Study of natural convection instabilities in closed cavities with non-isothermal walls

Sneha Rajeev Sondur

A dissertation

submitted in partial fulfillment of the

requirements for the degree of

Doctor of Philosophy

University of Washington

2020

Reading Committee:

Ann M. Mescher, Chair

John C. Kramlich

James J. Riley

Program Authorized to Offer Degree:

Mechanical Engineering

University of Washington

Abstract

Study of natural convection instabilities in closed cavities with non-isothermal walls

Sneha Rajeev Sondur

Chair of the Supervisory Committee:
Professor Ann M. Mescher
Mechanical Engineering

Natural convection inside closed cavities has been investigated extensively over the years owing to its application in several industrial processes. Amongst these, the most commonly studied configuration is that of natural convection in air-filled cavities with isothermal vertical walls maintained at different temperatures, which promote a unicellular base air-flow pattern. In the present work, natural convection of air in annular and rectangular cavities with non-isothermal walls supporting a bi-cellular base air-flow pattern is explored both experimentally and numerically. The experiments and numerical studies described in this work represent a significant departure from the more familiar problem of stability of unicellular convection in closed cavities and are therefore a novel addition to the body of literature available for natural convection systems.

Two experimental systems, one annular and one rectangular were constructed to study the stability of natural convection in tall, closed air-filled cavities with non-isothermal walls. The thermal boundary conditions applied on the cavities' vertical walls were such that the temperature of one vertical wall was higher than that of the opposing wall in the top portion of the cavity and lower than it in the bottom portion of the cavity. The Rayleigh number or buoyant potential of the bi-cellular (base) air-flow was successively increased/decreased over the course of several experiments, and the stability of flow inside these cavities was studied via monitoring of air temperatures. At low Rayleigh numbers, a steady flow regime was observed for both annular and rectangular cavities. With an increase in Rayleigh number transitions to 3D asymmetric periodic flows, quasi-periodic flows, intermittent flows, and chaotic flows were observed for the annular cavity. On the other hand, transitions from steady to 2D periodic flow, then to 3D periodic flow and finally to chaotic flow were observed for the rectangular cavity. The observed flow bifurcations, the resultant oscillation frequencies, phases, and amplitudes mapped relative to the wall thermal boundary conditions for both annular and rectangular experimental systems are presented in this work.

2D and 3D CFD models of the two experimental systems were developed using the commercial CFD code Simcenter StarCCM+ in order to numerically predict the experimentally observed unsteady natural convection flows. The experimentally imposed thermal boundary conditions were used as inputs for the CFD models. The accuracy of these CFD models in predicting experimental flows is discussed, and comparisons are made between the prediction capabilities of the 2D and 3D CFD models. Furthermore, the numerical simulations and frequency analysis of the experimental data are able to shed light on the primary instability modes causing

the transitions from steady to unsteady flows. These instability mechanisms responsible for bifurcations observed in the annular and rectangular cavity are discussed in detail.

This work also includes a benchmarking exercise for the commercial CFD code Simcenter StarCCM+ for problems of natural convection in cavities under both Boussinesq and non-Boussinesq temperature conditions. In addition, numerical simulations to understand the impact of non-Boussinesq temperature conditions and variable thermophysical fluid properties on the natural convection instabilities observed in closed, tall air-filled rectangular and annular cavities with isothermal walls are performed.

TABLE OF CONTENTS

LIST OF FIGURES

LIST OF TABLES

ACKNOWLEDGEMENTS

I would like to take this opportunity to thank my advisor Professor Ann M. Mescher for her support and guidance throughout my graduate school years. I am also deeply grateful to Professor James Riley for his lessons on turbulence modeling and fluid instabilities and also for guiding me on the numerical work for this project. I would like to thank Professor John Kramlich for the encouragement, guidance and support I received from him during my PhD journey. I would like to thank Professor Santosh Devasia and Professor Dana Dabiri for serving on my dissertation committee. Their advice and support throughout my dissertation has proved very helpful.

I would like to express my appreciation to the National Science Foundation (NSF) which was the principal funding source for this project. I would also like to acknowledge financial support of the Mechanical Engineering Department at University of Washington through teaching assistantships and fellowships. The numerical work done as part of this dissertation would have not been possible without the use of advanced computational, storage, and networking infrastructure provided by the HYAK supercomputer system at University of Washington. I would like to thank ME lab engineer Bill Kuykendall, my fellow graduate student Brek Meuris and undergraduate students Sari Barczay and Austin Park for their help with all the experimental work done as part of this project. I would also like to thank Wanwisa Kisalang for the unlimited support, encouragement and help she provided as my graduate academic advisor. Finally, I would like to thank my parents Rajeev Sondur and Anuradha Sondur, my brother Srinivas and all my friends here at UW and back at home in India for supporting me along this journey.

DEDICATION

To my family, friends and everyone who supported me throughout this long journey

Chapter 1

1 INTRODUCTION

1.1 Overview

Natural convection in closed cavities has been a subject of numerous studies over the years. One of the commonly investigated configurations is that of natural convection of air (Pr = 0.71) inside a closed cavity with two vertical isothermal walls maintained at two different temperatures ($T_1 > T_2$). The thermal boundary conditions at the walls promote a unicellular air-flow inside the cavity with fluid rising along the heated wall and falling along the cooled wall. Comparatively, there are very few experimental or numerical studies available in the literature for natural convection inside air-filled cavities with non-isothermally heated or cooled walls. In this dissertation, the stability of natural convection in annular and rectangular cavities with non-isothermal walls which support a bi-cellular base air-flow is explored both experimentally and numerically. The main motivation for studying flow stability in cavities with non-isothermal walls is its similarity to the polymer optical fiber (POF) drawing environment.

Chapter 1 discusses the motivation behind studying the present research problem and outlines the scope and objectives of this dissertation. The first part of Chapter 2 provides an overview of the POF drawing process and reviews literature on the effects of convective instabilities on POF drawing processes. A detailed review of the literature on natural convection instabilities in closed air-filled cavities is provided in the second part of Chapter 2. Chapter 3 discusses results from

numerical studies performed to benchmark the commercial CFD code Simcenter StarCCM+ for natural convection flows in closed cavities. The Simcenter StarCCM+ CFD code was used for all the numerical work performed as part of this dissertation. Chapters 4 and 5 provide details on numerical studies conducted to evaluate effects of non-Boussinesq thermal conditions on natural convection instabilities observed in tall, air-filled rectangular and annular cavities with isothermal vertical walls. Chapter 6 describes the experimental system constructed to study stability of natural convection in closed annular cavities with non-isothermal walls. Results from the experimental work and methods used for data analysis are presented in Chapter 7. Chapter 8 discusses results from 2D and 3D CFD modeling performed to predict and better understand the experimental observations of Chapter 7. Chapter 9 describes the construction of a rectangular cavity experimental system, which was used to study stability of natural convection in closed rectangular cavities with non-isothermal walls. Chapter 10 provides details of experimental results from the rectangular cavity system. Chapter 11 discusses the 2D and 3D CFD modeling work performed for prediction of the experimental observations of Chapter 10. Finally, concluding remarks are made in Chapter 12.

In this work, tall, closed, air-filled annular and rectangular cavities are constructed wherein the top portion of one vertical wall and bottom portion of the opposing vertical wall are actively heated. All the other surfaces of the cavity are passively cooled. Non-uniform temperature profiles develop on the two opposing vertical walls of the cavity due to a combination of conduction in the walls, convection and radiation heat transfer within the cavity. These thermal boundary conditions promote the existence of a base natural convection flow inside the cavity, which is comprised of two counter rotating convection cells, as shown in Fig.1.1.

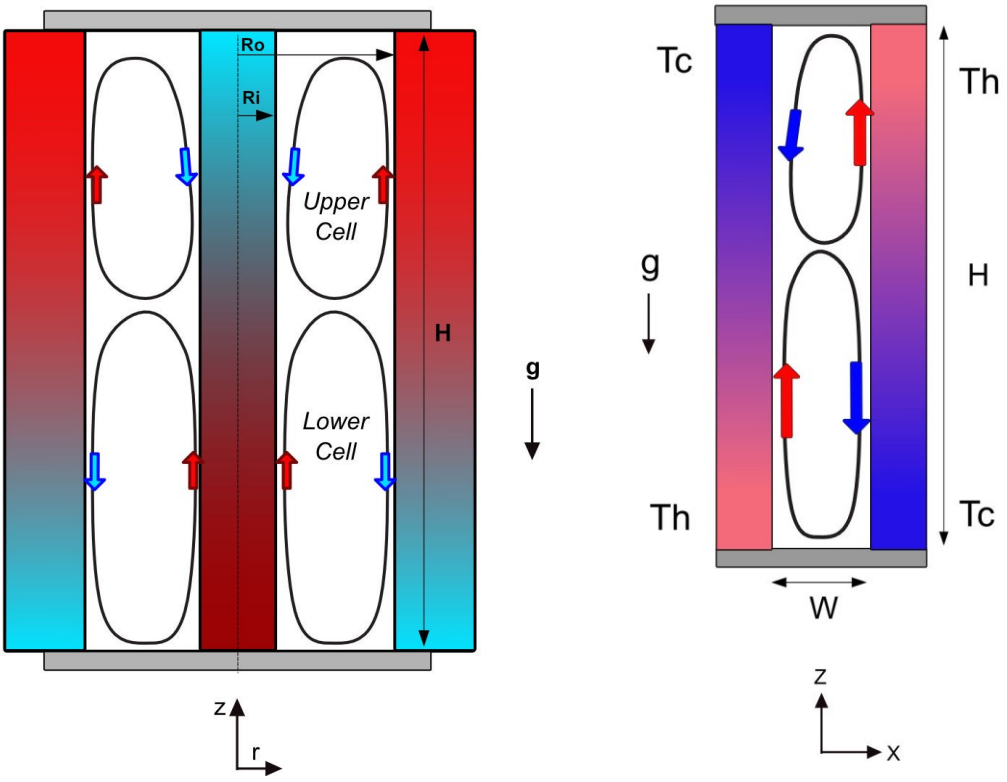

Figure 1.1: Closed annular cavity (left) and rectangular cavity (right) with thermal boundary conditions supporting bi-cellular natural convection.

The stability of this bi-cellular flow is studied experimentally by successively increasing/decreasing the buoyant potential of the flow. The sequence of bifurcations that cause the flow to transition from steady to unsteady oscillatory and ultimately to a chaotic flow are mapped relative to the wall thermal boundary conditions. The nature of the primary instability mode, whether 2D/axisymmetric or 3D/asymmetric, is also investigated. Finally, 2D and 3D CFD models of the annular and rectangular cavities are developed based on the experimentally imposed wall boundary conditions to numerically predict the transition from steady to unsteady natural convection and understand the instability mechanisms at play.

1.2 Motivation

The motivation behind studying the problem of bi-cellular natural convection in closed air-filled cavities with non-isothermal walls is its likeness to the air-flow pattern observed in a drawing process for polymer optical fiber (POF). Natural convection inside a closed furnace during the drawing of POF is known to become unsteady under certain operating conditions. This unsteady air-flow consists of oscillatory and chaotic regimes that result in cyclic and chaotic variations in the diameter of the drawn fiber. Convective flow oscillations in the gas phase during the POF drawing operation cause a time-varying heating/cooling of the necking polymer and fiber which leads to variations in the final fiber diameter. Even small temperature oscillations in the furnace can produce diameter variations greater than 1μm, which are sufficient in some applications to render the fiber unsuitable. To produce high quality uniform diameter fiber, steady air-flow inside the furnace is needed. Understanding the conditions under which steady, periodic and chaotic air flow conditions exist in an annular geometry can provide guidelines for efficient POF furnace design and control of the POF drawing operation. Previous investigations on the effects of convective oscillations in the gas phase on the diameter of POF have demonstrated that there is a direct correlation between the fundamental frequency of the oscillating gas phase and the variation in the fiber diameter produced. For certain specialized applications, a periodic variation in the fiber diameter is desirable. For such applications, knowledge of the thermal boundary conditions under which periodic flow is achieved and the oscillating frequency of the air flow, can be helpful in designing and manufacturing fiber with periodically varying diameter.

The non-uniform temperature profiles that develop on the furnace wall and polymer surface during the steady-state fiber drawing process support a base bi-cellular natural convection air-flow, which is comprised of two counter-rotating convection cells. Unsteady natural convection during

POF drawing processes is typically due to a loss of stability of this bi-cellular flow. In a steady state POF drawing system, the polymer diameter decreases from the preform diameter at the top to the fiber diameter at the bottom of the furnace. As a result, the air gap width formed between the furnace wall and the polymer surface increases monotonically along the draw direction. The radius ratio ($\eta = Ri/Ro$), as well as the aspect ratio of the cavity, is thus different at each Z-location along the height of the furnace. The geometrical parameters of the cavity, especially the aspect ratio (A) and the radius ratio (η) play an important role in the stability of the internal natural convection [26-34]. The drawing of POF in a furnace is a highly coupled system where the temperatures of the polymer preform and fiber depend on the natural convection of air within the furnace as well as on the radiative exchange between enclosure surfaces, including the changing free surface of the polymer. In the highly coupled POF system, it is difficult to precisely separate the radius ratio effects, and aspect ratio effects from the effects of increasing the Rayleigh number (buoyant potential) of the flow since all these parameters are varying in the system at the same time. Therefore, it is of interest to experimentally study this kind of bi-cellular natural convection in a simple annular or rectangular geometry where the radius ratio and aspect ratio remain fixed, allowing examination of the flow stability merely by increasing / decreasing the Rayleigh number.

1.3 Scope and Objectives

The unsteady flow observed during POF drawing was always 3D asymmetric [1]. Stability studies by McFadden et al. [33] and Prud'homme and Le Quéré [34] predict that natural convection in a tall, air-filled annular cavity loses stability to 3D asymmetric modes if the radius ratio of the cavity is less than $\eta < 0.4$. Following the conclusions of McFadden et al. [33], it is more probable to find 2D axisymmetric modes in annular cavities with high radius ratios ($\eta > 0.4$) or in rectangular

cavities since a long rectangular cavity can be thought of as an annular cavity in the limiting case of radius ratio $\eta \rightarrow 1$. Therefore, in this work, experimental investigations to examine the stability of natural convection with bi-cellular base flow pattern in cavities with non-isothermal walls were undertaken for two geometries:

1. Closed air-filled annular cavity of radius ratio $\eta = 0.5$ and aspect ratio A = 25.2.

2. Closed air-filled rectangular cavity of aspect ratio A = 10.

For each of the experiments in the annular and rectangular cavities, the buoyant potential of the natural convection flow was successively increased and the transition from steady air flow to oscillatory and chaotic flows was studied via measurement of air temperatures inside the cavity. Non-uniform thermal boundary conditions imposed on the walls of the annular and rectangular cavities to induce the bi-cellular convection flow were recorded for each experiment. These thermal boundary conditions were then used to develop 2D and 3D computational fluid dynamics (CFD) models of the experimental systems using the commercial finite volume code Simcenter StarCCM+. Findings from these experimental investigations present a map of the numerous flow bifurcations that can be observed in annular and rectangular cavity natural convection systems as the Rayleigh number of the flow is varied. Numerical predictions along with frequency analysis of the experimental data give insights on the instability mechanisms that cause flow transitions from steady to oscillatory flows.

Most of the studies available in the literature for natural convection inside closed cavities are for conditions where the temperature difference between the walls of the cavity is small, and the Boussinesq approximation is valid. However, for applications such as polymer fiber drawing, the typical temperature differences inside the furnace are much higher, and the assumptions of small

temperature differences and constant thermophysical properties under the Boussinesq approximation do not hold true. Further, stability analyses [40] and recent experimental studies [44,45] have shown that for natural convection in rectangular cavities, the nature of the 'cat's eye' instability varies significantly under non-Boussinesq conditions due to the high temperature differences and pronounced effects of variable thermophysical properties of fluid under these conditions. To my knowledge, no similar study exists for the annular cavity problem. Therefore, an attempt has also been made to quantify the effect of non-Boussinesq thermal conditions on the heat transfer and natural convection flow dynamics inside a tall, air-filled annular cavity with heated and cooled isothermal walls.

To summarize, the objectives of this dissertation are as follows:

1. To experimentally study the stability of base bi-cellular natural convection in tall, closed air-filled annular and rectangular cavities with non-isothermal walls.

2. To study the *radius ratio effect:* Determine the nature of oscillatory flow (whether 2D or 3D) observed in annular and rectangular cavity experiments.

3. To develop 2D and 3D computational models of the experimental systems using the commercial CFD code, Simcenter StarCCM+, and to numerically predict transitions from steady to unsteady natural convection flows.

4. To numerically study the effect of non-Boussinesq thermal conditions and temperature dependent thermophysical properties of air on the stability of unicellular, natural convection in an air-filled annular cavity with heated and cooled isothermal walls.

Chapter 2

2 LITERATURE REVIEW

In the first part of this chapter, an overview of the POF drawing process and literature pertaining to the effects of convective instabilities on the polymer fiber drawing process is provided. The remaining part of the chapter is dedicated to reviewing results from the literature on natural convection instabilities in closed air-filled cavities. First, previous experimental and numerical studies for natural convection flows in closed cavities with isothermally heated/cooled walls are reviewed. This is the most commonly investigated problem and provides the groundwork to study the more complex problem of natural convection in cavities with non-isothermal walls. Finally, the few studies that look at natural convection inside cavities with walls that are non-isothermally heated/cooled are reviewed.

2.1 Polymer Optical Fiber (POF) Drawing Process

The manufacturing of polymer optical fiber (POF) involves heating of a prefabricated polymer preform of diameter ‘D’ in a cylindrical furnace and then drawing the preform into fiber in a draw tower by applying a draw force. The polymer preform can have a radial refractive index profile which is used for manufacturing solid core multimode POF, or it can be composed of a pattern of holes which is used for manufacturing microstructured POF also known as hollow core photonic crystal fiber. A schematic of the drawing process is shown in Fig. 2.1.

Heating is applied to the upper part of the cylindrical furnace which results in a vertically non-uniform temperature profile on the interior furnace wall. The preform is fed into the furnace at a low feed velocity 'V_p' and is heated inside the furnace via natural convection and thermal radiation.

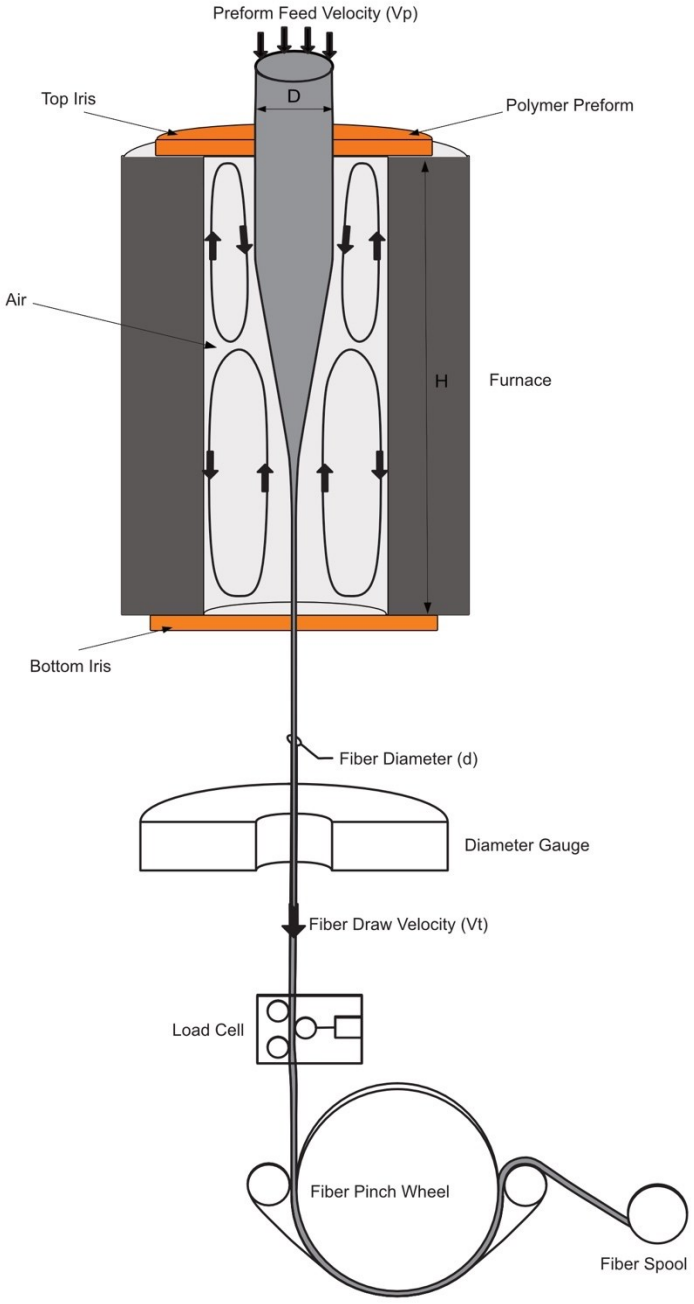

Figure 2.1: POF drawing system.

Unlike the glass fiber drawing process where radiation is the dominant mode of heat transfer, natural convection contributes about half of the total heat transfer to the preform. When the preform is sufficiently heated above its glass transition temperature, its viscosity drops drastically. The preform then begins to neck due to the applied tension force from the pinch wheel and exits the furnace as a fiber of diameter 'd' at a draw speed of 'V_t.' A diameter gauge located below the furnace measures in real time the diameter of the exiting fiber and a force gauge measures the tension acting on the fiber. Finally, the fiber is spooled after passing through a pinch wheel.

One of the major causes of optical losses in POF is fluctuations in fiber diameter, which occur during the manufacturing of POF in the furnace. Variations in fiber diameter lead to fiber misalignment during coupling of POF and additional losses along the length, causing significant losses during data transmission through the fiber. Diameter variations of more than 1 μm lead to high optical losses making the POF unusable for long distance data communication or commercial applications. Further, non-uniformity in the cross-section of the fiber can lead to a phenomenon known as birefringence, which affects data transmission at high frequencies and limits the bandwidth of data transmission [1].

Reeve [1] experimentally studied the drawing process of POF in a furnace and found that the transient drawing operation is highly sensitive to thermal perturbations in the furnace. He observed that under certain furnace operating conditions, the steady natural convection flow inside the closed furnace would become unsteady, leading to time-varying heating of the preform. The unsteady air-flow consisted of oscillatory and chaotic regimes which resulted in cyclic and chaotic variations in the diameter of the drawn fiber which were as high as $\pm$ 15 μm. This unsteady air-flow was always 3D asymmetric in nature. Figure 2.2 shows the air temperature measured at a

point inside the furnace during the drawing operation and the corresponding diameter of fiber manufactured during the same time period. Reeve et al. [1, 2] concluded that these thermal perturbations might be one of the primary causes of diameter variations in POF manufacturing, limiting its use for high bandwidth data transmission over long distances.

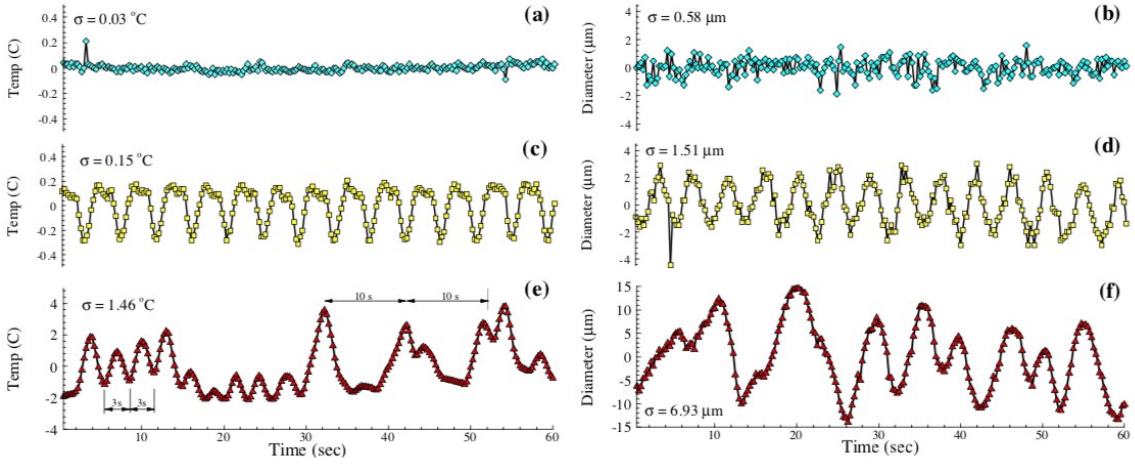

Figure 2.2: Excursion of the air temperature history (left) and fiber diameter history (right) from the sample mean, illustrating: (a) steady, (b) oscillatory, and (c) chaotic natural convection flow. **Note**: Different scales on the y-axis, Adapted from [2].

Other studies which looked at air-flow patterns in optical fiber drawing systems came to similar conclusions. Forest et al. [3] numerically studied the response of a stable fiber drawing system to unsteady disturbances in the drawing environment using a quasi-1D system of equations. They concluded that thermal fluctuations or fluctuations in the heat transfer rates to the fiber were the dominant source of diameter fluctuations, whereas mechanical effects like take-up rates, feed-in rates were less significant. Papamichael et al. [4] experimentally studied the natural convection flow in a fiber drawing environment and reported that natural convection induced disturbances in the furnace could affect the final diameter of fiber produced. Law et al. [5] conducted an extensive

experimental study to look at the causes of diameter variations in optical fibers based on real-time measurements made during fiber drawing. They concluded that the gas-flow instabilities within the furnace impact the local heat transfer to and from the neck-down region of the preform causing variations in the fiber diameter. They also suggested that the route to reducing variation in fiber diameter is to limit the extent to which short-time scale variations in the temperature and flow fields within the furnace interact with the preform neck-down region.

The drawing of POF in a furnace is a highly coupled system where the temperature profile of the polymer preform and fiber depends on the natural convection of air within the furnace as well as on the radiative exchange between the enclosure surfaces. Reeve et al. [6] numerically solved the steady-state axisymmetric conjugate problem of POF drawing in a cylindrical heated furnace. They predicted the final steady-state necked profile of the preform as well as the steady natural convection flow in the furnace. These numerical predictions of the POF drawing operation have shown that the convective flow inside the furnace is comprised of two counter-rotating cells [6] as shown in Fig. 2.3(a). The temperature difference between the hot upper furnace wall and the relatively cooler adjacent preform surface promotes the formation of an upper cell while the hotter, thinner necked preform surface and the relatively cooler adjacent lower furnace wall promotes the formation of a lower cell. Figure 2.3(b) shows a schematic of the thermal boundary conditions of the furnace wall and the preform surface, which support a base bi-cellular flow pattern. Unsteady natural convection phenomenon observed during POF drawing results from interplay between these two cells [1, 6].

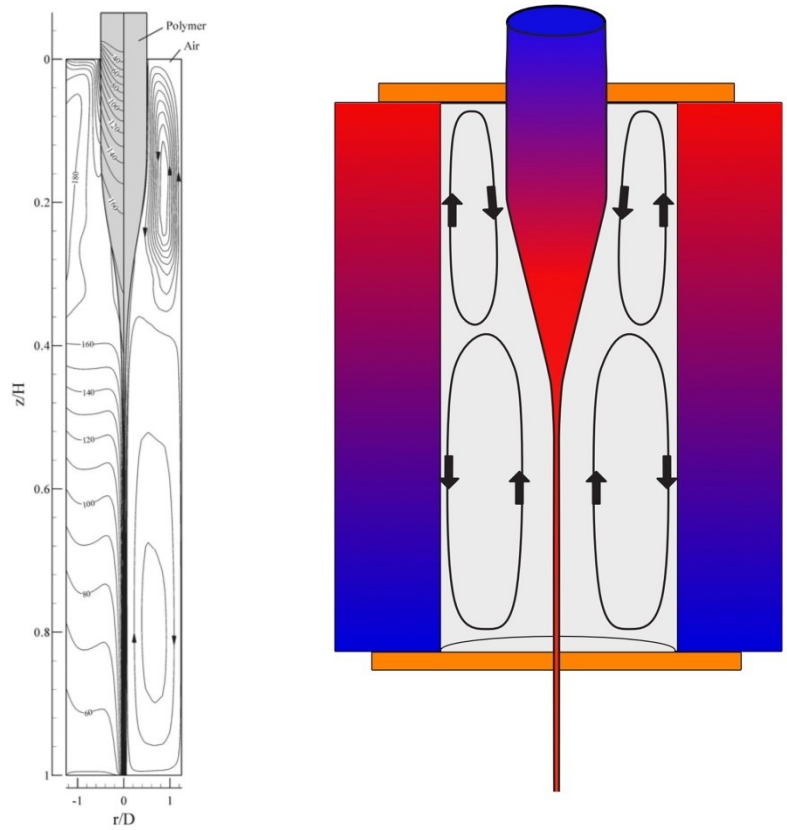

(a) (b)

Figure 2.3: (a) Steady-state natural convection flow inside the furnace, showing the presence of two counter-rotating cells as numerically predicted by Reeve et al. [6]; (b) Closed furnace cavity with thermal boundary conditions supporting bi-cellular air-flow.

2.2 Natural Convection in Closed Cavities

In the next few sections, several studies on natural convection instabilities observed in closed cavities are reviewed, and the geometrical conventions and the non-dimensional parameters relevant to natural convection in closed geometries are discussed.

2.2.1 Tall Rectangular Cavities with Isothermal Walls at Different Temperatures

The majority of literature available on natural convection instabilities in closed cavities is for the problem of natural convection of a fluid in a closed rectangular cavity with the two vertical walls of the cavity maintained at two different temperatures, both isothermal. The horizontal walls of the cavity are either adiabatic or conducting. This configuration is frequently referred to as the *differentially heated cavity with isothermal walls* and has received much attention over the years owing to its application in several industrial problems. Numerous experimental [8, 9, 10, 11, 12, 13], numerical [14, 15, 16, 17, 18, 19, 20], and analytical studies [21, 28, 23, 24, 25] for this problem have revealed the nature of heat transport and flow structure inside the cavity. We know from these studies that natural convection in a closed rectangular cavity is dependent on the Rayleigh number of the flow, aspect ratio of the cavity, and Prandtl number of the fluid enclosed. These parameters for a closed cavity height 'H' and air-gap width 'W' are defined as follows:

$$\text{Rayleigh number} = \text{Ra} = \frac{g\,\beta\,\Delta T\,L_c^3}{\upsilon\,\alpha} \tag{2.1}$$

$$\text{Prandtl number} = \text{Pr} = \frac{\upsilon}{\alpha} \tag{2.2}$$

$$\text{Aspect Ratio} = \text{A} = \frac{H}{W} \tag{2.3}$$

where β is the gas thermal expansion coefficient, υ is the kinematic viscosity, α is the thermal diffusivity, ΔT is the temperature difference driving the flow, g is local gravitational acceleration, and L_c is a characteristic length. Characteristic lengths L_c most commonly used in literature are either the air-gap width W or the height of the cavity H. The Grashoff number (Gr) is sometimes used in place of Rayleigh number (Ra) to describe flow bifurcations. The relationship between the Rayleigh number and Grashoff number is given by:

$$\text{Grashoff number} = \text{Gr} = \frac{g\,\beta\,\Delta T\,L_c^3}{\upsilon^2} = \frac{\text{Ra}}{\text{Pr}} \tag{2.4}$$

For natural convection inside a closed rectangular cavity with two vertical isothermal walls maintained at two different temperatures, the general flow structure is comprised of fluid rising along the heated wall, turning at the ends of the cavity and falling along the cooled wall giving rise to a unicellular flow pattern inside the cavity. At low Rayleigh numbers in tall cavities, the effects of the end regions are confined to a limited length, and parallel flow exists in the majority of the cavity. Here, the heat transfer occurs mainly by conduction, and hence, this regime is called the 'conduction regime.' This regime is characterized by isotherms parallel to the vertical walls of the cavity and a horizontal temperature gradient in the central part of the cavity. At high Rayleigh numbers, convection becomes the dominant mode of heat transfer in the cavity, and this regime is called the convection regime or the 'boundary layer regime.' The boundary layer regime is characterized by the presence of thin boundary layers along the cavity wall and a nearly stagnant core region. The horizontal temperature gradient exists only within the boundary layer while a vertical thermal stratification develops in the central region of the cavity. The internal flow at intermediate Rayleigh numbers is said to be in the 'transition regime.'

In tall cavities, the conduction regime is prone to an instability, the nature of which depends on the Prandtl number of the enclosed fluid in the cavity. Korpela et al. [28] found that the instability of the conduction regime takes the form of multiple stationary cells for Pr < 12.5 and the form of traveling waves for Pr > 12.5. As the aspect ratio of the cavity decreases or the Rayleigh number increases, a finite vertical temperature stratification develops in the cavity. Bergholz [23] used linear stability theory to study the effect of temperature stratification on the conduction regime instability for different Pr number fluids. He found that for low Pr numbers if the

stratification is sufficiently high, then there is a switch in the nature of the instability from multiple stationary cells to traveling waves and the opposite is true for high Pr number fluids. Thus, for low Pr number fluids (like air) in tall cavities (low vertical stratification) or high Pr number fluids (like silicon oil) in short cavities (high vertical stratification), the instability takes the form of *'multiple stationary convection cells.'* These multiple stationary cells resemble a cat's eye pattern, and so this instability of the conduction regime is often referred to as the *stationary 'cat's eye' instability*. The Rayleigh number or Grashoff number of the flow corresponding to the transition from unicellular flow to a multicellular cat's eye pattern marks the first bifurcation of the flow and is referred to as the critical Rayleigh number or the critical Grashoff number. The wavenumber of the cat's eye instability calculated based on the wavelength λ of the instability is given by:

$$K_w = \frac{2\pi L_c}{\lambda} \tag{2.5}$$

where λ, the wavelength of the instability, is equal to the length of the cells of the cat's eye pattern.

Elder [8] was the first to observe the stationary cat's eye pattern experimentally in high Pr number fluids while conducting experiments in differentially heated cavities filled with silicon oil (Pr = 1000). He observed that above a critical value of Rayleigh number, a secondary flow comprised of a regular cellular pattern becomes superimposed on the basic unicellular flow to form the 'cat's eye' instability. At even higher Rayleigh numbers, he observed that tertiary cells were generated between the counter-rotating secondary cells. For an infinitely tall cavity, the critical Grashoff number based on the cavity width (Lc = W) has been reported as Gr_{cr} = 7880 [9] which corresponds to a critical Rayleigh number of Ra_{cr} = 5595 for air-filled cavities (Pr = 0.71). The critical wavenumber is reported as 2.65. Vest and Arpaci [9] studied the stability of natural convection in vertical cavities analytically and verified their results with experimental

observations. They experimentally observed the 'cat's eye' instability in a tall air-filled (Pr = 0.71) cavity of aspect ratio A = 33 using smoke pattern visualizations, shown in Fig. 2.4(b). They reported a critical Grashoff number of 8700 $\pm$ 10 and a critical wavenumber of 2.74 for their experimental observations of stationary multicellular flow. Lee and Korpela [14] numerically studied multicellular flow in vertical slots and demonstrated the dependence of heat transfer on aspect ratio. Figure 2.4(a) shows the transition from steady unicellular flow to a stationary multicellular flow in an air-filled cavity of aspect ratio A = 15 as the Grashoff number is increased from 5000 to 15000 as predicted by Lee and Korpela [14].

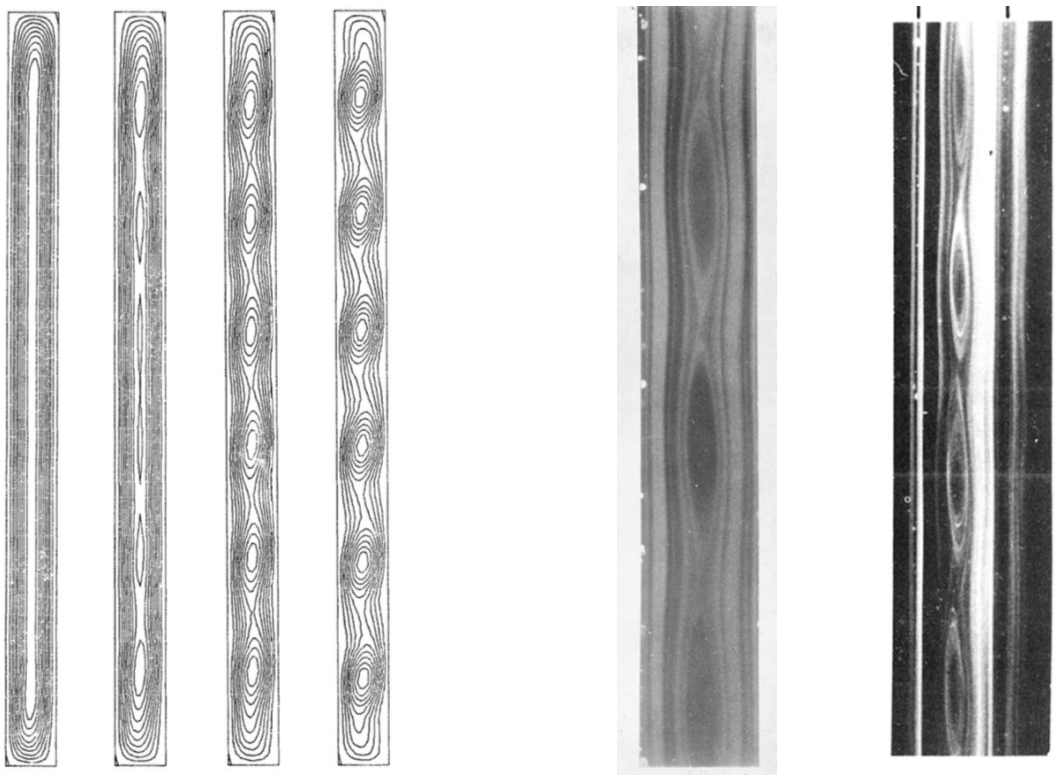

(a) (b) (c)

Figure 2.4: (a) Streamlines of flow in a rectangular cavity of A = 15 depicting the transition from unicellular to multicellular flows for a fluid of Pr = 0.71 as predicted numerically by Lee and Korpela [14] at Gr = 5000, 8000, 10000, 15000; (b) Smoke pattern photograph of stationary multicellular flow in an air-filled rectangular cavity of A = 33 at Gr = 9500, Pr = 0.71 as observed by Vest and Arpaci [9]; (c) Smoke pattern photograph of stationary multicellular flow in an air-filled cavity of A = 33 at Gr = 9000, Pr =0.71 as observed by Korpela [10].

At even higher Rayleigh numbers a transition back to the unicellular flow pattern from the multicellular cat's eye pattern followed by a second transition to unsteady flow has been observed by some researchers. Le Quéré [16] conducted a numerical investigation of the cat's eye instability in a tall air-filled cavity of aspect ratio A = 16 and predicted a reverse transition to unicellular flow from multicellular flow at a Rayleigh number of Ra = 40,000. In a similar numerical study for air-filled cavities, Wakitani [17] investigated the effect of initial conditions on the different flow transitions and predicted the presence of multiple solutions at higher Rayleigh numbers near the reverse transition. They reported a value of $Ra = 4 \times 10^5$ for a second transition from steady to unsteady flow. Other similar numerical [18, 19, 20] and analytical investigations [24, 25] in air-filled cavities focused on heat transfer and on mapping the sequence of flow bifurcations observed for various combinations of aspect ratios and Rayleigh number ranges.

To summarize the results from these numerous studies for tall air-filled (Pr = 0.71) differentially heated rectangular cavities with isothermal walls: the air-flow inside the cavity at low Rayleigh numbers is unicellular and the majority of the heat transfer occurs by conduction. On increasing the Rayleigh number, the unicellular flow becomes unstable to a 'cat's eye' instability consisting of multiple stationary cells. This instability is highly sensitive to the aspect ratio of the cavity and the Rayleigh number. With further increase in Rayleigh number, a reverse transition to steady flow is observed followed by a second transition to unsteady flow. This second transition exhibits hysteresis and is accompanied by the presence of multiple solutions. Figure 2.5 shows the summary of the different flow regimes for natural convection in tall, air-filled, closed rectangular cavities based on the Rayleigh number (Ra) and Aspect ratio (A) adapted from the work of [19] and [41].

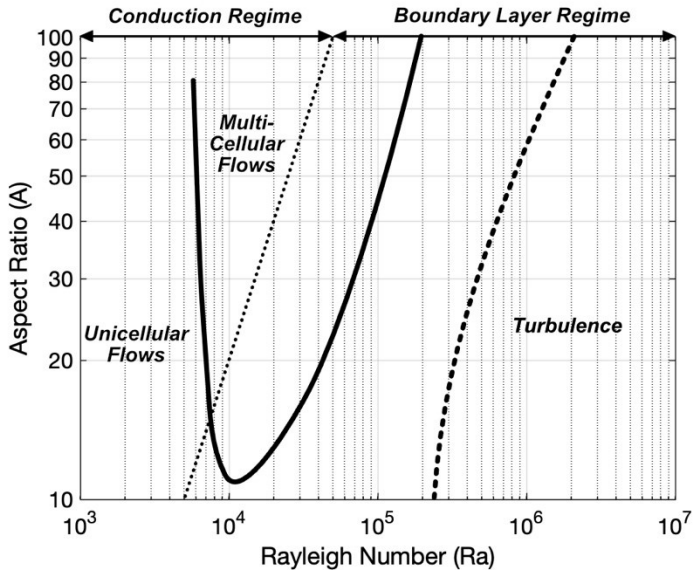

Figure 2.5: Summary of the different flow regimes for natural convection flow in tall, air-filled, closed rectangular cavities based on the Rayleigh number and Aspect ratio adapted from the work of [19] and [41].

Although majority of numerical studies for this problem have assumed the flow to be 2D, recent experimental investigation by Wright et al. [44] in an air-filled rectangular cavity of aspect ratio A = 40.8 has found that the 2D flow rapidly evolves into 3D flow at a Rayleigh number of Ra ≈ 10,000. Further, they have observed that the multicellular cat's eye pattern is not stationary as predicted by previous stability and numerical analysis but moves downwards with a constant velocity. A similar observation of downward drifting cells was made by Lartigue et al. [45] in their experimental investigations. The reason for this discrepancy between the previous studies on the cat's eye instability and the more recent experimental studies is due to the effect of variable thermophysical properties of the fluid and non-Boussinesq thermal conditions on the nature of the cat's eye instability. This *non-Boussinesq effect* is discussed in further detail in Chapters 3, 4 and 5 of this dissertation.

2.2.2 Short Rectangular Cavities with Isothermal Walls at Different Temperatures

Multiple investigators [70-72] reported on the transitions to unsteady flow inside short rectangular ($A < 8$) and square ($A = 1$) cavities. Kishor et al. [70] explored natural convection of air inside a closed rectangular cavity of aspect ratio $A = 3$ using Mach Zehnder interferometry, smoke pattern visualizations and numerical simulations. They observed steady flow at Ra = 9.7 x 10^5; upon increasing the Rayleigh number, they found the onset of periodic flow at Ra = 1.8 x 10^6. This periodic air-flow showed the presence of two dominant frequencies. Paolucci and Chenoweth [71] numerically explored natural convection of air in shorter cavities of aspect ratios $A = 0.5$ to 5. For cavities of aspect ratios $0.5 < A < 3$ they found that steady flow first transitions to a periodic flow showing one dominant frequency, then to quasi-periodic flow showing the presence of two frequencies, which then finally transitions to chaotic flow.

Several authors [72, 85-89] have looked at the different instability mechanisms that are responsible for transitions from steady to oscillatory flow. The three main instability mechanisms frequently found in closed air-filled cavities are the Rayleigh Bernard instability mechanism, the hydraulic jump mechanism and the Tollmien-Schlichting instability mechanism.

The Rayleigh Bernard instability mechanism is observed in the inviscid stratified core fluid region of the closed cavities. The flow is stable if the density of the fluid decreases with increasing height in the cavity and is unstable if density increases with height. Oscillatory flows occur because of internal gravity waves, and the frequency of oscillation is related to the $\mathrm{Brunt-Väisälä}$ frequency, $\frac{\sqrt{g\beta\Delta TH}}{H}$.

A hydraulic jump mechanism can occur in the corner of a closed cavity where the interaction between a high-speed horizontal fluid layer and a lower speed fluid layer takes place. If the change in speeds is too strong (large hydraulic jump), the fluid flow after the jump becomes unstable, and energy is dissipated via an unsteady oscillating wave pattern.

The Tollmien-Schlichting instability mechanism occurs in the natural convection boundary layer of a heated, vertical isothermal (semi-infinite) plate. Steady flows in tall closed cavities with heated/cooled walls often become unsteady via this mechanism. The frequency of unsteady oscillations caused by this instability mechanism is related to the viscous frequency $\left(\frac{(g\,\beta\,\Delta T\,)^{2/3}}{\upsilon^{1/3}}\right)$.

In their numerical studies, Henkes and Hoogendoorn [72] investigated natural convection of air in a square cavity with heated and cooled vertical (both isothermal) walls and either conducting or adiabatic (both non-isothermal) horizontal walls. For the case of conducting horizontal walls, the steady air-flow became unsteady at a critical Rayleigh number of 2 x 10^6. Periodic air-flow showed the presence of a single frequency and the instability mechanism was related to the Rayleigh-Bernard instability. For the second case of adiabatic horizontal walls, the onset of periodic flow happened at a much higher Rayleigh number of 2 x 10^8. The periodic air-flow then showed the presence of two frequencies and the instability mechanism was related to the Tollmien-Schlichting instability.

2.2.3 Annular Cavities with Isothermal Walls at Different Temperatures

The nature of natural convection inside a differentially heated annular cavity is similar to that of a rectangular cavity. However, the flow and heat transfer inside the cavity now depends on the curvature of the cavity in addition to the aspect ratio (A), Prandtl number (Pr), and Rayleigh

number (Ra). The curvature of the cavity is quantified in terms of the radius ratio, which is the ratio of the radius of the inner cylinder to outer cylinder (η).

$$\text{Radius ratio} = \eta = \frac{R_i}{R_o} \tag{2.6}$$

One of the first set of studies on natural convection in an annular cavity with vertical isothermal walls maintained at two different temperatures was done by de Vahl Davis and Thomas [26, 27]. They used a finite difference method to solve the problem for a wide range of parameters and provided empirical Nusselt number correlations for a range of Ra, A and η values based on their numerical results. They concluded that the heat transfer (Nusselt number) within the cavity was strongly affected by the curvature of the cavity.

Choi and Korpela [22] studied the stability of natural convection in a tall annulus with an isothermal, heated inner cylinder and an isothermal, cooled outer cylinder. They used linear stability analysis, considering only axisymmetric disturbances for fluids of Pr number ranging from Pr = 0.71 to 1000. They observed that for low Pr number fluids, the flow becomes unstable to an axisymmetric instability that is shear driven and sustained by energy transferred to the disturbance from the base flow. This shear-driven instability has been observed in experimental [22] and numerical studies [29, 30, 31] to take the form of a multicellular cat's eye pattern which drifts upwards in the cavity, opposite to the direction of gravitational force. The upward drift speed of the cat's eye instability increases with an increase in curvature. Further, increased curvature (or decrease in radius ratio) adds stability to the flow, thereby increasing the value of the critical Rayleigh number corresponding to the transition from steady to unsteady flow. Choi and Korpela [22] validated their stability analysis results by comparison with experiments in an air-filled

annular cavity of radius ratio $\eta = 0.68$ and aspect ratio A = 38.6. They were able to experimentally observe the predicted axisymmetric multicellular cat's eye pattern drifting upwards in the cavity using smoke visualizations, shown in Fig. 2.6(a) and 2.6(b). Lee, Korpela, and Horne [29] examined the stability and structure of natural convection of low Pr number fluids in a tall annulus using finite difference method. They concluded that for air-filled annular cavities of radius ratio $\eta = 0.8$, the minimum aspect ratio to observe unsteady multicellular flows is A = 13. This minimum aspect ratio value tends to be higher as the cavity radius ratio decreases.

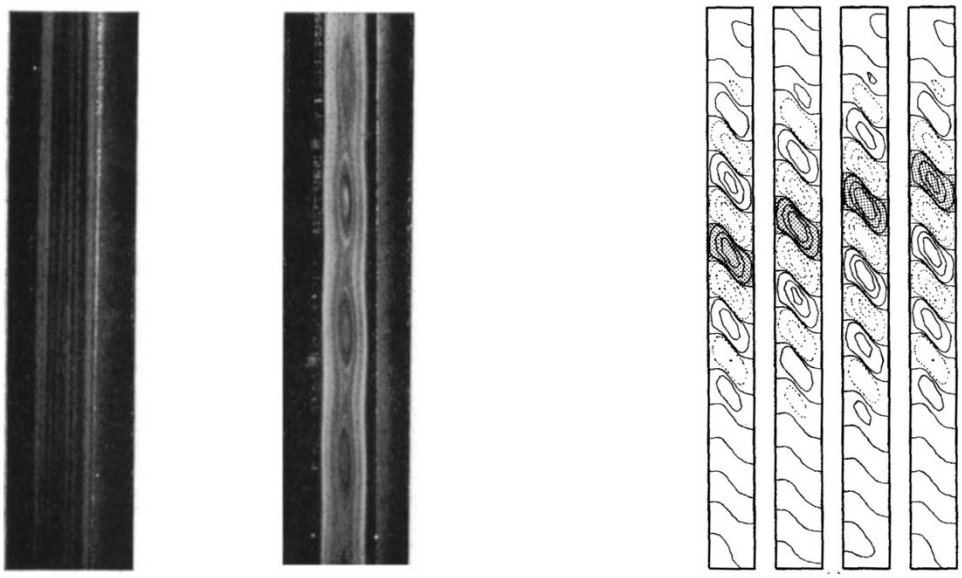

Figure 2.6: (a) Smoke pattern photograph of steady unicellular flow at Gr = 7400; (b) Unsteady multicellular cat's eye pattern drifting upwards at Gr = 9100 in an air-filled annular cavity of A = 38.6 and $\eta = 0.68$ observed by Choi and Korpela [22]; (c) Time sequence of fluctuating temperature field in an air-filled annular cavity of aspect ratio A = 16 and radius ratio $\eta = 0.8$ depicting the upward drifting cells as predicted by Le Quéré and Pécheux [30] at Ra = 7000.

Le Quéré and Pécheux [30] numerically studied the behavior of natural convection of air inside a differentially heated annular cavity of aspect ratio A = 16 and radius ratio $\eta = 0.8$ with an

isothermal heated inner cylinder and isothermal cooled outer cylinder; they solved the axisymmetric Navier-Stokes equations with the Boussinesq approximation. The main aim of their work was to study the bifurcations that occur when the Rayleigh number is varied gradually. The first bifurcation they observed was a transition from steady unicellular flow in the conduction regime to an unsteady multicellular cat's eye instability comprised of cells drifting upward in the cavity. This bifurcation was found to be a supercritical Hopf bifurcation, and the corresponding critical Rayleigh number reported was $Ra_c = 6850$. The unsteady multicellular convection they predicted is shown in Fig. 2.6(c). They found that the upward drifting cells move with an almost constant velocity, which decreases as the Rayleigh number is increased. With further increase in Rayleigh number, a period doubling bifurcation was observed at Ra = 12,000. At even higher Rayleigh number they found a reverse transition to steady flow through a series of subcritical bifurcations with hysteresis. They also considered a configuration with a heated outer cylinder and a cooled inner cylinder, predicting that the cells would drift downwards instead of upwards. For even taller cavities of aspect ratio A = 20 and 25, Le Quéré and Pécheux [30] found that the unsteady cat's eye instability occurred at a lower critical Rayleigh number than that predicted for the A = 16 cavity, indicating that an increase in aspect ratio has a destabilizing effect on the flow.

Pécheux, Le Quéré and Abcha [31] built on the results of Le Quéré and Pécheux [30] by studying the effects of curvature on the bifurcations in cavities of aspect ratio A = 16, at several different radius ratios. The first transition of the conduction regime from steady flow to unsteady periodic flow (drifting cat's eye pattern) was always a supercritical Hopf bifurcation for all the radius ratios they investigated. As the Rayleigh number was further increased, they predicted complex flow behaviors like quasiperiodic flows, intermittency, chaotic flows, reverse transitions to steady flows, multiple solutions and hysteresis depending on the radius ratio (η) of the cavity.

The main conclusion of their study was that "*curvature effects can dramatically influence the dynamics of the solutions resulting from the instability of the conduction regime in a tall differentially heated annulus".* Weng and Chu [32] investigated the combined natural convection and radiation in a differentially heated annular cavity and concluded that the inclusion of radiation effects makes the flow more stable and uniform.

McFadden et al. [33] added to the work of Choi and Korpela [22] by studying the stability of Pr = 0.71 (air) and Pr = 3.5 (water) subject to both 2D axisymmetric and 3D asymmetric perturbations. In air, they found that for radius ratios less than $\eta < 0.44$, the least stable disturbance is 3D asymmetric shear-driven, but for radius ratios greater than $\eta > 0.44$, the least stable disturbance is 2D axisymmetric shear-driven. Similar conclusions were reached by Prud'homme and Le Quéré [34] in their investigation of the stability of natural convection in a tall annular cavity with vertical thermal stratification. For low Pr number fluids, they found that the disturbances were always shear-driven and that 3D asymmetric disturbances occurred only when the radius radio was smaller than $\eta < 0.4$.

Based on the conclusions of McFadden et al. [33], studies in low radius ratio cavities filled with low Prandtl number fluids like air have been avoided by many researchers because of the likelihood of the instability being 3D asymmetric. However, 3D asymmetric instabilities have been observed in experimental studies with moderate to high Prandtl number fluids [35, 36, 37]. Weidman and Mehrdadtehranfar [35] conducted experiments with moderately high Prandtl number (Pr = 20 to 110) fluids in a differentially heated annular cavity of aspect ratio A = 64 and radius ratio $\eta = 0.62$. They observed that the instability consisted of waves traveling in opposite directions along opposing cylindrical walls. The instabilities were axisymmetric at the onset but

rapidly became asymmetric at higher Rayleigh numbers. Asymmetric instabilities were also observed by Fang et al. [36] in a vertical melt annulus between a coaxial heating wire and surrounding crystal-melt interface of succinonitrile (SCN). Recently, Lepiller et al. [37] experimentally investigated the bifurcations of the conduction regime in a differentially heated water-filled annular cavity of aspect ratio A = 114 and radius ratio $\eta = 0.8$. They observed that the flow first becomes unstable to axisymmetric upward moving rolls located in the central part of the cavity through a supercritical Hopf bifurcation. However, at slightly higher Rayleigh numbers than the critical state, the flow started to exhibit spatial-temporal defects indicating the onset of 3D asymmetric flow. Figures 2.7(a) and 2.7(b) show visualizations of the asymmetric flow patterns observed by Fang et al. [36] and Lepiller et al. [37] in moderate Prandtl number fluids.

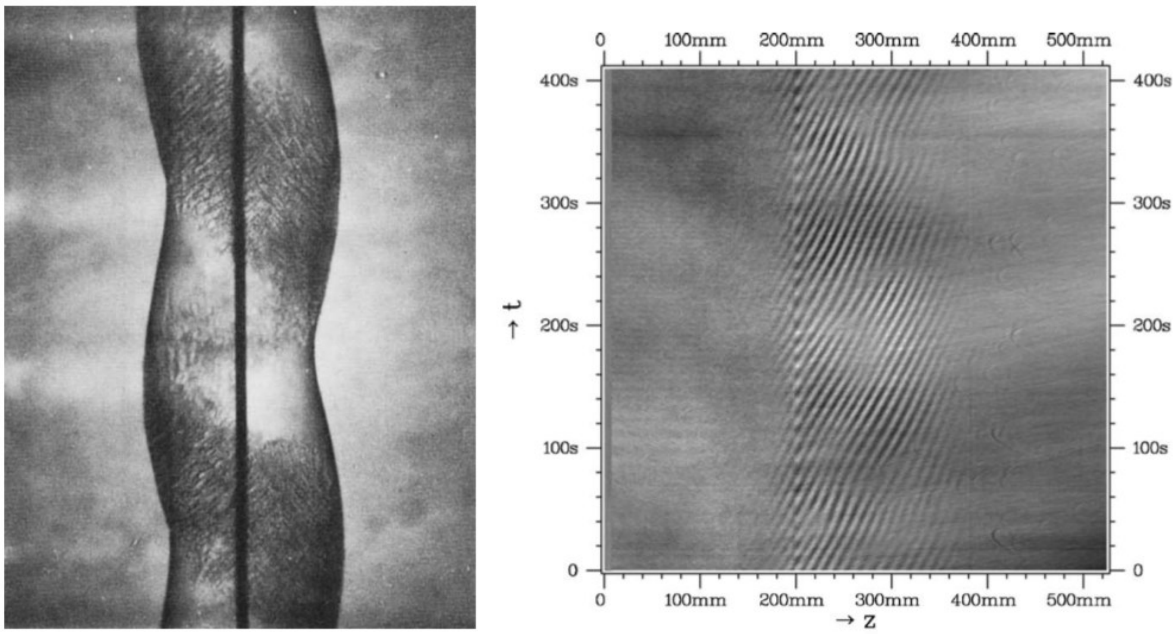

(a) (b)

Figure 2.7: (a) Helical (Asymmetric) crystal-melt interface observed in the experiments of Fang et al. [36]; (b) Space-time diagrams for Pr = 6.5, Gr = 7675 showing upward moving rolls with spatial-temporal defects in the experiments conducted by Lepiller et al. [37].

To my knowledge, there have been no experimental or numerical studies investigating the 3D asymmetric instability that is expected for low Pr number fluids like air in tall annular cavities with radius ratios $\eta \leq 0.44$. Most experimental studies of air-filled annular cavities have been for $\eta = 0.6$ or higher. The majority of previous numerical studies were also typically restricted to solving the axisymmetric Navier-Stokes equations. Natural convection flows in air-filled annular cavities of moderate to small radius ratios $\eta < 0.6$ is an area still needing exploration to improve our understanding of the nature of the unsteady 'cat's eye' instability in differentially heated annular cavities.

2.2.4 Annular Cavities with Iso-Flux Heating of Inner Cylinder.

Some investigators have studied the case of natural convection in a closed annular cavity with iso-flux (constant thermal flux) heating of the inner cylinder. Sheriff [46] conducted experiments with carbon-dioxide at high pressures in high aspect ratio annular cavities of radius ratio close to one, providing Nusselt number correlations for the iso-flux case. Keyhani et al. [47] experimentally investigated natural convection in an annular cavity of aspect ratio A = 27.6 and radius ratio η = 0.23, with the inner cylinder at constant heat flux and the outer cylinder at constant temperature. Air and helium were the enclosed fluids, and all of their heat transfer correlations were corrected for radiation. Khan and Kumar [48] numerically investigated the iso-flux inner wall case for air-filled cavities, and they found that heat transfer rates for iso-flux heating are higher than for the corresponding isothermal heating case. Rogers and Lao [49] investigated natural convection in an annular cavity with an inner iso-flux heated cylinder and an insulated outer cylinder. Using linear stability analysis, they found that for low Pr number fluids, the nature of the instability changes

from axisymmetric to azimuthal/asymmetric as the radius ratio decreases, similar to the isothermal case.

2.3 Non-Boussinesq Studies and Effect of Variable Thermophysical Properties

All numerical, analytical and experimental studies mentioned to this point have examined natural convection inside cavities where the temperature differences are small, and the thermophysical properties of the enclosed fluid do not vary significantly. These aforementioned numerical and analytical studies have used the Boussinesq approximation along with the assumption of constant thermophysical fluid properties. For air at standard atmospheric pressure, the Boussinesq approximation is reasonable up to $\Delta T = 28.6°C$, according to criterion established by Gray and Giorgini [38]. Recently, there has been interest in re-examining the nature of natural convection instabilities under conditions of high-temperature differences where the Boussinesq approximation does not apply. Stability analyses [39, 40] and numerical studies [41-43] conducted under non-Boussinesq conditions (high-temperature difference conditions) have shown that the natural convection flow deviates significantly from its predicted behavior under Boussinesq conditions. The role of temperature dependent thermophysical properties becomes increasingly important as temperature differences inside the cavity increase. For natural convection flows in cavities under non-Boussinesq conditions, the temperature difference becomes an additional parameter of importance. The temperature difference parameter is quantified in terms of the normalized wall temperature difference, ε, given by the ratio:

$$\varepsilon = \frac{\Delta T}{2T_m} = \frac{T_h - T_c}{T_h + T_c} \tag{2.7}$$

where T_h is the temperature of the heated wall, T_c is the temperature of the cooled wall and T_m is the mean temperature given by $(T_h + T_c)/2$. In the limit of very small temperature difference, the value of ε approaches 0, and these conditions are referred to as *Boussinesq conditions*.

Sulsov and Paolucci [40] investigated the stability of natural convection in a rectangular cavity under non-Boussinesq conditions and found that the instability of the conduction regime, which was previously predicted to be a *stationary* cat's eye instability, is in fact an *oscillatory* instability which takes the form of a downward drifting cat's eye pattern for any finite temperature difference $\Delta T > 0$. A stationary 'cat's eye' instability (zero wave-speed) is possible only in the limiting case of $\varepsilon \rightarrow 0$ along with an assumption of constant thermophysical properties. Linear stability analyses [40] also showed that the nature of this instability is shear-driven at low and intermediate temperature differences ($\varepsilon < 0.536$) and is buoyancy driven at high-temperature differences ($\varepsilon > 0.536$). The downward drift of the 'cat's eye' instability in tall air-filled rectangular cavities predicted by Sulsov and Paolucci [40] has been recently observed experimentally by Wright et al. [44] and Lartigue et al. [45]. Figure 2.8 shows the dependence of the critical Rayleigh number for the 'cat's eye' instability on the dimensionless temperature difference ε in the rectangular cavity, as predicted by Suslov and Paolucci [40].

To my knowledge, there have been no numerical or experimental investigations on effects of non-Boussinesq conditions on the nature of the unsteady 'cat's eye' instability in annular cavities. It is most likely that natural convection under non-Boussinesq conditions in annular cavities differs significantly from its behavior under Boussinesq conditions.

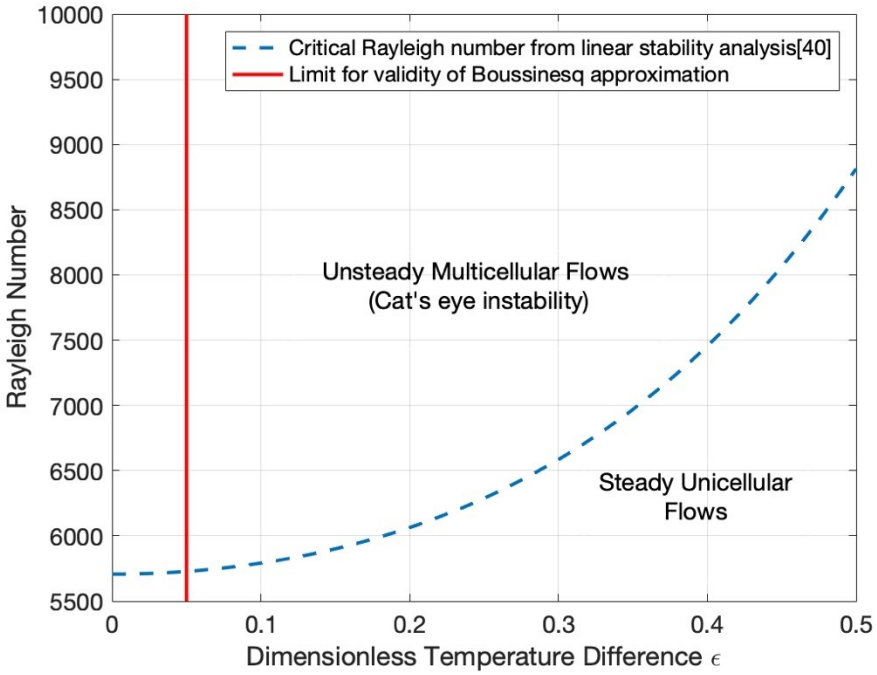

Figure 2.8: Critical Rayleigh numbers (dashed curve) from linear stability analyses for an infinitely tall rectangular cavity under non-Boussinesq conditions [40] and the limit of validity for the Boussinesq approximation based on results of Gray and Giorgini [38].

2.4 Cavities with Non-Isothermal Walls

Although there is an abundance of literature on natural convection flows in differentially-heated cavities with isothermal walls, there are relatively few studies on unsteady natural convection of air inside annular cavities with non-isothermal walls. Reeve et al. [50] were the first to investigate natural convection of air in an annular cavity of aspect ratio A = 10 and radius ratio $\eta = 0.6$ with linearly varying temperatures on the inner and outer cylinders. These thermal boundary conditions support a bi-cellular flow pattern similar to the flow pattern that can occur during the drawing operation for POF fiber [6]. Reeve et al. [50] studied the problem numerically by solving the transient axisymmetric Navier-Stokes equations with the Boussinesq approximation, using the

commercial finite element code FIDAP. At low Rayleigh numbers, the steady bi-cellular flow consisted of two counter-rotating cells. As the Rayleigh number was increased beyond a critical value, the interface between the two convection cells began to oscillate, leading to an unsteady oscillatory flow inside the cavity as shown in Fig. 2.9. The critical Rayleigh number for this transition based on the height of the cavity was reported as $Ra_{Hcr} = 2.165 \times 10^7$. With further increase in the Rayleigh number, complex phenomenon such as hysteresis, subharmonics, chaotic (nonperiodic) flow, multiple solutions, and a reverse transition back to a steady solution were predicted. Figure 2.10 maps the predicted oscillation frequencies as a function of Rayleigh number for the different flow regimes simulated by Reeve et al. [50].

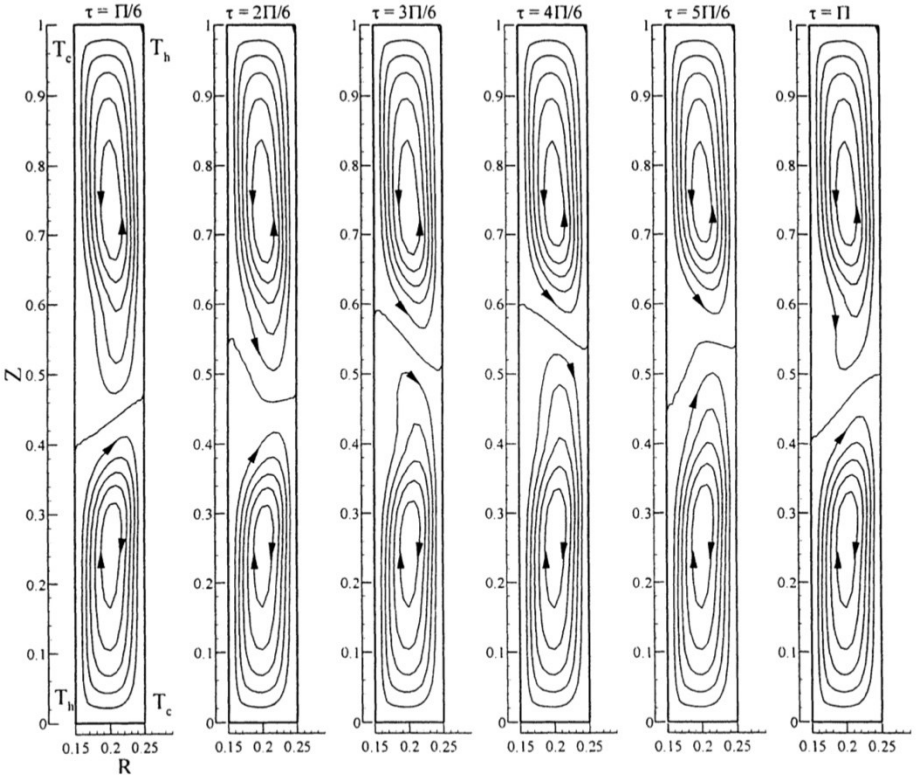

Figure 2.9: The stream function illustrating oscillation of a bi-cellular natural convection flow pattern through one period for $Ra_H = 2.5 \times 10^7$ in an air-filled annular cavity of aspect ratio A = 10 and radius ratio $\eta = 0.6$ as predicted by Reeve et al. [50].

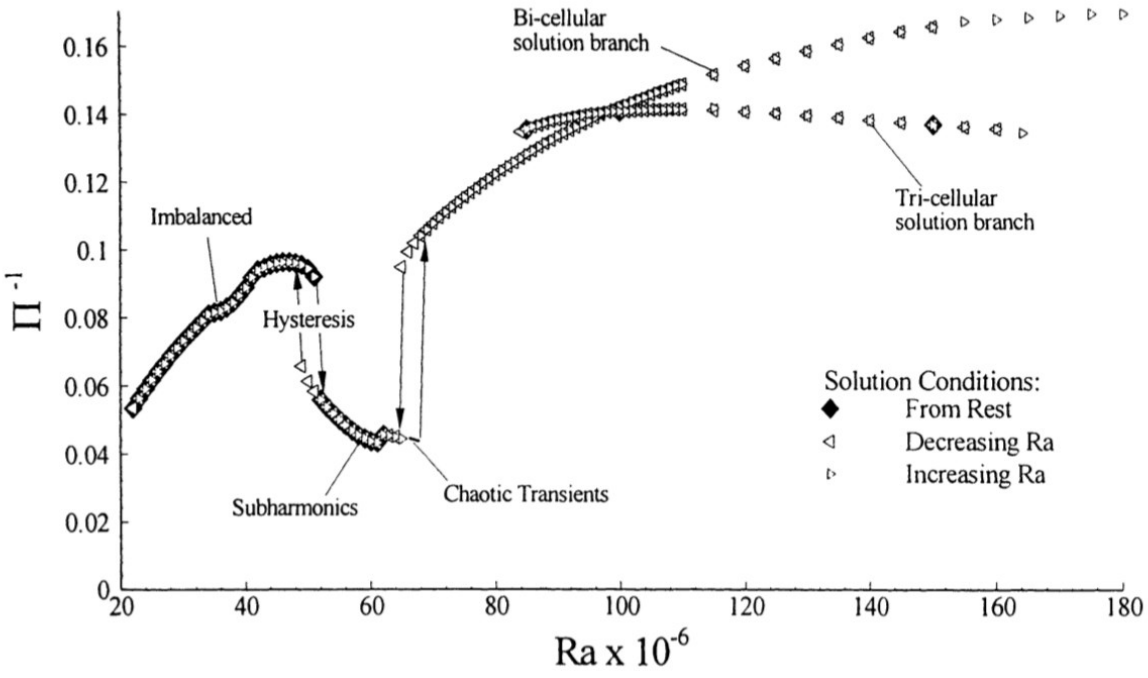

Figure 2.10: Map of predicted oscillation frequencies as a function of the Rayleigh number for an air-filled annular cavity of A = 10 and $\eta = 0.6$ as predicted by Reeve et al. [50].

Dillon et al. [51] built on the work of Reeve et al. [50] and studied the stability of bi-cellular natural convection in a rectangular cavity of aspect ratio A = 10 with linearly varying temperatures on the two vertical walls. They solved the 2D form of the Navier-Stokes equations with the Boussinesq approximation, using the commercial finite element code COMSOL. A similar sequence of flow bifurcations was predicted, as in Reeve et al. [50]. The steady flow first transitioned to oscillatory flow via a supercritical Hopf bifurcation at $Ra_{Hc} = 2.2 \times 10^7$. With further increase in Rayleigh number, the flow transitioned to chaotic at $Ra_H = 4.5 \times 10^7$. At an even higher Rayleigh number of $Ra_H = 1.27 \times 10^8$, a reverse transition from chaotic to oscillatory flow was predicted, accompanied by the creation of a third cell. Sanker et al. [68] studied convection in an annular cavity with discrete heat sources on the inner wall, and they analyzed the effects of heater

location, length, cavity aspect ratio, radii ratio, and Rayleigh number on the flow and heat transfer inside the cavity.

Natural convection in closed cavities with non-isothermal walls, supporting a base bi-cellular flow pattern, has yet to be fully explored. Numerical simulations by Reeve et al. [50] and Dillon et al. [51] for bi-cellular natural convection in annular and rectangular cavities with linearly varying wall temperatures have mapped the bifurcations that lead to transitions from steady to (transient) 2D oscillatory flows. However, these studies were with the assumption that flow inside the cavity is 2D, and that temperature differences inside the cavity are small. Whether unsteady flows in annular cavities, with thermal boundary conditions supporting a base bi-cellular flow pattern, are in fact 2D or 3D is not yet fully explored. Experimental observations of unsteady bi-cellular natural convection are from Reeve [1] in the POF drawing process, where the instability was always 3D asymmetric. Further investigation is needed to determine the radius ratios (if any exist) for which the bi-cellular flow losses stability to 2D/axisymmetric modes. For base bi-cellular natural convection in air-filled annular cavities, it is possible that the primary instability mode is always 3D asymmetric. In this case, full 3D numerical simulation is required to understand the instability mechanism(s) that lead(s) to transitions from steady to oscillatory and chaotic flows.

Chapter 3

3 BENCHMARKING STUDIES

The commercial finite volume CFD code Simcenter StarCCM+ is used for the computational fluid dynamics modeling of the natural convection flows described in Chapters 4, 5, 8, and 11. To test the capability of the CFD code in predicting natural convection instabilities in closed geometries, several benchmarking studies were performed for different geometries and boundary conditions. Results from these benchmarking studies are presented in this chapter.

3.1 Benchmarking Studies - Overview

The main category of problems used for benchmarking the Simcenter StarCCM+ code is the numerical and experimental work available for natural convection flows in tall, air-filled, differentially heated closed rectangular and annular cavities with isothermal walls. A detailed literature review on this category of natural convection flows has been presented in Chapter 2. In this configuration, the two vertical opposite facing walls of the cavity of height 'H' are maintained at two different constant temperatures T_h and T_c separated by an air-gap of width 'L' such that $T_h > T_c$ while, the top and bottom walls of the cavity are adiabatic. At low Rayleigh numbers, a unicellular, natural convection flow with fluid rising along the heated wall and falling along the cooled wall is observed in both the rectangular and annular geometries. As the Rayleigh number is increased above a critical value, the unicellular flow becomes unstable to a multicellular flow, also known as the 'cat's eye instability.' In rectangular cavities, the cat's eye instability is stationary and takes the form of stationary multiple cells/rolls. In annular cavities, the cat's eye

instability is convective and takes the form of constant drift speed upwards moving cells. The cat's eye instability of both the rectangular and annular cavity has been reported to be 2D/axisymmetric. Most of the literature available for this problem is for conditions of small temperature differences where the effect of the variable air temperature properties is negligible, and the Boussinesq approximation is valid. However, recent studies of natural convection in closed rectangular [40, 42] and square cavities [57, 58] have shown that under conditions of high-temperature differences, the variable thermophysical properties of air can affect the nature of the 'cat's eye' instability as well as the local heat transfer inside the cavity. Therefore, in this benchmarking operation, the accuracy of the Simcenter StarCCM+ code is evaluated under two conditions:

a) Flows under conditions of small temperature differences $\left(\frac{\Delta T}{T_h + T_c} = \frac{T_h - T_c}{2T_m} \approx 0\right)$ where the Boussinesq approximation is valid

b) Flows under conditions of high-temperature differences or non-Boussinesq conditions $\left(\frac{\Delta T}{T_h + T_c} = \frac{T_h - T_c}{2T_m} \gg 0\right)$

Accurate prediction of the critical Rayleigh number is an important metric for evaluating a commercial code. Critical Rayleigh number in this context is defined as the Rayleigh number at which flow transitions from steady unicellular to the multicellular cat's eye pattern. The average and local heat transfer rates at different Rayleigh numbers are readily available in the literature for this problem. Therefore, the main quantities used for the benchmarking operation were the average and local Nusselt numbers, critical Rayleigh numbers, wavenumbers, and wave-speeds. Qualitative comparisons of the velocity and temperature fields were also made. Table 3.1 gives a summary of the different numerical and experimental studies used for comparison in the benchmarking operation.

Table 3.1: Summary of numerical and experimental results for natural convection in closed air-filled cavities used for Benchmarking Simcenter StarCCM+.

Study	***Type***	***Geometry***	***Temperature Conditions and Air properties***	***Notes***
Lee and Korpela [14]	Numerical	Rectangular, A = 5 to 40	Boussinesq, constant thermophysical properties	Nusselt numbers, streamline contour plots and isotherms for select cases
Zhao et al. [19]	Numerical	Rectangular, A = 10.8 to 80	Boussinesq, constant thermophysical properties	Nusselt numbers, streamline contour plots and isotherms for select cases
Wakitani [18]	Numerical	Rectangular, A = 10 to 24	Boussinesq, constant thermophysical properties	Streamline contour plots and isotherms for select cases
Lartigue et al. [45]	Numerical	Rectangular, A = 40	Boussinesq, variable thermophysical properties	Nusselt numbers for select cases
Wright et al. [20]	Numerical	Rectangular, A = 40	Boussinesq, constant thermophysical properties	Nusselt numbers, streamline contour plots and isotherms for select cases
El Sherbiny et al. [11]	Experimental	Rectangular, A= 5 to 110	-	Empirical correlations for Average Nusselt number based on experiments
Vest and Arpaci [9]	Experimental	Rectangular, A = 33	-	Smoke pattern visualizations
Choi and Korpela [22]	Experimental	Annular, A = 38.6, η = 0.68	-	Smoke pattern visualizations
Le Quéré and Pécheux [30]	Numerical	Annular, A = 16, η = 0.8	Boussinesq, constant thermophysical properties	Nusselt numbers, streamline contour plots and isotherms for select cases
Pécheux, Le Quéré and Abcha [31]	Numerical	Annular, A = 16, η = 0.6 - 0.8	Boussinesq, constant thermophysical properties	Streamline contour plots and isotherms for select cases
Le Quéré et al. [57]	Numerical	Square, A = 1	Non-Boussinesq, Ideal gas, variable thermophysical properties	Reference solutions for non-Boussinesq convection based on several solutions collected at the "Mathematical and numerical aspects of low Mach number flows" conference organized by INRIA
Paillère et al.[58]	Numerical	Square, A = 1	Non-Boussinesq, Ideal gas, variable thermophysical properties	

3.2 Natural Convection in Tall Air-Filled Cavities Under Boussinesq Conditions

The first set of benchmarking studies was performed for the problem of natural convection inside tall, differentially heated air-filled rectangular and annular cavities with isothermal walls where the temperature differences in the cavity are small $\left(\frac{\Delta T}{T_h + T_c} = \frac{T_h - T_c}{2T_m} \approx 0\right)$, i.e. Boussinesq conditions. The dimensionless parameters which govern the flow inside a closed rectangular cavity of height 'H' and air-gap width 'L' are the Rayleigh number of the flow, the Prandtl number of the enclosed fluid, and the aspect ratio:

$$\text{Rayleigh number} = \text{Ra} = \frac{g\,\beta\,\Delta T\,L^3}{\upsilon\,\alpha} \tag{3.1}$$

$$\text{Prandtl number} = \text{Pr} = \frac{\upsilon}{\alpha} \tag{3.2}$$

$$\text{Aspect Ratio} = \text{A} = \frac{\text{H}}{\text{L}} \tag{3.3}$$

Where g is local gravitational acceleration, β is the gas thermal expansion coefficient, υ is kinematic viscosity, α is thermal diffusivity, ΔT is the temperature difference driving the flow between the inner and outer isothermal walls of the cavity, and 'L' is the air-gap width.

For closed annular cavities, in addition to the above three dimensionless parameters, the geometric parameter of radius ratio also affects the natural convection flow. For an annular cavity of height H with inner and outer radii of R_i and R_o, the radius ratio is defined as follows:

$$\text{Radius ratio} = \eta = \frac{\text{R}_\text{i}}{\text{R}_\text{o}} \tag{3.4}$$

The computational domain and boundary conditions for the rectangular cavity configuration and the annular cavity configuration are shown in Fig. 3.1(a) and Fig. 3.1(b).

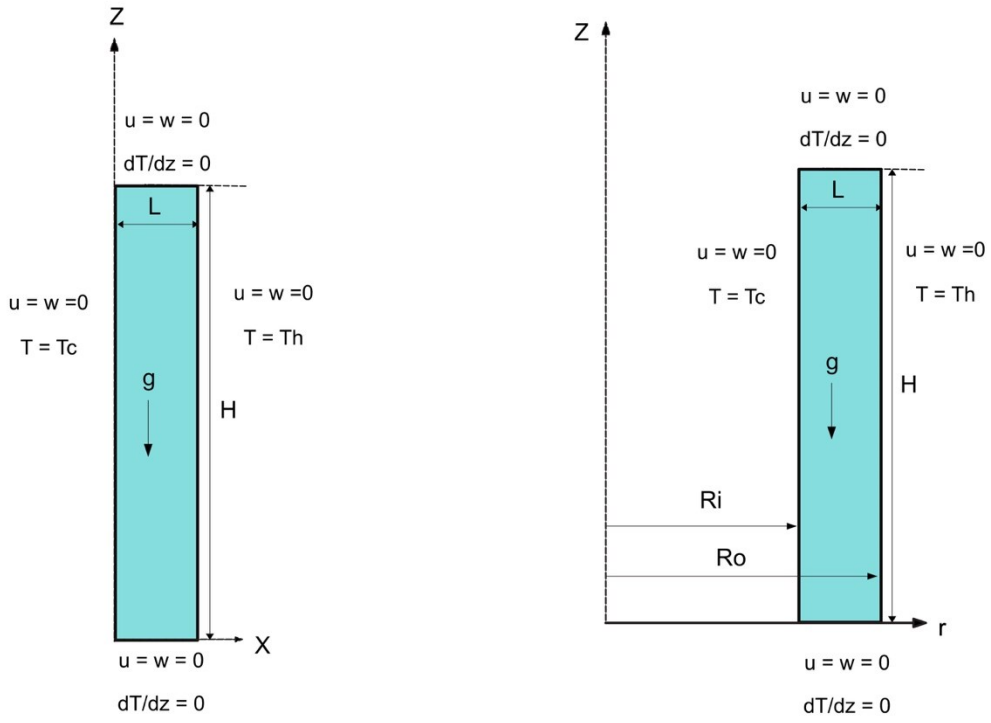

Figure 3.1: Computation domain and boundary conditions for (a) Rectangular cavity (b) Annular cavity.

Most of the numerical and experimental studies used in this benchmarking operation, report the average Nusselt numbers for different Rayleigh number and aspect ratios. In these studies, the local and average Nusselt numbers along the heated and cooled vertical walls are evaluated as:

$$\text{Local Nusselt} = \text{Nu}(z) = \frac{h(z).L}{k_m} = \frac{q(z).L}{(T_h - T_c).k_m} = \frac{L}{(T_h - T_c).k_m} k(T) \left|\frac{dT}{dx}\right|_{wall} \tag{3.5}$$

$$\text{Average Nusselt} = \overline{\text{Nu}} = \frac{1}{H}\int_{z=0}^{z=H} \text{Nu}(z)dz, \tag{3.6}$$

Where h(z) is the local heat transfer coefficient, k(T) is the temperature dependent thermal conductivity, k_m is the thermal conductivity at the mean wall temperature T_m, and $q(z) = k(T)\left|\frac{dT}{dx}\right|_{wall}$ is the local heat flux. The wavenumber and wave-speeds of the cat's eye instability are calculated based on the cell-length and drift speed of the cat's eye instability.

3.2.1 Governing Equations and Thermophysical Properties

For the benchmarking operation, both the incompressible and compressible form of the Navier-Stokes equations were solved. Some numerical studies for the differentially heated closed cavity problem solve the incompressible form of Navier-Stokes equations along with the Boussinesq approximation for the density, while assuming all other thermophysical properties as constant. This is a reasonable assumption since, for small temperature differences, the variation in the thermophysical properties of air is negligible. In order to be consistent with these studies, the incompressible form of Navier-Stokes equations, along with the Boussinesq approximation and constant thermophysical properties, was used for comparison with numerical studies that invoked this approximation.

For comparison with all experimental studies, and some numerical studies which treated thermophysical air properties to be temperature dependent, the compressible form of the Navier-Stokes equations were solved. Air was modeled as an ideal gas, and all other thermophysical properties of air like thermal conductivity (k), dynamic viscosity (μ), and specific heat (Cp) were treated as temperature dependent obtained from linear interpolation of tabulated values [56]. Furthermore, for the experimental studies of Vest and Arpaci [9] and Choi and Korpela [22], both the incompressible and compressible form of equations were solved to gauge which assumption provided better comparisons with experimental observations. Some interesting effects of using

variable thermophysical properties of air were observed. More details are presented in subsequent sections.

3.2.2 Solver Selection and Settings

The transient Navier-Stokes equations for a Newtonian fluid are solved using the coupled implicit solver of Simcenter StarCCM+. The assumption of 2D flow for the rectangular cavity case and axisymmetric flow for the annular cavity case is used. Simcenter StarCCM+ uses co-located finite volume discretization to convert the continuous system of Navier-Stokes equations to a set of discrete algebraic equations which are then solved using an algebraic multigrid solver. The Simcenter StarCCM+ user manual recommends using the coupled solver for flows dominated by natural convection [54]. The coupled solver is based on the approach of modifying a density-based hyperbolic solver using preconditioning schemes to be efficient and accurate under conditions of low Mach number flows. It solves the conservation equations for continuity, momentum, and energy simultaneously as a vector set of equations. To address ill-conditioning at low Mach number, the coupled solver in Simcenter StarCCM+ uses a low-Mach number pre-conditioning based on Turkel's family of pre-conditioners for ideal gas flows [54, 55]. This preconditioned form of the governing equations used by the Coupled Flow model makes it suitable for solving both incompressible and compressible flows [54].

3.2.3 Spatial and Temporal Discretization

A second-order-upwind spatial discretization for the convective flux terms and second-order central discretization for the diffusion terms is used. The Weiss-Smith Preconditioned Roe's Scheme is used for discretization of the inviscid fluxes. For time discretization, a second-order

implicit scheme is selected. The transient form of equations is solved by the coupled solver using a dual time-stepping approach with inner iterations in pseudo-time, and outer iterations are in real time. Grid refinement studies were performed to select the appropriate grid size and time step for each benchmarking operation. Orthogonal, non-staggered, quadrilateral mesh cells of square shape (grid-cell aspect ratio = 1) were used. 3-4 layers of prism layer cells were used at the wall boundaries to refine the grid at the horizontal and vertical walls further.

3.2.4 Results: Tall Air-Filled Rectangular Cavities Under Boussinesq Conditions

3.2.4.1 Cavities of Aspect Ratio A = 20 and A = 40

Simulations using the Simcenter StarCCM+ coupled implicit solver were performed for cavities of aspect ratios A = 20 and A = 40 at several different Rayleigh numbers. The results from these simulations were then compared with the empirical correlations for rectangular cavities by El Sherbiny et al. [11] and with the numerical studies of Lee and Korpela [14], Zhao et al. [19], Wakitani [18], Lartigue et al. [45], and Wright et al. [20]. The dimensions of the 2D cavities of aspect ratio A = 20 and A = 40 used in the Simcenter StarCCM+ simulations were 0.0289 m x 0.578 m and 0.0289 m x 1.156 m, respectively. The grid sizes for the A = 20 and A = 40 cavities were 50 x 1000 and 50 x 2000, respectively, which correspond to a unit cell size of 0.6 mm. The Boussinesq approximation was used for modeling the flow. A time step size of 0.01 seconds was used for the simulations. For air at standard atmospheric pressure, the Boussinesq approximation remains valid up to $\Delta T = 28.6°C$, according to the criterion established by Gray and Giorgini [38]. Therefore, to maintain the temperature conditions in the cavity well within the limit of the Boussinesq approximation, the temperature differences ΔT was varied from 0 to 7.8° C to vary the Rayleigh number of the flow from Ra = 0 to 17702. Table 3.2 reports the average Nusselt

numbers, at the hot wall, obtained from the numerical simulations performed using the Simcenter StarCCM+ coupled implicit solver, along with prior results at different Rayleigh numbers for rectangular cavities of aspect ratio 20 and 40.

Table 3.2: Comparison of numerically predicted average Nusselt numbers, $\overline{Nu}$, at heated wall with results from prior experimental and numerical studies at different Rayleigh numbers.

Ra	A	Simcenter StarCCM+ Coupled solver	Empirical co-relations	Numerical results			
			El Sherbiny et al. [11]	Lee and Korpela [14]	Zhao et al. [19]	Lartigue et al. [45]	Wright et al. [20]
5000	40	1.093	1.034	1.05	-	-	-
6800	40	1.163	1.096	-	1.158	1.167	1.15
8239	40	1.226	1.159	-	1.227	-	1.21
10102	40	1.287	1.244	-	1.277	1.292	1.28
12000	40	1.335	1.328	1.21	-	-	-
15000	40	1.418	1.448	1.28	-	-	-
7789	20	1.325	1.307	1.29	-	-	-
8497	20	1.358	1.339	1.32	-	-	-
10621	20	1.436	1.429	1.41	1.441	-	-
14162	20	1.545	1.562	1.53	1.547	-	-
17702	20	1.641	1.677	1.62	1.647	-	-

Many studies report the number of cells/rolls observed for different Rayleigh numbers and aspect ratios and use them as a means to track bifurcations observed in the flow. Table 3.3 compares the number of cells predicted using the coupled solver for rectangular cavities of aspect ratio 20 and 40 at different Rayleigh numbers with several numerical results from the literature. The coupled solver accurately captured the tendency of decrease in the number of cells/rolls in the cat's eye instability with an increase in Rayleigh number or a reduction in cavity aspect ratio.

Table 3.3: Comparison of the number of cells in the cavity predicted at different Rayleigh numbers with results from prior numerical studies in the Boussinesq regime.

Ra	A	Simcenter StarCCM+ coupled solver	Lee and Korpela [14]	Lartigue et al. [45]	Wright et al. [20]	Wakitani et al. [18]
5000	40	unicellular flow	unicellular flow	unicellular flow	unicellular flow	unicellular flow
6800	40	14	-	16	15	-
8239	40	13	14	-	15	-
10102	40	12	14	14	14	-
12000	40	11	-	-	-	-
15000	40	11	13	-	-	-
7789	20	5	5	-	-	5
8497	20	5	5	-	-	5
10621	20	4	5	-	-	5
14162	20	3	5	-	-	4
17702	20	3	5	-	-	

Figures 3.2 and 3.3 shows the streamlines and isotherms at different Rayleigh numbers in a cavity of aspect ratio A = 40 and A = 20 obtained using the coupled solver. Streamlines and isotherms from the Simcenter StarCCM+ simulations were compared with the flow descriptions in the numerical studies of Lee and Korpela [14], Wakitani [18], Lartigue [45], and Wright et al. [20]. The strongest cells are observed at the center of the cavity, while the cells near the cavity ends are elongated and weaker. Correct trends were observed in the Simcenter StarCCM+ simulations using the coupled solver, for aspect ratios A = 20 and 40, and reasonable agreement was found with all reported values from prior numerical simulations that invoked the Boussinesq approximation.

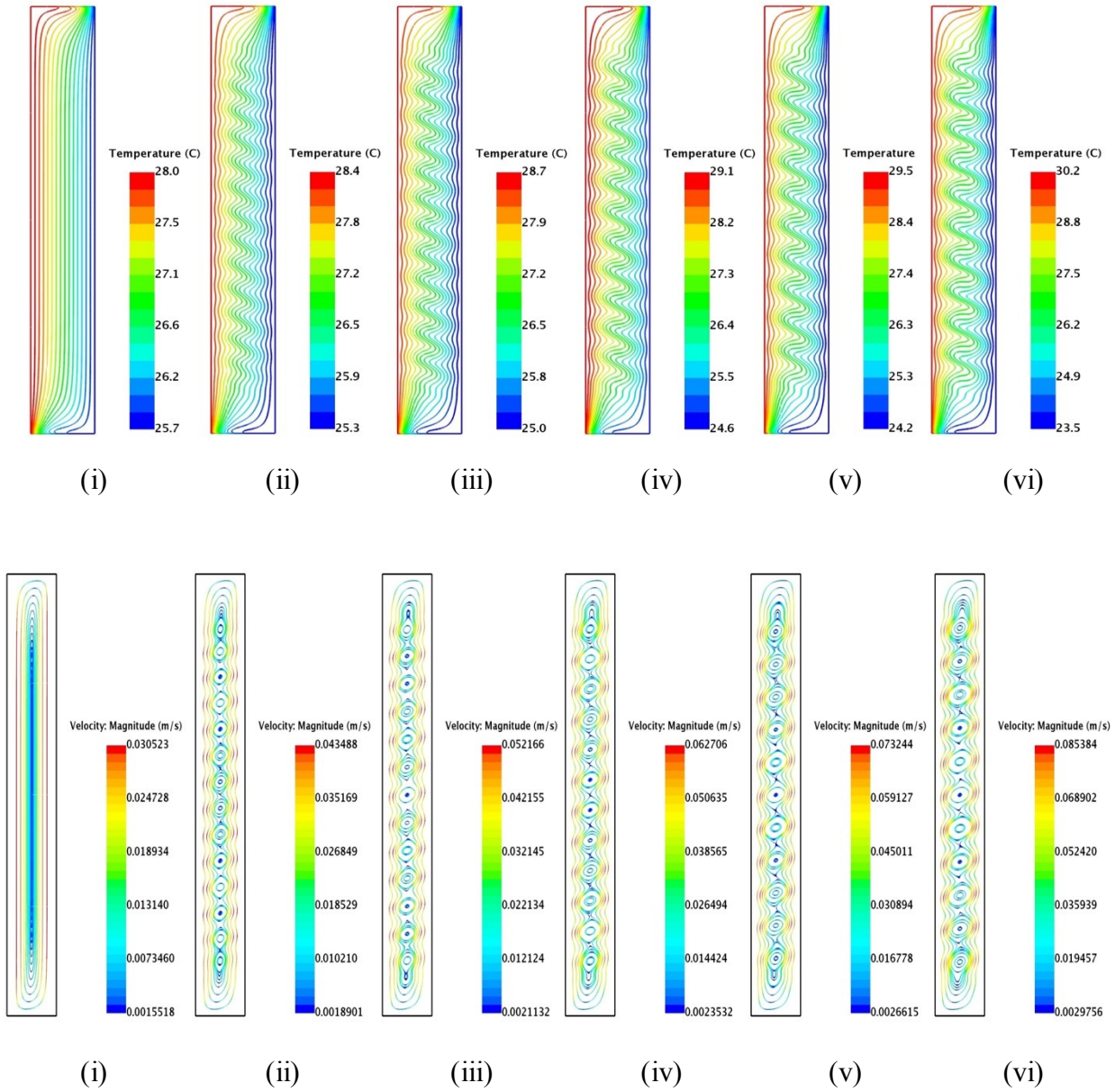

Figure 3.2: Isotherms (top) and Streamlines (bottom) for natural convection of air in a rectangular cavity of aspect ratio A = 40 at different Rayleigh numbers: (i) Ra = 5000 (ii) Ra = 6800 (iii) Ra = 8239 (iv) Ra = 10102 (v) Ra = 12000 (vi) Ra = 15000 obtained using Simcenter StarCCM+ coupled implicit solver.
Note: Width of the cavity is scaled by a factor of 6 for visualization purposes.

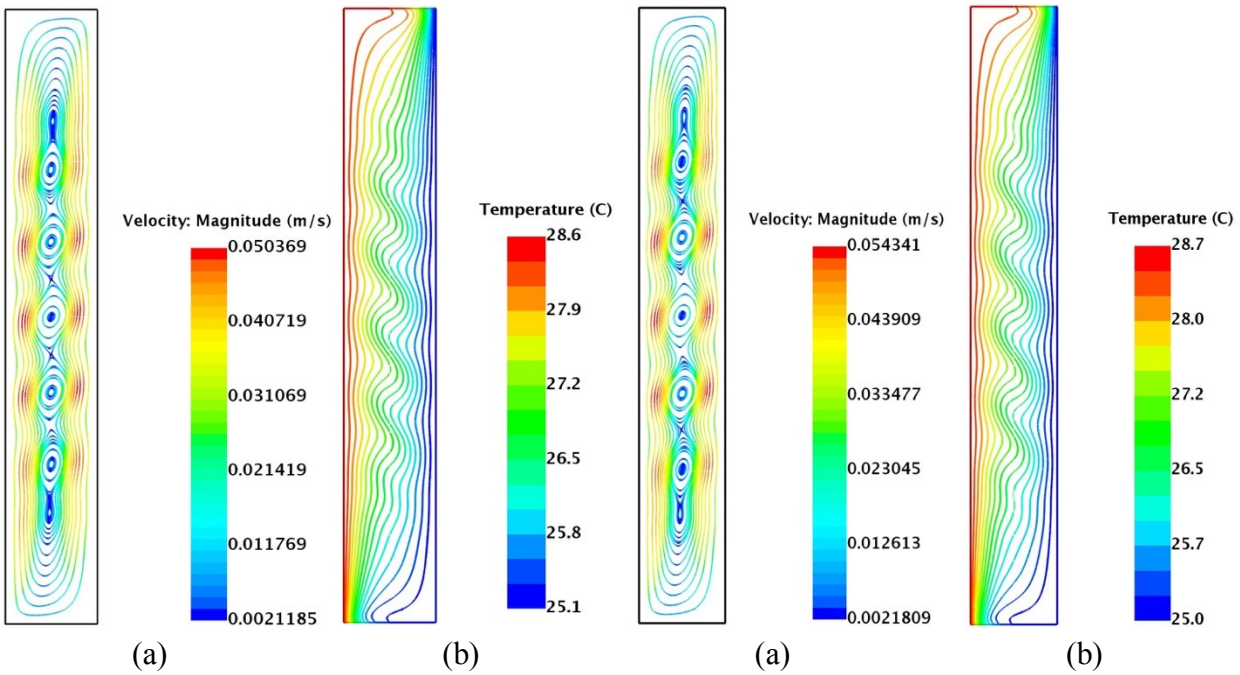

(a) (b) (a) (b)

(i) Ra = 7789 *(ii) Ra = 8497*

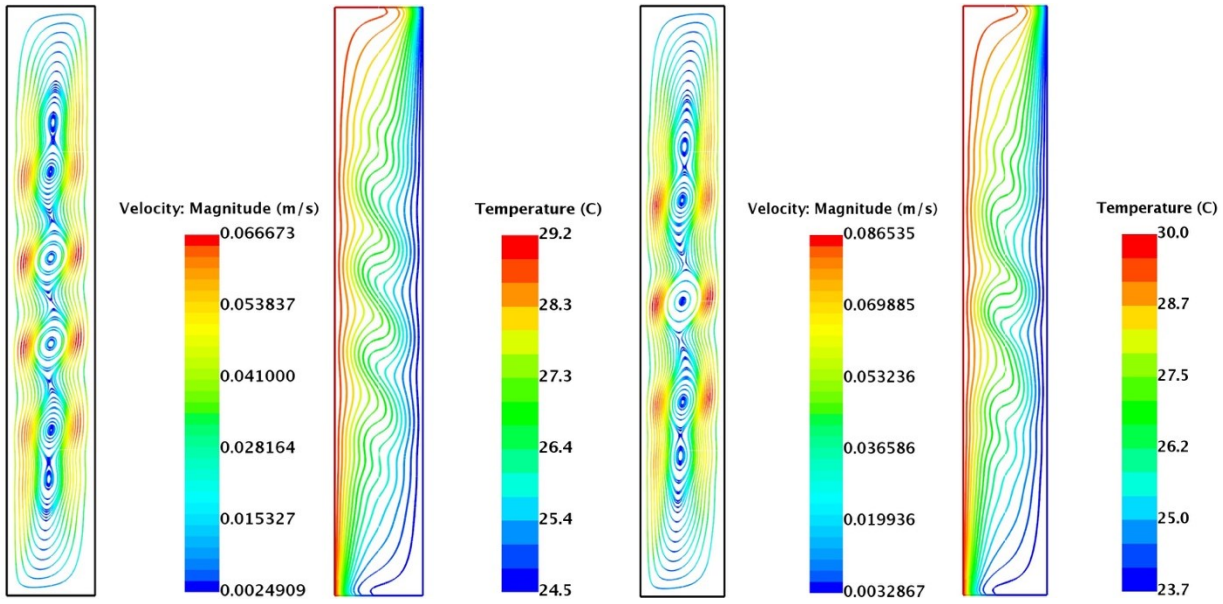

(a) (b) (a) (b)

(iii) Ra = 10621 *(iv) Ra = 14162*

Figure 3.3: (a) Isotherms and (b) Streamlines for natural convection of air in a rectangular cavity of aspect ratio A = 20 at different Rayleigh numbers: (i) Ra = 7789 (ii) Ra = 8497 (iii) Ra = 10621 (iv) Ra = 14162 obtained using Simcenter StarCCM+ coupled implicit solver.
Note: Width of the cavity is scale by a factor of 3 for visualization purposes.

3.2.4.2 Cavity of Aspect Ratio A=33

Next, the coupled solver was benchmarked against the experimental results of Vest and Arpaci [9], where they reported experimentally observed critical Rayleigh number and wavenumber for the 'cat's eye' instability in an air-filled rectangular cavity of aspect ratio A = 33 and an air-gap width L = 0.01905m. The grid size used for the Simcenter StarCCM+ simulation was 48 x 1600, which corresponds to a unit cell size of 0.4 mm. The timestep used was 0.01 seconds. Numerical simulations were conducted at several Rayleigh numbers to determine the critical state where the unicellular flow became unstable to the cat's eye instability. Air was treated as an ideal gas, and all other thermophysical properties of air were modeled as temperature dependent. Table 3.4 shows the predicted values of critical Rayleigh number and wavenumbers for the experimental observations of Vest and Arpaci [9] along with the Simcenter StarCCM+ coupled solver predictions. Figure 3.4 shows the streamlines from the Simcenter StarCCM+ simulations and photograph of the streamlines from the experimental observation of Vest and Arpaci at a Gr = 9700.

Table 3.4: Comparisons with experimental results of Vest and Arpaci [9].

	Critical Rayleigh Number	Wavenumber
Vest and Arpaci's Experiment for air-filled rectangular cavity of A = 33	6177± 10%	2.74
Simcenter StarCCM+ Coupled Implicit solver (Grid size = 48 x 1600, Time step = 0.01 sec)	5822	2.73

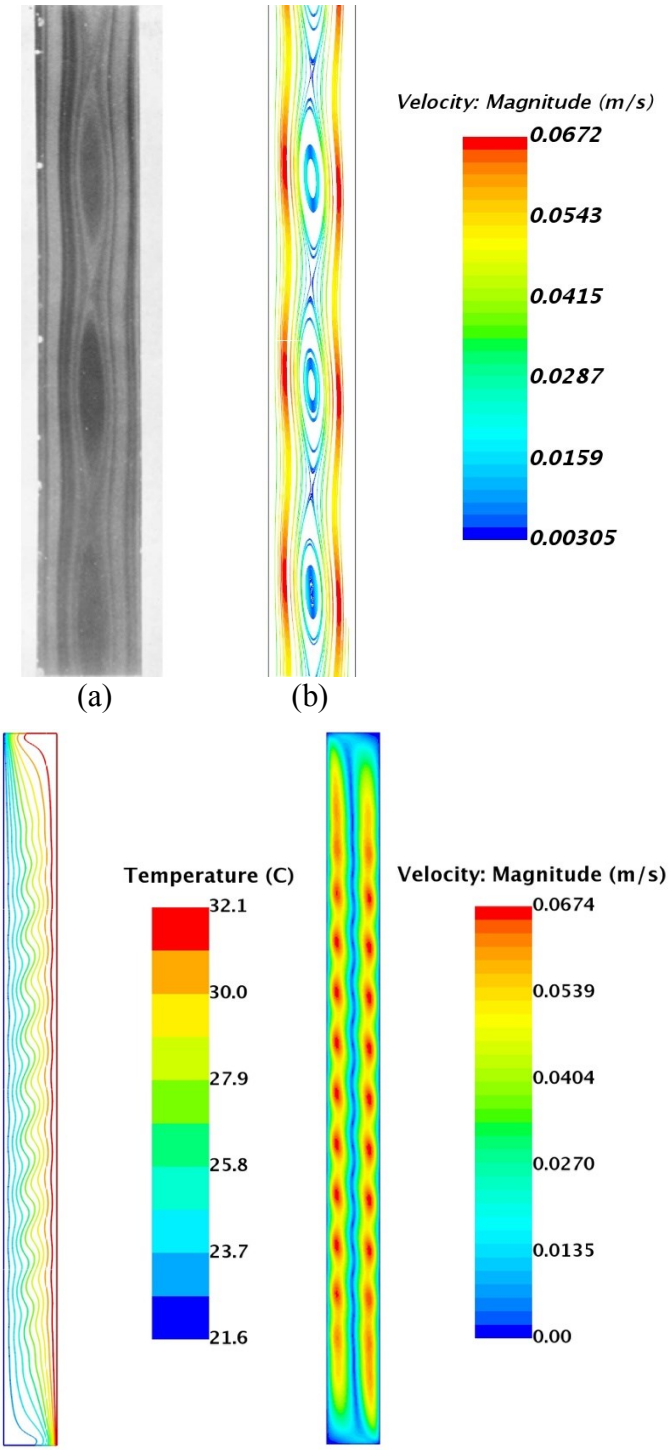

Figure 3.4: Streamlines from the central part of the cavity of aspect ratio A=33 at Gr = 9700 observed using (a) Photograph of the streamlines from the experimental observation of Vest and Arpaci [9]; (b) Simcenter StarCCM+ simulations using variable thermophysical properties; (c) Isotherms and streamlines for entire cavity length.

Although a good comparison was observed between the numerical prediction of critical Rayleigh number and wavenumber with the experimental observations of Vest and Arpaci [9], one significant discrepancy was evident: The Simcenter StarCCM+ numerical simulations predicted the instability as convective; moving downward at a very slow speed (Time period ≈ 100 seconds), whereas Vest and Arpaci [9] have reported the cat's eye instability in their experiment to be stationary. In order to understand the reason for the downward drifting of cells observed in numerical simulations, another set of numerical simulations were performed, this time using the Boussinesq approximation for density and treating all the other thermophysical properties of air as constant. Surprisingly, for this second set of numerical simulations, the instability was observed to be stationary consistent with the observations of Vest and Arpaci [9]. Figure 3.5 shows the evolution of temperature at the midpoint of the cavity for numerical simulations with variable and constant thermophysical properties.

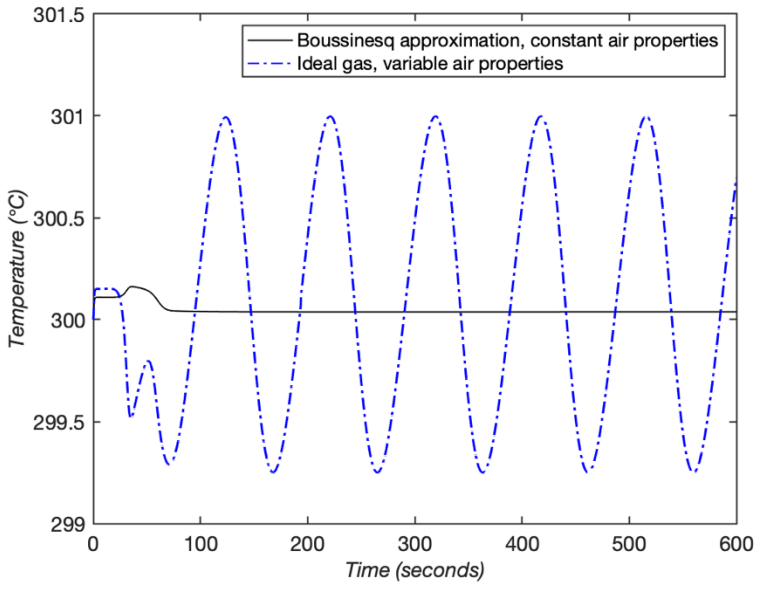

Figure 3.5: Temporal evolution of temperature at vertical and horizontal midpoint of the cavity from numerical simulations of experiments conditions of Vest and Arpaci [9] at Gr = 9500 with: Boussinesq approximation, constant thermophysical air properties assumption (black curve) and variable air thermophysical properties assumption (blue dotted curve).

The prediction of a stationary cat's eye instability is only possible if there is perfect symmetry in the numerical domain. For the case of variable thermophysical properties, this flow symmetry is broken, which leads to the instability drifting downward. More recent experimental investigations by Lartigue et al. [45] and Wright et al. [44] have reported the slow downward drift of the cat's eye instability in tall rectangular cavities, which was observed in our numerical simulations with Simcenter StarCCM+ using the temperature dependent thermophysical properties. This difference in numerical prediction prompted a more detailed investigation of the effects of variable thermophysical properties and non-Boussinesq temperature conditions on the cat's eye instability of the rectangular cavity. The results of this investigation will be discussed in Chapter 4.

3.2.4.3 Conclusion

The coupled implicit solver of Simcenter StarCCM+ was able to predict the correct trends and results with reasonable accuracy for the experimental and numerical studies for natural convection in tall rectangular cavities. The average Nusselt numbers predicted by the solver agreed with experimental measurement of El Sherbiny et al. [11] to within 2% for A = 20 cavities and within 6% for A = 40. Good agreement was also observed with the experimental results of Vest and Arpaci [9] with the error in critical Rayleigh number predicted by numerical simulations being less than 6%. Bifurcations and flow transitions observed in the Simcenter StarCCM+ simulations were in agreement with the descriptions provided in the numerical studies Lee and Korpela [14], Zhao [19], Wakitani [18], Lartigue [45], and Wright et al. [20].

3.2.5 Results: Annular Cavities Under Boussinesq Conditions

Compared to the rectangular cavity case, fewer studies are available in the literature for natural convection in tall air-filled annular cavities under Boussinesq conditions. For the annular cavity case, the cat's eye instability has been reported to be convective, moving upward in both experimental [22] and numerical studies [30, 31]. For this series of benchmarks, numerical predictions using the Simcenter StarCCM+ coupled implicit solver were compared against the numerical results of Le Quéré and Pécheux [30] and Pécheux, Le Quéré and Abcha [31] for an annular cavity of A = 16, η = 0.8, 0.7 and with experimental results of Choi and Korpela [22] for cavity of A = 38.6 and η = 0.68.

3.2.5.1 Cavity of Aspect Ratio A = 16 and Radius Ratio η = 0.8, 0.7

Le Quéré and Pécheux [30] and Pécheux, Le Quéré and Abcha [31] have reported the transitions observed in an annular cavity of A = 16 for several radius ratios. Numerical simulations were performed using Simcenter StarCCM+ coupled implicit solver for two annular cavities of A=16 and η = 0.8, 0.7, respectively. Both the reference numerical studies used for the benchmarking operations [30, 31] have used the Boussinesq approximation along with constant thermophysical properties to solve the axisymmetric form of equations; therefore, the same assumptions were used for the benchmark. A grid size of 48 x 752 and a time step size of 0.01 seconds was used. Figure 3.6 shows the steady and unsteady numerical solutions found by the coupled implicit solver for the cavity of radius ratio η = 0.8. The steady solution shows the presence of a unicellular flow while the unsteady solution shows a multicellular cat's eye pattern slowly drifting upward.

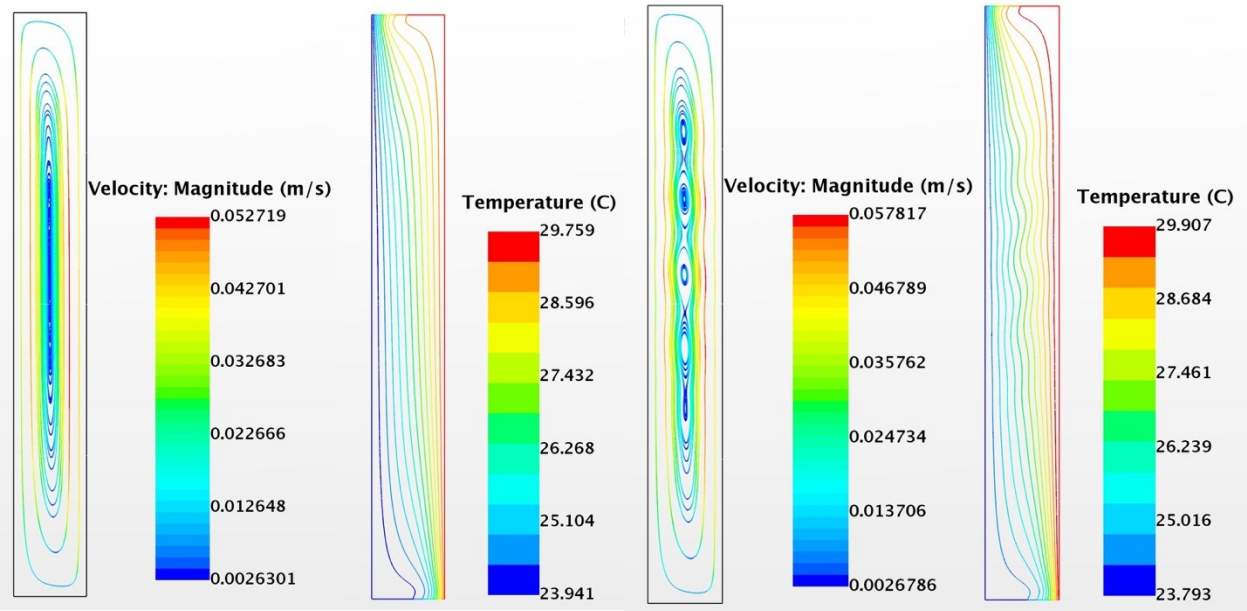

(i) *Ra = 6900* *(ii)* *Ra = 7250*

Figure 3.6: Streamlines and isotherms for steady and unsteady solutions found using the coupled implicit solver for an annular cavity of $\eta = 0.8$, A=16.
Note: Width of the cavity is scaled by a factor of x2 for visualization purposes.

Since the transition from steady unicellular to the unsteady upward-moving cat's eye instability happens via a supercritical Hopf bifurcation; in the vicinity of the critical state, the following relation holds:

$$(\mathrm{Ra} - \mathrm{Ra_{cr}}) \ \alpha \ (\text{amplitude of oscillations})^2 \tag{3.7}$$

This relation was utilized to determine the critical Rayleigh number by performing several simulations in the vicinity of the critical state and then extrapolating the values to the critical state (amplitudes $\rightarrow 0$). The determination of the critical Rayleigh number using this method for A = 16 and $\eta = 0.8$ is shown in Fig. 3.7. This same method has been used by Le Quéré and Pécheux [30] and Pécheux, Le Quéré and Abcha [31] in their numerical work.

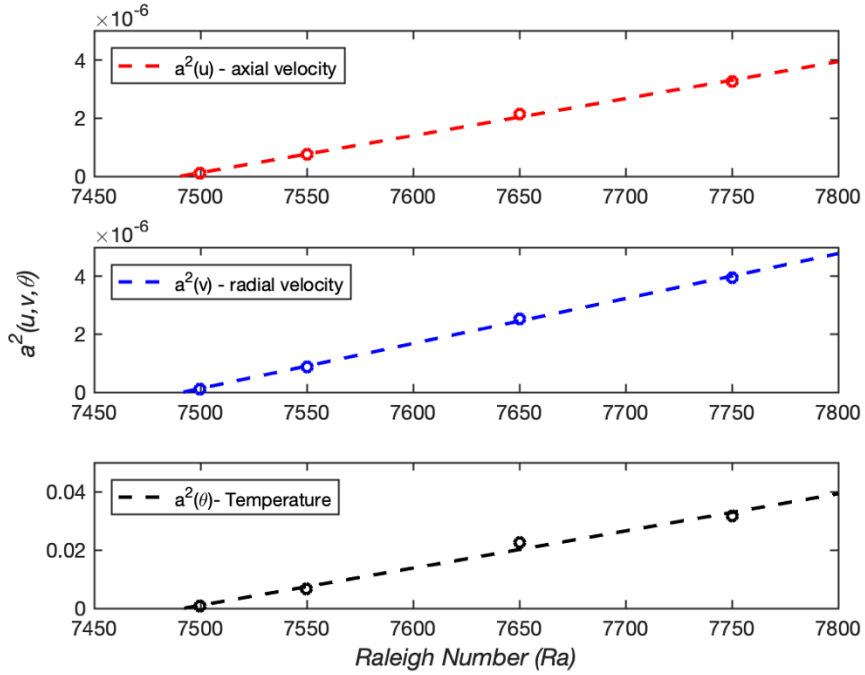

Figure 3.7: Critical Raleigh Number determined from extrapolation of temperature and velocity oscillations amplitudes obtained from Simcenter StarCCM+ simulations for the annular cavity of A = 16 and η = 0.7.

Table 3.5 and 3.6 shows comparison of critical Rayleigh numbers and dimensionless time period of oscillations predicted by the Simcenter StarCCM+ simulations for η = 0.7, 0.8, A = 16 with the numerical predictions of Le Quéré and Pécheux [30] and Pécheux, Le Quéré and Abcha [31].

Table 3.5: Critical Rayleigh number determination for A = 16, η = 0.8, 0.7 annular cavities.

Radius Ratio	A	Critical Ra – Simcenter StarCCM+	Critical Ra in Reference [30],[31]	Percentage Error
0.8	16	7041	6850	2.8
0.7	16	7492	7220	3.8

Table 3.6: Dimensionless time period of oscillations for A =16 and η = 0.8 annular cavity.

Raleigh Number	A	η	Simcenter StarCCM+ coupled solver Dimensionless Time Period	Reference [30],[31] : Dimensionless Time Period	Percent Error
8000	16	0.8	14.7	14.6	0.9
10000	16	0.8	18.5	18.7	1.2

3.2.5.2 Cavities of Aspect Ratio A = 38.6

Next, experimental results of Choi and Korpela [22] for an annular cavity of aspect ratio A= 38.6 and radius ratio η = 0.68 with air-gap width L = 0.0234m were used to benchmark StarCCM+. Numerical simulations were performed using both the Boussinesq approximation and the ideal gas assumption with variable thermophysical air properties. The grid size used for numerical simulations was 48 x 1816, which corresponds to a unit cell size of 0.5 mm. The timestep used was 0.01 seconds. Figure 3.8 shows the streamlines and isotherms at Gr = 9100 as predicted by Simcenter StarCCM+ simulations along with the smoke pattern photos of Choi and Korpela [22]. Table 3.7 shows the comparison with the experimental observations by Choi and Korpela [22] at a supercritical Rayleigh number for the 'cat's eye' instability. The prediction of the cell-length of the cat's eye instability was identical in the two numerical simulations invoking the Boussinesq approximation and ideal gas assumption with variable properties. However, different values for the upward drift speed of the instability were observed for both cases as seen in Table 3.7. This difference again demonstrates the sensitivity of the prediction of the cat's eye instability to variable thermophysical properties of air. A detailed investigation on the effects of non-Boussinesq

conditions and variable thermophysical properties on the cat's eye instability of the annular cavity was performed. Results of this investigation are presented in Chapter 5. Overall, a good agreement was observed between the reported quantities and flow descriptions from the experimental observations and the predictions of Simcenter StarCCM+.

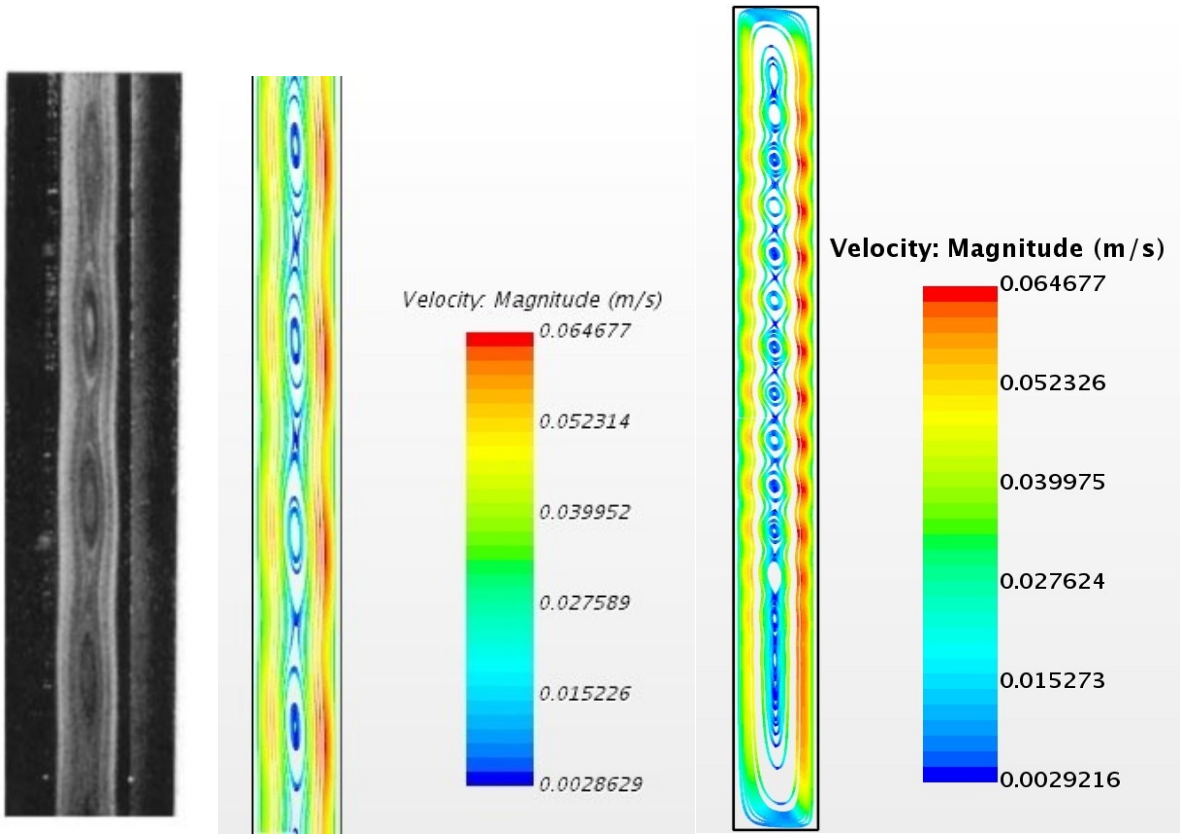

(a) (b) (c)

Figure 3.8: Streamlines from the central part of the annular cavity of aspect ratio A = 38.6 and radius ratio η = 0.68 at Gr = 9100 observed in (a) Photograph of the streamlines from the experimental observation of Choi and Korpela [22]; (b) Simcenter StarCCM+ simulations using variable thermophysical properties; (c) Streamlines for entire cavity length.
Note: Width of the cavity in Figure 3.8(c) is scaled by a factor of *x*4 for visualization purposes.

Table 3.7: Comparisons with experimental results of Choi and Korpela [22].

		Cell-length (cm)	Drift speed (cm/s)
Choi and Korpela's Experiment for air-filled annular cavity of A = 38.6 and $\eta = 0.68$ at Gr = 9100		5.4 ± 0.1	0.76 ± 0.04
Simcenter StarCCM+ Coupled Implicit solver	Ideal gas with variable air properties	5.20	0.74
	Boussinesq approximation with constant air properties	5.20	0.78

3.2.5.3 Conclusions

A good agreement between the predictions using the Simcenter StarCCM+ coupled solver and the reported values of critical Rayleigh number (< 3% discrepancy) and dimensionless period of oscillations (< 1.5 % discrepancy) by Le Quéré and Pécheux [30] and Pécheux, Le Quéré and Abcha [31] was observed. The predicted values by the coupled implicit solver also agreed well with the experimental observations of Choi and Korpela [22]. Some differences in the cell drift speed were observed in the numerical predictions with and without invoking the Boussinesq approximation for the same experimental case [22]. These differences further demonstrate how temperature dependent thermophysical properties of air can affect the prediction of natural convection flows. Therefore, care must be taken while using the Boussinesq approximation for numerical predictions of natural convection flows even if the temperature conditions inside the cavity are well within the Boussinesq limit.

3.3 Natural Convection in Air-Filled Cavities Under Non-Boussinesq Conditions

The second set of benchmarking studies were performed for natural convection flows in cavities under high-temperature difference conditions $\left(\frac{\Delta T}{T_h + T_c} = \frac{T_h - T_c}{2T_m} \gg 0\right)$ or non-Boussinesq conditions. These non-Boussinesq conditions are quantified using the normalized wall temperature difference 'ε', which is defined as the ratio of the temperature difference between the heated and cooled walls, $(T_h - T_c)$, to the sum of their absolute temperatures, $(T_h + T_c)$. For this set of benchmarks, reference solutions for the problem of natural convection in a differentially heated square cavity with isothermal walls under non-Boussinesq conditions were used [57, 58]. The reference solutions are based on the numerical results for non-Boussinesq convection in a square cavity submitted by several researchers at the "Mathematical and numerical aspects of low Mach number flows" conference organized by INRIA and LAB. The computation domain and boundary conditions for the square cavity problem are shown in Fig. 3.9.

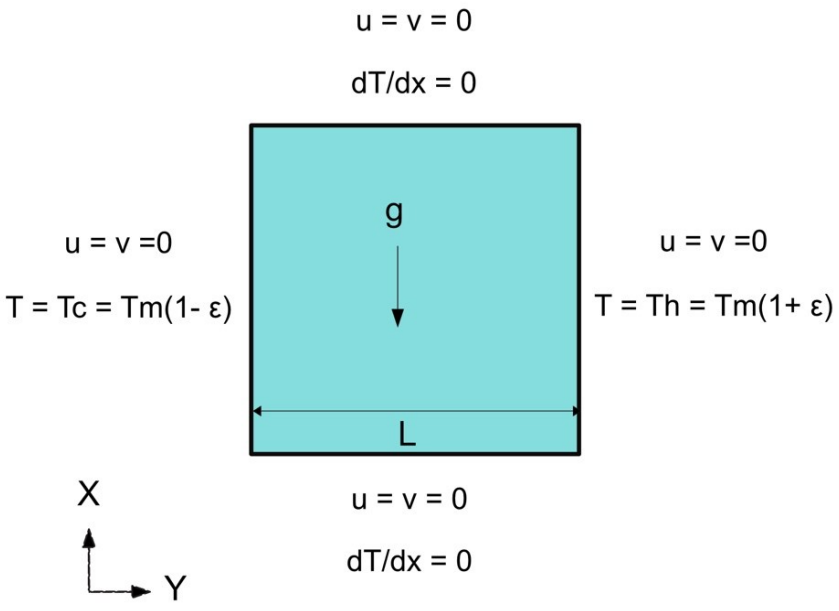

Figure 3.9: Computational domain and boundary conditions for non-Boussinesq convection of air in a closed square cavity.

3.3.1 Transport Properties

The viscosity of air μ and thermal conductivity of air k, are temperature dependent and vary according to Sutherland's law given by:

$$\mu(T) = \mu^* \left(\frac{T}{T^*}\right)^{\frac{3}{2}} \frac{T^* + S}{T + S} \tag{3.8}$$

$$k(T) = \frac{\mu(T)\gamma R}{(\gamma - 1)Pr}$$

Where

$\mu^* = 1.68 \times 10^{-5}$ kg/ms

$T^* = 273$ K

S = 110.5 K

γ = ratio of specific heats for air = 1.4

Pr = Prandtl number for air = 0.71

The air is assumed to be a calorically and thermally perfect gas. The density of air ρ follows the ideal gas equation given by:

$$p = \rho RT \tag{3.9}$$

Where R = gas constant for air

Note that the Prandtl number of the fluid is held constant at 0.71 while allowing for the variation in the viscosity and thermal conductivity with temperature according to the Sutherlands laws.

3.3.2 Dimensionless Governing Parameters

Unlike the Boussinesq convection, where the air properties practically remain constant, for non-Boussinesq convection, the thermophysical properties of air vary significantly within the cavity.

Therefore, the Rayleigh number inside the cavity needs to be evaluated using temperature properties at a specific reference temperature. Accordingly, a nominal Rayleigh number for this configuration is based on the air-properties evaluated at the mean wall temperature $T_o = \frac{T_h + T_c}{2}$. The natural convection flow inside an air-filled square cavity (Aspect ratio = 1, Pr = 0.71) then becomes a function of only two dimensionless parameters – Rayleigh number and dimensionless temperature difference which are evaluated as:

$$\mathrm{Ra} = \frac{g\,\beta_o\,\Delta T\,L^3}{\upsilon_o \alpha_o}\,, \tag{3.10}$$

$$\varepsilon = \frac{T_h - T_c}{T_h + T_c} = \frac{T_h - T_c}{2T_o}. \tag{3.11}$$

Where,

$\beta_o = \frac{1}{T_o}$ for ideal gas = Coefficient of thermal expansion evaluated at T_o

$\Delta T = T_h - T_c$

υ_o= kinematic viscosity evaluated at T_o

α_o = thermal diffusivity evaluated at T_o

3.3.3 Test Case Description

For the benchmarking operation, the Simcenter StarCCM+ coupled implicit solver was used to simulate three test cases, as shown in Table 3.8. The results were then compared to the reference solutions [57, 58].

Table 3.8: Description of Test Cases.

Test case number	Rayleigh number (Ra)	Dimensionless temperature difference (ε)	Density	Dynamic Viscosity and Thermal Conductivity
T1	10^6	0.6	Ideal gas equation	constant
T2	10^6	0.6	Ideal gas equation	Temperature dependent
T3	10^7	0.6	Ideal gas equation	Temperature dependent

3.3.4 Governing Equations and Solver Settings

The compressible form of the transient Navier-Stokes equations for a Newtonian fluid given by (3.12-3.14) along with the ideal gas equation and variable transport properties are solved using the Simcenter StarCCM+ coupled implicit solver.

$$\frac{\partial \rho}{\partial t} + \nabla \cdot (\rho \overline{V}) = 0 \tag{3.12}$$

$$\frac{\partial (\rho \overline{V})}{\partial t} + \nabla \cdot \left(\rho \overline{V} \times \overline{V} + p\bar{\bar{I}}\right) = \rho \overline{g} + \nabla \cdot \bar{\bar{\tau}} \tag{3.13}$$

$$\frac{\partial (\rho E)}{\partial t} + \nabla \cdot \left(\rho \overline{V} H\right) = \nabla \cdot (k \nabla T) + \rho \overline{g} \cdot \overline{V} + \nabla \cdot \left(\bar{\bar{\tau}} \cdot \overline{V}\right) \tag{3.14}$$

Where,

$\overline{V}$ = velocity vector

ρ = density

p = pressure

H = Specific total enthalpy

E = Specific total energy

T = Temperature

$\overline{\overline{\tau}} = \mu\left(\nabla\overline{V} + \nabla^T\overline{V} - \frac{2}{3}(\nabla\cdot\overline{V})\overline{\overline{I}}\right)$ = viscous stress tensor for a Newtonian fluid

$\overline{\overline{I}}$ = Identity matrix

k = thermal conductivity

μ = dynamic viscosity

A second-order-upwind scheme for discretization of convective flux terms, a second-order central-difference scheme for the diffusion terms, and the Roe Flux-Difference Splitting Scheme for the inviscid fluxes is used. A second-order implicit scheme was used for time stepping. The coupled implicit solver is based on modifying a compressible density-based solver with a suitable preconditioning matrix. Refer to Appendix A for details of the solution scheme implemented by the coupled implicit solver for solving low Mach number compressible flows.

3.3.4.1 Heat transfer rates

The local and average Nusselt number is evaluated as follows:

$$\mathrm{Nu(y)} = \frac{\mathrm{h(y).L}}{\mathrm{k_o}} = \frac{\mathrm{q(y).L}}{(\mathrm{T_h}-\mathrm{T_c}).\mathrm{k_o}} = \frac{\mathrm{L}}{(\mathrm{T_h}-\mathrm{T_c}).\mathrm{k_o}}\mathrm{k(T)}\left|\frac{\mathrm{dT}}{\mathrm{dx}}\right|_{\mathrm{wall}} \tag{3.15}$$

$$\overline{\mathrm{Nu}} = \frac{1}{\mathrm{L}}\int_{\mathrm{y=0}}^{\mathrm{y=L}}\mathrm{Nu(y)dy} \tag{3.16}$$

Where

h(y) = local heat transfer coefficient,

k_0 = thermal conductivity evaluated at T_o

$q(y) = k(T)\left|\frac{dT}{dx}\right|_{wall}$ = local heat flux.

Reference solutions report a quantity called the thermodynamic pressure ratio which is defined as follows:

$$P_t = P_o \frac{\int \frac{1}{T_o} d\forall}{\int \frac{1}{T} d\forall} \tag{3.17}$$

Where $\forall$ = volume of the system

This ratio signifies the net change in the pressure from the initial pressure P_o as the closed system reaches a steady state. This quantity is based on the conservation of mass of the system and is evaluated for the coupled implicit solver.

3.3.5 Spatial and Temporal Discretization

Three successively finer grids were used in this study, namely, 160 x 160 (Grid 3), 320 x 320 (Grid 2) and 640 x 640 (Grid 1). These grids are uniform, and no local-refining of the grid was done. The time step used was 0.001 seconds. Grid convergence studies according to techniques described by Roache [69] are used for numerical error estimation, and determination of the asymptotic order of convergence/accuracy of the Simcenter StarCCM+ coupled solver.

3.3.6 Results

The reference solutions were successfully reproduced using the Simcenter StarCCM+ coupled implicit solver, and good agreement was observed for local as well as average Nusselt numbers

values. Table 3.9 shows a comparison of the coupled implicit solver with the reference solutions [57, 58] for the case of dimensionless temperature difference $\varepsilon = 0.6$ and Rayleigh number 10^6.

Table 3.9: Comparison of Simcenter StarCCM+ coupled implicit solver with reference solution [57]

Test case T2: Ra = 10^6 and $\varepsilon = 0.6$ and variable thermophysical properties average quantities				
	Simcenter StarCCM+ Coupled implicit solver			Reference solution [57]
GRID size	160 x 160	320 x 320	640 x 640	
$\overline{Nu}$ (h)	8.75372	8.703645	8.69091	8.6866
$\overline{Nu}$ (c)	8.75372	8.703645	8.69091	8.6866
Pt/P_o	0.921371	0.923679	0.924283	0.924487

Table 3.10 shows results from the coupled implicit density-based solver on the 640 x 640 grid for all three benchmark cases. The maximum error in the computation of the average Nusselt numbers and thermodynamic pressure is 0.16%. The relative error observed in the T3 case solution is higher than that of the T2 case. This implies that a finer grid is required to maintain the same level of accuracy for computations at higher Rayleigh numbers. The second row from the bottom shows the actual order of convergence calculated from the results for the coupled implicit solver on the three successively finer grids. We can see that for the T1 case, the actual observed order of convergence of the solution is the same as the formal order of convergence i.e. '2'. For the T2 and T3 cases for which the thermophysical properties were assumed to be temperature dependent, the observed order of convergence is lower than 2. This shows that a finer grid would be required to achieve a grid-independent solution when the computations have to include the effect of thermophysical properties at high Rayleigh number flows as compared to computations with

constant thermophysical properties at lower Rayleigh numbers. The time required for the evolution of the flow from the initial condition to a steady state is dependent on the flow Rayleigh number. The final row of the table shows the physical time in seconds required for the flow to evolve and reach a steady state. The T1 case requires the smallest amount of time to evolve as the flow is at a lower Rayleigh number, and we do not include the temperature dependent thermophysical properties. The time required to reach steady state is more than double when the Rayleigh number is increased by a factor of 10 (T2 vs T3).

Table 3.10: Results for average Nusselt numbers and thermodynamic pressures from the Simcenter StarCCM+ coupled implicit density-based solver on the 640 x 640 grid.

	Case		
	T1	**T2**	**T3**
Average Nusselt number	8.86285	8.69091	16.26630
Reference Average Nusselt number	8.85978	8.68660	16.24100
Percentage error	-0.03%	-0.05%	-0.16%
Pt/Po	0.856243	0.924283	0.92194
Reference Pressure Ratio	0.856338	0.924487	0.92263
Percentage error	0.01%	0.02%	0.07%
Actual order of convergence	2.0	1.9	1.8
Physical Time required to reach steady state (seconds)	26	32	79

For a thorough benchmark of Simcenter StarCCM+, the results from the coupled implicit solver were compared to the most accurate reference solution submitted to the conference organized by INRIA and MAB in 2004 [57, 58]. This solution was by Vierendeels et al. [58]. The authors computed the solutions to the three test cases by solving the compressible Navier-Stokes equations

using an explicit third-order discretization for convective fluxes and line implicit discretization for diffusive fluxes on a 2048 x 2048 grid. Table 3.11 shows the local Nusselt numbers at six different locations and maximum local pressure in the cavity for the three test cases compared to the solutions provided by Vierendeels et al. [58]. For the T1 and T2 cases, the maximum local Nusselt number error is 0.3%. For the T3 case, the maximum error in the local Nusselt number is 1.30% and is observed at the cold wall. The streamlines and isotherms for the T2 and T3 cases computed on the 320 x 320 grid are shown in Figure 3.10.

Table 3.11: Results for local Nusselt numbers and pressures for the Simcenter StarCCM+ coupled implicit density-based solver for the 640 x 640 grid.

		Grid Size (N x N)	Nu-hot (0.5)	Nu-cold (0.5)	Nu-hot (max)	Nu-hot (min)	Nu-cold (max)	Nu-cold (min)	Pmax/Po
T1	Simcenter StarCCM+	N = 640	7.82027	8.79616	19.61498	1.07361	16.39134	0.85409	0.856247
	Vierendeels	N= 2048	7.81938	8.79636	19.59642	1.07345	16.36225	0.85512	0.856340
	% Error		-0.01	0.00	-0.09	-0.01	-0.18	0.12	0.01
T2	Simcenter StarCCM+	N = 640	7.4615	8.6370	20.2920	1.0670	15.5654	0.7554	0.924295
	Vierendeels	N= 2048	7.4593	8.6372	20.2704	1.0667	15.5194	0.7575	0.924489
	% Error		-0.03	0.00	-0.11	-0.03	-0.30	0.28	0.02
T3	Simcenter StarCCM+	N = 640	13.201	15.509	46.587	1.456	34.747	1.077	0.92195
	Vierendeels	N= 2048	13.189	15.512	46.379	1.454	34.272	1.089	0.92264
	% Error		-0.09	0.02	-0.45	-0.13	-1.39	1.11	0.07

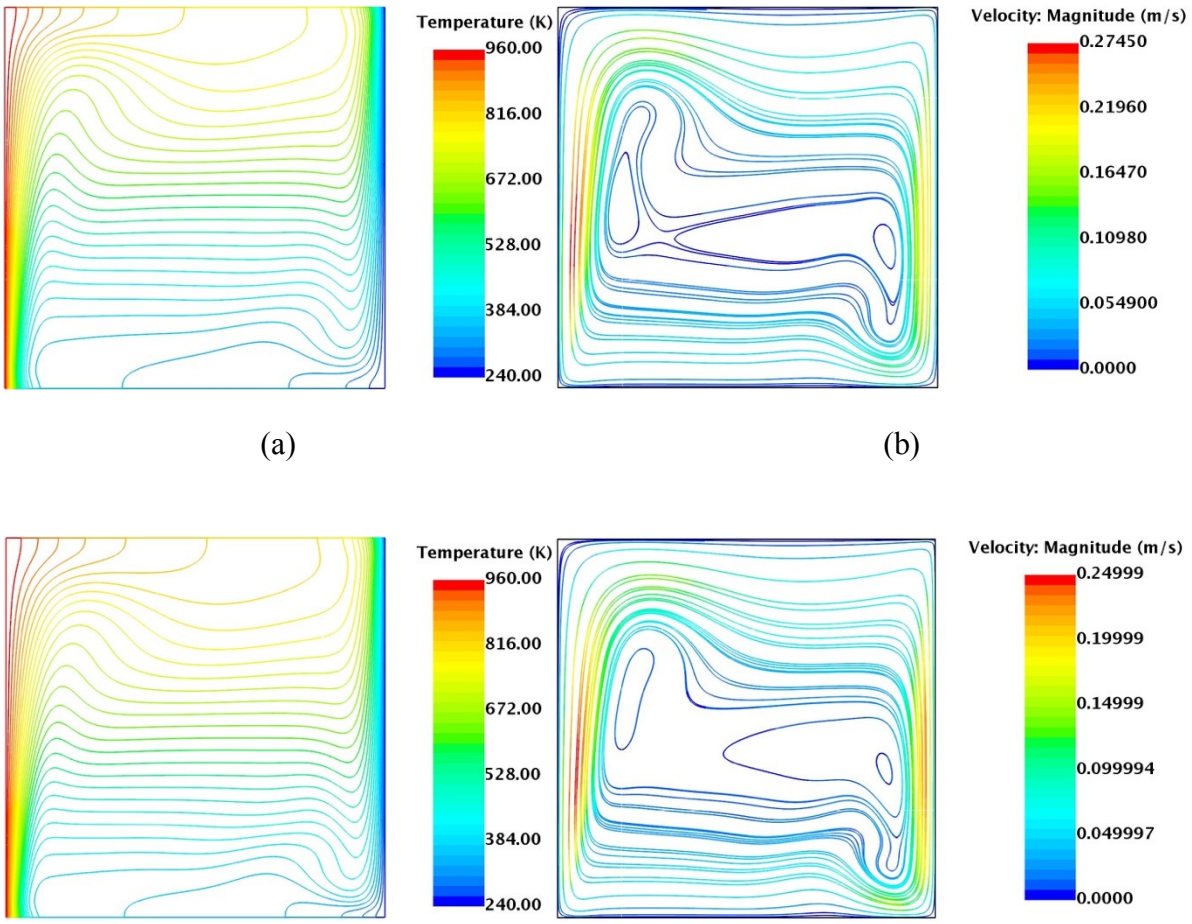

Figure 3.10: (a) Velocity vectors and (b) dimensionless temperature fields obtained using the coupled implicit solver for the T1 case (top figures) and T2 case (bottom) on a 640x640 grid.

Figures 3.11(a) and 3.11(b) show the temperature distribution along the horizontal and vertical midplane of the cavity for the T3 case computed on the 640 x 640 grid. In Fig. 3.11 (a) we can see the presence of the thermal boundary layers along the hot and cold walls. At this Rayleigh number Ra = 10^7, an almost linear temperature gradient exists inside the cavity. This is evident in Fig. 3.11(b) which shows the temperature distribution along the vertical midplane. The approximate value of the slope of this linear temperature gradient for a Rayleigh number of 10^7 is 42.8854 degrees.

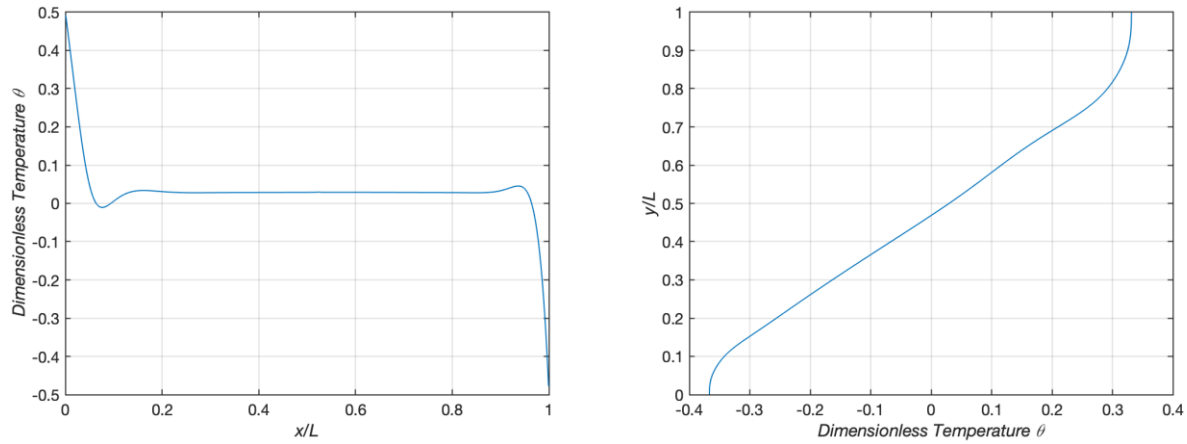

(a) (b)

Figure 3.11: (a) Dimensionless temperature along the horizontal midplane of the cavity y/L= 0.5; (b) Dimensionless temperature along the vertical midplane of the cavity x/L = 0.5 for T3 case.

Figure 3.12 (a) shows the vertical velocity distribution along different horizontal planes for the T3 case, and Figure 3.12(b) shows the total magnitude of velocity at these planes. The maximum velocity in the cavity occurs long the hot wall of the cavity, as seen in Fig. 3.12 (b).

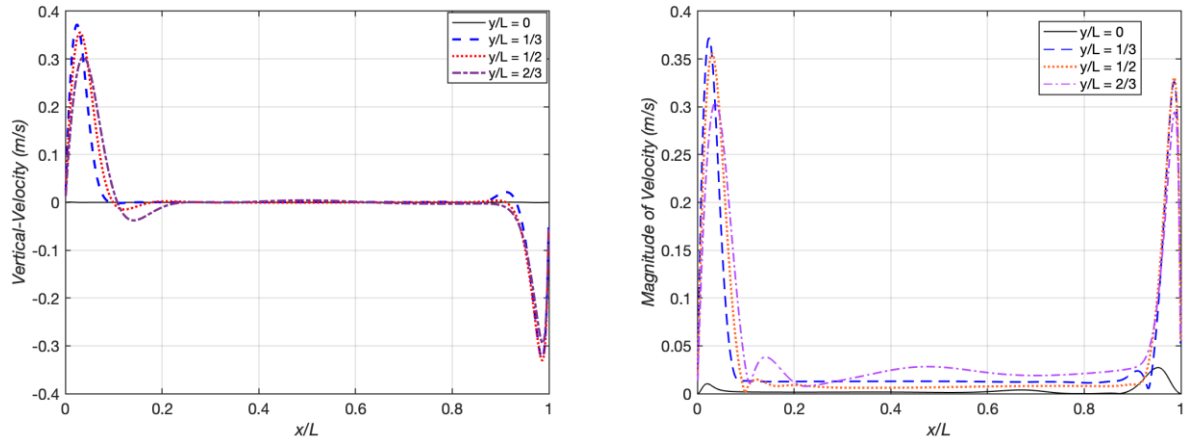

(a) (b)

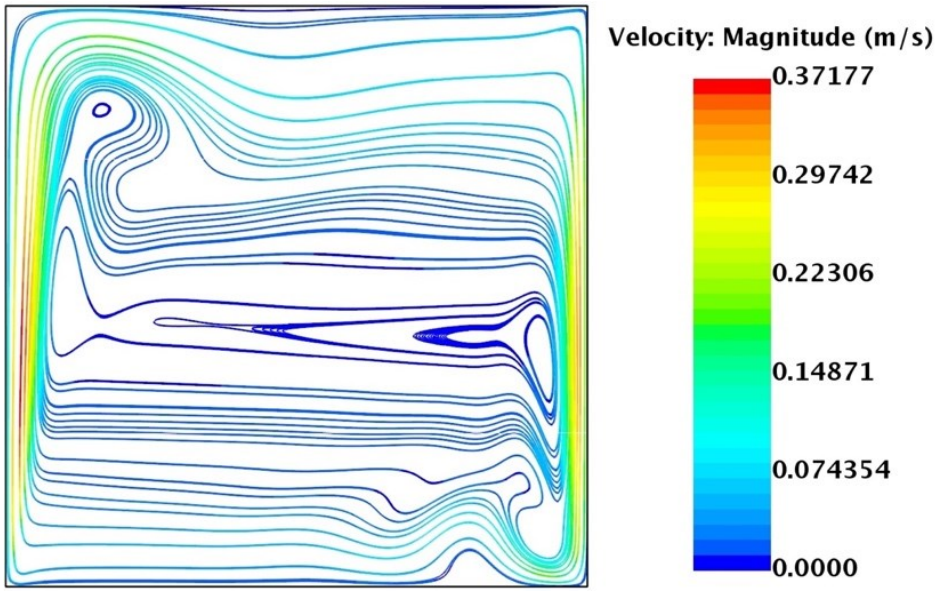

(c)

Figure 3.12: (a) Magnitude of velocity along four planes in the cavity y/L = 0, y/L = 1/3, y/L = 1/2, y/L = 2/3; (b) Vertical velocity along four planes in the cavity y/L = 0, y/L = 1/3, y/L = 1/2, y/L = 2/3; (c) Streamlines for T3 case.

There are two circulating cells present in the cavity, each located close to the cavity walls. The presence of these cells is evident from Fig. 3.12(a) and more clearly seen in Fig. 3.12(c). The velocity distributions in the cavity are not symmetric. The loss of symmetry is on account of the non-Boussinesq nature of the flow.

3.4 Key Results and Conclusions from Benchmarking Operation

The coupled implicit solver of Simcenter StarCCM+ was able to predict with reasonable accuracy the natural convection flows under both Boussinesq and non-Boussinesq conditions. Therefore, this solver will be used for the development of CFD models for simulating the experimental results for natural convection flows in annular and rectangular cavities with non-isothermal boundary conditions.

During the benchmarking operation it was also discovered that the variable thermophysical properties of air can have a profound effect on the nature of the cat's eye instability. In order to further investigate this effect, detailed numerical studies on the effects of non-Boussinesq temperature conditions and variable thermophysical properties on the nature of the cat's eye instability were performed. Results from these studies are presented in the next two chapters.

Chapter 4

4 EFFECT OF NON-BOUSSINESQ CONDITIONS ON NATURAL CONVECTION IN A TALL RECTANGULAR CAVITY

During the benchmarking operation for the experimental results of Vest and Arpaci [9] different predictions were obtained when air thermophysical properties were assumed either as constant or variable. This indicates that the nature of instability is sensitive to the temperature dependent thermophysical properties of air. In this chapter, the effects of variable air temperature properties and non-Boussinesq temperature conditions on the cat's eye instability of the rectangular cavity are investigated numerically for a tall air-filled rectangular cavity of aspect ratio A = 40.8. Assumptions of constant thermophysical properties can lead to a significant error in the prediction of local quantities for transient natural convection flows. Therefore, an effort has been made in this study to quantify the error associated with the assumption of constant thermophysical properties for non-Boussinesq flow conditions.

4.1 Introduction

There have been stability analyses [39, 40, 73, 74] and numerical studies [41-43] on flows inside differentially heated rectangular cavities under non-Boussinesq conditions which have shown that the flow structure depends on normalized wall temperature difference ε in addition to the Rayleigh number, Prandtl number, and aspect ratio.

$$\varepsilon = \frac{T_h - T_c}{T_h + T_c} = \frac{T_h - T_c}{2T_m}. \quad (4.1)$$

Linear stability analyses by Sulsov and Paolucci [40] showed that the instability of the conduction regime inside an infinitely tall cavity for any finite temperature difference is always an oscillatory instability, which manifests as a travelling wave drifting downward in the cavity. The same linear stability analyses showed that the nature of this instability is shear driven at low and intermediate temperature differences and is buoyancy driven at high temperature differences [40]. Non-linear analyses conducted by the same authors [73, 74] shed more light on the nature of these shear driven and buoyancy driven modes and their energy transfer mechanisms. The downward drifting waves predicted by stability theory have been experimentally observed by Simpkins [75], and more recently by Wright et al. [44] and Lartigue et al. [45] in tall cavities. The predicted *stationary* instability from studies in the Boussinesq limit results from an artificially imposed symmetry of the flow due to constant gas properties.

Majority of previous numerical studies for non-Boussinesq flows have focused on cavities of aspect ratios A< =10 [42, 43] while multicellular flows (cat's eye pattern) can be observed only for aspect ratio more than 12.5 [14]. The extensive study by Chenoweth et al. [41] does look at natural convection flows for non-Boussinesq conditions for aspect ratios between A = 1 to 100. However, the focus of their work is on the boundary layer regime in low aspect ratio air-filled cavities. Furthermore, they report that the increase in temperature difference parameter leads to a lower critical Rayleigh number for the conduction regime instability, whereas, the stability theory results by Suslov and Paolucci [40] predict the exact opposite trend. Thus, there is some ambiguity with respect to the flow behavior inside cavities with high aspect ratios which needs further investigation.

4.2 Objective and Scope of Study

The objective of the current study is to explore in detail effects of the dimensionless temperature difference ε on the two-dimensional flow structure and local heat transfer in a tall, differentially heated, air-filled rectangular cavity. An aspect ratio of A = 40.8 was chosen for comparison with experimental results [44, 45] from the literature; this cavity is also tall enough so that effects of stratification due to top and bottom walls are minimal; and the flow is in the conduction regime for the Rayleigh number range investigated. For infinitely tall rectangular cavities in the Boussinesq limit ($\varepsilon \rightarrow 0$), the critical Rayleigh number is $Ra_{c0} \approx 5707$ [40]. From experimental observations [44], the flow becomes three-dimensional when the Rayleigh number is increased beyond 10,000. This study is therefore restricted to the Rayleigh number range $Ra_{c0} < Ra < 9000$ for which, the flow is expected to be two-dimensional.

Prior results from linear stability theory by Suslov and Paolucci [40] with varying thermophysical properties (non-Boussinesq conditions) are illustrated by the dashed curve in Fig. 4.1(a). According to the criterion established by Gray and Giorgini [38], for air at standard atmospheric pressure, the Boussinesq approximation remains valid up to $\Delta T = 28.6°$ C, corresponding to a value of $\varepsilon \approx 0.05$ for a mean temperature of 300 K. The region left of the vertical line in Fig. 4.1(a) shows where the Boussinesq approximation remains valid. Between the dashed and vertical lines is a region of transient multicellular air-flows which have been, until now, remained relatively unexplored.

To study effects of the dimensionless temperature difference ε on the flow structure, simulations at Rayleigh numbers of 6000, 6800, 7800, and 8600 were performed. Simulations were carried out for each Rayleigh number while increasing the value of dimensionless temperature difference ε gradually until a critical state ε_c was reached and the flow transitioned from transient

multicellular convection to steady unicellular convection. Figure 4.1(b) summarizes all of the simulations carried out as part of present study.

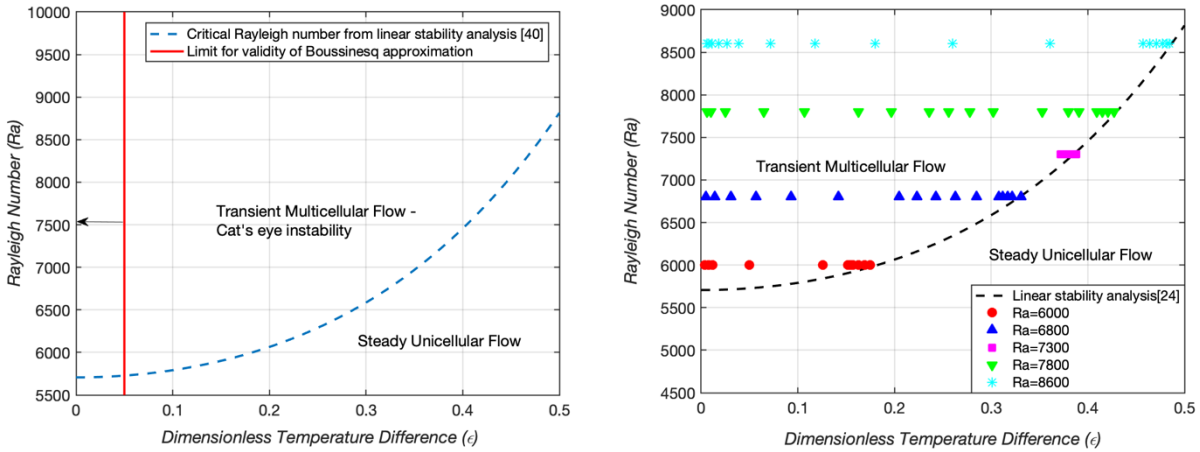

(a) (b)

Figure 4.1: (a) Critical Rayleigh numbers (dashed curve) from linear stability analyses for an infinitely tall rectangular cavity, non-Boussinesq conditions [40]; (b) Summary of simulations for air-flows in a tall rectangular cavity of A = 40.8, carried out in the present study.

4.3 Numerical Method

The fully compressible, transient, two-dimensional Navier-Stokes equations are solved for a Newtonian fluid using the commercial CFD code Simcenter StarCCM+ (Version 11.02.009-R8). Air is treated as an ideal gas, and its density ρ, dynamic viscosity μ, thermal conductivity k, and specific heat C_p are all temperature dependent properties. Dynamic viscosity and thermal conductivity are obtained by linear interpolation of tabulated data [76] as shown in Fig 4.2. Specific heat is expressed as a cubic polynomial fitted to tabulated data [76].

Since the coupled implicit solver of Simcenter StarCCM+ was able to predict with good accuracy natural convection flows under both Boussinesq and non-Boussinesq conditions, this

solver was used for solving the compressible Navier-Stokes equations. The compressible form of the transient Navier-Stokes equations for a Newtonian fluid given by equations (3.12) - (3.14) along with the ideal gas equation and variable transport properties are solved.

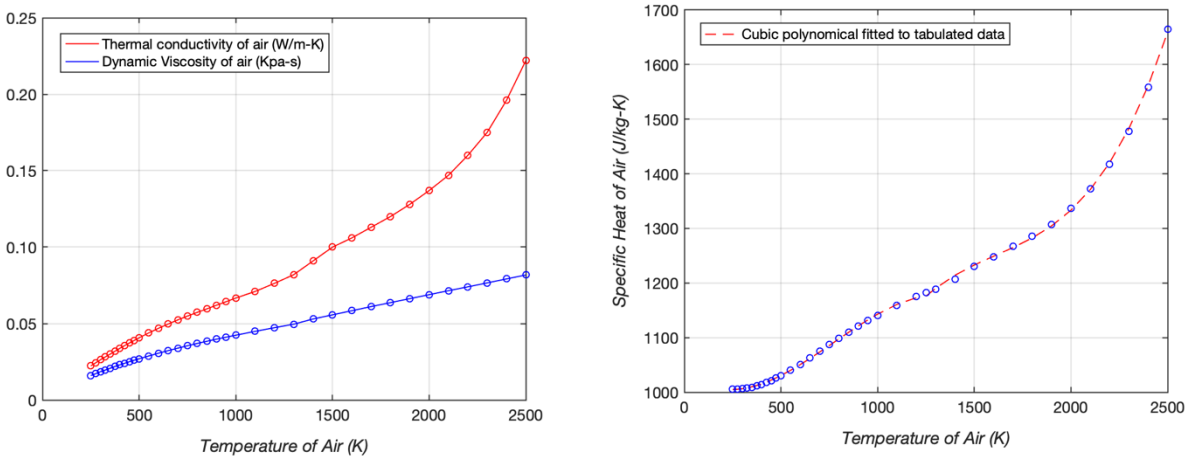

(a) (b)

Figure 4.2: (a) Variation of thermal conductivity and dynamic viscosity of air with temperature; (b) Variation of specific heat of air with temperature.

A second-order up-winding scheme for spatial discretization and an implicit second-order scheme for time discretization is used. The number of inner iterations is set so that the residuals for energy, continuity, and momentum equations are below 10^{-8}. Velocity and temperature fields are monitored to ensure the solution is converged at each time step. Time-steps from 0.01 to 0.0005 second are used depending on the values of the Rayleigh number and ε.

The physical dimension of the cavity used for the simulation is 0.0289 x 1.156 m. An orthogonal, non-staggered, quadrilateral mesh is used. The mesh is uniform everywhere except near the boundaries of the cavity where it is further refined using prism layer cells. The grid has 48 nodes in the horizontal x-direction and 2000 nodes in the vertical z-direction. The grid was

selected after a grid refinement study according to methods of Roache [69]. All simulations were done with an initial condition of motionless, isothermal air inside the cavity.

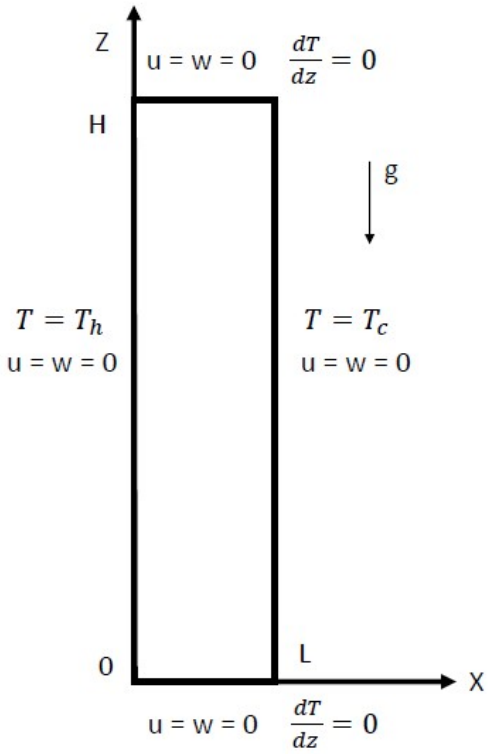

Figure 4.3: Geometry and boundary conditions for the two-dimensional problem.

4.4 Results and Discussion

Simulation results are first compared with predictions from linear stability analyses of Suslov and Paolucci [40]; the influence of the dimensionless temperature difference ε on the flow structure and heat transfer is subsequently described. For all simulations with $\varepsilon \leq \varepsilon_c$, the instability of the conduction regime was found to be a traveling wave that drifts downward in the cavity. This is in agreement with previous stability analyses [40, 73] and experimental results [44, 45, 75]. The observed downward drift of the cells can be attributed to the variation in air properties with

temperature. Instability of the conduction regime is shear driven and first appears near the inflection point of the cubic base-flow velocity profile where the shear is maximized. As the value of ε increases, the inflection point shifts closer to the cooled wall of the cavity due to thermally variable air properties. The air velocity is downward near the cooled wall and hence the instability also moves downward in the cavity [40].

From current numerical simulations, wavenumbers are found to change only slightly with ε, except near critical transitions between multicellular and unicellular flows; wave-speeds, on the other hand, are strongly affected by ε. Close to the Boussinesq limit ($\varepsilon \to 0$), wave-speeds for each of the four Rayleigh numbers are very small, yet finite. As the value of ε is increased for each Rayleigh number, there is a corresponding increase in the wave-speed. For all values of $\varepsilon > \varepsilon_c$, the simulated flow is steady and unicellular, i.e. the wave-speed is zero.

Although the dimensional form of Navier-Stokes equations were solved; for sake of presentation and comparison with previous studies, results in the subsequent sections are non-dimensionalized using suitable reference quantities for length, velocity, time, and temperature. Dimensionless velocities are given by

$$\bar{V} = \frac{V}{u_r} \tag{4.2}$$

where the reference velocity u_r is the thermal diffusion speed, $u_r = \frac{\alpha_m}{L}$, [40] and α_m is the thermal diffusivity of air evaluated at the mean wall temperature T_m. Dimensionless times are given by

$$\bar{t} = \frac{t}{t_r} \tag{4.3}$$

where the reference time t_r is $t_r = \frac{L}{u_r}$. Dimensionless temperatures are given by

$$\Theta = \frac{T - T_m}{T_h - T_c} \tag{4.4}$$

The downward drifting cells originate at the top of the cavity and then move downward at a constant speed till they reach the bottom portion of the cavity where they are destroyed. In the central portion of a tall cavity, the drift speed and the length of cells are constant. Therefore, the frequency of the oscillations in the velocity and temperature field caused by the downward drifting cells also remains constant in the central portion of the cavity. The wave-length 'λ' of the cat's eye instability is calculated based on the length of the central cell of the multicellular pattern. The reciprocal of the wavelength is expressed in terms of a dimensionless wavenumber given by

$$K_w = \frac{2\pi L}{\lambda} \tag{4.5}$$

The dimensionless wave-speed of the instability 'C' is calculated based on the wavenumber and the dimensionless time-period of velocity oscillations measured at the midpoint of the cavity.

$$C = \frac{2\pi L}{\bar{t}_p . K_w} \tag{4.6}$$

4.4.1 Comparison with Stability Theory

Stability theory for an infinitely tall rectangular cavity (A → ∞) under non-Boussinesq conditions predicts a dependence of critical Rayleigh numbers and critical wave-speeds on the dimensionless temperature difference ε. Critical Rayleigh numbers predicted by linear stability theory (A → ∞) [40] and critical Rayleigh numbers obtained by the current simulations (for A = 40.8) compare very well as shown in Fig. 4.4 (a). Although a tall cavity of finite aspect ratio has some degree of vertical stratification that is expected to stabilize the flow and enhance the transition from multicellular to unicellular flow, it appears that for a tall cavity of A = 40.8 under non-Boussinesq conditions, stratification produced by the ends of the cavity has only a small effect on critical

Rayleigh numbers. The maximum difference in critical Rayleigh numbers predicted from linear stability theory [40] and from Simcenter StarCCM+ simulations is less than 3.5%.

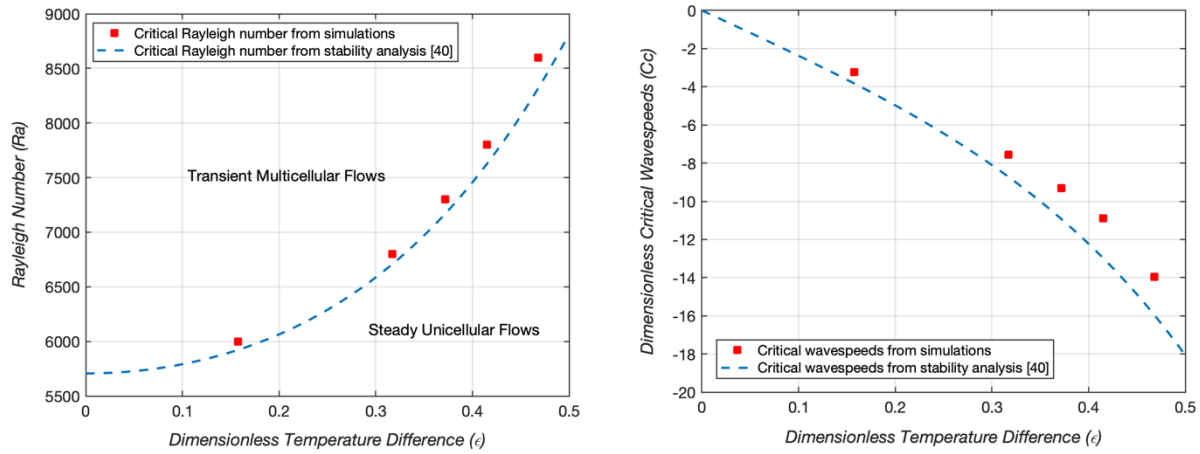

(a) (b)

Figure 4.4: (a) Critical Rayleigh numbers and (b) dimensionless critical wave-speed predicted by numerical simulations and linear stability analyses [40] as a function of dimensionless temperature difference ε.

Figure 4.4 (b) compares dimensionless critical wave-speed from linear stability theory [40] with results from current numerical simulations. Wave-speed within a finite cavity are likely to be reduced by end effects and vertical stratification. Critical wave-speed from numerical simulations at A = 40.8 are somewhat lower in magnitude, yet consistent with stability theory results from Suslov and Paolucci [40] for a rectangular cavity of infinite height.

4.4.2 Effect of ε on Simulated Wave-speed

For Rayleigh numbers $6000 \leq Ra \leq 8600$, and for every dimensionless temperature difference $0 < \varepsilon \leq \varepsilon_c$, the secondary cells drift downward in the cavity, i.e. the wave-speed is negative. Figure 4.5(a) shows simulated wave-speed for Rayleigh numbers 6000, 6800, 7800 and 8600. Although

there is strong dependence of wave-speed on ε, there is little dependence of dimensionless wave-speed on Rayleigh number in the range of $6000 \leq Ra \leq 8600$.

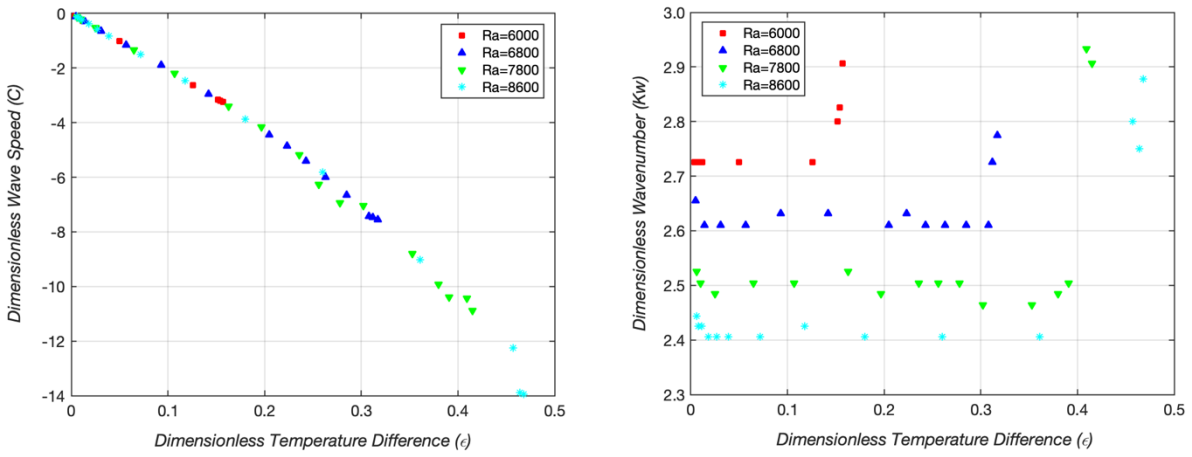

(a) (b)

Figure 4.5: Predicted dimensionless (a) wave-speed and (b) wavenumbers for Rayleigh numbers 6000, 6800, 7800, and 8600 as a function of dimensionless temperature difference ε.

Early experimental investigations [10, 9] close to the Boussinesq limit found the instability of the conduction regime to be a stationary wave based on photographs of smoke patterns. From Fig. 4.5 (a), the wave-speed approaches zero for small values of ε, and at such low values the instability might appear stationary. This could explain why experimenters who used smoke pattern visualizations [10, 9] reported the instability as a stationary wave. Early experimental investigation by P. Simpkins [75] reported non-zero wave-speed under high temperature difference conditions (high ε). Recent experimental studies [44, 45] which use techniques like particle image velocimetry and laser interferometry have observed non-zero wave-speed even for conditions of low temperature differences (low ε). These experiments further validate the observations from the

stability theory that the instability always has a non-zero wave-speed for any *finite* temperature difference.

4.4.3 Effect of ε on Simulated Wavenumber

Wavenumbers for $6000 \leq Ra \leq 8600$ are shown in Fig. 4.5 (b) to be a relatively weak function of ε except near the critical values ε_c. In the Boussinesq limit ($\varepsilon \rightarrow 0$), wavenumbers at Rayleigh numbers of 6000, 6800, 7800 and 8600 are 2.73, 2.66, 2.52 and 2.44, respectively. As ε is increased, the wavenumber decreases slightly then remains almost constant until ε approaches ε_c. Near the critical values of ε_c (transition between transient multicellular flow and steady unicellular flow) the wavenumbers increase to values between 2.75 and 2.95 for $6000 \leq Ra \leq 8600$. Here, the wavenumber K_w has stronger dependence on Rayleigh number and weaker dependence on ε, except as ε approaches ε_c.

4.4.4 Comparison with Experimental Results

Lartigue et al. [45] studied natural convection of air inside a rectangular cavity of aspect ratio 40 using particle image velocimetry. The heated and cooled walls in this experiment were not perfectly isothermal. Using their reported temperature variations, the value of ε could have been in the range $0.044 < \varepsilon < 0.054$ and the effective Rayleigh number could have been between $8300 < Ra < 10{,}100$ for an experiment in which they reported a downward drift of the secondary cells at 1.3 mm/s. The investigators also numerically simulated the flow using a scheme that allowed for temperature dependent properties. The predicted wave-speed from their numerical simulation was 1.34 mm/s.

To compare with Lartigue's results, Simcenter StarCCM+ numerical simulations were carried out at the minima and maxima of the Rayleigh number range and the range of ε corresponding to

their experimental conditions. Table 4.1 shows reasonable comparison between simulated values for wave-speed and wavenumber with the experimental values reported by Lartigue et al. [45].

Table 4.1: Comparison of Lartigue's experimental results [45] with numerically predicted wave-speed and wavenumbers.

	Wave-speed (m/s)	Wavenumber
Experimental Results, Lartigue et al. [45]	1.30E-03	2.386
Simcenter StarCCM+ Simulation: Ra = 10,100, $\varepsilon = 0.054$	1.87E-03	2.285
Simcenter StarCCM+ Simulation: Ra = 8300, $\varepsilon = 0.044$	1.45E-03	2.488

Wright et al. [44] also reported a downward drift of cells in experiments with a rectangular cavity of aspect ratio 40.8. At a Rayleigh number of 8600, they observed a downward wave-speed of 9.8 mm/s. The value of ε corresponding to their experimental conditions was 0.00566. From Simcenter StarCCM+ numerical simulations at a Rayleigh number of 8600 and $\varepsilon = 0.00566$, the predicted wave-speed for Wright's experimental conditions is 0.085 mm/s. This predicted wave-speed is two orders of magnitude lower than the experimental observation by Wright et al. [44]. The reason for this discrepancy is not fully understood. As the values of ε for experiments conducted by Wright et al. [44] and simulations done in the present study are of same magnitude and close to the Boussinesq limit, the velocity of the downward drifting cells should have been comparable. Linear stability theory results by Suslov and Paolucci [40] show presence of a buoyancy driven mode which exhibits much higher wave-speed compared to the shear driven mode. However, this buoyancy driven mode only exists for very high values of dimensionless temperature difference $\varepsilon > 0.5$ whereas the experiments by Wright et al. [44] were at a much lower ε value. Therefore, the higher wave-speed observed by Wright et al. [44] cannot be attributed to

the presence of a buoyancy driven mode of instability. A more plausible explanation could be presence of multiple solutions. All the simulations done as part of this study were done starting from a motionless isothermal state whereas the experiments of Wright [44] were done by continuously increasing the Rayleigh number. Presence of multiple solutions and hysteresis effects are commonly observed in natural convection flows. It is possible that the higher wave-speed mode observed by Wright et al. [44] is another shear driven mode which was captured by the experiments on account of different initial conditions than the ones used in our simulations.

4.4.5 Effect of ε on Local Nusselt Numbers

Local heat transfer rates along the heated and cooled vertical walls were evaluated using the local Nusselt number,

$$\mathrm{Nu}(z) = \frac{h(z).L}{k_m} = \frac{q(z).L}{(T_h - T_c).k_m} = \frac{L}{(T_h - T_c).k_m} k(T) \left|\frac{dT}{dx}\right|_{wall} \tag{4.7}$$

where h(z) is the local heat transfer coefficient, k(T) is the temperature dependent thermal conductivity, k_m is the thermal conductivity at the mean wall temperature T_m, and $q(z) = k(T) \left|\frac{dT}{dx}\right|_{wall}$ is the local heat flux.

The downward drift of the cells causes both spatial and temporal oscillations in local Nusselt numbers along the heated and cooled walls. The amplitude and time-period of these oscillations are strong functions of the dimensionless temperature difference ε. Figure 4.6 (a)-(d) show instantaneous spatial variations of local Nusselt numbers along the heated and cooled walls for a Rayleigh number of 6800, as the dimensionless temperature difference ε is increased from ε = 0.005 to the critical point ε_c = 0.317. Amplitudes diminish as the critical state is approached.

Beyond the critical point, e.g. at $\varepsilon = 0.322$ shown in Fig. 4.6 (d), the flow has transitioned from transient multicellular flow to steady unicellular flow, and the fluctuations have vanished.

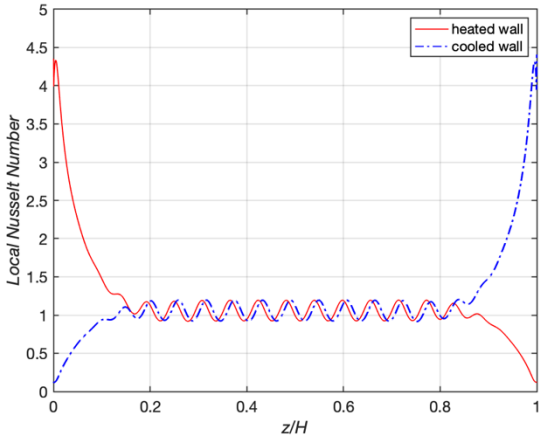

(a) $\varepsilon = 0.005$, Ra = 6800

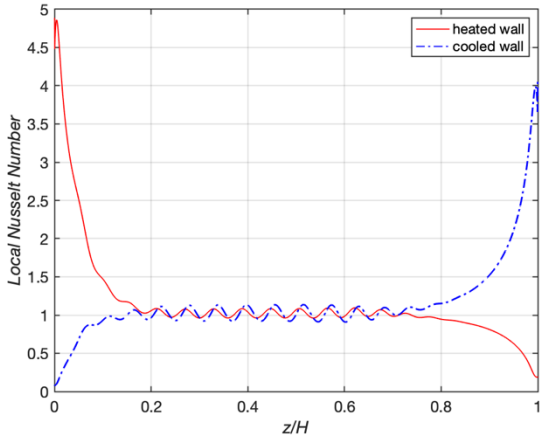

(b) $\varepsilon = 0.285$, Ra = 6800

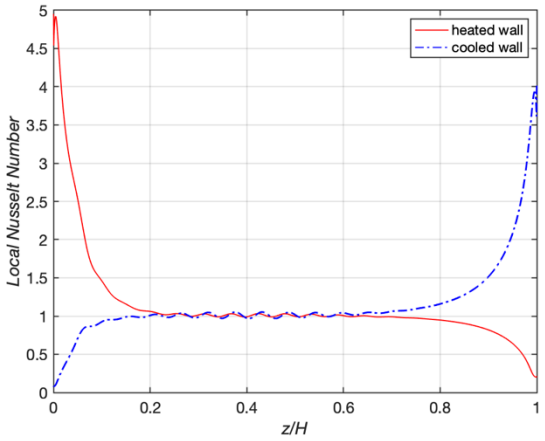

(c) $\varepsilon = 0.317$, Ra = 6800

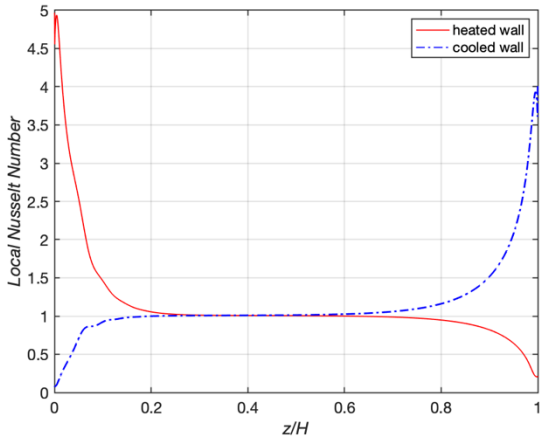

(d) $\varepsilon = 0.322$, Ra = 6800

Figure 4.6: (a)-(d) Local Nusselt numbers along the heated and cooled walls for a Rayleigh number of 6800 at selected values of the dimensionless temperature difference $\varepsilon = 0.005$ (a), $\varepsilon = 0.285$ (b), $\varepsilon = 0.317$ (c), and $\varepsilon = 0.322$ (d).

Drifting of the cells causes the local Nusselt number at a fixed location along the cavity wall to vary in time. Time-period of oscillations decreases as the value of ε is increased from $\varepsilon \approx 0$ to the critical state, $\varepsilon = \varepsilon_c$. Table 4.2 reports the maximum percent deviation in local Nusselt number

from its respective, temporal mean value at the vertical midpoints of the heated (x = 0, z = H/2) and cooled (x = L, z = H/2) walls for a Rayleigh number of 6800 at selected values of ε. The dimensionless time period over which the oscillations occur is also reported in Table 4.2. At small values of ε, deviations in local Nusselt numbers are as high as 14.8%, and the oscillation time period is large; at higher values of ε, deviations in local Nusselt numbers are smaller, and the oscillation time period is much shorter. Local Nusselt number deviations as high as 20% were predicted for Ra = 8600.

Table 4.2: Oscillation time periods and percent deviation in local Nusselt numbers at the midpoints of the heated (x = 0, z = H / 2) and cooled (x = L, z = H / 2) walls for Ra = 6800.

ε	Percent Deviation in Local Nusselt Number at the Heated Wall	Percent Deviation in Local Nusselt Number at the Cooled Wall	Dimensionless Time Period of Oscillation
0.005	12.75	12.86	20.85
0.014	13.75	14.08	7.86
0.057	13.48	14.82	2.08
0.142	10.71	13.84	0.81
0.308	4.94	9.62	0.32
0.317	1.96	3.56	0.30

An important point to be considered here is that, assumption of constant thermophysical properties leads to a prediction of stationary instability inside the cavity with the local Nusselt number at a given point not varying with time. However, in reality, the local Nusselt number at any point in the cavity varies significantly with time on account of the travelling wave nature of the instability. Therefore, assumption of constant thermophysical properties for these types of problems can lead to erroneous prediction of local heat transfer.

4.4.6 Small Effect of ε on Average Nusselt Numbers

Spatially averaged Nusselt numbers, $\overline{\mathrm{Nu}} = \frac{1}{H}\int_{z=0}^{z=H} \mathrm{Nu(z)}dz$, along the two vertical walls of the cavity are shown in Table 4.3 for the selected Rayleigh numbers in the Boussinesq limit ($\varepsilon \rightarrow 0$). These average Nusselt numbers change very little as the value of the dimensionless temperature difference is increased from $\varepsilon \approx 0$ to the critical state $\varepsilon = \varepsilon_c$. For all Rayleigh numbers in the range $6000 \leq \mathrm{Ra} \leq 8600$, the average Nusselt number along the vertical walls under non-Boussinesq conditions varies by no more than 2.5 percent of its value in the Boussinesq limit. In this Rayleigh number range therefore, the average Nusselt number remains almost unchanged as the dimensionless temperature difference is increased from $\varepsilon \approx 0$ to $\varepsilon = \varepsilon_c$, for fixed Ra.

Table 4.3: Spatially averaged Nusselt number $\overline{\mathrm{Nu}}$ ($0 \leq z \leq H$) at the wall, in the Boussinesq limit, and maximum percent deviation in $\overline{\mathrm{Nu}}$ as ε is varied from $0 < \varepsilon \leq \varepsilon_c$.

Rayleigh Number	Average Nusselt Number $\overline{\mathrm{Nu}}$ in the Boussinesq Limit	Maximum Percent Deviation in Average Nusselt Number $\overline{\mathrm{Nu}}$ under non-Boussinesq Conditions
6000	1.120	0.6
6800	1.161	1.8
7800	1.205	1.8
8600	1.237	2.5

4.4.7 Effect of ε on Flow Structure

For a Rayleigh number of 7800, and for respective ε values of 0.006 and 0.380, Figs. 4.7(a) and 4.7(b) show contour plots of instantaneous velocity magnitude (left plots) and horizontal velocity component (center plots). In these simulation results, the left wall is heated, and the right wall is cooled. Since multicellular flow does not occur in the cavity's upper and lower end regions, the

contour plots show velocities only in the central, multicellular flow regions. The plots on the far-right sides of Figs. 4.7(a) and 4.7(b) show instantaneous, dimensionless horizontal velocity components along the full height H of the cavity's mid-plane ($x = L / 2$, $0 \le z \le H$).

For small values of ε, the cell centers lie close to the vertical midplane of the cavity, as shown in Fig. 4.7(a) by the velocity contour plots and the horizontal velocity component along the z-axis at the cavity's mid-plane. At a dimensionless temperature difference of $\varepsilon = 0.006$, maximum velocities near the heated and cooled walls are almost equal.

For higher values of dimensionless temperature difference, e.g. $\varepsilon = 0.380$ as shown in Fig. 4.7(b) the cell centers have shifted toward the cooled wall. This is a result of lower air density adjacent to the heated wall and higher air density adjacent to the cooled wall. These effects become more pronounced at higher Rayleigh numbers.

The presence of multiple cells and their relative strengths are shown by plots at the far right of Figs. 4.7(a) and 4.7(b). Due to stratification effects near the cavity ends [14], cells near the vertical center of the cavity are strongest and cells closest to the ends of the cavity are weakest. In the two regions of the cavity where multicellular flow does not occur, a comparison can be made between penetration distances Z_{e1} for the upper end and Z_{e2} for the lower end of the cavity. At small values of ε, as shown in the far-right plot of Fig. 4.7(a) for $\varepsilon = 0.006$, the penetration distances from the upper and lower cavity ends are almost equal ($Z_{e1} \approx Z_{e2}$). As the dimensionless temperature difference is increased to $\varepsilon = 0.380$ as shown in the far-right plot of Fig. 4.7(b), the penetration distance from the upper end of the cavity, Z_{e1}, is increased while the penetration distance Z_{e2} from the lower end is decreased. For larger values of ε, Z_{e1} continues to increase relative to Z_{e2}. The penetration distance Z_{e1} reaches its maximum value at the critical state, ε_c. Hence, for a fixed Rayleigh number, as the critical state is approached with increasing values of ε

and Z_{e1}, there is a corresponding decrease in wavelength/increase in wavenumber, as previously shown in Fig. 4.5(b).

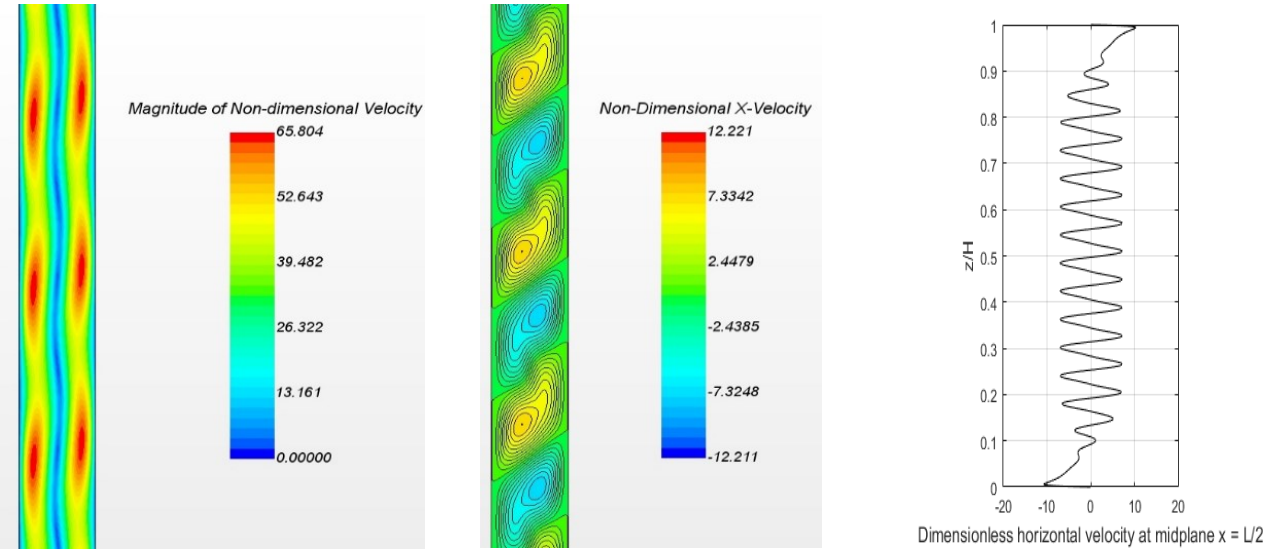

(a) $\varepsilon = 0.006$, Ra = 7800

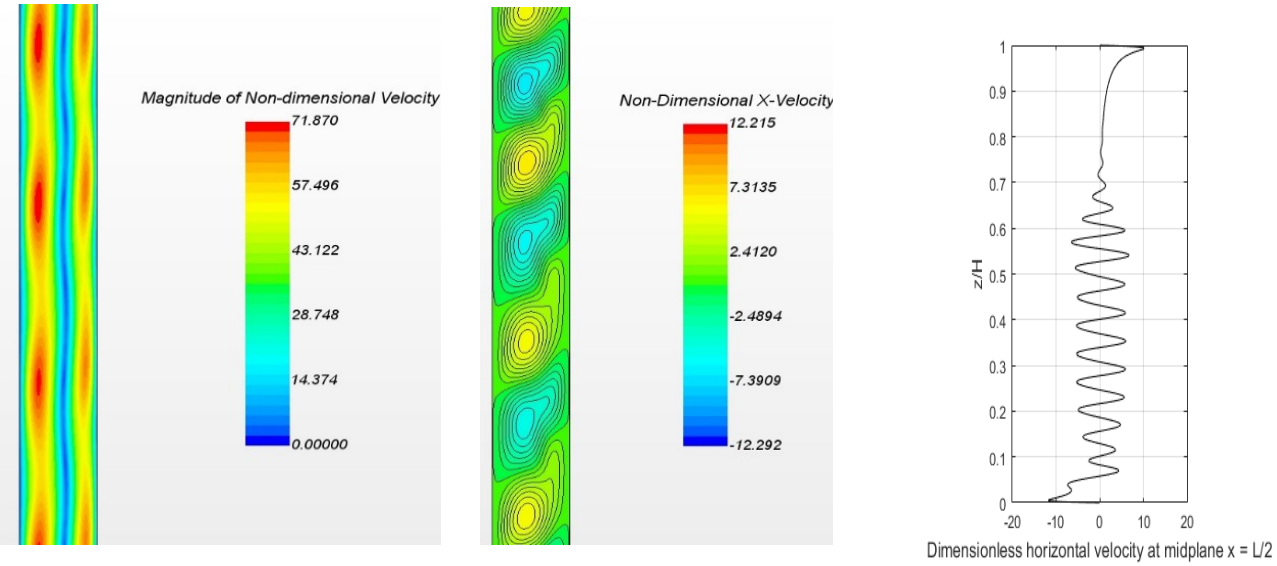

(b) $\varepsilon = 0.380$, Ra = 7800

Figure 4.7: Contour plots of dimensionless velocity (left) and dimensionless horizontal velocity component (center) with dimensionless horizontal velocity component (right) on the cavity's mid-plane ($x = L / 2$, $0 \leq z \leq H$), for values of (a) $\varepsilon = 0.006$ and (b) $\varepsilon = 0.380$ at Ra = 7800.

4.4.8 Transient Mono-Periodic and Quasi-Periodic Flows

At a Rayleigh number of 6000, temporal evolutions of dimensionless temperature at the center point of the cavity (x = L / 2, z = H / 2) are given in Fig. 4.8(a)-(d) for values of ε = 0.004 (a), ε = 0.012 (b), ε = 0.050 (c), and ε = 0.152 (d).

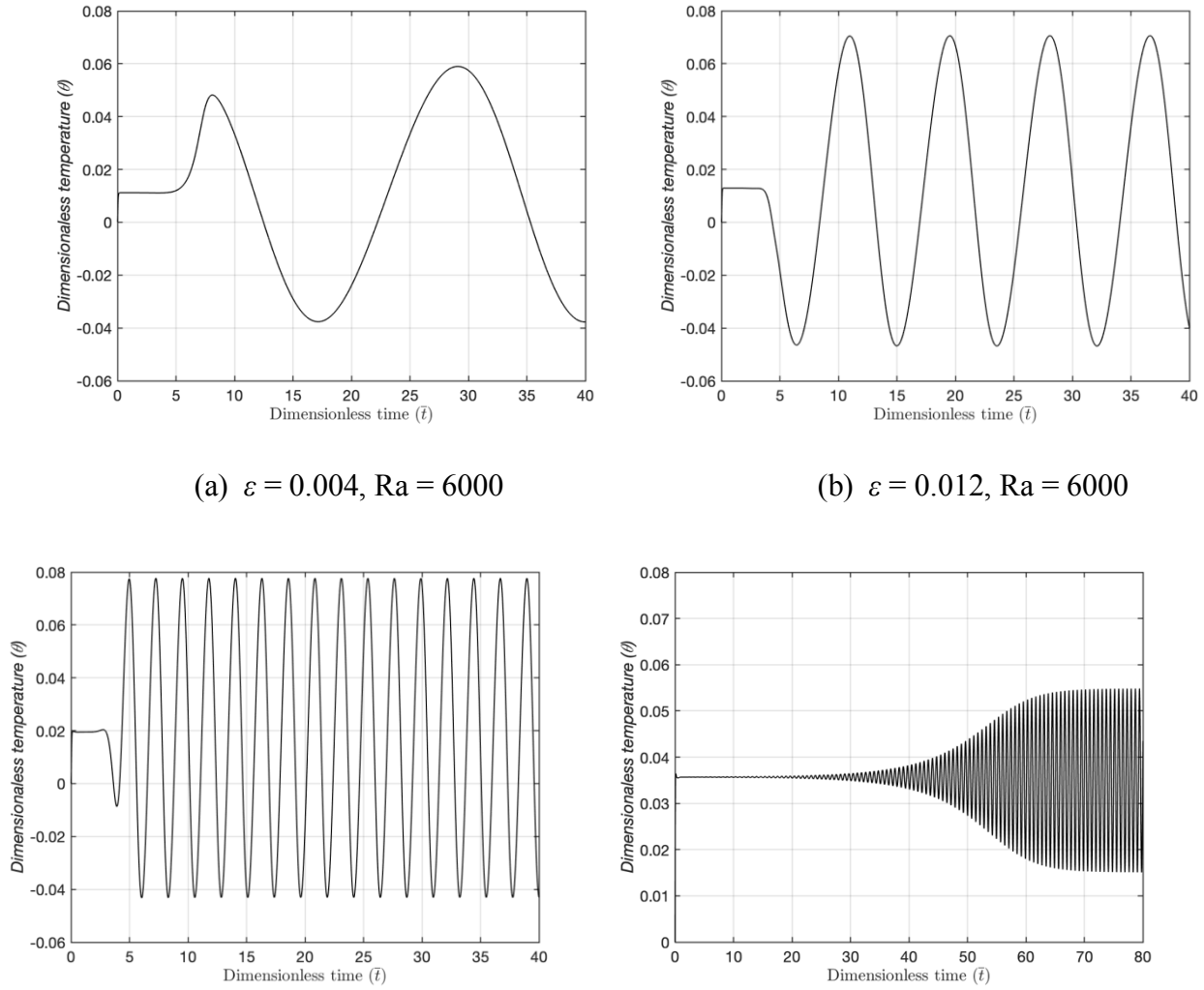

(a) ε = 0.004, Ra = 6000

(b) ε = 0.012, Ra = 6000

(c) ε = 0.050, Ra = 6000

(d) ε = 0.152, Ra = 6000

Figure 4.8: (a)-(d) Temporal evolution of dimensionless temperature θ at the cavity center (x = L / 2, z = H / 2) for a Rayleigh number of 6000 and selected values of ε = 0.004 (a), ε = 0.012 (b), ε = 0.050 (c), and ε = 0.152 (d).

For a fixed Rayleigh number, at small values of the dimensionless temperature difference ε, the frequency of oscillations is low; as the value of ε is increased, the frequency of oscillations increases and becomes highest at the critical state ε_c. With increasing value of ε, the amplitude of the oscillations first increases, then diminishes as the critical state is approached. Thus, the time evolution of temperature in the flow field strongly depends on the dimensionless temperature difference ε.

For Rayleigh numbers 6000, 6800, and 7800, all simulated transient flows were mono-periodic. At a Rayleigh number of 8600, all simulated flows were mono-periodic for $\varepsilon \leq 0.361$, but quasi-periodic for $0.457 < \varepsilon \leq \varepsilon_c$. Figure 4.9(a) shows the temporal evolution of dimensionless temperature near the cavity center point, and Fig. 4.9(b) shows the power spectral density function for a simulated quasi-periodic flow at Ra = 8600 and $\varepsilon = 0.464$.

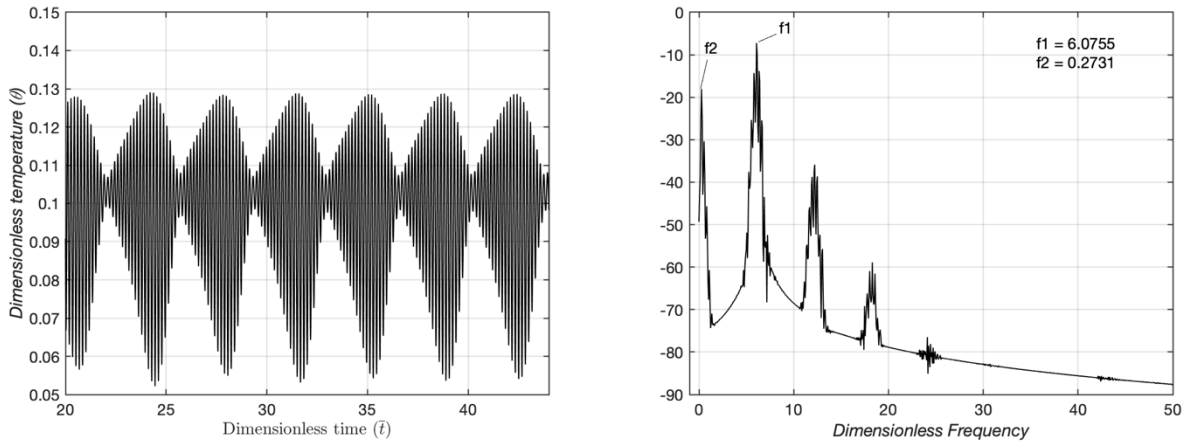

(a) (b)

Figure 4.9: (a) Dimensionless temperature θ near the cavity center (x = L / 2, z = H / 3), and (b) power spectral density function for simulated quasi-periodic flow at a Rayleigh number of 8600 and $\varepsilon = 0.464$.

The power spectral density function shows the presence of two fundamental frequencies; all other frequencies are linear combinations of these two frequencies. The ratio of the lower to higher frequency is 0.045. The first dominant frequency, f_1, observed in the quasiperiodic flows seems be the frequency corresponding to the shear-driven mode from making order of magnitude comparisons of its wave-speed to the linear stability theory. The second dominant frequency, f_2, is a lower frequency compared to f_1. Since the buoyancy driven mode (observed at high ε values) is significantly faster as compared to the shear driven mode, f_2 cannot be associated with the buoyant mode as it is almost 22 times *lowe*r than f_1. In the time trace of temperature shown in Figure 4.9(a), f_2 appears as a low frequency modulating the higher frequency f_1. Similar behavior of a fundamental frequency being modulated by a lower frequency has been observed experimentally by Le Quéré and Penot [61] in their experiments with rectangular cavities of aspect ratio A = 4 in the boundary layer regime.

4.4.9 A Final Note on Variable Thermophysical Properties

Downward drifting cells in the cavity results from a loss of flow symmetry due to temperature dependent thermophysical properties, which include density, viscosity, thermal conductivity and specific heat of air. To ascertain which properties, play the greater roles in transient flow behavior, seven different simulations (cases 1 - 7) were run and compared for Ra = 6000 and $\varepsilon = 0.05$. Case 1 simulation (most accurate) allowed all properties to vary and did not invoke the Boussinesq approximation. Case 2 simulation allowed density and viscosity to vary, while holding thermal conductivity and specific heat constant. Cases 3 through 6 held three properties constant while allowing a single property to vary. A final simulation (case 7, least accurate) held all four properties constant and invoked the Boussinesq approximation.

Wavenumbers, wave-speed and oscillation time periods for each of the cases are reported in Table 4.4. Although wavenumbers are practically unaffected by variable / constant properties, wave-speed and the time period of oscillations are most strongly affected by temperature dependent density and viscosity and are least affected by variations in the specific heat of air.

Table 4.4: Effects of variable / constant thermophysical properties on predicted dimensionless wave-speed for Ra = 6000 and $\varepsilon = 0.05$.

Case	Density	Viscosity	Thermal Conductivity	Specific Heat	Wave-number	Wave-speed (Dimension-less)	Time Period (Dimension-less)
1	V	V	V	V	2.70	1.027	2.26
2	V	V	C	C	2.70	0.879	2.65
3	V	C	C	C	2.70	0.482	4.83
4	C	V	C	C	2.73	0.393	5.87
5	C	C	V	C	2.73	0.143	16.14
6	C	C	C	V	2.73	-	> 72.7
7	C	C	C	C	2.70	Stationary Cells	-

* **Note:** V = variable and C = constant

4.5 Key Results and Conclusions

The aim of this study was to examine air-flows inside a tall, differentially heated rectangular cavity under Boussinesq and non-Boussinesq conditions and to determine the effects of the dimensionless temperature difference ε on the nature of flow and heat transfer inside the cavity. As was previously established, flows inside the rectangular cavity in the conduction regime are prone to a shear driven instability. Solving the Navier-Stokes equations and allowing all fluid properties to vary with temperature revealed that the instability of the conduction regime is not a stationary wave, as has been previously reported, but rather a travelling wave that drifts downward in the cavity. The

wave-speed is a strong function of the dimensionless temperature difference ε. Recent experiments in tall rectangular cavities confirmed the existence of finite wave-drift velocities; however, the observed wave-speed in an experiment from Lartigue et al. [45] showed good agreement, while the wave-speed from Wright et al. [44] showed poor agreement compared to predicted wave-speed from Simcenter StarCCM+ simulations.

While the wave-drift speed can be very small, it is not identically zero for any finite value of the dimensionless temperature difference ε. Previous numerical simulations that invoked the Boussinesq approximation did not show a downward drift of the cells because the equations did not allow for variation in the thermophysical properties of air. To accurately predict the downward drift speed of the cells it is essential to allow for variation of all the thermophysical air properties including density, viscosity, thermal conductivity and specific heat.

For the range of Rayleigh numbers that were studied, the cell centers begin to shift towards the cold wall of the cavity with increasing values of the dimensionless temperature difference ε. For small values of ε, at any Rayleigh number in the range between $5707 < Ra < 9000$ flow consisted of slowly downward drifting cells centered very close to the cavity's mid-plane at $x = L / 2$. With increasing values of ε, the velocity of the downward drift of the cells increases and the cells become centered closer to the cavity's cooled wall. For a fixed Rayleigh number, as the dimensionless temperature difference ε approaches the critical value ε_c, flow stratification becomes increasingly important. End effects from the upper wall extend further into the cavity, resulting in shorter cell wavelengths as $\varepsilon \rightarrow \varepsilon_c$.

While heat transfer in a tall rectangular cavity depends on the Rayleigh number, the average heat transfer rate across the cavity is practically unaffected by changes in the dimensionless

temperature difference ε. At a fixed Rayleigh number, the spatially averaged Nusselt number along a vertical wall varies by no more than 2.5% for values of ε ranging from $0 < \varepsilon \leq \varepsilon_c$.

On the other hand, local heat transfer rates and flow structure are strongly affected by the dimensionless temperature difference ε. The frequency of local Nusselt number oscillations increases with higher values of ε, reaching a maximum frequency at $\varepsilon = \varepsilon_c$ for a fixed Rayleigh number. As the dimensionless temperature difference is varied between $\varepsilon \approx 0$ and ε_c, local Nusselt numbers at the midpoint of a vertical wall of the cavity were found to vary by as much as 20% for a Rayleigh number of 8600. For a fixed Rayleigh number, as ε nearly approaches ε_c, the amplitude of local Nusselt number oscillations is diminished, and for $\varepsilon > \varepsilon_c$, the flow field becomes steady unicellular. Therefore, for applications where local heat transfer rates are crucial, the effect of the dimensionless temperature difference ε must be considered for the purpose of accurately predicting the local transient flow structure and heat transfer rates.

Chapter 5

5 EFFECT OF NON-BOUSSINESQ CONDITIONS ON THE UNSTEADY CAT'S EYE INSTABILITY OF THE ANNULAR CAVITY

Many numerical and experimental studies have investigated the unsteady cat's eye instability observed in air-filled annular cavities under low-temperature difference or Boussinesq conditions. However, to my knowledge, no experimental or numerical study has looked at the effects of non-Boussinesq conditions on the nature of this instability. In the previous chapter, it was established that temperature dependent air properties and non-Boussinesq conditions could significantly alter behavior of the cat's eye instability observed in rectangular cavities. Therefore, it is highly probable that a similar effect of non-Boussinesq conditions will also be observed for the annular cavity case. In this chapter, the effects of non-Boussinesq temperature conditions on bifurcations observed with increasing Rayleigh numbers in an air-filled annular cavity (Pr = 0.71) will be investigated.

5.1 Scope of Study

An air-filled annular cavity of aspect ratio A = 40 and radius ratio $\eta = 0.8$ is considered for this study. For a cavity of this large an aspect ratio, the effects of the top and bottom walls are limited to the end regions and parallel base flow exists in the central region of the cavity. Therefore, comparisons with stability theory ($A \rightarrow \infty$) based on the flow in the central part of the cavity can be made. The radius ratio of $\eta = 0.8$ was chosen to avoid the possibility of asymmetric disturbances

[33, 34] expected in cavities with $\eta < 0.44$. Non-Boussinesq conditions for this problem are quantified in terms of a dimensionless temperature difference parameter 'ε' which is the normalized wall temperature difference and is given by the ratio

$$\varepsilon = \frac{\Delta T}{2T_m} = \frac{T_h - T_c}{T_h + T_c} = \frac{T_h - T_c}{2T_m}. \tag{5.1}$$

Where $\Delta T = T_h - T_c$ is the temperature difference between inner and outer isothermal cylinders of the cavity and $T_m = \frac{T_h + T_c}{2}$ is the mean wall temperature. Three values of the normalized wall temperature difference ε namely, 0.005, 0.1, 0.2 are investigated. Figure 5.1 shows a summary of all the simulations done as part of this study. The region to the left of the dashed vertical line shows the well-explored region where the Boussinesq approximation is valid for air-filled cavities, while, the region to right of the dashed line is where non-Boussinesq effects are to be expected.

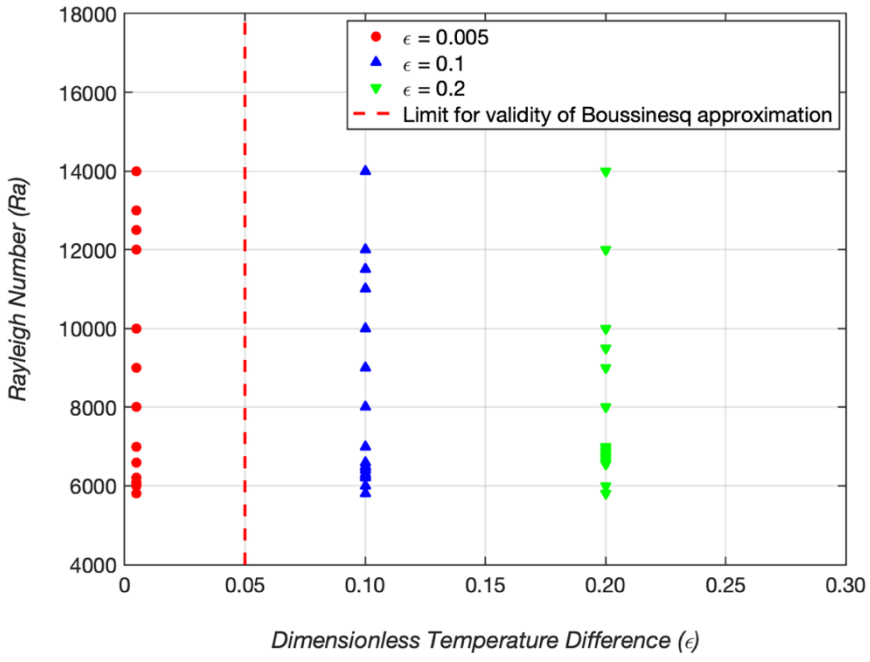

Figure 5.1: Summary of simulations for air-flows in a tall annular cavity A = 40, η = 0.8 carried out in the current study. Dashed curve represents limit of Boussinesq approximation for air [38].

5.2 Problem Definition

Consider an annular cavity comprising of an inner cylinder of radius r_i, outer cylinder of radius r_o and height H. The annular air-gap width 'L' is given by $r_o - r_i$ and the aspect ratio 'A' is given by A = H/L. The radius ratio 'η' is given by $\eta = r_i/r_o$. The outer cylinder is heated isothermally at a temperature T_h and the inner cylinder is cooled isothermally a temperature T_c, where, T_h and T_c are absolute temperatures and $T_h > T_c$. The horizontal top and bottom surfaces are insulated. The fluid inside the cavity is air at atmospheric pressure. The aspect ratio of the cavity is A = 40 and radius ratio is $\eta = 0.8$. For this geometry, the flow inside the cavity is assumed axisymmetric following conclusions of McFadden [33]. u is the axial component and v is the radial component of velocity. Figure 5.2 shows the simulation domain and boundary conditions for this problem.

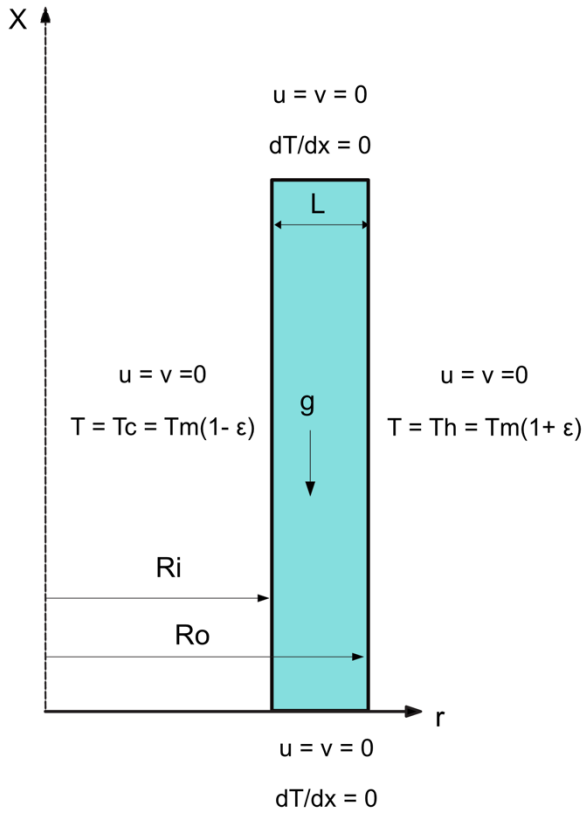

Figure 5.2: Geometry of problem and temperature boundary conditions.

The initial conditions used for the problem are as follows:

$$u(x,r) = u_o = v(x,r) = v_o = 0$$
$$T(x,r) = T_o = T_m \qquad (5.2)$$
$$\rho(x,r) = \rho_o = \frac{P_o}{RT_o}$$

$$P(x,r) = P_o = P_{atm} + \frac{P_{atm}}{RT_m} g(H-x) \text{ and } P_{atm} = 101325 \text{ Pa}$$

Rayleigh number of the flow is given by,

$$Ra = \frac{g\,\beta\,\Delta T\,L^3}{\upsilon\,\alpha} = \frac{2\,\varepsilon\,g\,L^3}{\upsilon\,\alpha} \qquad (5.3)$$

Where, the temperature dependent air properties, including the thermal expansion coefficient β, kinematic viscosity υ, and thermal diffusivity α, are evaluated at the mean wall temperature T_m, g is the local gravitational acceleration and L is the air-gap width.

Three independent cases of normalized wall temperature difference ε, are investigated:

Case (1) ε = 0.005 (Boussinesq conditions)

Case (2) ε = 0.1 (Moderately non-Boussinesq conditions)

Case (3) ε = 0.2 (non-Boussinesq conditions)

The first condition $\varepsilon = 0.005$ corresponds to flow under Boussinesq conditions. The next two conditions, $\varepsilon = 0.1$ and $\varepsilon = 0.2$, correspond to increasingly non-Boussinesq temperature conditions. For each fixed value of dimensionless temperature difference ε, Rayleigh number of the flow is progressively increased starting from a value at which steady unicellular flow is predicted up to a

value of 14000. For this Rayleigh number range, flow in tall air-filled annular cavities is in the conduction regime and is prone to the cat's eye instability characteristic of this regime.

5.3 Governing Equations and Numerical method:

The fully compressible, transient, axisymmetric Navier-Stokes equations (3.12) - (3.14) are solved for flow of a Newtonian fluid. Air is treated as an ideal gas, and its density ρ, dynamic viscosity μ, thermal conductivity k, and specific heat C_p are all temperature dependent properties. Dynamic viscosity and thermal conductivity are obtained by linear interpolation of tabulated data in [56]. Specific heat is expressed as a cubic polynomial fitted to tabulated data in [56].

The coupled implicit solver available in the commercial CFD software Simcenter StarCCM+ is used for solving the equations. The coupled solver algorithm is based on the approach of modifying a compressible density-based hyperbolic solver using preconditioning schemes to be efficient and accurate under conditions of low Mach number compressible flows. The coupled density-based implicit solver solves the conservation equations for continuity, momentum, and energy simultaneously as a vector set of equations. Pre-conditioning methods based on Turkel's family of pre-conditioners for ideal gas flows are used to prevent ill conditioning at low Mach numbers by this solver [55]. In Chapter 3, this Simcenter StarCCM+ solver was thoroughly benchmarked against several available solutions for Boussinesq and non-Boussinesq natural convection closed cavity flow problems.

For spatial discretization, a second-order up-winding scheme for convective terms and a second-order central discretization scheme for diffusive terms is selected. For time discretization, an implicit second-order scheme is selected. The transient form of equations is solved by the coupled solver using a dual time-stepping approach with inner iterations in pseudo-time. Time-

steps ranging from 0.01 to 0.001 seconds are used based on the values of the ε and Rayleigh number. An orthogonal, non-staggered, quadrilateral mesh which is uniform everywhere except near the boundaries of the cavity where it is further refined using prism layer cells is used. A fine mesh with 50 nodes in the radial-direction and 2000 nodes in the axial-direction based on grid refinement studies is used in order to capture all the flow features accurately.

5.4 Results

For this study, the dimensional form of Navier-Stokes equations is solved. However, for the sake of presentation and comparison with previous results from literature all the results in the subsequent sections will be presented in terms of dimensionless quantities. The results are non-dimensionalized using suitable characteristic scales for length, velocity, time, and temperature.

Dimensionless lengths are given by

$$\bar{x} = \frac{x}{L} \quad \text{and} \quad \bar{r} = \frac{r}{L} \tag{5.4}$$

Dimensionless velocities are given by

$$\bar{u} = \frac{u}{V_r} \quad \text{and} \quad \bar{v} = \frac{v}{V_r} \tag{5.5}$$

where characteristic velocity V_r is given by, $V_r = \frac{\nu_m \sqrt{Ra}}{L}$ and ν_m is the kinematic viscosity of air evaluated at mean wall temperature T_m. The velocity scale V_r was selected as it is an appropriate scale for convective flows of moderate and low Pr number fluids [43].

Dimensionless times are given by

$$\bar{t} = \frac{t}{t_r} \tag{5.6}$$

where the characteristic time t_r is $t_r = \frac{L}{V_r}$.

Dimensionless temperatures are given by

$$\Theta = \frac{T - T_m}{T_h - T_c}. \tag{5.7}$$

In the following sections, the structure of steady unicellular flow, first onset of cat's eye instability and subsequent flow bifurcations observed with an increasing Rayleigh number are discussed for each value of dimensionless temperature difference ε. Finally, the effect of ε, on the local and average heat transfer is discussed.

5.4.1 Steady Flow

For all three values of ε, a steady unicellular flow comprising of fluid rising along the hot outer cylinder and falling along the cold inner cylinder is observed for a Rayleigh number of 5800. Figure 5.3 shows the axial velocity along the horizontal midplane and Fig. 5.4 (a) and (b) shows the isotherms and velocity field for ε = 0.005, 0.2 at Ra = 5800. Under Boussinesq temperature conditions (ε = 0.005), the location of maximum velocity occurs close to the cold inner cylinder while the location of zero velocity occurs at the midpoint of the cavity width. As temperature conditions become non-Boussinesq (ε = 0.1 and 0.2), location of zero-flow velocity and location of maximum flow velocity both begin to shift more and more towards the cold inner cylinder . For both Boussinesq and non-Boussinesq conditions, velocity field in most part of the cavity except for top/bottom end regions, is parallel to the cavity axis. The temperature fields for all three cases of ε at Ra = 5800 are very similar and consist of almost vertical isotherms indicative of the conduction regime.

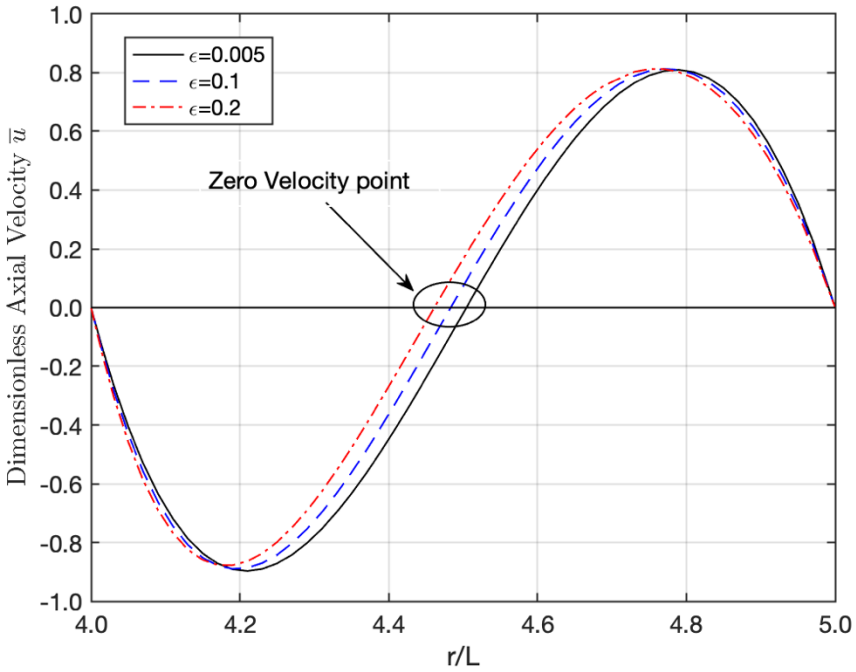

Figure 5.3: (a) Dimensionless axial velocity profiles at the horizontal midplane of the cavity ($\bar{x}$ = H/2L) for ε = 0.005, 0.1 and 0.2 at Ra =5800.

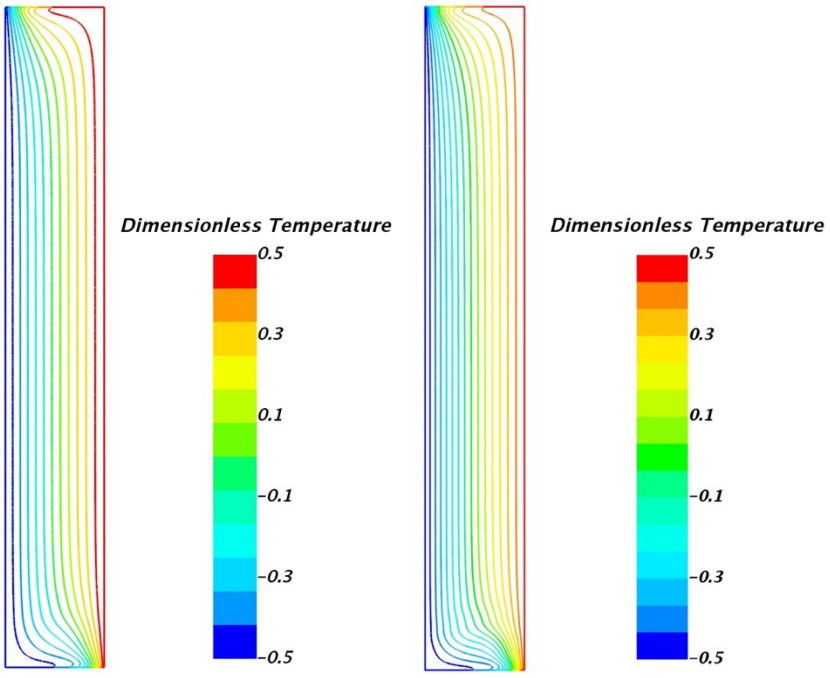

(a)

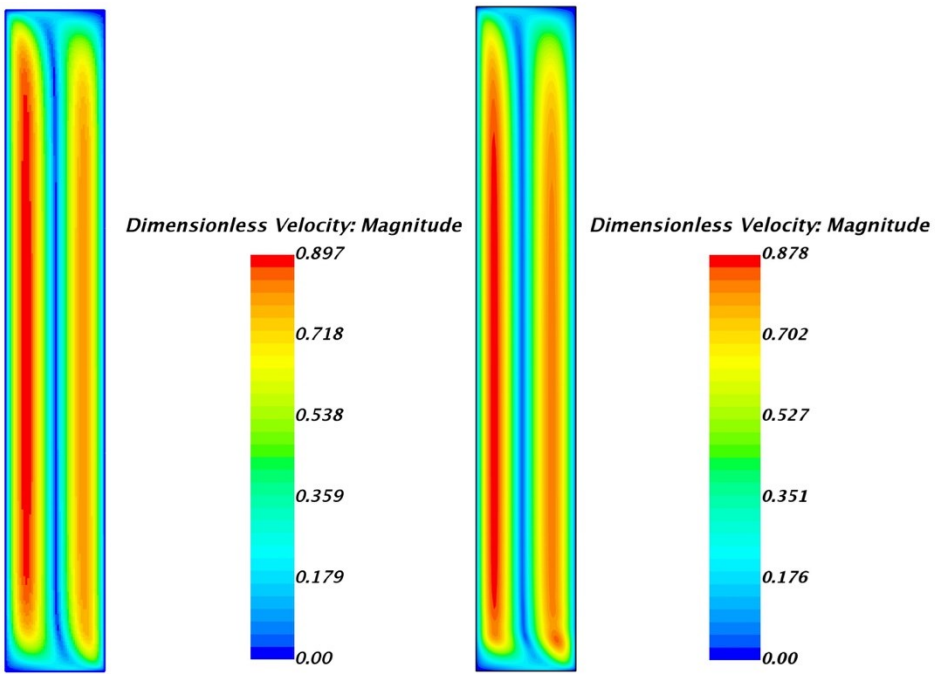

(b)

Figure 5.4: (a) Isotherms and (b)Velocity field for ε = 0.005 (left) and 0.2 (right) at Ra = 5800.
Note: Width of the cavity is scaled by a factor of 6 for visualization purposes.

5.4.2 Onset of Oscillatory Flow – First Bifurcation

As the Rayleigh number is further increased transition from steady unicellular flow to mono-periodic oscillatory flow is observed for all three cases of dimensionless temperature difference ε. For the Boussinesq case (ε = 0.005), a downward drifting multicellular flow is first observed at Rayleigh number of 6000. The numerical solution produces an unsteady, periodic flow showing constant amplitude oscillations in temperature and velocity fields. The unsteady oscillatory flow is caused due to the multicellular cat's eye pattern drifting downward inside the cavity. The fluctuations originate at the top part of the cavity, then slowly drift downward and diminish as they reach the bottom part of the cavity. Le Quéré and Pécheux [30] studied the different flow transitions under Boussinesq conditions for an air-filled cavity for the same radius ratio as this

study (η=0.8) and a smaller aspect ratio of 16. They observed the transition from steady flow to unsteady periodic flow at a critical Rayleigh number of 6850. A smaller aspect ratio is known to stabilize the flow inside the cavity; therefore, the slightly lower critical Rayleigh number observed in our study as compared to Le Quéré and Pécheux [30] is to be expected.

For non-Boussinesq cases of ε = 0.1 and ε = 0.2, the downward drifting multicellular pattern was first observed at progressively higher Rayleigh numbers of 6200 and 6550 respectively. These observations suggest that the first onset of the cat's eye instability in annular cavities gets delayed as we transition from Boussinesq conditions to non-Boussinesq temperature conditions. A similar effect of delayed onset of the cat's eye instability has been previously reported by Sulsov and Paolucci [40] for differentially heated rectangular cavity under non-Boussinesq conditions. Figures 5.5(a) and 5.5(b) show the isotherms and velocity fields at the first onset of the cat's eye instability for the three dimensionless temperature cases.

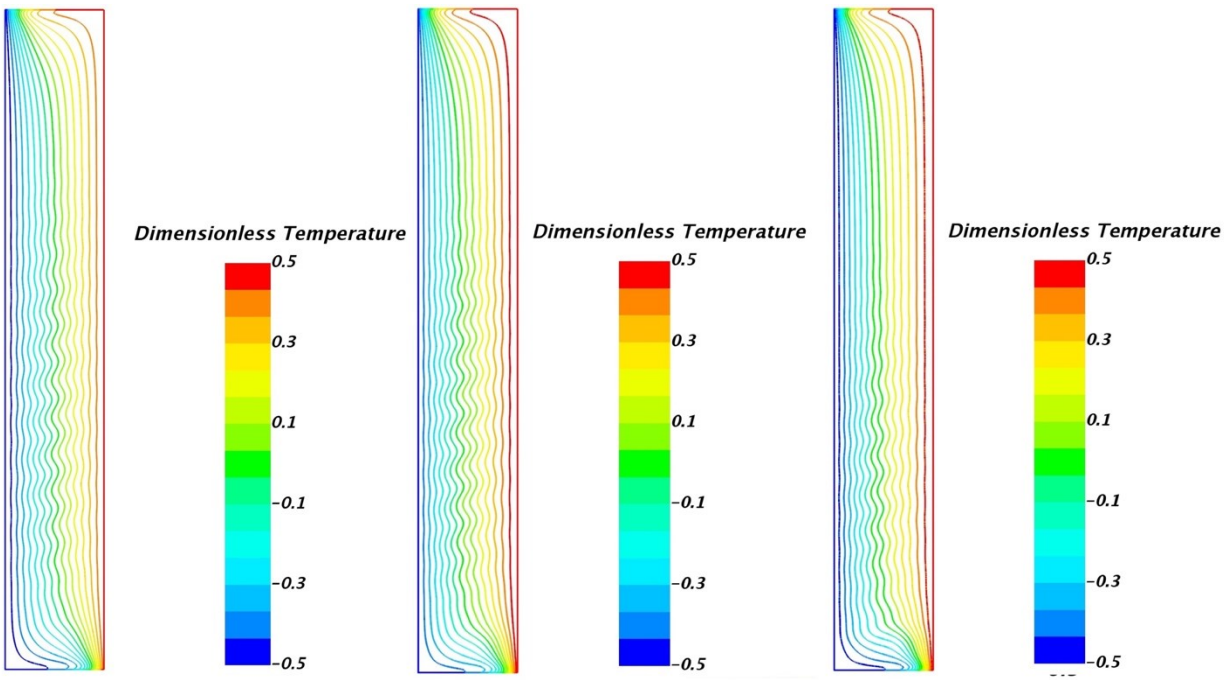

(a)

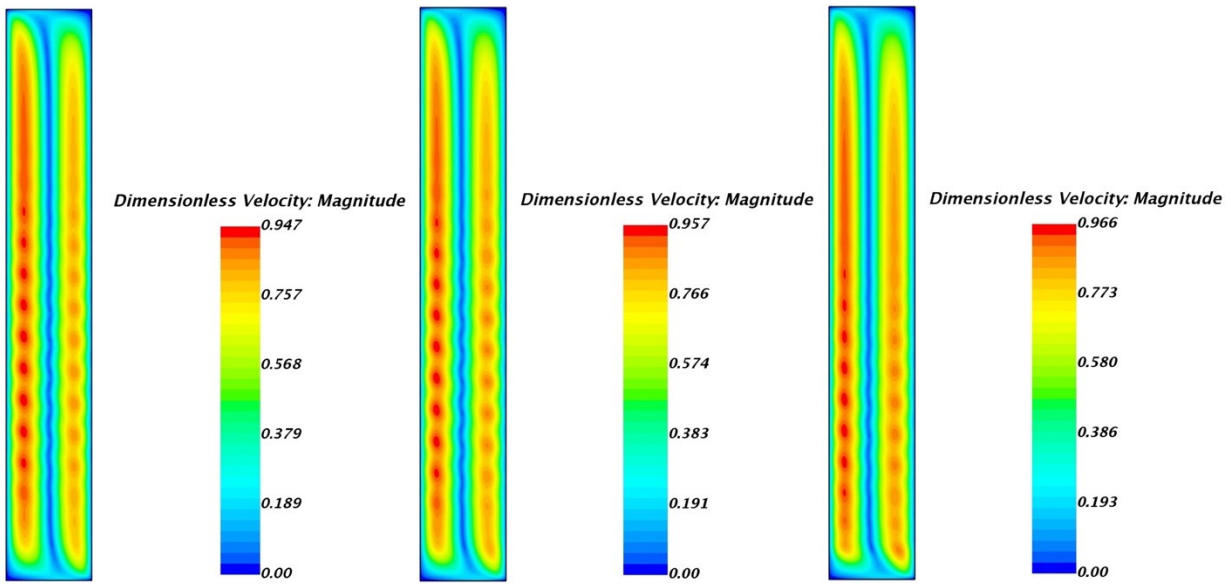

(b)

Figure 5.5: (a) Isotherms and (b) Velocity field for ε = 0.005, 0.1 and 0.2 at first onset of the downward drifting cat's eye instability at Ra = 6000, Ra = 6200 and Ra = 6550 respectively.
Note: Width of the cavity is scaled by a factor of 6 for visualization purposes.

5.4.2.1 Critical parameters determination

The transition from steady unicellular flow to downward drifting cat's eye instability for both Boussinesq (ε = 0.005) as well as non-Boussinesq cases (ε = 0.1,0.2) seems to follow the three characteristics of supercritical Hopf bifurcation as described by Le Quéré and Pécheux [30]. The first characteristic is that in the vicinity of the critical Rayleigh number the amplitude of oscillation behaves as $\sqrt{Ra - Ra_{cr}}$. The second is that above the critical Rayleigh number the time required to reach the final asymptotic solution varies as $(Ra - Ra_{cr})^{-1}$. The final characteristic is that in the vicinity of the critical Rayleigh number, the time period of oscillation is a continuous function of the Rayleigh number. These three characteristics of the supercritical Hopf bifurcation were used to accurately determine the critical parameters of the bifurcation from the simulation results.

Based on the first characteristic, immediately above the critical Rayleigh number, a linear relationship exists between the square of amplitude of oscillations and the Rayleigh number.

$$a(\bar{u}, \bar{v}, \bar{\theta})^2 \propto Ra - Ra_{cr} \tag{5.8}$$

For each ε case, amplitude of temperature and velocity oscillations were recorded for several Rayleigh numbers close to the Rayleigh number at which oscillatory flow was first observed. The monitoring point was located at $\bar{x}$ = H/3L and $\bar{r}$ = (r_o/L + ½). In order to estimate the value of critical Rayleigh number, amplitudes of recorded oscillations were extrapolated back to the Rayleigh number corresponding to zero amplitude. Figure 5.6(a) and 5.6(b) show this process for ε = 0.005 and ε = 0.1 cases. Critical Rayleigh numbers for the three dimensionless temperature difference cases were calculated as 5847 for ε = 0.005, 5987 for ε = 0.1 and 6449 for ε = 0.2. The maximum uncertainty associated with calculation of critical Rayleigh numbers is +/- 0.3 %.

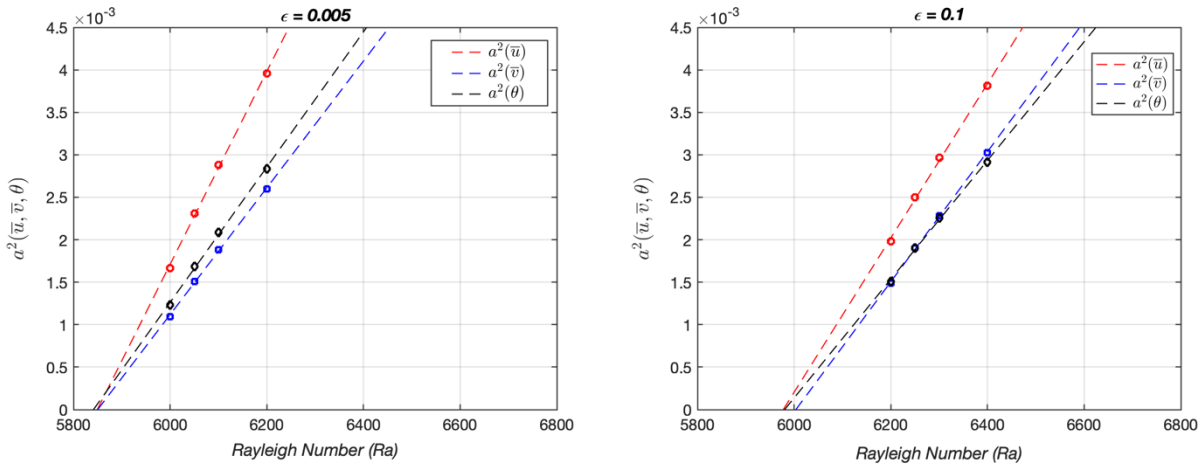

Figure 5.6: Squared amplitude of oscillations in temperature, axial velocity and radial velocity at several Rayleigh numbers in the vicinity of the critical Rayleigh number for dimensionless temperature difference (a) ε = 0.005 and (b) ε = 0.1.

Choi and Korpela [22] studied the linear stability of flow inside a differentially heated air-filled cavity of infinite aspect ratio and various radius ratios under Boussinesq temperature conditions. Although their results are for an infinite cavity they will be used here for comparison as they represent the limiting case of $\varepsilon \rightarrow 0$. For a radius ratio of 0.8, the critical Rayleigh number reported by them is 5769. Figure 5.7 shows the plot of critical Rayleigh number versus ε. The value of critical Rayleigh number from linear stability theory results of Choi and Korpela [22] is plotted against a dimensionless temperature difference value of '0' along with the results from the present study. The critical Rayleigh number increases as the value of ε is increased as seen in Fig. 5.7. Thus, the non-Boussinesq temperature conditions have a stabilizing effect on the flow which leads to a delay in the onset of the cat's eye instability.

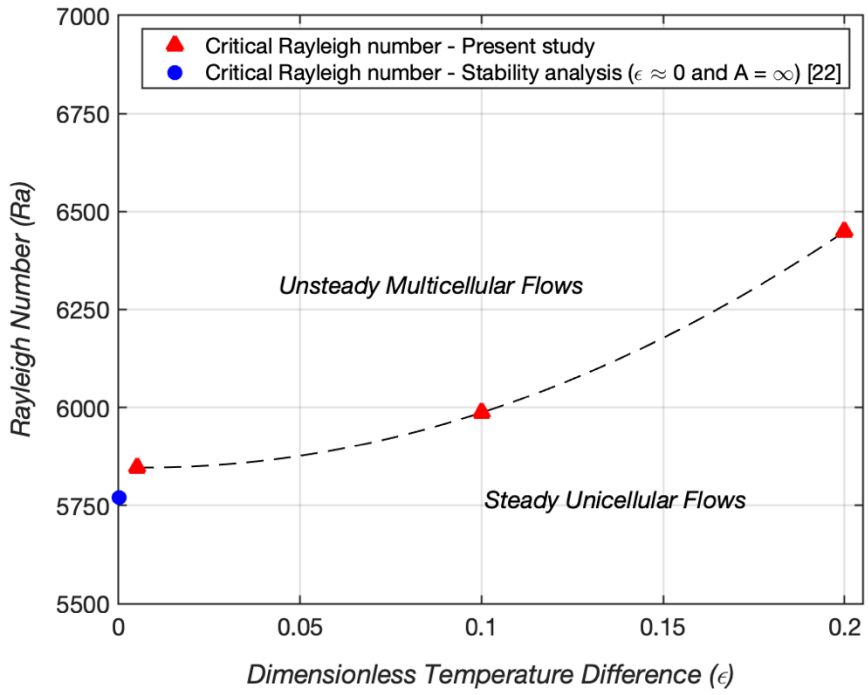

Figure 5.7: Critical Rayleigh number as a function of dimensionless temperature difference.

Figure 5.8 shows the plot of the absolute value of the dimensionless critical wave-speed for the 3 dimensionless temperature difference cases along with the critical wave-speed from the linear stability studies of Choi and Korpela [22]. From the plot, we can see that the increase in the value of ε is accompanied by a corresponding increase in the critical wave-speed of the instability.

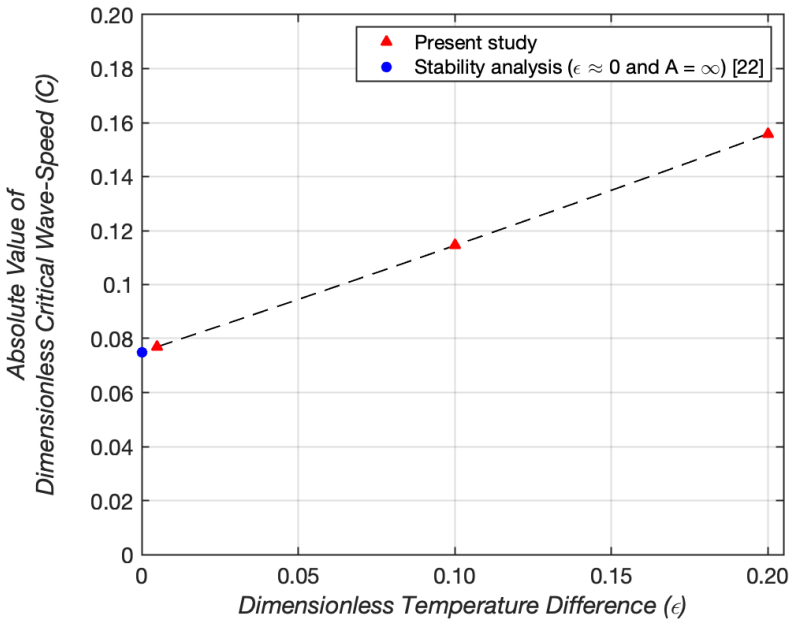

Figure 5.8: Critical wave-speed as a function of dimensionless temperature difference.

Based on results, the functional dependence of critical Rayleigh number and dimensionless critical wave-speed on ε for 0 <= ε <= 0.2 for a cavity of aspect ratio 40 is given by,

$$\mathrm{Ra_{cr}}(\varepsilon) = 1.612\mathrm{x}10^4\varepsilon^2 - 216.9785\varepsilon + 5847.7 \qquad (5.9)$$

$$\mathrm{C_{cr}}(\varepsilon) = 0.0986\varepsilon^2 + 0.3843\varepsilon + 0.075$$

Thus, the downward drifting cat's eye instability in annular cavities under non-Boussinesq conditions occurs at a higher critical Rayleigh number and drifts downward at a faster pace as compared to under Boussinesq conditions.

According to the third characteristic of the supercritical Hopf bifurcation the dimensionless time period of oscillation is a continuous function of the Rayleigh number. Time-period of oscillations were calculated for several Rayleigh numbers close to the critical Rayleigh number. A power-law relationship between the dimensionless time period of oscillation and the Rayleigh number was then determined for each case of dimensionless temperature difference ε given by:

$$\tau = \tau_{cr} \cdot \left(\frac{Ra}{Ra_{cr}}\right)^{m} \tag{5.10}$$

The exponent 'm' was found to be positive for all 3 dimensionless temperature difference cases. This suggests that for both Boussinesq and non-Boussinesq conditions, the time period of oscillations increases as the Rayleigh number is increased. A similar trend was observed in the Boussinesq conditions studies conducted by Le Quéré and Pécheux [30]. The value of the exponent 'm' along with the critical time period of oscillation for the 3 dimensionless temperature difference cases is shown in Table 5.1.

Table 5.1: Critical parameters for the three dimensionless temperature difference cases.

Dimensionless temperature difference (ε)	Critical Rayleigh number (Ra_{cr})	Dimensionless Critical time period of oscillation (τ_{cr})	Exponent of Power-law relation (m)
0.005	5847	28.8	0.451
0.1	5987	19.2	0.345
0.2	6449	14.1	0.166

5.4.3 Monoperiodic Oscillatory Flows

As the Rayleigh number is further increased the oscillatory flow persists for all three dimensionless temperature cases. However, the range of Rayleigh numbers over which monoperiodic oscillatory flows are observed is different for each case. Mono-periodic flows are observed up to a Rayleigh number of 1.25×10^4 for the $\varepsilon = 0.005$ case, up to a Rayleigh number of 1.10×10^4 for the $\varepsilon = 0.1$ case and up to a Rayleigh number of 6.75×10^3 for the $\varepsilon = 0.2$ case. Figure 5.9 (a-b) shows the temperature fluctuations measured at a point inside the cavity for monoperiodic flow at Ra =12000 and corresponding power spectral density function for the Boussinesq case of $\varepsilon = 0.005$. The PSD shows presence of a single fundamental frequency 'f_1' and its first three harmonics. Figures 5.9 (c-d) show the isotherms and streamlines inside the cavity for this case. Figures 5.10 (a-b) and 5.11(a-b) shows the temperature fluctuations and PSD for the monoperiodic flow observed at Ra = 11000 and Ra = 6550 for the non-Boussinesq cases of $\varepsilon = 0.1$ and $\varepsilon = 0.2$ respectively. Figures 5.10 (c-d) and 5.11 (c-d) show the isotherms and streamlines inside the cavity for the same. Table 5.2 gives a summary of the monoperiodic flow regime for the three ε cases.

Table 5.2: Summary of monoperiodic regime for three dimensionless temperature differences.

Dimensionless Temperature difference (ε)	Rayleigh number range for monoperiodic flows (Ra)	Dimensionless Frequency Range (f)
0.005	$5847 < Ra < 12500$	0.0232 – 0.0343
0.1	$5987 < Ra < 11000$	0.0352 – 0.0514
0.2	$6449 < Ra < 6750$	0.0704 – 0.0707

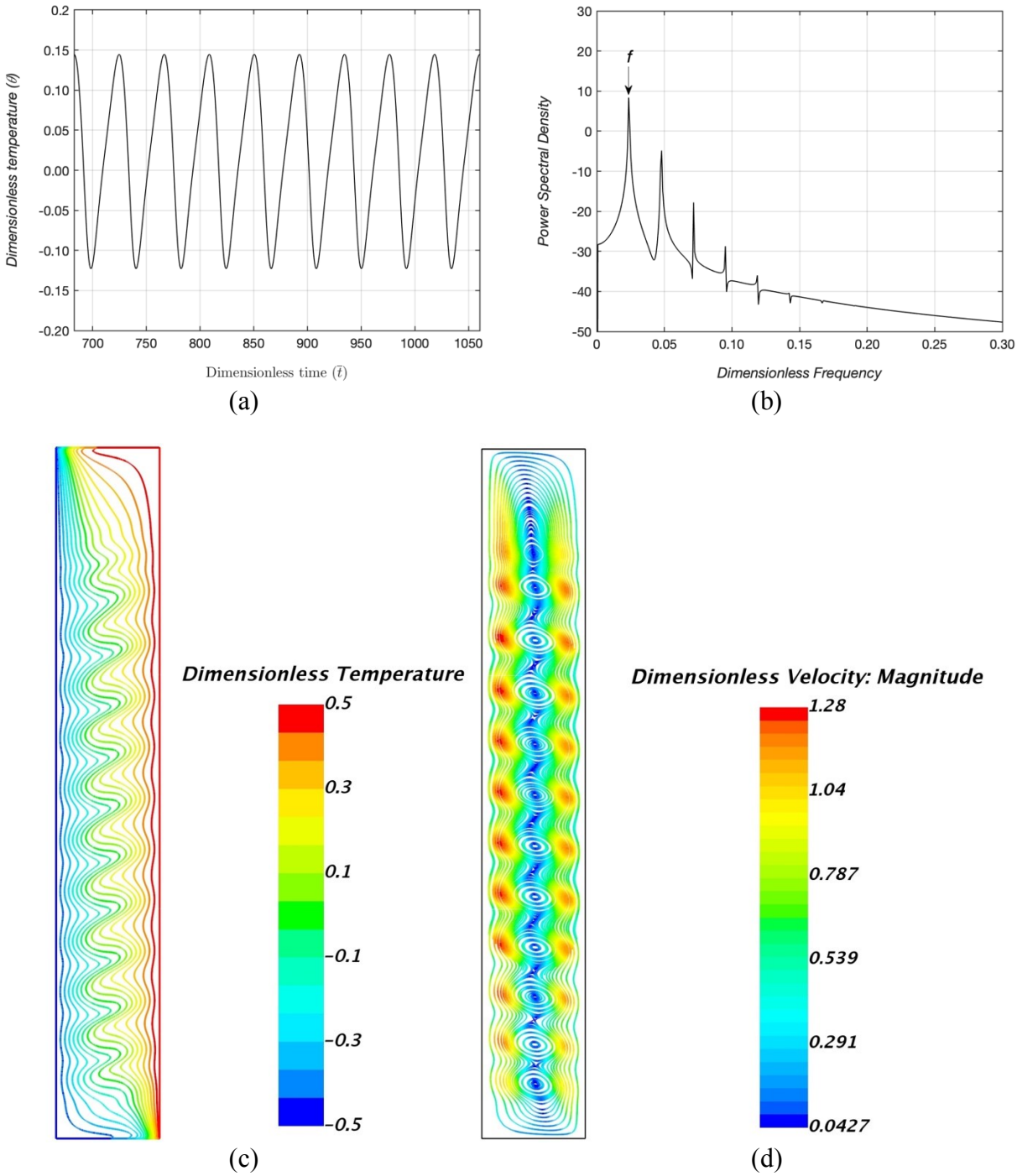

Figure 5.9: (a) Temporal evolution of dimensionless temperature θ at the monitoring point located at $\left(\bar{x} = \frac{H}{3L}, \bar{r} = \frac{R_i + R_o}{2L}\right)$; (b) Power spectral density for temperature signal measured at monitoring point. (c) Isotherms and (d) Streamlines for Ra = 12000 and ε = 0.005 in an air-filled annular cavity of A = 40 and radius ratio η = 0.8.
Note: Width of the cavity is scaled by a factor of 6 for visualization purposes.

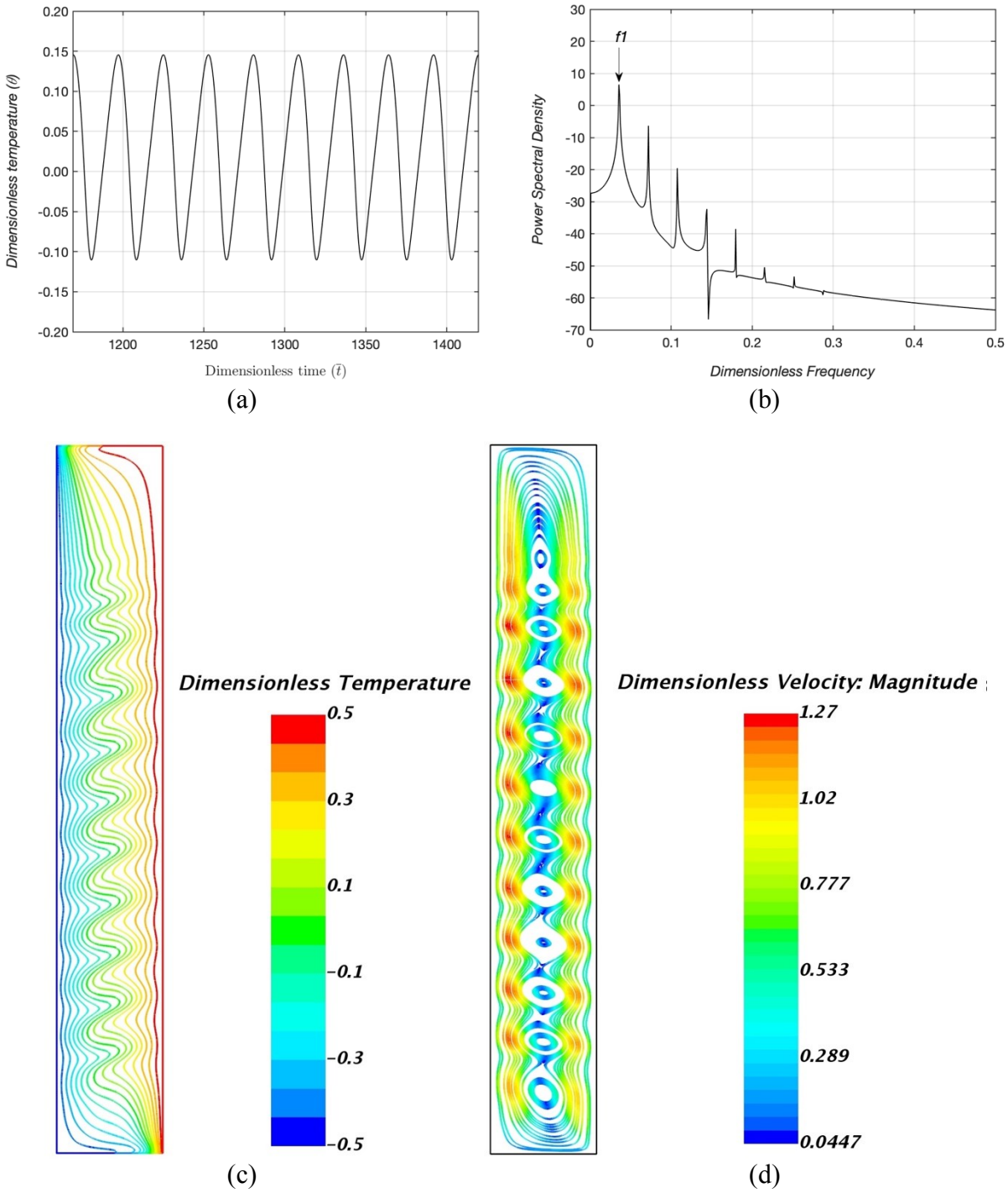

Figure 5.10: (a) Temporal evolution of dimensionless temperature θ at the monitoring point located at $\left(\bar{x} = \frac{H}{3L},\ \bar{r} = \frac{R_i + R_o}{2L}\right)$; (b) Power spectral density for temperature signal measured at monitoring point. (c) Isotherms and (d) Streamlines for Ra = 11000 and ε = 0.1 in an air-filled annular cavity of A = 40 and radius ratio η = 0.8.
Note: Width of the cavity is scaled by a factor of 6 for visualization purposes.

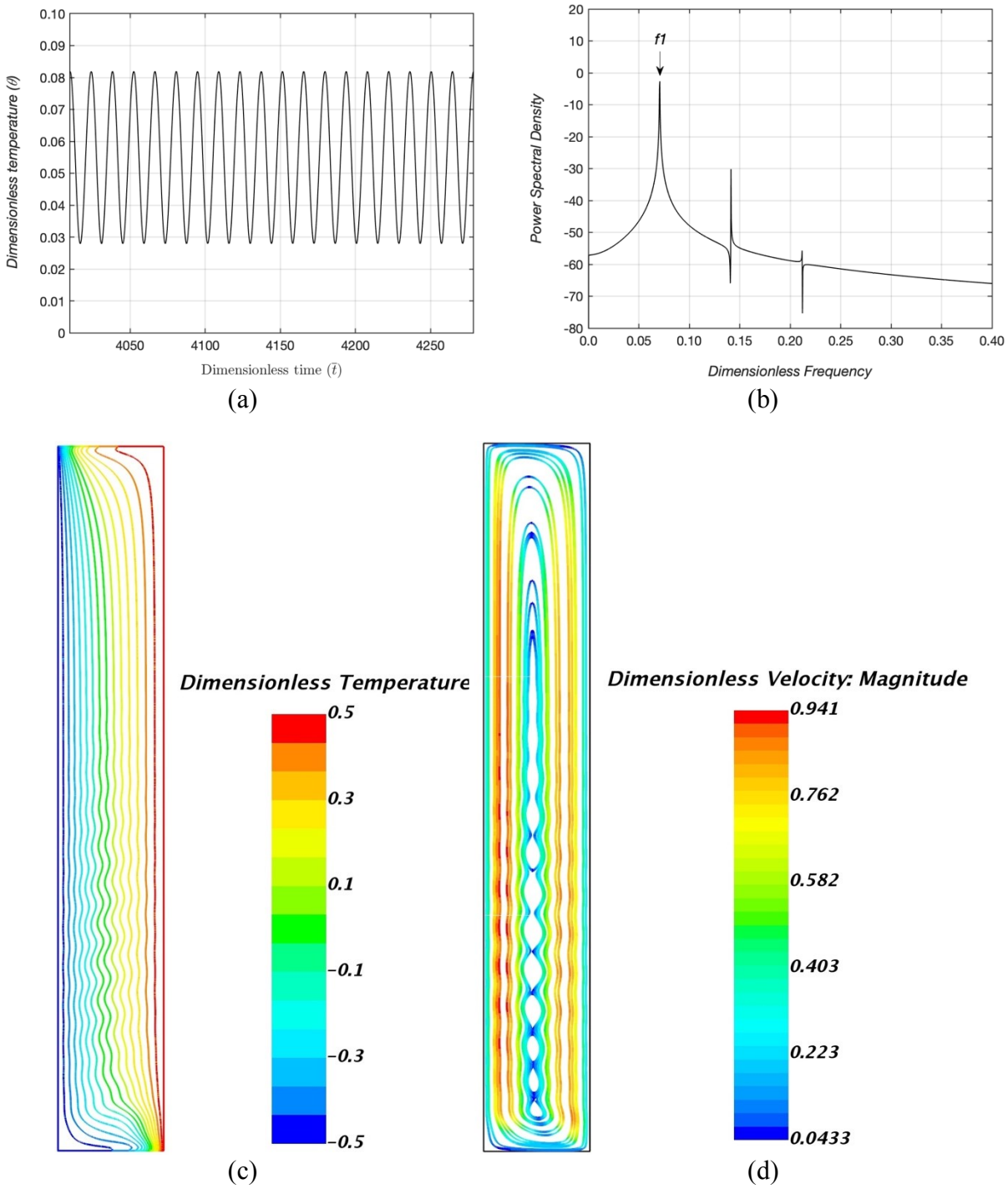

Figure 5.11: (a) Temporal evolution of dimensionless temperature θ at the monitoring point located at $\left(\bar{x} = \frac{H}{3L},\ \bar{r} = \frac{R_i + R_o}{2L}\right)$; (b) Power spectral density for temperature signal measured at monitoring point. (c) Isotherms and (d) Streamlines for Ra = 6550 and ε = 0.2 in an air-filled annular cavity of A = 40 and radius ratio η = 0.8.

Note: Width of the cavity is scaled by a factor of 6 for visualization purposes.

The nature of the time-space structure of the flow in the monoperiodic regime for all three temperature difference conditions remains similar; consisting of cells of similar size continuously drifting downwards with an almost constant velocity. For each dimensionless temperature difference 'ε' case, the increase in Rayleigh number is accompanied by an increase in the time-period and amplitude of oscillations. Dimensionless time-periods and wave-speed for the three 'ε' cases are shown in Fig 5.12(a) and (b).

For the mono-periodic flows, the time-periods of oscillations were calculated by calculating a temporal average over 10 oscillations measured at the monitoring point $\left(\bar{x} = \frac{H}{3L},\ \bar{r} = \frac{R_i + R_o}{2L}\right)$ once the asymptotic solution was reached by the solver. The measurement of the time-period/frequency of oscillation is independent of the location of the monitoring point since all points in the interior of the cavity oscillate at the same frequency. Wavelengths of the multicellular cat's eye instability were calculated based on the length of the central cell in the multicellular pattern. The wave-speed for the mono-periodic oscillatory flows were calculated by dividing the wavelength by the time-period of oscillations.

The general trends established for time-period of oscillations and wave-speeds for small supercritical Rayleigh numbers described in the previous section seem to hold true for even higher values of Rayleigh numbers. Dimensionless time-periods increase with increasing Rayleigh numbers and decreases with increasing values of ε. The dimensionless wave-speed of the instability decreases slowly with increasing Rayleigh numbers and increases rapidly when ε is increased. The wave-speeds and time periods have a much stronger dependence on ε as compared to the Rayleigh number as can be seen in Fig 5.12(a) and (b).

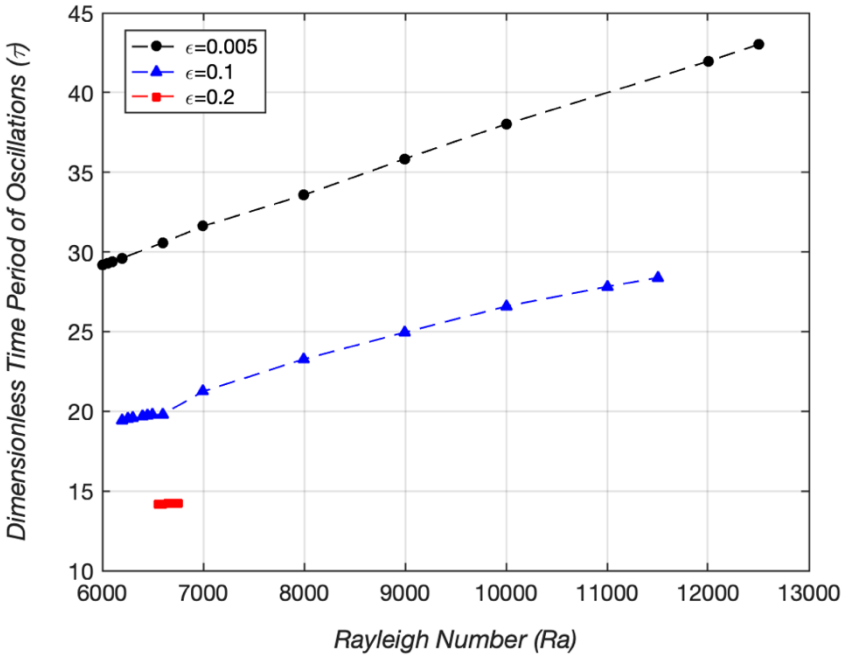

(a)

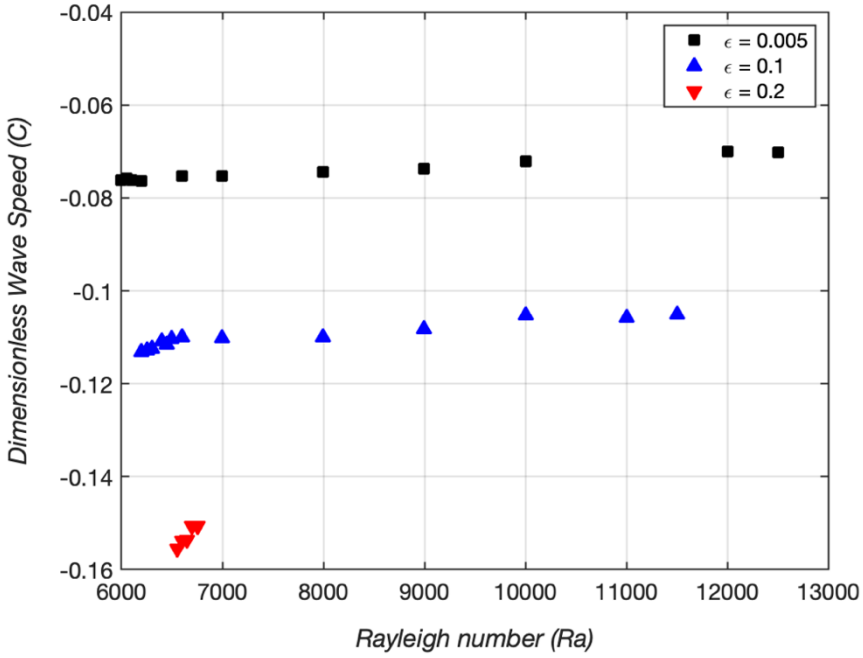

(b)

Figure 5.12: (a) Plot of dimensionless time-period v/s Rayleigh number; (b) Plot of dimensionless wave-speed v/s Rayleigh number for mono-periodic oscillatory flows for the three dimensionless temperature cases.

5.4.4 Period Doubling, Quasiperiodic and Quasi-Chaotic Flows

With further increase in Rayleigh number, a period doubling bifurcation is observed at Ra = 13000 for the Boussinesq case (ε = 0.005). Power spectral density function and temperature signal measured at a monitoring point located at $\bar{x} = \frac{H}{3L}$ and $\bar{r} = \frac{R_i+R_o}{2L}$, is shown in Fig. 5.13(a) and (b). The PSD indicates presence of two key dimensionless frequencies f_1 = 0.22 and the subharmonic $f_2 = \frac{f_1}{2}$ = 0.11; the ratio of $\frac{f1}{f2}$ = 2. All the other peaks are linear combinations of m. f_1 + n. $\frac{f_1}{2}$. This is consistent with the observations of period doubling bifurcation by Le Quéré and Pécheux [30] for an annular cavity of radius ratio 0.8 and aspect ratio 16 under Boussinesq conditions. Multiple cells/rolls are visible in the isotherms and streamlines captured at a specific instance in time for Ra = 13000, as shown in 5.13 (c) and (d). Similar to the monoperiodic regime, the multiple cells/rolls still drift downward inside the cavity. However, unlike the monoperiodic regime, the velocity of the downward drifting cells is not constant but varies as the cell moves along the cavity thereby causing the periodic doubling or quasiperiodicity in the temperature and velocity signals.

When the Rayleigh number is increased starting from the monoperiodic flow regime for the two non-Boussinesq temperature difference cases (ε = 0.1, 0.2); instead of period doubling, quasiperiodicity is observed. For the moderately non-Boussinesq case (ε = 0.1), a quasiperiodic flow behavior is first observed at Ra = 12000. Power spectral density function for temperature signal measured at a monitoring point, as shown in Fig. 5.14(a) and (b) indicates presence of two key dimensionless frequencies f_1= 0.034 and f_2 = 0.006. The ratio of the frequencies is $\frac{f1}{f2}$ = 5.60. All the other peaks are linear combinations of these two frequencies m. f_1+n.f_2. The isotherms and streamlines corresponding to this flow are shown in Fig 5.14(c) and (d).

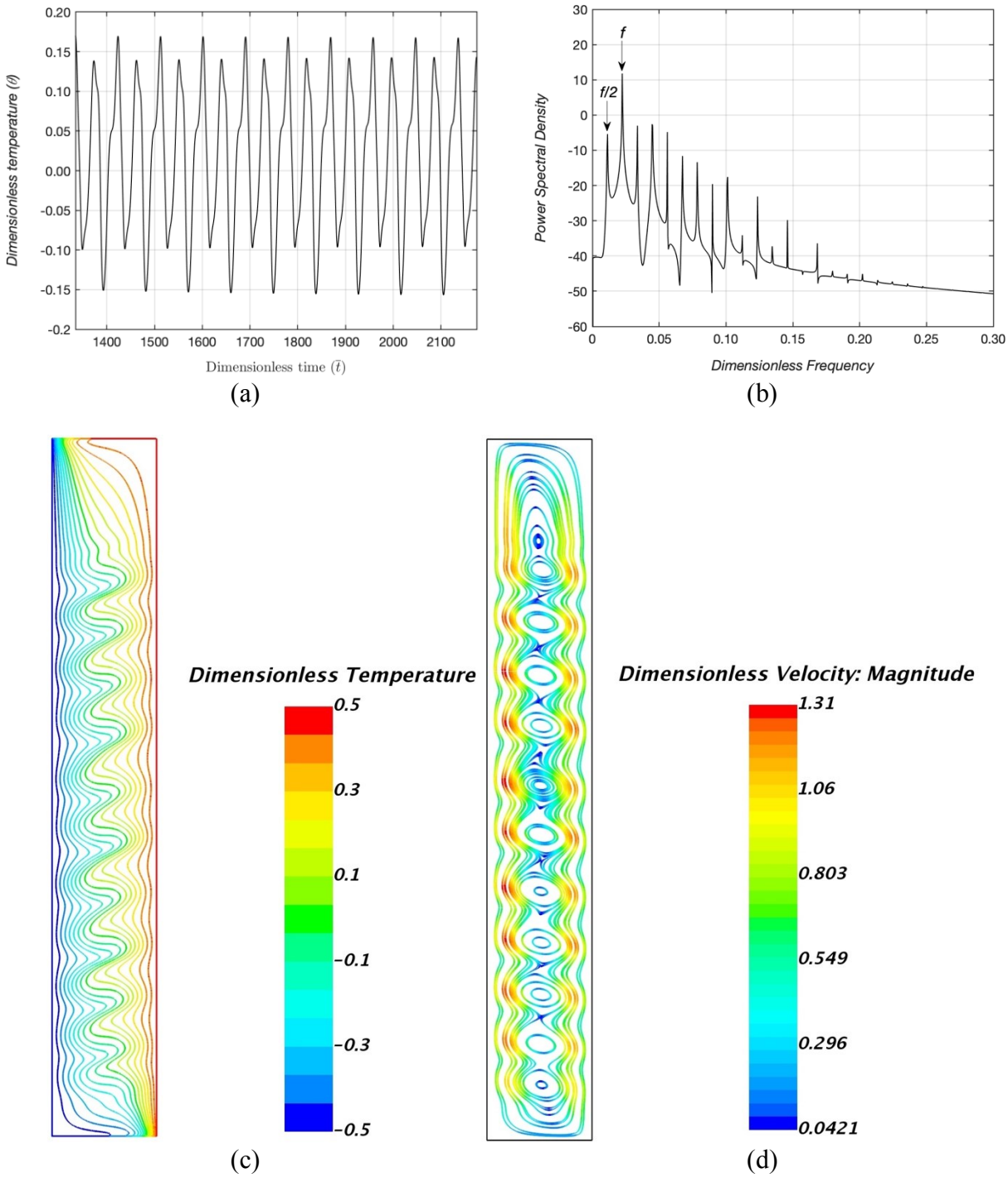

Figure 5.13: (a) Temporal evolution of dimensionless temperature θ at the monitoring point located at $\left(\bar{x} = \frac{H}{3L},\ \bar{r} = \frac{R_i + R_o}{2L}\right)$; (b) Power spectral density for temperature signal measured at monitoring point. (c) Isotherms and (d) Streamlines for Ra = 13000 and ε = 0.005 in an air-filled annular cavity of A = 40 and radius ratio η = 0.8.
Note: Width of the cavity is scaled by a factor of 6 for visualization purposes.

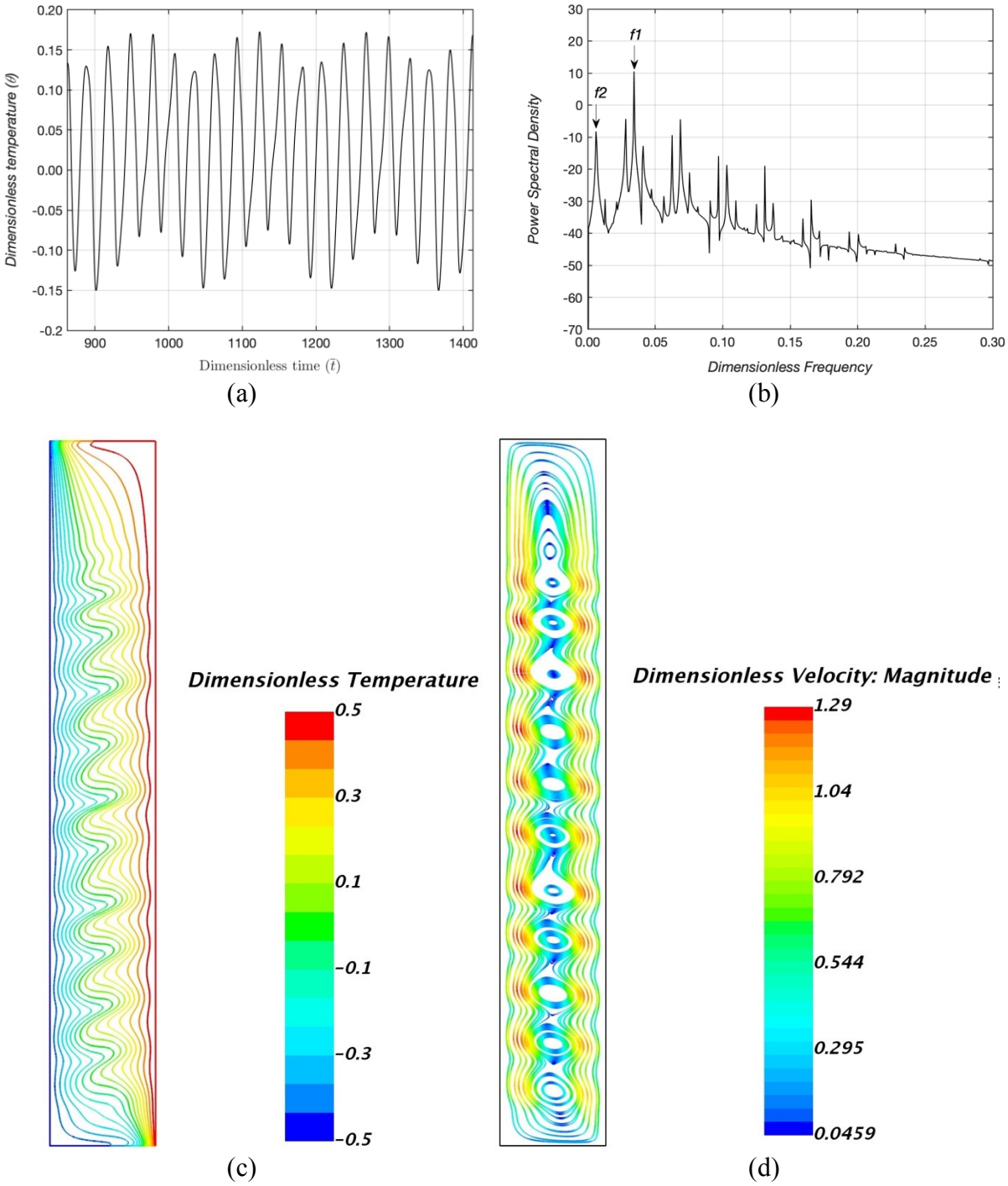

Figure 5.14: (a) Temporal evolution of dimensionless temperature θ at the monitoring point located at $\left(\bar{x} = \frac{H}{3L},\ \bar{r} = \frac{R_i + R_o}{2L}\right)$; (b) Power spectral density for temperature signal measured at monitoring point. (c) Isotherms and (d) Streamlines for Ra = 12000 and ε = 0.1 in an air-filled annular cavity of A = 40 and radius ratio η = 0.8.
Note: Width of the cavity is scaled by a factor of 6 for visualization purposes.

For the non-Boussinesq case (ε = 0.2), the quasiperiodic flow is first observed at Ra = 6800. Power spectral density function of the temperature signal at monitoring point shown in Fig 5.15(a) and (b) shows two key frequencies f_1= 0.068 and f_2 = 0.003. The ratio of the frequencies is $\frac{f1}{f2}$ = 26.2. The quasiperiodic time-series signal appears almost like a high frequency signal modulated with a low frequency signal. Similar behavior of a fundamental frequency being modulated by a lower frequency has been observed experimentally by Le Quéré and Penot [61] in their experiments with air-filled rectangular cavities. The isotherms and streamlines corresponding to this flow are shown in Fig 5.15(c) and (d). The second bifurcation from monoperiodic flow is observed for all three ε cases. The ratio of this second frequency to the fundamental frequency f_1/f_2 is different for each case of ε, and varies as the ε^2. Based on the simulation data, an estimate of this functional dependence is given by:

$$\frac{f_1}{f_2} = 877.46\varepsilon^2 - 54.239\varepsilon + 2.24 \tag{5.11}$$

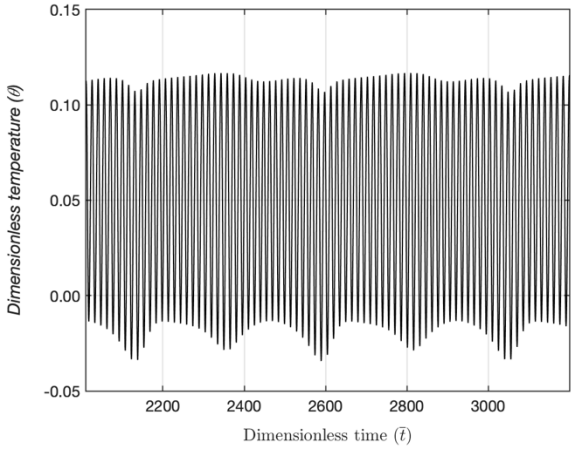

(a)

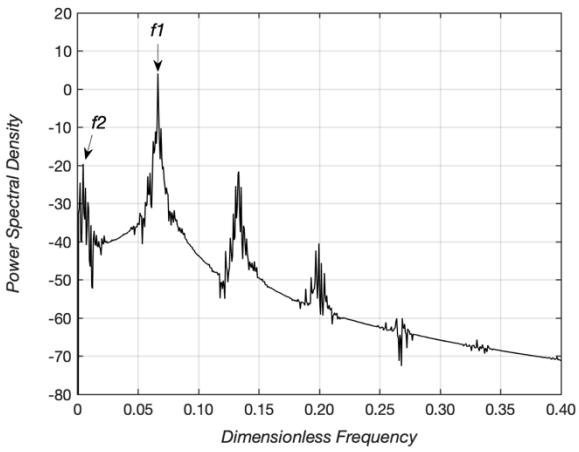

(b)

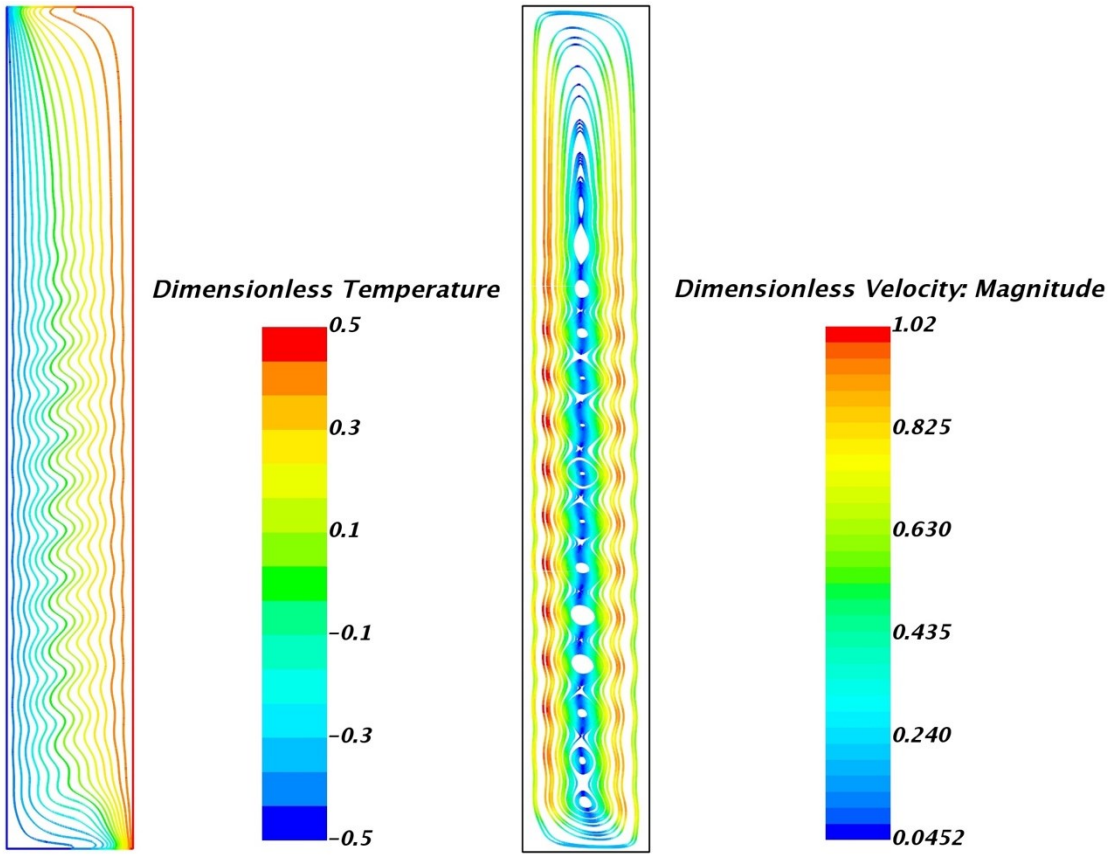

Figure 5.15: (a) Temporal evolution of dimensionless temperature θ at the monitoring point located at $\left(\bar{x} = \frac{H}{3L},\ \bar{r} = \frac{R_i+R_o}{2L}\right)$; (b) Power spectral density for temperature signal measured at monitoring point. (c) Isotherms and (d) Streamlines for Ra = 7000 and ε = 0.2 in an air-filled annular cavity of A = 40 and radius ratio η = 0.8.
Note: Width of the cavity is scaled by a factor of 6 for visualization purposes.

As the Rayleigh number is further increased more and more frequency peaks are visible and the flow progresses towards becoming chaotic for each case of ε. Previous experimental investigations in similar cavities have shown that the flow likely becomes 3D around Ra = 14000 and therefore one would need to solve the 3D unsteady Navier-Stokes equations in order to capture the dynamics of the flow. Therefore, 2D numerical solutions were obtained only up to a Rayleigh number of Ra = 14000 for each dimensionless temperature difference case. Figure 5.16 (a) and (b) shows the temperature signal and corresponding PSD for ε = 0.2 case at Ra = 14000.

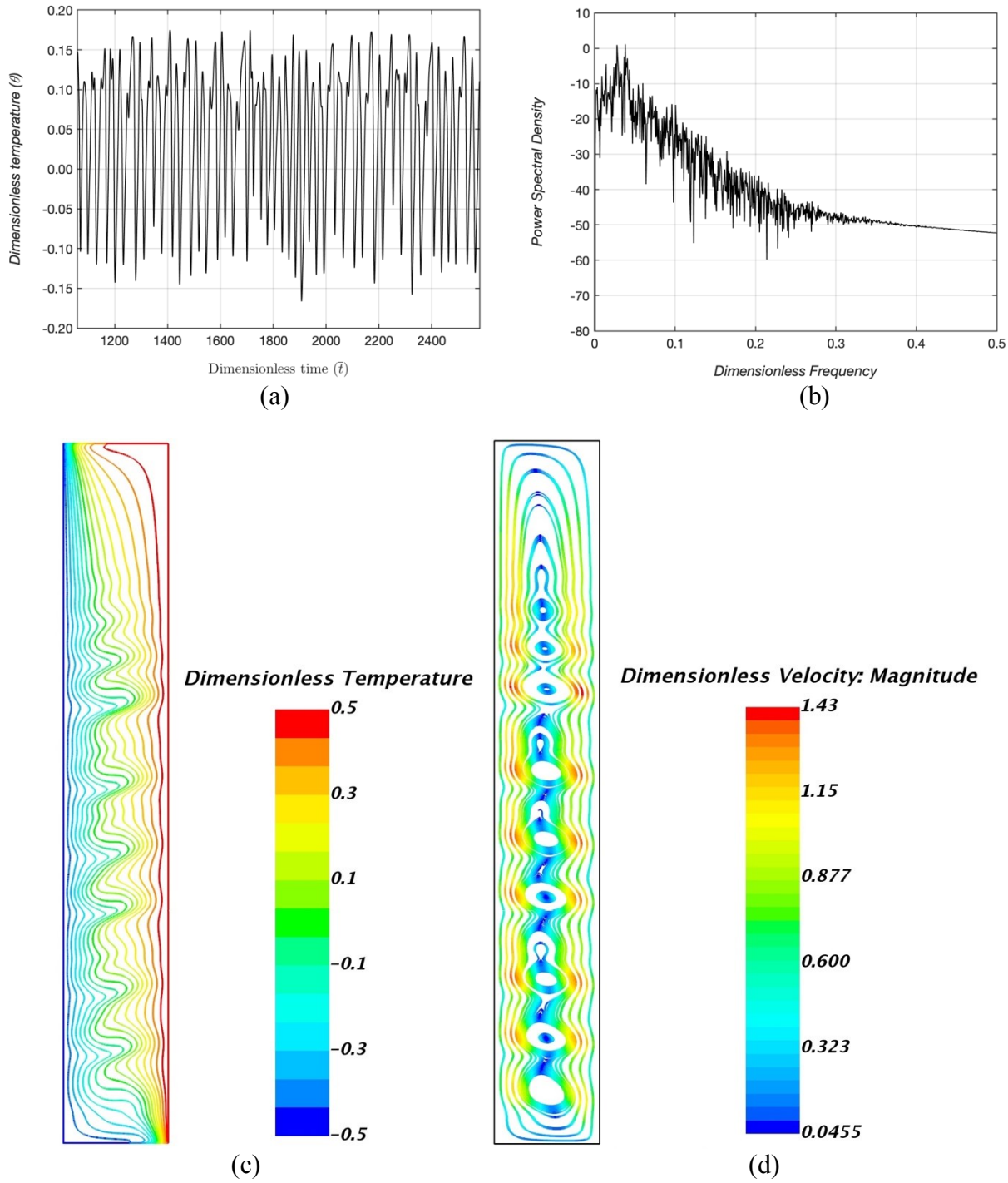

Figure 5.16: (a) Temporal evolution of dimensionless temperature θ at the monitoring point located at $\left(\bar{x} = \frac{H}{3L},\ \bar{r} = \frac{R_i + R_o}{2L}\right)$; (b) Power spectral density for temperature signal measured at monitoring point. (c) Isotherms and (d) Streamlines for Ra = 14000 and ε = 0.2 in an air-filled annular cavity of A = 40 and radius ratio η = 0.8.
Note: Width of the cavity is scaled by a factor of 6 for visualization purposes.

The PSD of the temperature signals shows presence of several peaks, however, few peaks with significant power are still visible. Thus, the flow is on the route to becoming chaotic but is not fully chaotic yet. Figures 5.16 (c) and (d) shows the isotherms and streamlines for this case. The structure of the cat's eye multicellular flow is still visible at this Rayleigh number. However, the movement of the cells is not in strictly in downward direction but random, where the two adjacent cells either move close to each other or further away from each other at any given time instant.

5.4.5 Stability of Dynamical System and Transition to Chaotic Flow

The transition from steady flow to chaotic flow can be understood further by studying the velocity phase space at a sample point as the Rayleigh number is increased. Figures 5.17 (a) –(d) show the velocity phase space for the non-Boussinesq case of $\varepsilon = 0.2$ for four different values of Rayleigh number. At Ra = 6000 flow inside the cavity is steady corresponding to the steady unicellular flow solution. For this case, the velocity phase-space shows the trajectory following a stable spiral and ultimately approaching the stable limit point at the center of the spiral. At a higher Rayleigh number of Ra = 6600 the flow is in the monoperiodic regime corresponding to a downward drifting multicellular flow. For this case, a stable limit cycle appears in the phase space with the trajectories staying on the limit cycle for an infinite time. At a still higher Rayleigh number of Ra = 7000 the flow has just started to show quasiperiodicity. The trajectories of the phase space do not follow the limit cycle exactly but rather change their path by a small amount in every loop which is characteristic of a quasiperiodic flow. Finally, at Ra = 14000, flow is quasi-chaotic (approaching chaotic behavior). The corresponding phase space has trajectories which do not follow a specific

path (random path) making the phase space appear more crowded. Least three loops are still visible indicating that the flow has still not lost all its periodicity. The phase spaces for the different flow regimes are distinct and give a good picture of the stability of this system.

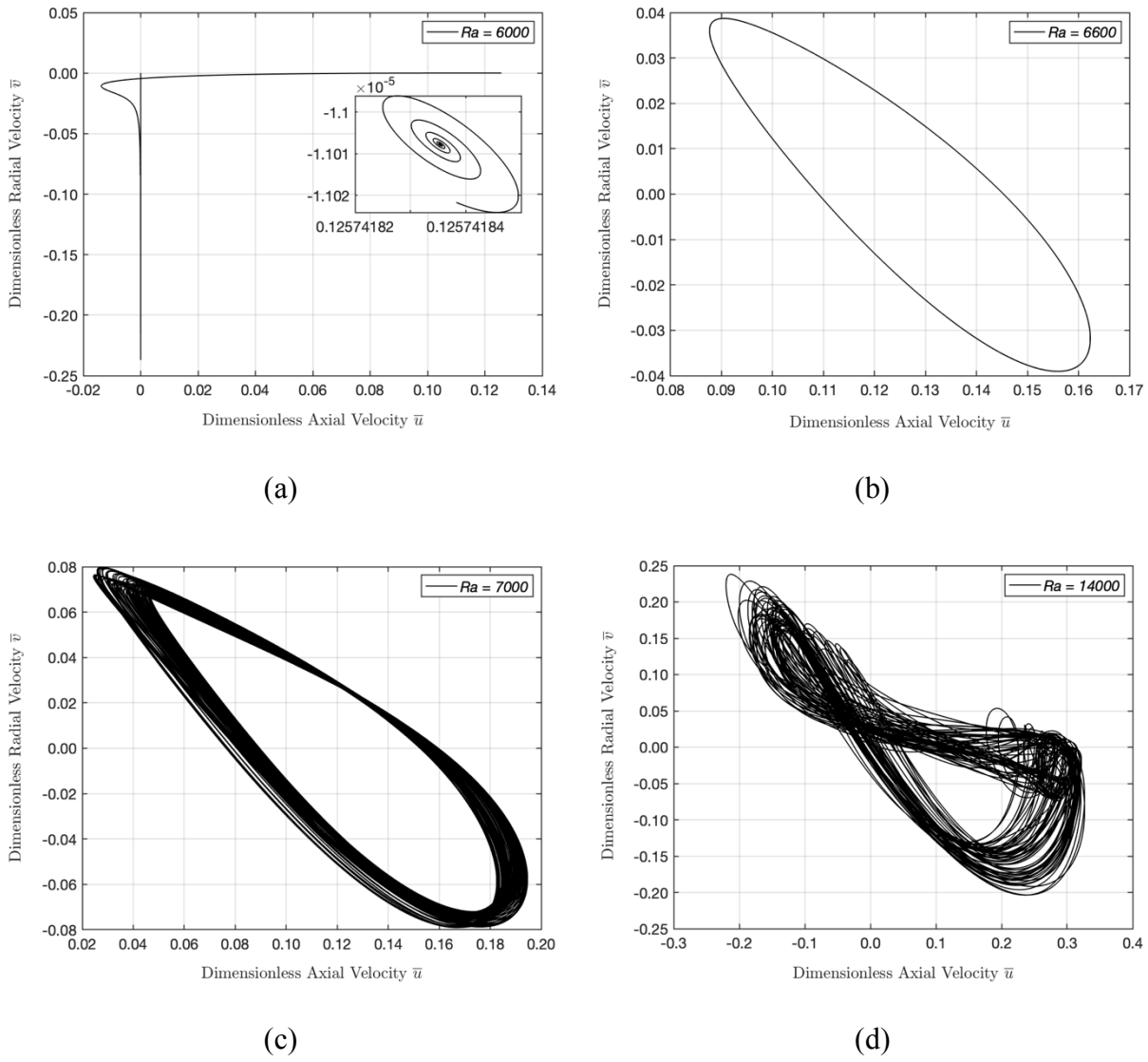

Figure 5.17: Phase space of velocity at the monitoring point located at $\left(\bar{x} = \frac{H}{3L},\ \bar{r} = \frac{R_i + R_o}{2L}\right)$ for non-Boussinesq case - $\varepsilon = 0.2$ for Ra = 6000 (a), Ra = 6600 (b), Ra = 7000 (c), Ra = 14000(d).

5.4.6 Frequency and Amplitude Maps

The different flow bifurcations and the corresponding evolution of the frequencies can be easily observed in the plot of frequency versus Rayleigh number plots for the three dimensionless temperature difference cases, as shown in Fig. 5.18.

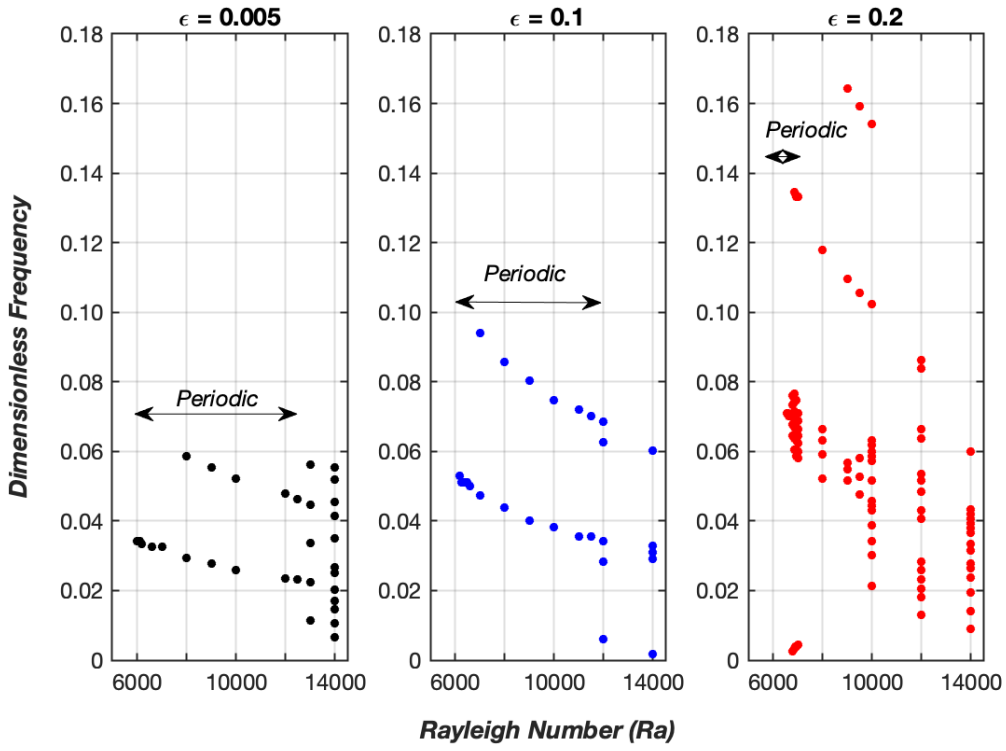

Figure 5.18: Frequency Map for different temperature conditions (Boussinesq / non-Boussinesq) based on numerical simulations for an annular cavity (A = 40, η = 0.8).

Figure 5.19 shows the average amplitude of temperature oscillations (in dimensionless units) at different Rayleigh numbers for the three ε cases. In each case, the amplitude of oscillations increases with an increase in Rayleigh number. The amplitude of oscillations is around 2 percent of the maximum temperature difference inside the cavity ΔT at the onset of the multicellular flow and increases up to 14 percent of ΔT at Ra =14000 for each case.

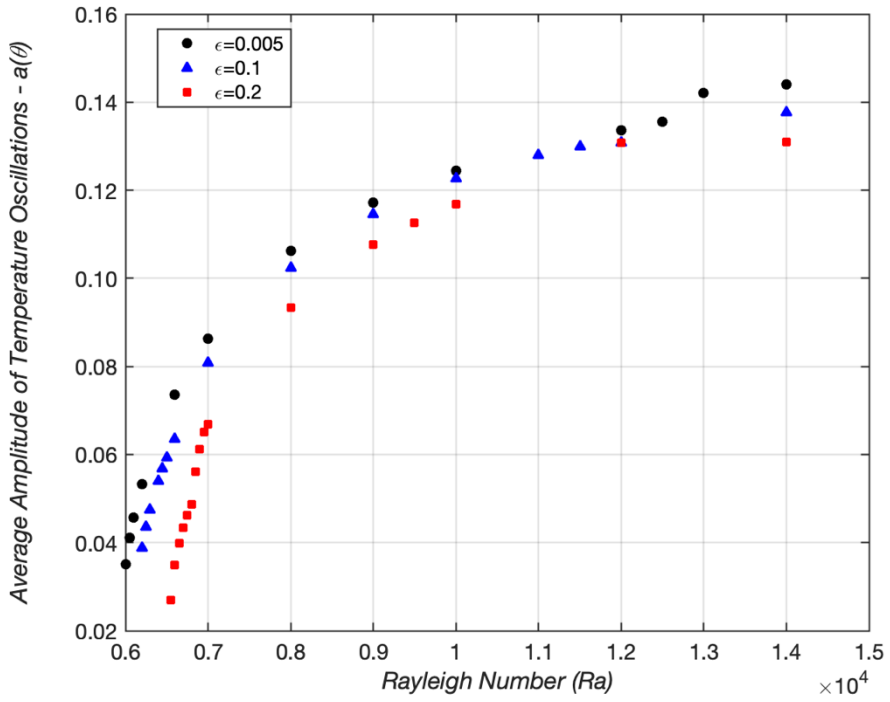

Figure 5.19: Average amplitude of temperature oscillations measured at the monitoring point located at $\left(\bar{x} = \frac{H}{3L},\ \bar{r} = \frac{R_i+R_o}{2L}\right)$ at different Rayleigh numbers for $\varepsilon = 0.005$, $\varepsilon = 0.1$ and $\varepsilon = 0.2$.

5.4.7 Effect of ε on Spatial Flow Structure

For the cartesian cavity case studied in the previous chapter, it was observed that the non-Boussinesq temperature conditions affected the area of the cavity where the multicellular flow is observed. A similar effect is observed in the annular cavity case as well. Figure 5.20 shows the radial velocity along the cavity's vertical midplane at a Rayleigh number of 7000 for the three ε cases. Multicellular flow does not occur in the top and bottom regions of the cavity shown in the figure by penetration distances Z_{e1} for the upper end and Z_{e2} for the lower end of the cavity. For the Boussinesq case, the penetration distances from the upper and lower cavity ends are almost equal ($Z_{e1} \approx Z_{e2}$). As the conditions become more non-Boussinesq (higher values of ε), the top

penetration distance Z_{e1} increases while the bottom penetration distance Z_{e2} decreases. As a result, for the ε = 0.2 case, the multicellular flow is mainly observed in the lower 2/3rd part of the cavity.

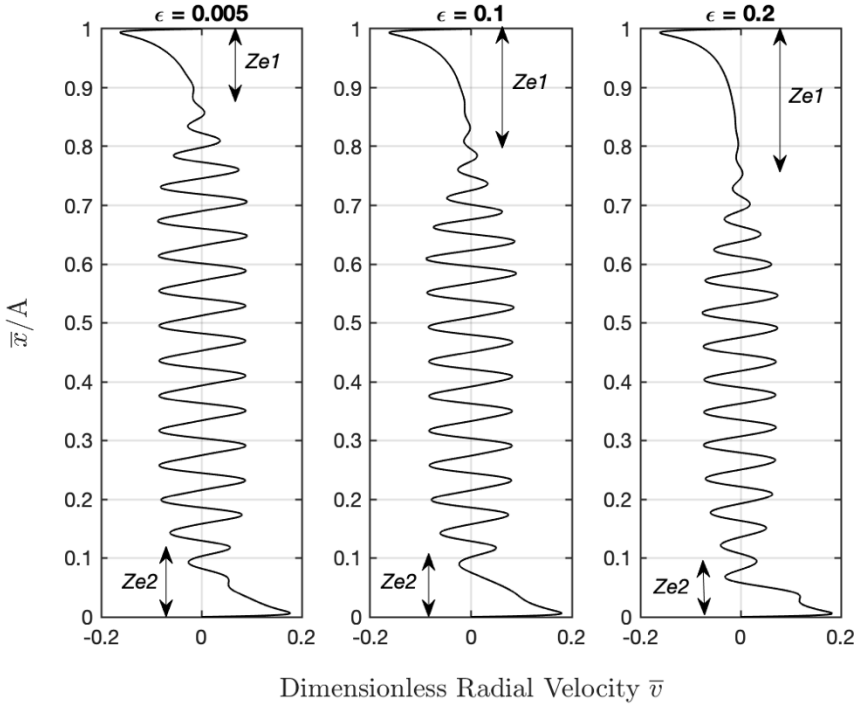

Figure 5.20: Dimensionless Radial velocity along the cavity's vertical midplane $\left(\bar{r} = \frac{R_i+R_o}{2L}\right)$ at Ra = 7000 for ε = 0.005 (left), ε = 0.1 (center) and ε = 0.2 (right).

5.4.8 Effect on Heat Transfer

Local Nusselt number along the heated and cooled cylinder walls is evaluated as

$$Nu(x) = \frac{h(x).L}{k_m} = \frac{q(x).L}{(T_h - T_c).k_m} = \frac{L}{(T_h - T_c).k_m} k(T) \left|\frac{dT}{dr}\right|_{wall} \quad (5.12)$$

where h(x) is the local heat transfer coefficient, k(T) is the temperature dependent thermal conductivity, k_m is the thermal conductivity at the mean wall temperature T_m, and $q(x) =$

$k(T)\left|\frac{dT}{dr}\right|_{wall}$ is the local heat flux. The downward drift of the cells causes both spatial and temporal oscillations in local Nusselt numbers along the cylinder walls. The amplitude and time-period of these oscillations are strong functions of the dimensionless temperature difference ε. In addition, local Nusselt number distribution along the cavity walls for a given Raleigh number can also vary significantly depending on the values of ε. Figure 5.21 shows instantaneous spatial variations of local Nusselt numbers along the heated and cooled cylindrical walls for a Rayleigh number of 12000, for the three dimensionless temperature difference ε cases. For the Boussinesq case ε = 0.005, the flow inside the cavity is monoperiodic at Ra = 12000, which cause regular spatial oscillations in the local Nusselt number along the cavity walls as seen in Fig. 5.21 (left). For the two non-Boussinesq cases ε = 0.1 and 0.2, the flow is quasiperiodic for Ra = 12000. As a result, the spatial oscillations in the local Nusselt number are not regular along the cavity length as seen in Fig 5.21(center and right).

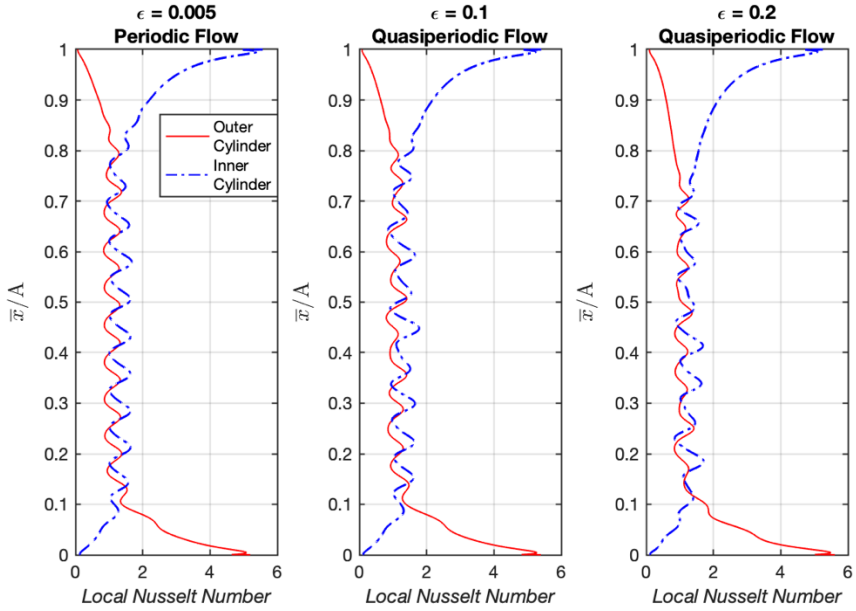

Figure 5.21: Local Nusselt numbers along the heated outer and cooled inner (dashed) cylinder walls for Ra = 12000 and dimensionless temperature difference ε = 0.005 (left), ε = 0.1(center), and ε = 0.2 (right).

Although the non-Boussinesq temperature conditions can significantly alter the local Nusselt number distribution, the net effect on the spatially averaged Nusselt number $\overline{\mathrm{Nu}} = \frac{1}{H}\int_{x=0}^{x=H} \mathrm{Nu(x)}dx$, is negligible as can be seen in the Fig. 5.22. A similar trend of negligible effect of non-Boussinesq conditions on the average Nusselt numbers was observed for the cartesian case described in the previous chapter.

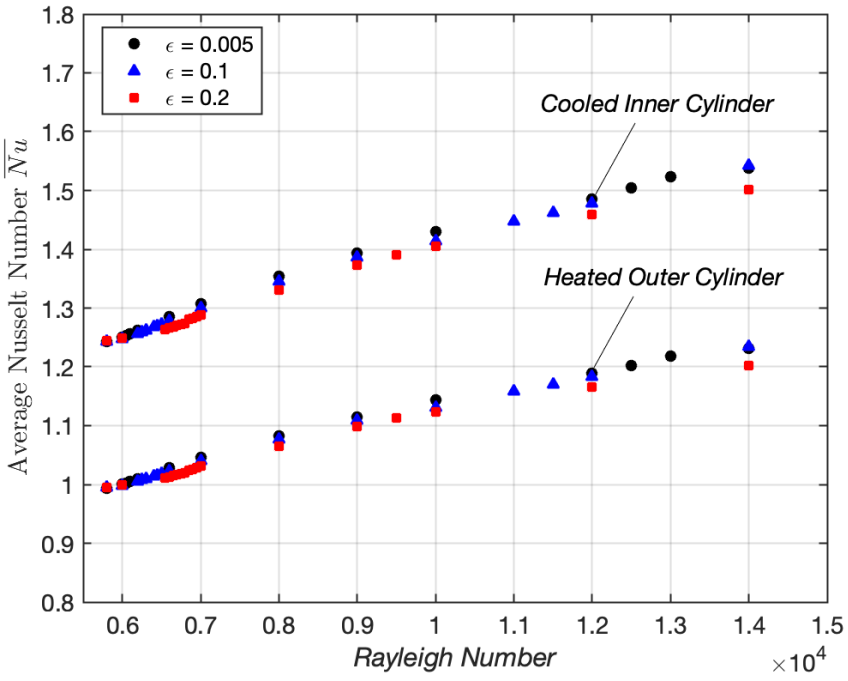

Figure 5.22: Average Nusselt numbers along the heated outer and cooled inner cylinder walls for dimensionless temperature difference ε = 0.005, 0.1 and 0.2.

5.5 Key Results and Conclusion

This numerical study found that non-Boussinesq temperature conditions have a pronounced effect on the onset of the 'cat's eye' instability in the annular cavity, subsequent flow bifurcations, wave-speeds, oscillation time-periods as well as on the local heat transfer rates. The value of the critical Rayleigh number which signifies the transition from steady flow to the downward drifting 'cat's

eye' instability increases as the conditions become non-Boussinesq (value of ε increases). The fundamental frequency of the monoperiodic oscillatory flows is found to increase with an increasing ε and decrease with increasing Rayleigh numbers. Further, the range of Rayleigh numbers over which monoperiodic oscillatory flows are observed is significantly reduced under non-Boussinesq temperature conditions compared to Boussinesq conditions. A second bifurcation from monoperiodic flow to quasiperiodic flow is observed for both Boussinesq and non-Boussinesq temperature conditions. However, the ratio of the two frequencies of quasiperiodic regime $\frac{f_1}{f_2}$ is found to increase as the temperature conditions become more and more non-Boussinesq. A stability map based on the results of the study indicating the steady, monoperiodic and quasiperiodic flow regimes for $0 \leq \varepsilon \leq 0.2$ and $0 \leq Ra \leq 14000$ is shown in Fig 5.23.

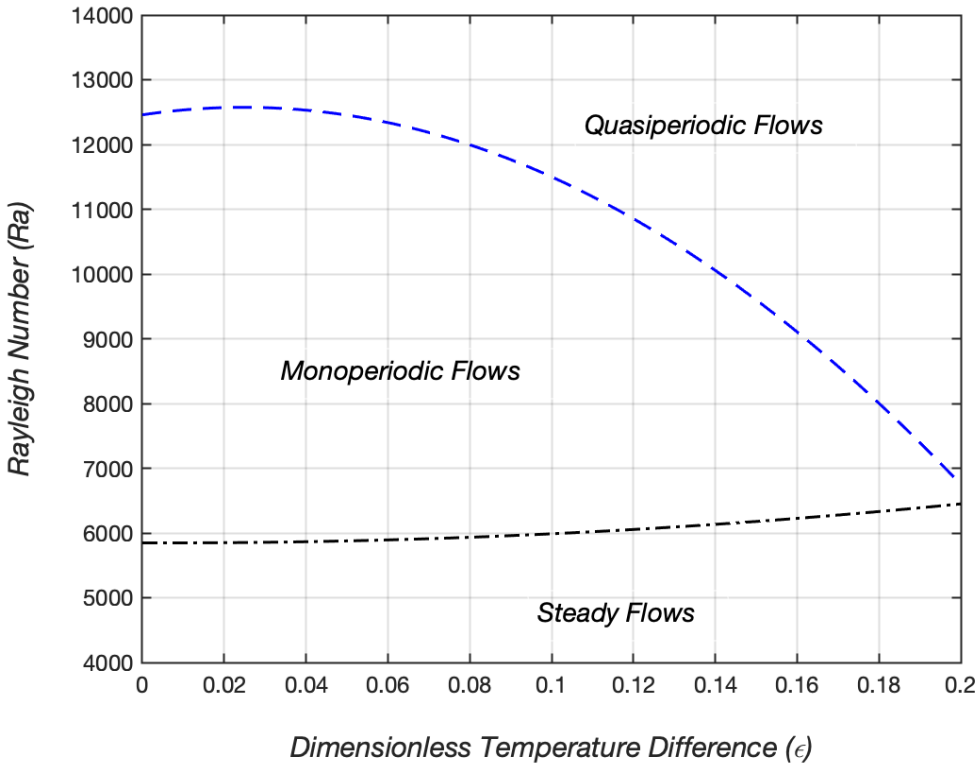

Figure 5.23: Stability map based on numerical simulations for an annular cavity (A = 40, η = 0.8).

Chapter 6

6 DESCRIPTION OF ANNULAR CAVITY EXPERIMENTAL SYSTEM

Natural convection of air inside a closed, tall annular cavity with a constant radius ratio $\eta = 0.50$, aspect ratio A = 25.2 and with non-isothermal vertical walls is investigated experimentally. Goal of the study is to map stability of the dynamical system and to understand instability mechanisms at play. Construction of experimental system, its various components and methods used for data collection and analysis are described in this chapter. Details of boundary conditions used for experiments and results from experiments will be presented in the next chapter.

6.1 Objectives of the Experiment

An experimental system is constructed to study unsteady periodic and chaotic natural convection flow of air inside a closed, tall, annular cavity wherein boundary conditions of opposing vertical walls support a base flow pattern similar to that observed by Reeve [1] in the polymer optical drawing system. Cavity walls consist of an inner cylinder of radius R_i, a concentric outer cylinder of radius R_o, and horizontal top and bottom surfaces. In the top part of the cavity, temperature of outer cylinder is higher than that of inner cylinder at the corresponding height, whereas in the bottom part of the cavity temperature of inner cylinder is higher than that of adjacent outer cylinder. These thermal boundary conditions, imposed on vertical walls of the cavity, support a bi-cellular base flow pattern consisting of two counter-rotating convection cells as shown in Fig. 6.1(a). This bi-cellular base flow is very similar to base flow observed during drawing of polymer optical fibers in an annular furnace [1,6] as shown in Fig. 6.1(b). Temperature difference in top

portion of the cavity drives the "upper convection cell" while temperature difference in bottom portion of the cavity drives the "lower convection cell." When temperature differences in either top or bottom part of the cavity are increased beyond critical values, the two counter-rotating cells begin to interact with each other, resulting in an unsteady air-flow inside the cavity. Transition from steady to unsteady air-flow is monitored via air temperatures measured inside the cavity at the interface region where the two counter-rotating cells are expected to interact. Nature of unsteady air-flow, whether axisymmetric or asymmetric, is also monitored via measured air temperature data.

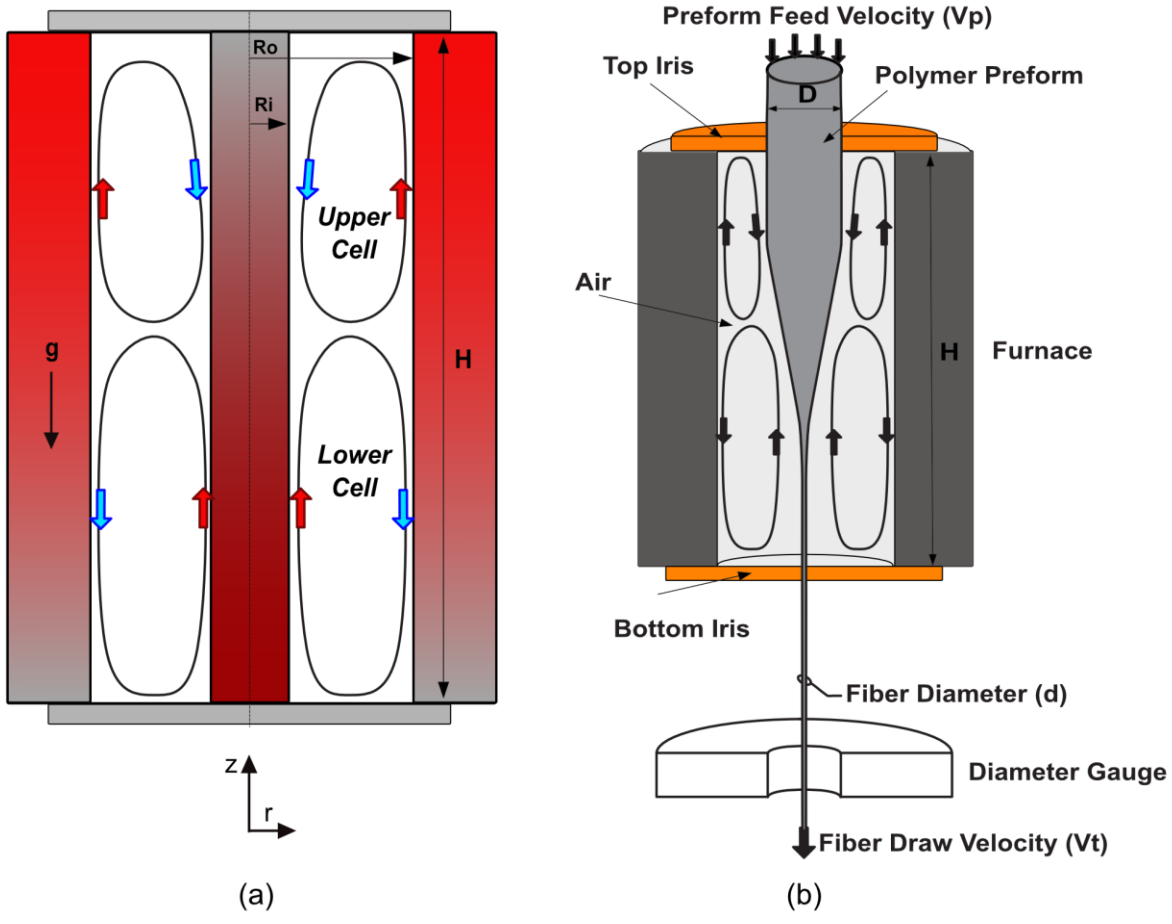

Figure 6.1: (a) Closed annular cavity with thermal boundary conditions supporting bi-cellular air-flow (b) Polymer fiber drawing system.

6.2 Experimental System

The experimental system is comprised of a tall, closed, air-filled annular cavity wherein the top portion of outer cylindrical wall and the bottom portion of inner cylindrical wall are actively heated while all other surfaces of the cavity are passively cooled. As the entire experimental system is passively cooled, ambient air temperature is important in the control of the cavity's thermal boundary conditions. To minimize changes in surrounding ambient air temperature, the entire experimental system was operated inside of a large tent enclosure in which ambient air temperature was maintained within $\pm$ 0.5°C. Tent enclosure housing the experimental system was set up inside a large laboratory where the room air conditioner cycled every 20 minutes. Due to cavity wall's relatively large thermal inertia, and with the aid of a thermal controller, furnace wall temperatures varied temporally no more than $\pm$ 0.08°C, with a time period of about 20 to 25 minutes, in response to ambient air temperature changes.

A schematic of the experimental system is shown in Fig. 6.2. Annular cavity is formed by holding a polycarbonate tube within a cylindrical refractory furnace with the help of two horizontal copper irises. Outer cylinder is a custom-made refractory furnace, and inner cylinder is a thick-walled black polycarbonate tube. Two horizontal surfaces at the top and bottom are precision made copper irises, with O-ring seals to seal gap between iris and polycarbonate tube. Aspect ratio of the cavity is $A = 25.2$, and radius ratio is $\eta = 0.50$. Temperature profiles along furnace inner wall and along cavity-side surfaces of polycarbonate tube and copper irises are monitored using an array of thermocouples. These 'wall thermocouples' are used for monitoring, measuring and controlling the surface temperature profiles of the walls of the annular cavity.

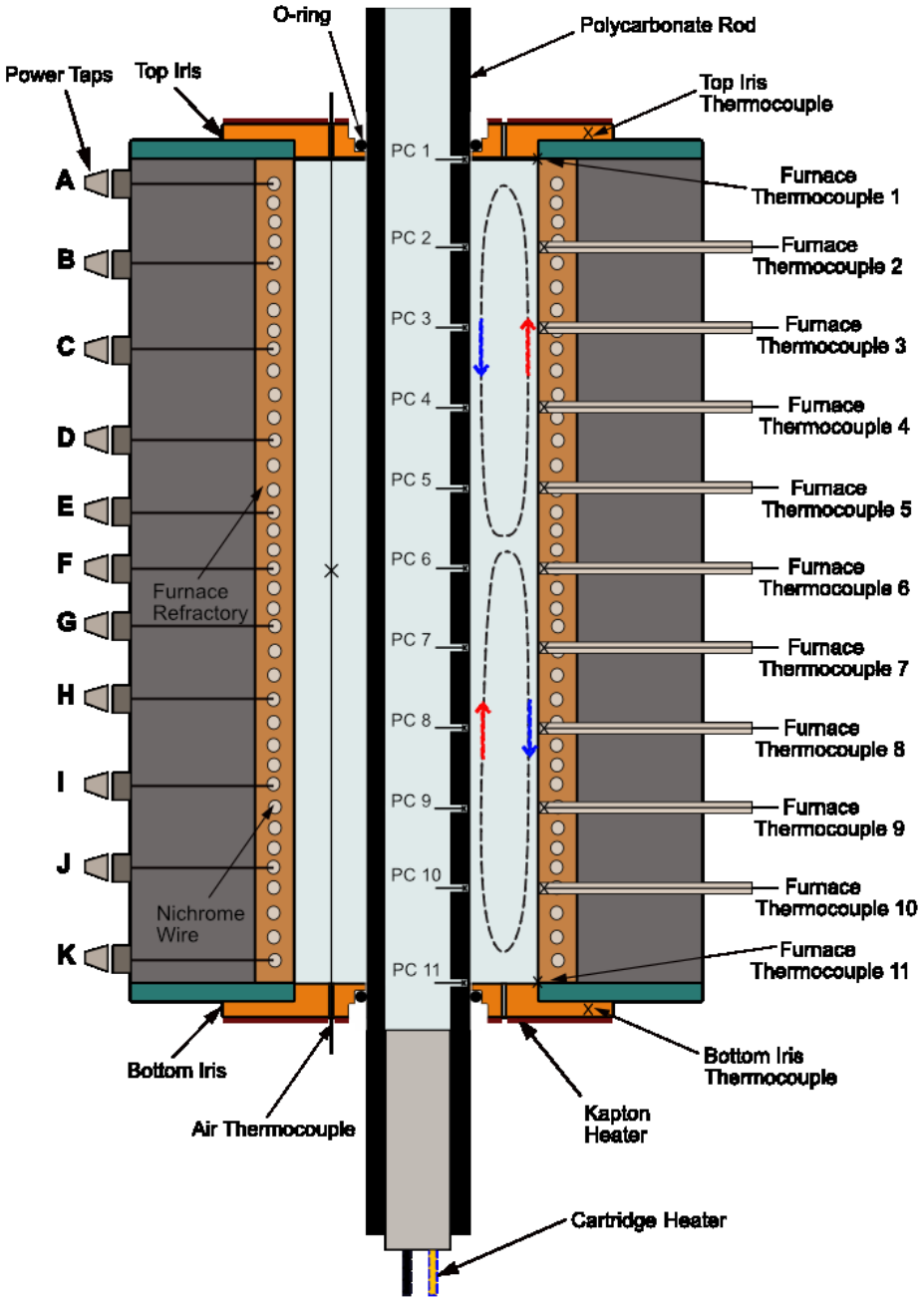

Figure 6.2: Schematic of the experimental system.

Wall thermal profiles serve two purposes:

1. Wall temperature profiles are used to calculate temperature differences observed in the top and bottom portions of the cavity. These are then used for determination of nominal Rayleigh number, which serves as an estimate of flow buoyant potential.

2. Wall thermal profiles are used as input boundary conditions for numerical predictions of natural convection inside cavity using computational fluid dynamics models of experimental system. Results from CFD simulations will be presented in Chapter 8.

Air temperatures inside the cavity are measured using four very fine wire thermocouples suspended at the vertical and radial midpoint of the cavity, and at four azimuthal coordinates, separated by $\Delta\theta = \pi / 2$ radians. These fine wire thermocouples are used for measuring temperature oscillations as well as for characterizing two-dimensional or three-dimensional nature of air flow.

6.3 Components of Experimental System

Components of the experimental system are :

1. Annular cavity, comprised of the furnace, polycarbonate rod and copper irises.
2. Power and control circuitry which is used to supply electrical power for heating furnace wall, polycarbonate tube wall and copper irises and also to control wall temperatures. Components providing electrical heating to the annular cavity are the nichrome wire embedded in furnace refractory wall, cartridge heater positioned at bottom of polycarbonate tube and Kapton heaters fixed to the outer surface of copper irises. VARIAC (Variable Transformer) AC power supplies are used for powering the nichrome wire coil and cartridge heater while a DC power supply is used for powering the Kapton heaters.

3. Data acquisition circuitry which is used to monitor and record cavity wall and air temperatures. This system is comprised of an array of thermocouples installed inside the cavity and along the cavity walls, a HP3852A DAQ data acquisition system and a computer running LabVIEW 2015.0 to interface with the DAQ.

Power circuitry and data acquisition circuitry are physically separated and do not share any common electrical input lines. This is done to prevent any electromagnetic noise from the power circuitry affecting thermocouple signals going to the data acquisition system. Wherever possible extension wires carrying thermocouple signals are enclosed inside a metal sleeve to prevent effects of stray electromagnetic fields on signals. Metal brackets around the furnace act as a faraday's cage and help in reducing electromagnetic interferences in the thermocouple signals. Care was also taken to properly ground the power and control circuitry. Figure 6.3 shows a diagram of power, control and data acquisition circuitry. Figure 6.4 shows a photograph of the actual experimental system.

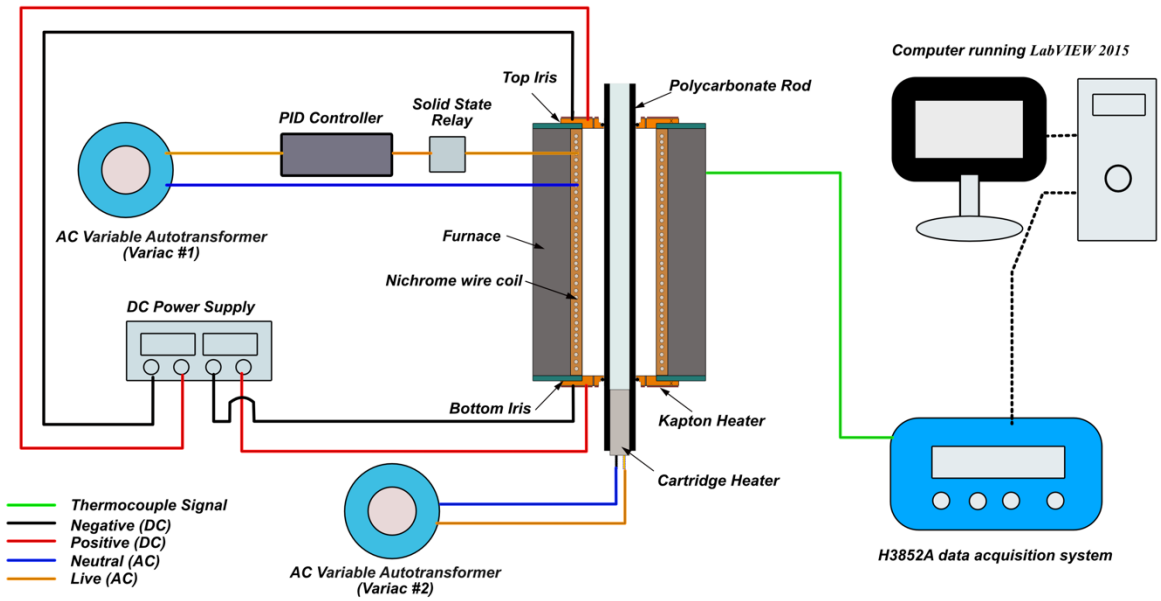

Figure 6.3: Power, control and data acquisition circuitry.

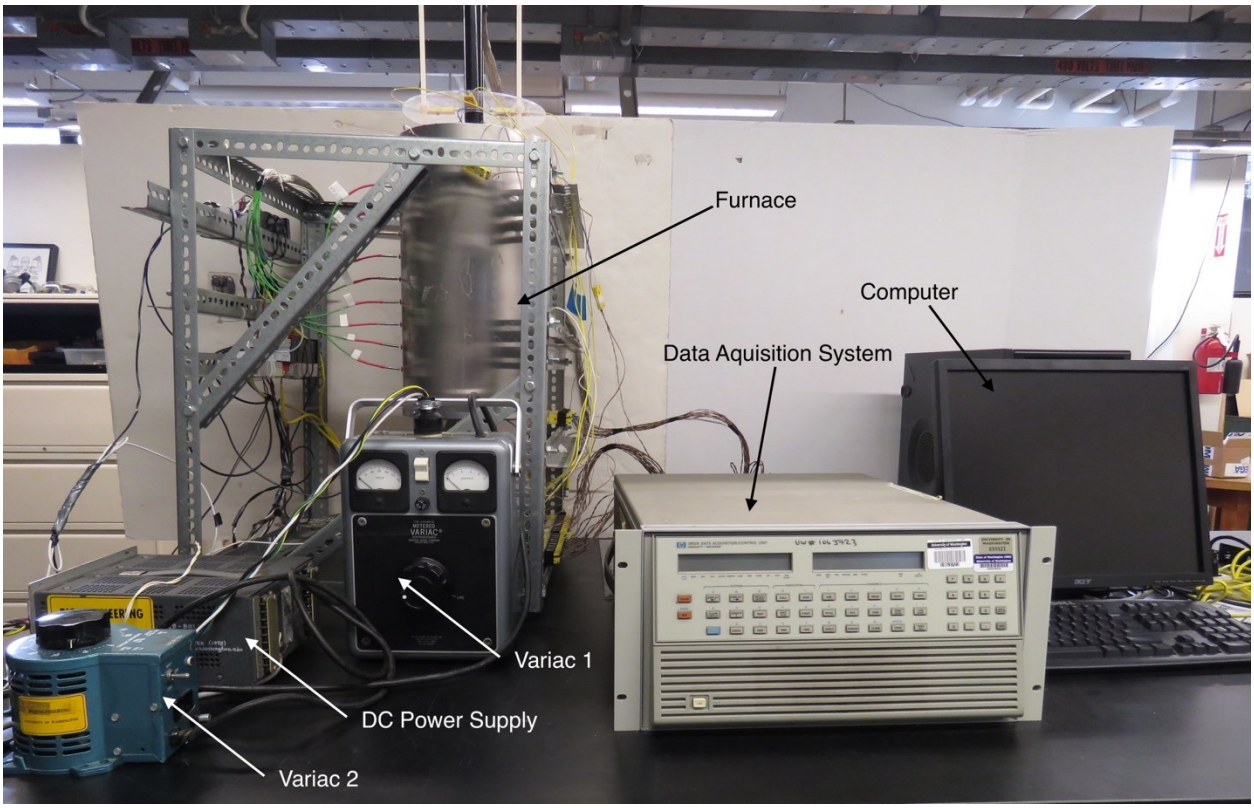

Figure 6.4: Photograph of the actual experimental system.

6.3.1 Furnace Wall

The furnace is a custom designed Thermcraft Inc. Marshall 1100 series furnace. Height of the furnace (H) is 0.400 m (15.75 inches), and its inner diameter is 0.0635 m (2.50 inches). Furnace wall is heated by a nichrome wire coil, embedded within the furnace refractory and powered by a Variable Autotransformer (Variac AC) unit of maximum rated capacity 0-280 V, 10A. Power can be applied to a variable length of nichrome wire using 11 taps labeled A-K located on the side of furnace. Thermal profile of furnace wall can be controlled by applying power across different combinations of power taps. Table 6.1 shows z-locations of power taps and resistance of nichrome wire coil between consecutive power taps.

Table 6.1: Location of furnace power taps, normalized location of power taps, and resistance between consecutive power taps (extreme right).

Power Taps	z (m)	z/H	Resistances between Taps (Ohms)
A	0.381	0.9525	1.8 (A-B)
B	0.331	0.8275	1.5 (B-C)
C	0.281	0.7025	1.1 (C-D)
D	0.245	0.6125	1.0 (D-E)
E	0.218	0.545	0.9 (E-F)
F	0.195	0.4875	0.9 (F-G)
G	0.172	0.4300	1.0 (G-H)
H	0.145	0.3625	1.1 (H-I)
I	0.109	0.2725	1.5 (I-J)
J	0.059	0.1475	1.8 (J-K)
K	0.009	0.0225	

Inner furnace wall temperature profile is monitored using 11 type K, prefabricated thermocouples. Nine of these thermocouples are 1 mm (0.04 inch) diameter thermocouples (numbered 2 through 10) installed flush along the furnace inner wall inside ceramic sheaths, and two additional thermocouples made of 0.13 mm (0.005 inch) diameter wire are attached to top and bottom edges of the furnace wall (numbered 1 and 11). Z-locations of these 11 thermocouples are shown in Table 6.2.

Table 6.2: Location and sensor numbers of furnace and polycarbonate tube wall thermocouples.

z/H	z (m)	Furnace Thermocouple Number	Furnace Sensor Name	Polycarbonate Tube Thermocouple Number	Polycarbonate Tube Sensor Name
1.000	0.400	1	210	1	104
0.873	0.349	2	200	2	105
0.778	0.311	3	201	3	106
0.683	0.273	4	202	4	107
0.588	0.235	5	203	5	108
0.492	0.197	6	204	6	109
0.397	0.159	7	205	7	110
0.301	0.120	8	206	8	111
0.207	0.083	9	207	9	112
0.111	0.044	10	208	10	113
0.000	0.000	11	209	11	114

Peak furnace wall temperature is actively controlled using a PID controller, Omega CN9112A, and a solid-state relay (Omega SSRL24DC25). The controller cycles power on and off to the nichrome wire to control peak wall temperature. Fig. 6.5 shows a close-up view of the furnace. 11 power taps are visible at the front side of furnace and wall thermocouple wires are visible on the right side of furnace. Furnace is held in place and supported by a steel frame as seen in Fig 6.5.

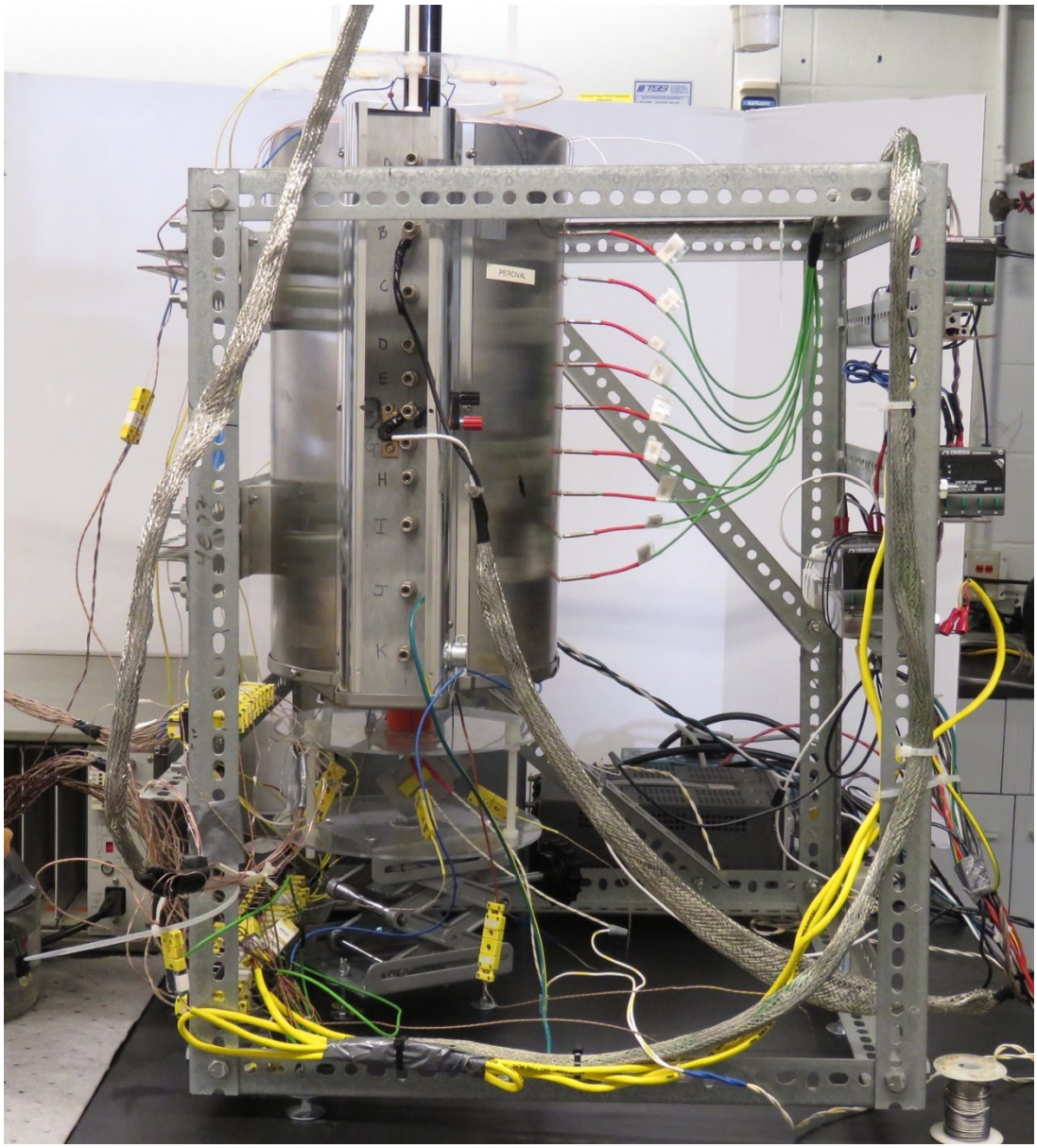

Figure 6.5: Thermcraft Inc. Marshall 1100 series furnace.

Nichrome wire is uniformly coiled along the refractory cylinder which makes up the furnace. This ensures uniform heat flux from coil to refractory cylinder in the azimuthal direction. This provides furnace thermal boundary conditions that are close to axisymmetric. Although no efforts were made to quantify the variation in furnace temperature profile in azimuthal direction, previous

investigations using a furnace of same dimensions have found furnace temperature profiles to be axisymmetric to within 0.3 degrees [1].

6.3.2 Polycarbonate Tube

Thick-walled black polycarbonate tube has an inner diameter of 0.0254 m (1.00 inch) and an outer diameter of 0.0318 m (1.25 inches). The polycarbonate tube is held concentrically inside the furnace by two copper irises. Two high-temperature O-rings are used to seal the gap between the polycarbonate tube and copper irises, preventing air from escaping from the cavity. An assembly of two acrylic plates supported on a leveling table is placed below the bottom of the polycarbonate rod. The acrylic plate structure serves two purposes; it provides additional mechanical support for the polycarbonate tube and provides a base for holding 'taut' thermocouple wires coming out of bottom iris. A similar assembly of two acrylic plates is placed on top of the furnace which provides a base for holding 'taut' thermocouple wires emerging from top iris. Polycarbonate tube and inner cylindrical furnace wall are held vertically to within 0.1 degree, for all experimental runs. Total length of the polycarbonate tube is 0.7874 m. Out of this 0.4 m is inside the furnace forming inner cylinder of the annular cavity. Length of tube below the bottom iris is 0.0762 m.

A low-density cartridge heater with a sheath length of 0.0762m (3.0 inches) and a maximum rated wattage flux of 4.9 W/cm^2 is positioned inside the polycarbonate tube at its bottom. The cartridge heater is powered by a Variable Autotransformer (Variac AC) unit of maximum rated capacity 0-120 V and 10A. Eleven type-K, prefabricated insulated 0.25 mm (0.010 inch) diameter wire thermocouples, are installed flush with cavity-side (outer) surface of polycarbonate tube. These 11 thermocouples are used for monitoring the temperature profile that develops on the polycarbonate tube. To install these thermocouples, a series of 1 mm (0.04 inch) diameter holes

were drilled through the wall thickness of polycarbonate tube. Thermocouples were then embedded and potted flush with the outer tube surface using a low thermal conductivity epoxy, *OMEGABOND*® OB-100. Z- locations of these 11 thermocouples are exactly the same as those of the 11 thermocouples assembled on furnace wall (shown in Table 6.2).

6.3.3 Copper Irises

Two copper irises are machined with high precision so that they can be used for maintaining the cylindrical surfaces concentric and vertical. Thickness of each iris is 8.26 mm (0.325 inch) and their outer diameter is 0.0762 m (3-inch). Fig. 6.6 shows a CAD drawing of top and bottom irises along with tolerances on each surface. After assembly of the two irises, inner surfaces of top and bottom irises are exactly perpendicular to the furnace wall surface.

Ten-millimeter deep holes were machined from the periphery of the irises to install 0.51 mm (0.020 inch) diameter wire, prefabricated type K thermocouples. A high thermal conductivity epoxy, *OMEGABOND*® OB-200, was used to bond these thermocouples to interior of the irises. These thermocouples are used for monitoring iris temperatures. Four small holes of diameter 1.5 mm (0.06 inch) were drilled in the copper irises at a radial location of r = 0.0238 m and azimuthal locations separated by 90º angles, as shown in Fig. 6.6. These small holes are used to thread fine thermocouple lead wires (used for monitoring air temperatures) inside the cavity through the top and bottom irises. Radial locations of these holes corresponds to the midpoint of air-gap width formed between the polycarbonate tube and furnace walls. Inner surfaces of these holes were coated with *MG CHEMICALS*® Red insulating varnish to prevent electrical contact between thermocouple lead wires and copper irises.

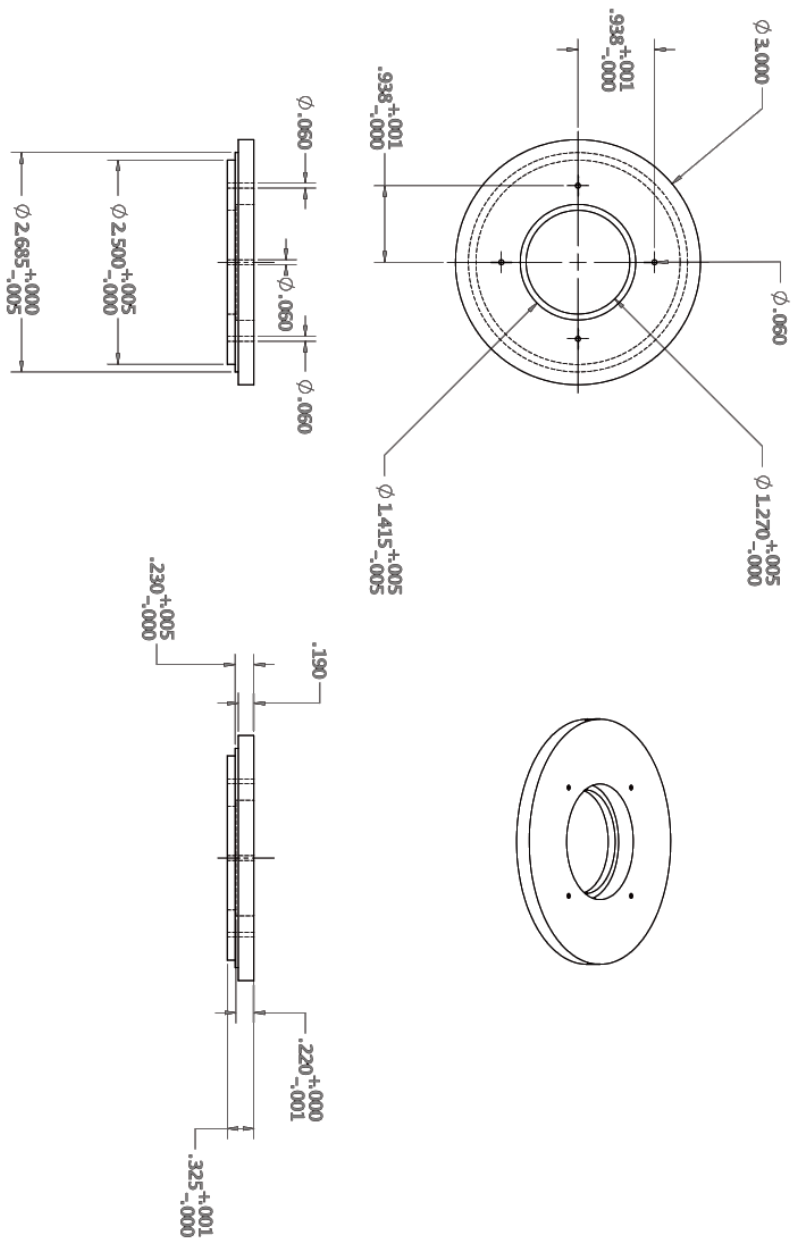

Figure 6.6: Drawing of the top/bottom iris along with tolerances on each surface. All dimensions are in inches.

Custom designed Kapton heaters with a 0.0762 m (3-inch) outer diameter and 40-watt capacity are installed on the outer surface of each iris using pressure sensitive adhesive. Kapton heaters, shown in Fig 6.7, are powered with a DC power supply unit of maximum rated capacity

40 V and 1 A. Top iris temperature was held temporally within $\pm$ 0.06°C and bottom iris temperature was held within $\pm$ 0.08°C for all experimental runs.

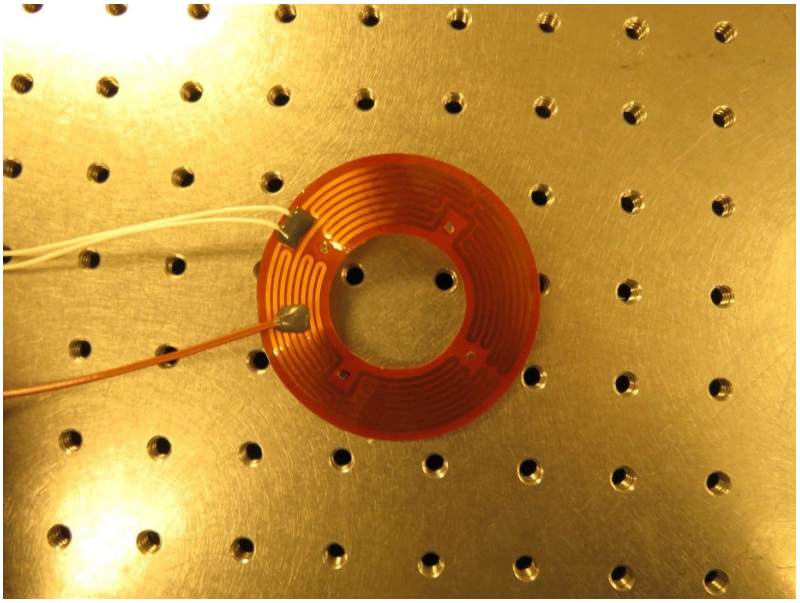

Figure 6.7: Photograph of the Kapton heater before being installed on the bottom iris.

6.3.4 Air Temperature Measurements

Four 0.125 mm (0.005 inch) fine diameter wire, butt-welded, type K, prefabricated Omega© thermocouples are installed inside the cavity to measure air temperatures. Thermocouple wires are installed via small holes drilled through the thickness of each iris, with positive and negative leads coming out through top and bottom irises, respectively. These four thermocouples are positioned at azimuthal angles $\theta = 0°, 90°, 180°$ and 270° at the vertical mid-plane of the cavity ($z/H = 0.500$) and at radial midpoint locations $r = (Ro + Ri) / 2$. Small air gaps formed between the iris holes and threaded thermocouple lead wires are completely sealed using a series of shrink-wraps fitted on thermocouple lead wires exiting from top and bottom irises. An assembly of two acrylic plates

placed below the polycarbonate tube and above the furnace, are used to install connectors for thermocouple wires. Special care is taken to maintain the same vertical position for all four thermocouple sensors. Uncertainty associated with vertical location of each thermocouple's junction is within $\pm$ one mm. Air temperatures from these thermocouples are recorded and are used to determine whether air-flow inside the cavity is 2D axisymmetric or 3D asymmetric. Butt-welded thermocouples were used because they have no visible bead and their response times are faster as compared to a beaded thermocouple. All four thermocouples have the same time constant of 0.1 seconds [62] and same wire specifications, thereby reducing possibility of a phase lag between signals from two thermocouples on account of difference in response times.

6.3.5 Data Acquisition System

Voltage signals from thermocouples measuring wall and air temperatures were sent to a data acquisition system consisting of a HP3852A DAQ and a computer running LabVIEW 2015.0. A total of 29 thermocouple temperatures were recorded for each experiment which included 24 wall temperatures, 1 ambient air temperature and 4 air temperatures inside cavity. Two cards of HP3852A were configured to measure thermocouple voltages. For a typical experimental run, furnace and polycarbonate tube wall temperatures were recorded at a lower sampling frequency of 0.00417 Hz while the four air temperatures inside the cavity and iris temperatures were recorded at a higher sampling frequency of 2.5 Hz . Block diagram of the LabVIEW VI designed for measuring thermocouple voltages is shown in Fig.6.8. Thermocouple voltages were converted into temperatures based on the NIST ITS-90 datasheets for direct and inverse polynomial functions for type K thermocouples [63].

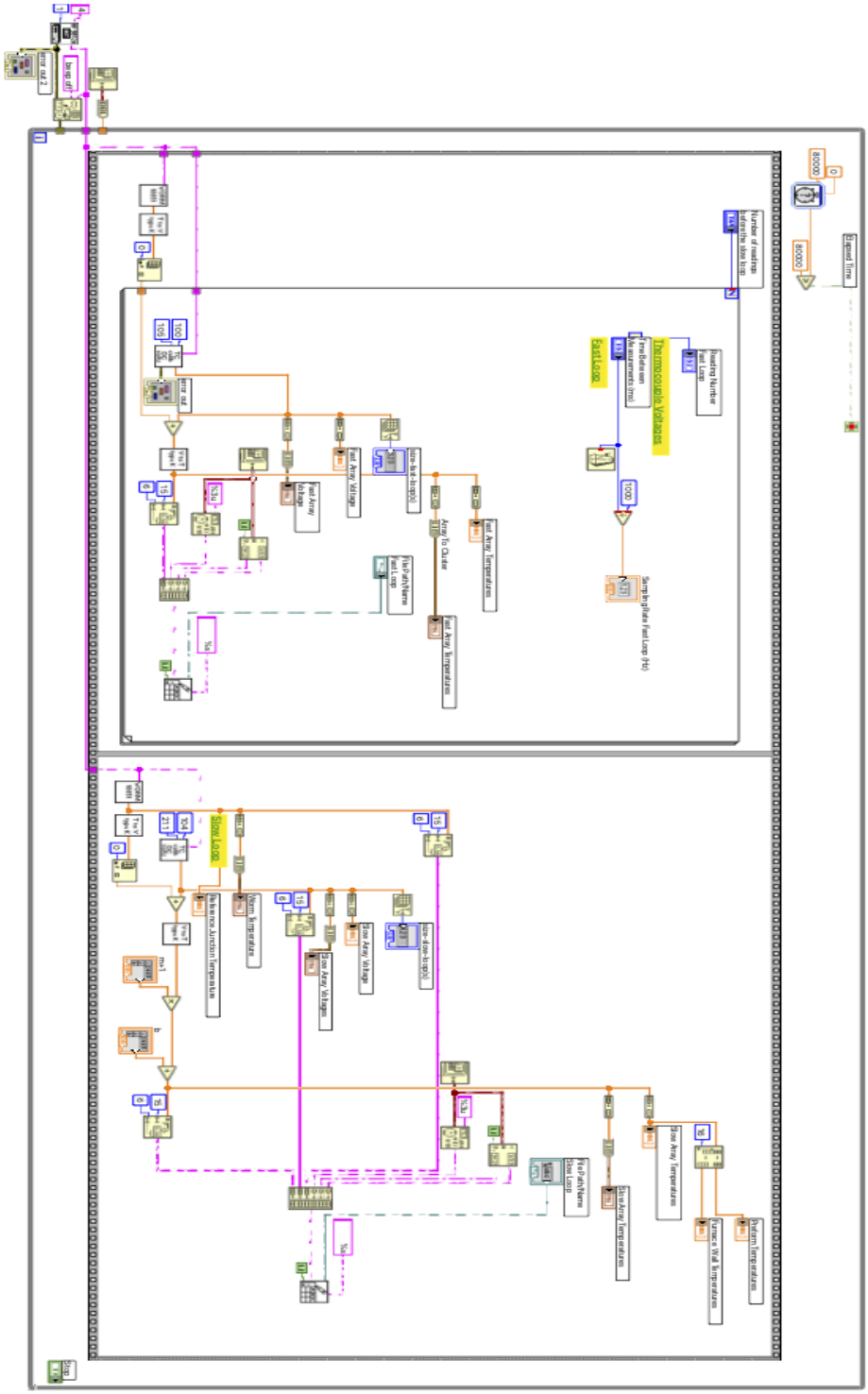

Figure 6.8: LabVIEW 2015.0 VI block diagram for temperature measurement of annular cavity experimental system.

6.4 Temperature Measurement Uncertainty

6.4.1 Wall Temperatures

Precision and bias of the 24 wall thermocouples were checked at three reference temperatures: an ice bath at 0.00°C, still air at a room temperature of 22.70°C and a boiling water bath at 99.7°C. Based on bias errors obtained at 0.00°C and 99.7°C, linear temperature corrections were implemented in the LabVIEW 2015.0 VI to correct bias (systematic error) for each wall thermocouple. Precision (random error) of wall thermocouples at the three reference temperatures is shown in Table 6.3.

Table 6.3: Wall thermocouple precision at three reference temperatures.

Reference temperatures	Precision
Ice bath at 0.00°C	$\pm$ 0.03°C
Still air at 22.70°C	$\pm$ 0.03°C
Boiling water bath at 99.7°C	$\pm$ 0.5°C

6.4.2 Air Temperatures

Thermocouples for measuring air temperatures are made of fine wire, which is prone to forming kinks if immersed in an ice bath or boiling water bath. Therefore, a single precision check was performed after thermocouples were installed at the vertical mid-plane of the cavity and at (selected four) radial midpoint locations. Precision of thermocouples for measuring temperature in still air was within $\pm$ 0.03°C. Baseline noise levels are also evident by examining air-temperature residuals for the four thermocouples and their Power spectral density function in still

air at 23°C. Fig. 6.9 shows residuals of air temperatures measured by the four thermocouples to be within $\pm$ 0.025°C over a time period of six minutes for steady air-flow inside the cavity. Power spectral density function shown in Fig. 6.10 shows a baseline noise-level less than -40 dB for all four thermocouples.

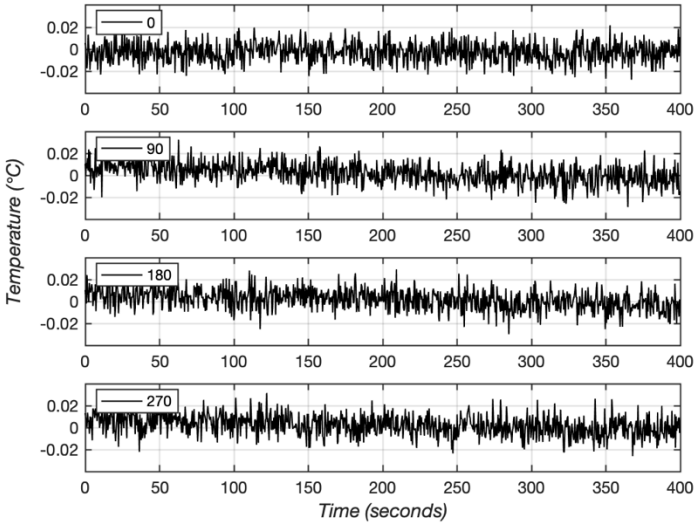

Figure 6.9: Air temperature residuals measured at θ = 0°, 90°, 180° and 270° for still air at 23° C.

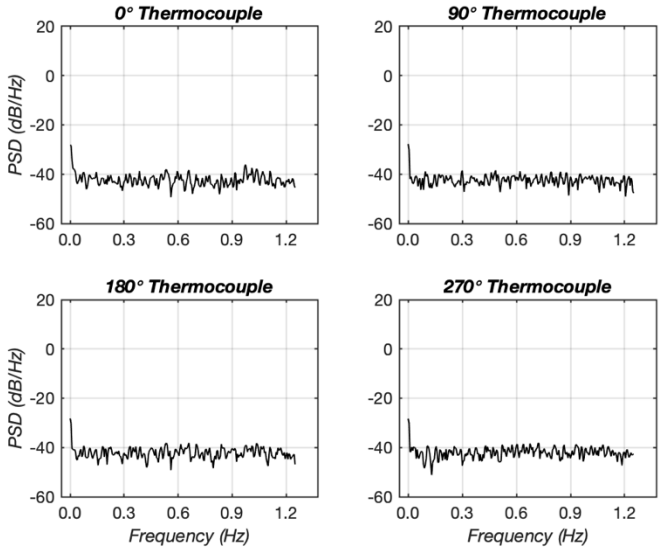

Figure 6.10: Power spectral density of air temperatures measured at θ = 0°, 90°, 180° and 270° for still air at 23° C.

6.5 Data Collection

Control parameters for the experiments were the furnace wall peak temperature and bottom iris temperature. For each experiment, control parameter was set, and all of the wall temperatures were monitored. It took approximately 10-12 hours for the furnace wall and polycarbonate surface temperatures to be fully established without temporal change. After this transient period of wall heating / cooling was complete, air temperatures, iris temperatures, polycarbonate surface and furnace wall temperatures were collected for two hours. For each two-hour duration, the maximum temporal variation in surface boundary temperature was less than $\pm$ 0.08°C.

A typical experimental run consisted of the following steps:

1. Control parameter is set to get the required wall temperature profiles.
2. Wall and air temperatures are continuously monitored, and data collection is started when the wall temperatures start to reach stable conditions.
3. 8-10 hours of data is recorded, and the last two hours of data recorded data is used for frequency analysis and post processing.
4. Control parameter is changed, and process is repeated.

Each experimental run took a total of 10-14 hours to complete. Fig. 6.11 shows the temperatures of the polycarbonate tube wall, furnace wall and ambient air temperature over a duration of 10 hours for an experimental run. In the last 2-3 hours of the run the wall temperature variations have dropped to below $\pm$ 0.08°C. The air temperature data and wall temperature data collected during this duration of time were used for post-processing. Periodic variation visible in in the room air temperature is on account of the room air conditioner cycling every 20 minutes.

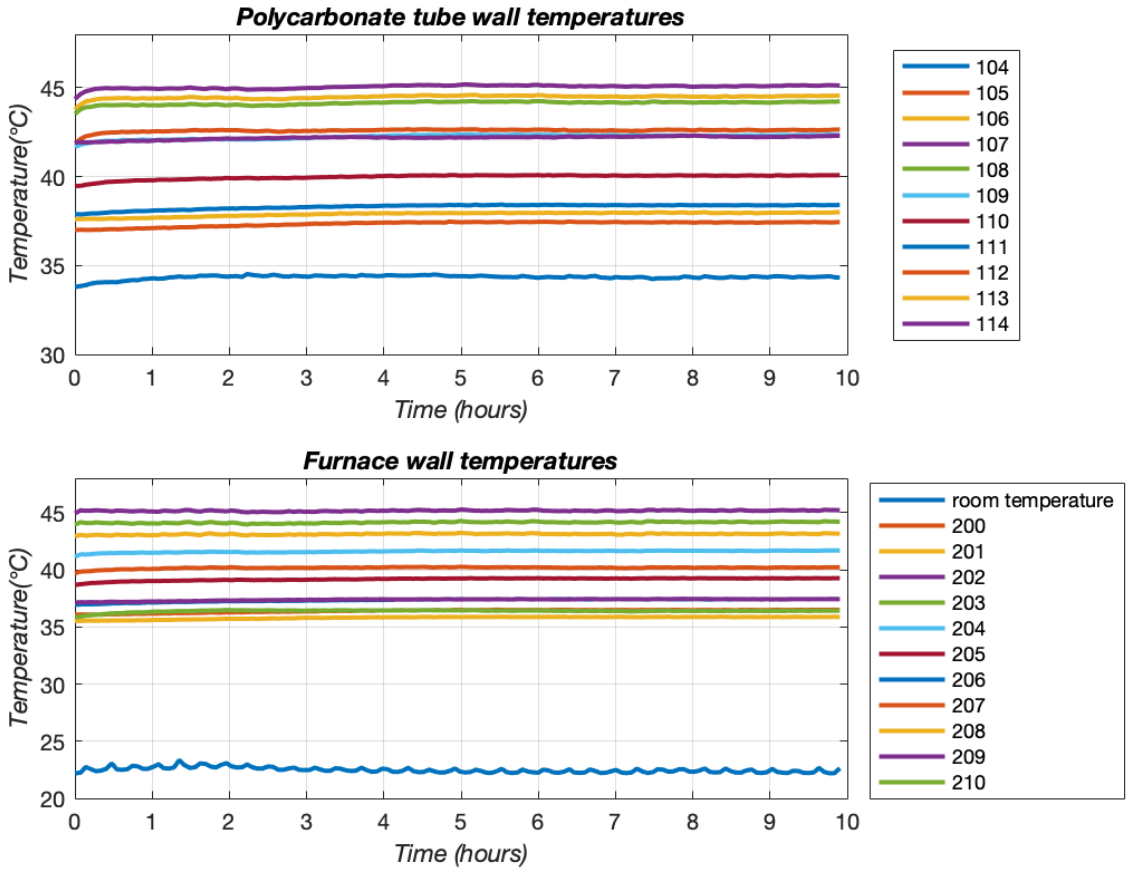

Figure 6.11: Temperature data of furnace wall (Sensors 200 to 210), polycarbonate tube wall (Sensors #104 to #114) and ambient room temperature over a time period of 10 hours.

6.6 Data Analysis

Air temperature data from thermocouples inside the cavity collected over a time period of two hours at a sampling frequency of 2.5 Hz, is used to determine the frequency content, amplitude and phase-lags between air temperature oscillations. Next few sections will go through the methods utilized for data analysis. Algorithms for data analysis were implemented in MATLAB R2019a [64].

6.6.1 Frequency Content

Recorded time series of air temperature data is first de-trended by subtracting the mean. De-trended time series of air temperature data is referred to as temperature residuals.

$$T_{residual} = T_{raw} - T_{mean} \tag{6.1}$$

Key frequencies present in the time series are then obtained from the power spectral density (PSD) of signal. Power spectral density also known as the spectral density function (SDF) of a time series specifies the distribution of power into the frequency content of time series signal. PSD for a wide-sense stationary random process can be estimated by a number of methods.

6.6.1.1 Periodogram

For a wide-sense stationary process X = { X_0, X_1, X_2 … X_N } recorded at evenly spaced time intervals t = { t_0, t_1, t_2 … t_N }the periodogram which is a non-parametric direct estimator of the PSD is given by [52],

$$\widehat{P}(f) = \frac{\Delta t}{N}\left|\sum_{j=0}^{N-1} X_j e^{-i2\pi jf\Delta t}\right|^2 \quad \text{for} -\frac{1}{2\Delta t} \le f \le \frac{1}{2\Delta t} \tag{6.2}$$

Where,

N = Total number of data samples

f = Frequency

Δt = Sampling interval

Fs= $1/\Delta t$ = Sampling Frequency

Fs/2 = $1/2.\Delta t$ = Nyquist Frequency

6.6.1.2 Modified Periodogram

The main drawback of the periodogram is that it introduced significant bias and variability in the PSD estimate [52]. To reduce the bias in the periodogram, time-series can be multiplied with a windowing function or a data taper before calculating the PSD. This is called a modified periodogram. A window function can be any function which has a value of zero at the start point and end points and which is non-negative. This technique of multiplying a time series with a window function is called 'Tapering' and it helps in reducing bias associated with the periodogram [52]. If h_j is a window function, the modified periodogram is defined by [52],

$$\widehat{P}(f) = \frac{\Delta t}{N}\left|\sum_{j=0}^{N-1} h_j X_j e^{-i2\pi jf\Delta t}\right|^2 \quad \text{for} -\frac{1}{2\Delta t} \leq f \leq \frac{1}{2\Delta t} \tag{6.3}$$

A number of windowing functions like the Rectangular window, Hamming window, Bartlett window, Blackmann window, Hann window and Kaiser window are used for calculating the periodogram. The Hann window is commonly used for time series exhibiting chaos [65,66] and is given by [52],

$$h_j = \frac{1}{2}\left[1 - \cos\left(\frac{2\pi j}{N}\right)\right] \text{ for } j = 0,1,2,3,\ldots N \tag{6.4}$$

6.6.1.3 Welch's Overlapped Segment Averaging Method (WOSA)

Welch's overlapped segment averaging method is based on breaking the time series into overlapping segments of data, computing modified periodograms of the data segments and then averaging the modified periodograms to obtain an estimate of the power spectral density. Modified

periodograms for overlapping segments are computed using an appropriate windowing function, such as the Hann window. Averaging process of modified periodograms reduces the variance in PSD estimate while the overlapping of segments helps in preventing the loss of information from the ends of the segments due to the windowing function. Thus, for large datasets Welch's overlapped segment method is recommended, since modified periodograms of segments of data provide unbiased estimates of PSD and the averaging of periodograms reduces variability [3, 4].

Consider a time series X = { X_0, X_1, X_2 … X_N }with power spectral density function P(.). The direct spectral estimator based on the modified periodogram for a segment of data containing Ns samples staring at index '*l*' is given by [52],

$$\widehat{P}(f) = \frac{\Delta t}{N_s}\left|\sum_{j=1}^{N_s} h_j X_{j+l-1} e^{-i2\pi jf\Delta t}\right|^2 \quad \text{for } 1 \le l \le N+1-N_s \tag{6.5}$$

WOSA based estimate of the power spectral density is given by [52],

$$\widehat{P}^{(WOSA)}(f) = \frac{1}{N_B}\sum_{j=0}^{N_B-1} \widehat{P}_{jn+1}(f) \quad \text{for } 1 \le l \le N+1-N_s \tag{6.6}$$

Where,

N_B = Total number of data segments

N_S = Number of data samples in each segment

l = index of data segment

N = Total number of data samples

$\left(1-\frac{n}{Ns}\right)x\ 100$ = Percentage of overlap between segments where 'n' is an integer value shift factor satisfying $0 \le n \le N_s$ *and* $n(N_B-1) = N - N_s$

Due to advantages of Welch's overlapped segment averaging method explained in previous sections, it was selected for computing the power spectral density of temperature time series. The time series signal was divided into 20 windows with 50% overlap, and each segment was windowed with a Hann window given by equation (6.4). Dominant frequencies present in the signal were then determined from the PSD. The frequency resolution achieved by using the WOSA method is +/- 0.0015 Hz and the maximum frequency than can be represented on the PSD is the Nyquist frequency $\frac{F_S}{2}$ = 1.25 Hz.

6.6.2 Amplitude

Oscillation amplitudes for periodic flows are calculated by determining mean peak to peak amplitude of periodic temperature oscillations over duration of experiment and then dividing it by a factor of 2. An amplitude of x°C thus represents $\pm$ x°C change from mean temperature. Amplitudes calculated for quasi-chaotic flows, intermittent flows and quasi-periodic flows are average amplitudes of oscillations for the temperature data series over duration of experiment.

6.6.3 Time Delay

In case of axisymmetric flows, all four thermocouples measuring air temperatures at the cavity's vertical and radial midpoints would likely be in phase. A phase lag in air temperature measurements indicates 3D asymmetric (swirling) flow. For all four temperature time series, time lags are obtained by calculating the cross-correlation function of each of the θ = 90°, 180° and 270° thermocouple temperature signals with reference to the θ = 0° thermocouple temperature signal. Cross-correlation function measures the correlation between two time series as a function

of lag or displacement of one series with respect to the other. Estimate of the cross-correlation function between two discrete time series (temperature signals) A_n and B_n is given by [67],

$$\hat{\varphi}_{xy}(k) = \begin{Bmatrix} \sum_{n=0}^{N-k-1} A_{n+k} B_n^* \text{ for } k \geq 0 \\ \widehat{\varphi^*}_{xy}(-k) \text{ for } k < 0 \end{Bmatrix} \quad (6.7)$$

Where,

k = lag or displacement

N = total number of samples in series A and B

* = Complex conjugate

After calculation of cross-correlation function $\hat{\varphi}_{xy}(k)$ between the two temperature signals, lag value 'k' for which function value is maximum is determined to estimate time delay between the two temperature signals. Phase lag for each thermocouple temperature signal with respect to reference ($\theta = 0°$) thermocouple temperature signal is calculated based on time-lag values and oscillation frequency as follows:

$$\text{Phase lag (in degrees)} = \frac{\text{Time} - \text{lag (seconds)}}{\text{Time period of oscillations (seconds)}} \text{ x } 360^o \quad (6.8)$$

6.6.4 Time-frequency Analysis

Power spectral density function of a time signal is able to give information on all frequencies that are present in a signal. However, we cannot get any information on specific time instances at which particular frequencies were produced. For some experimental runs chaotic and intermittent flow phenomena were observed; where the frequency content alone cannot provide a complete picture

of the flow behavior. Therefore, a time-frequency analysis is performed for quasi-periodic, intermittent and quasi-chaotic flows. For time-frequency analysis, the total time signal is decomposed into small time windows. Frequency content of each time window is then extracted using fast Fourier transform (FFT). In order to extract frequency content from only one time-window at a time (localized time and frequency), the FFT kernel is modified using a Gabor function. This new transform is called the short-time Fourier transform or the Gabor Transform [53] and is given by:

$$G[f](t,\omega) = \int_{-\infty}^{\infty} f(\tau)\bar{g}(\tau - t)e^{-i\omega\tau}\, d\tau = (f, \bar{g}_{t,\omega}) \tag{6.9}$$

Where f(t) = signal and $g_{t,\omega} = g(\tau - t)e^{-i\omega\tau}$ is the Gabor kernel.

Thus, Gabor transform is a function of the two variables t(time)and ω(Frequency). Transform window is centered at time instance 'τ' with a width 'a' of the signal. 'τ' is the translation parameter which moves the Gabor transform in time domain and 'a' is the scaling parameter which decides the width of filter function used in the transform. A Gaussian Gabor function is used for calculating the Gabor Transform of temperature data from the experiments and is given by

$$g(t) = e^{-a(t-\tau)^2} \tag{6.10}$$

Where a = 0.005 and b = 0.5.

The process of Time-Frequency analysis of a temperature data set from one of the experiments exhibiting quasi-chaotic behavior is shown in Fig. 6.12.

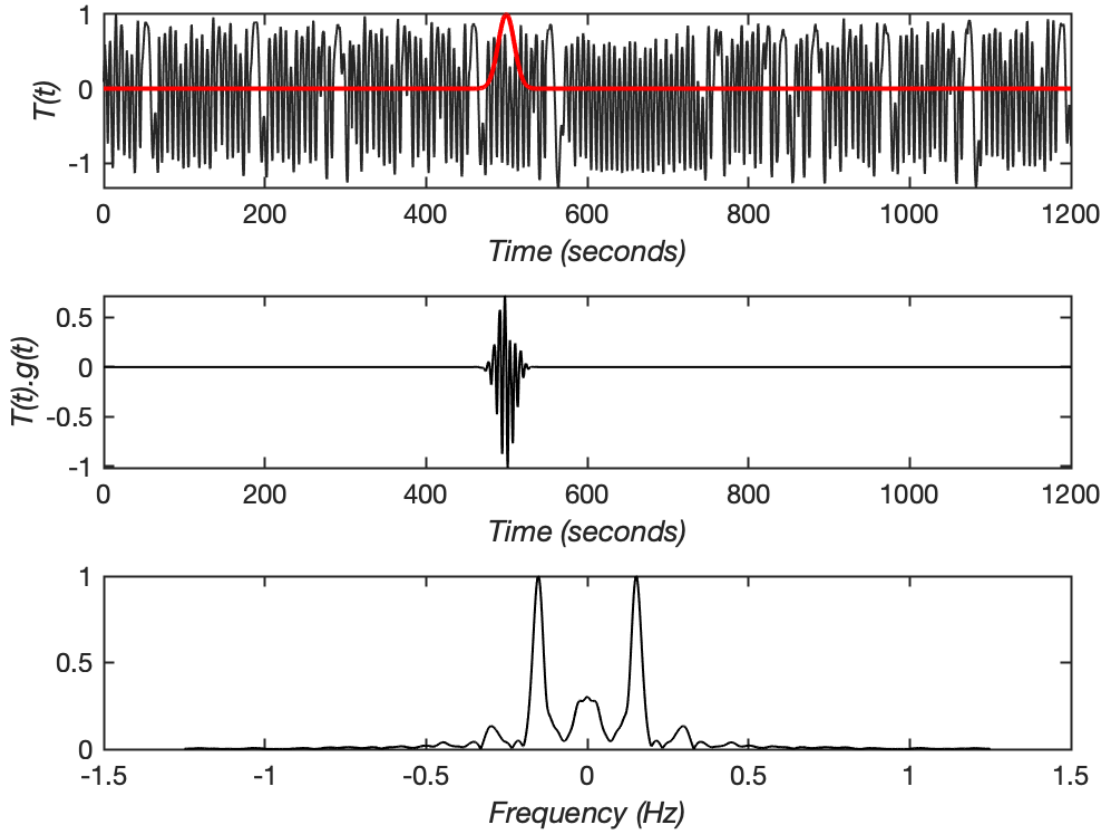

Figure 6.12: Temperature residuals showing quasi-chaotic behavior (Top plot) and Gaussian Gabor function (red), product of Gabor function with temperature data at a specific time instant (Middle plot) and Gabor transform at a specific time instant (Bottom plot).

Top plot shows residuals of temperature data and the Gaussian Gabor function**.** Middle plot shows the product of Gabor function with temperature data at a specific time instant and bottom plot shows the value of Gabor transform at a specific time instant. A spectrogram is a graphical representation of the Gabor transform in the time and frequency domain. Various frequencies produced at each instance in time are represented on the spectrogram for easy visual observation.

Chapter 7

7 NATURAL CONVECTION IN ANNULAR CAVITY – EXPERIMENTAL RESULTS

7.1 Wall Thermal Profiles for Experiments

In order to induce a bi-cellular base flow inside the cavity, the top portion of the furnace wall is heated by applying power to taps B-F, and the lower portion of the polycarbonate tube wall is heated by applying power to the cartridge heater near the tube base and by applying power to the bottom iris. The resulting thermal boundary conditions are such that the furnace wall (outer cylinder) has a higher temperature than the adjacent polycarbonate tube wall (inner cylinder) in the top part of the cavity, and the polycarbonate tube wall (inner cylinder) has a higher temperature than the adjacent furnace wall (outer cylinder) at the bottom part of the cavity as shown in Fig. 7.1. The final temperature profiles that develop on the polycarbonate tube and furnace wall interior surfaces are a combined result of conduction in the walls of the cavity, convection of air inside the cavity and radiative exchange between the inner surfaces of the annular cavity. The thermal profiles for the furnace wall and polycarbonate tube wall were determined by fitting a 5^{th} order polynomial to the temperature measurements from the thermocouples installed on the cavity walls. Fig. 7.2 shows the temperature profile of the furnace wall, polycarbonate tube wall and top and bottom irises for a typical experimental run. For all experimental runs reported in this study, the cavity's interior surfaces, including the furnace wall, polycarbonate tube wall, and bottom iris,

varied by no more than ± 0.08°C temporally, and the top iris interior surface temperature varied by no more than ± 0.06°C temporally over the duration of the two hour data collection.

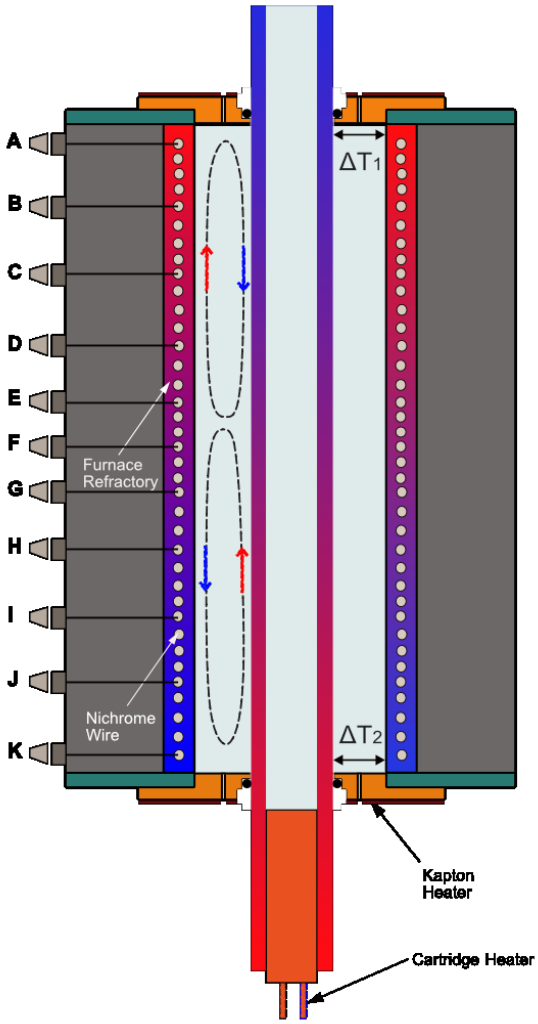

Figure 7.1: Schematic of the experimental system showing regions where active heating is applied to nichrome wire, cartridge heater and iris Kapton heaters.

Note: During the course of the experiments it was discovered that the location of two furnace wall thermocouples in the custom made Thermcraft Inc. Marshall 1100 series furnace were more than 7 mm away from the inner surface of the furnace wall. This resulted in a significant error in the temperature measurement at these two locations. Therefore, for the purposes of the determination of the furnace wall temperature profile the temperature measurements from those two sensors were not included in the polynomial fit. Further details about uncertainty associated with furnace wall thermocouples is provided in Appendix B.

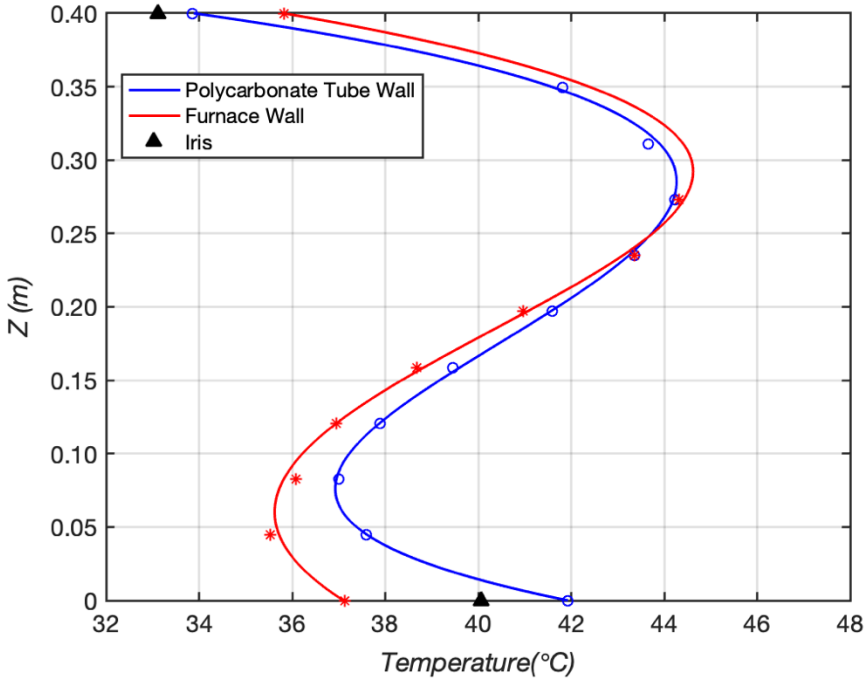

Figure 7.2: Temperature profile of the furnace wall, polycarbonate tube wall and top and bottom irises for an experimental run with peak furnace wall temperature $T_p = 44.6°C$.

7.2 Experimental Data Sets

7.2.1 Organization of Experiments

Temperature differences in the top and bottom parts of the cavity are indicative of the buoyant potentials of the upper and lower cells of the base bi-cellular flow as shown in Fig. 7.1. Two sets of experiments were conducted to study the effects of changing a cell's buoyant potential on the stability of air-flow inside the cavity.

Set A: In the first set of experiments, the buoyant potential of the upper cell was successively increased by increasing the peak furnace wall temperature (T_p). During these experiments, the heat flux applied to the polycarbonate tube via the cartridge heater and the heat flux applied to the

bottom iris via the Kapton heater were both held constant. The peak furnace wall temperature T_p is the control parameter for this set A of experiments. As the buoyant potentials of the top and bottom convection cells were increased different air-flow regimes were observed in the cavity. The data from the 4 thermocouples measuring air-temperatures was processed using methods described in Chapter 6. The experimental runs were then classified into steady, mono-periodic, quasi-periodic and chaotic air-flow regimes based on the analysis of the frequency content present in the temperature data. Further information on the frequency content of each air-flow regime is presented in the subsequent sections. Figure 7.3 shows examples of iris and wall temperature profiles (iris temperatures and cylindrical surface temperature profiles) that result in three different air-flow regimes for set A experiments.

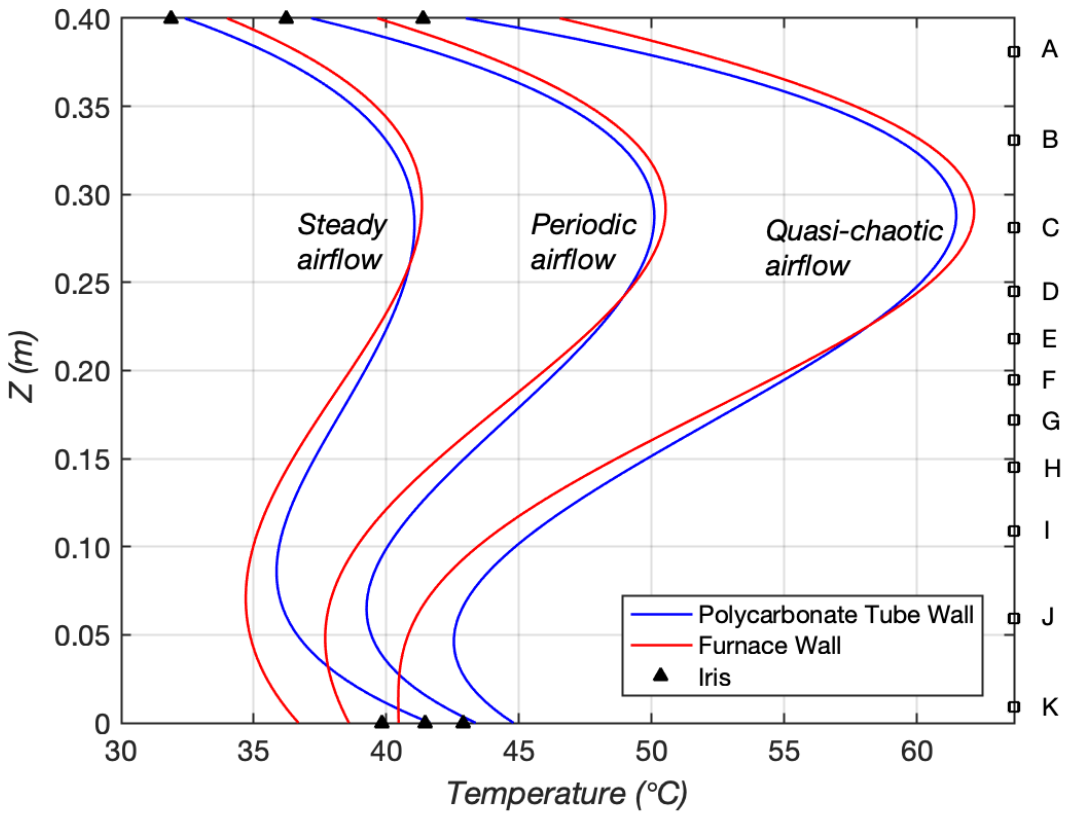

Figure 7.3: Sample temperature profiles of the furnace wall, polycarbonate surface and irises for steady, periodic and quasi-chaotic air-flow regimes with peak furnace wall temperature T_p as the control parameter.

Set B: In the second set of experiments, the buoyant potential of the lower cell was successively increased by increasing the bottom iris temperature (BI). During these experiments, the peak furnace wall temperature was held constant. The bottom iris temperature BI is the control parameter in this case. Figure 7.4 shows examples of iris and wall temperature profiles (iris temperatures and cylindrical surface temperature profiles) that result in different air-flow regimes.

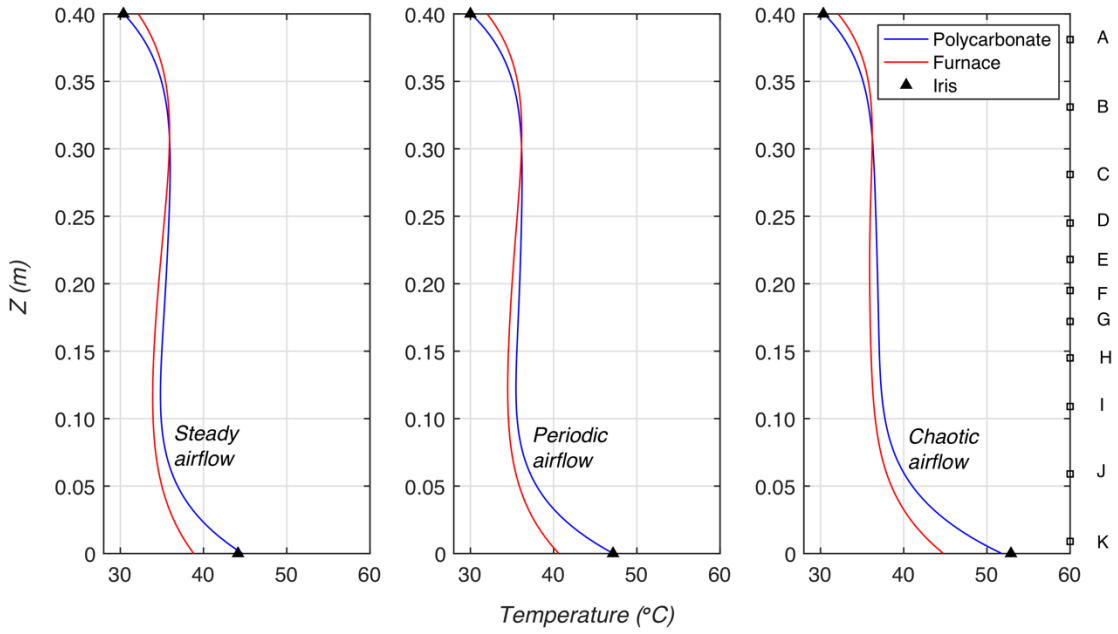

Figure 7.4: Sample temperature profiles of the furnace wall, polycarbonate surface and irises for steady and periodic flow regimes with bottom iris temperature BI as the control parameter.

7.2.2 Nominal Rayleigh Number

For all of set **A** and set **B** experiments, neither of the cavity's cylindrical surfaces are isothermal, as is apparent from examples of the thermal boundary conditions shown in Figs. 7.3 and 7.4; it is therefore not evident at first glance which temperature difference across the annular cavity should

be used to evaluate experimental Rayleigh numbers as a standardized basis for comparison with previous and potential future literature. The temperature difference between the furnace wall and the adjacent polycarbonate tube goes on decreasing as we move downward along the height of the cavity and becomes zero at the intersection point of the furnace wall and polycarbonate tube thermal profiles (cross-over point). Thereafter, as we move towards the bottom of the cavity, the temperature difference goes on increasing till the bottom edge of the cavity. This divides the cavity in two parts, namely the top portion which is the area above the cross-over point and the bottom portion which is the area below the cross-over point. The maximum temperature difference in the top part of the cavity is found at the top edge of the cavity and the maximum temperature difference in the bottom part of the cavity is found at the bottom edge.

For set **B** experiments in which the buoyant potential of the lower convection cell is varied, careful examination of the thermal boundary conditions in Fig. 7.4 reveals that the maximum temperature difference across the cavity's cylindrical walls occurs at the bottom edge of the cavity; thus this bottom edge ΔT is used to evaluate Rayleigh numbers for set **B** experiments. For set **A** experiments in which the buoyant potential of the upper convection cell is varied, careful examination of the thermal boundary conditions in Fig. 7.3 reveals that the maximum temperature difference across the cylindrical walls in the upper part of the cavity occurs at the top edge of the cavity; thus this top edge ΔT is used to evaluate Rayleigh numbers for set **A** experiments.

Experimental Rayleigh numbers calculated with the top edge ΔT (set **A**) or bottom edge ΔT (set **B**) are useful for comparison within these data sets; however, care must be exercised when comparing the current non-isothermal annular wall results to literature results for cavities with isothermal walls. The characteristic length chosen for evaluating Rayleigh numbers in this study

is the height of the annular cavity, $L_c = H$, and all of air's thermophysical properties are evaluated at the cavity's weighted mean wall temperature. For set **A** experiments, the nominal Rayleigh number range explored was 8.18 x 10^6 to 1.71 x 10^7. For set **B** experiments, the nominal Rayleigh number range explored was 3.08 x 10^7 to 3.57 x 10^7. The maximum uncertainty associated with these experimental Rayleigh numbers is $\pm$ 4%. The data presented in this chapter are from the analysis of over 60 sets of experimental data. Air temperature data and iris temperatures were all collected at a frequency of 2.5 Hz. Furnace wall and polycarbonate surface temperatures were collected at a frequency of 0.00417 Hz.

7.3 Results and Discussion

7.3.1 Varying Buoyant Potential of Upper Cell

In the first set A of experiments, the buoyant potential of the upper cell of the bi-cellular flow was successively increased by gradually increasing the peak furnace wall temperature. The first experiment was at a peak furnace wall temperature of T_p = 41.3°C corresponding to a nominal Rayleigh number of Ra = 8.18 x 10^6. For this experiment, natural convection flow inside the furnace is steady. Figure 7.5 shows the residuals of temperatures recorded by the air thermocouples over a time duration of three minutes for this experiment at T_p = 41.3°C. The temperatures recorded by the thermocouples are constant over the duration of the experiment and show no periodic variation. The PSD of the temperature data in Fig. 7.6 does not show the presence of any peak frequencies, indicating that the air-flow is steady. With further increase in T_p, steady flows were observed up to a peak furnace wall temperature of T_p = 44.6°C.

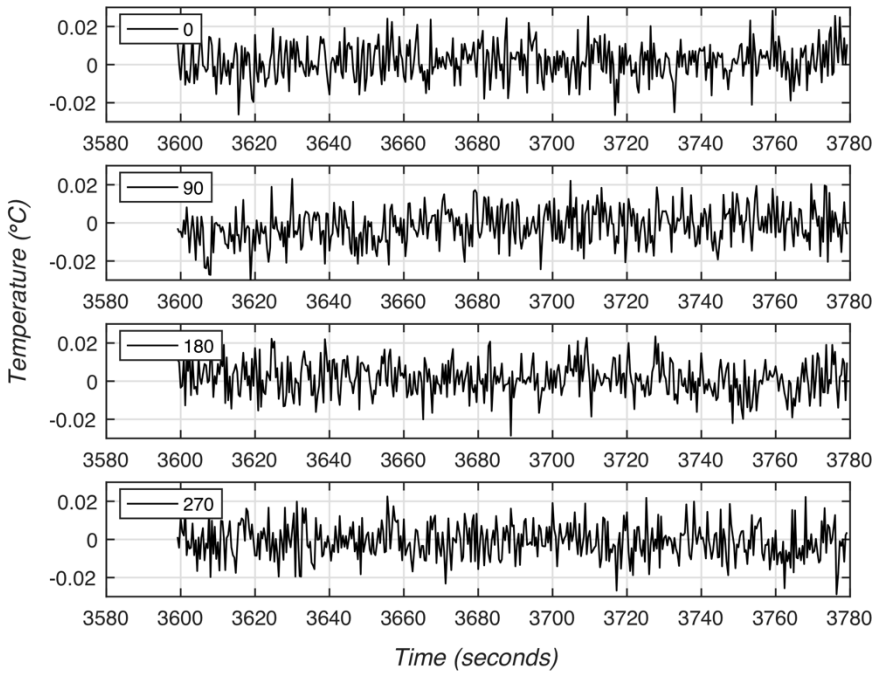

Figure 7.5: Air temperature residuals measured at θ = 0°, 90°, 180° and 270° for an experiment with peak furnace wall temperature T_p = 41.3° C.

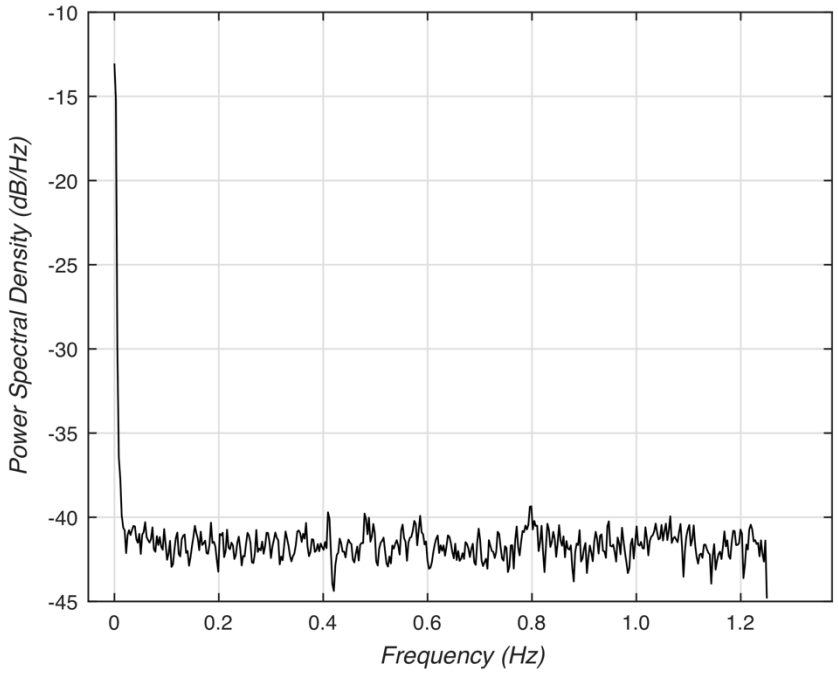

Figure 7.6: Power spectral density of air temperature data set recorded at reference thermocouple (θ = 0°) for steady flow regime with peak furnace wall temperature T_p = 41.3°C.

7.3.1.1 Periodic Flow Regime

When the peak furnace wall temperature was increased to T_p = 45.5°C, the system transitioned from steady flow to a mono-periodic flow. This is the first bifurcation of the system, and the nominal Rayleigh number for this transition is Ra = 1.00 x 10^7 ± 4%. With further increase in T_p, periodic flows were observed up to a peak furnace wall temperature of T_p = 56.4°C. Figure 7.7 shows the residuals of air temperatures for flow in the periodic regime at T_p = 55.5°C, and Fig. 7.8 shows the corresponding PSD of measured air temperatures at θ = 0°.

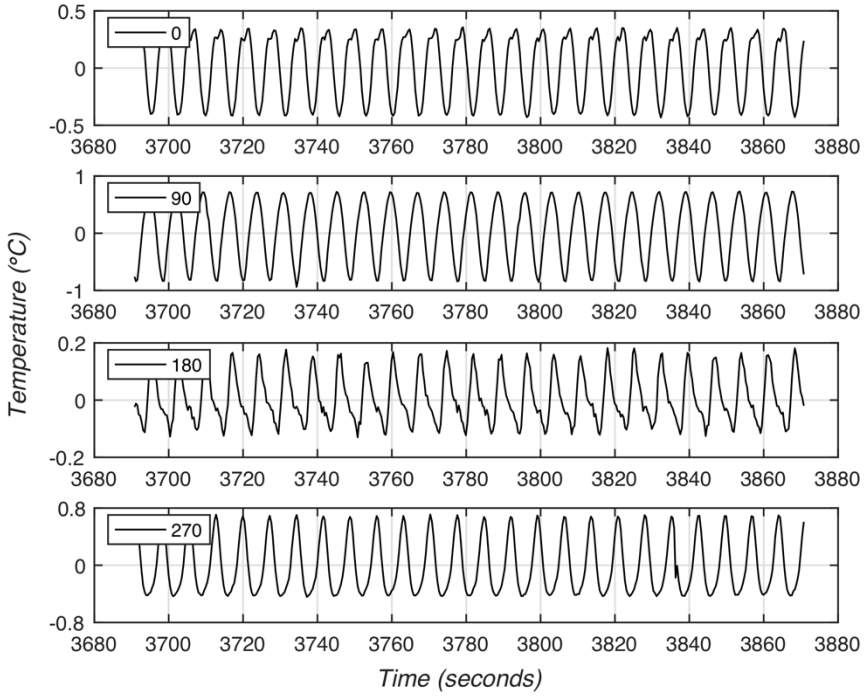

Figure 7.7: Air temperature residuals measured at θ = 0°, 90°, 180° and 270° for flow in the periodic regime with peak furnace wall temperature T_p = 55.5°C.

This PSD shows the presence of one fundamental frequency (f_1 = 0.139 Hz) and its harmonics indicating mono-periodic flow behavior. For the mono-periodic flow regime, the fundamental frequency of the oscillations increased from f_1 = 0.110 Hz to 0.140 Hz as the peak furnace wall

temperature was increased from T_p = 45.5°C to 56.4°C. The frequency content of temperature signals in the periodic regime is comprised of the fundamental frequency of oscillation f_1 and its harmonics $n.f_1$ (n=1,2,3...). The amplitude of temperature oscillations also increased with increase in peak furnace wall temperature.

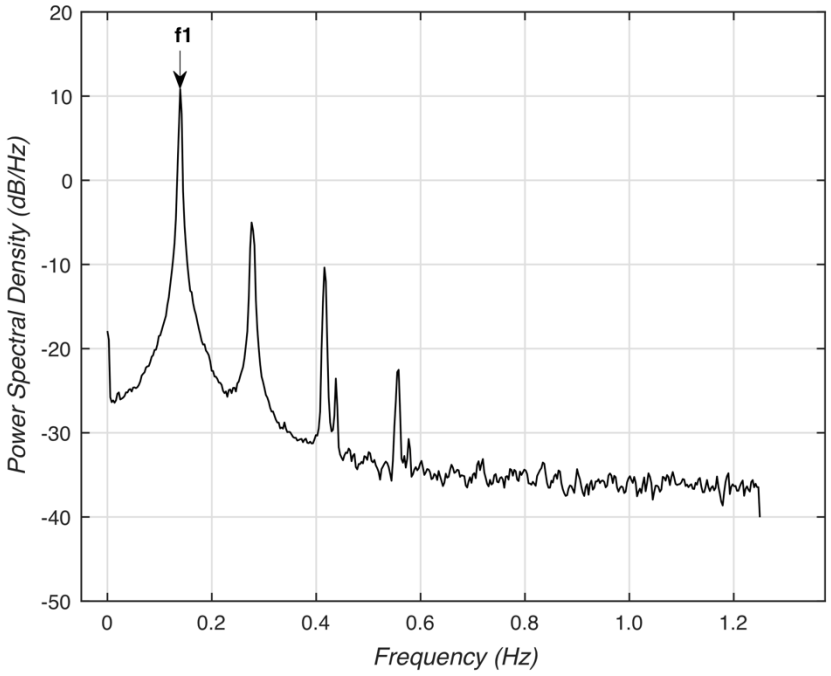

Figure 7.8: Power spectral density of air temperature data set recorded at reference thermocouple ($\theta = 0°$) for periodic flow regime with peak furnace wall temperature T_p = 55.5°C.

When the peak temperature of the furnace was decreased from 51.5°C to 41.3°C over a sequence of set **A** experiments, the system exhibited hysteresis. Periodic flow was observed in the previously steady flow regime through a peak furnace wall temperature of 43.6°C. With further decrease in T_p, the flow transitioned back to steady from periodic. Thus, the first bifurcation from steady to mono-periodic oscillatory flow is subcritical and exhibits a small amount of hysteresis between 43.6°C ≤ T_p ≤ 45.5°C as shown in Fig. 7.9.

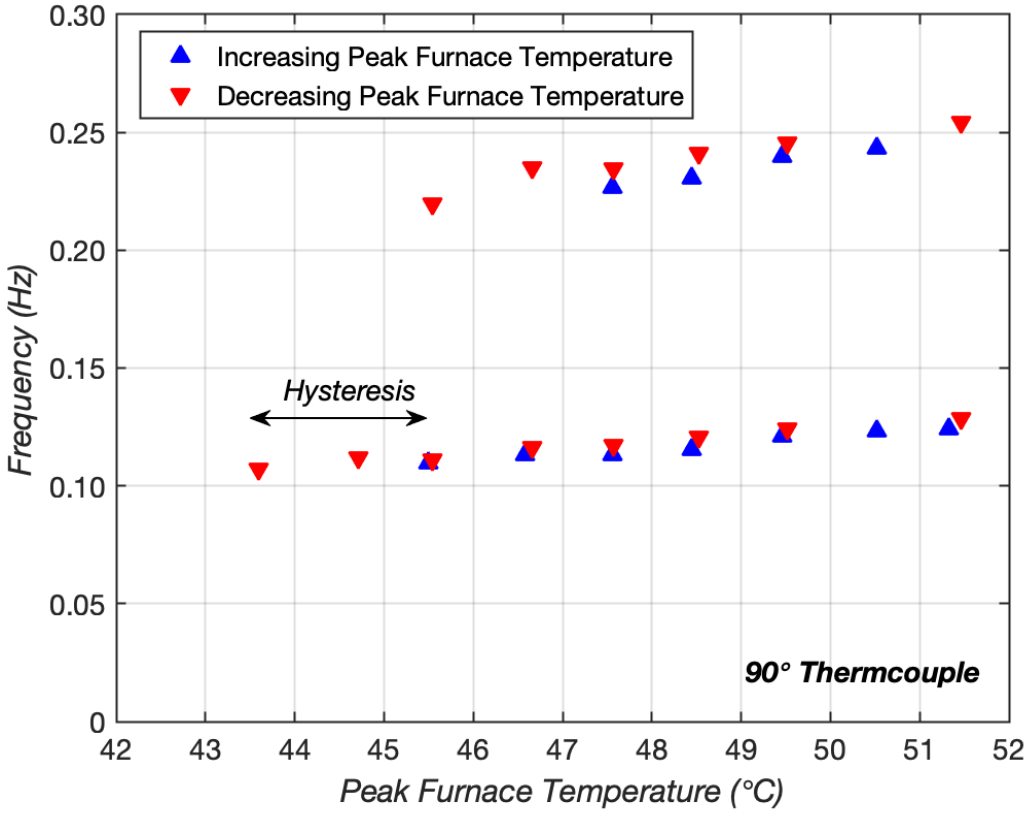

Figure 7.9: System exhibiting hysteresis for first bifurcation from steady to monoperiodic flow.

7.3.1.2 Three-Dimensional Asymmetric Flow

Recorded air temperature oscillations in the periodic regime were not in phase, indicating that the flow is 3D asymmetric. Time-lags between measured air temperature signals and their corresponding phase-lags for experiments in the periodic regime and for the first few runs of the quasi-periodic regime are shown in Fig. 7.10. For all periodic flows, the $\theta = 90°$, 180° and 270° thermocouple signals lagged the $\theta = 0°$ thermocouple signal by different phase angles as shown in Fig. 7.10. At the start of the periodic regime, the phase lag between the thermocouples at 270° and 180° is small but continues increasing as the peak furnace wall temperature is increased. By the

end of the periodic regime, the phase lags between the four thermocouples do not vary as much and are nearly constant with further increase in peak furnace wall temperature.

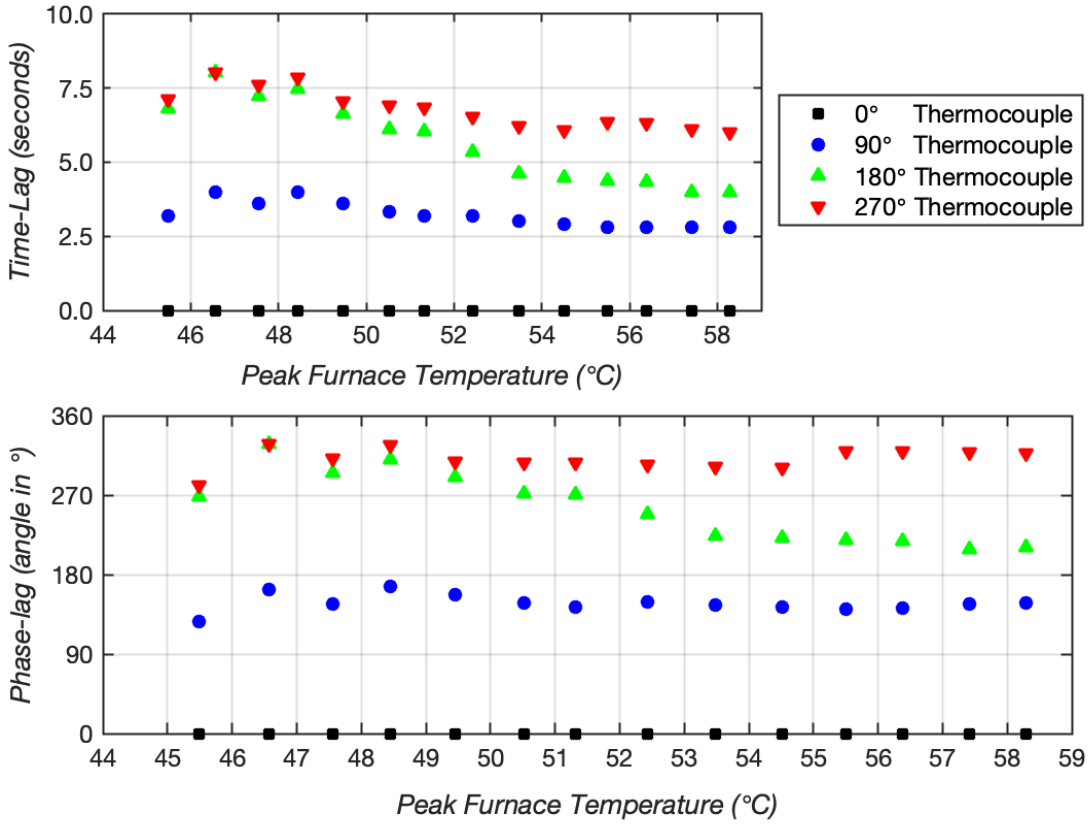

Figure 7.10: Time-lags and phase-lags of the four air temperature signals in the periodic regime for various peak furnace wall temperatures.

The time-lag sequence indicates that the motion of the air in the plane of the thermocouples (Z / H = 0.500) consists of a gentle swirling motion in the anticlockwise direction. This unsteady natural convection in the periodic regime is thus asymmetric, consisting of oscillating motion in the vertical Z direction and a gentle swirling motion in the azimuthal θ direction. Figure 7.11 shows the temperatures measured by at the θ = 90°, 180° and 270° for a peak furnace temperature of T_p = 56.4°C where the time-lag between the four temperature measurements is clearly visible.

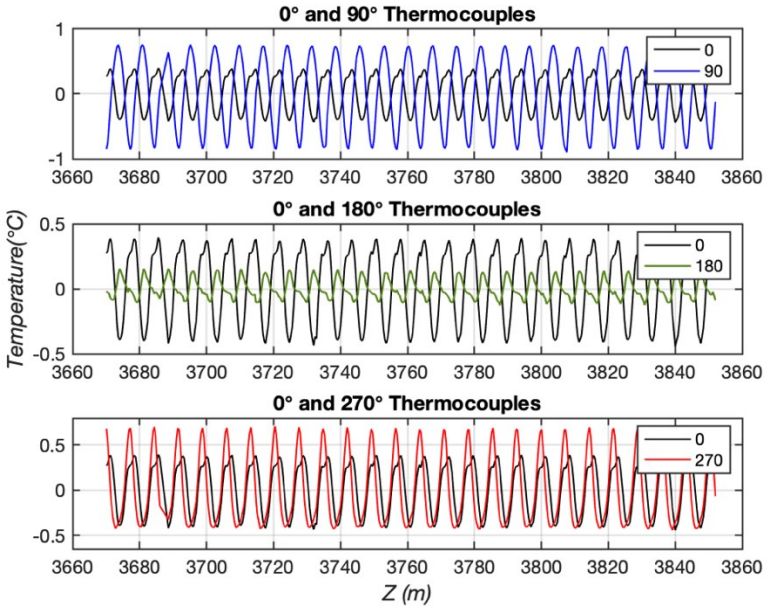

Figure 7.11: Air temperature residuals measured at θ = 0°, 90°, 180° and 270° for flow in the periodic regime with peak furnace wall temperature T_p = 56.4°C.

7.3.1.3 Bifurcations to Quasi-Periodic Flows

As the peak furnace wall temperature was increased to T_p = 57.4°C, the system exhibited quasi-periodic flow behavior. This is the second bifurcation of the system from mono-periodic flow to quasi-periodic flow, and the nominal Rayleigh number for this transition is 1.41 x 10^7 ±4%. Figure 7.12 shows the residuals of quasi-periodic air temperature signals recorded at a peak furnace wall temperature of T_p = 58.3°C. Figure 7.13 shows the PSD of the quasi-periodic temperature signal recorded by the reference (θ = 0°) thermocouple. The PSD shows the presence of two key frequencies: f_1 = 0.147 Hz and f_2 = 0.036 Hz. All other frequencies appearing in the PSD correspond to linear combinations of these two frequencies. The ratio f_1 / f_2 is 4.083 at T_p = 58.3°C. The frequency content of temperature signals in the two-frequency quasiperiodic regime is comprised of the 2 frequencies f_1, f_2 and frequencies = m.f_1 + n.f_2, where m and n are integers.

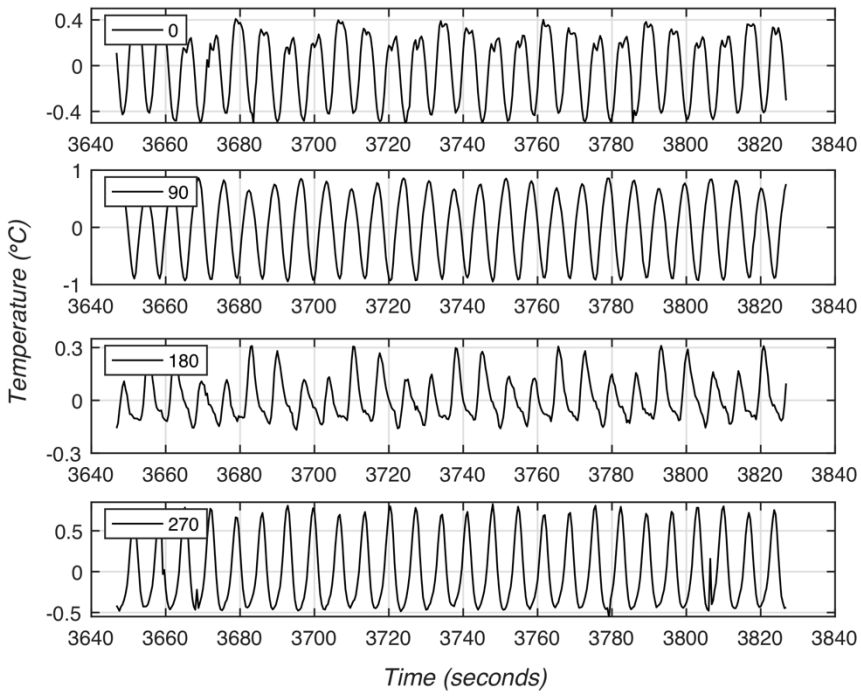

Figure 7.12: Air temperature residuals measured at θ = 0°, 90°, 180° and 270° for flow in the quasi-periodic regime with T_p = 58.3°C.

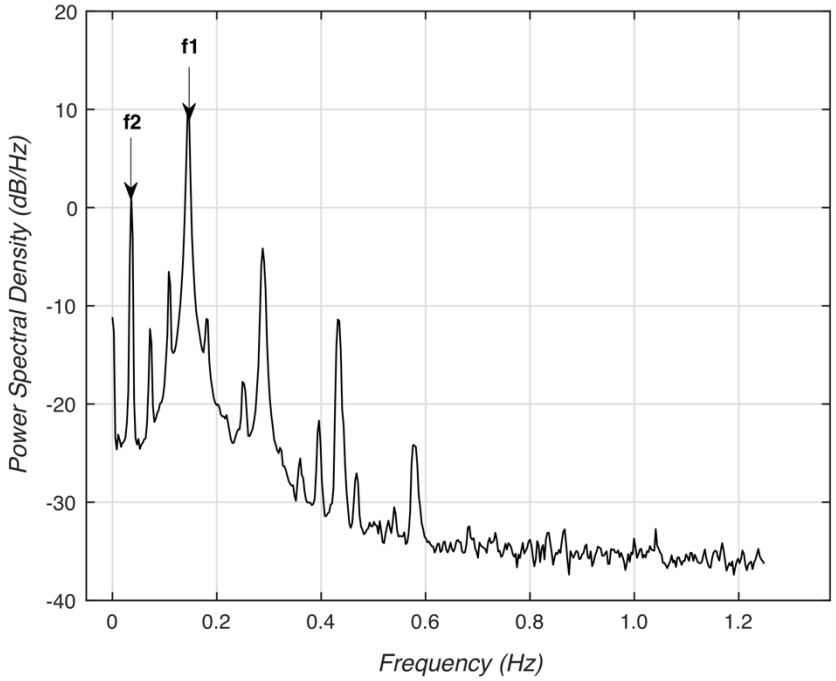

Figure 7.13: Power spectral density of air temperature data set recorded at reference thermocouple (θ = 0°) for quasi-periodic flow regime with T_p = 58.3°C.

With further increase in peak furnace wall temperature, a third frequency appears in the quasi-periodic regime. This is the third bifurcation of the system from a 2-frequency quasi-periodic flow to a 3-frequency quasi-periodic flow. Figures 7.14 and Figure 7.15 shows the temperature residuals of the four temperature signals and PSD of the 3-frequency quasi-periodic temperature signal for a peak furnace wall temperature T_p = 59.2°C. The PSD of the temperature signal shows the presence of three key frequencies: f_1 = 0.141 Hz, f_2 = 0.047 Hz, f_3 = 0.025 Hz. All other frequencies appearing in the PSD correspond to linear combinations of these three frequencies. (PSD peaks = f_1, f_2, f_3, $m.f_1 + n.f_2 + p.f_3$, where m,n,p are integers).

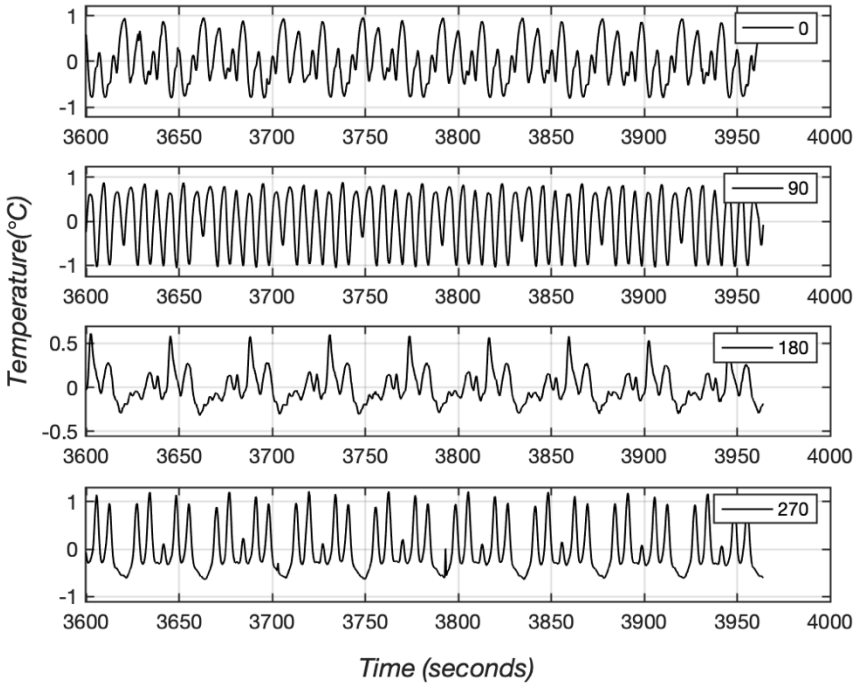

Figure 7.14: Air temperature residuals measured at θ = 0°, 90°, 180° and 270° for flow in the quasi-periodic regime with T_p = 59.2°C.

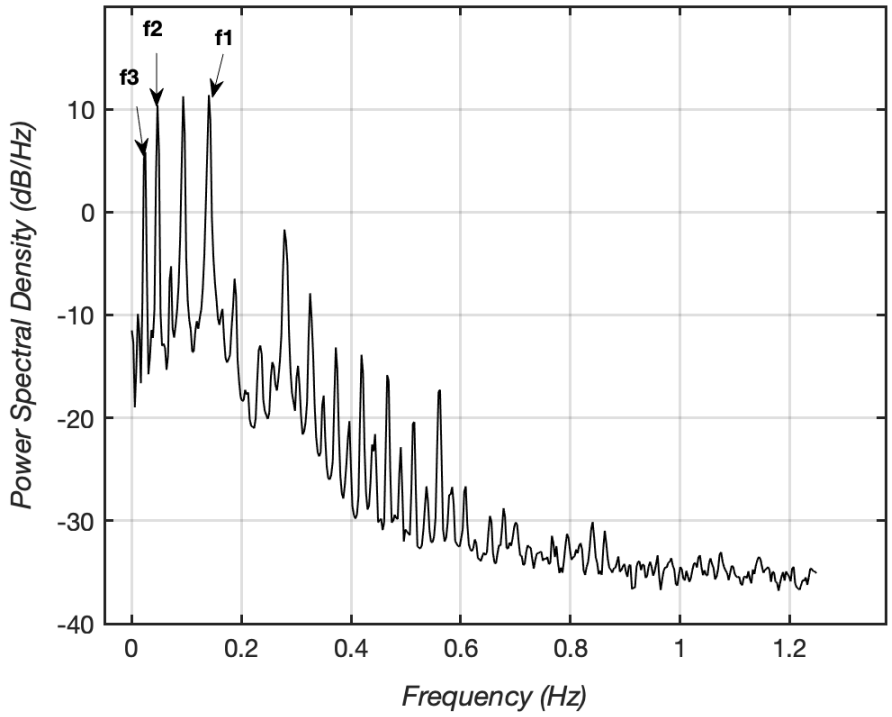

Figure 7.15: Power spectral density of air temperature data set recorded at reference thermocouple ($\theta = 0°$) for quasi-periodic flow regime with $T_p = 59.2°C$.

7.3.1.4 Transition to Quasi-Chaotic Flow

Increasing the peak furnace wall temperature even further causes more bifurcations to appear, and the flow starts to exhibit characteristics of chaotic behavior. Figure 7.16 shows air temperature residuals over six minutes duration for a peak furnace wall temperature of $T_p = 66.2°C$.

The PSD of the reference temperature signal at $\theta = 0°$ for $T_p = 66.2°C$ is shown in Fig. 7.17. This PSD is characteristically different from the PSDs of the periodic and quasi-periodic regimes, showing a banded presence of multiple frequency peaks. A fully chaotic flow has a power spectrum with power distributed equally at all frequencies. The PSD of the flow observed for $T_p = 66.2°C$ is characteristic of a chaotic flow; however, a few peaks with higher power are still visible, indicating

that the flow is not fully chaotic, but is on the route to chaos. This regime is referred to as the quasi-chaotic flow regime. A time series and spectrogram of measured air temperatures for quasi-chaotic flow with T_p = 68.0°C is shown in Fig. 7.18. The presence of different frequencies at different time windows is clearly evident from the spectrogram. A summary of all these air-flow regimes with increasing peak furnace wall temperature is given in Table 7.1.

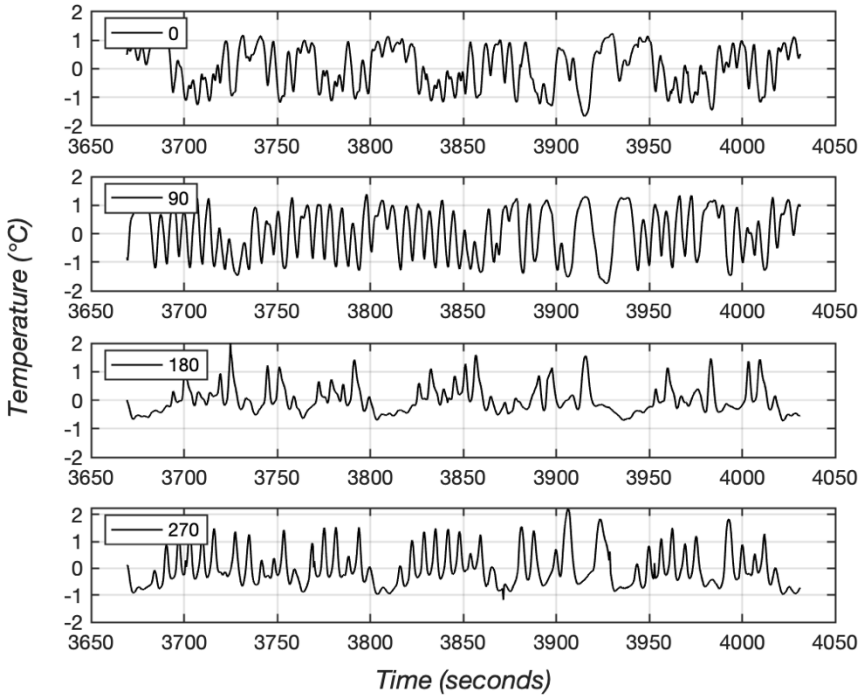

Figure 7.16: Air temperature residuals measured at θ = 0°, 90°, 180° and 270° for flow in the quasi-chaotic regime with T_p = 66.2°C.

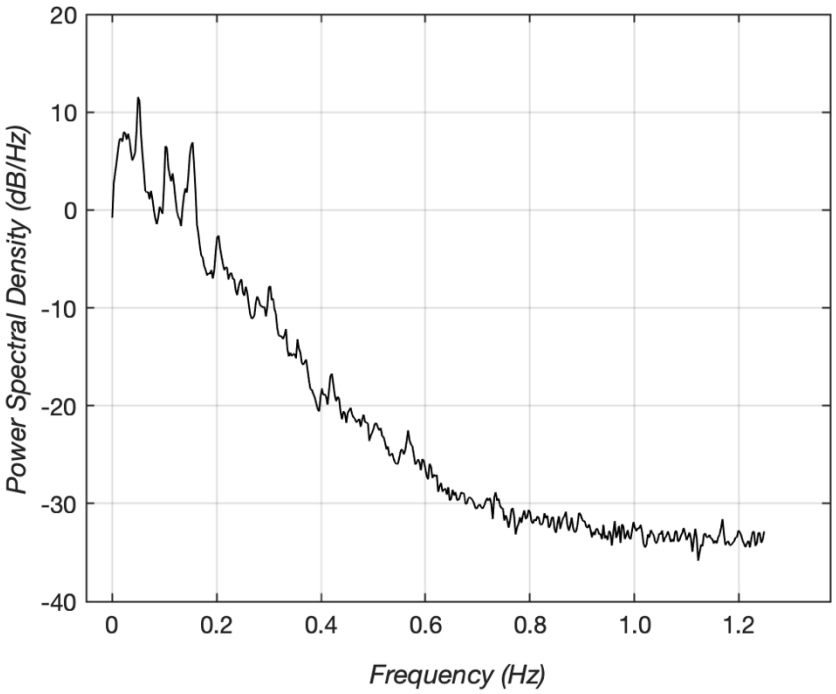

Figure 7.17: Power spectral density of air temperature data set recorded at reference thermocouple ($\theta = 0°$) for quasi-chaotic flow regime with $T_p = 66.2°C$.

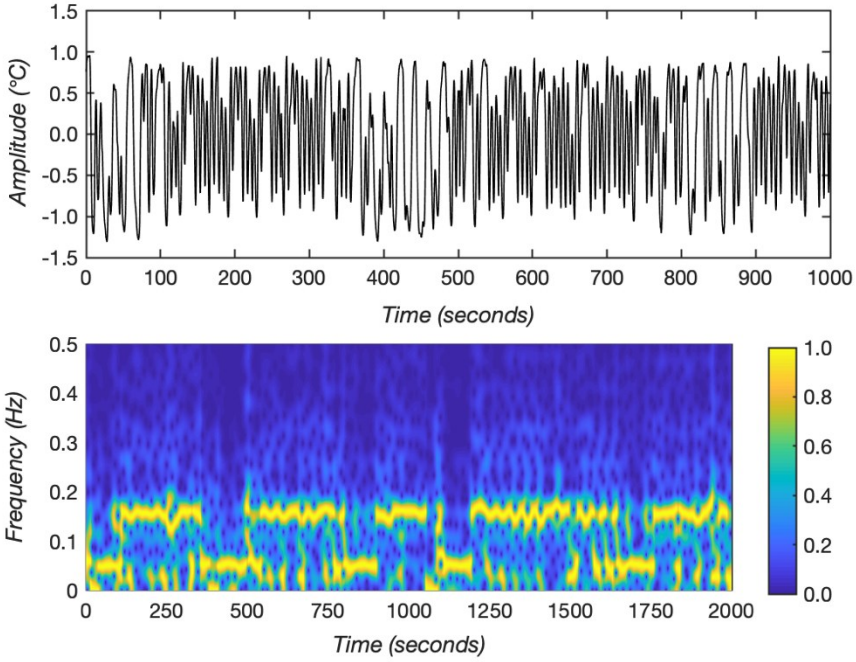

Figure 7.18: Time series (top) and spectrogram (bottom) of air temperatures recorded at $\theta = 90°$ for quasi-chaotic flow with $T_p = 68.0°C$.

Table 7.1: Air-flow regimes with increasing peak furnace wall temperature T_p as control parameter.

Air-flow Regime	***Peak Furnace Wall Temperature Range***	***Nominal Rayleigh Number Range***	***Frequency peaks***
Steady	$T_p \leq 44.6°C$	$Ra \leq 9.68 \times 10^6$	No peaks visible
Mono-periodic	$45.5°C \leq T_p \leq 56.4°C$	$1.00 \times 10^7 \leq Ra \leq 1.36 \times 10^7$	f_1, and harmonics $n.f_1$
Quasi-periodic	$57.4°C \leq T_p \leq 59.2°C$	$1.41 \times 10^7 \leq Ra \leq 1.44 \times 10^7$	f_1, f_2 and $m.f_1+n.f_2$ for two frequency quasiperiodic f_1, f_2, f_3 and $m.f_1+n.f_2+p.f_3$ for three frequency quasiperiodic
Quasi-chaotic	$T_p \geq 60.3°C$	$Ra \geq 1.46 \times 10^7$	Banded presence of multiple frequency peaks

In each of the quasi-chaotic, quasi-periodic, and mono-periodic flows, frequencies above 0.6 Hz show negligible contribution in the PSD and spectrograms. Furthermore, all fundamental frequencies f_1, f_2, and f_3 are well below 0.2 Hz throughout both the mono-periodic and quasi-periodic flow regimes. In earlier experiments with temperature data collection at 4 Hz and 8 Hz from air-flow in a furnace of the same design [1], all measured oscillation frequencies were consistently well below 0.5 Hz; therefore, an air-temperature sampling frequency of 2.5 Hz was appropriately chosen for these experiments.

In nearly all of the flow regimes for these set **A** experiments, the amplitude of air temperature oscillations increases continuously with increasing T_p. Figure 7.19 shows the average amplitudes from measured air temperature oscillations over the full range of peak furnace wall temperatures that were explored. These amplitudes are reasonably consistent among the four thermocouples but show variations that likely result from 3D asymmetric flow behavior and an estimated $\pm$ two mm uncertainty for each of the thermocouple junction's vertical z-location.

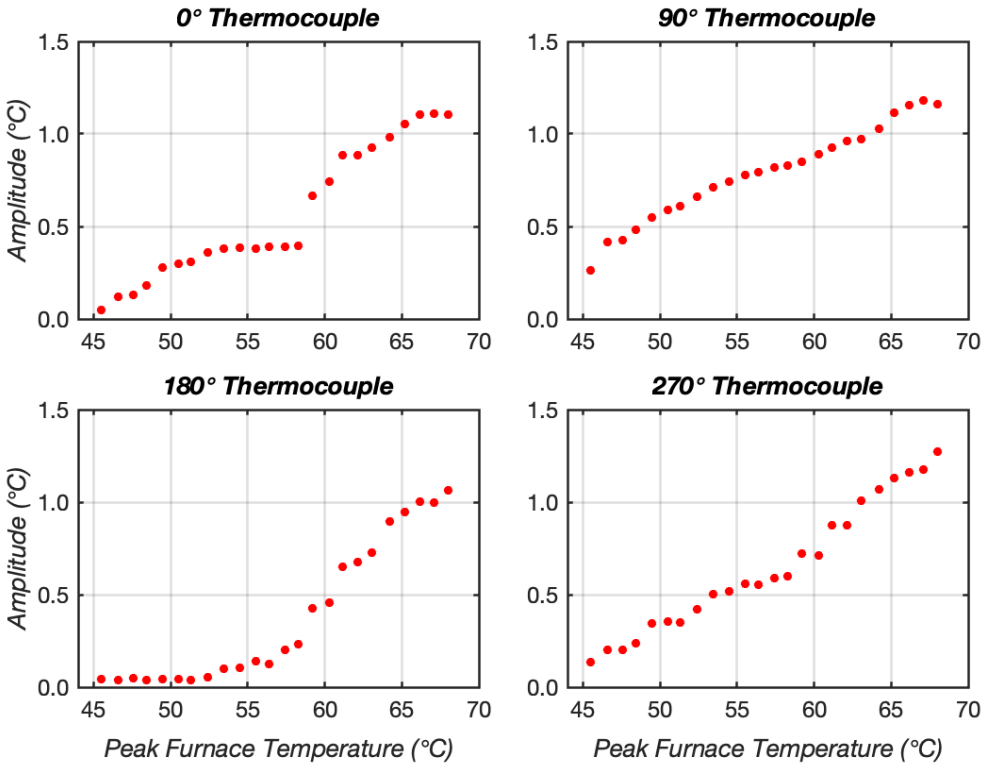

Figure 7.19: Average amplitude of air temperature oscillations measured at θ = 0°, 90°, 180° and 270° as peak furnace wall temperature is increased.

Transitions from steady to periodic and quasi-chaotic flows are readily identified in the frequency maps shown in Fig. 7.20. With transition of the flow from periodic to quasi-chaotic regimes, the total signal power is distributed amongst more and more frequencies. Figure 7.21 shows the frequency with the highest power and the percentage of total power in that frequency. In the periodic regime, the fundamental frequency f_1 = 0.11 Hz to 0.14 Hz is the dominant frequency with the highest percentage of total signal power (40% to 50%). With transition of the flow from periodic to quasi-chaotic regimes, the total signal power is distributed amongst more and more frequencies and the percentage power at the dominant frequency goes on decreasing. For the quasi-chaotic regime, the dominant frequency is around 0.05 Hz.

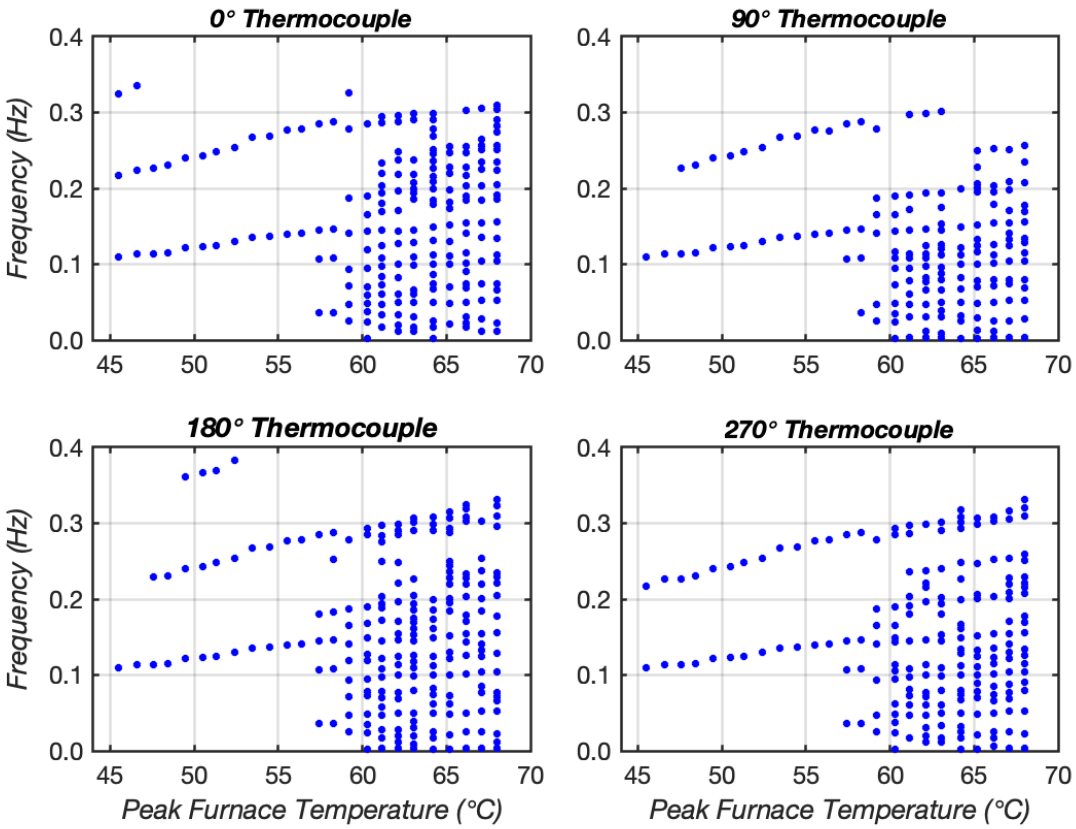

Figure 7.20: Frequency map of the system as peak furnace wall temperature is increased.

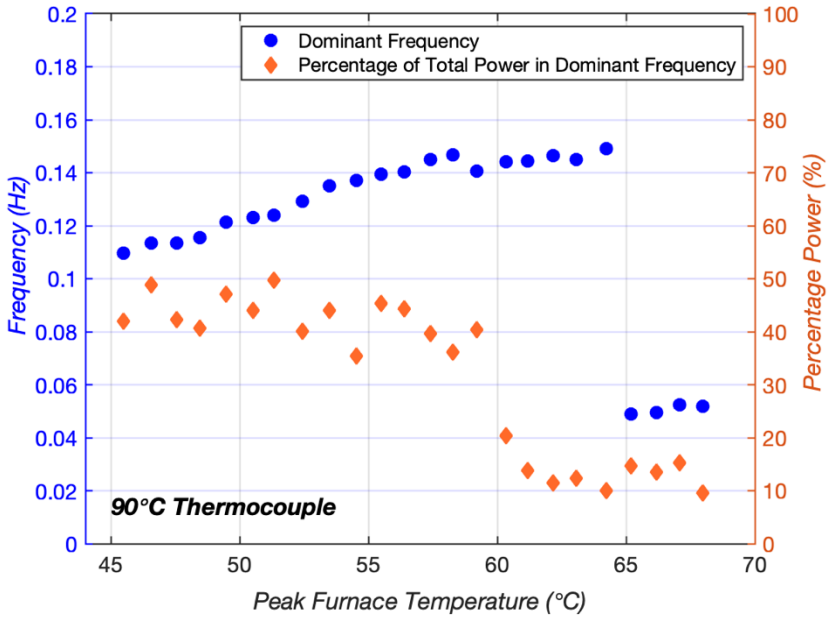

Figure 7.21: Dominant frequencies and percentage power in dominant frequencies as peak furnace wall temperature is increased.

7.3.1.5 Summary and Discussion of Set A Experimental Results

The following air-flow regimes are identified, based on analyses of frequency spectra for set **A** experiments in which T_p is successively increased: steady flows are followed by mono-periodic flows, leading to 2-frequency quasi-periodic flows, followed by 3-frequency quasi-periodic flow, finally transitioning to quasi-chaotic flows. This sequence of bifurcations is consistent with a quasi-periodic route to chaos; the very same route to chaos via quasi-periodicity was observed in other low Prandtl number fluid systems including classic Rayleigh-Bernard convection [59]. A typical sequence of bifurcations for a quasi-periodic route to chaos is as follows: first, the flow bifurcates from a steady regime to a periodic regime with frequency f_1; next, the flow bifurcates from a periodic regime to a quasi-periodic regime, exhibiting two frequencies f_1 and f_2 with the ratio f_1 / f_2 being irrational; next, 2-frequency quasi-periodic flow bifurcates to 3-frequency quasi-periodic flow, and with further increase in the control parameter, 3-frequency quasi-periodic flow transitions towards chaotic flow.

For comparison with a geometry much closer to this study, quasi-periodic flows within an air-filled annular cavity of A = 16 and radius ratio η = 0.74 were reported by Pécheux, Le Quéré and Abcha [6]. As Rayleigh number was increased, mono-periodic flow first transitioned to quasi-periodic flow, showing two frequencies with a ratio of ¼. At even higher Rayleigh number, a transition to chaotic flow was reported, similar in trend to observations in these set **A** experiments.

Similar to the trend of increasing fundamental frequencies from 0.110 Hz to 0.140 Hz in the periodic regime of set **A** experiments, there were also observed increases in the fundamental frequency of periodic oscillations (0.23 to 0.38 Hz) in the polymer fiber drawing environment, as the buoyant potential of the upper convection cell was increased [2]. Periodic flows in the polymer fiber drawing environment were also 3D asymmetric, with the temperature signals at locations θ

= 90°, 180°, and 270° lagging behind the temperature signal at location $\theta = 0°$ by phase angles of approximately 48°, 160°, and 323° respectively [2]. For comparison, in the periodic 3D flows observed in these set **A** experiments, temperature signals from thermocouples at $\Delta\theta = 90°$ intervals were found to lag (Fig. 7.10) a reference thermocouple by as little as 10° and by as much as 330°, extending over the range of phase lags (48° to 323°) previously observed.

Reeve et al. [50] simulated axisymmetric natural convection in an annular cavity of A = 10 and radius ratio η = 0.6 with linearly varying temperatures along the inner and outer cylindrical walls; they predicted the first bifurcation from steady to mono-periodic flow at a Rayleigh number based on cavity height of $Ra_H = 2.165 \times 10^7$.

In a separate numerical study of (base) bi-cellular flow in a rectangular cavity of aspect ratio A = 10, Dillon et al. [51] predicted the critical Rayleigh number for the first bifurcation from steady to mono-periodic flow at $Ra_H = 2.2 \times 10^7$. For comparison with the current set **A** experiments, the nominal Rayleigh number at which the flow transitioned from steady to mono-periodic was $Ra_H = 1.00 \times 10^7 \pm 4\%$. Both Reeve et al. [50] and Dillon et al. [51] predicted increases in the frequency of periodic oscillations with increasing Rayleigh number, which is the same trend observed in these set **A** experiments. While some degree of comparison is possible with the aforementioned 2D numerical studies on account of the similarity in (base) bi-cellular flows, it is important to note that all of the periodic flows observed in these set **A** experiments were fully 3D in nature.

7.3.2 Varying Buoyant Potential of the Lower Convection Cell

In set **B** experiments, the buoyant potential of the lower cell was successively increased (or successively decreased), by increasing (decreasing) the bottom iris temperature BI. The power to the cartridge heater was maintained at the highest possible setting without softening the

polycarbonate tube, and the peak furnace wall temperature was maintained at $T_p = 36.1 \pm 0.2°C$ for the entirety of set **B** experiments. The first experiment in set **B** was with the bottom iris temperature at BI = 43.2°C; for this first experiment, air-flow inside the cavity was steady.

7.3.2.1 Transition to Mono-Periodic Flows

When the bottom iris temperature was increased to BI = 44.8°C, the flow transitioned from steady to mono-periodic flow. Mono-periodic flows were observed up to a bottom iris temperature of BI = 49.2°C. In set **B** experiments, the transition from steady to mono-periodic flow was very similar to observations in set **A** experiments. The fundamental frequencies of the mono-periodic regime (f_1 = 0.111 Hz to 0.148 Hz) were also very similar to those in set **A** experiments. Similarities with set **A** experiments are expected since the buoyant potential of the same (base) bi-cellular flow is merely being changed in two different ways. Temperature differences in the top part of the cavity were varied in set **A** experiments; alternately, in set **B** experiments, temperature differences in the bottom part of the cavity were varied. The key distinction between experimental results from set **A** and set **B** was the pathway by which flows transitioned from mono-periodic to chaotic.

7.3.2.2 Intermittent Flows

Subsequent to the mono-periodic regime, when the bottom iris temperature was further increased to BI = 50.7°C, intermittent flow behavior was observed via all four air temperature signals. Intermittency in this context means nearly periodic flow interrupted by irregular bursts of chaotic flow. The time interval between these chaotic bursts is random [60]. As the bottom iris temperature was further increased, the frequency of the chaotic bursts increased, and for bottom iris

temperatures above 51.4°C, the flow began to exhibit characteristics of chaotic flow. A summary of air-flow regimes with increasing bottom iris temperature BI is given in Table 7.2.

Table 7.2: Air-flow regimes with increasing bottom iris temperature BI as the control parameter.

Air-flow Regime	***Bottom Iris Temperature Range***	***Nominal Rayleigh Number Range***	***Frequency peaks***
Steady	$BI \leq 44.1°C$	$Ra \leq 3.10 \times 10^6$	-
Mono-periodic	$44.8°C \leq BI \leq 49.2°C$	$3.17 \times 10^7 \leq Ra \leq 3.48 \times 10^7$	f_l, and harmonics $n.f_l$
Intermittent	$50.7°C \leq BI \leq 51.4°C$	$3.51 \times 10^7 \leq Ra \leq 3.52 \times 10^7$	f_l + chaotic bursts
Quasi-chaotic	$BI > 51.4°C$	$Ra > 3.52 \times 10^7$	Banded presence of multiple frequency peaks

7.3.2.3 Hysteresis

The frequency map in Fig. 7.22 for all set **B** experiments, both increasing and decreasing bottom iris temperatures, illustrates hysteresis. Quasi-chaotic flow with BI = 51.7°C transitioned to intermittent flow after BI was decreased to 50.8°C. Intermittent flow persisted from BI = 50.2°C down to BI = 49.2°C. (Previously at BI = 49.2°C the flow was mono-periodic.) Intermittent flow at BI = 49.2°C gave way to mono-periodic flow with further decrease in the bottom iris temperature to BI = 48.0°C. Mono-periodic flows were observed down to BI = 46.5°C, as expected; however, with further decrease in the bottom iris temperature below 46.5°C, the flow transitioned back to steady. Figure 7.22 illustrates hysteresis between $44.8°C \leq BI < 46.5°C$, where flows are mono-

periodic for ascending BI, but steady for descending BI in this same temperature range, indicating that this bifurcation is subcritical.

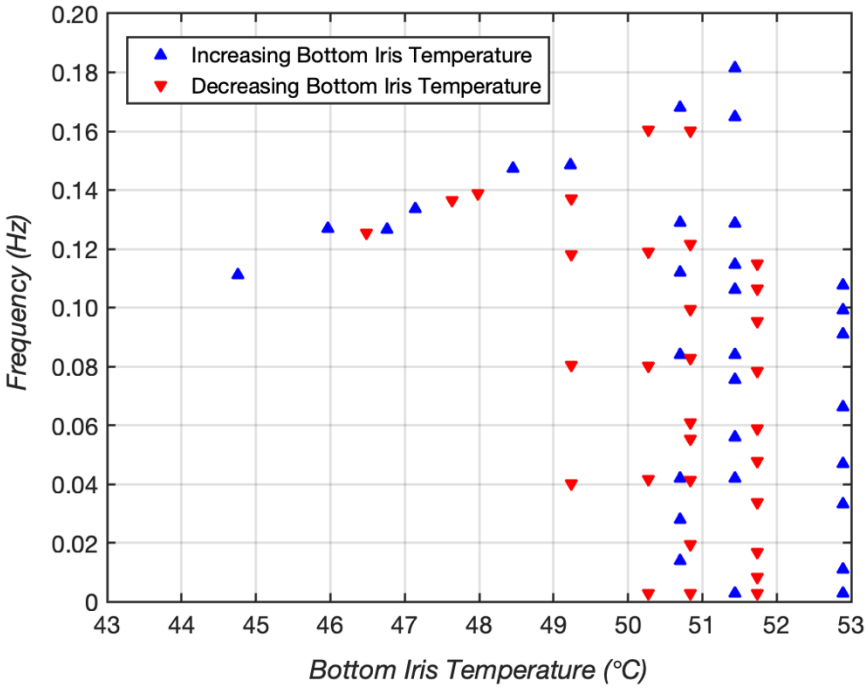

Figure 7.22: Frequency map of the air-flows for set B experiments, as the bottom iris temperature is increased and decreased.

Figure 7.23 shows intermittent air-flow temperature residuals measured at $\theta = 90°$ for 1000 seconds, and a spectrogram for 2000 seconds of data with the bottom iris temperature at BI = 49.2°C. As evident in Fig. 7.23, periodic flows at a fundamental frequency of 0.137 Hz are interrupted by random bursts of chaotic flow. This intermittent flow in the case of BI descending to 49.2°C provides yet another example of hysteresis as shown in Fig. 7.22, where mono-periodic flow occurs instead for the case of BI ascending to 49.2°C.

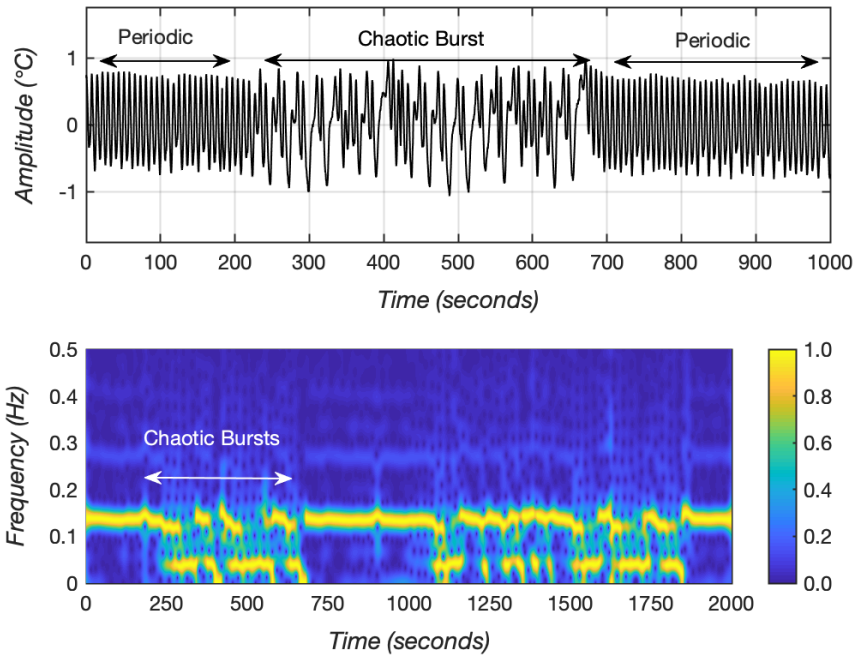

Figure 7.23: Time series (top) and spectrogram (bottom) of air temperatures recorded at θ = 90° for air-flow exhibiting intermittency in set B experiment with BI = 49.2°C (decreasing BI temperature).

7.3.2.4 Summary and Discussion of Set B Experimental Results

Intermittent flows have been predicted in systems transitioning to chaos, and such have been described for natural convection flows in air-filled annular cavities [31, 50]. Pécheux, Le Quéré and Abcha [31] predicted intermittent flow behavior (axisymmetric) in an air-filled annular cavity of A = 16 and radius ratio η = 0.76 at Rayleigh numbers between those for periodic and chaotic solutions. For an annular cavity of A = 10 and radius ratio η = 0.6 with linearly varying temperatures along the inner and outer cylinder walls, Reeve et al. [50] predicted intermittent flow behavior (axisymmetric) which was described then as "intermittent pseudo-periodic oscillations within the chaotic behavior".

In the current set **B** experiments, intermittency occurred when the control parameter – the bottom iris temperature BI – was increased and moved away from the periodic flow regime. As the control parameter is increased and moved farther away from the periodic regime, chaotic bursts become more frequent until finally the system transitions to chaotic flow. According to Strogatz [60] this progression of events is classified as an intermittent route to chaos and is called Type I intermittency [59, 60]. Type I intermittency indicates that transition from periodic to chaotic flow most likely takes place by a saddle node type bifurcation [59, 60]. The progression of bifurcations exhibited by this natural convection system when the bottom iris temperature is increased (set **B** experiments), appears to follow an intermittent route to chaos [59].

7.4 Key Findings

The stability of natural convection air-flows in an annular cavity with A = 25.2 and $\eta = 0.50$ and non-isothermal vertical walls was studied experimentally. When the buoyant potential of the upper cell of the bi-cellular flow was successively increased (set **A** experiments), the flow transitioned from steady to mono-periodic flow and then followed a quasi-periodic route to chaos. When the buoyant potential of the lower cell was successively increased (set **B** experiments), the flow transitioned from steady to mono-periodic flow, and then followed an intermittent route to chaos showing a Type I Intermittency. The fundamental frequencies of the periodic regime were found to be between 0.11 to 0.14 Hz. The dominant frequency of the quasi-chaotic regime was found to be approximately 0.05 Hz. In both sets (**A** and **B**) of experiments, the very first bifurcations from steady bi-cellular flow to mono-periodic flows were subcritical and exhibited hysteresis. All of the observed mono-periodic, quasi-periodic, and quasi-chaotic air-flow behaviors were 3D asymmetric.

These current experimental results are reinforced by previous experimental observations from Reeve et al. [2] of steady, periodic and chaotic air-flows in drawing processes for polymer optical fiber. In those earlier experiments, oscillation frequencies in the periodic regime increased with increasing Rayleigh number [1], as in all of the current experiments. Periodic flows in the fiber drawing environment were also 3D asymmetric, with phase lags comparable to those obtained in the current experiments from air temperature measurements at azimuthal intervals of $\Delta\theta = \pi / 2$ radians.

Previous numerical studies [26,27,30,31,50,68,59,60,1,9,16,17,51,70,71,72] for various Cartesian and annular cavities with either isothermal or non-isothermal vertical walls, indicate similar if not identical chaotic flow pathways to those identified in these set **A** and **B** experiments, further reinforcing the observations of this study. Since the majority of these previous numerical studies are 2D however, still lacking are quantitatively accurate 3D predictions of those critical transitions from steady to mono-periodic flow regimes, to quasi-periodic and quasi-chaotic flow regimes as observed in these set **A** experiments. Accurate 3D simulations of the critical transitions from steady to mono-periodic, then intermittent and quasi-chaotic flow regimes are likewise needed for comparison with these set **B** experimental results.

For air-filled square cavities with isothermal vertical walls and conducting horizontal walls, Henkes and Hoogendoorn [72] predicted that steady flow would become oscillatory at a Rayleigh number of $Ra_c = 2.1 \times 10^6$. For supercritical Rayleigh numbers, the non-dimensional frequencies of periodic flows were found to be independent $\left(\frac{f*H}{\sqrt{g\beta\Delta TH}} = 0.248\right)$ of Rayleigh number if the frequencies f were scaled with the $\mathrm{Brunt} - \mathrm{Väisälä}$ frequency $\frac{\sqrt{g\beta\Delta TH}}{H}$.

For all set **A** experiments in the mono-periodic regime, observed fundamental frequencies f_1 were scaled with the Brunt – Väisälä frequency; the resulting dimensionless frequencies range from 0.27 to 0.29 and are thus relatively independent of the nominal Rayleigh number. The dimensionless critical frequency for these set **A** experiments is 0.274, comparable to the value of 0.248 predicted for the onset of periodic air-flow in Henkes and Hoogendoorn's square cavity. This similarity in dimensionless frequencies and relative invariance over the range of nominal Rayleigh numbers explored suggests that an instability mechanism in the current set **A** experiments might likewise be the Rayleigh-Bernard instability mechanism previously predicted for air-flow in square cavities with vertical isothermal walls and conducting horizontal walls [72].

Tollmien-Schlichting instability mechanism is a well-documented instability in the vertical boundary layers of tall rectangular cavities [71, 72,89]. While scaling with the Brunt – Väisälä frequency suggests interaction with an inviscid core, scaling with the viscous frequency $\left(\frac{(g\,\beta\,\Delta T)^{2/3}}{\upsilon^{1/3}}\right)$ suggests instability in the vertical boundary layers. For all set **A** experiments in the mono-periodic regime, scaling the fundamental frequencies f_1 with this viscous boundary layer frequency yields relatively invariant dimensionless values of 0.017 to 0.018 over the range of nominal Rayleigh numbers explored. Such invariance of dimensionless frequency suggests that another instability mechanism in set **A** experiments might be the Tollmien-Schlichting instability as previously demonstrated in tall rectangular cavities.

Chapter 8

8 NATURAL CONVECTION IN ANNULAR CAVITY – CFD MODELING

This chapter presents results from CFD models developed to understand observations of unsteady natural convection flows in annular cavity experiments described in Chapter 7. At first, a 2D axisymmetric model of the annular cavity experimental system was developed to understand the base convection flow pattern. This axisymmetric model was able to predict steady-state flows but had difficulty predicting the oscillatory flows observed in the system. Since all oscillatory flow observations in the annular cavity experiments were 3D asymmetric, a full 3D CFD model of the annular cavity was developed to more accurately model the system. The coupled implicit solver of Simcenter StarCCM+ predicted with reasonable accuracy natural convection flows under both Boussinesq and non-Boussinesq conditions, as demonstrated by the benchmarking operations described in Chapter 3. Therefore, this solver was used for performing both 2D axisymmetric and 3D numerical simulations of the annular cavity experimental system.

8.1 2D Axisymmetric CFD Model

An axisymmetric CFD model of the annular cavity experimental system is developed in Simcenter StarCCM+, where only the fluid portion of the annular cavity is modeled. Temperature profiles of inner and outer cylindrical walls of the cavity and top and bottom horizontal walls are set corresponding to experimentally measured wall temperature profiles of the furnace wall, polycarbonate tube wall, and top and bottom irises.

8.1.1 Governing Equations and Fluid Properties

Axisymmetric, compressible, transient form of Navier-Stokes equations for a Newtonian fluid given by equations (3.12) - (3.14) are solved. Air is treated as an ideal gas, and its density ρ, dynamic viscosity μ, thermal conductivity k, and specific heat Cp are all temperature dependent properties. Dynamic viscosity and thermal conductivity are obtained by linear interpolation of tabulated data [56]. Specific heat is expressed as a cubic polynomial fitted to tabulated data [56].

8.1.2 Solver Settings, Grid Size, and Time-Step

Solver settings similar to those used for benchmarking studies described in Chapter 3 are selected. The transient form of governing equations is solved using Simcenter StarCCM+ coupled implicit solver. A second-order up-winding scheme is selected for spatial discretization, and for time discretization, a second-order implicit scheme is selected. The number of inner iterations is set so that residuals for energy, continuity, and momentum equations fall below 10^{-8} at each time step. Velocity and temperature fields are monitored to ensure the solution is converged at each time step. An orthogonal, non-staggered, quadrilateral mesh is used, which is uniform everywhere except near the cavity boundaries, where it is further refined using prism layer cells. A mesh size of 80 x 2000 with 80 nodes in the radial direction and 2000 nodes in the axial-direction is selected based on grid refinement studies. A time step of 0.001 seconds is used.

8.1.3 Boundary Conditions

The no-slip boundary condition and Dirichlet thermal boundary condition are applied at all four walls of the axisymmetric cavity domain. The temperature along outer and inner cylindrical surfaces of the cavity is specified as a function of axial location ‘T(z)’ based on temperature

measurements from thermocouples installed along the length of furnace and polycarbonate tube wall. Top and bottom surfaces of the cavity are assumed to be at a constant temperature corresponding to the top and bottom iris temperatures measured for each experimental run. Computational domain and boundary conditions are shown in Fig 8.1 (a) and (b).

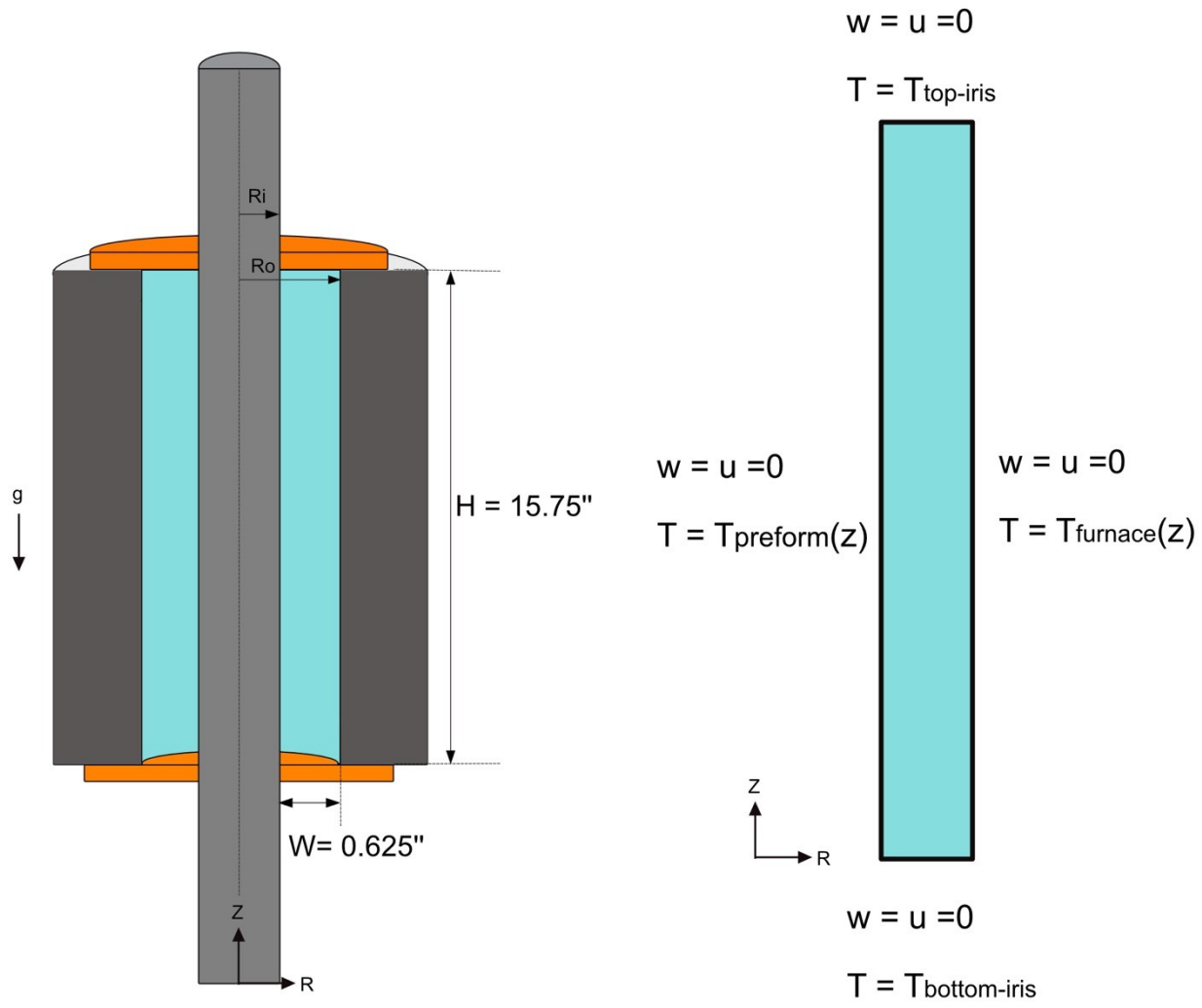

Figure 8.1: (a) Computational domain for axisymmetric CFD model (b) Boundary conditions for annular cavity.

For the experiments in the annular cavity, described in Chapters 6 and 7, the peak furnace wall temperature was progressively increased, starting with the flow field of a prior experimental run. To emulate this, a previous simulation's velocity and temperature fields were used as initial conditions for each subsequent simulation. The only exception was the very first simulation for which initial conditions were set to stationary air at ambient temperature.

8.2 Results

To predict the transition from steady to oscillatory flows, simulations were performed corresponding to each experiment, starting with an experiment for which steady flow was observed inside the cavity.

8.2.1 Steady Flow

The first simulation was performed at Ra = 9.68 x 10^6 corresponding to an experiment with peak furnace wall temperature of T_p = 44.6°C. A steady bi-cellular air-flow was predicted for this simulation. Isotherms and streamlines for the predicted steady flow are shown in Fig. 8.2(a) and (b). Two convection cells are visible in the streamline plot with the lower convection cell showing a higher maximum velocity as compared to the upper cell. Mean air temperature measured by the four thermocouples located at $z = 0.5H, r = \frac{R_i+R_o}{2}, \theta = \frac{n\pi}{2}$ $(n = 0,1,2,3)$ over a period of 2 hours was 42.1°C. Air temperature at the point corresponding to location of thermocouples predicted by the model is 41.5°C. The axisymmetric CFD model was able to successfully predict experimentally observed steady flow inside the cavity. Starting with this steady flow solution at Ra = 9.68 x 10^6 , Rayleigh number was then increased to Ra = 1.00 x 10^7.

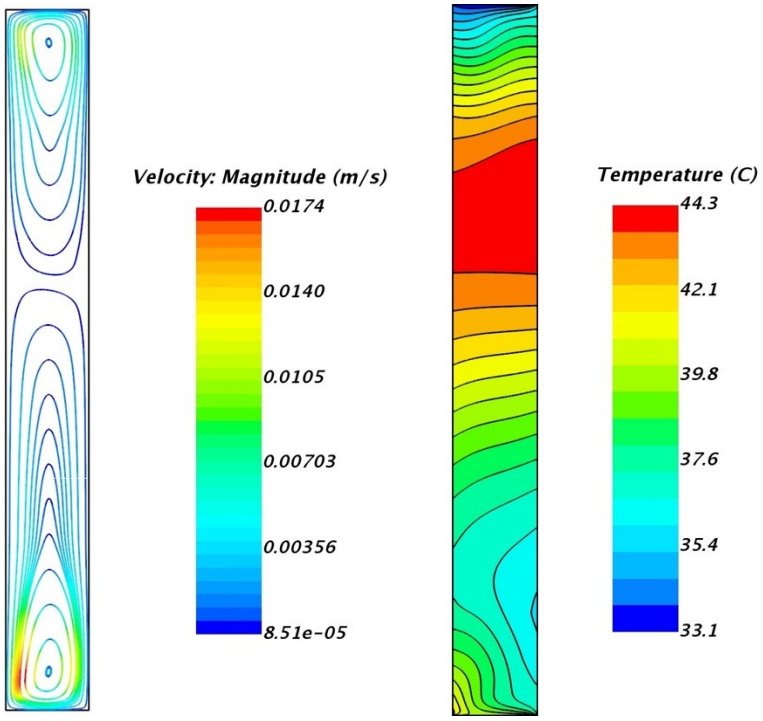

(a) (b)

Figure 8.2: (a) Streamlines (b) Isotherms for steady bi-cellular flow predicted at Ra = 9.68 x 10^6 which corresponds to an experimental run with peak furnace temperature of T_p = 44.6°C using the axisymmetric CFD model of the annular cavity.
Note: Width of cavity (r-dimension) is scaled by *x*3 times for visualization purposes.

For the experimental run at Ra = 1.00 x 10^7, an unsteady monoperiodic flow was first observed inside the cavity. In contrast, for the simulation at Ra = 1.00 x 10^7, the axisymmetric CFD model could not predict an oscillatory flow and instead predicted a steady bi-cellular flow. After this a simulation with boundary conditions corresponding to the next experimental run (T_p = 46.5 °C) was performed. Again, the model predicted a steady bi-cellular flow instead of an unsteady monoperiodic flow observed in experiments. Numerical simulations corresponding to all experimental runs of the monoperiodic oscillatory regime and quasiperiodic regimes were performed in a similar manner. The axisymmetric CFD model was not able to predict unsteady flow in any of these simulations. Furthermore, the model predicted a steady bi-cellular flow even

for thermal boundary conditions corresponding to experimental runs for which quasi-chaotic flow behavior was observed. Steady air-flow patterns predicted in all these simulations were always bi-cellular with the upper cell showing higher velocities with each successive simulation. Isotherms and streamlines for a steady flow predicted by the axisymmetric model at Ra = 1.52 x 10^7 corresponding to an experimental run in the quasi-chaotic regime are shown in Fig. 8.3(a) and (b). For this bi-cellular flow, the upper cell has a higher maximum velocity than the lower cell, which is the opposite of what was observed for the bi-cellular flow shown in Figure 8.2.

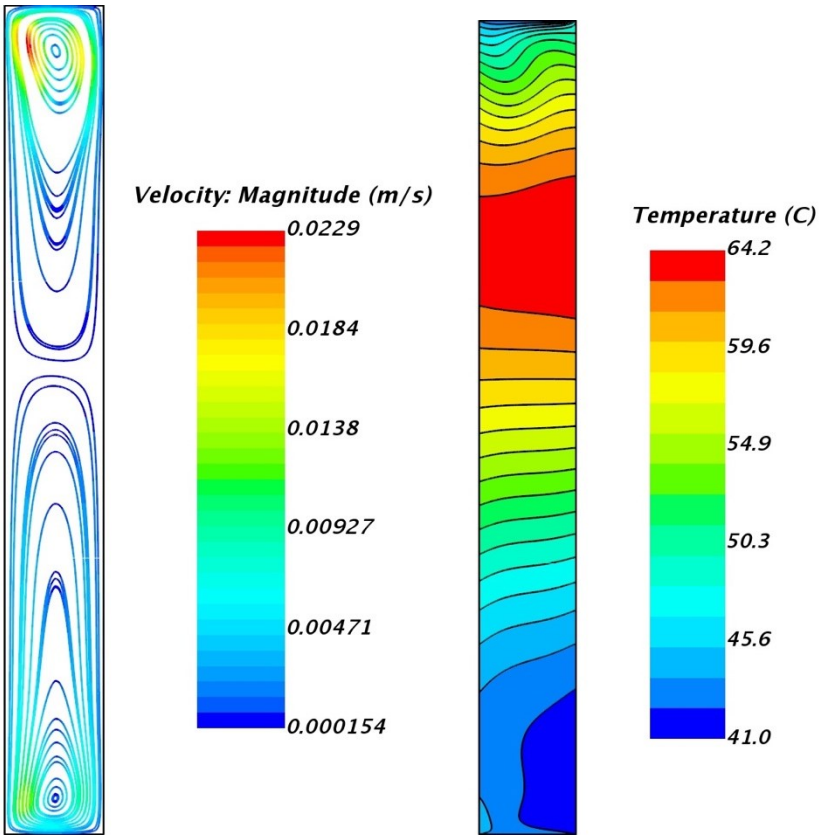

Figure 8.3: (a) Streamlines (b) Isotherms for a steady bi-cellular flow predicted at Ra = 1.52 x 10^7 which corresponds to an experimental run with peak furnace temperature of T_p = 64.2°C using the axisymmetric CFD model of the annular cavity.
Note: Width of cavity (r-dimension) is scaled by *x*3 times for visualization purposes.

8.2.2 Comparison of Axisymmetric Model with Experiments

As the axisymmetric CFD model was unable to predict any unsteady flows, comparisons are only possible between mean temperatures measured by thermocouples for the different flow regimes and those predicted by the model. Mean temperature measured at $\theta = 270°$ thermocouple for experimental runs starting from $T_p = 44.6°C$ upto $T_p = 64.2°C$ are shown in Fig.8.4. Error bars indicate amplitude of fluctuations about mean temperatures for unsteady flows observed in experiments. Temperatures predicted by the axisymmetric simulations at the point $z = 0.5H, r = \frac{R_i+R_o}{2}$ are also shown in Fig 8.4 for comparison.

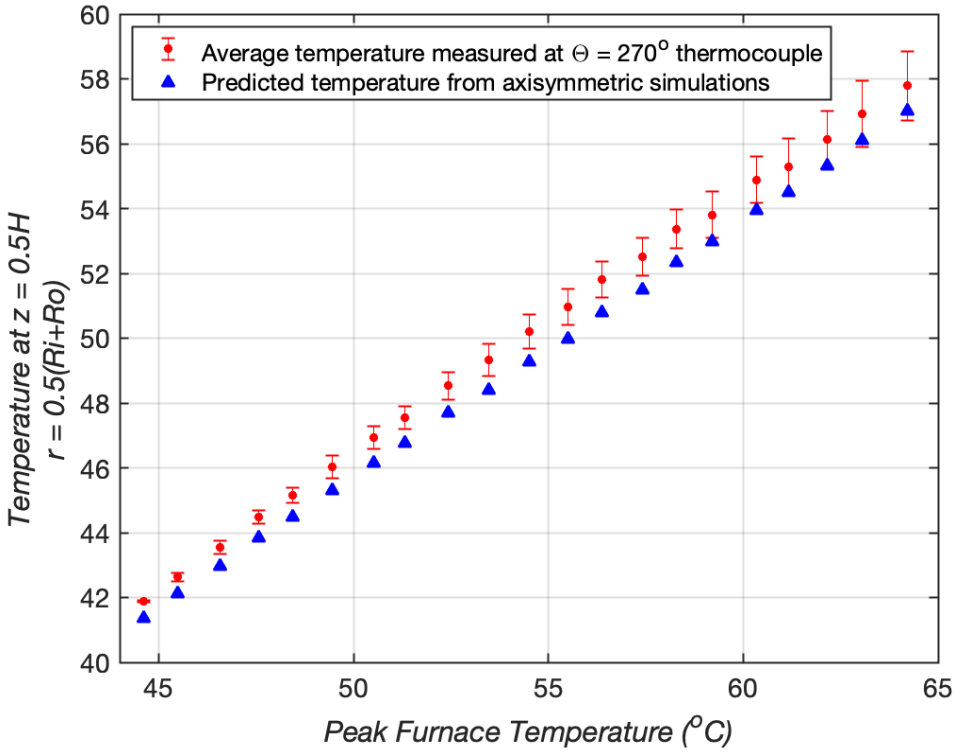

Figure 8.4: Average temperature at point $z = 0.5H, r = \frac{R_i+R_o}{2}$ from experimental measurements and from axisymmetric CFD model predictions.

With each successive experimental run, error between experimentally observed mean temperature at $z = 0.5H, r = \frac{R_i+R_o}{2}$ and mean temperature prediction from the axisymmetric model increases. This discrepancy is caused because the axisymmetric model could not predict any unsteady flows.

8.3 3D CFD Model

As the axisymmetric model was not able to predict either periodic or chaotic flows observed in the experiments, it was decided to develop a full 3D CFD model of the annular cavity. Results from the 3D CFD model are presented in subsequent sections.

8.3.1 Numerical Method and Fluid Thermophysical Properties

Three-dimensional, compressible, transient form of the Navier-Stokes equations for a Newtonian fluid given by equations (3.12) - (3.14) are solved. Air is treated as ideal gas and thermophysical properties are assigned similar to those mentioned in Section 8.1.1.

8.3.2 Solver Settings, Grid Size, and Time-Step

The 3D model is developed in Simcenter StarCCM+ using the coupled implicit solver. Computational domain is discretized using a second-order accurate up-winding scheme. A second-order accurate implicit scheme is used for time discretization. A symmetric grid in azimuthal direction and a structured, flow-aligned grid in the axial direction was created by utilizing the directed mesher in Simcenter StarCCM+. After a grid refinement study according to methods of Roache [69, 92], a grid size of 28 x 336 x 700 with 28 elements in the radial direction, 336 elements in azimuthal direction and 700 elements in the axial direction was selected. At this grid size the 3D annular computational domain contains approximately 6.6 million cells. A time-

step size of 0.05 seconds was selected after performing time-discretization error studies as per methods of Roache [69,92].

8.3.3 Computational Domain, Boundary Conditions and Initial Conditions

Temperature boundary conditions for the annular cavity's inner and outer cylindrical walls were prescribed based on a 5th order polynomial fitted to experimentally measured temperatures from the furnace and polycarbonate wall thermocouples. A logarithmically varying temperature profile was prescribed for the top and bottom horizontal walls based on the assumption of conduction heat transfer through horizontal walls. The no-slip velocity boundary condition was assigned at all four walls of the cavity. Figure 8.5 shows the computational domain used for simulations.

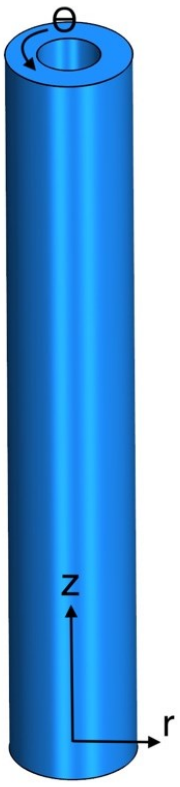

Figure 8.5: Computational domain for 3D CFD model of the annular cavity experimental system.

Equations (8.1) - (8.4) show the temperature boundary conditions assigned at cavity walls. Figure 8.6 shows boundary conditions for simulation at Rayleigh number of 1.05 x 10^7 which corresponds to an experimental run with peak wall temperature of T_p = 46.7°C. Initial condition for each new 3D transient simulation was set to the flow field obtained from a prior simulation at a lower Rayleigh number. For the very first simulation, initial conditions of stationary air at ambient temperature were assigned.

$$\text{Inner cyliner at } r = R_i = 0.015875\text{m}: \; T_1(z) = T_{preform}(z) \tag{8.1}$$

$$\text{Outer cyliner at } r = R_o = 0.03175\text{m}: \; T_2(z) = T_{furnace}(z) \tag{8.2}$$

$$\text{Top surface at } z = H = 0.4\text{m}: \quad T_3(r) = \frac{T_1(H) - T_2(H)}{\ln\left(\frac{R_i}{R_o}\right)} . \ln\left(\frac{r}{R_o}\right) + T_2(H) \tag{8.3}$$

$$\text{Bottom surface at } z = 0: \; T_4(r) = \frac{T_1(0) - T_2(0)}{\ln\left(\frac{R_i}{R_o}\right)} . \ln\left(\frac{r}{R_o}\right) + T_2(0) \tag{8.4}$$

Note: In the annular cavity experiments described in Chapter 7, a steady flow regime was observed for nominal Rayleigh numbers between 8.18 x 10^6 and 9.68 x 10^6. This range corresponds to only four experiments with peak wall temperatures ranging between T_p = 41.3°C to 44.6°C. In order to ensure that the 3D CFD model accurately captures transitions from steady to periodic flows, it was deemed necessary to have more experimental data for the steady flow regime. To generate

temperature boundary conditions for which steady flow was observed in the cavity, additional experiments were done at lower peak wall temperatures between T_p = 30.6°C to 41.3°C, which correspond to nominal Rayleigh numbers between to 4.58 x 10^6 to 8.18 x 10^6. A steady flow was observed for all of these newly conducted experiments. 3D transient simulations described in this chapter are done starting from these lower Rayleigh number experiments where the steady flow was observed.

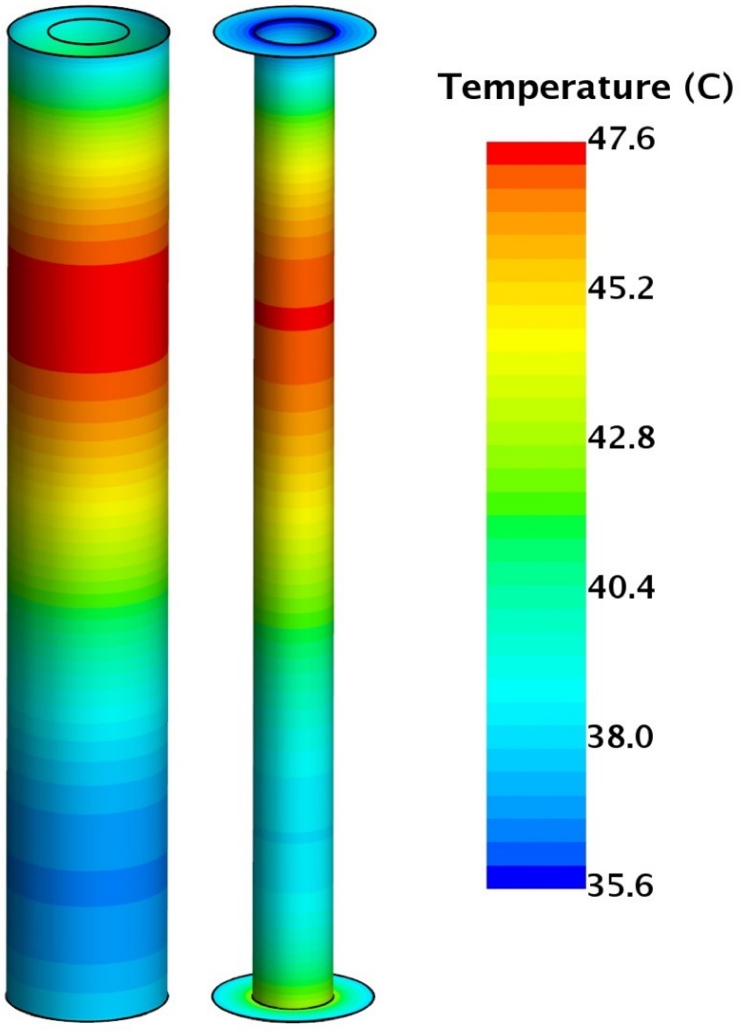

Figure 8.6: Temperature boundary conditions applied at four walls of cavity for a simulation at Rayleigh number of 1.05 x 10^7 corresponding to an experimental run with peak wall temperature of T_p = 46.7°C.

8.4 Results

The 2D axisymmetric CFD model predicted a steady bi-cellular base flow at low Rayleigh numbers. A cell or roll in an annular geometry takes the form of a torus. Therefore, when visualized in a 3D annulus, a bi-cellular flow comprises two counter-clockwise rotating tori. Our expectation when starting with the 3D CFD simulations was to observe these axisymmetric tori at low Rayleigh numbers. However, flow patterns predicted by the 3D model, even for very low Rayleigh numbers, were neither axisymmetric nor steady. The next few sections describe the surprising results from these 3D numerical simulations.

8.4.1 Eight Convection Cells

The first 3D simulation was performed for a Rayleigh number of 4.58×10^6 corresponding to an experiment with peak furnace wall temperature of $T_p = 30.6°C$. An unsteady oscillatory flow solution comprising of several convection cells/rolls was predicted for this simulation. The oscillatory flow resulted from a back and forth rotating movement of convection cells and their interaction. Descriptions and visualizations of the flow are presented before discussing the physical phenomenon responsible for flow oscillations.

8.4.1.1 Description of Convection Cells.

A total of eight unsteady convection cells/rolls are seen inside the annular cavity for the simulation at $Ra = 4.58 \times 10^6$. The cells are arranged in sets of four in two rows along the cavity height: four cells/rolls in the upper half of cavity and four cells/rolls in the lower half. Cells are oriented along the circumference of the annular space in the azimuthal direction, and they circulate fluid perpendicular to the radial direction (radially directed). This orientation of cells is very different

from the symmetric bi-cellular (toroidal) base flow predicted by the 2D axisymmetric CFD model, where two tori (upper cell/torus and lower cell/torus) oriented in the radial direction circulate fluid perpendicular to the azimuthal direction. Each of the eight convection cells rotates in a direction opposite to that of the adjacent cell. Consequently, there are two clockwise and two counterclockwise rotating cells in the cavity's top and bottom halves. Figure 8.7 shows the streamlines inside the annulus visualized from the front and backside. An even number of cells is conducive from an energetics perspective since an odd number of cells would result in a shear layer between adjacent cells/rolls.

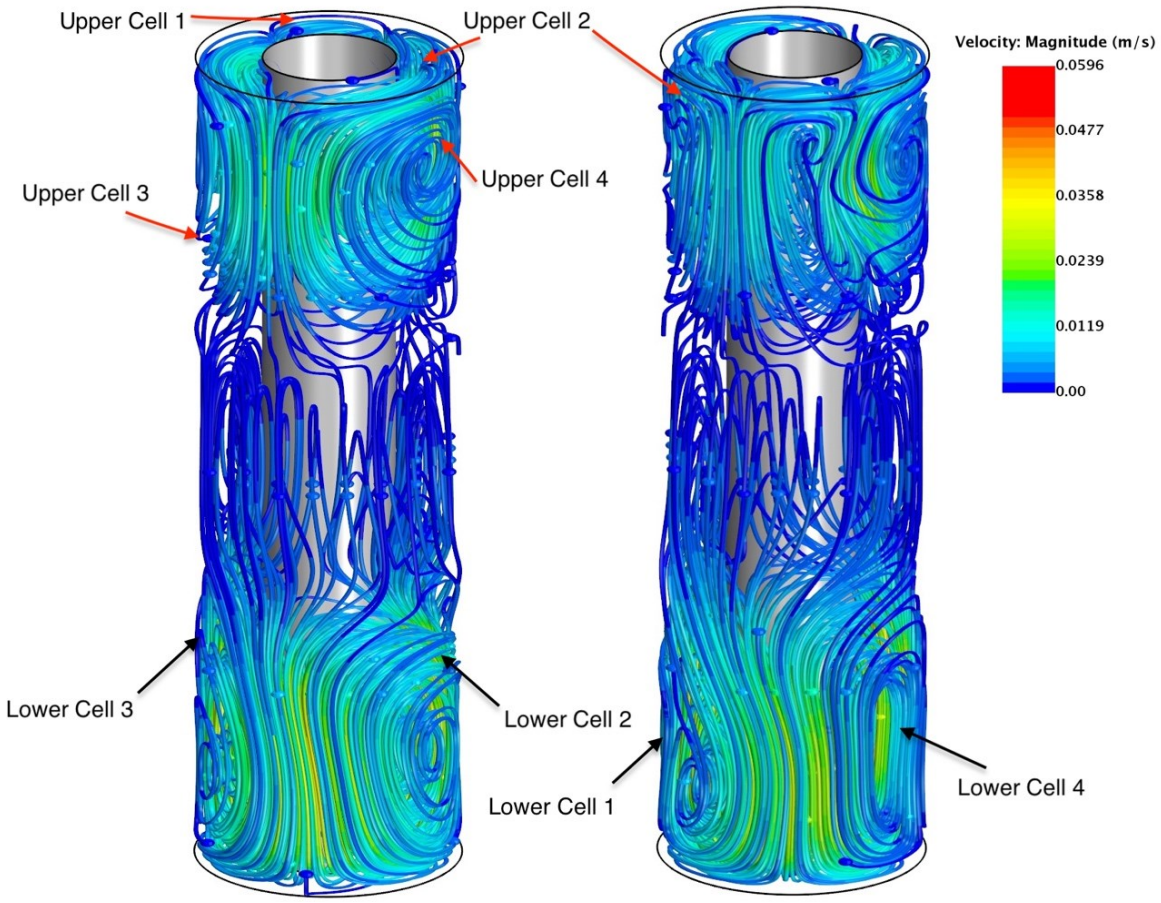

Figure 8.7: Streamlines in annular space of cavity visualized from frontside (left) and backside (right) for a simulation at Ra = 4.58 x 10^6 which corresponds to an experimental run with peak wall temperature of T_p = 30.6°C.
Note: Radial dimension of cavity is scaled by *x*1.5 times for visualization purposes.

Number of convection cells and their orientation is evident looking at axial velocities along planes perpendicular to axial (Z) direction. Figures 8.8 shows axial velocities on three planes namely, z = 0.1m, 0.15m and z = 0.35m. Planes z = 0.1m and z = 0.15m intercept the lower convection cells while the z = 0.35m plane intercepts the upper convection cells. Areas of negative and positive axial velocity are marked by '+' and '-' signs.

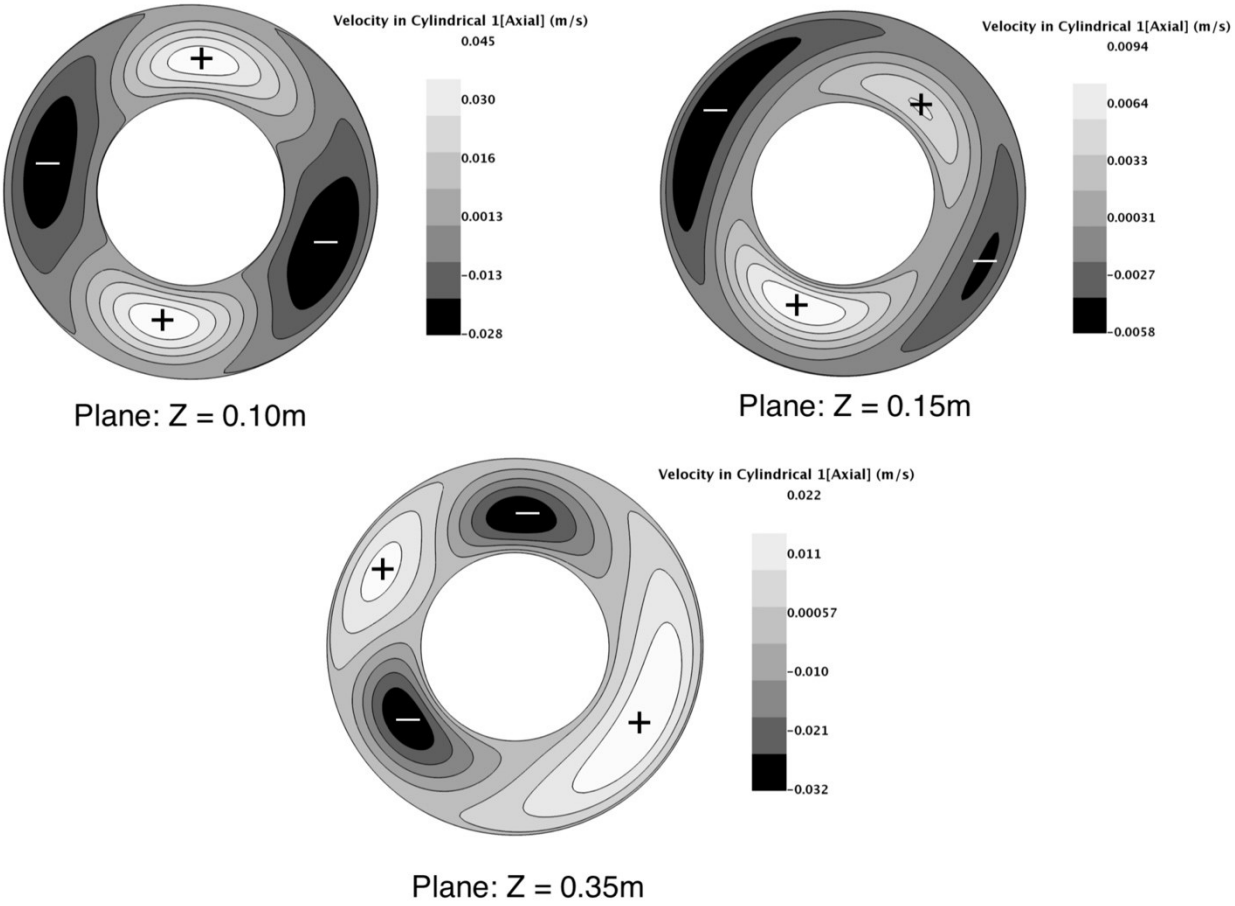

Figure 8.8: Axial velocities on planes z = 0.1m, 0.15m and z = 0.35m for a simulation at Ra = 4.58 x 10^6 which corresponds to an experimental run with peak wall temperature of T_p = 30.6°C. Dark and light regions indicate negative and positive axial velocities respectively.

Each convection cell passes through one positive axial velocity area (marked in light color) and an adjacent negative axial velocity area (marked in dark color). All three planes show two areas each of positive and negative axial velocities indicating presence of four cells. This convention of denoting number of cells from axial velocity will be used throughout this chapter. Four upper and lower convection cells and their direction of rotation is also easily observable in Figure 8.9 which shows temperature fields on three Z planes along with projected velocity vectors.

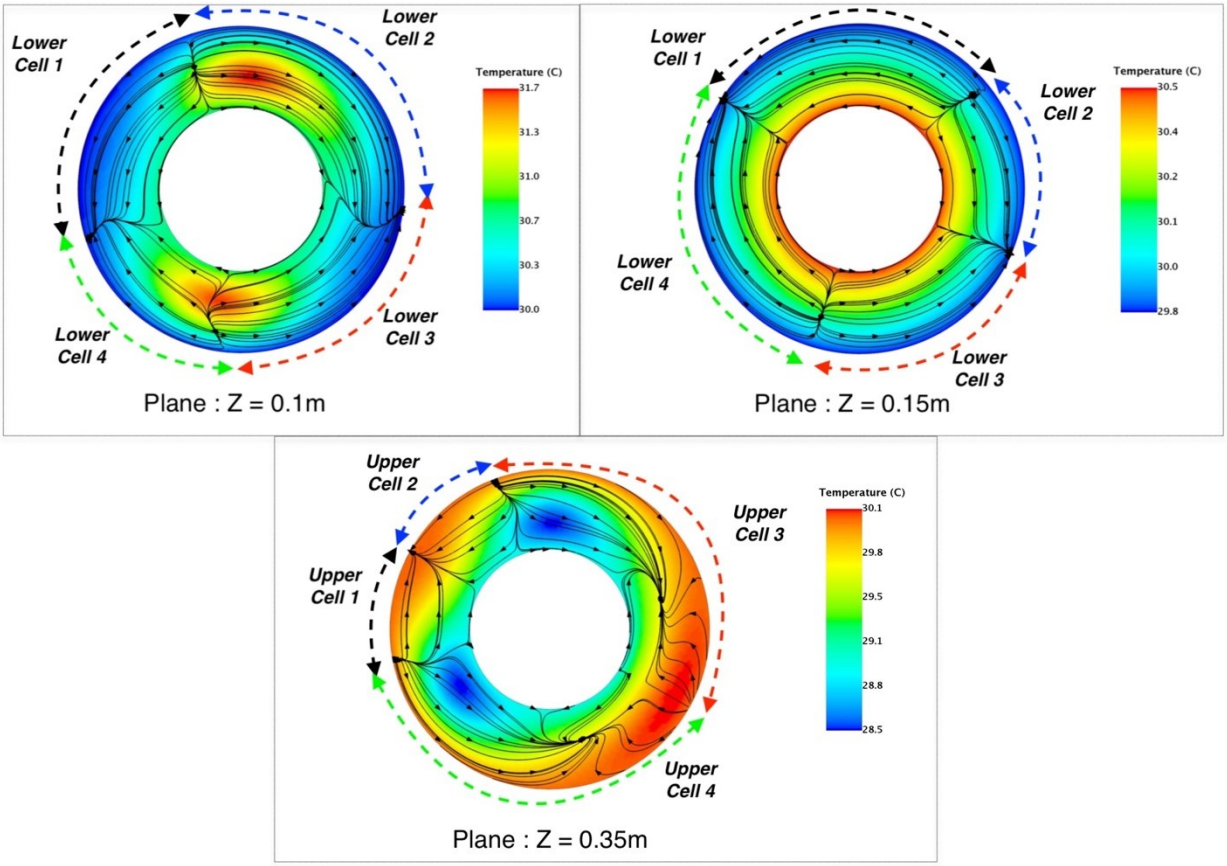

Figure 8.9: Temperature fields superimposed with projection of velocity vectors on planes z = 0.1m, 0.15m and z = 0.35m for a simulation at Ra = 4.58 x 10^6 which corresponds to an experimental run with peak wall temperature of T_p = 30.6°C.

Note: In order to get the visualizations shown in Fig 8.9 and Fig 8.10 the velocity field was modified by first subtracting from it dot product of the local velocity with the surface normal and then projecting the resultant field onto the surface.

Figure 8.10 shows temperature fields and projected vectors on fours azimuthal planes namely, θ = 0°, 90°, 180° and 270°. Here we can see two rows of cells (top and bottom) in which the upper and lower convection cells reside. Isotherms inside the cavity shows steep gradients along the axial direction at the extremities and an almost isothermal central region. Cold horizontal fluid layers lay on top of hot fluid layers in both upper and lower portions of cavity indicating unstable flow stratification in these two areas.

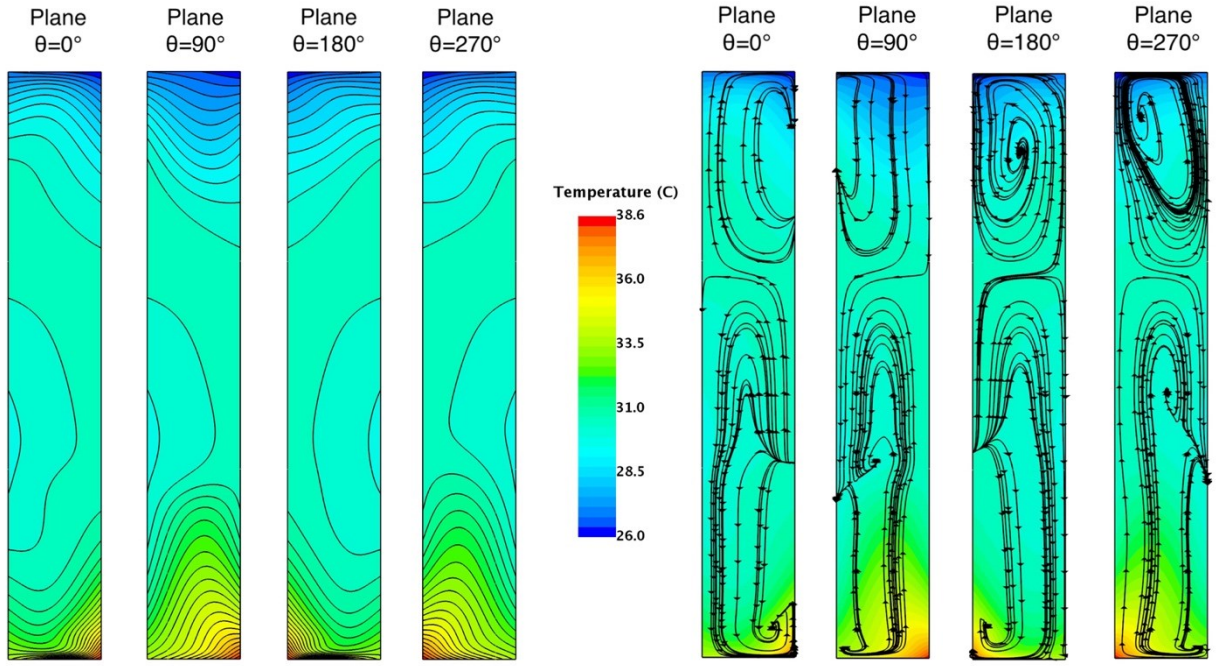

Figure 8.10: Temperature fields superimposed with projection of velocity vectors on planes θ = 0°, 90°, 180° and 270° for a simulation at Ra = 4.58 x 10^6 which corresponds to an experimental run with peak wall temperature of T_p = 30.6°C.
Note: Radial dimension of cavity is scaled by *x*4 times for visualization purposes.

Figure 8.11 shows the velocity vectors in top and bottom potions of the cavity where circulations created by upper and lower convection cells can be seen. Flow oscillations in are mostly restricted to top and bottom extremes while the central portion of cavity is relatively unperturbed.

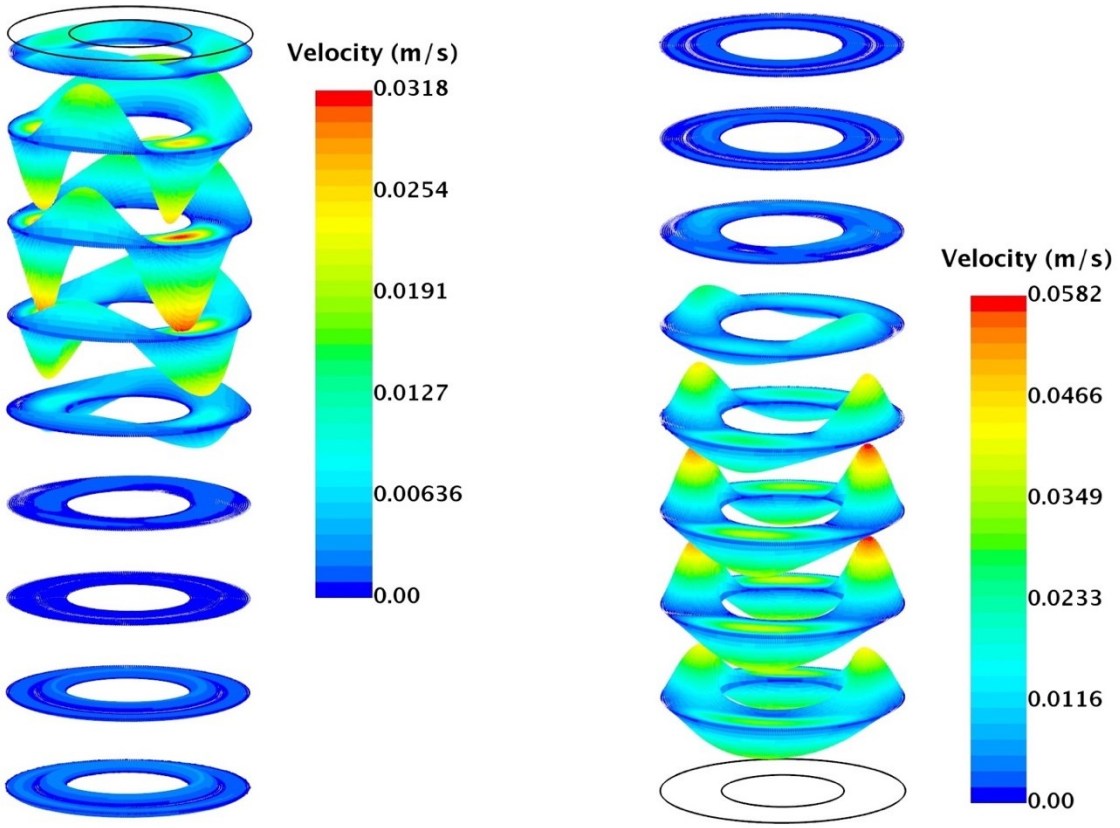

Figure 8.11: Velocity vectors on planes z = 0.2m, 0.225m, 0.25m, 0.275m, 0.3m, 0.325m, 0.350m, 0.375, 0.395m located in top part of cavity and z = 0.2m, 0.175m, 0.15m, 0.125m, 0.10m,0.075m,0.05m,0.025m located in bottom part of cavity for a simulation at Ra = 4.58 x 10^6 which corresponds to an experimental run with peak wall temperature of T_p = 30.6°C.

8.4.1.2 Physical Description of Oscillatory Phenomenon

In the top and bottom portions of cavity where fluid is unstably stratified, azimuthally oriented (or radially directed) cells/rolls are formed due to the Rayleigh-Bernard instability mechanism. Similar observations of azimuthal cells (radially directed) have been made by Rubinov et al. [93], Selver et al. [94] and Ma et al. [95] in their study of vertical cylindrical cavities partially heated from the sides. Ma et al. [95] found that a steady, axisymmetric, toroidal flow becomes unstable to azimuthal modes resulting in one-roll or two-roll oscillating patterns. For large aspect ratio

cylinders, they observed that the oscillatory flow was a result of Rayleigh Bernard type instability caused by unstably stratified top portion of fluid in cylindrical cavity. Figure 8.12(a) shows the axial velocity at a different time instances on z = 0.875H plane for the two-roll rotating pattern predicted by Ma et al. [95]. Rayleigh-Bernard instability in annuli and cylinders heated from the bottom has also been reported to create azimuthally oriented (or radially directed) rolls [91,96]. Figure 8.12 (b) shows multiple rolls observed in an annulus by Stork and Müller [91] in their experiments with annular cavities heated from the bottom. Azimuthally oriented cells observed in our current study are similar to these two configurations where cells/rolls develop due to the Rayleigh-Bernard instability mechanism.

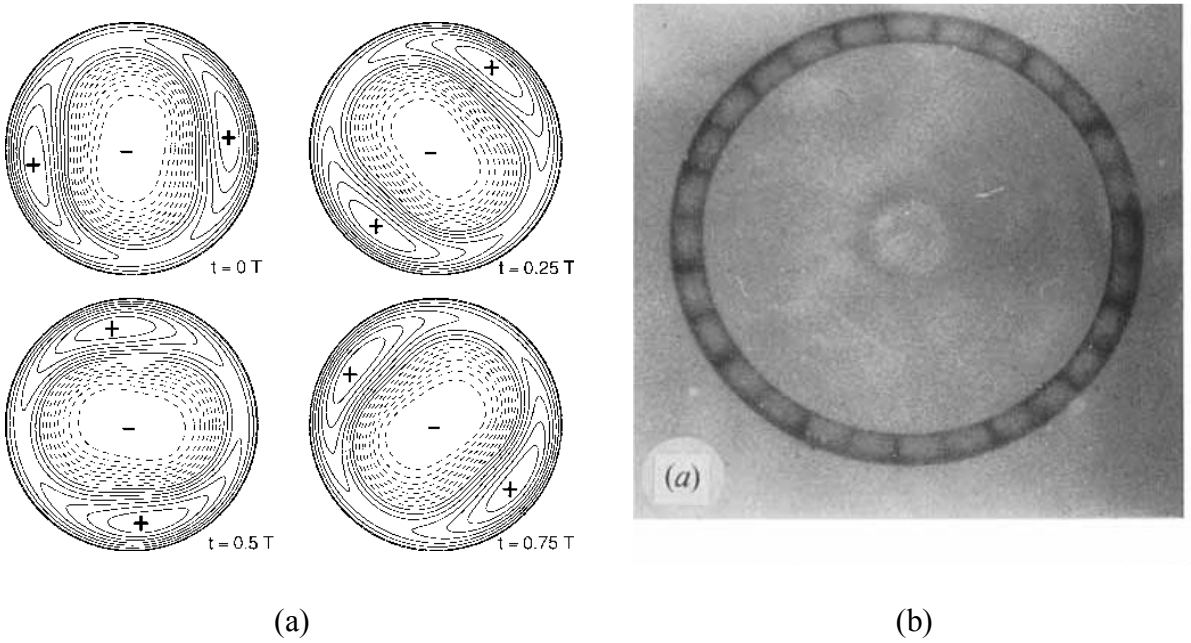

(a) (b)

Figure 8.12: (a) Axial velocity at z = 0.875H plane showing the two-roll oscillatory pattern for convection in cylindrical cavity heated from side as predicted by Ma et al. [95], adapted from [95]; (b) Radially directed (azimuthally oriented) convection rolls observed by Stork and Müller [91] in their experiments with annular cavities heated from the bottom, adapted from [91].

Figures 8.13 and 8.14 show the variation in temperature fields and velocity vectors during one oscillation cycle of unsteady periodic flow predicted at Ra = 4.58 x 10^6.

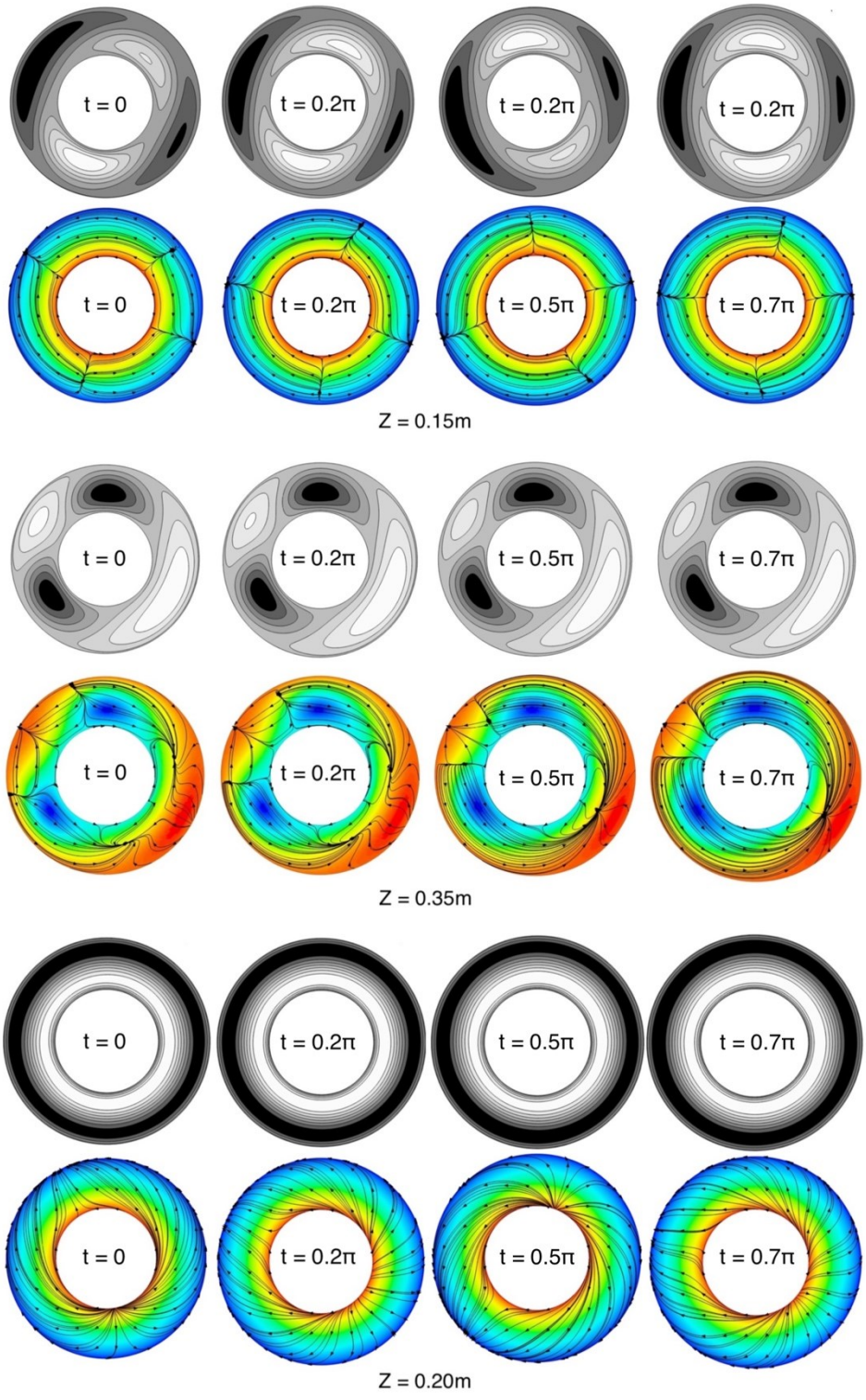

Figure 8.13: Axial velocities (top row) and temperature fields superimposed with projection of velocity vectors (bottom row) over one oscillation period ($\pi = 22.05\ seconds$) for a simulation at Ra = 4.58 x 10^6 which corresponds to an experimental run with peak wall temperature of T_p = 30.6°C. Dark and light regions indicate negative and positive axial velocities respectively.

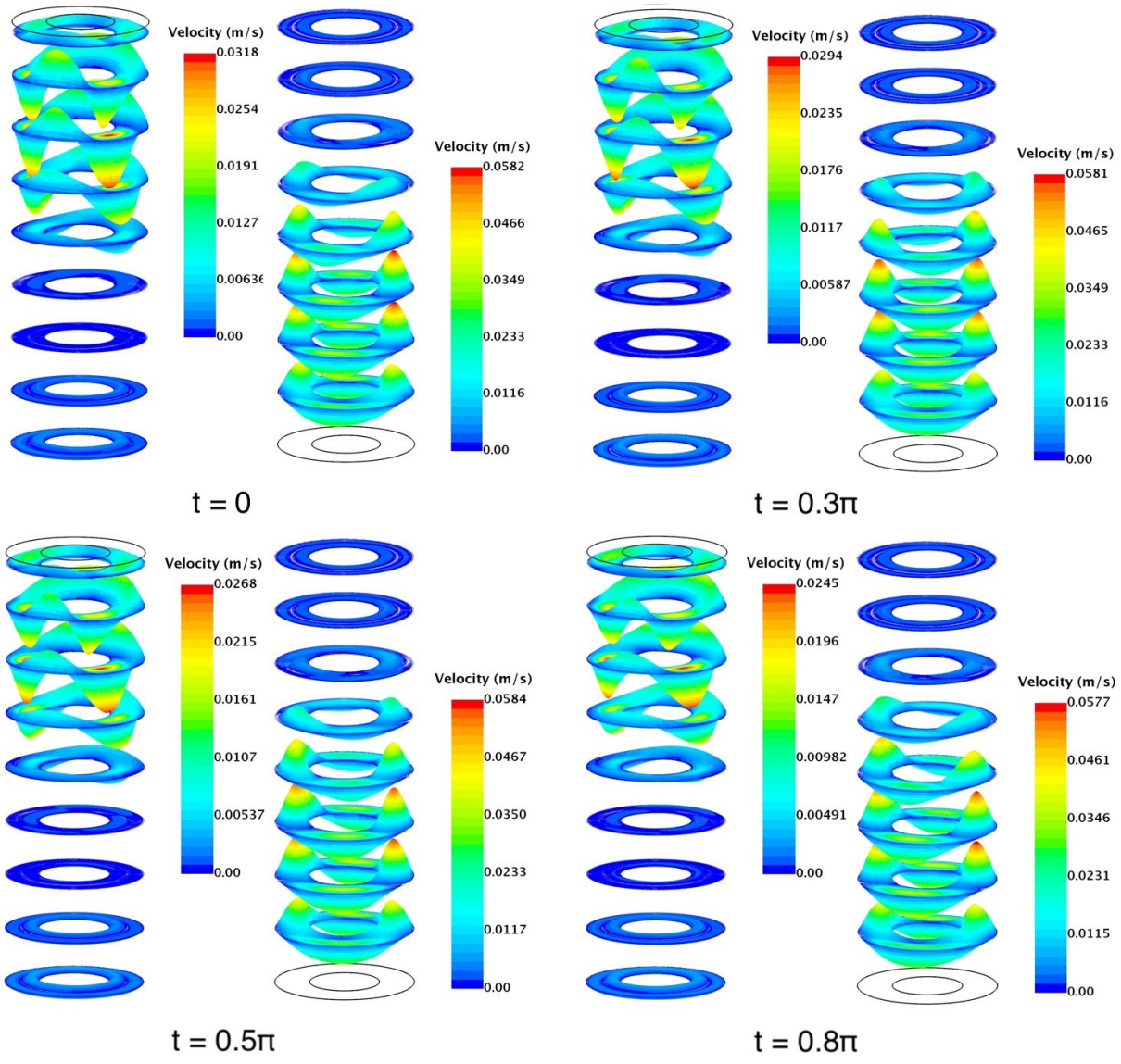

Figure 8.14: Velocity vectors in top and bottom halves of cavity over one oscillation period ($\pi = 22.05\ seconds$) for a simulation at Ra = 4.58 x 10^6 which corresponds to an experimental run with peak wall temperature of T_p = 30.6°C.

In one oscillation cycle, the lower convection cells rotate back and forth along the axis of the annulus, as can be seen in plots for planes z = 0.15m and z = 0.2m. On the other hand, the two larger upper convection cells first move closer and then farther away from the other two smaller convection cells over the course of an oscillation, as can be seen in the plots for plane z = 0.35m.

This back and forth motion of the upper and lower convection cells is the cause of asymmetric oscillatory flow inside the cavity.

8.4.1.3 Frequency and Amplitude of Oscillatory Flow

Oscillatory flow is monoperiodic and all points in cavity oscillate at the same fundamental frequency of 0.046 Hz. Further, fundamental frequency of oscillations for temperature and velocity fields is the same. Figure 8.15(a) shows power spectral density plots for velocity and temperature time-series. Oscillation amplitudes are highly sensitive to azimuthal location as can be seen in Fig. 8.15 (b) showing oscillations measured at different azimuthal locations on z = 0.1m plane.

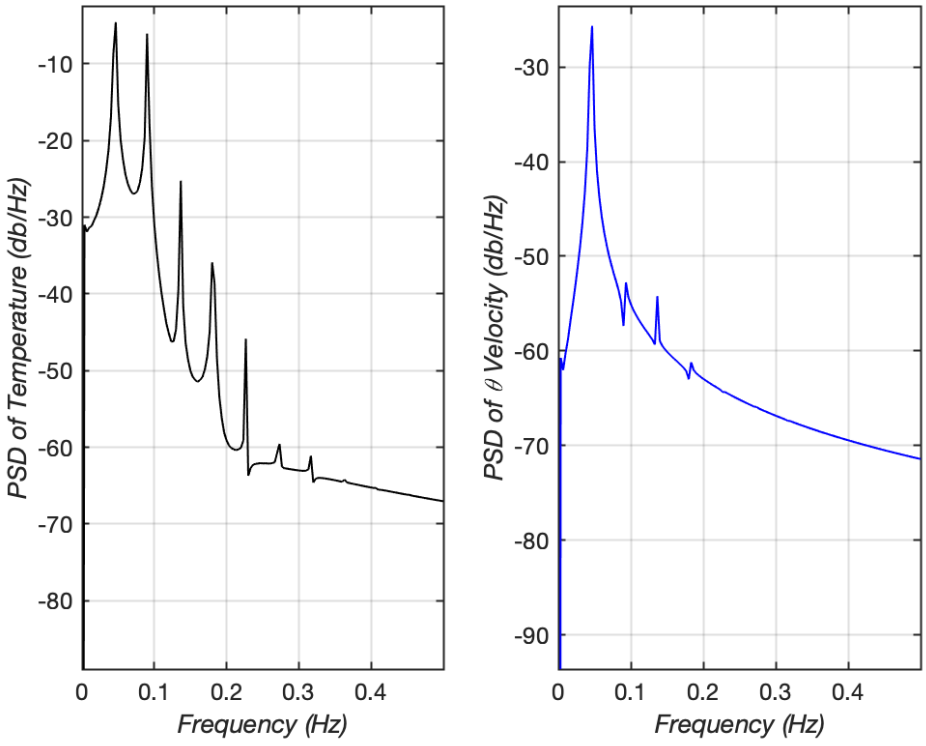

(a)

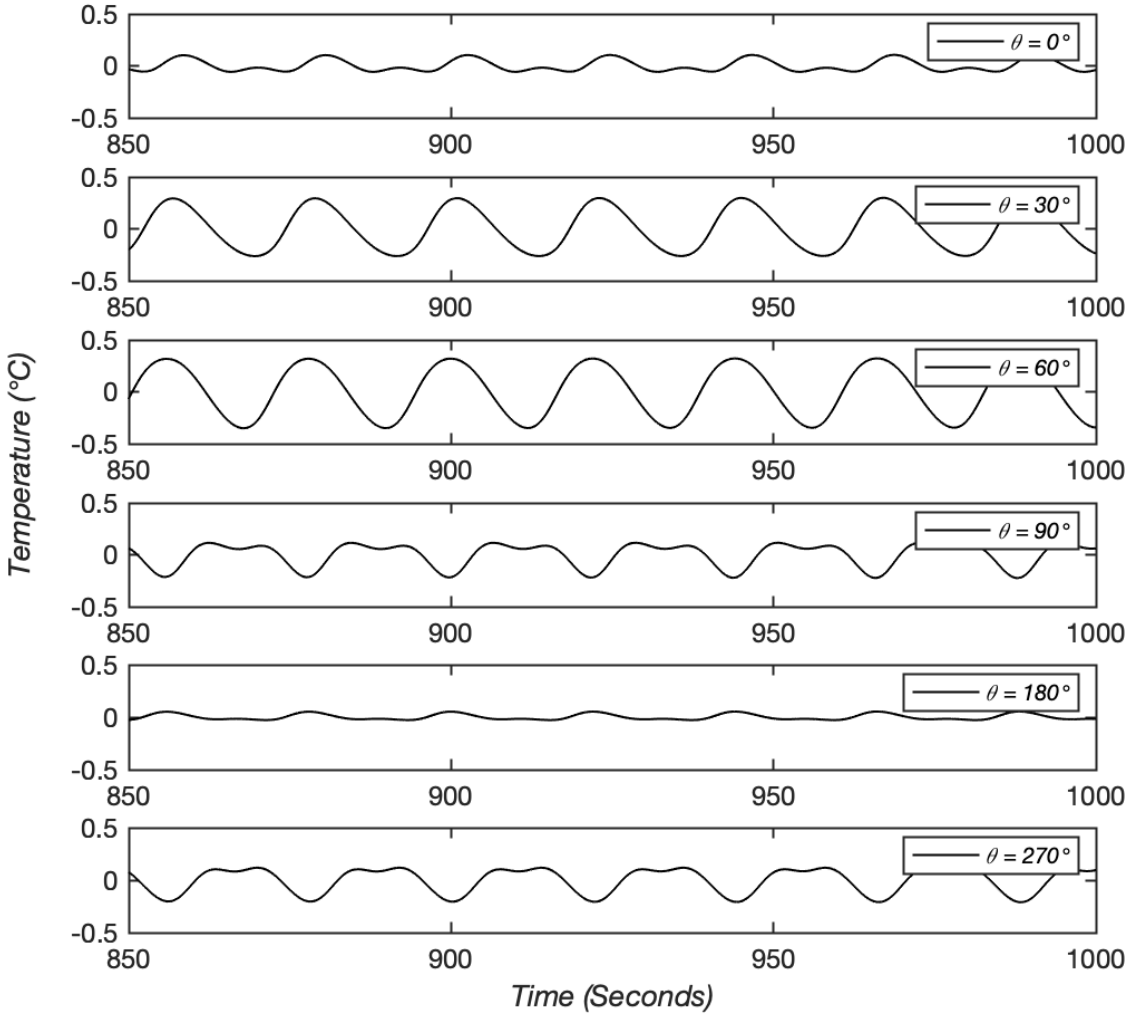

(b)

Figure 8.15: (a) Power spectral density (PSD) of temperature (left) and azimuthal velocity (right) measured at monitoring point (r = 0.0079375m, z = 0.10, θ = 0°); (b) Temperature time series for six points on the plane z = 0.1m, located at radial distance of r = 0.0079375m and at six different azimuthal angles θ = 0°, 30°, 60°, 90°, 180°, 270°, for a simulation at Ra = 4.58 x 10^6.

Oscillatory flow solutions with eight convection cells were predicted for a few more simulations until Rayleigh number of 8.18 x 10^6 at which point a flow bifurcation was observed.

8.4.2 Six Convection Cells

Starting with the solution obtained at Ra = 8.18 x 10^6, when Rayleigh number was further increased to 8.68 x 10^6 (experimental run at T_p = 43.5°C), a different flow pattern with a total of six convection cells was observed. The main change in this new six cell flow from the previous eight cell flow was that the number of upper convection cells reduced from four to two. Figure 8.16 shows the vector plots on several planes in top and bottom parts of cavity.

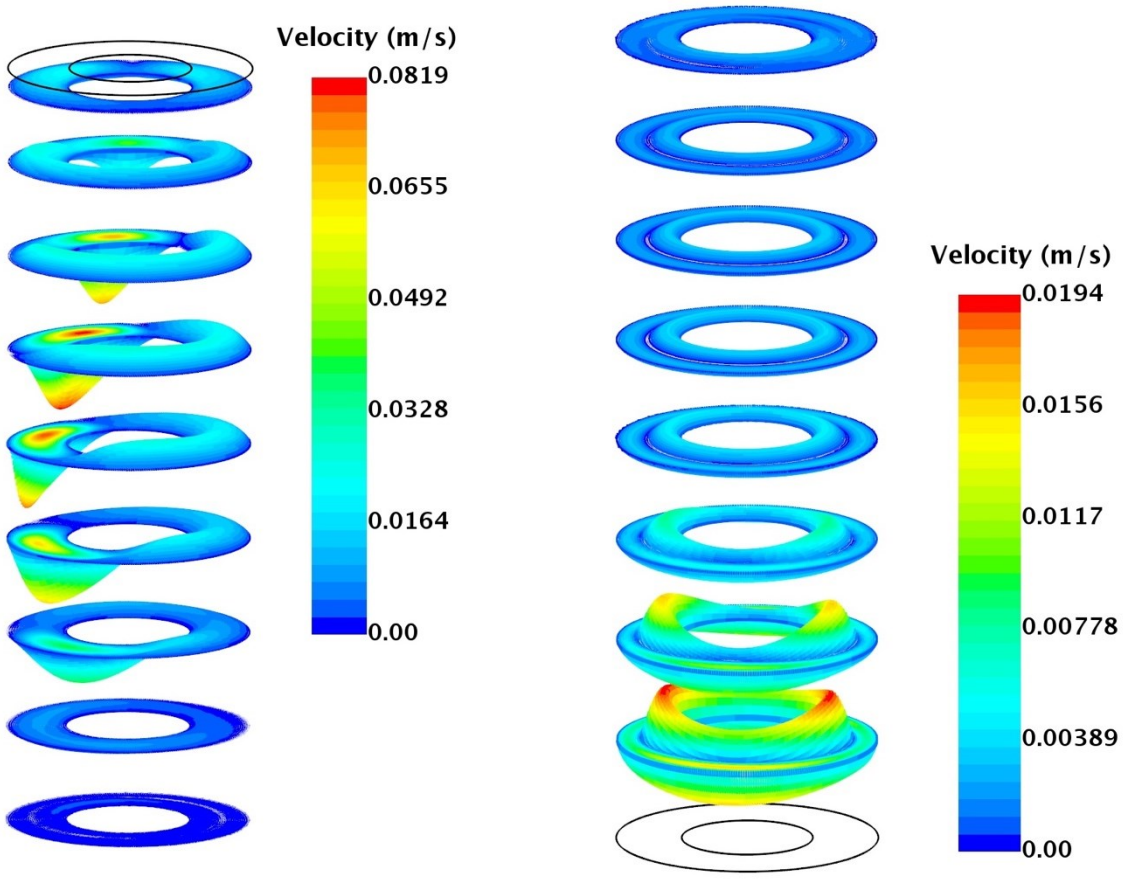

Figure 8.16: Velocity vectors on planes z = 0.2m, 0.225m, 0.25m, 0.275m, 0.3m, 0.325m, 0.350m, 0.375, 0.395m located in top part of cavity and z = 0.2m, 0.175m, 0.15m, 0.125m, 0.10m,0.075m,0.05m,0.025m located in bottom part of cavity for a simulation at Ra = 8.68 x 10^6 which corresponds to an experimental run with peak wall temperature of T_p = 43.5°C.

Axial velocity plots shown in Fig 8.17 show four convection cells in bottom part of cavity (planes z = 0.05 m). These cells are similar to what were predicted for the eight-cell flow solution. Axial velocity at the z = 0 .1m plane appears symmetric which indicates that the lower convection cells have reduced in length (axial Z- dimension) compared to their size in the eight cells solution. Top portion of the cavity (planes z = 0.30m,0.2m) which previously had four convection now shows presence of only two cells.

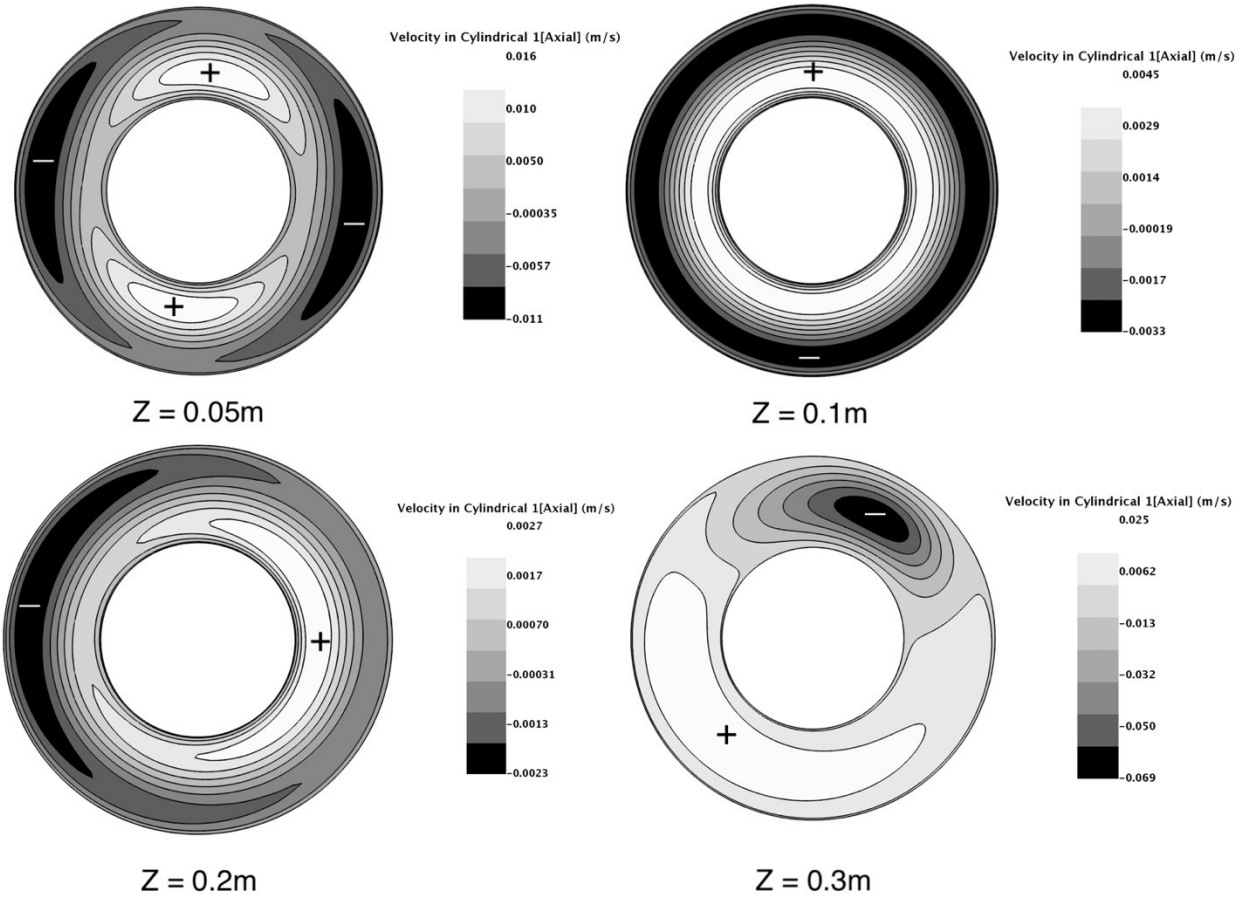

Figure 8.17: Axial velocities on planes z = 0.1m, 0.15m and z = 0.35m for a simulation at Ra = 8.68 x 10^6 which corresponds to an experimental run with peak wall temperature of T_p = 43.5°C. Dark and light regions indicate negative and positive axial velocities respectively.

Figure 8.18 shows temperature fields on four azimuthal planes : θ = 0°, 90°, 180° and 270°. Isotherms in bottom part of cavity look almost symmetric, while those in the top portion look distorted showing a strong presence of convection in azimuthal direction. Further, unstable temperature stratification responsible for the Rayleigh-Bernard instability is much more pronounced in the top portion of the cavity. This leads to higher flow velocities in upper convection cells as compared to lower cells. Figures 8.19 and 8.20 show the variation in temperature fields and velocity vectors during one oscillation cycle of unsteady periodic flow at Ra = 8.68 x 10^6.

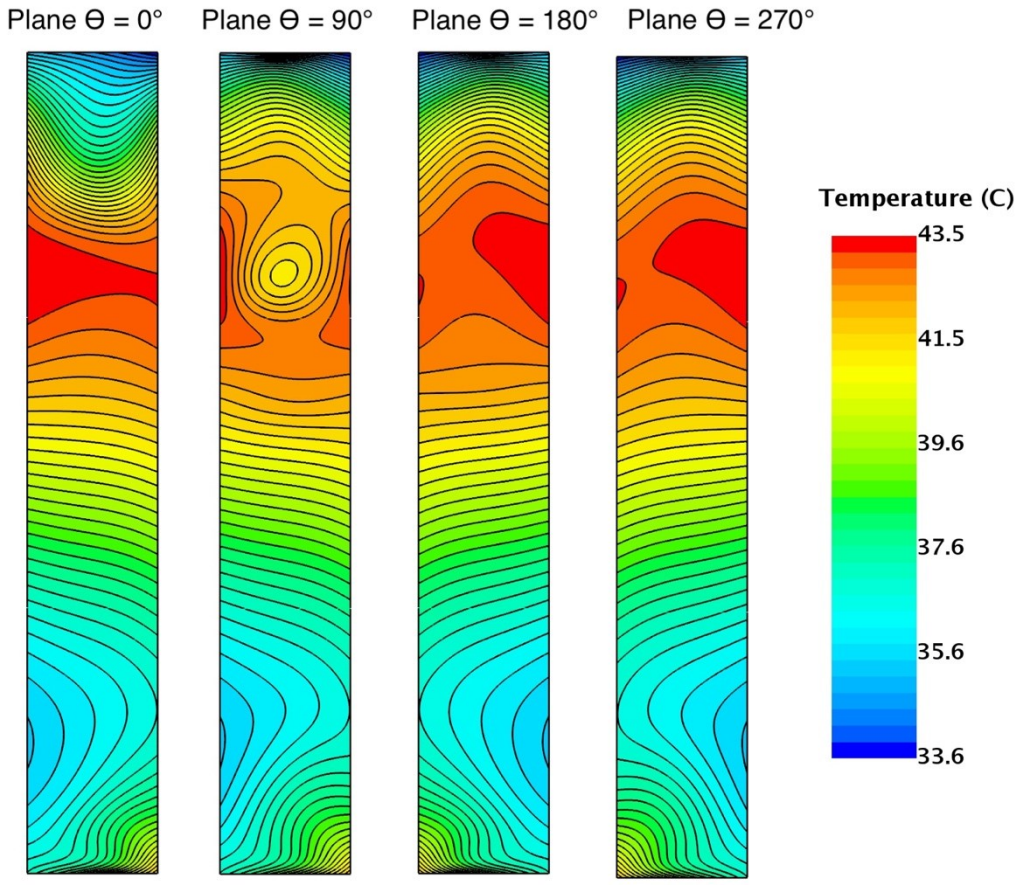

Figure 8.18: Temperature fields on planes θ = 0°, 90°, 180° and 270° for a simulation at Ra = 8.68 x 10^6 which corresponds to an experimental run with peak wall temperature of T_p = 43.5°C.
Note: Radial dimension of cavity is scaled by *x*4 times for visualization purposes.

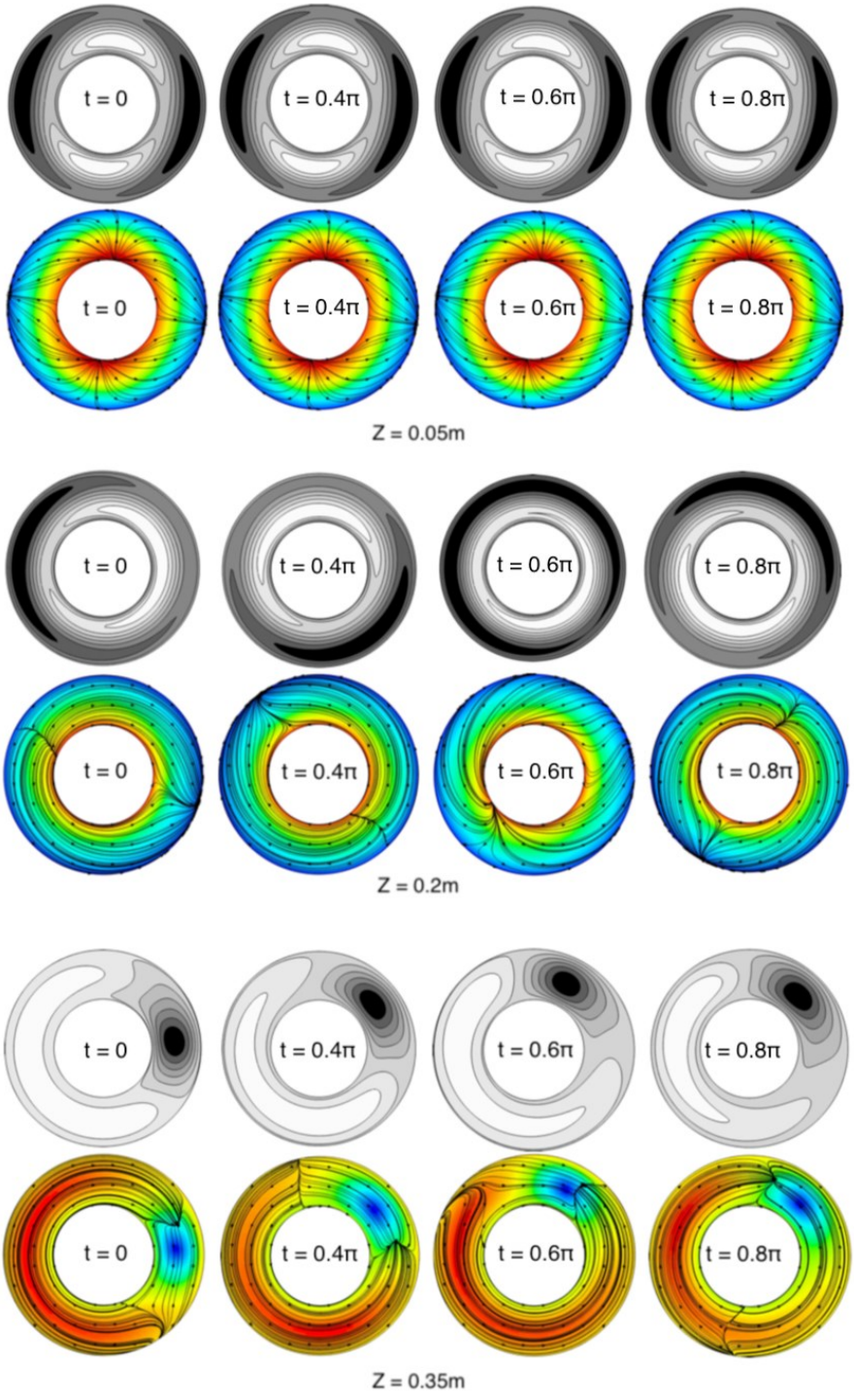

Figure 8.19: Axial velocities (top row) and temperature fields superimposed with projection of velocity vectors (bottom row) over one oscillation period ($\pi = 15.3\ seconds$) for a simulation at Ra = 8.68 x 10^6 which corresponds to an experimental run with peak wall temperature of T_p = 43.5°C. Dark and light regions indicate negative and positive axial velocities respectively.

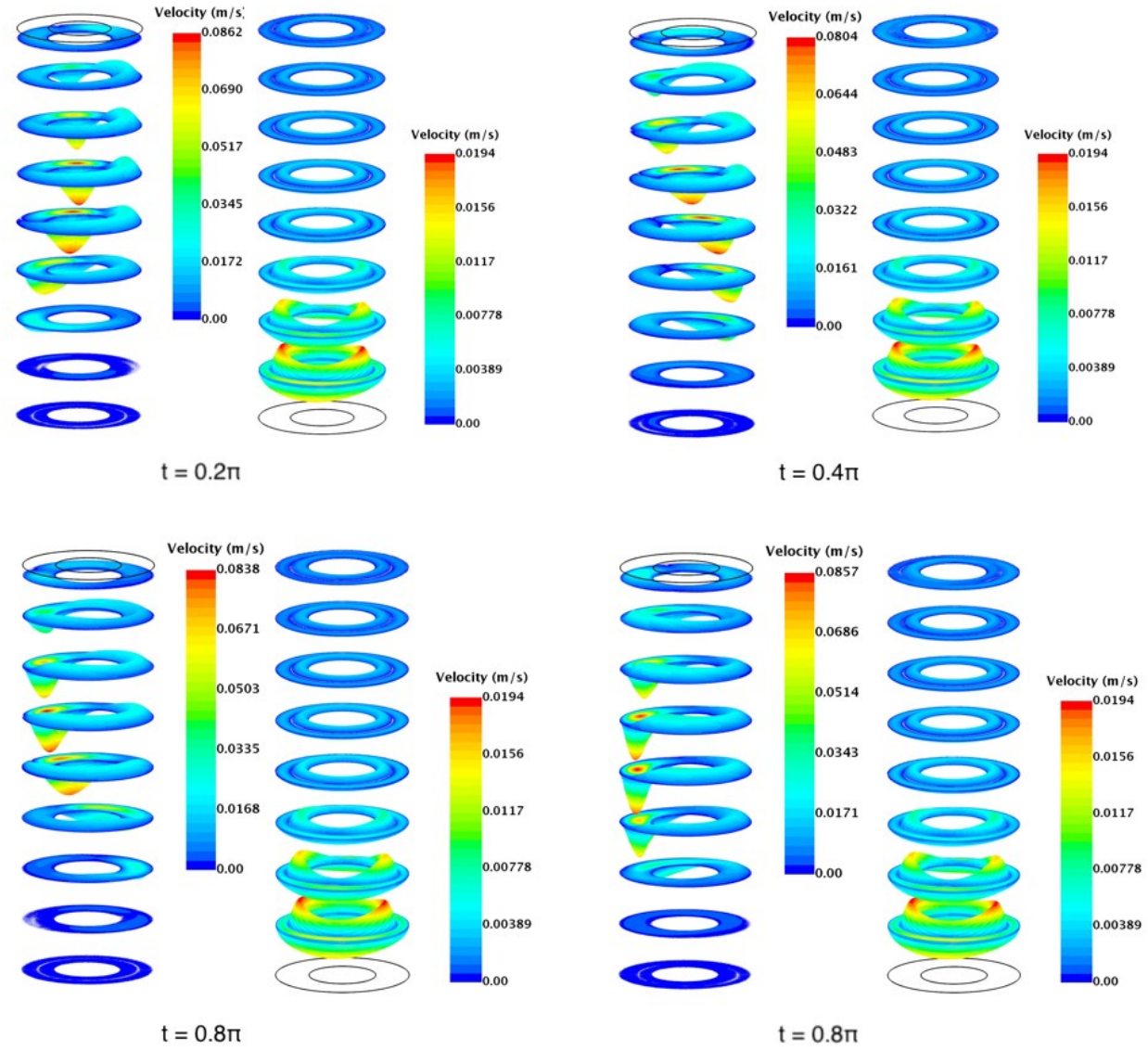

Figure 8.20: Velocity vectors in top and bottom halves of cavity over one oscillation period ($\pi = 15.3\ seconds$) for a simulation at Ra = 8.68 x 10^6 which corresponds to an experimental run with peak wall temperature of T_p = 43.5°C.

Despite the change in the flow structure from eight to six cells, oscillatory flow observed inside the cavity is still mono-periodic. Figures 8.21 and 8.22 shows the oscillation amplitudes at four points on the z = 0.2m plane and corresponding power spectral densities. A fundamental frequency of 0.065 Hz along with its first few harmonics are visible. Oscillation time period of this six-cell convection is lower than that observed for the eight-cell convection.

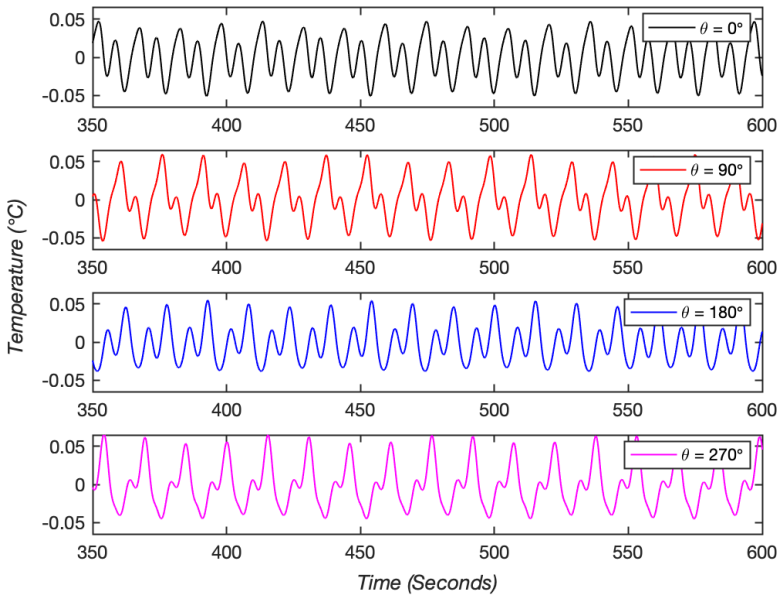

Figure 8.21: (a) Time series for temperature measured on the plane z = 0.2m, located at radial distance of r = 0.0079375m and at four different azimuthal angles θ = 0°, 90°, 180°, 270°, for a simulation at Ra = 8.68 x 10^6.

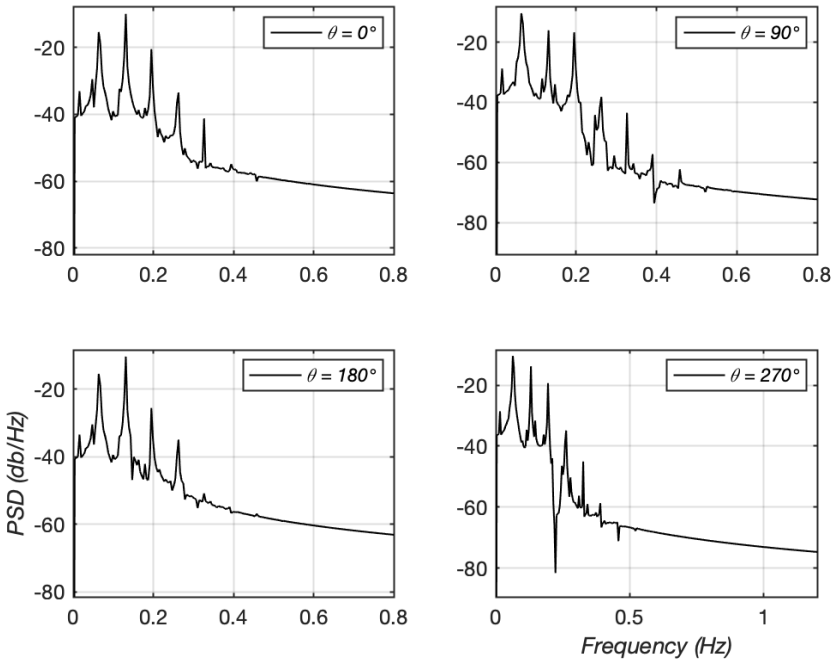

Figure 8.22: Power spectral density (PSD) of temperature measured on the plane z = 0.2m, located at radial distance of r = 0.0079375m and at four different azimuthal angles θ = 0°, 90°, 180°, 270°, for a simulation at Ra = 8.68 x 10^6.

8.4.3 Two Convection Cells and Weakly Asymmetric Toroidal Structure

Starting from the six-convection cell solution when Rayleigh number was increased to 1.00 x 10^7 corresponding to a peak wall temperature of T_p = 45.5°C, a further reduction in number of convection cells was observed. This time, the lower four convection cells disappeared, and, in their place, a weakly asymmetric toroidal structure appeared. This flow structure was extremely stable and was observed for all the subsequent simulations up to a Rayleigh number of 1.71 x 10^7. Figure 8.23(a) and (b) show streamlines and vectors in top and bottom portions of the cavity where these structures can be identified for a simulation at Ra = 1.05 x 10^7 corresponding to a peak wall temperature of T_p = 47.6°C. The toroidal structure is slightly asymmetric at base of cavity and becomes distorted closer to cavity mid-height where it interacts with the two upper convection cells.

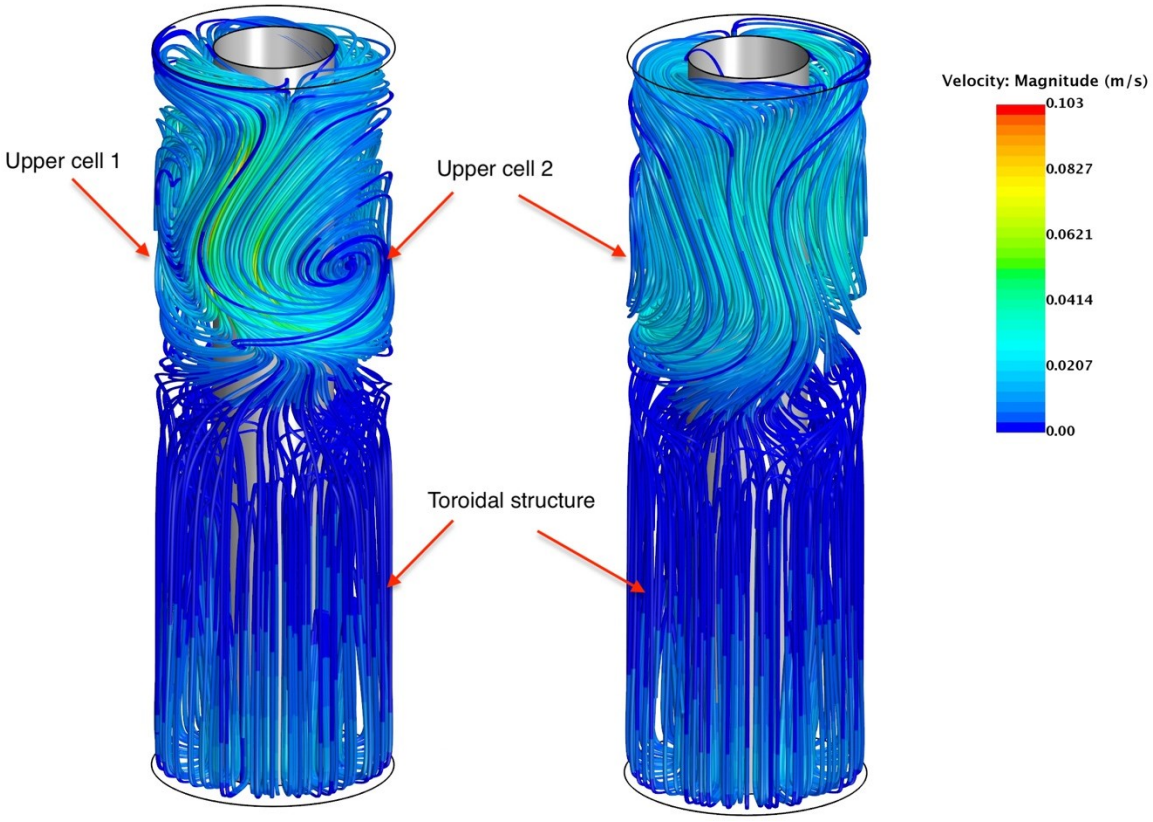

(a)

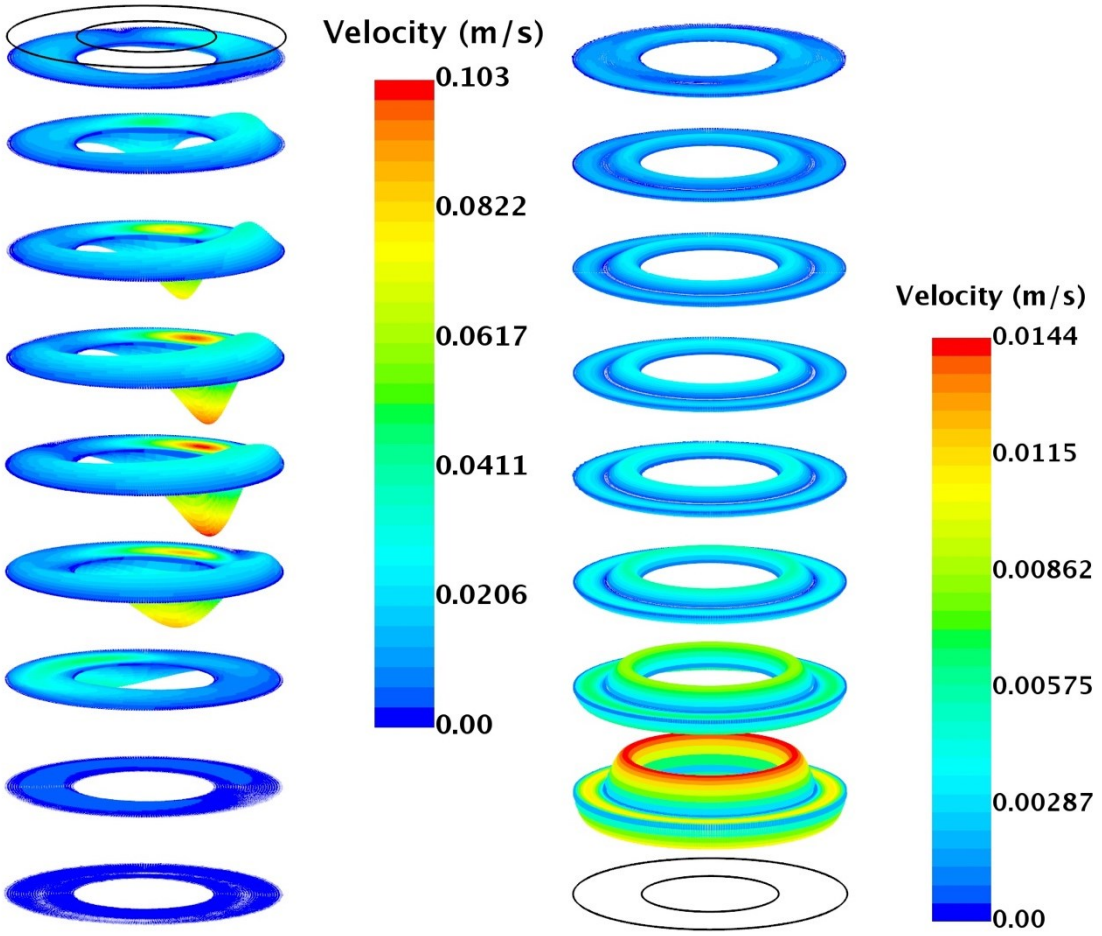

(b)

Figure 8.23: (a) Streamlines in annular space visualized from frontside (left) and backside (right) for a simulation at Ra = 1.05 x 10^7 which corresponds to an experimental run with peak wall temperature of T_p = 47.6°C; (b)Velocity vectors on planes z = 0.2m, 0.225m, 0.25m, 0.275m, 0.3m, 0.325m, 0.350m, 0.375, 0.395m located in top part of cavity and z = 0.2m, 0.175m, 0.15m, 0.125m, 0.10m,0.075m,0.05m,0.025m located in bottom part of cavity for a simulation at Ra = 1.05 x 10^7 which corresponds to an experimental run with peak wall temperature of T_p = 47.6°C.
Note: Radial dimension of cavity is scaled by *x*1.5 times for visualization purposes.

Axial velocity plots along several Z planes for solution at Ra = 1.05 x 10^7 shown in Fig 8.24 demonstrate this transition from two convection cells in top to a toroidal structure in the bottom

portions of the cavity. Although the axial velocity plots in the lower planes look 'almost' axisymmetric, very small amplitude asymmetric oscillations in temperature and velocity are still measurable on these planes.

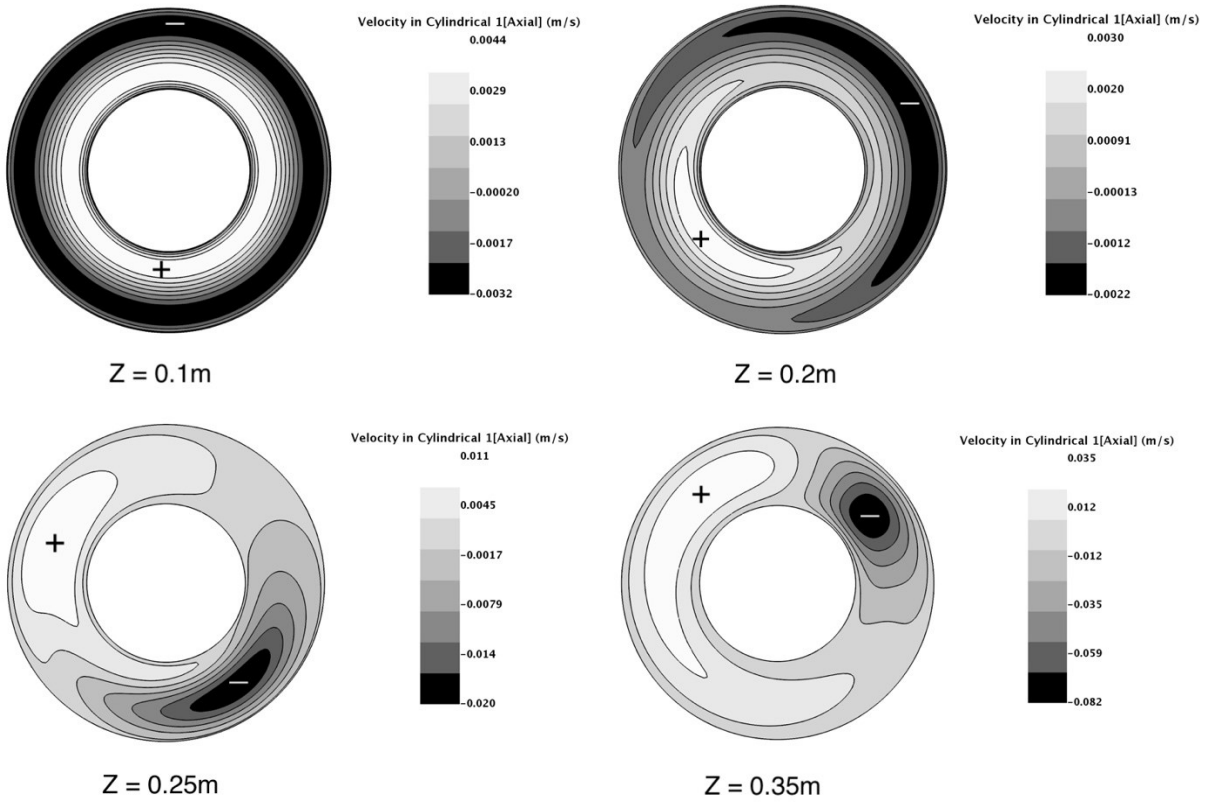

Figure 8.24: Axial velocities on planes z = 0.1m, 0.15m and z = 0.35m for a simulation at Ra = 1.05×10^7 corresponding to an experimental run with peak wall temperature of $T_p = 47.6°C$. Dark and light regions indicate negative and positive axial velocities respectively.

Figure 8.25 shows temperature fields on four azimuthal planes : $\theta = 0°$, 90°, 180° and 270° for the same two cell convection solution obtained at Ra = 1.05×10^7. Fluid in most of the lower parts of the cavity is stably stratified. In contrast, a strong unstable thermal stratification exists in the top portion of the cavity. In the two upper convection cells, fluid is circulated at velocities almost ten

times higher than those in the toroidal structure at the bottom part of the cavity. Oscillations experienced in the lower half of the cavity are mainly due to interaction of the toroidal structure with the upper convection cells. Consequently, variations in temperature and velocity fields are much more prominent in the upper half of the cavity where the two upper convection cells rotate in a back and forth motion about the axis of the annulus than in the toroidal structure.

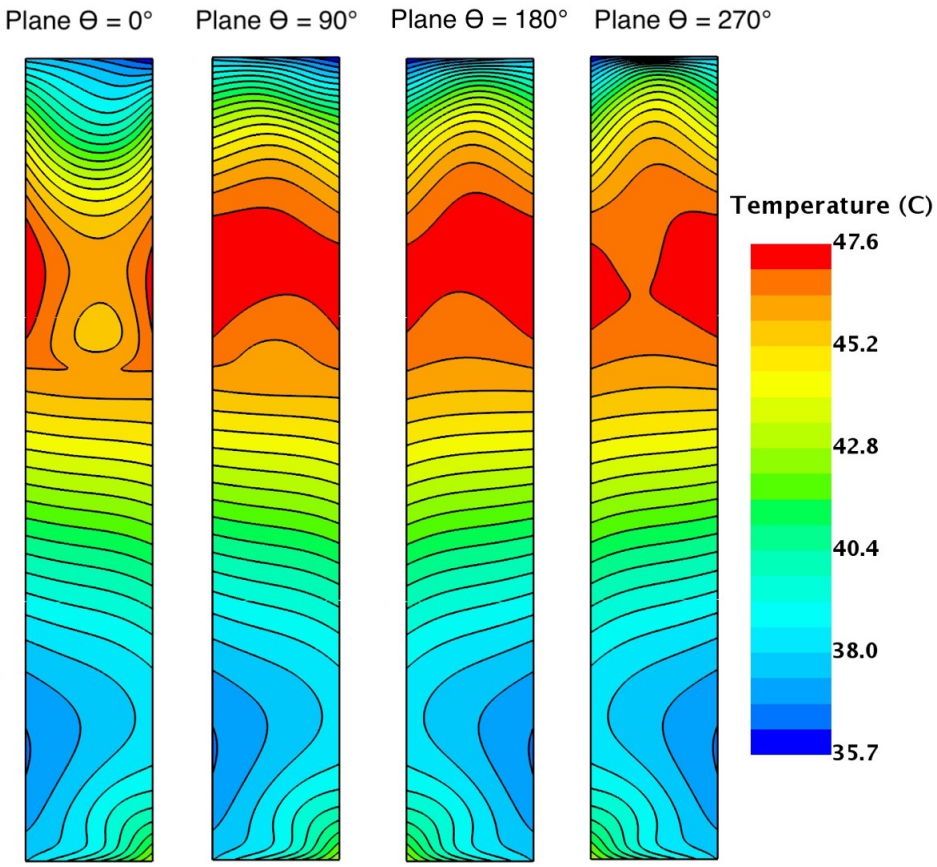

Figure 8.25: Temperature fields on planes θ = 0°, 90°, 180° and 270° for a simulation at Ra = 1.05 x 10^7 which corresponds to an experimental run with peak wall temperature of T_p = 47.6°C.
Note: Radial dimension of cavity is scaled by *x*4 times for visualization purposes.

Figures 8.26 and 8.27 show the variation in temperature fields and velocity vectors during one oscillation cycle of unsteady periodic flow predicted at Ra = 1.05 x 10^7.

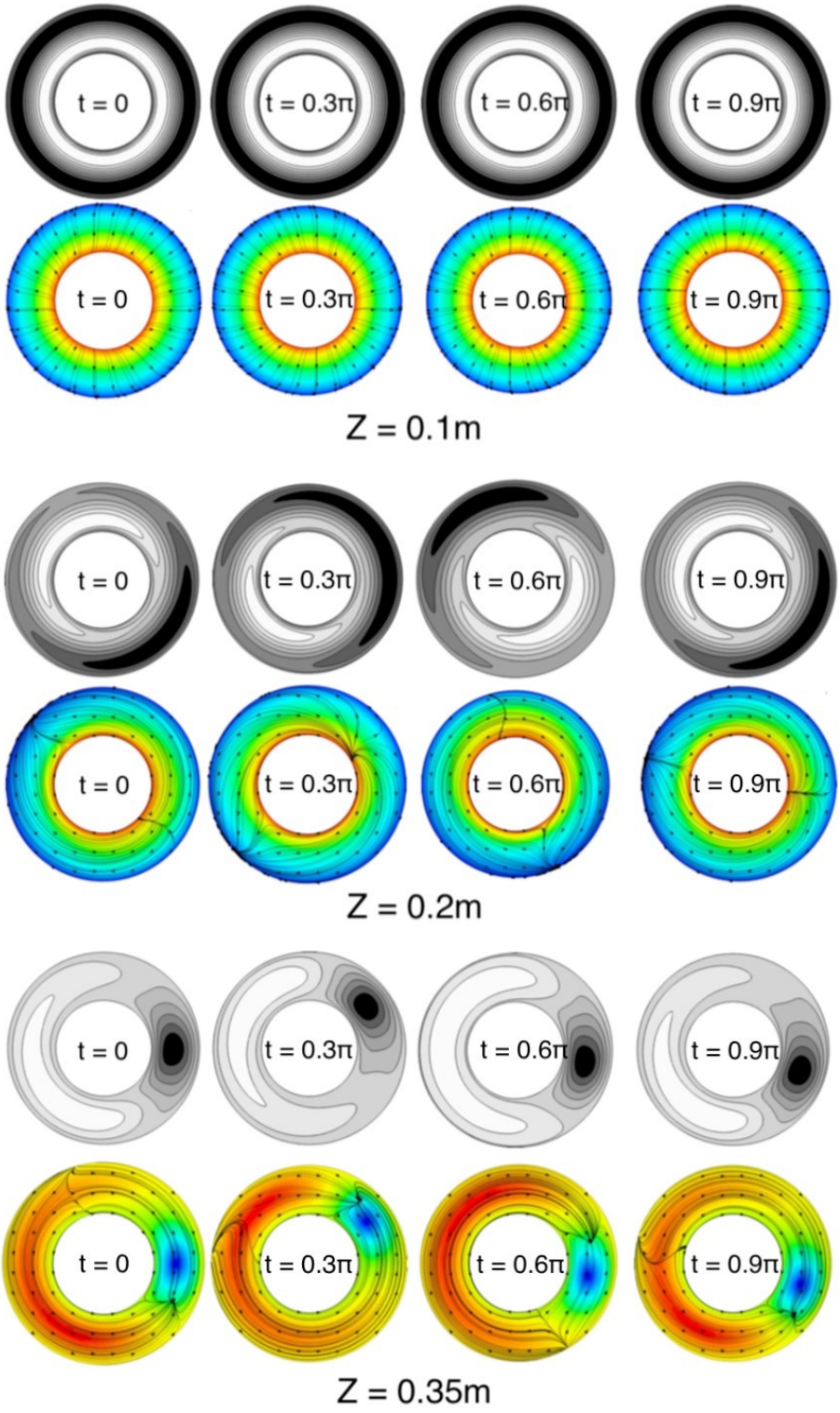

Figure 8.26: Axial velocities (top row) and temperature fields superimposed with projection of velocity vectors (bottom row) over one oscillation period ($\pi = 13.21\ seconds$) for a simulation at Ra = 1.05 x 10^7 which corresponds to an experimental run with peak wall temperature of T_p = 47.6°C. Dark and light regions indicate negative and positive axial velocities respectively.

The back and forth motion of the cells are clearly visible on the z = 0.35m, 0.2m planes while an almost axisymmetric flow with velocity vectors going from the heated portion of inner cylinder to the cooler portion of the outer cylinder is visible in the projected velocity plot for z = 0.1m plane.

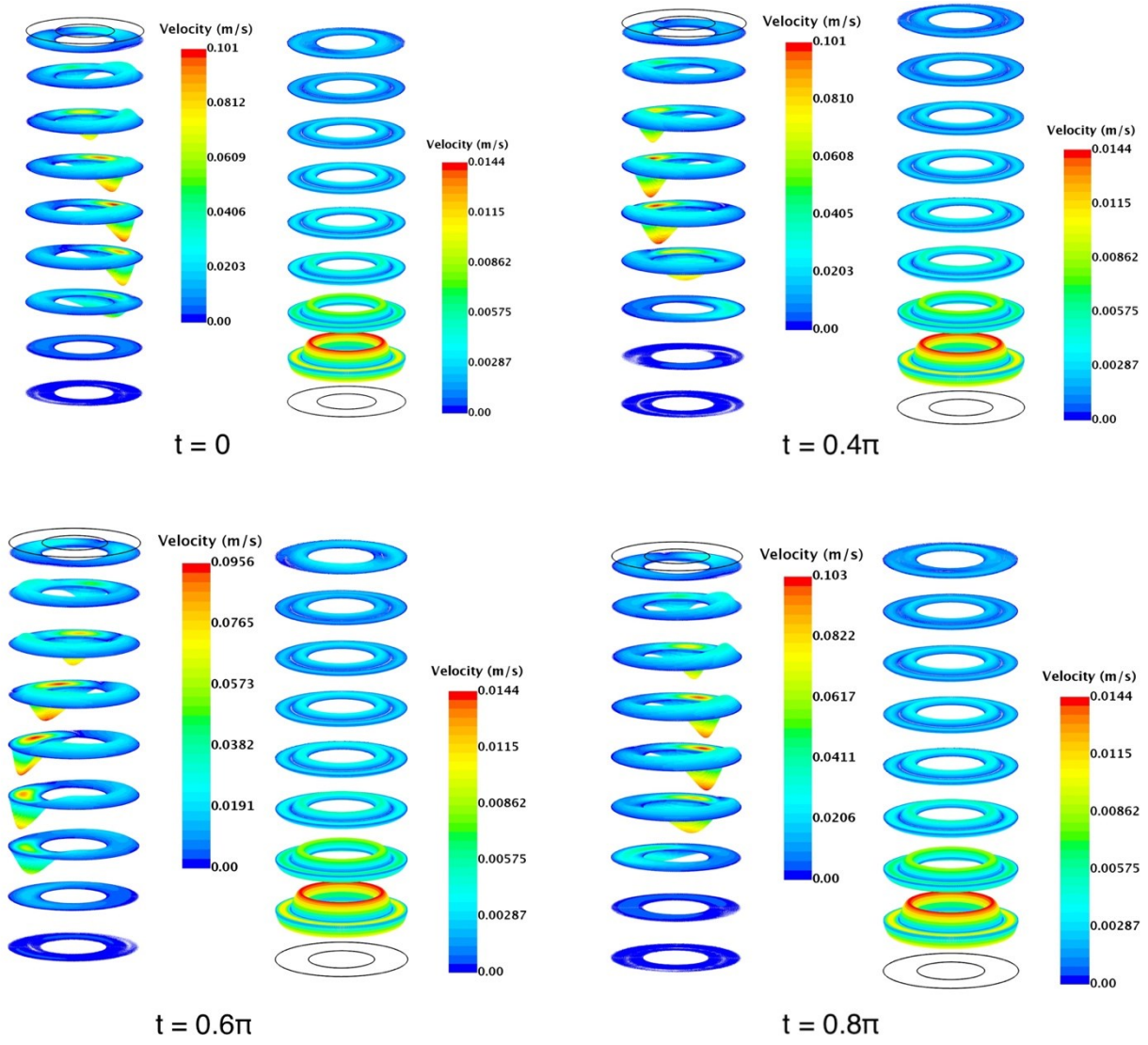

Figure 8.27: Velocity vectors in top and bottom halves of cavity over one oscillation period ($\pi = 13.21\ seconds$) for a simulation at Ra = 1.05 x 10^7 which corresponds to an experimental run with peak wall temperature of T_p = 47.6°C.

The asymmetric oscillatory flow of the two-cell convection solution obtained at Ra = 1.05 x 10^7 is monoperiodic with a fundamental frequency of 0.076 Hz. Figures 8.28 shows the oscillations in azimuthal velocity measured at four locations on the z = 0.2m plane. Interestingly, the waveforms at θ = 0° and 270° and those at θ = 90° and 180° appear to be mirror reflections of each other; a result of the back and forth motion of cells.

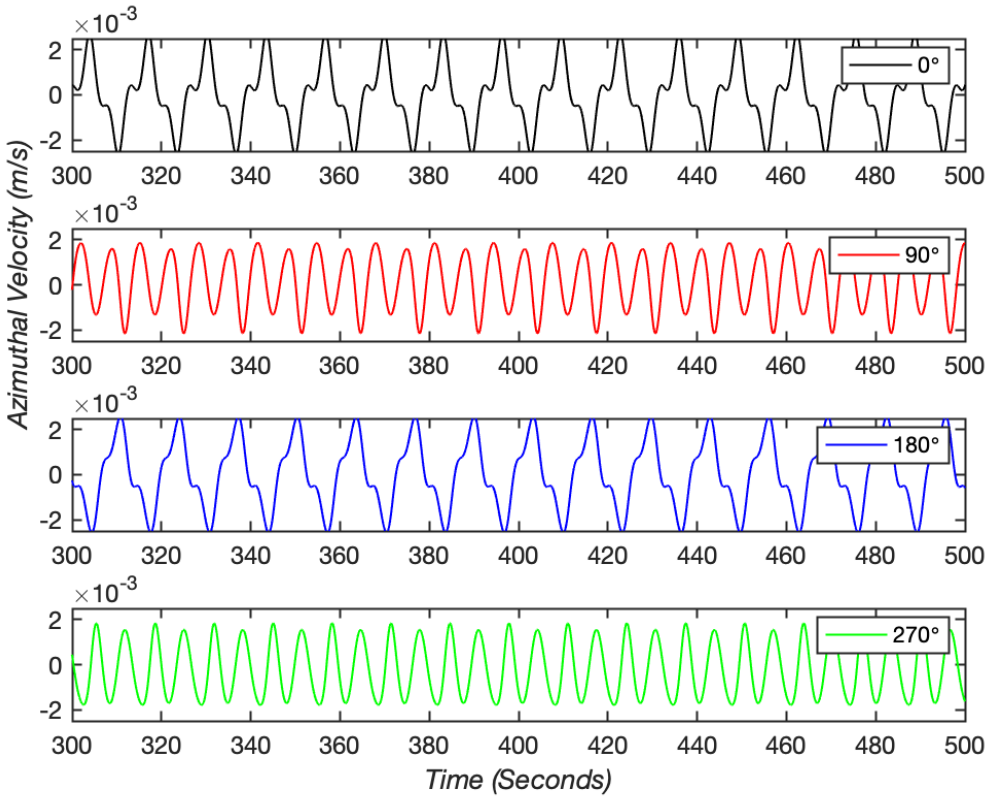

Figure 8.28: Azimuthal velocity time-series for four points on the plane z = 0.2m, located at radial distance of r = 0.0079375m and at four different azimuthal angles θ = 0°, 90°, 180°, 270°, for a simulation at Ra = 1.05 x 10^7.

Figure 8.29 shows the velocity phase-space at four locations in the cavity. The non-intersecting infinity shape of stable limit cycle in phase-space is again an indication of the back and forth motions of convection cells.

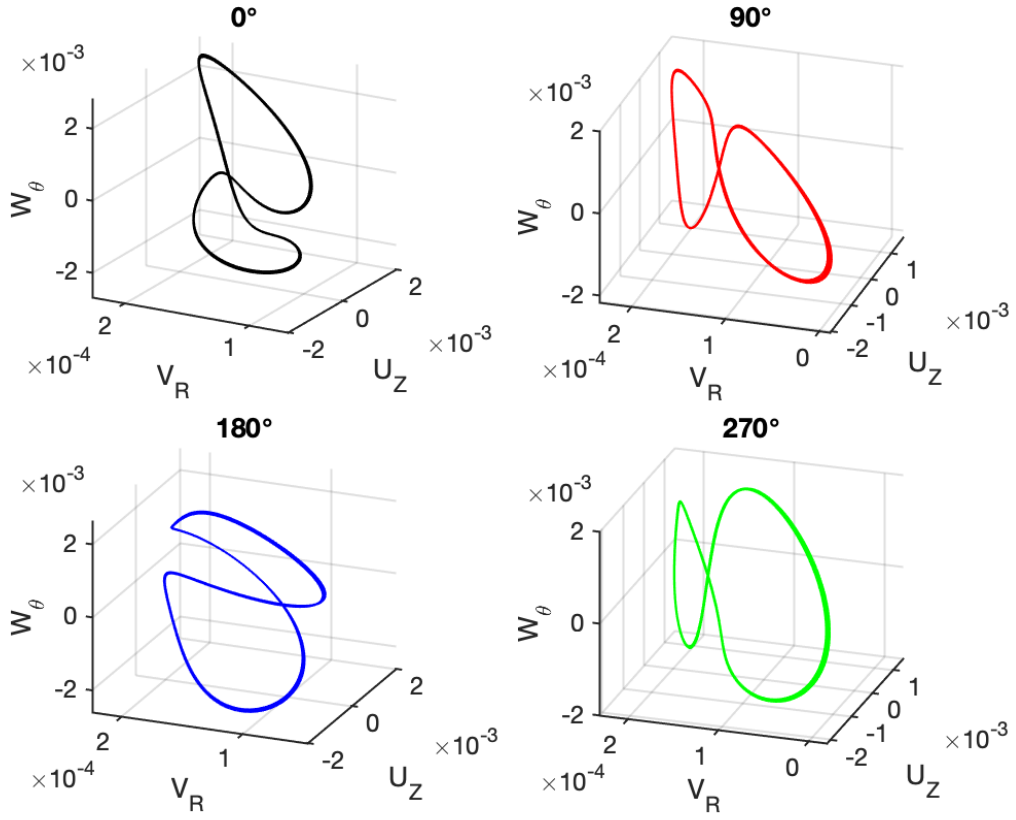

Figure 8.29: Velocity phase space for four points on the plane z = 0.2m, located at radial distance of r = 0.0079375m and at four different azimuthal angles θ = 0°, 90°, 180°, 270°, for a simulation at Ra = 1.05 x 10^7 showing a stable limit cycle.

During the course of an oscillation cycle shown in Fig 8.26, temperature and velocity fields on the z = 0.1m plane seem almost unperturbed while those on the z = 0.35m vary significantly. This is also reflected in the amplitudes of temperature oscillations experienced in different Z-planes inside the cavity. Figure 8.30 shows the oscillation amplitudes for simulation at Ra = 1.05 x 10^7, measured along different Z-planes. Here we see an almost exponential increase in oscillation amplitudes as we move from bottom to top.

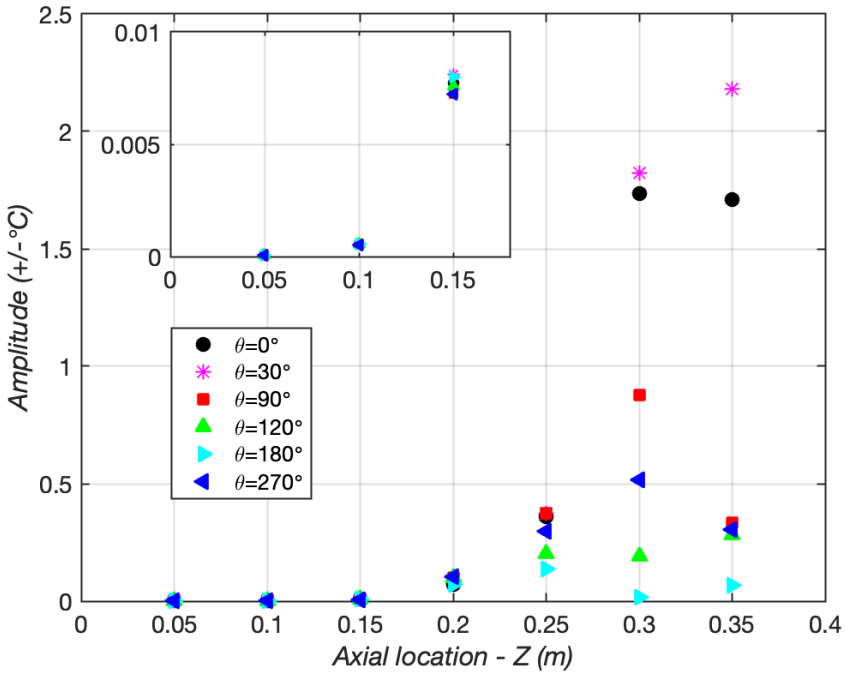

Figure 8.30: Amplitude of oscillations as a function of the axial distance for six points located at radial location r = 0.0079375m and azimuthal angles θ = 0°, 30°, 90°, 120°, 180° and 270° from simulation at Ra = 1.05 x 10^7. (Inset figure for emphasis on low amplitudes at z = 0.05m to 0.15m planes).

8.4.4 Two-Cell Convection Solution at Higher Rayleigh Numbers

As the Rayleigh number was increased even further, the two-cell convection solution was continually observed for all simulation from Ra = 1.05 x 10^7 to 1.71 x 10^7. The only change observed was that at higher Rayleigh numbers with peak wall temperatures increasing even further, the unstratified top zone inside the cavity caused high frequency, high amplitude oscillations. Figures 8.31 and 8.32 shows the amplitudes, frequencies and time-periods observed for temperature oscillations at four points in the cavity midplane (z = 0.2m) for all simulations predicting the two-cell convection pattern. Here, we can see that the oscillation amplitudes continuously increase on account of increasing unstably stratified zones in the top potion of cavity.

Fundamental frequency of oscillations increases continuously as peak wall temperature/Rayleigh number is increased.

Note**:** Two-cell convection solutions were obtained corresponding to experimental runs with peak wall temperatures between T_p = 45.5°C to 68°C which correspond to Rayleigh numbers between Ra = 1.00 x 10^7 to 1.71 x 10^7. For easy of comparison with experimental data, frequencies and amplitudes are plotted as function of peak wall temperature and not Rayleigh number. Also, for easy of comparison to experiments, monitoring points for measuring amplitudes were chosen same as the location of four air thermocouples in the experimental system.

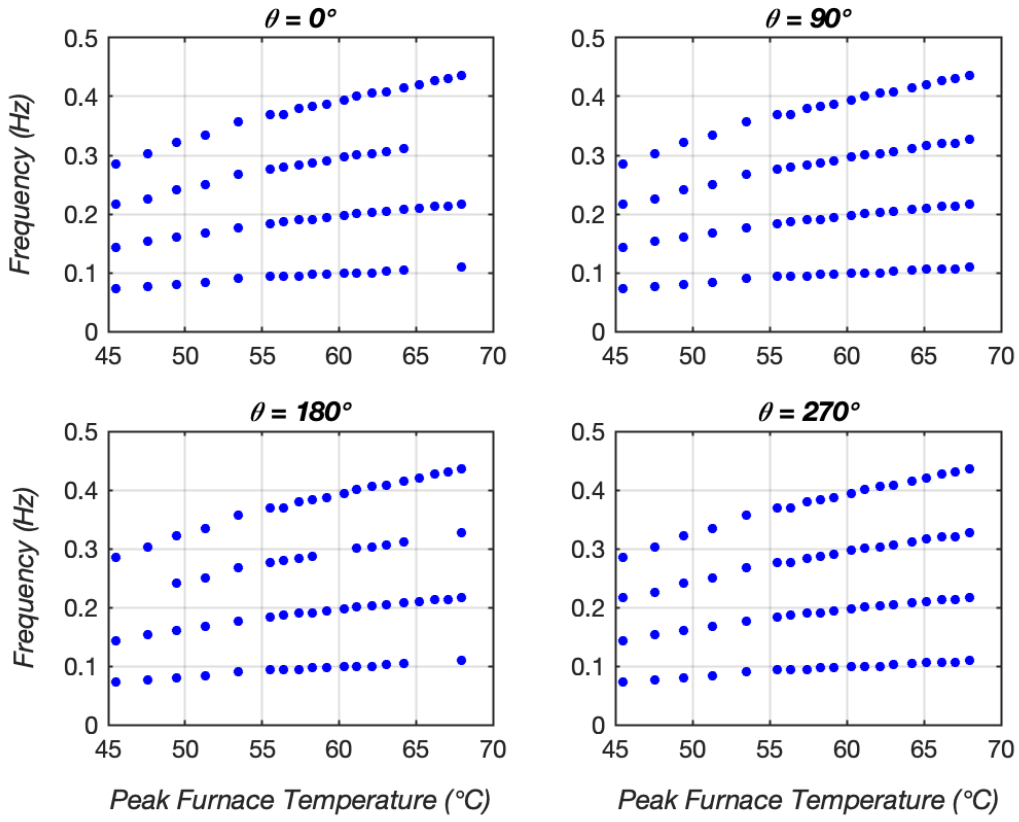

Figure 8.31: Frequency map for two-cell convection solutions obtained for peak furnace wall temperature between T_p = 45.5°C to 68°C (or Rayleigh numbers between 1.00 x 10^7 to 1.71 x 10^7).

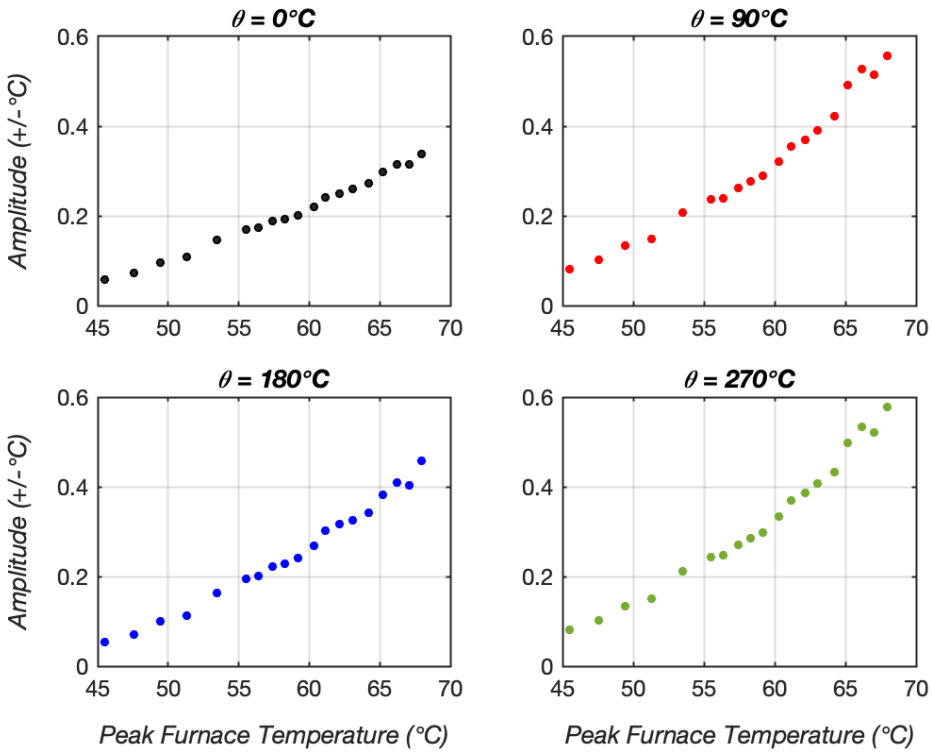

(a)

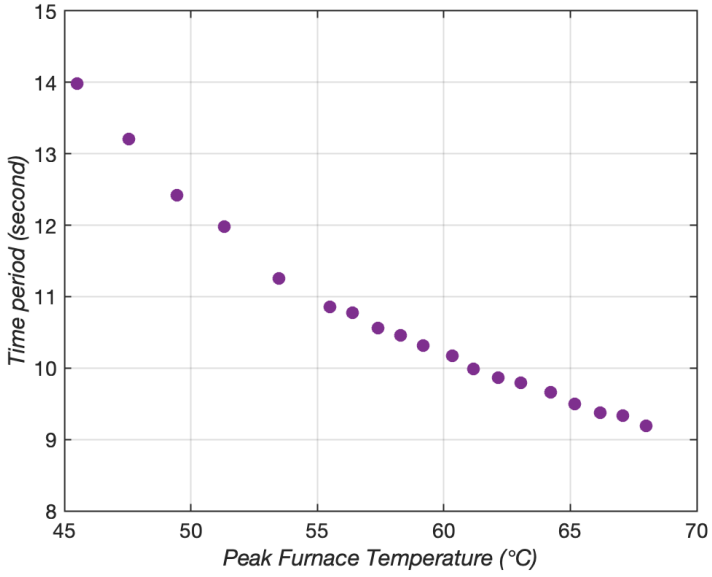

(b)

Figure 8.32:(a) Amplitude and (b) Time period of oscillations measured at four points on the plane z = 0.2m, located at radial distance of r = 0.0079375m and at four different azimuthal angles θ = 0°, 90°, 180°, 270° for two-cell convection solutions obtained for peak furnace wall temperature between T_p = 45.5°C to 68°C (or Rayleigh numbers between 1.00 x 10^7 to 1.71 x 10^7).

8.5 Key Results and Conclusions

8.5.1 Summary

In the 3D numerical study of the annular cavity of $\eta = 0.50$, aspect ratio $A = 25.2$ and with non-isothermal walls, asymmetric oscillatory flows were predicted for all the Rayleigh numbers corresponding to experimental conditions described in Chapter 7. At low Rayleigh numbers, a convection flow comprising of eight unsteady cells/rolls was observed. The cells were arranged in pairs of four in the top and bottom parts of the cavity. Cells were azimuthally oriented similar to those observed by Stork and Müller [91] in their study of classical Rayleigh-Bernard instability in an annulus. Oscillatory flows were caused due to the back and forth rotation of these cells about the axis of the cavity. The dominant mechanism responsible for creating of these oscillating cells/rolls was identified as the Rayleigh Bernard instability which is triggered as result of unstably stratified fluid regions in the upper and lower sections of the cavity.

The oscillatory flow was monoperiodic with amplitude of oscillations sensitive to location. Maximum amplitudes were observed in regions where the azimuthally oriented cells interacted. As the Rayleigh number was further increased at first a transition to an oscillatory six-cell convection pattern comprising of four lower cells and two upper cells was observed. With even further increase in Rayleigh number an oscillatory two-cell convection pattern comprising of two upper convection cells and a weakly asymmetric toroidal stricture was observed. The amplitude and fundamental frequencies of the oscillatory flow increased continuously with increase in Rayleigh number. No further bifurcations or transitions to chaotic flow were observed.

8.5.2 Comparisons with Experiments and 2D CFD Model

8.5.2.1 Steady Flow Regime

A steady flow regime was observed in the experiments for certain boundary conditions based on temperatures measured by sensors located at cavity midpoint. For the same experimental steady flow regime boundary conditions, 2D Axisymmetric CFD simulations predicted a steady bi-cellular flow while 3D CFD simulations predicted an asymmetric and oscillatory flow. However, findings from the 3D simulations suggest that amplitude of oscillations caused by asymmetric oscillations is highest in the upper portions of the cavity far away from the thermocouple placement locations. In addition, thermocouple baseline noise levels are +/- 0.03ºC, which is the same order of magnitude or higher than the amplitudes predicted by the 3D simulations at temperature sensor locations. Therefore, it is entirely plausible that the flows observed as 'steady' in the experiments were oscillatory, but the sensor was unable to detect the oscillations till they exceeded the baseline noise levels. On the other hand, the steady flow predictions made by the 2D model seem to be an artifact of the axisymmetric flow assumption, which prevents any velocity components in the azimuthal direction. Besides, the 3D asymmetric oscillations were caused by rotation of the convection cells along the azimuthal direction based on the results of the 3D CFD model. Any assumption preventing this movement in azimuthal direction will likely give a steady flow prediction.

8.5.2.2 3D Periodic Regime

3D CFD simulation were able to accurately predict asymmetric, oscillatory, monoperiodic flows observed in the annular cavity experiments. Scaling the experimentally observed fundamental frequencies of the set A experiments in the mono-periodic regime by the $\mathrm{Brunt}-\mathrm{Väisälä}$

frequency had suggested that the instability mechanism observed in the experiments was related to the Rayleigh Bernard instability mechanism. This experimental observation is in agreement with the 3D simulation results where the primary instability mechanism for the asymmetric oscillations was identified as the Rayleigh-Bernard instability. For both experiments and 3D simulations the amplitude and fundamental frequency of oscillation for the monoperiodic regime were found to increase with Rayleigh number. Figures 8.33 and 8.34 show the comparison between fundamental frequencies predicted by simulations and those observed in experiments. The error bars on the simulation amplitudes correspond to the uncertainty associated with placement of thermocouples.

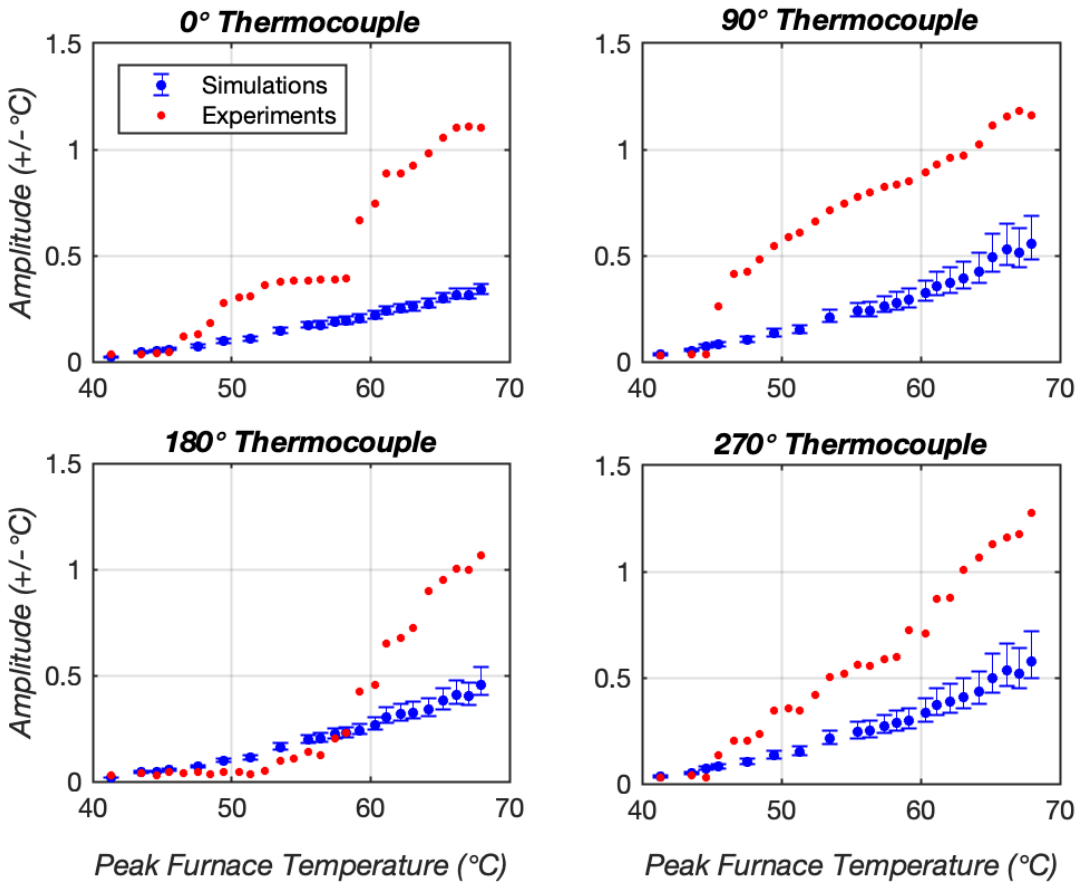

Figure 8.33: Comparison between amplitudes measured at thermocouple sensor locations as peak furnace wall temperature is increased, as observed in experiments and predicted by 3D CFD simulations.

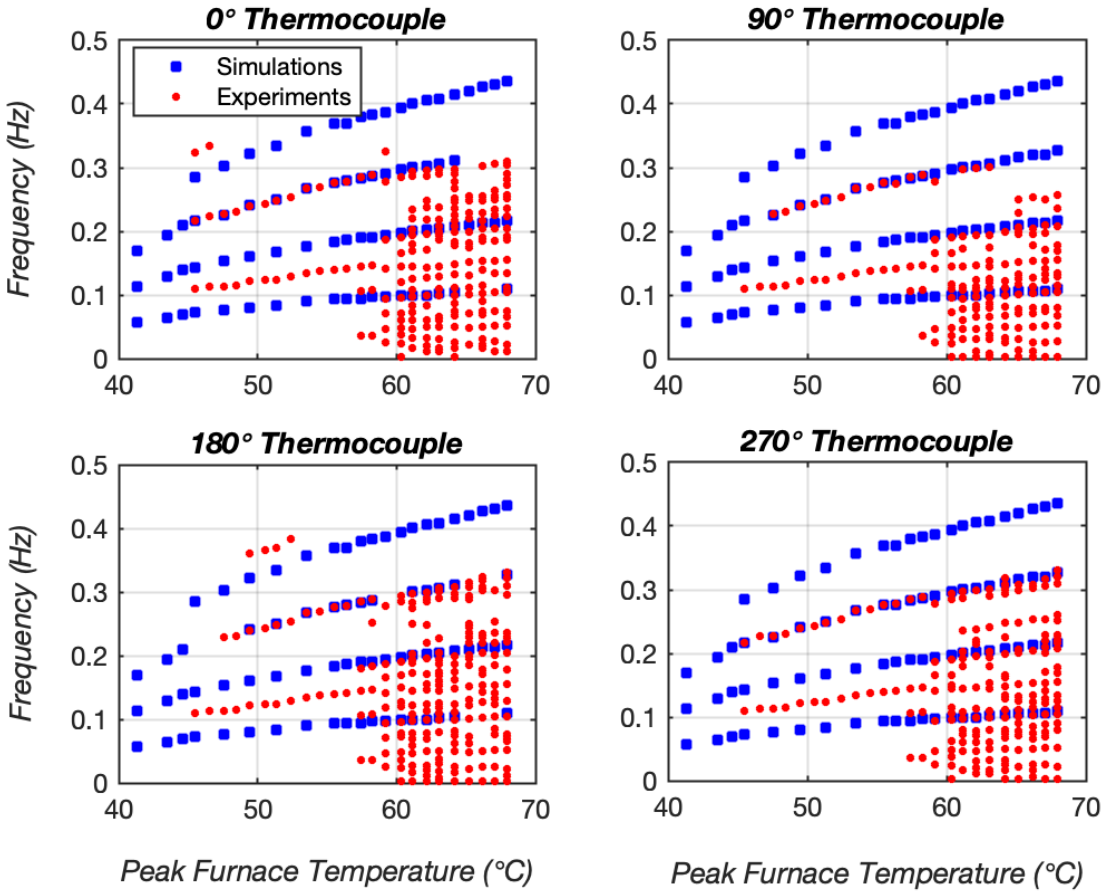

Figure 8.34: Comparison between frequency map of the system as peak furnace wall temperature is increased as observed in experiments and predicted by 3D CFD simulations.

The amplitudes and fundamental frequencies predicted by 3D simulations are lower as compared to that of experiments. However, 3D model results suggest that the amplitudes can vary significantly depending on azimuthal locations. The direction in which the asymmetric flow orients itself in the experiment is triggered by asymmetries inherent in the experimental system. Therefore, the azimuthal orientation of the asymmetric flow structure in the simulation and in the experiment might not match, making amplitude comparisons based on point measurements difficult. Nonetheless, all the correct trends are predicted by the 3D model for the monoperiodic regime and 3D simulation results are comparable to experimental observations for this flow regime.

8.5.2.3 Quasiperiodic Regimes and Chaotic Regime.

The 3D model was unable to predict any quasiperiodicity or chaotic flow behavior observed in experiments. As the flow begins to become chaotic, the smallest size of eddies in the flow decreases. The grid size of 0.6mm used by the current 3D model might be insufficient to correctly capture interactions at smaller length scales that would arise in a chaotic flow. A finer grid than the one used for the current 3D CFD model could not be used due to computational resource constraints. In future work for this problem, a 3D DNS of the flow using a higher order spectral method might be able to capture the chaotic and quasiperiodic regimes observed in experiments.

Chapter 9

9 DESCRIPTION OF RECTANGULAR CAVITY EXPERIMENTAL SYSTEM

An experimental investigation of natural convection flows in a rectangular cavity with aspect ratio A = 10 and non-isothermal walls is performed. The goal of this study is to map the sequence of bifurcations that cause transitions from steady flow to 2D/3D oscillatory and chaotic flows. In this chapter, construction of the experimental system, its various components and methods used for data collection and analysis are described.

9.1 Objectives of the Experiment

2D numerical studies by Reeve et al. [50] and Dillon et al. [51] have shown that steady bi-cellular natural convection inside a closed, air-filled, rectangular cavity with temperatures on opposing walls varying along the cavity length, becomes unstable to 2D oscillatory modes. No analogous 3D numerical study or experimental study is available for this configuration to verify whether the unsteady oscillatory flow is in fact 2D in nature or whether the flow is actually 3D oscillatory. Experiments conducted in annular cavities with similarly varying temperature boundary conditions (discussed in Chapters 6 and 7) could not find any 2D axisymmetric oscillatory flows; all oscillatory flows observed were 3D asymmetric in nature. Further, based on the findings of McFadden et al. [33] and Prud'homme and Le Quéré [34], the highest likelihood of finding a 2D instability mode for this type of natural convection is in a rectangular cavity which represents the

limiting case of an annular cavity with a radius ratio of $\eta \rightarrow 1$. Therefore, it is of interest to determine the nature of flow bifurcations that can be expected in a tall, closed, air-filled, rectangular cavity with non-linearly varying wall temperatures.

An experimental system is constructed to study the stability of natural convection of air in a tall, closed, rectangular cavity with non-isothermal walls which support a bi-cellular base flow pattern. The cavity (H x W x L) (Z x X x Y) consists of two long, tall opposing vertical walls of height 'H' and length 'L' which are separated by a gap width 'W' and four other walls that cover top, bottom front and back sides of the cavity. The vertical walls are maintained at temperatures varying along cavity height, such that, temperature of one vertical wall increases from top to bottom, and temperature of the opposing vertical wall decreases from top to bottom. These boundary conditions promote the existence of a bi-cellular base flow consisting of two counter rotating cells; an upper and lower convection cell as shown in Fig 9.1.

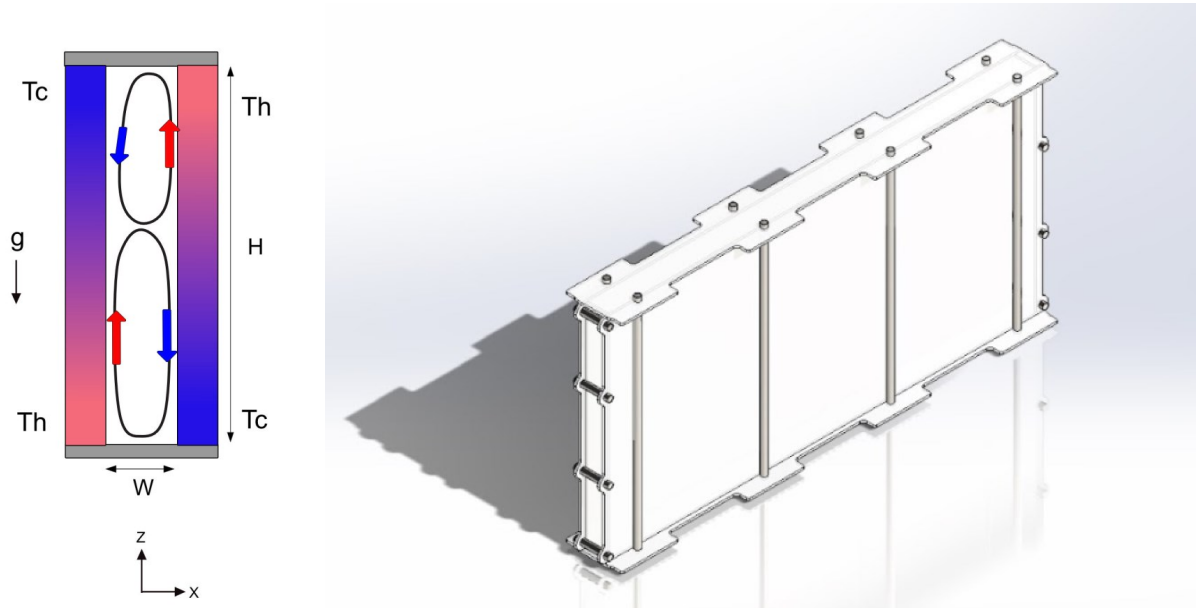

Figure 9.1: (a) Closed rectangular cavity with thermal boundary conditions supporting bi-cellular air-flow; (b) CAD model of the rectangular cavity.

As buoyant potential of the flow is increased by increasing temperature difference between the vertical walls, steady natural convection inside the cavity first transitions to unsteady periodic flow and then to chaotic flow. These different flow bifurcations are observed by monitoring air temperatures inside the cavity at the region where the two convection cells interact with each other. The nature of unsteady natural convection flow, whether 2D or 3D is determined via measured air temperature data.

9.2 Experimental System

The experimental system is comprised of a long, closed, rectangular cavity of dimensions 0.30 m x 0.030 m x 0.60 m (H x W x L). The cavity is filled with air (Pr = 0.71) and has an aspect ratio of A = 10. The rectangular cavity is made up of six clear acrylic plates of thickness 3.175mm. The two long vertical walls of the cavity are separated by an air-gap of width 3 cm. The length (0.60 m) of the cavity is kept more than 20 times its width to reduce effect of the end walls on the flow at the interior of the cavity. Heating bands are installed on the outside of the two, long, opposing vertical walls, which actively heat the top $1/3^{rd}$ and bottom $1/3^{rd}$ portions of the respective walls. The remaining $2/3^{rd}$ portion of the vertical walls and the other four wall surfaces of the cavity are passively cooled. The heat flux applied to the vertical walls can be changed by changing the power supplied to the heating bands. Bi-cellular natural convection is induced in the rectangular cavity by applying same amount of power to the top and bottom heating bands. To control effect of the ambient air temperature fluctuations on the wall temperature boundary conditions, the entire experiment was operated inside a large tent enclosure. The tent enclosure housing the experimental system was set up inside a large laboratory where the room air conditioner was controlled within $\pm$ 1.5°C. For all the experiments conducted on this system, the cavity wall varied temporally no

more than $\pm$ 0.1°C. A schematic of the experimental system is shown in Fig. 9.2. An array of thermocouples is installed along the height of the two long vertical sidewalls. These 'wall thermocouples' are used for monitoring, measuring and controlling the temperature profiles of the vertical walls. Wall temperature profiles are used to calculate temperature differences observed in the cavity and to determine nominal Rayleigh number for each experimental condition. These temperature profiles are also used as the input boundary conditions for the numerical prediction of the natural convection inside the cavity using 2D and 3D CFD models (discussed in Chapter 11).

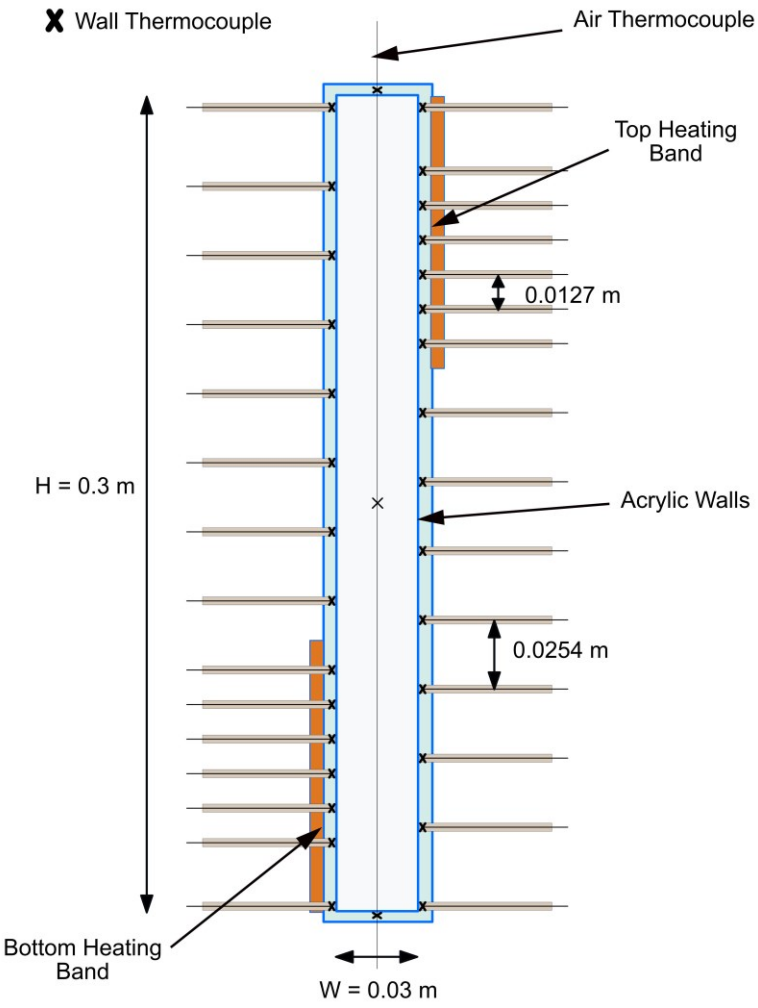

Figure 9.2: Schematic of the experimental system.

Three very fine wire thermocouples are suspended at the vertical midplane of the cavity along the length of the cavity at locations separated by 15.44 cm. These fine wire thermocouples are used for measuring the temperature oscillations as well as for characterizing the two-dimensional or three-dimensional nature of the unsteady air flow.

9.3 Components of Experimental System

The components of the experimental system are :

1. A rectangular cavity made up of 6 acrylic plates. A support structure made up of plywood and steel rods is used to help hold and level the rectangular cavity on an optical table. The support structure is also fitted with a mechanism to suspend 3 fine wire thermocouples inside the cavity. Figure 9.3(a) shows the rectangular cavity mounted on an optical table. A tent enclosure is constructed around the optical table to reduce the effect of ambient room temperature fluctuations, shown in Fig. 9.3(b).
2. Two Heating bands which heat up the top and bottom thirds of the two opposing vertical plates of dimensions 0.6m x 0.3m. Both heating bands are powered using a single Variac AC power supply. The voltage on the power supply can be changed in increments of 0.5V. A digital voltmeter connected to the Variac reads the voltage supplied to the heating bands.
3. Data acquisition circuitry which is comprised of an array of thermocouples installed inside the cavity and along the cavity walls, a HP3852A data acquisition system with a computer running LabVIEW 2017.0. Care was taken to physically separate the data acquisition and the power circuitry to prevent electromagnetic interference.

Fig. 9.4 shows a photograph of the actual experimental system and Fig. 9.3. shows a diagram of the power and data acquisition circuitry.

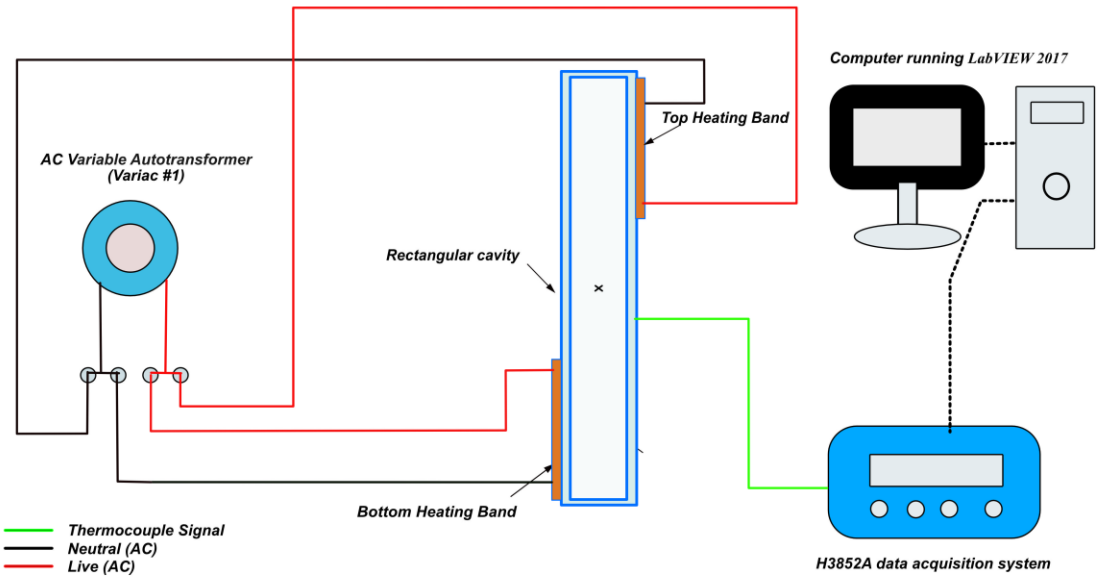

Figure 9.3: Power and data acquisition circuitry.

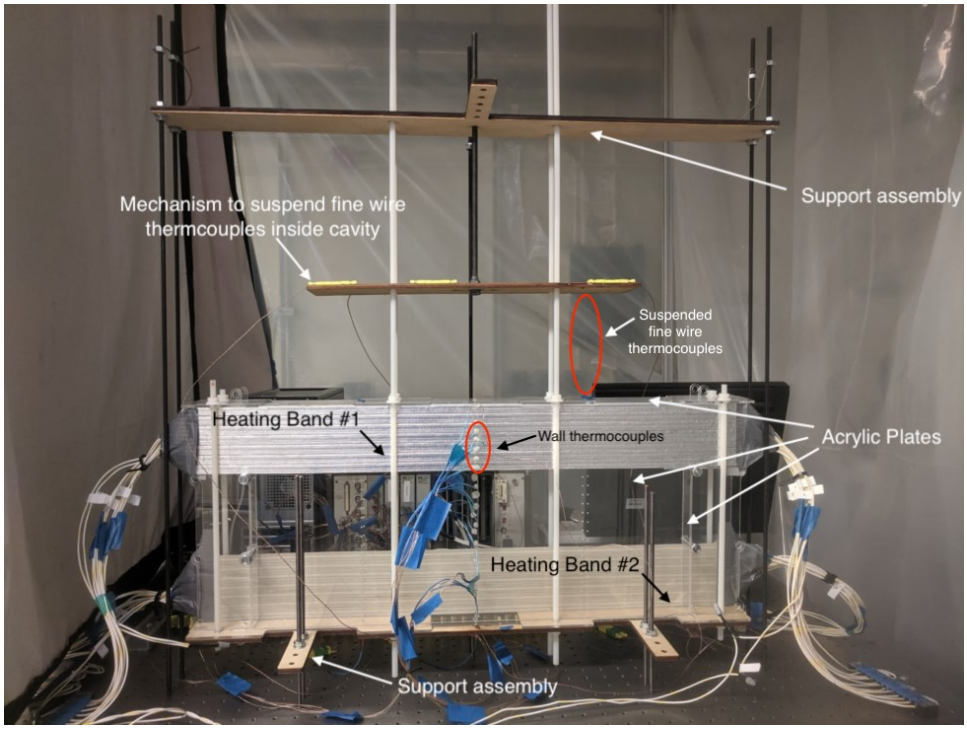

(a)

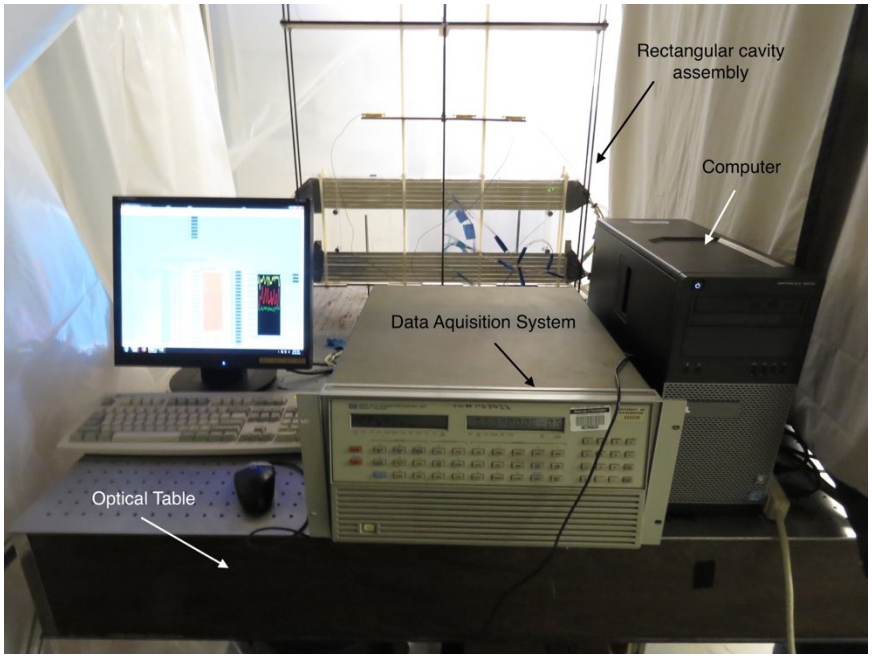

(b)

(c)

Figure 9.4: (a) Photograph of the actual rectangular cavity showing its different components and mechanism for supporting thermocouple assembly; (b) Photograph of the entire experimental system; (c) Photograph showing the enclosure constructed around the experimental system.

9.4 Construction of Cavity

The rectangular cavity is constructed using two side walls, a top and bottom plate and two end plates all fabricated from 3.175mm thick clear, scratch-resistant acrylic plates. The acrylic plates were cut to the appropriate dimensions, using a laser cutter (Kern LC50 Laser – 400W CO_2 laser). The cavity sits on a stabilizer plate made up of ¼ inch thick plywood which is held up on a Newport RS4000 optical table by six threaded steel rods. Figure 9.5 shows the assembled cavity and its different components.

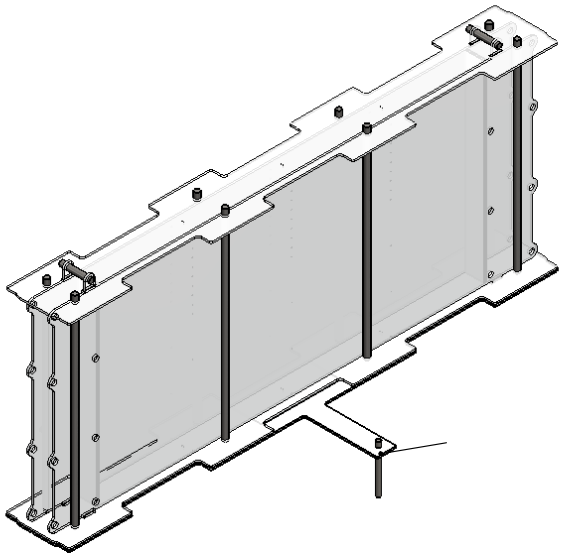

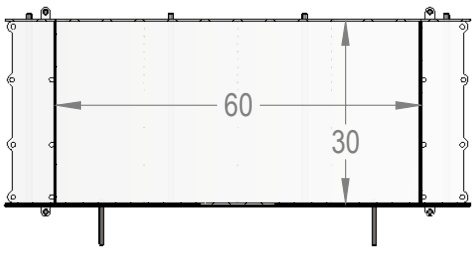

SECTION A-A

(a)

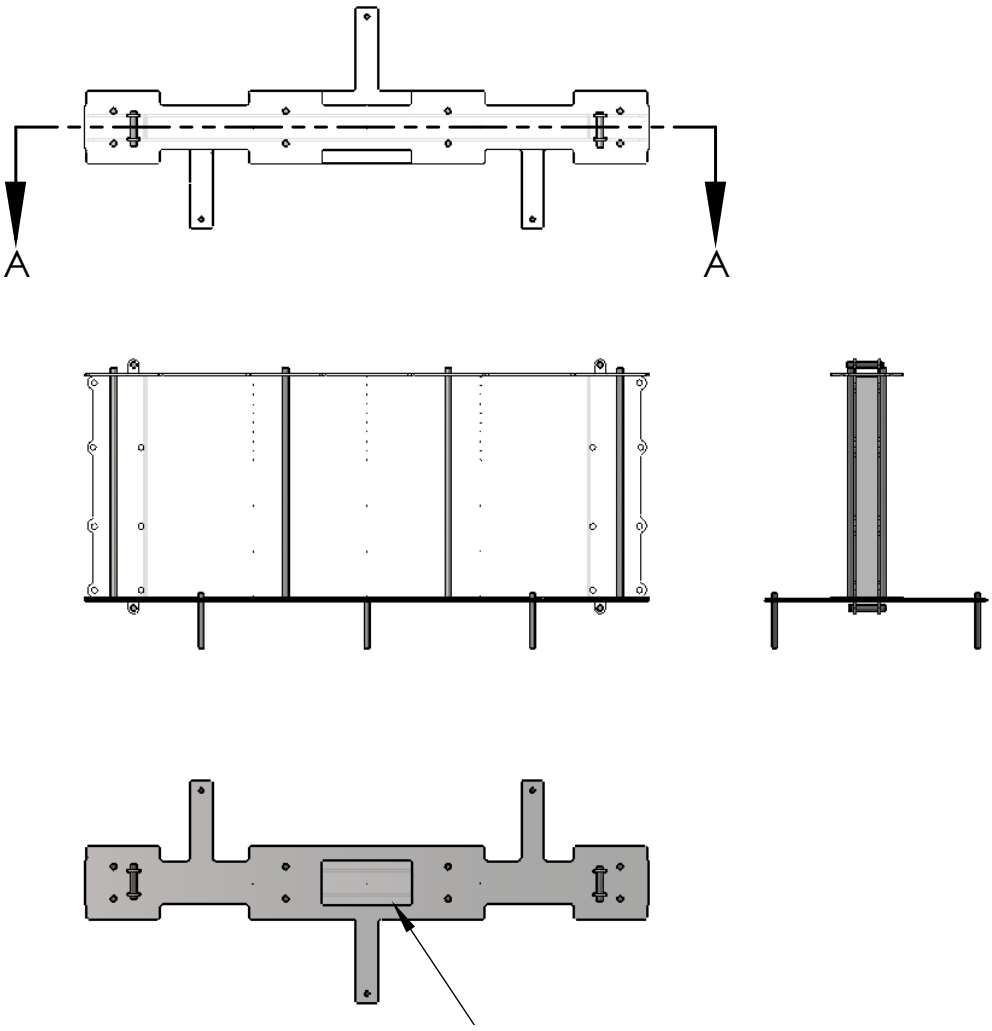

(b)

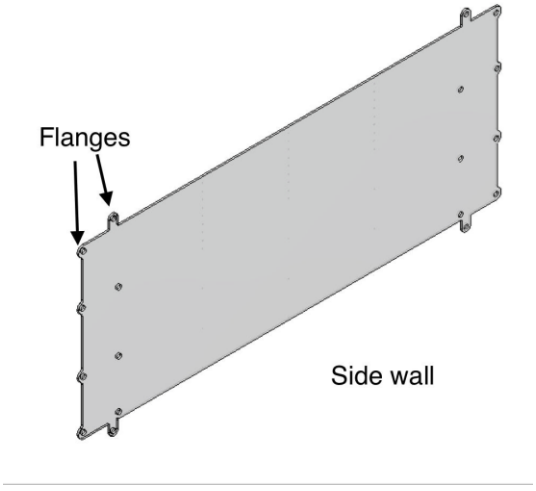

(c)

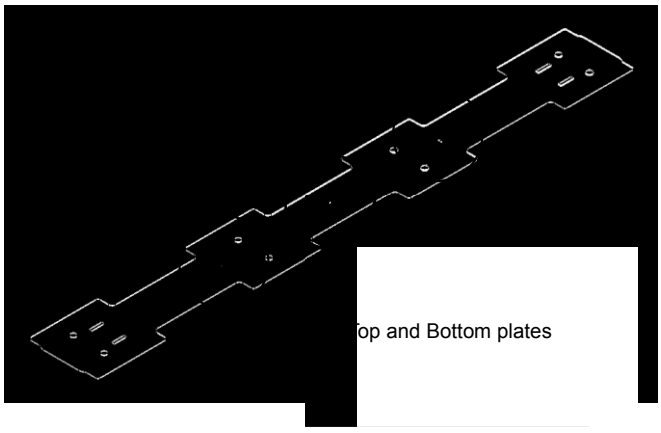

(d)

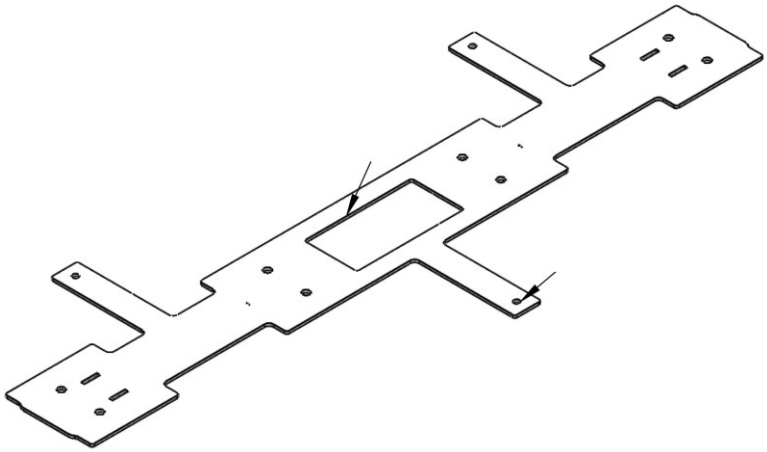

(e)

Figure 9.5: CAD drawing of the (a) Entire cavity (b) Exploded view of components of the cavity (c) Side walls (d) Top and bottom wall plates (e) Stabilizer plate.

The assembly of the cavity was done in several steps. Prior to installing all the cavity, all the acrylic plates were cleaned with iso-propyl alcohol. The stabilizer plate, shown in Fig. 9.5(e), is made from ¼ inch thick plywood and has 3 appendages with holes drilled in it. To assemble the cavity, the stabilizer plate was first supported on the optical table by means of six threaded rods. Using a digital level, the stabilizer plate was made exactly parallel to the horizontal. The bottom plate was then assembled on the stabilizer plate. Each of side wall (0.74 m x 0.3m) shown in Fig 9.5 (c) is fabricated so that end of the wall has a total of twelve flanges, six flanges on either side, and six holes, three on each side, separated by a horizontal distance of 0.6m. Next, the two side walls were installed by inserting four bottom flanges on the side walls into rectangular slots machined on bottom and stabilizer plates. Eighteen short, threaded-rods were then passed through the flanges. Two end plates of dimensions 0.3m x 0.03 m were inserted between the two side walls and nuts were assembled on either side of the eighteen threaded-rods to hold the two side walls at a fixed distance of 0.03m.The top and bottom plates are long narrow plates with four tabs, which

each have two equally spaced holes as shown in Fig 9.5(d). After assembling the side walls and end plates, the cavity was closed by assembling the top walls using 8 threaded nylon rods and nuts that go on both sides on the threaded rods. Once the cavity was assembled, the edges of the cavity were glued from the outside using TAP acrylic cement. The acrylic cement was inserted on the edges of the cavity walls with the help of a hypodermic needle. The TAP acrylic cement has a very low viscosity and thus wicks itself between the acrylic sheets surfaces to create a perfectly sealed joint. The acrylic cement is clear, dries off quickly and ensures an air-tight finish. After applying the adhesive, the cavity was allowed to sit, and the acrylic cement was allowed to dry. To make sure the cavity was perfectly sealed, air was pumped into the cavity and the edges were checked for any escaping air using soapy water. A second around of adhesive was added at the corners and all the outer edges were caulked using a transparent caulking paste for extra precaution against air leakage.

9.4.1 Heating Bands

Each side wall is installed with a heating band that runs along the longer dimension of the wall; one side wall with a heating band covering the top 1/3rd area, and other side wall with a similar heating band covering the bottom 1/3rd area. The resistance of each heating band is 55.2 Ω. The top and bottom heating bands are connected in parallel to an AC Variac unit, so that, same amount of heat is generated by either heating band. Each heating band is comprised of 7 Clayborn C-16 heat tapes of connected in series [84]. Each heat tape is 1.27 cm (0.5 inch) wide and is comprised of four resistive wires. The wires have squiggles on them to account for thermal expansion of the metal wires during heating. The outer surface of the heat tape is reflective (high emissivity) and acts as a radiation shield while the inner surface is lined with an adhesive material for application

to plane acrylic surfaces. Figure 9.6 shows a picture of the Clayborn C-16 heat tape [84]. The location of each heating tape along the cavity height is given is Table 9.1.

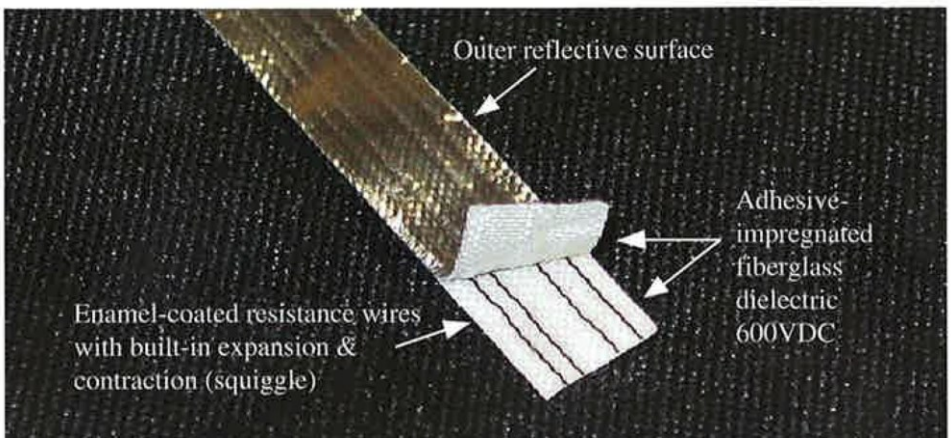

Figure 9.6: Clayborn C-16 heat tape [84].

Table 9.1: Z – Locations of heat taps installed on the two side walls.

	Side wall with bottom heating band		Side wall with top heating band	
Heating Tape #	z (m)	z/H	z (m)	z/H
1	0.006	0.02	0.294	0.98
2	0.019	0.06	0.281	0.94
3	0.032	0.11	0.268	0.89
4	0.044	0.15	0.256	0.85
5	0.057	0.19	0.243	0.81
6	0.070	0.23	0.230	0.77
7	0.083	0.28	0.217	0.72

After installation of both heating bands, IR images of the side walls were taken to ensure that both heating bands were functional and were uniformly heating the cavity side walls along the horizontal direction. Figure 9.7 shows the IR images for the top heating band installed on one of the side walls. The IR image shows uniform temperature along the side wall length, with variation in temperature only along the side wall height.

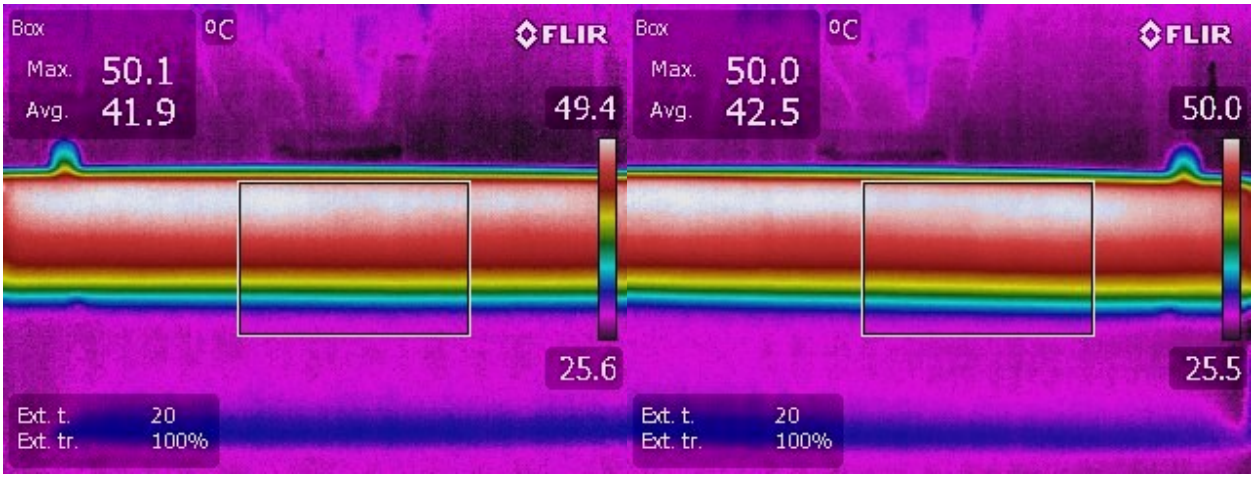

Figure 9.7: IR images of the cavity side wall installed with a heating band.

9.4.2 Wall Thermocouples

Each side wall was installed with 15 type K thermocouples made of 0.25 mm (0.010 inch) diameter wire to capture the temperature profile of the wall. In order to install the thermocouples, each of the two side walls of 3.175 mm thickness, were machined with divots along its vertical center line, at 1.27 cm intervals. The divots are 2 mm in diameter and have a depth of 2.73 $\pm$0.03 mm. The spacing in the divots matches the width of the heating tape, thereby allowing the thermocouples to be integrated into the assembly without interrupting consistency of heating. To attach the

thermocouples to walls, the thermocouple bead was dipped into a low thermal conductivity epoxy, *OMEGABOND*® OB-100 and then inserted into the divot. In order to gain access to the divots located in the portions of the cavity covered by heating tape, small incisions were made in the heating tape itself at the appropriate locations using a very fine needle. The thermocouples were then inserted into the divots following the previously mentioned procedure. Prior to adhering the thermocouples to the cavity, each divot was cleaned with isopropyl alcohol to ensure that there were no debris and the thermocouple bead made perfect contact with the acrylic wall surface. Figure 9.8 shows a picture of the thermocouples installed on one of the sidewalls of the cavity.

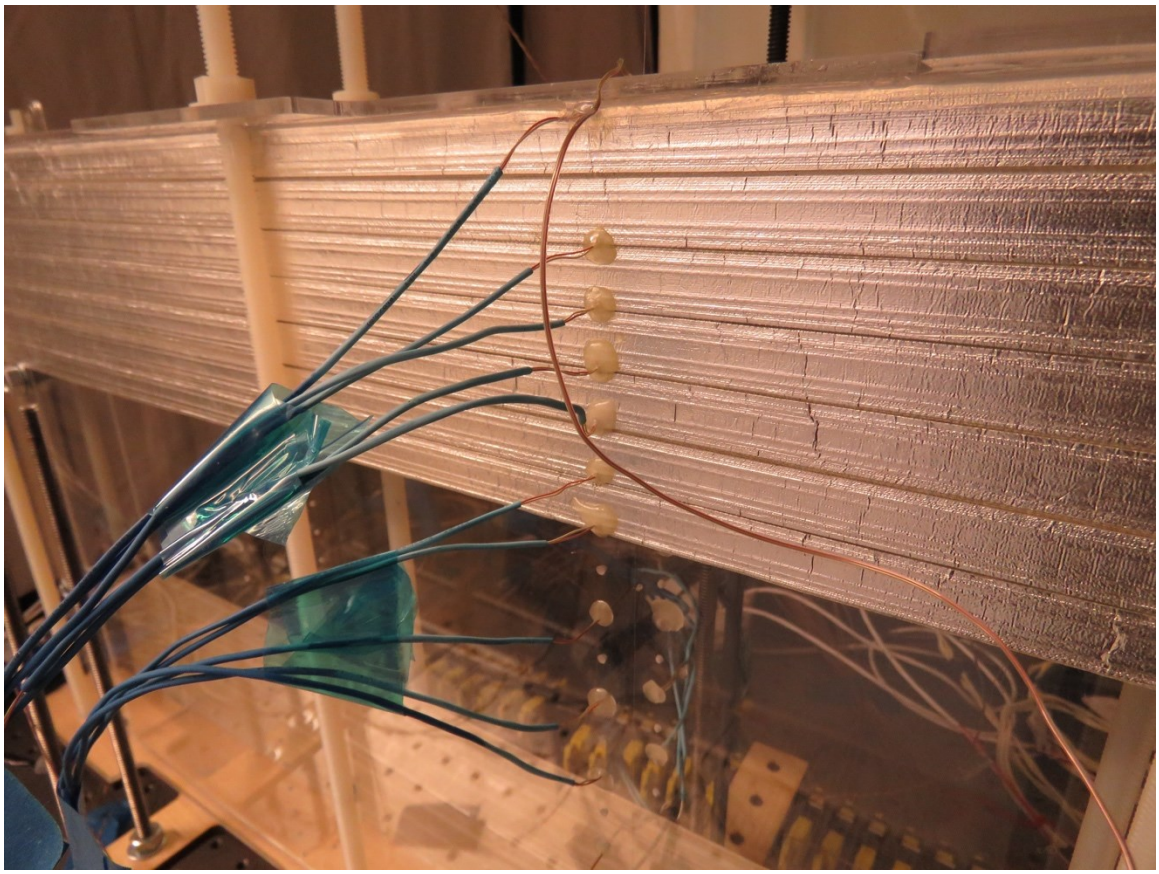

Figure 9.8: Photograph showing installation of thermocouples on side wall of the cavity.

Divots were also machined on top and bottom plates at their mid-lengths. Two thermocouple of 0.25 mm (0.010 inch) diameter wire were installed in these divots to monitor temperatures of top and bottom plates. Table 9.2 shows location of the 32 thermocouples installed on cavity walls.

Table 9.2: Z-Locations and Sensor numbers of thermocouples installed on sidewalls and top and bottom walls of the cavity.

Side wall with bottom heating band			Side wall with top heating band			Top and bottom horizontal plates		
Thermocouple sensor name	z (m)	z/H	Thermocouple sensor name	z(m)	z/H	Thermocouple sensor name	z(m)	z/H
100	0.002	0.01	116	0.008	0.03	212	0.0	0
101	0.025	0.08	117	0.033	0.11			
102	0.038	0.13	119	0.059	0.20			
103	0.051	0.17	200	0.084	0.28			
104	0.064	0.21	201	0.110	0.37			
105	0.076	0.25	202	0.135	0.45			
106	0.089	0.30	203	0.160	0.53			
107	0.114	0.38	204	0.186	0.62			
108	0.140	0.47	205	0.211	0.70			
109	0.165	0.55	206	0.224	0.75			
110	0.191	0.64	207	0.237	0.79			
112	0.216	0.72	208	0.249	0.83			
113	0.241	0.80	209	0.262	0.87			
114	0.267	0.89	210	0.275	0.92			
115	0.292	0.97	211	0.298	0.99	213	0.3	1

9.4.3 Air Temperature Measurements

The air temperatures inside the cavity are measured using three 0.125 mm (0.005 inch) fine diameter wire, prefabricated butt-welded type K pre-manufactured thermocouples. The thermocouple junctions are located in the vertical midplane of the cavity (z/H = 0.5, x/W =0.5), and three locations along the cavity length y/L = 0.24, 0.50, 0.76. Table 9.3 gives the x-y-z locations of the thermocouples.

Table 9.3: X-Y-Z Locations of thermocouples used for measuring air temperatures.

Air thermocouple #	y (m)	x (m)	z (m)
1	0.1456	0.015	0.15
2	0.3000	0.015	0.15
3	0.4544	0.015	0.15

In order to maintain thermocouples perfectly suspended inside the cavity, with the thermocouple wire being taut at all times, a support mechanism was installed in the plane above the top wall of the cavity. The support mechanism is comprised of a ½ inch thick plywood support-plate installed on four threaded steel rods fixed on the optical table, and a ¼ inch thick plywood moving-plate attached to the support-plate. The support mechanism was levelled to within 0.1 degree using a digital level to be perfectly parallel to the top and bottom walls of the cavity. The moving-plate which is parallel to the plane of the top cavity wall is assembled on the support mechanism by means of a threaded steel rod. The end of the steel rod attached to the moving-plate is fixed while the other end is attached to the support-plate using two lock nuts. The moving plate can be moved only up-down along the z-direction by changing location of the lock nuts on the threaded steel rod.

The top and bottom plates of the cavity are machined with 0.8mm diameter holes at the x-y locations shown in Table 9.3. The fine wire thermocouples are threaded into the cavity through these holes with the positive and negative leads coming out through the top and bottom walls respectively. Lead wires coming out of the bottom wall are installed with shrink wrap to restrict movement of fine wire above the bottom plate. Positive lead wires immerging out from the top plate are attached to thermocouple connectors installed on the moving plate of the support mechanism. The moving plate is then moved upwards along the Z direction to make the thermocouple wires perfectly taut. With this assembly, the uncertainty associated with the vertical location of each thermocouple's junction is within $\pm$ one mm.

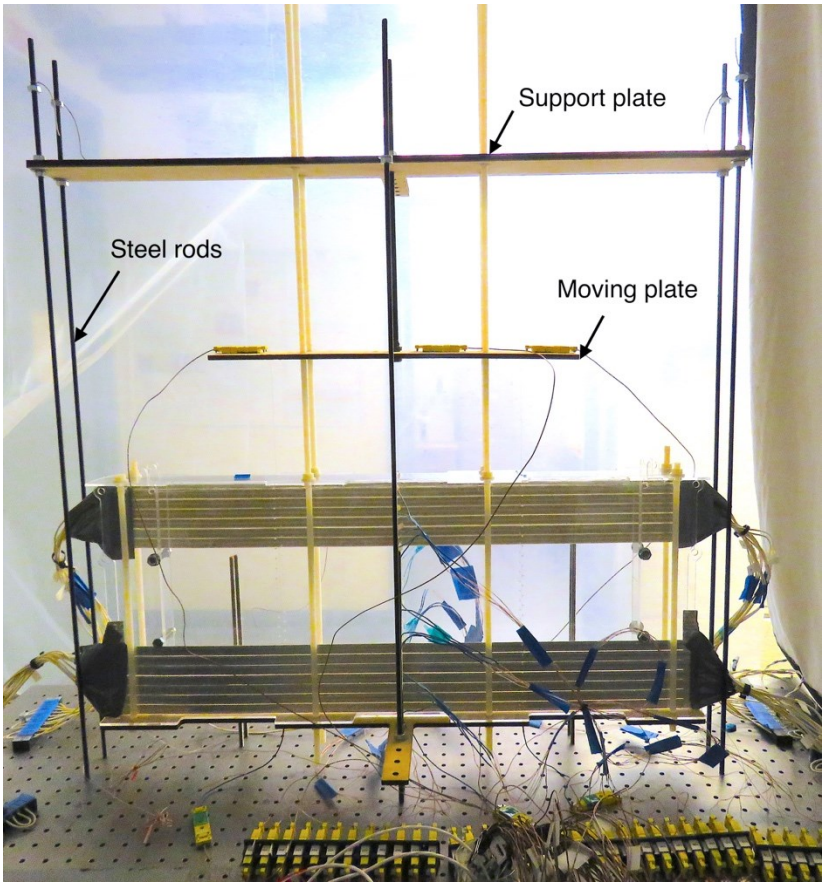

Figure 9.9: Photograph showing support mechanism installed on the cavity to accommodate the thermocouples measuring air temperatures inside the cavity.

9.4.4 Data Acquisition System

The data acquisition system for this experiment is similar to the one used for the annular cavity experiments. A total of 35 thermocouples temperatures, 32 wall thermocouple temperatures and 3 air temperatures inside the cavity were measured using a data acquisition system consisting of a HP3852A DAQ and a computer running LabVIEW 2017. Thermocouple voltages were converted into temperatures based on the NIST ITS-90 datasheets for direct and inverse polynomial functions for type K thermocouples [63]. The wall temperatures were recorded at a lower sampling frequency of 0.00417 Hz while the three air temperatures inside the cavity were recorded at a higher sampling frequency of 2.5 Hz. The block diagram of the LabVIEW VI designed for measuring the thermocouple voltages is shown in Fig.9.10.

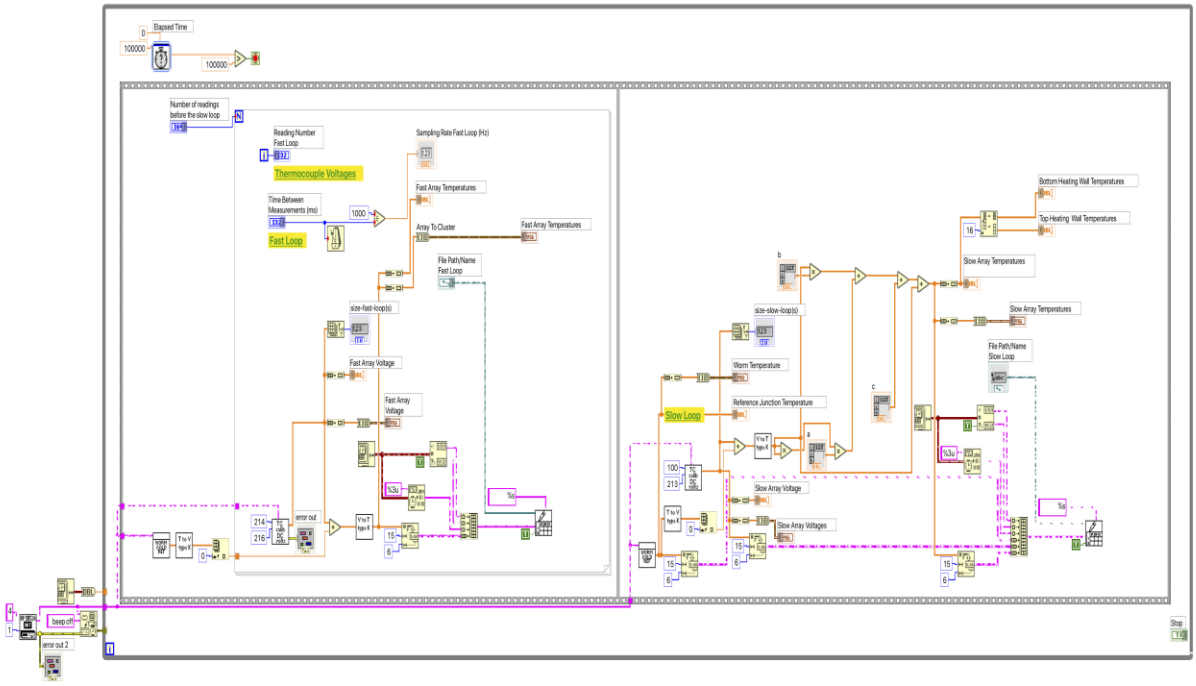

Figure 9.10: LabVIEW 2017.0 VI block diagram for temperature measurement for rectangular cavity experimental system.

9.5 Temperature Measurement Uncertainty

The precision and bias of the 32 wall thermocouples were checked at three reference temperatures: an ice bath at -0.01°C, still air at a room temperature of 22.21°C and a boiling water bath at 100.05°C. The reference temperatures were measured by a NIST calibrated Class 'A' 4-wire platinum RTD of 100 Ω . Bias errors for the 32 thermocouples were obtained at -0.01°C, 22.21°C and 100.05°C, and temperature corrections were implemented in the LabVIEW 2017.0 VI to correct the bias (systematic error) for each wall thermocouple. The precision (random error) for the 32 wall thermocouples is shown in Table 9.4 at the three reference temperatures.

Table 9.4: Wall thermocouple precision at three reference temperatures.

Wall thermocouples at three reference temperatures:	Precision
Ice bath at -0.01°C	± 0.04°C
Still air at 22.21°C	± 0.06°C
Boiling water bath at 100.05°C	± 0.53°C

Similar to fine wire thermocouples installed for the annular cavity system, a single precision check at room temperature was performed for all three thermocouples measuring air temperatures inside the cavity after the thermocouples were installed. Precision of fine thermocouples in still air inside the cavity was within ± 0.04°C. Fig. 9.11(a) shows the residuals of the air temperatures measured by the three thermocouples in still air at 22.8°C . Figure 9.11(b) shows the power spectral density functions for each of the three thermocouples in still air showing a baseline noise-level of around -40 dB.

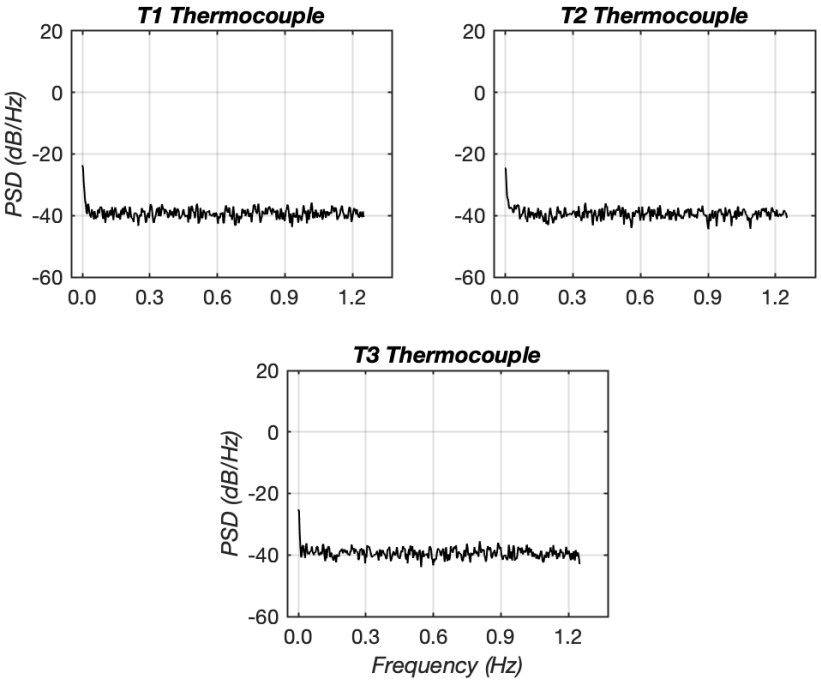

(a)

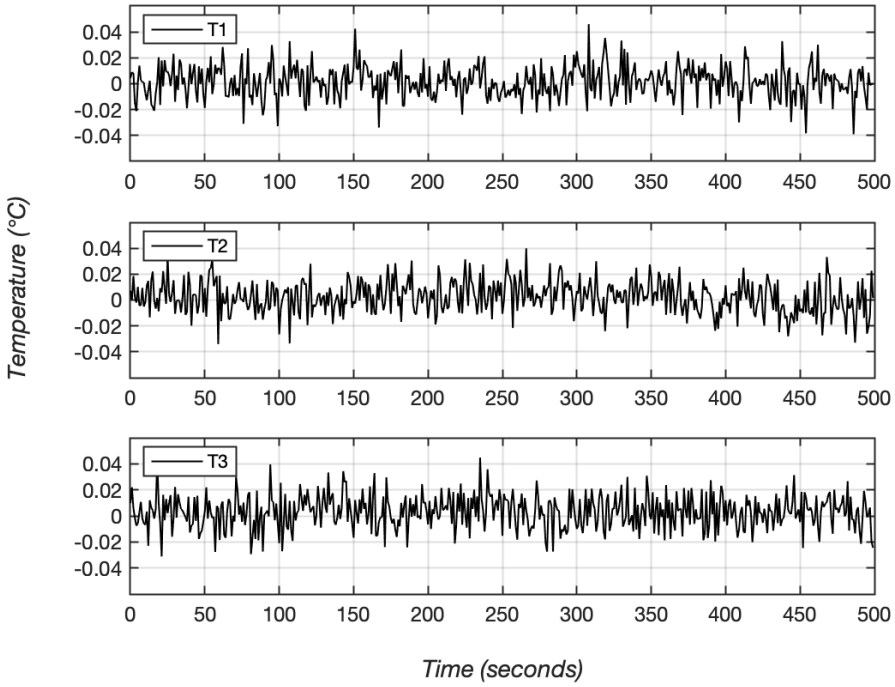

(b)

Figure 9.11: (a) Air temperature residuals for three thermocouples at y/L = 0.24, 0.50, 0.76 for still air at 22.8° C; (b) Power spectral density of air temperatures measured by three thermocouples at y/L = 0.24, 0.50, 0.76. for still air at 22.8° C.

9.6 Data Collection and Analysis

To study stability of bi-cellular base flow inside the cavity, the heat flow from the top and bottom heating bands was progressively increased over several sets of experiments. The control parameter for these sets of experiments is the maximum temperature difference between the two side walls. The heat flux from the heating bands was changed by changing the voltage supplied by the Variac to the heating bands. Since both heating bands are connected in parallel to the power supply, by changing the voltage by a certain amount the heat flux increased by the same for amount for either bands. For each experiment, the control parameter was set (voltage), and all of the wall temperatures were monitored. It took approximately 3-4 hours for the wall temperatures to be fully established without temporal change. After this transient period of wall heating / cooling was complete, the air temperatures and cavity temperatures were collected for two hours. For each two-hour duration, the maximum temporal variation in surface boundary temperature was less than $\pm 0.1°C$. This data was then used to determine the frequency content, amplitude for air temperature oscillations, type of flow (2D/3D) and to determine wall temperature profiles and nominal Rayleigh numbers for each experimental run using the same data analysis techniques as previously discussed in Chapter 6.

Chapter 10

10 NATURAL CONVECTION IN RECTANGULAR CAVITY – EXPERIMENTAL RESULTS

10.1 Wall Thermal Profiles for Experiments

To induce a bi-cellular baseflow inside the long, tall, rectangular cavity, top portion of one vertical wall and bottom portion of the opposing vertical wall are heated via heating bands installed on upper and lower thirds of corresponding walls. When no heat is applied to the walls, the opposing walls are isothermal and air inside the cavity is stationary. When heating bands are turned on, the resulting boundary conditions are such that in the top portion of the cavity one wall has a higher temperature that the adjacent wall, and visa-versa in the bottom portion of the cavity. These boundary conditions support presence of a stable bi-cellular base flow as shown in Fig. 10.1.

A combination of conduction heat transfer within the acrylic walls, internal and external convection of air, and radiative heat transfer within the cavity surfaces as well as with ambient air are responsible for the final temperature profiles that develop on the cavity walls. Thermal profiles for the vertical opposing walls were determined by a cubic piecewise spline fitted to temperature measurements from 30 thermocouples installed on the cavity walls. Temperature profiles for the vertical opposing walls for a typical experimental run are shown in Fig. 10.2 For all experimental runs reported in this study, the cavity's wall surfaces, varied by no more than $\pm$ 0.1°C temporally over the duration of the two hour data collection.

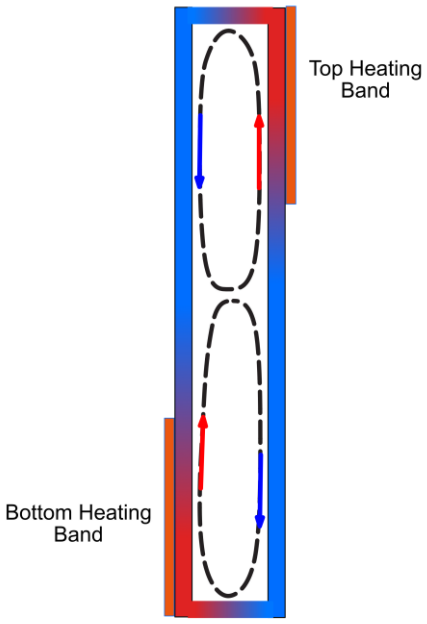

Figure 10.1: Schematic of the experimental system showing regions where active heating is applied to top and bottom heating bands and the resulting bi-cellular baseflow pattern.

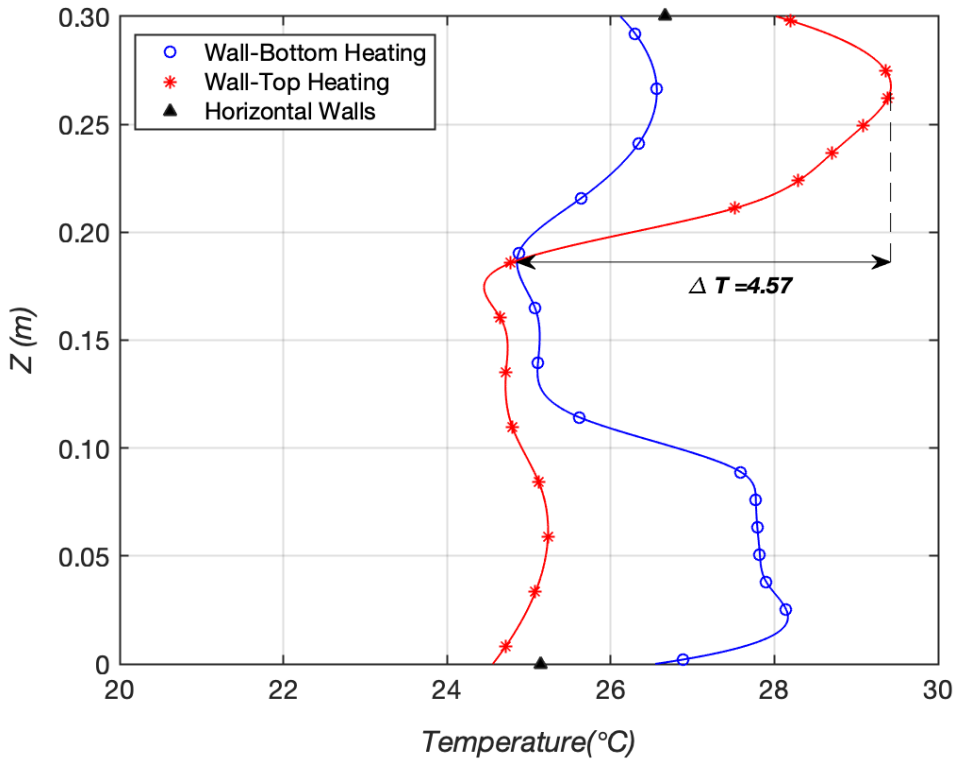

Figure 10.2: Temperature profiles for the two opposing vertical walls for a typical experimental run.

10.2 Experimental Data Sets

10.2.1 Organization of Experiments

Buoyant potentials of the upper and lower convection cells of the bi-cellular base flow are dependent on temperature differences in the top and bottom parts of the cavity, as shown in Fig. 10.1. Temperature differences in these two regions were simultaneously increased by increasing heat flux to top and bottom heating bands installed on opposing vertical walls by equal amounts. Over the course of several experiments, heat flux to the two heating bands was increased in small steps to study effects of increasing buoyant potential of convection cells on the stability of flow. Difference between maximum temperature of wall installed with top heating band and minimum temperature of wall installed with bottom heating band is denoted by 'ΔT'. This temperature difference is used to quantify the increase in buoyant potential of the convection cells in response to increase in heat flux to heating bands. Temperature difference 'ΔT' can be directly controlled by changing the heat flux to the heating bands and is, therefore, the control parameter for these sets of experiments. As the buoyant potential of the cells was successively increased, the convection flow inside the cavity underwent different flow regimes. Air temperature data collected from the three thermocouples suspended in the cavity was processed using the methods described in Chapter 6. The experimental runs were classified into steady, 2D periodic, 3D periodic, and quasi-chaotic flow regimes based on frequency and phase content of the air temperature data. Figure 10.3 shows examples of temperature profiles of the two opposing vertical walls that result in three different air-flow regimes – steady, periodic, and quasi-chaotic. Temperatures of top and bottom walls of the cavity measured at the midpoint of the walls as well as the locations of the heating bands are shown in Fig 10.3. Proxy for the buoyant potential, viz. temperature difference 'ΔT' for each case is also shown in Fig.10.3.

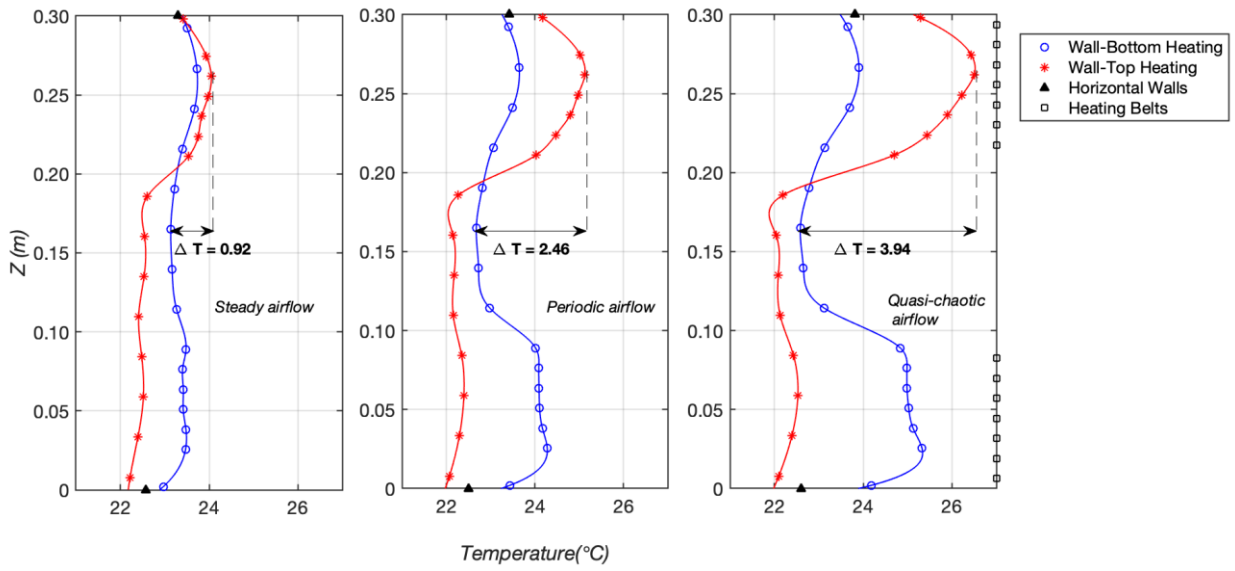

Figure 10.3: Sample temperature profiles of the opposing vertical walls for steady, periodic and quasi-chaotic air-flow regimes with ΔT as the control parameter.

10.2.2 Nominal Rayleigh Number

Temperature differences between vertical opposing walls of the cavity are different at each Z location along cavity height. Temperature difference first increases and then decreases as we move downwards from the top edge of the cavity. It then becomes zero at the intersection point (cross-over point) of temperature profiles of the two opposing vertical walls. As we move towards even further towards the bottom of the cavity, temperature difference again increases and then decreases till the bottom edge of the cavity. The cross-over point of wall thermal profiles divides the cavity into two parts: the top portion, which is the area above the cross-over point, and the bottom portion, which is the area below the cross-over point (seen in Fig.10.3). The upper and lower convection cells of the bi-cellular flow develop in these two distinct regions. Temperature difference 'ΔT' can be found by taking the difference between the maxima of thermal profile of the wall installed with the top heating belt and the minima of thermal profile of the wall installed with the bottom heating

belt. 'ΔT' is used to calculate a nominal Rayleigh number for each experimental run. Height of the rectangular cavity, $L_c = H$, is chosen as the characteristic length for evaluating Rayleigh numbers. All of the air's thermophysical properties are assessed at the cavity's weighted mean wall temperature. This convention of using the temperature difference inside the cavity (ΔT) and height of the cavity (H) for calculation of nominal Rayleigh number is similar to that used for the annular cavity experiments described in Chapters 6,7 and non-isothermal cavity results of Reeve et al. [50] and Dillon et al. [51]. Nominal Rayleigh numbers are useful for comparisons within experimental data sets and for comparison with previous results from literature for non-isothermal cavities and annular cavity experimental results described in Chapters 6 and 7. The range of nominal Rayleigh number explored for these rectangular cavity experiments was 2.04 x 10^6 to 2.03 x 10^7. The maximum uncertainty associated with Rayleigh numbers is $\pm$ 5.7%. The data presented in this chapter are from the analysis of over 39 sets of experimental data. Air temperature was data collected at a frequency of 2.5 Hz, while cavity wall temperature data was collected at a rate of 0.00417 Hz.

10.3 Results and Discussion

10.3.1 Steady Bi-cellular Flow

The first experimental was conducted at ΔT =0.77°C which corresponds to a nominal Rayleigh number of 2.04 x 10^6. For this experimental run the bi-cellular natural convection flow inside the cavity was found to be steady. When ΔT was further increased over subsequent experimental runs, steady flow was observed for experiments with ΔT up to ΔT = 2.17°C. Figure 10.4 shows the wall temperature profiles for one such run of the steady flow regime with ΔT = 1.15°C. Temperature

differences in the top and bottom parts of the cavity can be indicative of the relative strengths of the upper/lower convection cells. Careful observation of the temperature profiles show that the temperature differences in the top part of the cavity (upper convection cell) are smaller as compared to that in the bottom part of the cavity (lower convection cell).

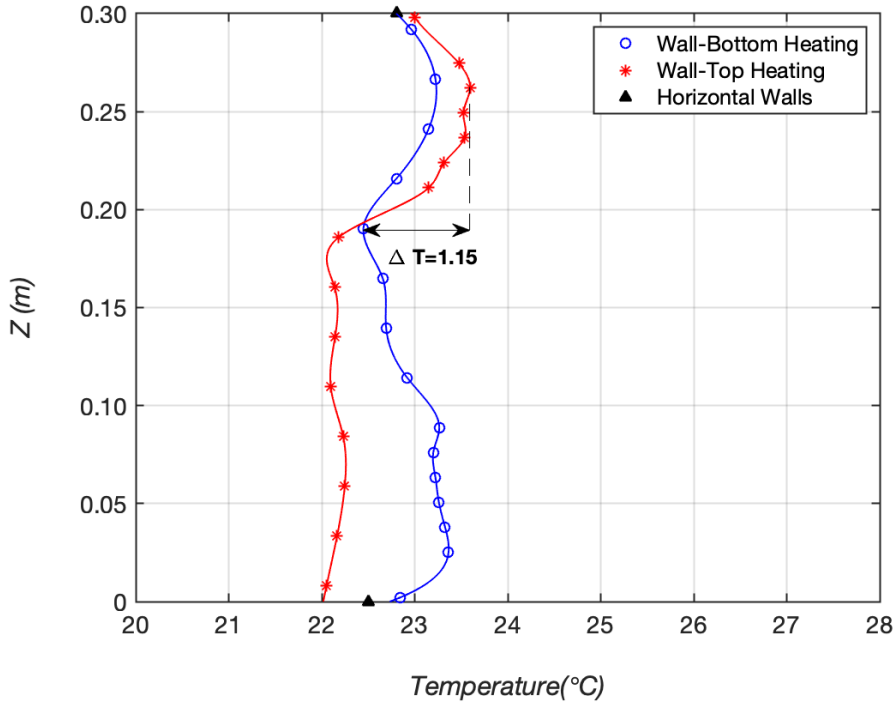

Figure 10.4: Temperature profiles for the two opposing vertical walls for an experimental run in the steady flow regime with ΔT= 1.15°C.

Figure 10.5 shows the residuals of temperatures recorded by the three air thermocouples over a time duration of three minutes while Fig. 10.6 shows the PSD of temperature data for the same experiment at ΔT = 1.15°C. Air temperature data is constant with baseline noise levels over the duration of the experiment and shows no periodic variations. Further, no frequency peaks are observed in the PSD of temperature data indicating the flow inside the cavity is steady.

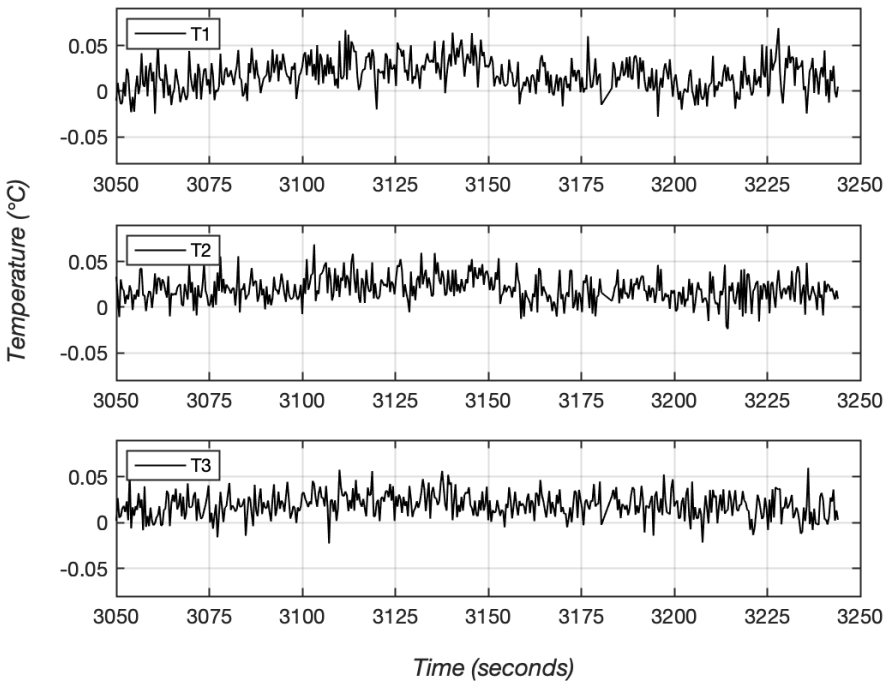

Figure 10.5: Air temperature residuals measured at three thermocouples located along the vertical midplane of the cavity (z/H = 0.5, x/W =0.5), and three locations along the cavity length y/L = 0.24, 0.50, 0.76 for an experiment run in the steady flow regime with ΔT =1.15°C.

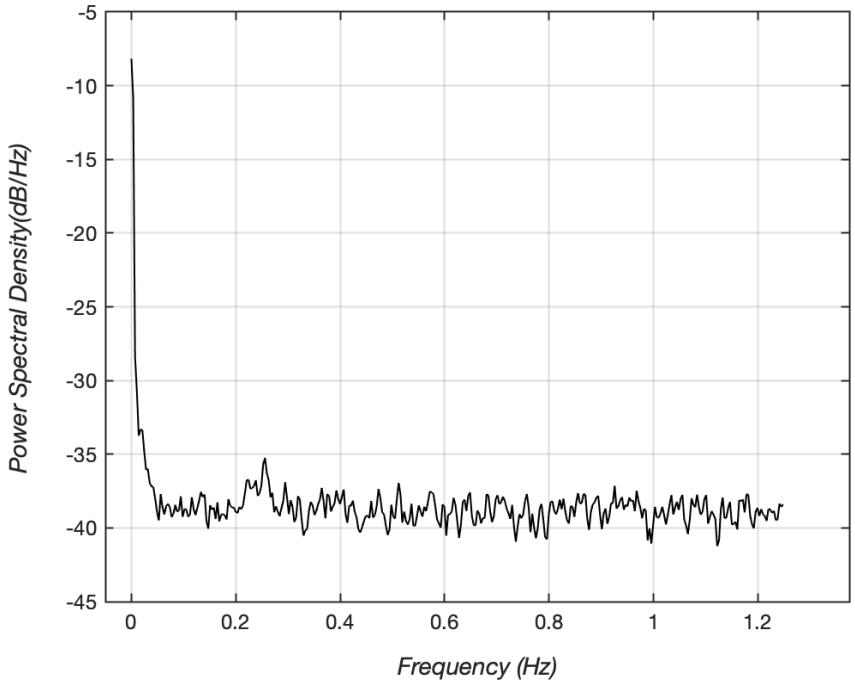

Figure 10.6: Power spectral density of air temperature data set recorded at thermocouple located at z/H = 0.5, x/W =0.5, y/L = 0.5 for an experiment run in the steady flow regime with ΔT =1.15°C.

10.3.2 Two-Dimensional Periodic Flow Regime

As the ΔT between the cavity walls was increased beyond ΔT=2.17 the first bifurcation of the system from steady to periodic flow was observed at ΔT=2.30. The nominal Rayleigh number corresponding to this transition is Ra = 6.27 x 10^6 $\pm$ 3%. Figure 10.7 shows the wall temperature profiles for one such experimental run of the periodic flow regime observed at ΔT = 2.46°C. The temperature differences in the top and bottom portions of the cavity are now comparable indicating that the upper and lower convection cells are of comparable strength.

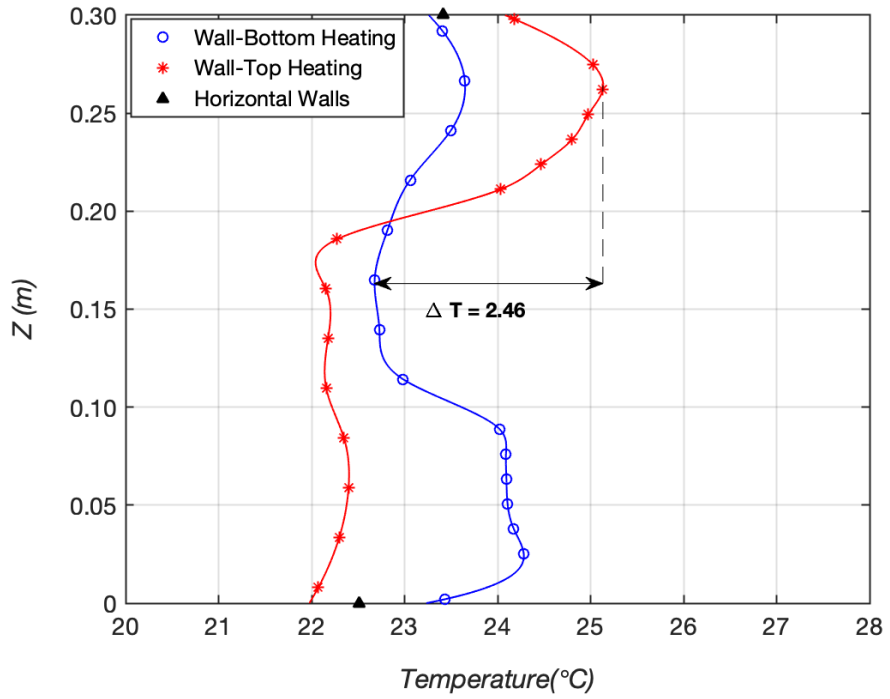

Figure 10.7: Temperature profiles for the two opposing vertical walls for an experimental run in the 2D periodic flow regime with ΔT= 2.46°C.

Figure 10.8(a) shows the residuals of temperatures recorded by the three air thermocouples over a time duration of six minutes for flow in periodic regime at ΔT = 2.46°C and Fig. 10.9 shows the corresponding PSD. The PSD shows the presence of one fundamental frequency (f_1 = 0.051 Hz)

and its harmonics n.f_l (n=1,2,3...). indicating periodic flow behavior. Three air temperature signals, seen in Fig 10.8(a), are of comparable amplitude and the waveforms of signals have a similar triangular shape. Further, the three air temperature signals are in phase as seen in Fig 10.8(b) which shows the three temperature signals superimposed on each other. The similar amplitude, phase and shape of the air temperature signals from three different points along the cavity length indicate that the unsteady periodic flow is 2D in nature with fluid movement only in the x-z plane. This flow regime is therefore classified as '2D periodic flow'. The fundamental frequency of the oscillations increased from f_l = 0.032 Hz to 0.051 Hz as the ΔT was increased from ΔT = 2.30°C to 2.46°C. 2D periodic flow regime was observed for experimental runs upto ΔT=2.46°C. This 2D periodic regime was observed over a relatively small ΔT (Rayleigh number) range. Transition from steady convection to 2D unsteady period flow exhibiting a single frequency dependence indicates that this flow transition occurs via a Hopf bifurcation [60,72].

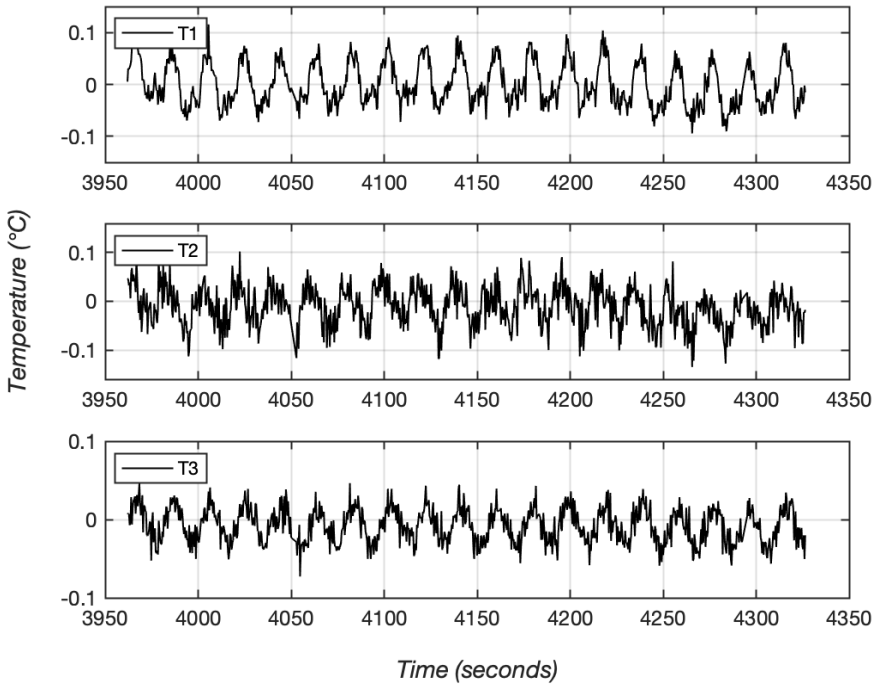

(a)

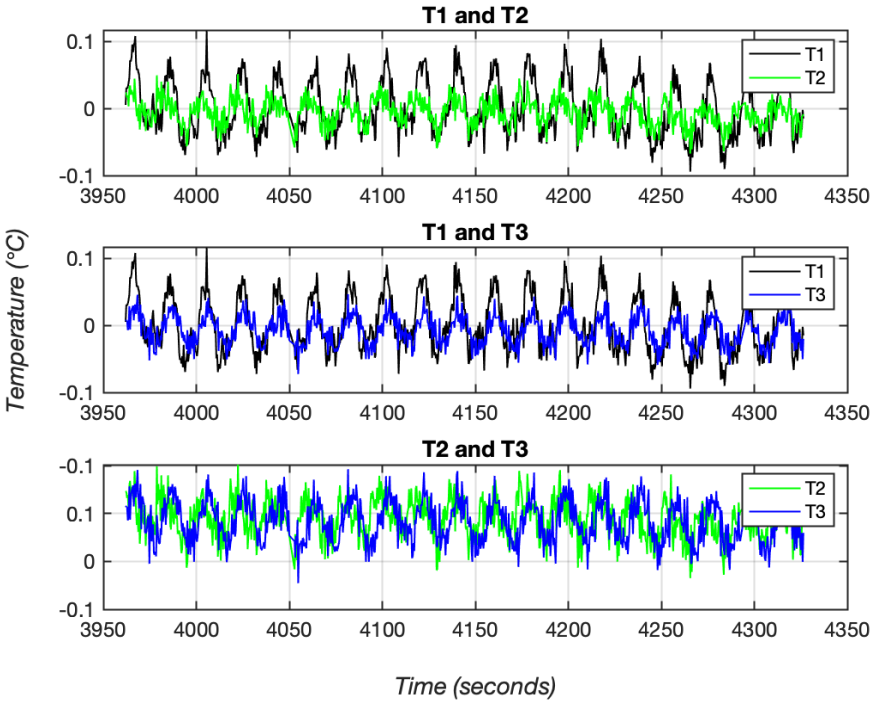

(b)

Figure 10.8: (a) Air temperature residuals measured at three thermocouples located along the vertical midplane of the cavity (z/H = 0.5, x/W =0.5), and three locations along the cavity length (y/L = 0.24, 0.50, 0.76) for an experiment run in the 2D periodic flow regime with ΔT =2.46°C; (b) Comparison of three temperature signals showing the three signals in-phase.

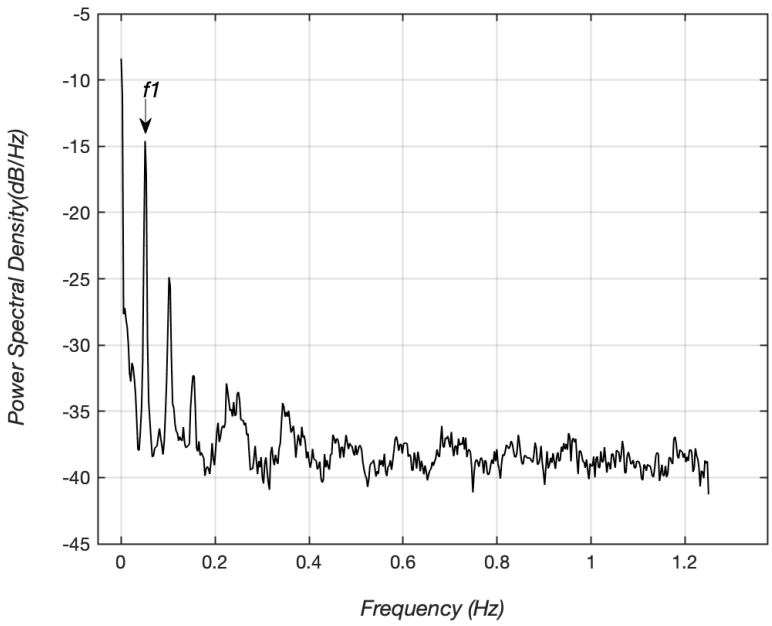

Figure 10.9: Power spectral density of air temperature recorded at thermocouple located at z/H = 0.5, x/W =0.5, y/L = 0.5 for an experiment run in the 2D periodic flow regime with ΔT =2.46°C.

10.3.3 Three-Dimensional Periodic Flow Regime

With further increase in ΔT, the periodic flow regime continued. However, the nature of the air-flow inside the cavity changed from 2D to 3D as was indicated by the change in phase and waveform shape of the air temperature signals. The change of instability from 2D periodic to 3D periodic flow was first observed for an experimental run at ΔT = 2.66°C. This is the second bifurcation of the system and the corresponding nominal Rayleigh number is Ra = 6.99 x 10^6 $\pm$ 3%. This 3D periodic regime was observed for experimental runs with ΔT between ΔT = 2.66°C to 3.55°C. The fundamental frequency of the oscillations observed for the 3D periodic flow regime varied between f_l= 0.019 Hz to 0.042 Hz. The amplitude of oscillation increased continuously with increase in ΔT from $\pm$ 0.13°C to $\pm$ 0.4°C.

Figure 10.7 shows the wall temperature profiles for an experimental run in the 3D periodic flow regime observed at ΔT = 3.29°C. Figure 10.11(a) shows the residuals of temperatures recorded by the three air thermocouples over a time duration of six minutes for flow in 3D periodic regime at ΔT = 3.29°C and Fig. 10.12 shows the corresponding PSD. Periodic flow behavior is evident from the PSD which shows the presence of one fundamental frequency (f_l = 0.024 Hz) and several of its harmonics n.f_l (n=1,2,3..).The amplitudes of the three air temperature signals are not comparable; with the amplitudes of the two extreme thermocouples (y/L = 0.24 and 0.76) being close to $\pm$ 0.4°C. while that of the central thermocouple (y/L = 0.5) being $\pm$ 0.2°C. . Each of the three-thermocouple signal waveform is significantly different from each other which is in contrast to the similar triangular waveform of the 2D periodic regime. Further, the three air temperature signals are in not in phase as seen in Fig 10.11(b) which shows the three temperature signals superimposed on each other. The different amplitudes, out of phase temperature signals and

dissimilar waveforms of temperature signals indicate that the unsteady flow is 3D in nature. Simultaneous fluid movement occurring in the x-z and y-z plane can cause such a 3D oscillatory flow. This behavior of each air temperature signal having a differently shaped waveform is reminiscent of the temperature signal waveforms of the 3D asymmetric periodic flow observed in the annular cavity experiments.

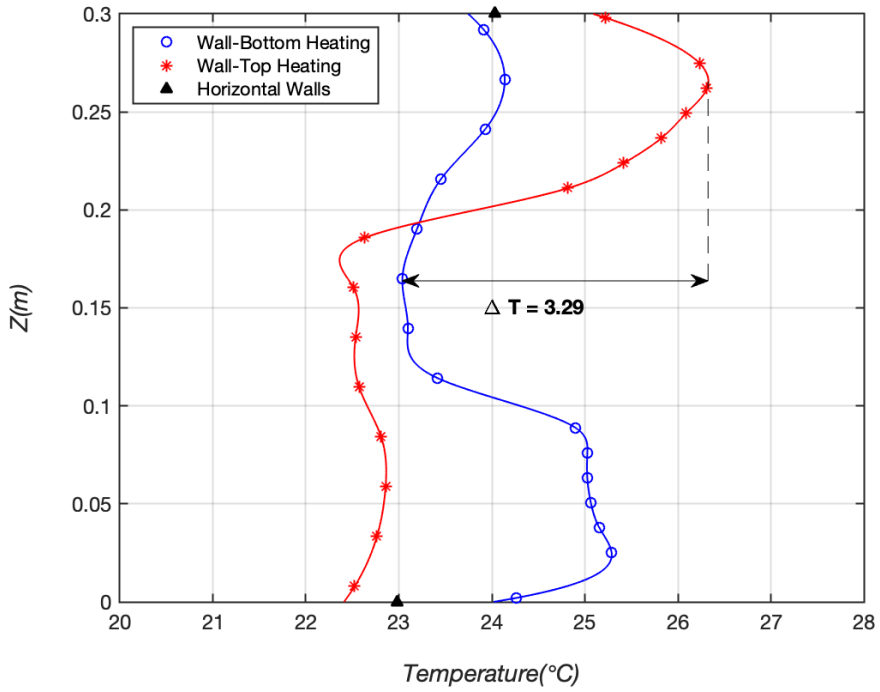

Figure 10.10: Temperature profiles for the two opposing vertical walls for an experimental run in the 3D periodic flow regime with ΔT= 3.29°C.

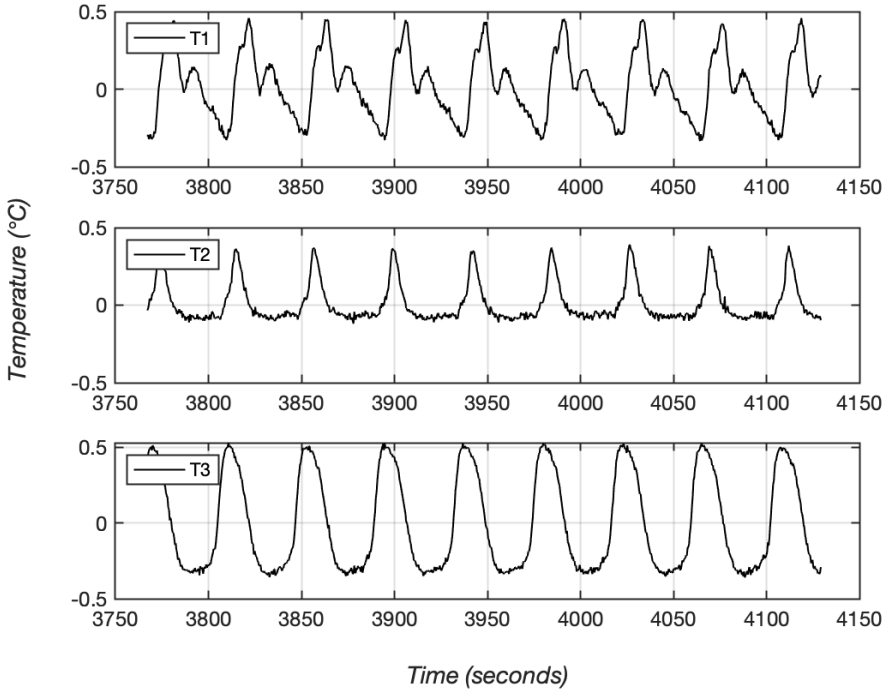

(a)

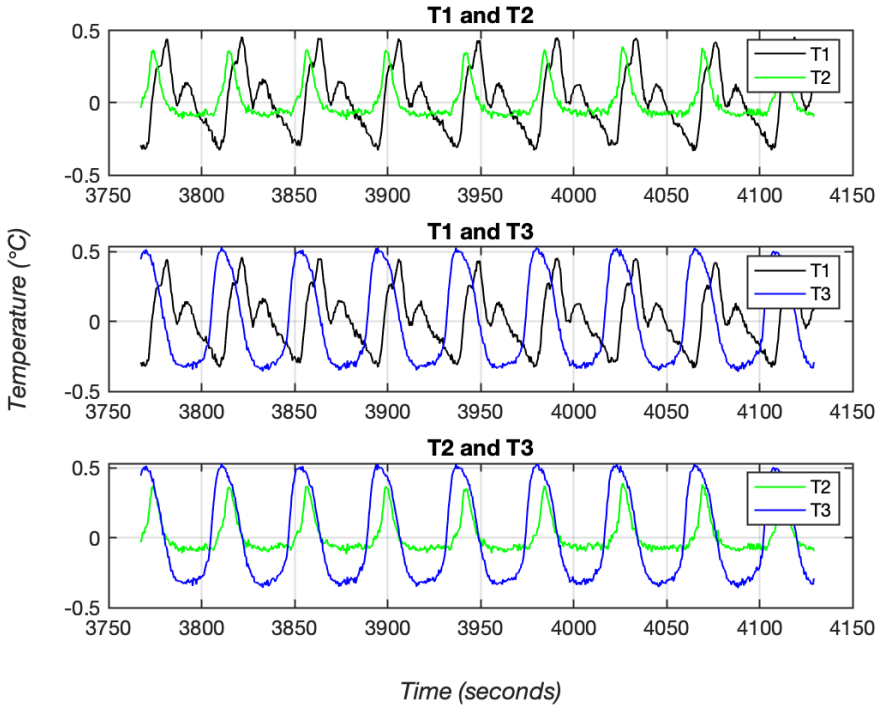

(b)

Figure 10.11: (a) Air temperature residuals measured at three thermocouples located along the vertical midplane of the cavity (z/H = 0.5, x/W =0.5), and three locations along the cavity length (y/L = 0.24, 0.50, 0.76) for an experiment run in the 3D periodic flow regime with ΔT =3.29°C; (b) Comparison of three temperature signals showing the three signals out of phase.

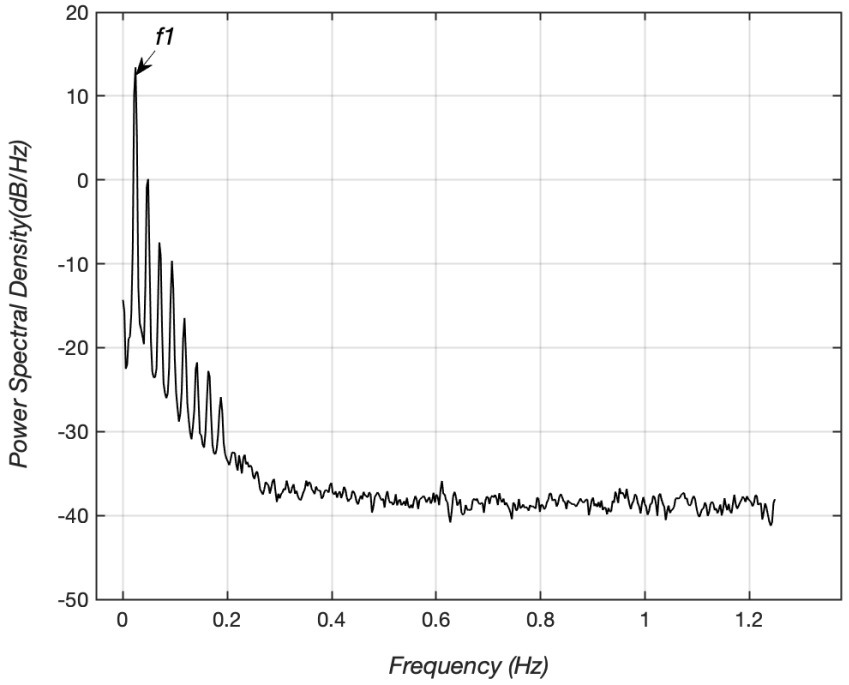

Figure 10.12: Power spectral density of air temperature data set recorded at thermocouple located at z/H = 0.5, x/W =0.5, y/L = 0.5 for an experiment run in the 3D periodic flow regime with ΔT =3.29°C.

10.3.4 Transition to Chaotic flow

When the ΔT was further increased to ΔT = 3.94°C, the flow transitioned from 3D periodic behavior to aperiodic flow behavior. This is the third bifurcation of the system and the corresponding nominal Rayleigh number is Ra = 1.05 x $10^7 \pm 2\%$. Increasing the ΔT even further caused more bifurcations to appear, and the flow starts to exhibit characteristics of chaotic behavior. As compared to the annular cavity experiments, the transition from periodic to chaotic flow in these experiments was much faster which made it difficult to identify the bifurcations that cause the transition from periodic to chaotic flow. Figure 10.13 shows the wall temperature profiles for one such experimental run in the chaotic flow regime observed at ΔT = 4.27°C. Figure

10.14 shows the residuals of temperatures recorded by the three air thermocouples over a time duration of sixteen minutes for flow in chaotic regime at ΔT = 4.27°C and Fig. 10.15 shows the corresponding PSD. The PSD shows a banded presence of multiple frequency peaks, characteristic of a chaotic flow. However, a significant amount of power is still present in the frequencies close to f = 0.014 Hz, indicating that the flow is not fully chaotic, but is on the route to chaos. Therefore, this regime is referred to as the quasi-chaotic flow regime. This quasi-chaotic flow regime was observed over several experimental runs as the ΔT was increased from ΔT = 3.94°C to 8.03°C. This corresponds to a Rayleigh number range of Ra = 1.05 x 10^7 to 2.03 x 10^7 over which system exhibited quasi-chaotic flow behavior. Even at the experimental run of ΔT =8.03°C, the flow was still quasi-chaotic with significant power in frequencies between f = 0.019 to 0.077 Hz.

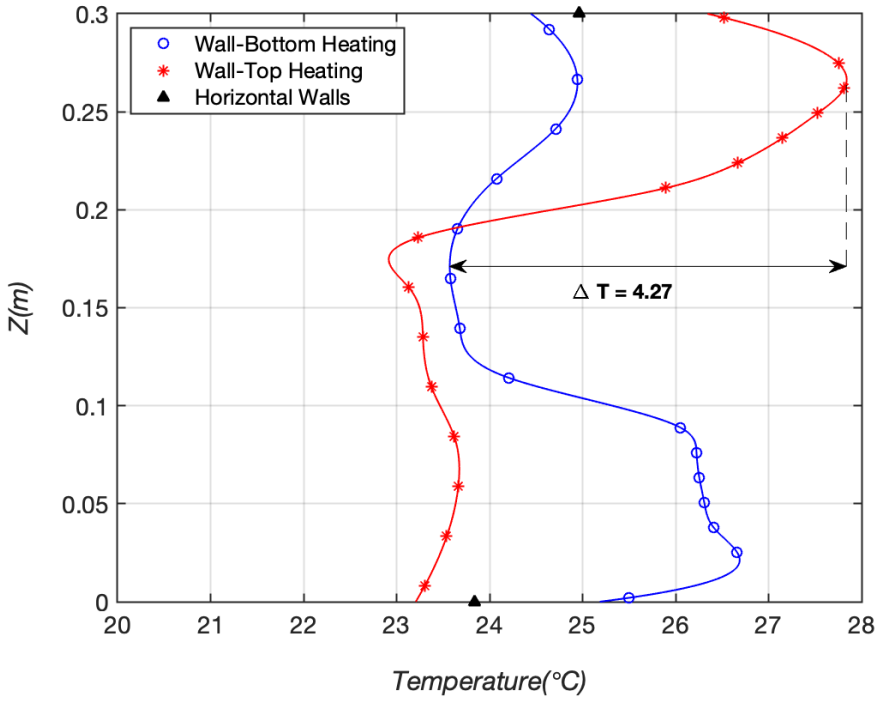

Figure 10.13: Temperature profiles for the two opposing vertical walls for an experimental run in the quasi-chaotic flow regime with ΔT= 4.27°C.

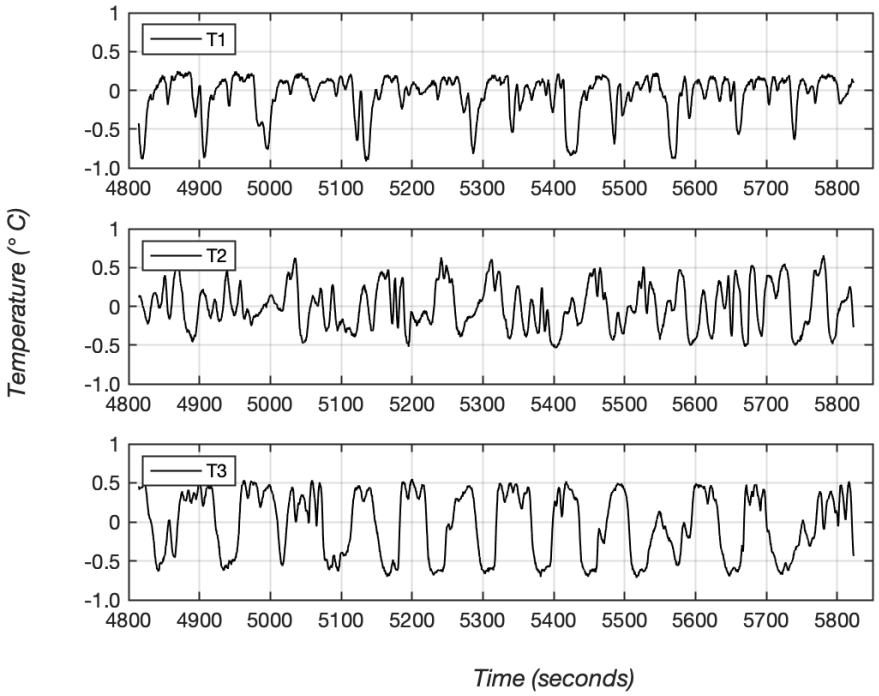

Figure 10.14: Air temperature residuals measured at three thermocouples located along the vertical midplane of the cavity (z/H = 0.5, x/W =0.5), and three locations along the cavity length y/L = 0.24, 0.50, 0.76 for an experiment run in the quasi-chaotic flow regime with ΔT =4.27°C.

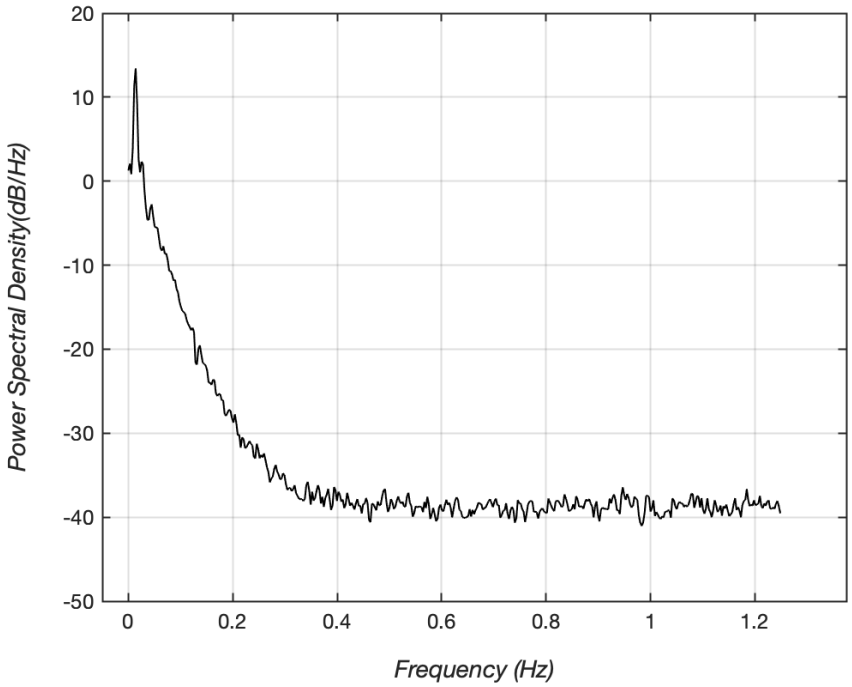

Figure 10.15: Power spectral density of air temperature data set recorded at thermocouple located at z/H = 0.5, x/W =0.5, y/L = 0.5 for an experiment run in the quasi-chaotic regime with ΔT =4.27°C.

A fully chaotic flow with power distributed equally at all frequencies was not observed in any of the experimental runs. After the experimental run at ΔT =8.03°C, the heat flux to the heating tapes was not increased any further for fear of damaging/deforming the acrylic plates. Unlike the annular cavity experiments, no quasiperiodic regime was observed as an intermediate regime between periodic and chaotic/aperiodic flow. There is a possibility that the quasiperiodic regime does exist but was not captured in the current experiments on account of limitation on the resolution of the AC Variac (Variable Transformer). The ΔT across the two vertically opposing walls is controlled by controlling the voltage supplied to the heating tapes. The lowest increment possible on the voltage supplied to the heating tapes is 0.5V. When the voltage was increased by 0.5V starting with the experiment with 3D periodic flow, the system transitioned from periodic behavior to aperiodic or quasi-chaotic behavior. If a finer control on the voltage and thereby on the ΔT is made available, it might be possible to capture a quasiperiodic regime which might provide some insight to the route to chaotic flow. A summary of all the air-flow regimes observed with increasing ΔT is given in Table 10.1.

Table 10.1: Air-flow regimes with increasing ΔT as control parameter.

Air-flow Regime	ΔT	*Nominal Rayleigh Number Range*	*Frequency peaks*
Steady	$\Delta T \leq 2.17°C$	$Ra \leq 5.78 \times 10^6$	No peaks visible
2D periodic	$2.30°C \leq \Delta T \leq 2.46°C$	$6.27 \times 10^6 \leq Ra \leq 6.56 \times 10^6$	f_1, and harmonics $n.f_1$
3D periodic	$2.66°C \leq \Delta T \leq 3.55°C$	$6.99 \times 10^6 < Ra \leq 9.35 \times 10^6$	f_1, and harmonics $n.f_1$
Quasi-chaotic	$\Delta T \geq 3.94°C$	$Ra \geq 1.05 \times 10^7$	Banded presence of multiple frequency peaks

Frequency maps for air temperature signals as a function of ΔT are shown in Fig. 10.16 where transitions from periodic to quasi-chaotic flows can be observed. For these experiments, the transition from steady to chaotic flow occurred very fast (over a small range of ΔT) resulting in a smaller periodic flow regime. As compared to the annular cavity experiments described in Chapter 7, the fundamental frequencies observed in the periodic regime for the rectangular cavity are of a lower magnitude. Further, similar to the annular cavity, for all flow regimes observed in these experiments, the dominant frequency content is below 0.2 Hz and frequencies above 0.6 Hz show negligible contribution in the PSD.

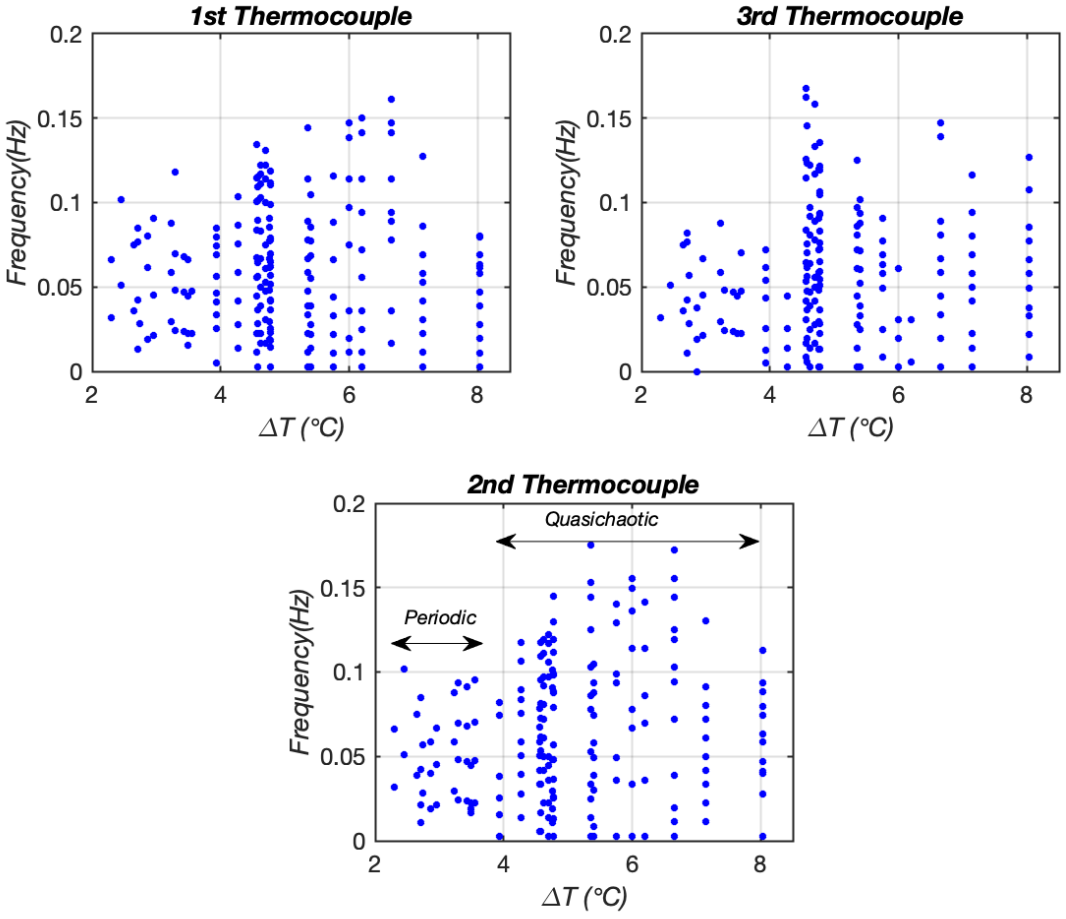

Figure 10.16: Frequency map of the system as ΔT is successively increased.

Throughout the 2D, 3D periodic and quasi-chaotic regimes the amplitude of air temperature oscillations increased continuously with increase in ΔT. Figure 10.17 shows the average amplitudes of air temperature oscillations measured at the three thermocouples over the full range of ΔT that were explored. An amplitude of x°C represents $\pm$ x°C change from the mean temperature. The amplitude of oscillations increase from $\pm$ 0.06°C in the 2D periodic flow regime to $\pm$ 0.91°C in the quasi-chaotic regime.

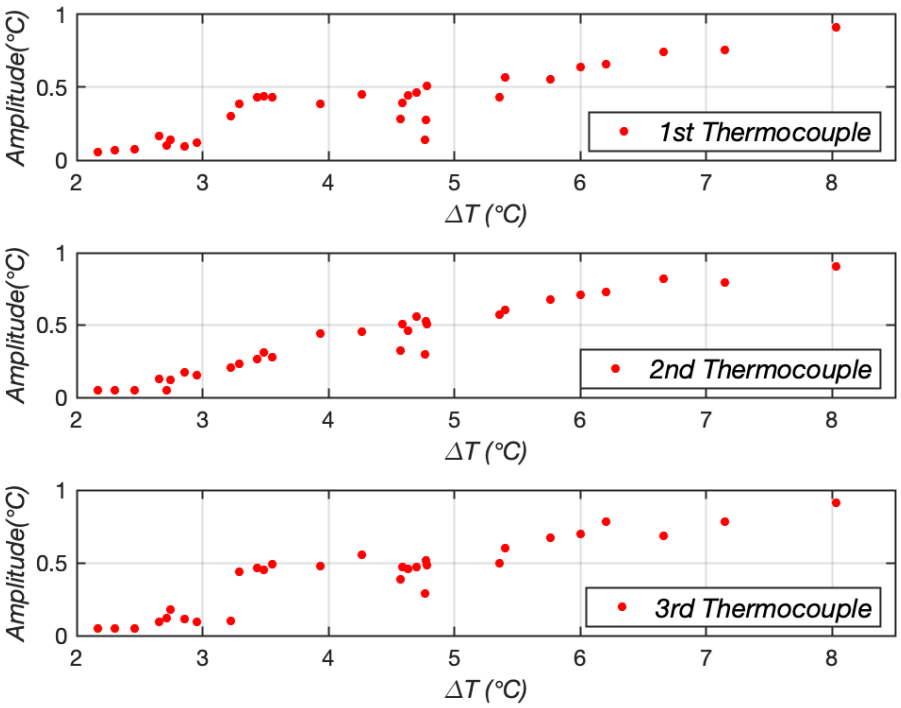

Figure 10.17: Average amplitude of air temperature oscillations measured at three thermocouples located along the vertical midplane of the cavity (z/H = 0.5, x/W =0.5), and three locations along the cavity length y/L = 0.24, 0.50, 0.76 as ΔT is successively increased.

The maximum temperature difference above and below the cross over point indicates the strength of the upper and lower convection cells respectively. Figure 10.18 shows the different flow

regimes marked on the experimental runs plotted as a function of maximum temperature differences above/below the cross-over point. For the steady flow regime, the maximum temperature difference in the lower portion of the cavity is higher than that in the upper portion of the cavity. As the flow transitions from steady to periodic to chaotic, this difference begins to decrease and at the end of the chaotic flow regime, the upper and lower maximum temperature differences are almost equal.

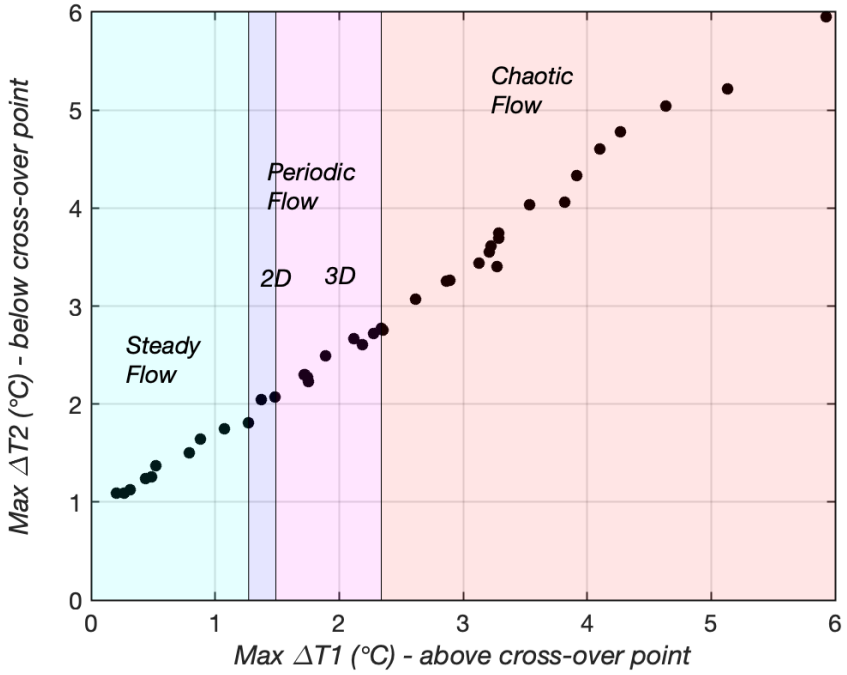

Figure 10.18: Experimental runs and flow regimes mapped as a function of maximum temperature differences above/below the cross-over point of the vertical wall temperature profiles.

10.4 Key Findings

The stability of bi-cellular natural convection for air in a long, tall rectangular cavity of aspect ratio A=10 was studied experimentally. When the buoyant potential of the convection cells of the bi-cellular base flow was increased, the flow transitioned first from steady to 2D unsteady mono-

periodic flow via a Hopf bifurcation. With further increase in flow buoyant potential (Rayleigh number), first a transition from 2D mono-periodic flow to a 3D mono-periodic flow followed by a transition from periodic to chaotic flow was observed.

In previous experimental investigations in closed annular cavities supporting a bi-cellular base flow pattern, the first bifurcation from steady to periodic flow has always been 3D in nature. The observation of 2D periodic flow in the rectangular cavity is important because it establishes that 2D oscillatory modes can exist for air-filled closed cavities with a bi-cellular base flow. Another major difference between the annular cavity experiments described in Chapter 7 and current rectangular cavity experiments was observed in the way in which periodic flows transitioned to chaotic. Mono-periodic flows of the annular cavity system transitioned to an intermediate quasi-periodic regime, which showed a presence of two or more fundamental frequencies before transitioning to chaotic flows. No such intermediate quasi-periodic regime was identified for the rectangular cavity experiments; with the monoperiodic flows directly transitioning to quasi-chaotic flows, which showed a banded presence of frequencies.

In their numerical study of (base), bi-cellular flow in a rectangular cavity of aspect ratio A = 10, Dillon et al. [51] predicted the critical Rayleigh number for the first bifurcation from steady to 2D mono-periodic flow at $Ra_H = 2.2 \times 10^7$. Reeve et al. [50] predicted the first bifurcation from steady to 2D axisymmetric mono-periodic flow at a critical Rayleigh number of $Ra_H = 2.165 \times 10^7$ for natural convection in an annular cavity of A = 10 and radius ratio $\eta = 0.6$ with bi-cellular base flow. Critical Rayleigh number for transition from steady to 3D monoperiodic flow was observed to be $Ra_H = 1.00 \times 10^7$ for the flows observed in annular cavity with non-isothermal walls (described in Chapter 7). For comparison with the current experiments of bi-cellular base flow in

a rectangular cavity, steady flow first transitioned to 2D mono-periodic at a critical Rayleigh number of $Ra_H = 6.27 \times 10^6$.

The oscillatory flows observed in current experiments were caused by a relatively slow fluid movement, with the fundamental frequencies of the periodic regime ranging between 0.019 to 0.051 Hz. When the fundamental frequencies of the 3D periodic regime are scaled with the $\text{Brunt} - \text{Väisälä}\ \frac{\sqrt{g\beta\Delta TH}}{H}$ the resulting dimensionless frequencies remain almost constant at value of 0.04 and appear to be independent of the nominal Rayleigh number. This invariance of dimensionless frequency suggests that the instability mechanism in the rectangular cavity experiments might be related to the Rayleigh-Bernard instability mechanism previously observed for air-flow in cavities with vertical isothermal walls and conducting horizontal walls [72].

Within the periodic regime, the 2D periodic regime was observed over a very small Rayleigh number range, and the flow quickly transitioned from 2D periodic to 3D periodic modes. With a further increase in Rayleigh number, the 3D periodic flow transitioned to a chaotic flow. A similar pattern of bifurcations has been reported by Wright et al. [44] in their experiments in a tall rectangular cavity with isothermal walls. Wright et al. [44] observed that the steady flow first transitioned to a 2D periodic flow and then very quickly transitioned to first to a 3D periodic and subsequently to a chaotic flow. Many numerical studies for cavities with both isothermal [14,17,29,30,31] as well as non-isothermal walls [6,50,51,68] often use the 2D flow assumption for studying natural convection in closed air-filled cavities. The current experiments study along with observations of Wright et al. [44] point to the fact that while this 2D assumption proves useful for getting a general sense of fluid flow within the cavity, it should be used with caution for predicting unsteady flows and bifurcations especially at higher Rayleigh numbers.

Chapter 11

11 NATURAL CONVECTION IN RECTANGULAR CAVITY – CFD MODELING

Natural convection flows observed in the rectangular cavity experiments showed transitions from steady flow to 2D/3D periodic and chaotic flows. Two CFD models, a 2D model and a full 3D model were developed to predict these experimentally observed flow transitions and to understand the instability mechanisms at play. In this chapter, numerical predictions from these two models are presented and results from each model are compared to experimental observations. Accuracy of models and differences in their predictions are addressed.

11.1 2D CFD Model

The first transition from steady flow to periodic flow observed in rectangular cavity experiments was 2D in nature. Further, since length of cavity is 20 times it's width, effect of end-walls on flow at the cavity interior should be negligible, at least at low Rayleigh numbers and flow in central part of the cavity can be assumed as 2D. Therefore, it was decided to first develop a 2D CFD model to study natural convection inside the cavity prior to developing a full 3D CFD model.

The 2D model was developed in Simcenter StarCCM+ where only fluid domain of cavity was modeled and boundary conditions at cavity walls were set corresponding to experimentally measured wall temperatures. In total, 24 transient simulations corresponding to experiments in rectangular cavity were performed.

11.1.1 Numerical Method and Fluid Thermophysical Properties

Two-dimensional, compressible, transient form of Navier-Stokes equations for a Newtonian fluid given by equations (3.12) - (3.14) are solved using the coupled solver of Simcenter StarCCM+. Air is treated as an ideal gas with temperature dependent thermophysical properties. Specific heat is expressed as a cubic polynomial fitted to tabulated data [56] while dynamic viscosity and thermal conductivity are obtained by linear interpolation of tabulated data [56].

11.1.2 Solver Settings, Grid Size, and Time-Step

The transient equations are solved using the coupled solver of Simcenter StarCCM+ with a second-order-upwind spatial discretization for the convective flux terms, a second-order central discretization for diffusion terms and Weiss-Smith Preconditioned Roe's Scheme for discretization of inviscid fluxes. A second-order implicit scheme is used for time discretization and a time step of size of 0.005 seconds is used. A grid size of 20 x 2000 was selected after a grid refinement study based on methods described by Roache [69, 92]. A 2D, orthogonal, uniform, non-staggered, quadrilateral mesh is used with further refinement near walls using prism layer cells. Details of the grid refinement study and error quantification are described in Appendix C. Velocities, temperatures at several points in the flow field and equation residuals were monitored to ensure convergence at each time step.

11.1.3 Boundary Conditions and Initial Conditions

For the opposing vertical walls, temperature profiles based on cubic piecewise splines fitted to experimentally measured temperatures from 30 wall thermocouples were used as boundary conditions. The precise depth of each thermocouple bead embedded in vertical walls is known. The acrylic wall thickness is 3.175mm while thermocouple bead is located at an average depth of

2.73 $\pm$0.03 mm. Consequently, the thermocouple measures temperatures at an average distance of 0.445 mm away from the inner surface of the acrylic wall. For thermocouples located in the heating-band regions, temperature measurement is slightly more than that of the wall inner surface, while in passively cooled regions, the measurement is slightly less. To precisely determine wall temperatures for 2D and 3D numerical work, an estimate of this 'conduction error' due to thermocouple location was made using 1D thermal analysis. Figure 11.1 shows thermal profiles for vertical walls before and after applying temperature correction for experimental run at nominal Rayleigh number of 1.47 x 10^7.

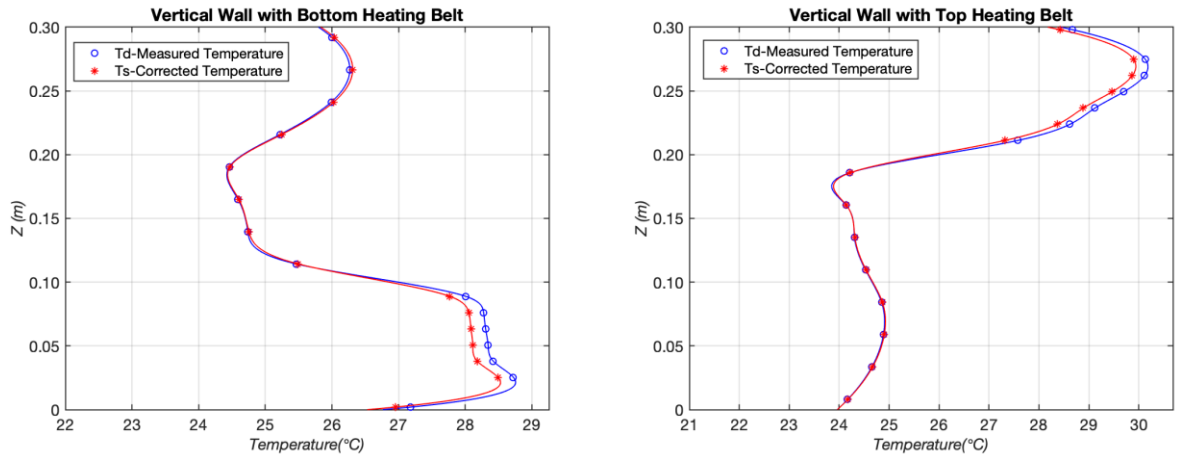

Figure 11.1: Measured and corrected vertical wall temperature profiles for vertical wall with bottom heating belt (left) and vertical wall with top heating belt (right) for an experimental run at nominal Rayleigh number Ra = 1.47 x 10^7.

For top and bottom horizontal walls, a linearly varying temperature profile was prescribed based on the assumption of conduction heat transfer through horizontal walls. This boundary condition is close to reality and also prevents any corner discontinuities in simulation domain due to sudden change in temperature at cavity corners. Figure 11.2 shows the computational domain and boundary conditions applied at each wall. Figure 11.3 shows boundary conditions used for simulating experimental run at nominal Rayleigh number of Ra = 1.47 x 10^7.

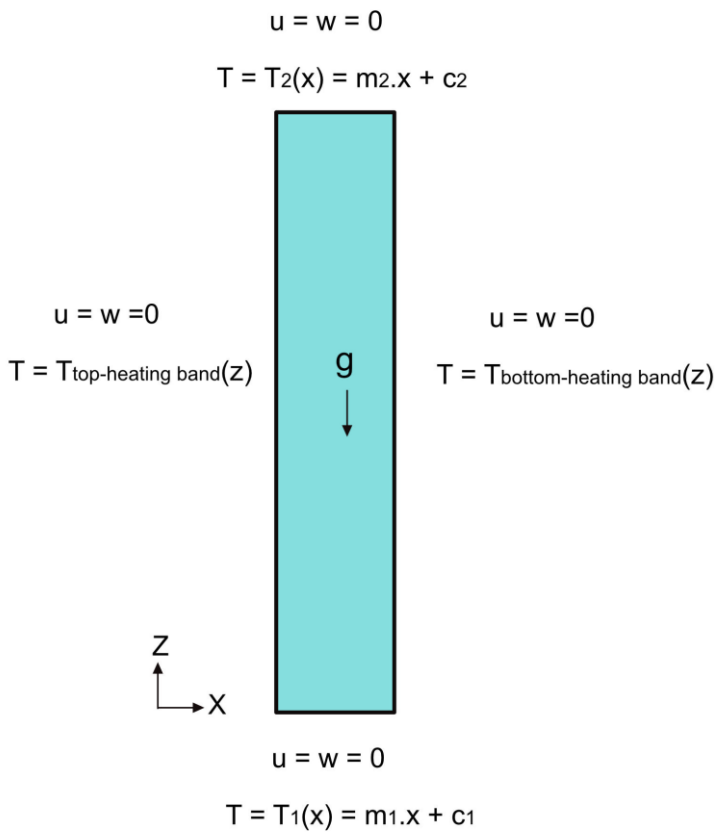

Figure 11.2: Computational domain and boundary conditions for 2D CFD model of rectangular cavity

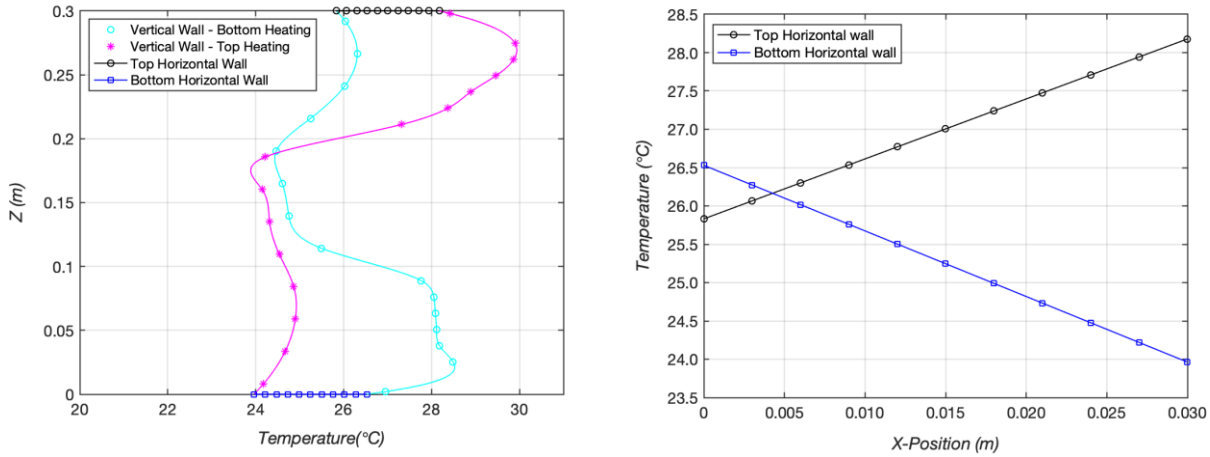

Figure 11.3: Boundary conditions applied at two opposing vertical walls (left) and top and bottom horizontal walls (right) for a simulation corresponding to experimental run at nominal Rayleigh number Ra = 1.47 x 10^7.

In the rectangular cavity experimental setup, flow Rayleigh number was progressively increased over several sets of experiments. The system was never shut-off and each experimental run (except for first experiment) started with flow field of a previous experimental run. Therefore, for numerical simulations corresponding to each experimental run, velocity and temperature fields from a simulation corresponding to a prior experimental run were used as initial conditions. The only exception was the very first simulation for which initial conditions were set corresponding to stationary air at ambient temperature.

11.2 Results

Several 2D simulations were performed corresponding to experimental runs in the rectangular cavity starting with the run for which steady flow was observed in experiments. Flow regimes observed in 2D simulations at different Rayleigh number are discussed in next few sections.

11.2.1 Steady Bi-Cellular Flow

A steady bi-cellular flow was predicted for the very first simulation corresponding to an experimental run at Rayleigh number of 2.26×10^6. For the next few simulations, at successively higher Rayleigh numbers a similar flow pattern was observed. Figures 11.4 (a),(b) show isotherms and streamlines for flow predicted for an experimental run at Rayleigh number of 4.66×10^6. Fluid rises along heated portions of the vertical walls, turns and then falls along the passively cooled portions of opposing vertical walls. This establishes a steady bi-cellular flow comprising of two counter-rotating cells as seen in Fig.11.4(b).

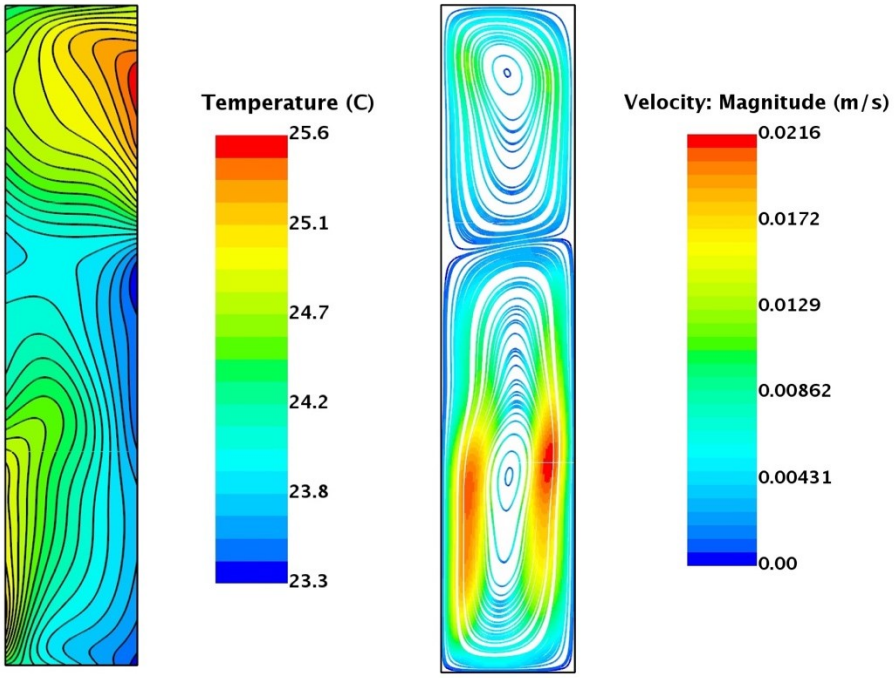

(a) (b)

Figure 11.4: (a) Isotherms and (b) Streamlines showing steady bi-cellular flow for simulation at Ra = 4.66 x 10^6 using the 2D CFD model of rectangular cavity.
Note: Width of cavity (x-dimension) is scaled by *x*2 times for visualization purposes.

Fig. 11.5 shows velocity vector plots for the same simulation. Here, the lower cell is seen rotating in a clockwise direction and the upper cell in an anti-clockwise direction. Velocities in lower cell are much higher as compared to that in upper cell. The weaker upper cell occupies top 1/3rd part of the cavity while the larger and stronger lower cell occupies remainder portion. Figure 11.6 shows X and Z-velocity profiles along the z = H/4 and z = 3H/4 planes located in upper and lower halves of the cavity for a simulation at Rayleigh number of 4.66x 10^6. Fig.11.7 shows Z-velocity and magnitude of velocity along the x = W/3 and x = 2W/3 planes located in right and left halves of the cavity. The direction of motion (clockwise, anticlockwise) and relative magnitudes of upper and lower convection cells are evident from these four plots.

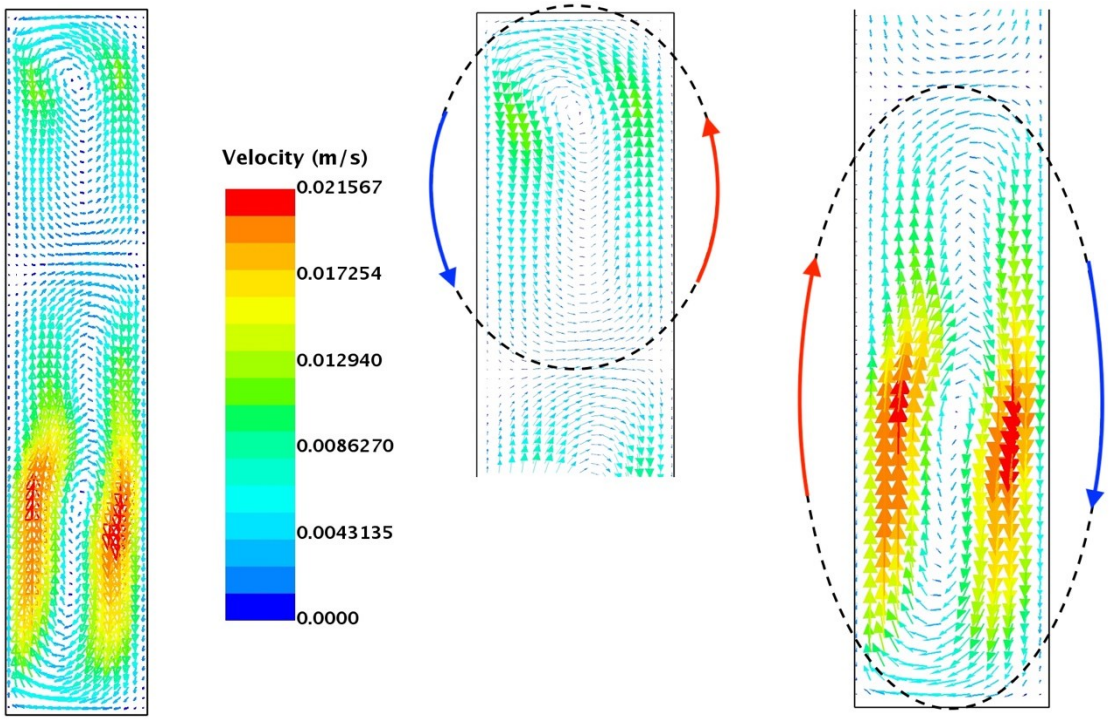

Figure 11.5: Vector plots showing steady bi-cellular flow comprising of upper (center) and lower (right) cells for simulation at Ra = 4.66x 10^6 using the 2D CFD model of rectangular cavity.
Note: Width of cavity (x-dimension) is scaled by *x*2 times for visualization purposes.

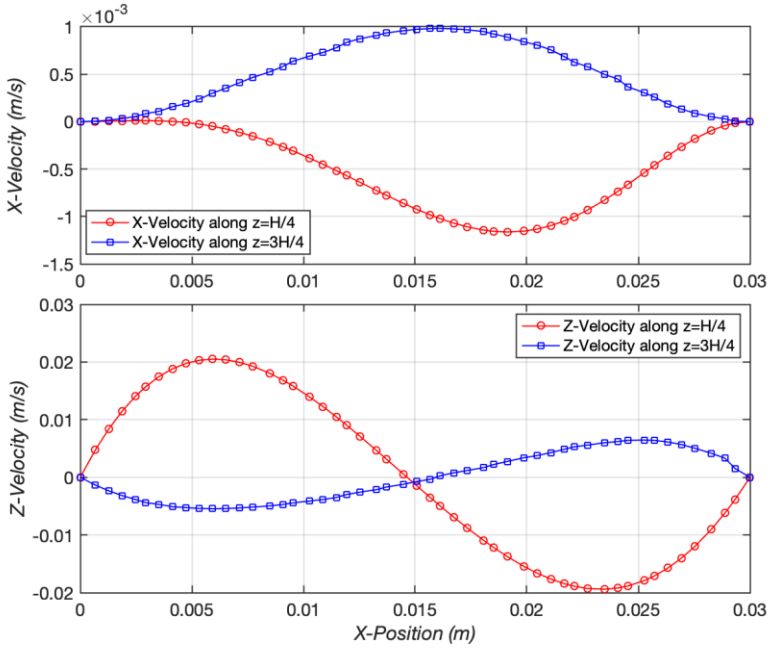

Figure 11.6: X-Velocity(top) and Z-velocity (bottom) along the planes z = H/4 and z = 3H/4 predicted for an experimental run at Ra = 4.66x 10^6.

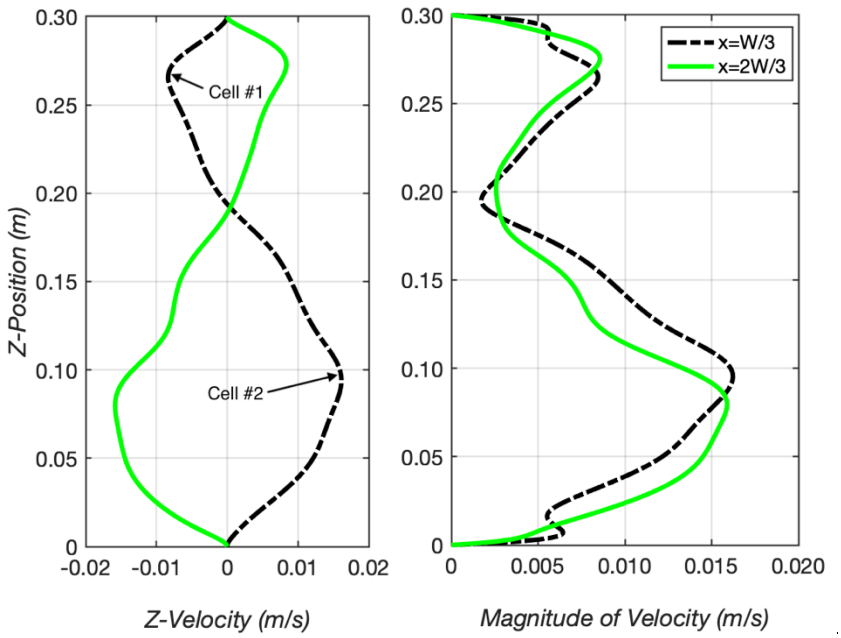

Figure 11.7: Z-Velocity (left) and magnitude of velocity (right) along the planes x = W/3 and x = 2W/3 predicted for an experimental run at Ra = 4.66x 10^6.

Velocity at center of both cells is close to zero, indicating two relatively stagnant cores. The two cells interface each other in the region between planes z = 0.2 m and z = 0.18 m. On account of counter-rotating cells, the Z-velocity is positive above interface and negative below interface for plane x = W/3 and vice-versa for plane x = 2W/3. For steady-bi-cellular flows, interface location between two counter-rotating convection cells was stable and time invariant. The maximum velocities in upper and lower convection cells and relative strength of the upper convection cell increased with increase in Rayleigh number. A steady bi-cellular flow regime was observed for all simulations between Ra = 2.26 x 10^6 to 8.71 x 10^6. Figures 11.8(a),(b) (d) and (e) show the isotherms and streamlines for simulations at Ra = 3.08 x 10^6 and Ra = 6.99 x 10^6.

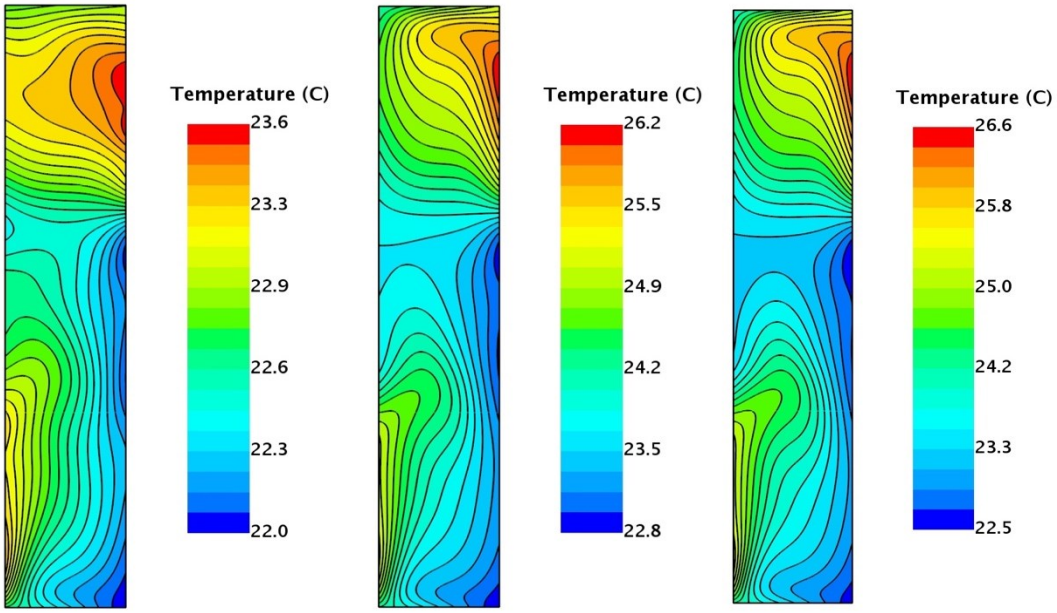

(a) (b) (c)

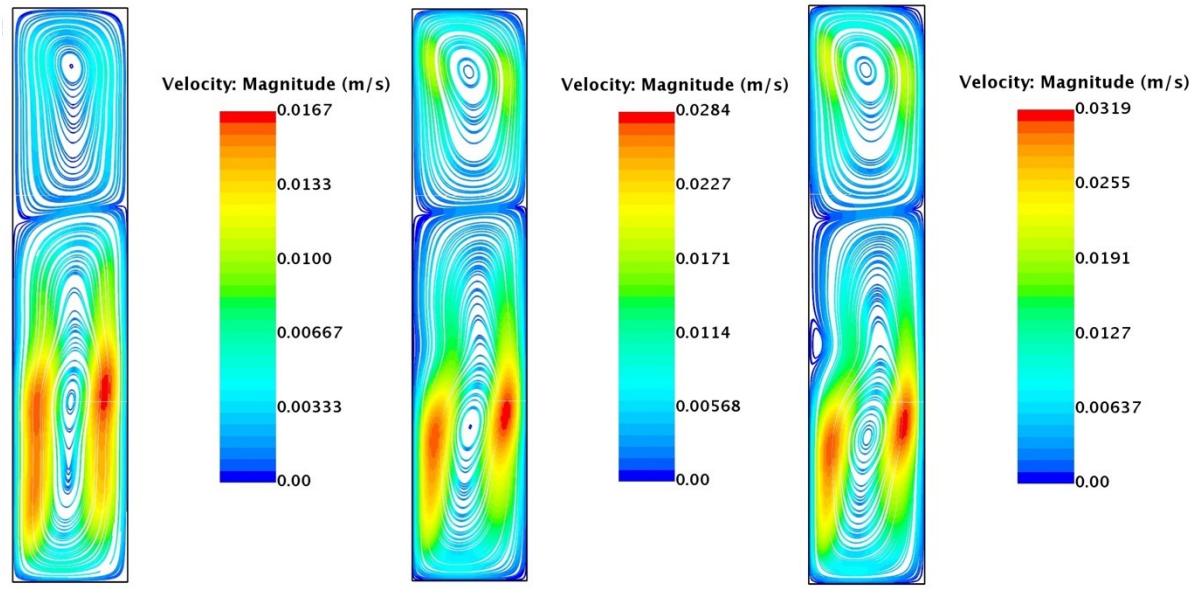

(d) (e) (f)

Figure 11.8: (a),(b)Isotherms and (d),(e)Streamlines showing steady bi-cellular flow for simulations at Ra = 3.08 x 10^6 and Ra = 6.99 x 10^6; (c)Isotherms and (f)Streamlines showing steady tri-cellular flow for simulation at Ra = 9.06 x 10^6 using the 2D CFD model of rectangular cavity.

Note: Width of cavity (x-dimension) is scaled by *x*2 times for visualization purposes.

11.2.2 Steady Tri-cellular Flow

When Rayleigh number was increased to Ra = 9.06 x 10^6 starting from a steady bi-cellular flow solution at Ra = 8.71 x 10^6, a third smaller convection cell first appeared adjacent to the lower convection cell. Isotherms and streamlines with steady tri-cellular flow observed for simulation at Ra = 9.06 x 10^6 are shown in Figs. 11.8(c) and (f). The same pattern was continually observed for simulations between Ra = 9.06 x 10^6 and Ra =1.38x 10^6. Figure 11.9 shows isotherms and streamlines for simulations at Ra = 1.11 x 10^7 , Ra = 1.26 x 10^7 and Ra = 1.38 x 10^7 respectively. For each consecutive simulation of this regime, size of the smaller third convection cell went on increasing, as can be seen in Fig. 11.9 (d)-(f).

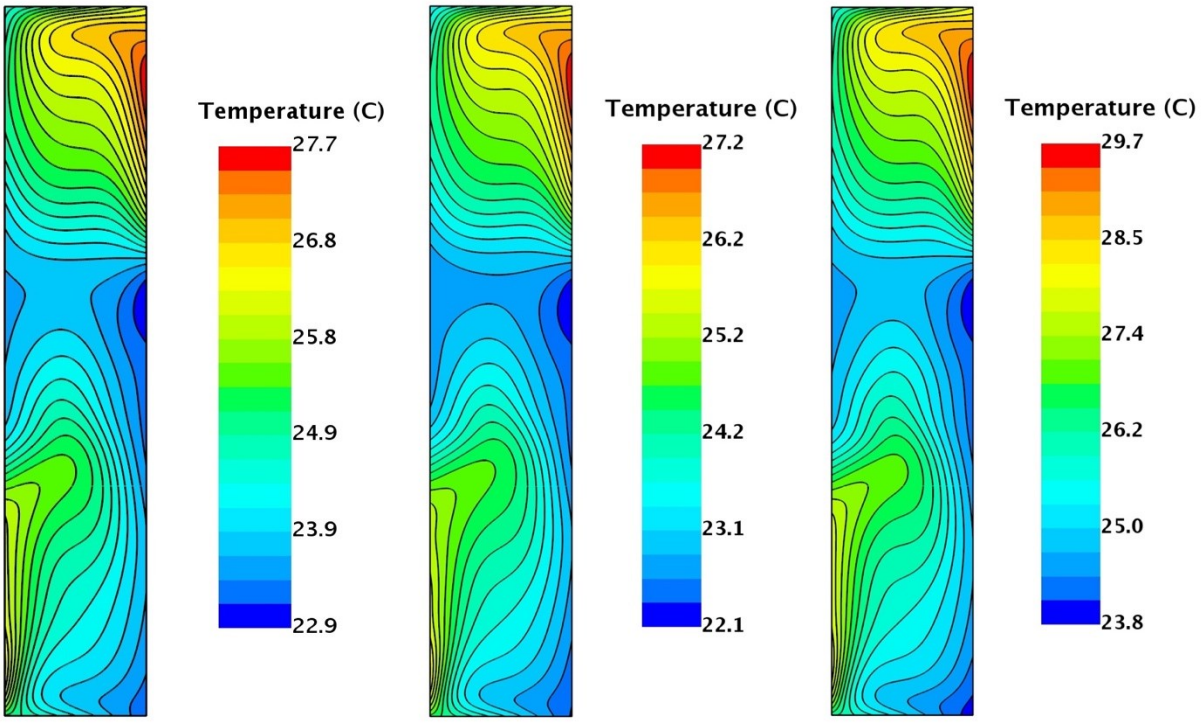

(a) (b) (c)

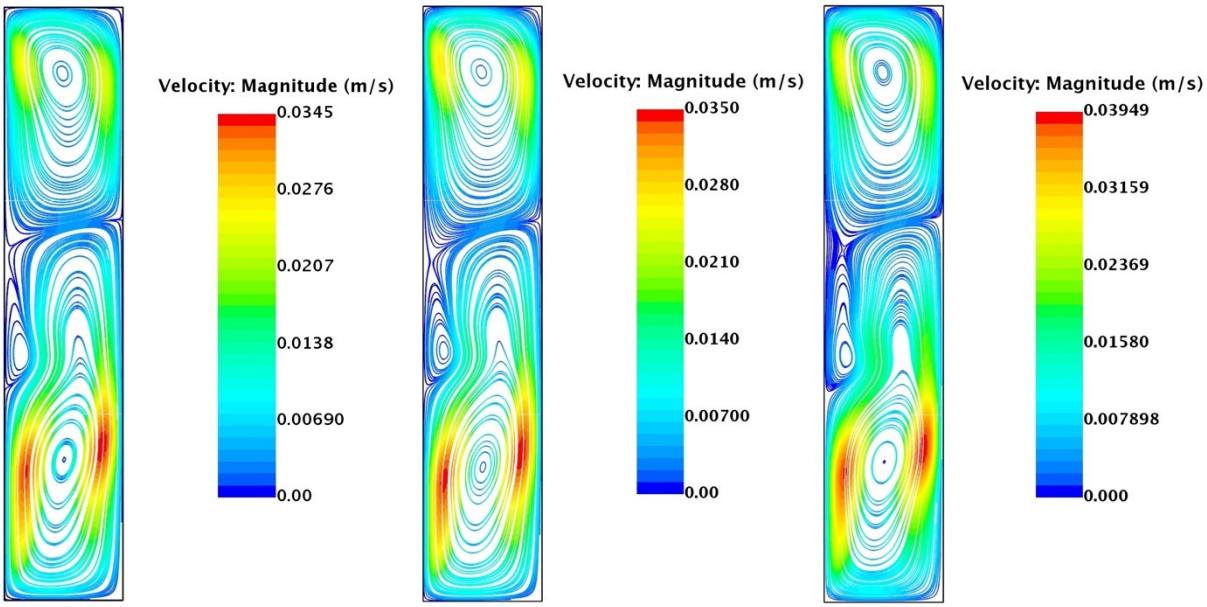

(d) (e) (f)

Figure 11.9: (a),(b),(c) Isotherms and (d),(e),(f) Streamlines showing steady tri-cellular flow for simulations at Ra = 1.11 x 10^7 , Ra = 1.26 x 10^7 and Ra = 1.38 x 10^7 using the 2D CFD model of rectangular cavity.
Note: Width of cavity (x-dimension) is scaled by *x*2 times for visualization purposes.

For the simulation at Ra = 1.38 x 10^7, initial perturbations in temperature and velocity fields oscillated for a long time before decaying and reaching a time-invariant solution. This behavior indicates that the system is close to a bifurcation point. Figure 11.10 (a) shows velocity and temperature time series for two points inside the cavity over a time period of 200 seconds for simulation at Ra = 1.38 x 10^7. Velocity and temperatures are seen to asymptote to a steady state with gradually decaying oscillations. In the velocity phase-space plot for the same simulation, shown in Fig. 11.10(b), we can see the trajectory following a stable spiral and ultimately approaching a stable limit point at center of the spiral.

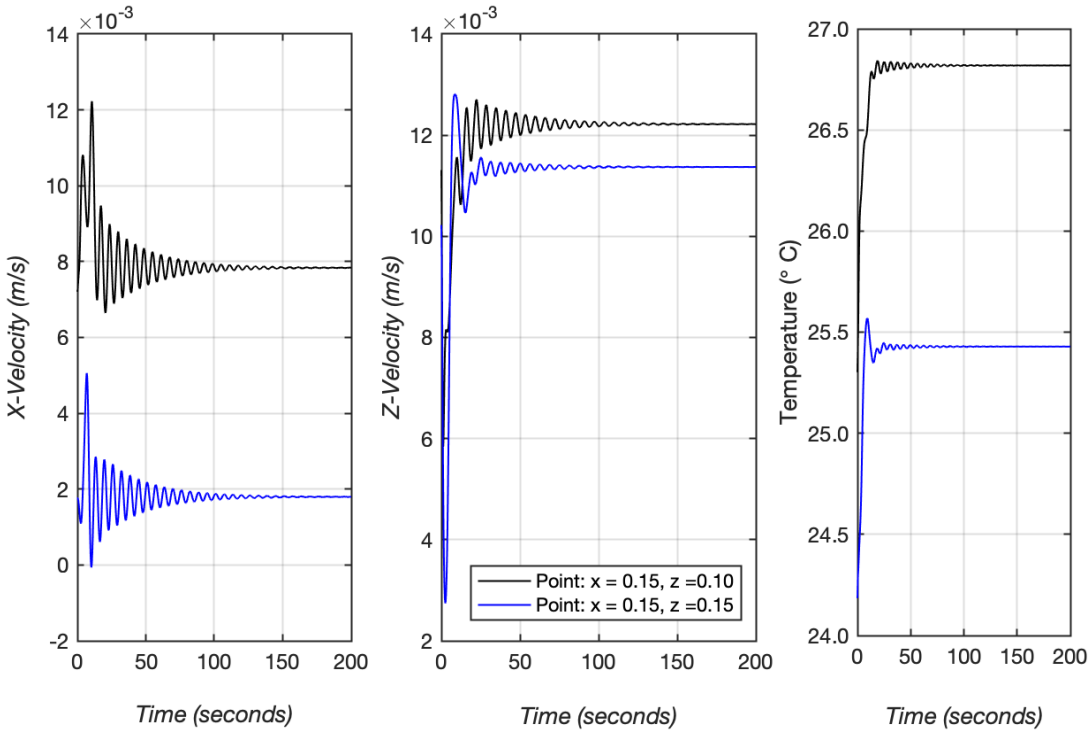

(a)

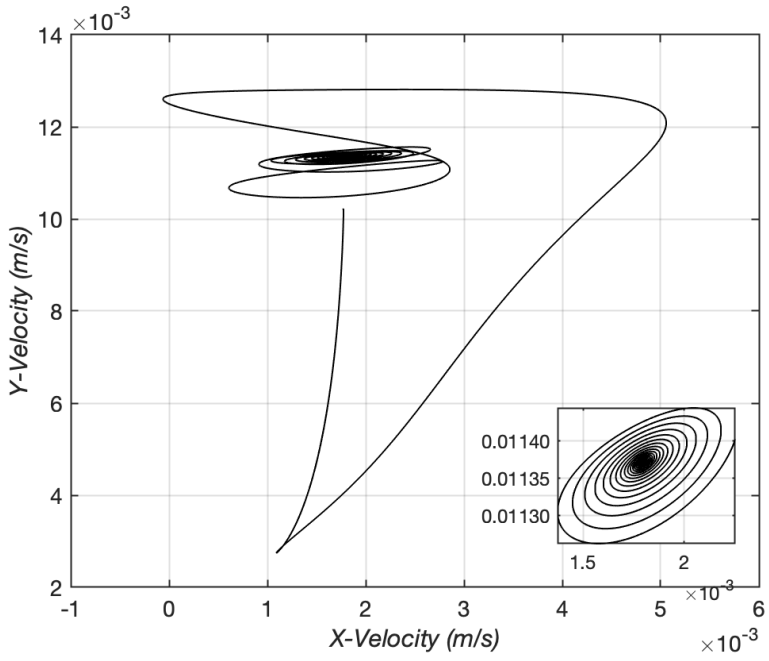

(b)

Figure 11.10: (a) Velocity and temperature time series for two points (x = 0.015m, z = 0.15m) and (x = 0.015m, z = 0.10m) for simulation at Ra = 1.38 x 10^7; (b) Velocity phase space at point (x = 0.015m ,z = 0.15m) for simulation at Ra = 1.38 x 10^7.

Fig. 11.11 shows velocity vector plots for the simulation at Ra = 1.38 x 10^7. Out of the three cells seen in Fig. 11.11, the larger lower cell rotates in clockwise direction whereas the upper cell and smaller third cell adjacent to lower cell, rotate in an anticlockwise direction. Velocities in the smaller third cell are much lower compared to the other two cells, nonetheless, a weak circulation does exist inside in this cell.

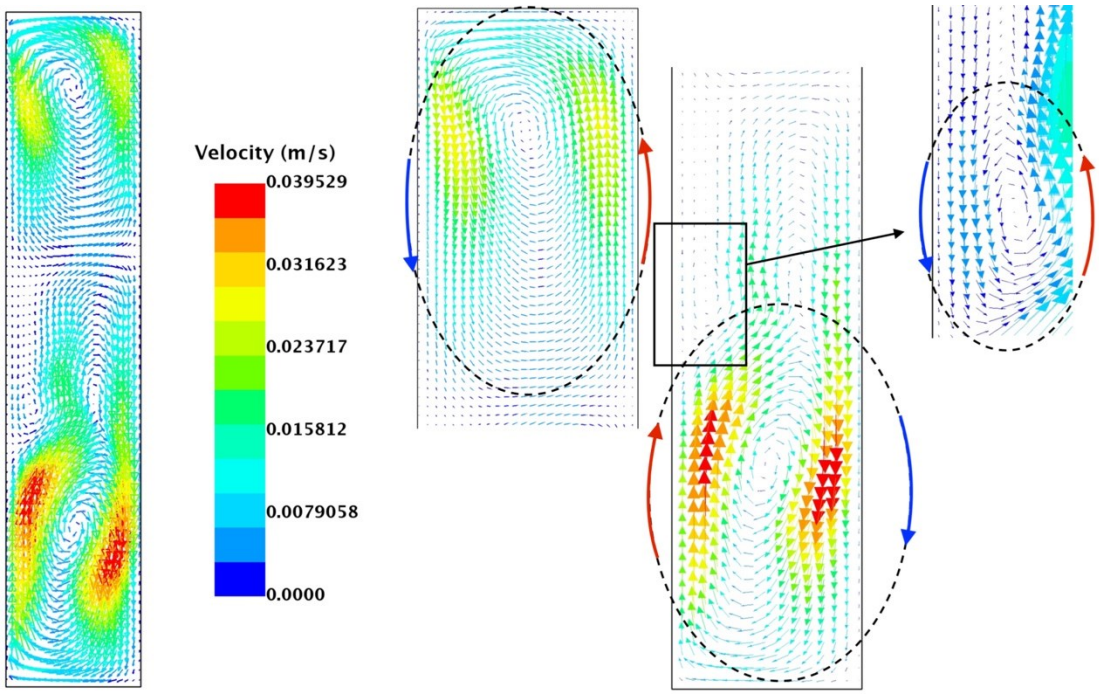

Figure 11.11: Vector plots showing steady tri-cellular flow(left) comprising of an upper (center-left), a lower (center-right) and a smaller lower cell(right) for simulation at Ra = 1.38 x 10^7 using the 2D CFD model of rectangular cavity.
Note: Width of cavity (x-dimension) is scaled by *x*2 times for visualization purposes.

Careful observation of the isotherms and streamlines in Fig. 11.9 shows that the smaller third convection cell is formed when a fraction of cool air from upper convection cell moves further downwards along the cooler section of the left cavity wall (wall with bottom heating) and occupies space previously occupied by the larger lower cell. The downward moving fluid in this third

smaller convection cell picks up heat as it moves along the left wall and then turns and begins to move upwards when it encounters the warm upward moving stream of air from the lower convection cell. The larger clockwise rotating lower cell now interfaces two anticlockwise rotating cells, one on top and one on its left side. These interfaces are stable and time invariant. Figure 11.12 shows the X and Z-velocity profiles along three planes z = 3H/4, z = 41H/100 and z = H/4 located in the upper and lower halves of cavity for a simulation at Rayleigh number of 1.38 x 10^7. The plane z = 41/100H passes though the center of the third convection cell. Fig. 11.13 shows the Z-velocity and magnitude of velocity along the x = W/3 and x = 2W/3 planes located on the right and left halves of cavity for the same simulation. Three peaks visible on the Z-velocity plot along the x = W/3 planes indicate the relative locations and strengths of the three convection cells.

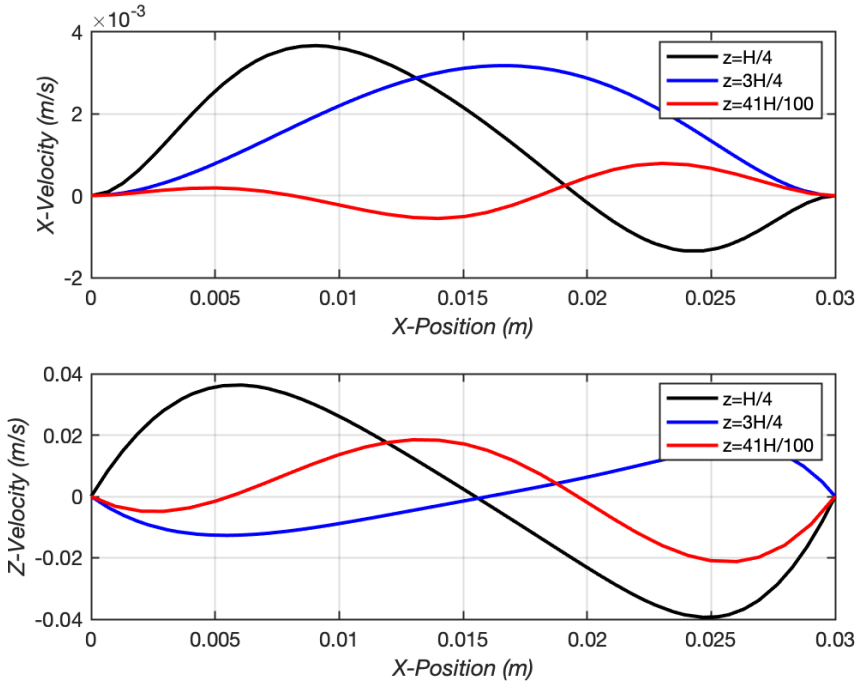

Figure 11.12: X-Velocity(top) and Z-velocity (bottom) along the planes z = H/4, z = 41H/100 and z = 3H/4 for simulation at Ra = 1.38 x 10^7.

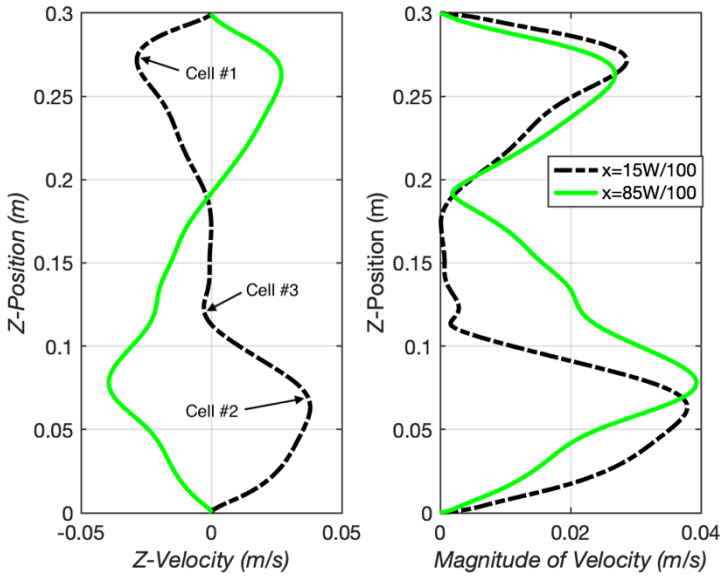

Figure 11.13: Z-Velocity (left) and magnitude of velocity (right) along the planes x = W/3 and x = 2W/3 for simulation at Rayleigh number Ra = 1.38 x 10^7.

11.2.3 Oscillatory Flow – Three/Four Unsteady Cells

Starting from the tri-cellular steady flow solution at Ra = 1.38 x 10^7, when the Rayleigh number was further increased to Ra = 1.47 x 10^7, an unsteady oscillatory flow solution was obtained. Figure 11.14(a) show oscillations in velocity and temperature fields that develop within the flow. Oscillation amplitudes grows exponentially till around t = 350 seconds after which they asymptote to a constant value. The oscillatory flow is monoperiodic with a fundamental frequency of 0.161 Hz. A single stable limit cycle is visible in the velocity phase-space plot shown in Fig. 11.14(b). Power spectral density plots for velocity and temperature measured at a monitoring point are shown in Fig. 11.14(c). PSD plots indicate that both velocity and temperature fields oscillate with same fundamental frequency. This transitional behavior from steady to 2D monoperiodic flow is characteristic of a supercritical Hopf bifurcation [30,31,50].

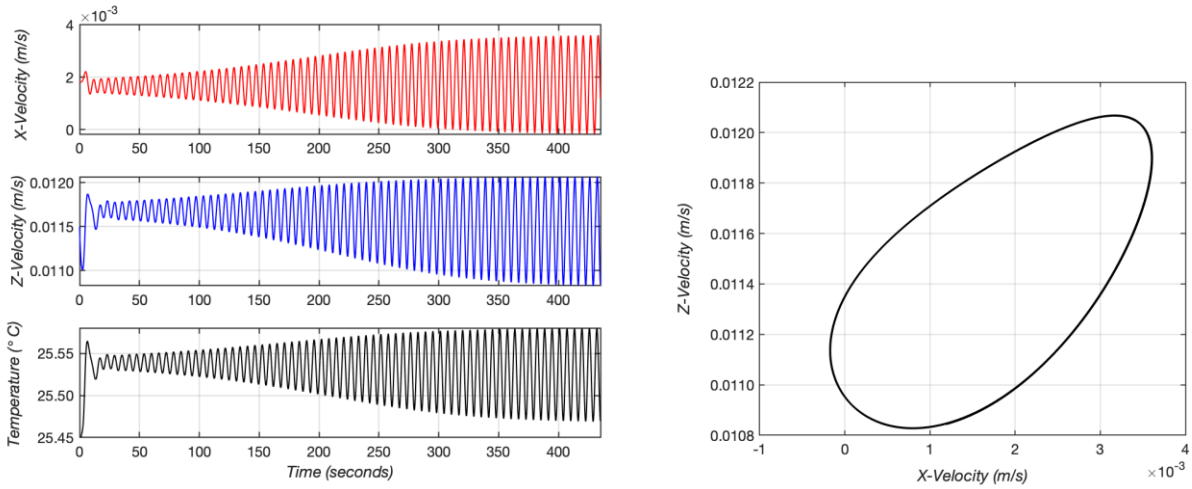

(a)

(b)

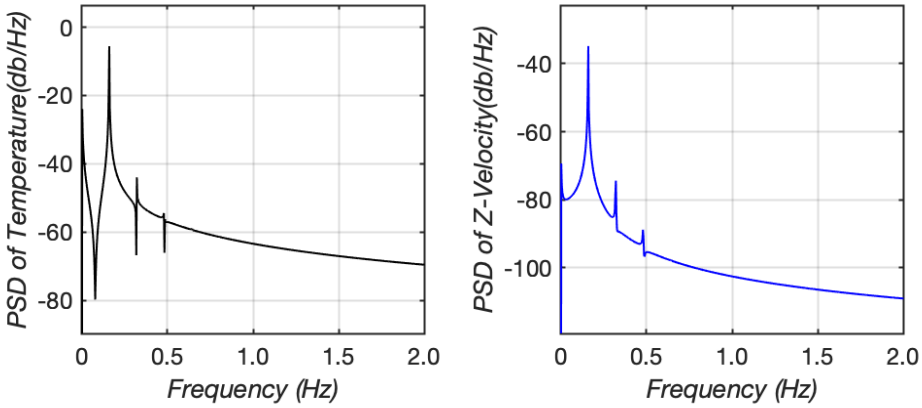

(c)

Figure 11.14: (a) X-velocity, Z-velocity and temperature time series for monitoring points x = 0.015m, z = 0.15m for simulation at Ra = 1.47 x 10^7; (b) Velocity phase space of at point (x = 0.015m, z = 0.15m) for simulation at Ra = 1.47 x 10^7 showing a stable limit cycle; (c) Power spectral density(PSD) of temperature (left) and Z-velocity (right) measured at monitoring point (x = 0.015m, z = 0.10m) for simulation at Ra = 1.47 x 10^7.

As the Rayleigh number was increased further, more unsteady periodic flows with progressively higher oscillation amplitudes and fundamental frequencies were predicted. Figures 11.15(a),(b), (c),(d) show the evolution of isotherms and streamlines for a periodic flow observed at Ra = 1.54 x 10^7 over one period of oscillation (π = 6.3 seconds). In first half of oscillation cycle, the smaller third convection cell begins to increase in size and simultaneously move downwards

in the cavity. In the process, it encroaches into space previously occupied by lower convection cell. The larger lower convection cell then splits into two smaller cells to accommodate this downward-moving and now larger third convection cell. By the end of the first half of the oscillation cycle, there are four cells inside the cavity: two clockwise and two counterclockwise rotating. In the second half of oscillation cycle, the third convection cell, now unable to move further downwards due to splitting of the lower convection cell, begins to move upwards while also shirking in size. As the third convection cell moves upwards, the two split parts of the lower convection cell, start to merge back. At end of the oscillation cycle, the lower convection cell is back to its original size, and there are again three cells inside the cavity. This back and forth movement of convection cells causes oscillations in temperature and velocity fields.

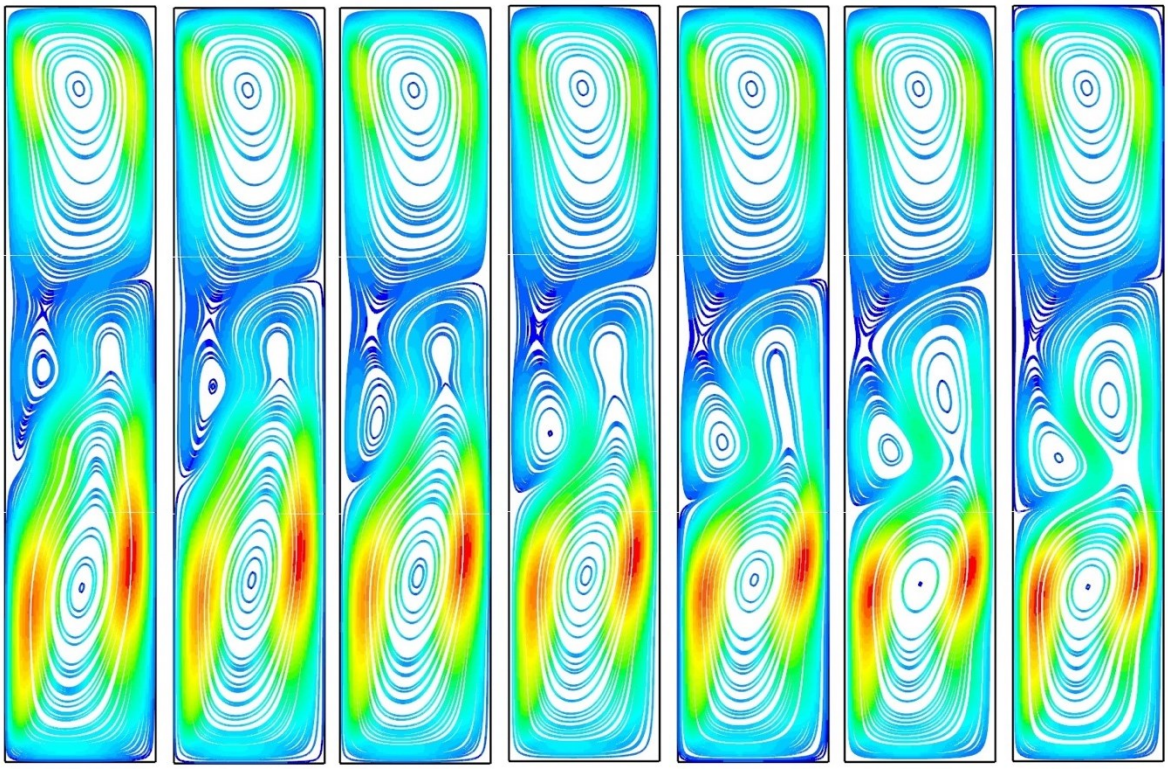

$t = 0$ $t = 0.08\pi$ $t = 0.16\pi$ $t = 0.24\pi$ $t = 0.32\pi$ $t = 0.40\pi$ $t = 0.48\pi$

(a)

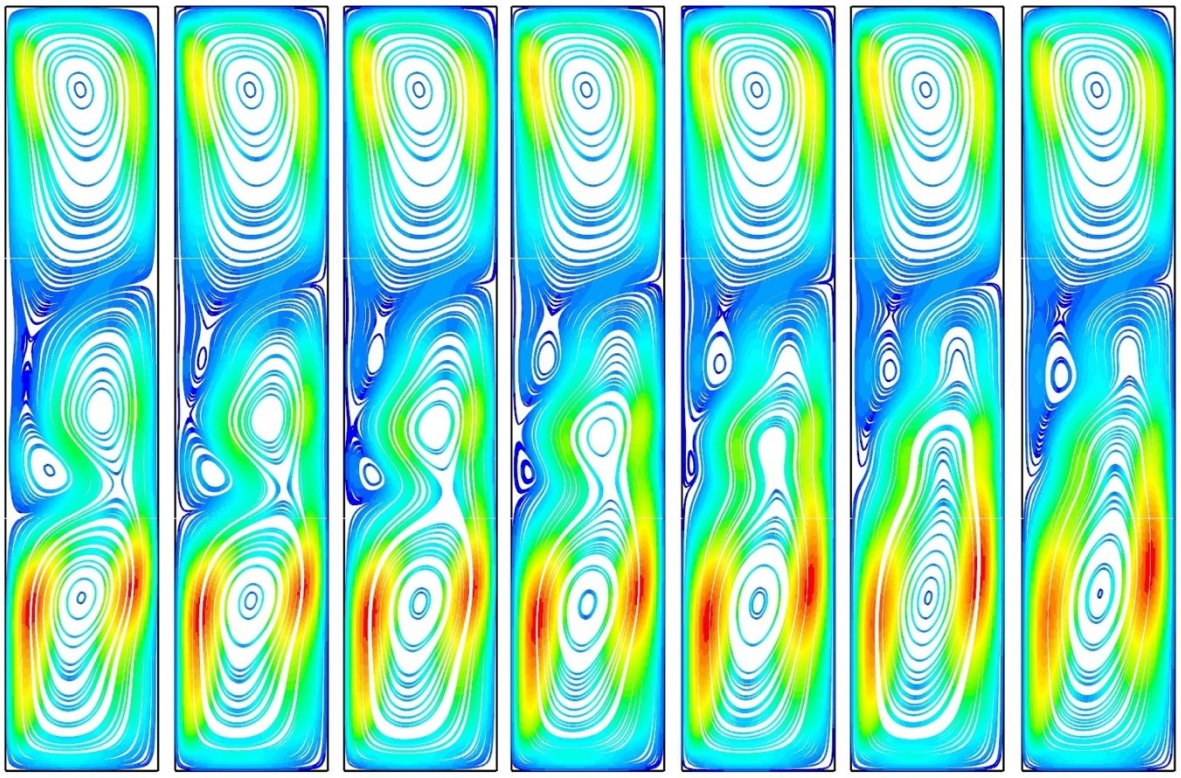

t = 0.57π t = 0.65π $t = 0.73\pi$ $t = 0.81\pi$ $t = 0.89\pi$ $t = 0.97\pi$ $t = \pi$

(b)

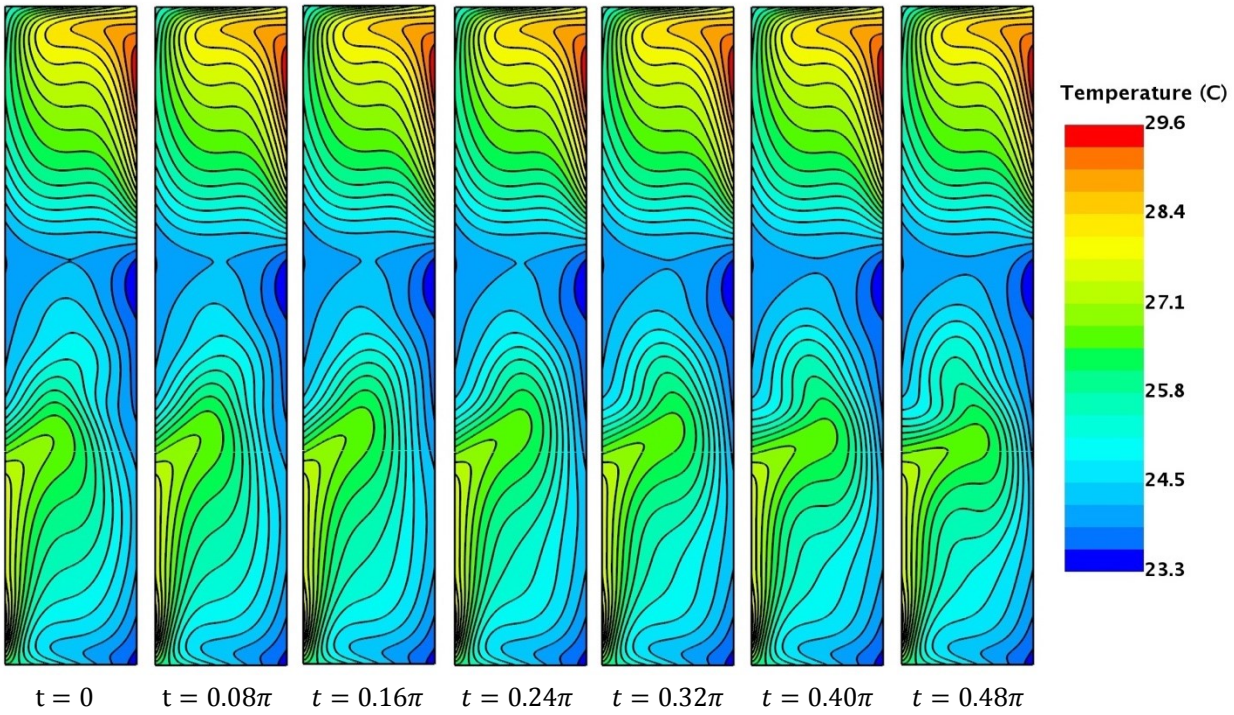

t = 0 t = 0.08π $t = 0.16\pi$ $t = 0.24\pi$ $t = 0.32\pi$ $t = 0.40\pi$ $t = 0.48\pi$

(c)

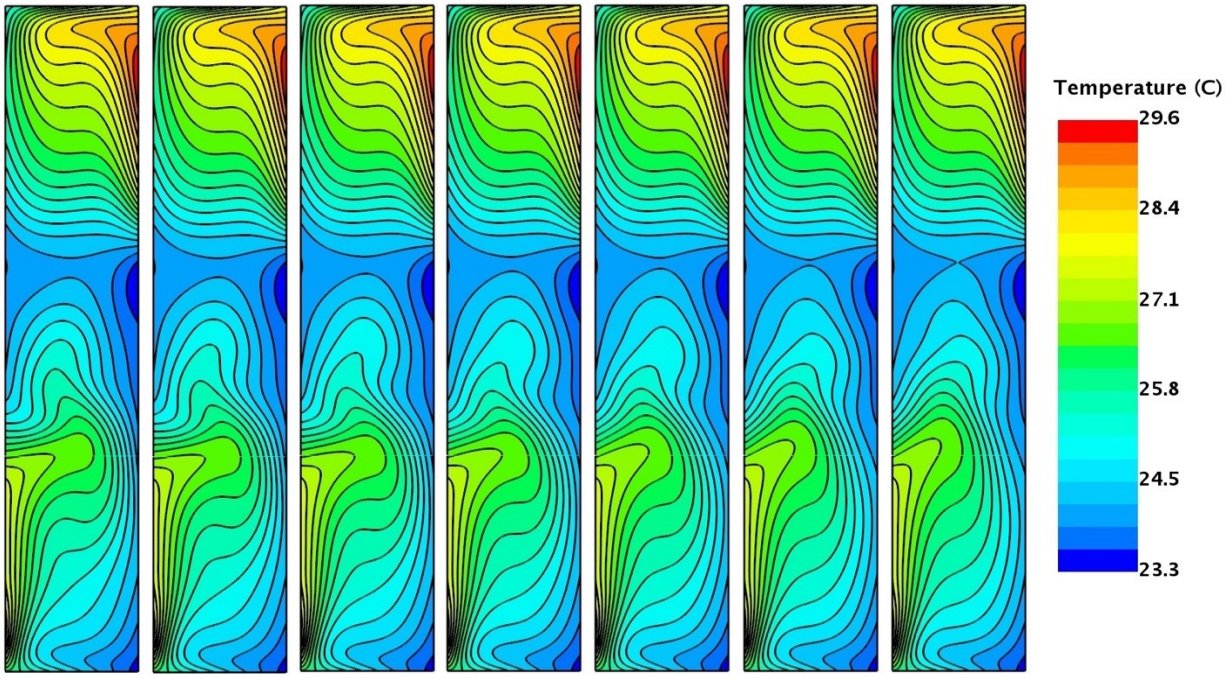

(d)

Figure 11.15: (a),(b) Streamlines and (c),(d) Isotherms for unsteady periodic flow over one oscillation period ($\pi = 6.3\ seconds$) for simulation at Ra = 1.54 x 10^7 using the 2D CFD model of rectangular cavity.
Note: Width of cavity (x-dim) is scaled by *x*2 times for visualization purposes

Physical description of the oscillatory phenomenon is as follows: A portion of cool air from downward moving stream of upper convection cell moves further down along the left wall of the cavity. As it moves downwards it picks up heat from the wall and then begins to move upwards. This circulation brings into existence the smaller third convection cell. Initially, this system of three convection cells is stable: steady tricellular flow. With an increase in Rayleigh number (temperature difference), more and more fluid from the upper convection cell moves into the smaller third convection cell, making it larger and more energetic. The increased strength increases interaction between anticlockwise rotating third convection cell and clockwise rotating lower

convection cell. On account of this interaction, the relatively cooler upward moving air from third convection cell picks up heat from the much warmer upward moving air from lower convection cell. Resultant rise in air temperature inside the third convection cell aids in its circulation causing it to progress further downward in the cavity and increase in size.

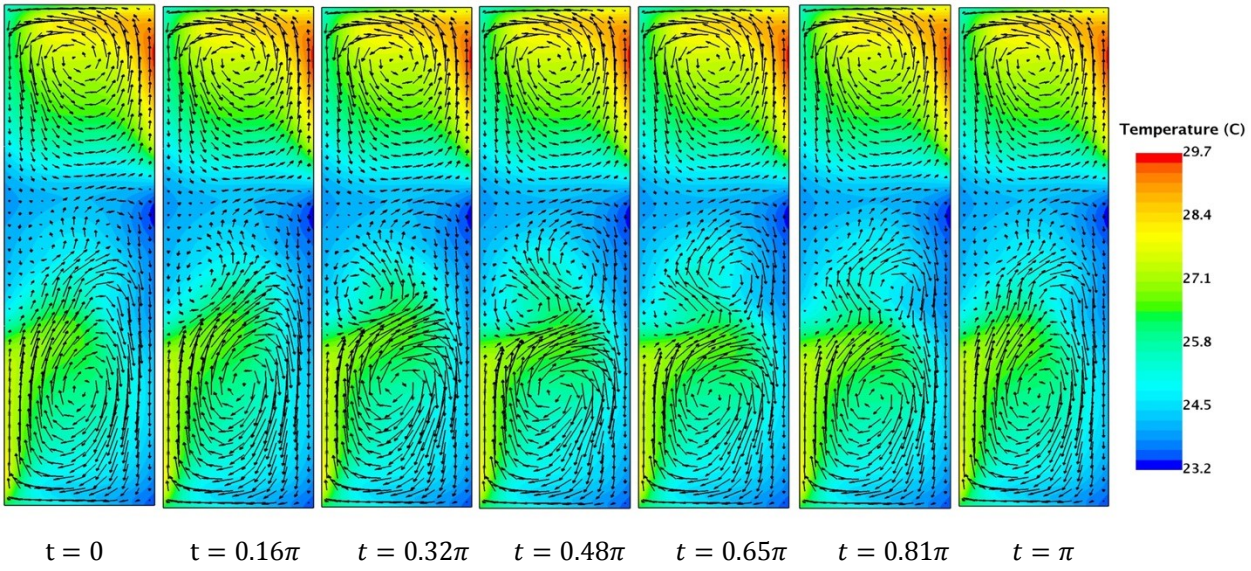

Figure 11.16: Flow vectors superimposed on temperature field for unsteady periodic flow over one oscillation period ($\pi = 6.3\ seconds$) for simulation at Ra = 1.54 x 10^7 using the 2D CFD model of the rectangular cavity.
Note: Width of cavity (x-dim) is scaled by x3 times for visualization purposes

On the other hand, loss of heat from lower convection cell to third convection cell causes it to shirk in strength and size. Third convection cell now occupies some of the space previously occupied by lower convection cell. Change in location and size of third and lower convection cells leads to a fourth convection cell forming adjacent to the third convection cell. This fourth clockwise rotating cell interfaces the third anticlockwise rotating cell and feeds into the lower clockwise rotating cell. In the process, some of the heat circulated in third convection cell is picked up by fourth convection cell and moved back into lower convection cell. The lower convection

cell aided by this heated air from fourth convection cell begins to grow in strength and size. At the same time, the third convection cell, stripped of some of its heated air, shrinks in size and retreats upwards. When it finally moves back to its original position, the fourth convection cell merges back into the lower convection cell. This process repeats continuously, giving rise to the oscillatory motion. Figure 11.16 shows the temperature contour plots superimposed with velocity vectors over a single period for oscillation for simulation at Ra = 1.54 x 10^7 . Physical phenomenon described in the above section above can be observed in these snapshots.

Figure 11.17 and 11.18 show the variation in Z-Velocity and X-Velocity along several horizontal and vertical planes inside the cavity over time duration of one oscillation cycle.

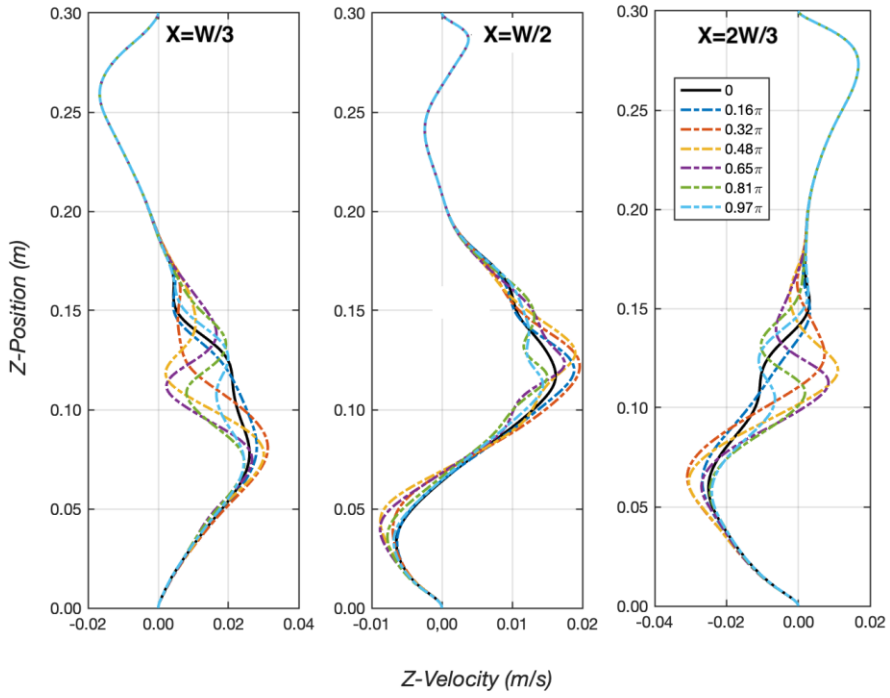

Figure 11.17: Z-velocity along the planes x = W/3, W/2 and 2W/3 over one oscillation period ($\pi = 6.3\ seconds$) for simulation at Ra = 1.54 x 10^7.

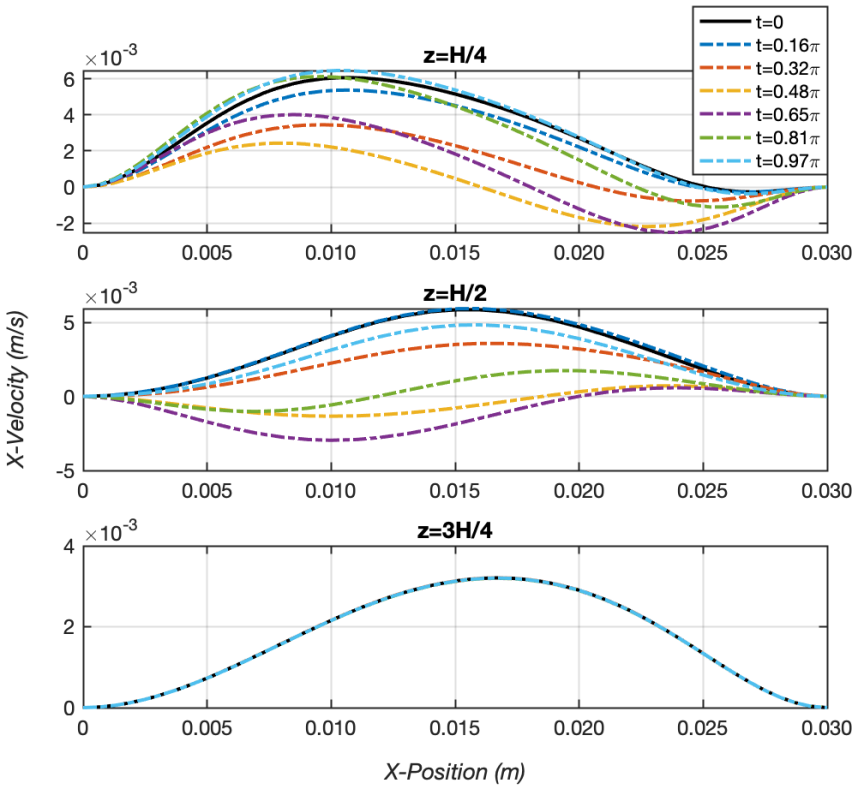

Figure 11.18: X-velocity along the planes Z = H/4, H/2 and 3H/4 over one oscillation period ($\pi = 6.3\ seconds$) for simulation at Ra = 1.54 x 10^7.

It is evident from Figs. 11.17 and 11.18 that most of the fluid movement occurs in the cavity region between planes Z = 0.05m and Z = 0.18m. Fluid in top portion of cavity occupied by upper convection cell (Z = 0.30m to Z = 0.20m) and bottom end of cavity (Z = 0 m to Z = 0.04m) remains almost unperturbed throughout the oscillation cycles. Maximum amplitude of temperature/velocity oscillations is observed at interface of convection cells near the plane Z = 0.12m. Figures 11.19 and 11.20 show oscillation amplitudes and PSD for temperature measurements at several points on the plane z = W/2 for periodic flow predicted at Ra = 1.59 x 10^7. Fundamental frequency of oscillations remains the same no matter where the monitoring point is located inside the cavity. However, oscillation amplitude and number of harmonics observed in PSD seem to depend on location of measurement.

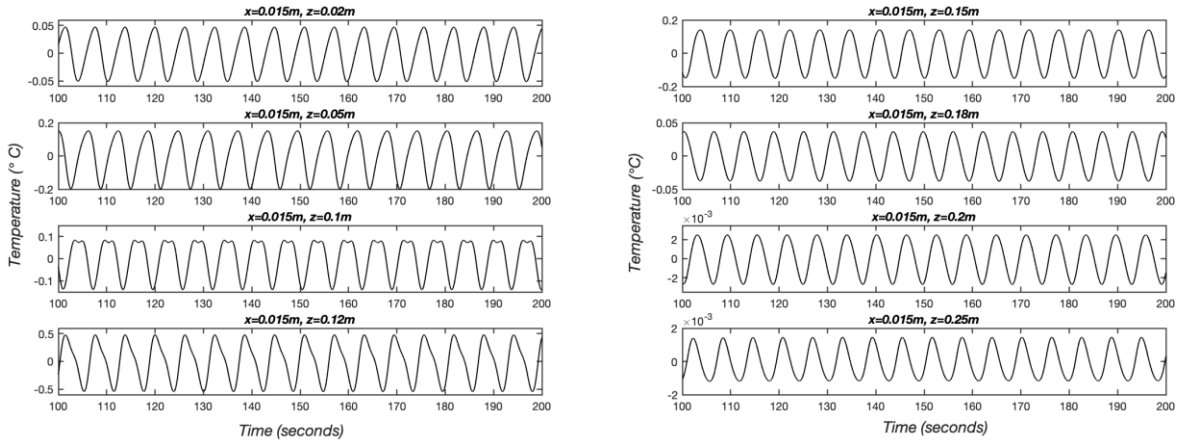

Figure 11.19: Temperature time series for eight points on the plane z = W/2 for periodic flow predicted at Ra = 1.59 x 10^7.

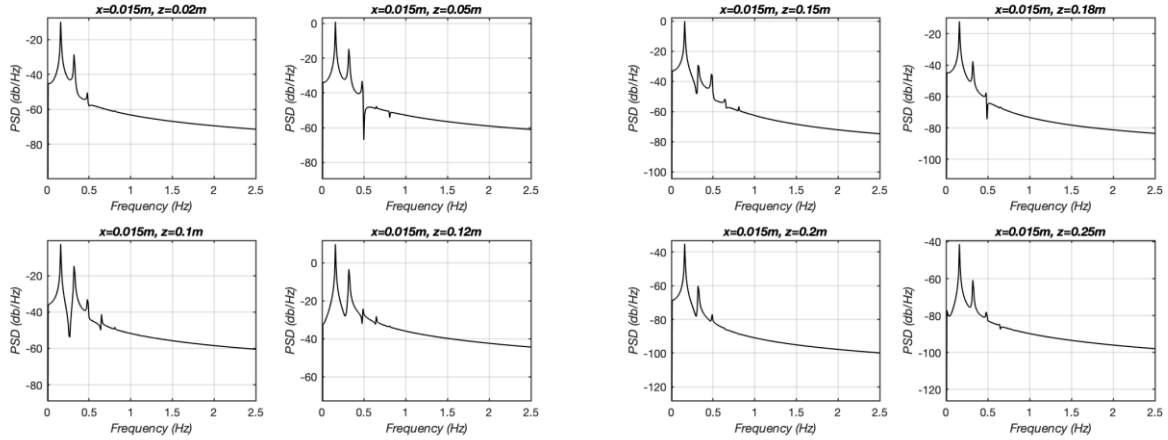

Figure 11.20: Power spectral density of temperature measurements at eight points on the plane z = W/2 for periodic flow predicted at Ra = 1.59 x 10^7.

With a further increase in Rayleigh number, more periodic flow solutions were predicted by the 2D model. Even for simulation corresponding to the very last experimental run at Ra = 2.03 x 10^7 where chaotic flow was observed in experiments, the 2D model still predicted a monoperiodic flow. A transition from periodic to chaotic flow was never seen in the 2D numerical study. Figure 11.21 shows the variation in amplitude and time-period of oscillation measured at monitoring point

x = 0.015m, z = 0.15m for simulations predicting 2D periodic flows. Oscillation time-period decreases, and oscillation amplitude increases with increase in Rayleigh number. This trend is similar to observations for 2D periodic flow in rectangular cavity experiments.

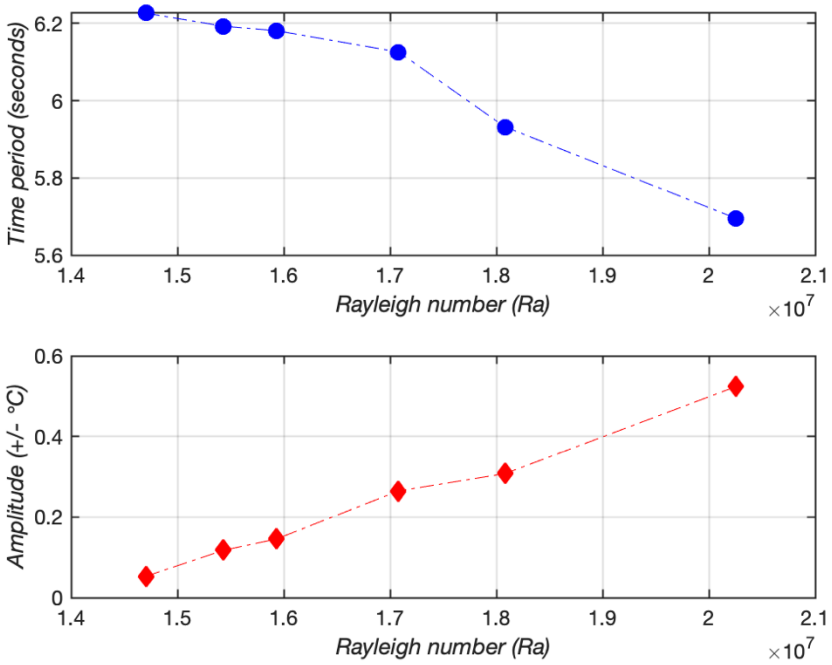

Figure 11.21: Variation in amplitude and time-period of oscillation with Rayleigh number for simulations that predict 2D periodic flows.

11.3 Key Results of 2D CFD Model and Comparison with Experiments

In 2D numerical study of rectangular cavity of aspect ratio A = 10 with non-isothermal walls, a steady bi-cellular flow was observed at low Rayleigh numbers. With increase in Rayleigh number, the steady bi-cellular flow bifurcated to a steady tri-cellular flow at Ra = 9.06 x 10^6. A second bifurcation from steady tri-cellular flow to unsteady 2D periodic flow occurred via a Hopf bifurcation at Ra = 1.47x 10^7. For periodic flows, the number of cells inside the cavity fluctuates between three and four over one oscillation cycle. An interplay between these three/four

convection cells is responsible for periodic oscillations in temperature and velocity fields. Table 11.1 summarizes different flow regimes predicted by the 2D CFD model.

Table 11.1: Air-flow regimes with increasing Rayleigh number predicated by the 2D CFD model.

Flow Regimes	Rayleigh Number Range
Steady Bi-Cellular	$Ra \leq 8.71 \times 10^6$
Steady Tri-cellular	$9.06 \times 10^6 \leq Ra \leq 1.38 \times 10^7$
2D Periodic	$Ra \geq 1.47 \times 10^7$

Table 11.2 draws a comparison between the periodic regimes observed in experiments and those predicted by the model.

Table 11.2: Rayleigh numbers ranges for flow regimes, fundamental frequencies and oscillation amplitudes for periodic flows observed in experiments and those predicted by the 2D CFD model.

	Flow Regimes	Nominal Rayleigh Number Range (Ra)	Frequencies (Hz)	Amplitude (ºC)
Simulations	2D Periodic	$1.47 \times 10^7 \leq Ra \leq 2.03 \times 10^7$	0.160 to 0.177	0.05 to 0.5
Experiments	2D Periodic	$6.27 \times 10^6 \leq Ra \leq 6.56 \times 10^6$	0.032 to 0.051	0.05 to 0.06
	3D Periodic	$6.99 \times 10^6 < Ra \leq 9.35 \times 10^6$	0.019 to 0.042	0.1 to 0.4

The 2D model correctly predicts transition from steady flow to 2D mono-periodic flow observed in the experiments. However, this bifurcation is predicted at a much higher Rayleigh number than

observed in experiments and the fundamental frequencies predicted for 2D periodic regime are almost five times higher than in experiments. The experimentally observed periodic regime is comprised of 2D and 3D monoperiodic flows. Oscillation amplitudes over this entire periodic regime (2D/3D) is comparable to those from the 2D periodic flows predicted by 2D model.

Some comparisons can also be drawn to 2D numerical study of Dillion et al. [51] for a rectangular cavity of the same aspect ratio (A = 10) and linearly varying wall temperatures. The steady bi-cellular flow predicted by the 2D model resembles the observations of steady flow predicted by Dillon. Critical Rayleigh predicted by Dillion et al. [51] for transition from steady to 2D periodic flow is $Ra_H = 2.2 \times 10^7$, which is slightly higher than that predicted by the current 2D model. However, periodic flow in Dillion's numerical study is caused due to movement of interface between the upper and lower convection cells, while in the current 2D model periodic flow is caused by interplay between four convection cells.

In the rectangular cavity experimental system, with an increase in Rayleigh number, 3D periodic flows transitioned to chaotic flows. The 2D CFD model could not predicted an analogous transition from 2D periodic flows to chaotic flows. The inability of the 2D model to predict chaotic flows hints to the fact that 3D effects play an essential role in the transition from periodic to chaotic flows. Besides, the 3D periodic regime most likely has an instability mechanism different than that of the 2D periodic regime, which is responsible for transitions to chaotic flows. In their analytical study for tall air-filled cavities with isothermal walls, Chait and Korpela [15] found that both 2D and 3D instability modes co-existed for the system; with the 2D mode being stable for a very small Rayleigh number range. A similar case seems to be true for the rectangular cavity experimental system where both 2D and 3D oscillatory modes co-exist, and the 2D mode becomes unstable first.

11.4 3D CFD Model

The 2D CFD model has provided a qualitative explanation for instability mechanisms that can cause 2D periodic flows observed in rectangular cavity with non-isothermal walls. However, to understand the experimental observations of 3D periodic and chaotic flow regimes, a full 3D CFD model is necessary. The main aims of these 3D simulations are to identify instability mechanisms responsible for 3D periodic flow and to predict numerically transition to chaotic flow.

11.4.1 Numerical Method, Fluid Thermophysical Properties

Three-dimensional, compressible, transient form of the Navier-Stokes equations for a Newtonian fluid given by equations (3.12) - (3.14) are solved. Air was treated as ideal gas and thermophysical properties were assigned similar to those mentioned in Section 11.1.1.

11.4.2 Solver Settings, Grid Size, and Time-Step

The coupled implicit solver of Simcenter StarCCM+ is used for developing the 3D model. A second-order up-winding scheme for spatial discretization and a second-order implicit scheme for time discretization is selected. After a grid refinement study, a significantly fine grid of 50 x 1000 x 500 cells (X x Y x Z) was found necessary for predicting periodic flows. At this grid size the 3D computational domain contains approximately 25 million cells. The trimmed cell mesher of Simcenter StarCCM+ which generates uniform hexahedral cells elements is used for generating the grid. Four prism layers are applied near cavity walls with a total thickness of 0.6 mm. A time-step size of 0.05 seconds is used. Each simulation was run for around 800 -1000 seconds of physical time. Such long-time durations were necessary since thermal instabilities responsible for periodic flow are slow moving with long time-periods of oscillation. For simulations predicting

periodic flows, the first 3 - 5 oscillations after flow reaches an asymptotic state were captured. With the large computational time and resources required for the 3D simulations, it was not possible to perform simulations corresponding to all 39 experiments for the rectangular cavity. Therefore, eight experiments at successively higher Rayleigh numbers were selected for the 3D numerical study.

11.4.3 Computational Domain, Boundary Conditions and Initial Conditions

Boundary conditions at the two opposing vertical walls and top and bottom walls were prescribed similar to those mentioned in Section 11.1.3. For the front and back vertical walls, temperature profiles corresponding to conduction heat transfer through the acrylic walls were assumed. The no-slip condition was assigned at all cavity walls. Temperature boundary conditions prescribed at surfaces numbered 1- 6 in Fig. 11.22 are given in equations (11.1) - (11.6).

$$\text{Surface 1 at } x = W = 0.03\text{m}: \; T_1(z) = T_{\text{top-heating}}(z) \tag{11.1}$$

$$\text{Surface 2 at } x = 0\text{m}: \; T_2(z) = T_{\text{bottom-heating}}(z) \tag{11.2}$$

$$\text{Surface 3 at } z = H = 0.3\text{m}: \; T_3(x) = \frac{T_1(H) - T_2(H)}{W}.x + T_2(H) \tag{11.3}$$

$$\text{Surface 4 at } z = 0\text{m}: T_4(x) = \frac{T_1(0) - T_2(0)}{W}.x + T_2(0) \tag{11.4}$$

Surface 5 at $y = L = 0.6m$ and Surface 6 at $y = 0m$:

$$T_5(x,z) = T_6(x,z) = \frac{T_1(z) - T_2(z)}{W}.x + T_2(z) \tag{11.5}$$

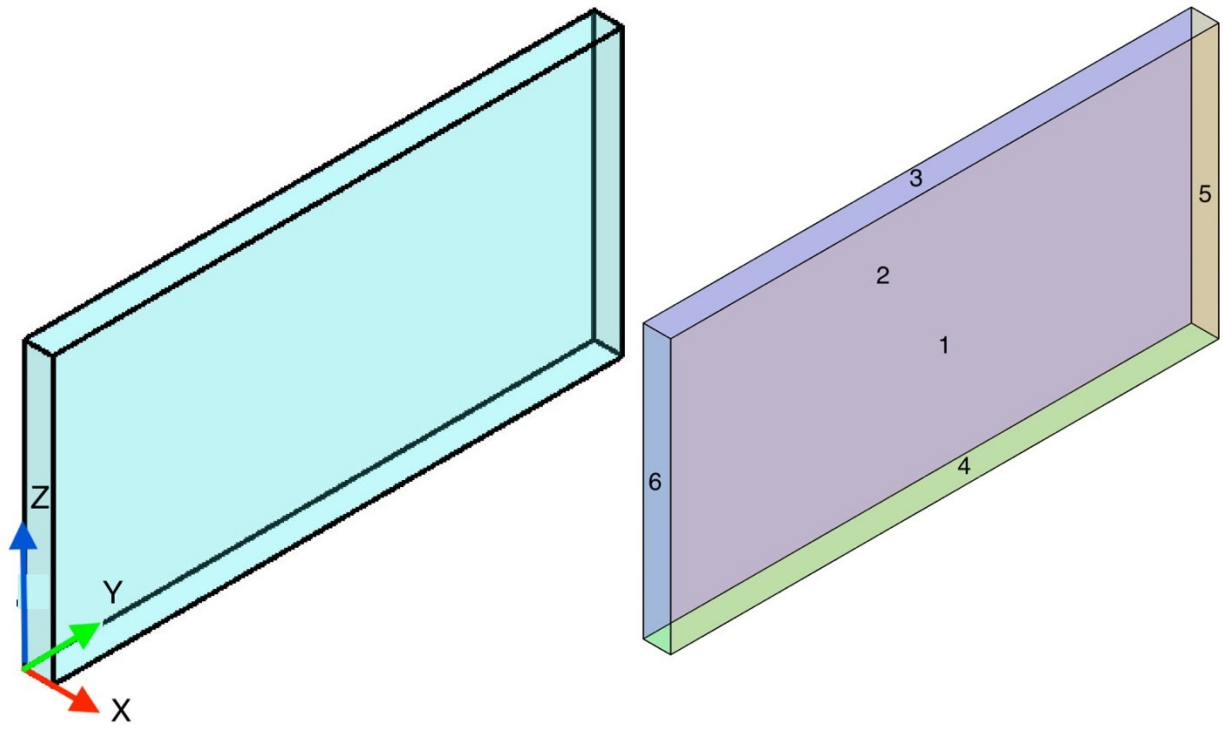

Figure 11.22: Computational domain and boundary conditions for 3D CFD model of rectangular cavity experimental system.

The boundary conditions applied for simulations at Rayleigh number of 8.71 x 10^6 are shown in Fig.11.23 . Initial conditions for 3D transient simulations were set similar to those described for the 2D CFD model: flow fields from simulations at a lower Rayleigh numbers were used as initial conditions for subsequent simulations at higher Rayleigh numbers.

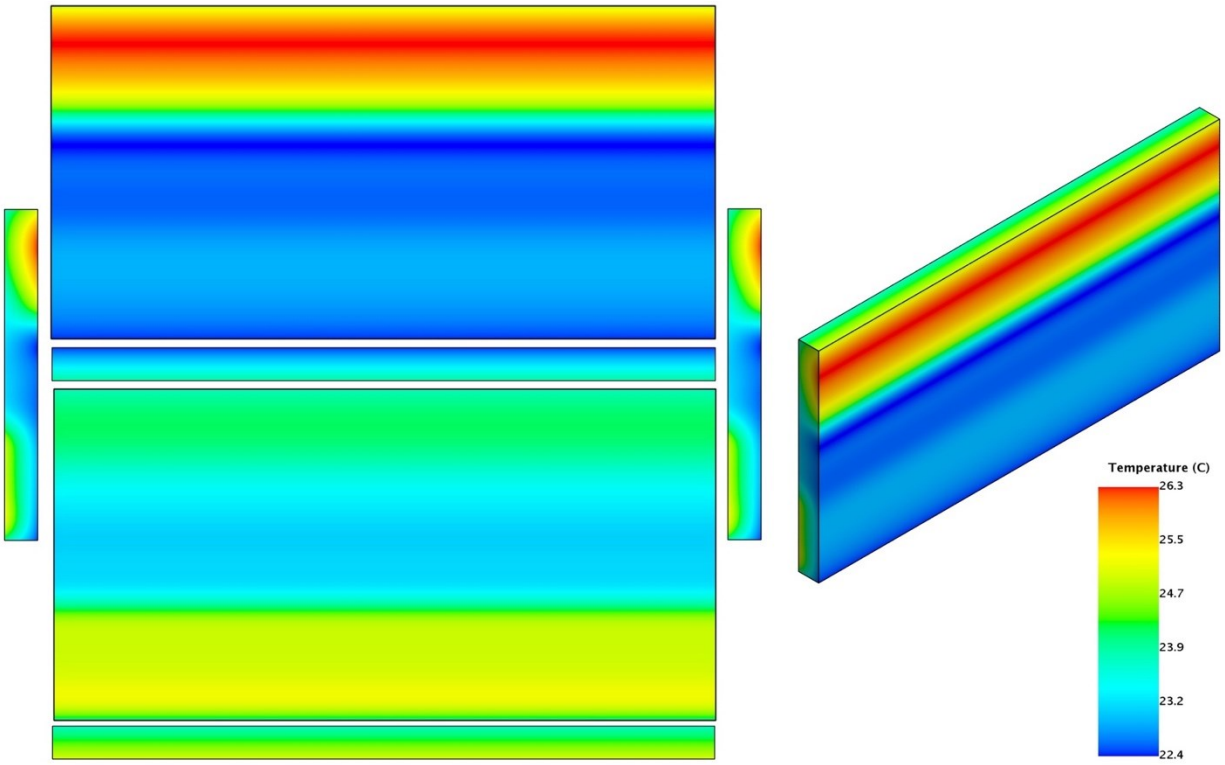

Figure 11.23: Temperature boundary conditions applied at six walls of cavity for a simulation corresponding to experimental run at nominal Rayleigh number of 8.71 x 10^6.

11.5 Results

The 3D CFD model was able to predict steady, 3D periodic and chaotic flow regimes observed in the rectangular cavity experiments. In subsequent sections, results from 8 full 3D CFD simulations for the rectangular cavity are presented.

11.5.1 2D Steady Flow

The first simulation was performed corresponding to an experimental run at Ra = 3.08 x 10^6. For this simulation a steady flow was predicted inside the cavity. Figures 11.24 and 11.25 shows isotherms, streamlines, and vector plots at different planes along cavity length. Streamlines inside

cavity show presence of two long, vertical counter-rotating cells: upper convection cell and lower convection cell. Isotherms and velocity vectors on XZ planes along cavity length look almost identical showing presence of upper and lower convection cells.

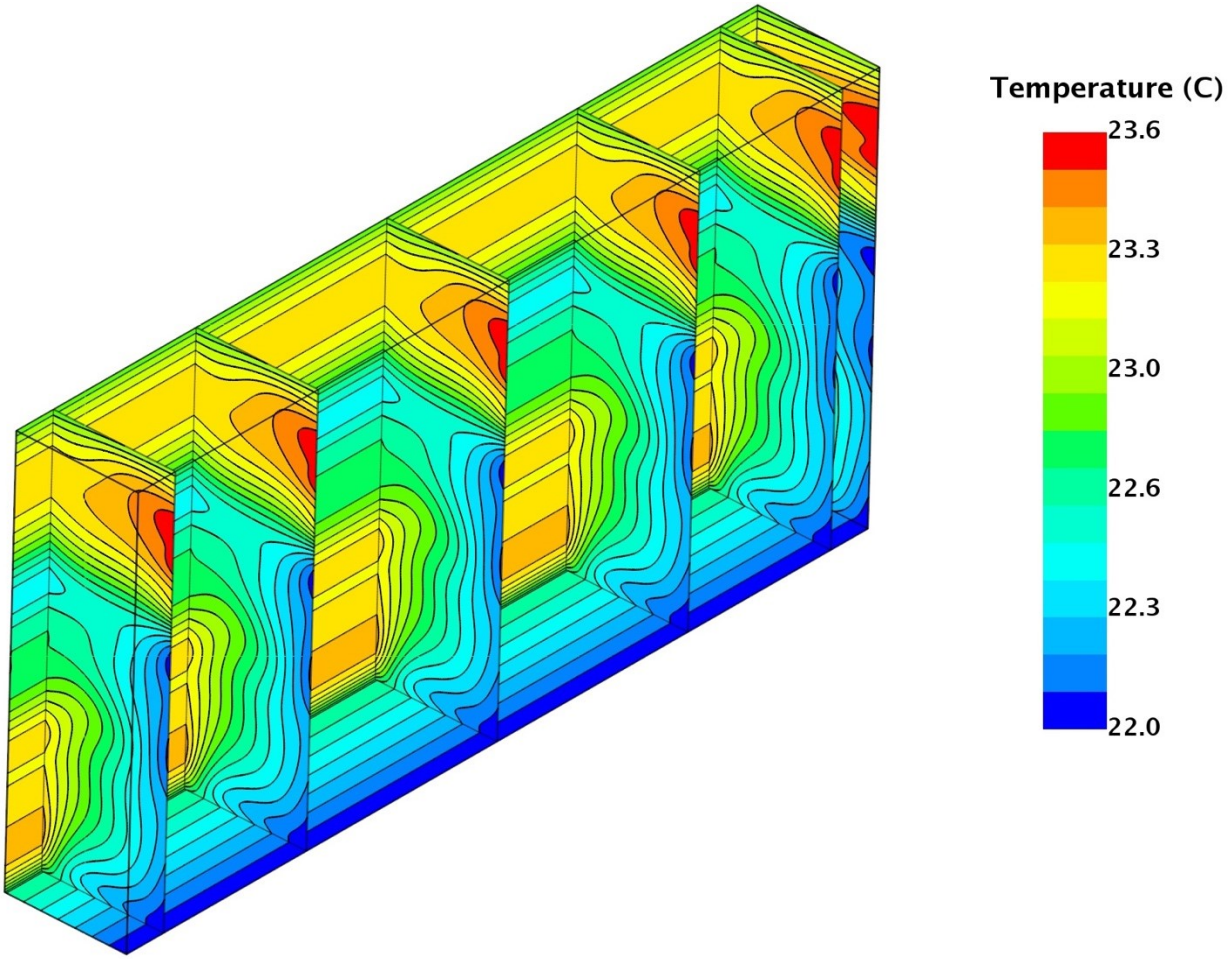

Figure 11.24: Isotherms at planes y = 0.03m, 0.1456m, 0.3m,0.4544m,0.57m,0.6m for Rayleigh number Ra = 3.08 x 10^6 using the 3D CFD model of rectangular cavity.
Note: Width of cavity (x-dimension) is scaled by *x*3 times for visualization purposes.

This is more evident when we look at vector plots superimposed on temperature fields along YZ planes, as shown in Fig. 11.26. Small recirculation zones develop near front and back end-walls; however, these zones do not impact the flow in the cavity interior. Consequently, the flow is 2D

in nature, with velocity vectors having only two components (X and Z components) in the majority of the cavity. A similar flow pattern is observed for two more simulations at successively higher Rayleigh number of Ra = 4.66 x 10^6 and 6.56 x 10^6. With increase in Rayleigh number, recirculation zones or small horizontal cells at fronts and back end-walls become larger and more energetic, causing a 3D flow pattern to emerge near the cavity ends. As a result, the 2D flow is restricted to a smaller volume at the cavity interior. The increasing influence of horizontal end-cells can be observed in vector plots for a simulation at Ra = 4.66 x 10^6 shown in Fig.11.27. Here, the horizontal cells at cavity ends occupy almost 20% of cavity volume. Flow is symmetric across the vertical midplane of the cavity located at y = 0.3m, as can be seen in Figs. 11.26 and 11.27.

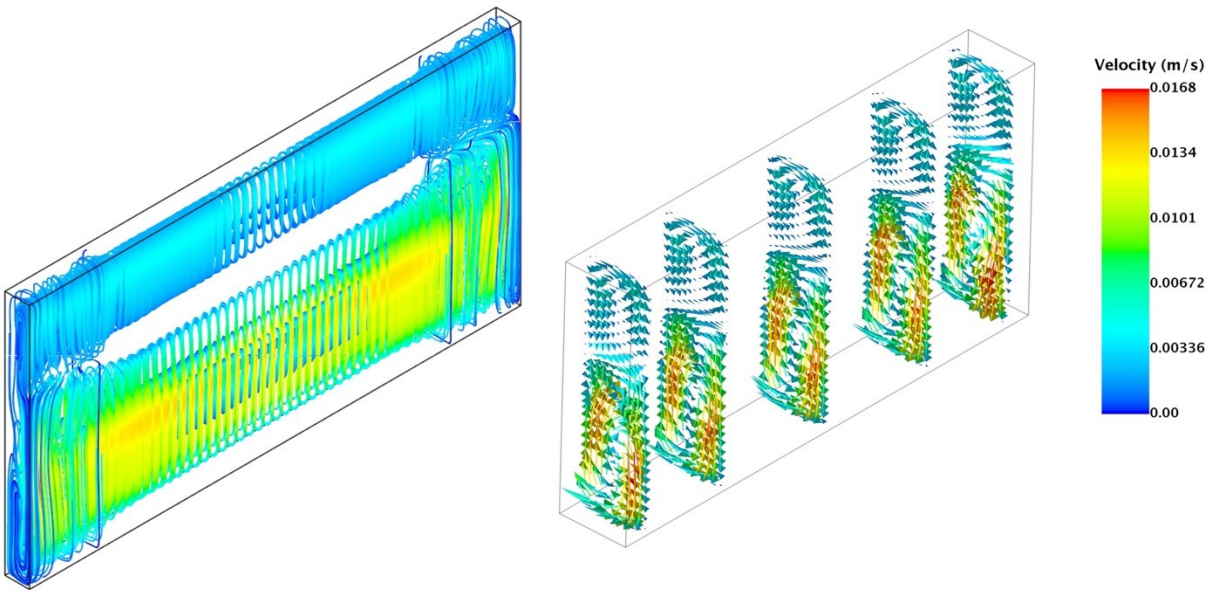

Figure 11.25: Streamlines (left) and vector plots(right) at planes y = 0.03m, 0.1456m, 0.3m, 0.4544m, 0.57m for steady bi-cellular flow predicted at Ra = 3.08 x 10^6 using the 3D CFD model of rectangular cavity.
Note: Width of cavity (x-dimension) is scaled by *x*3 times in vector plots (right)

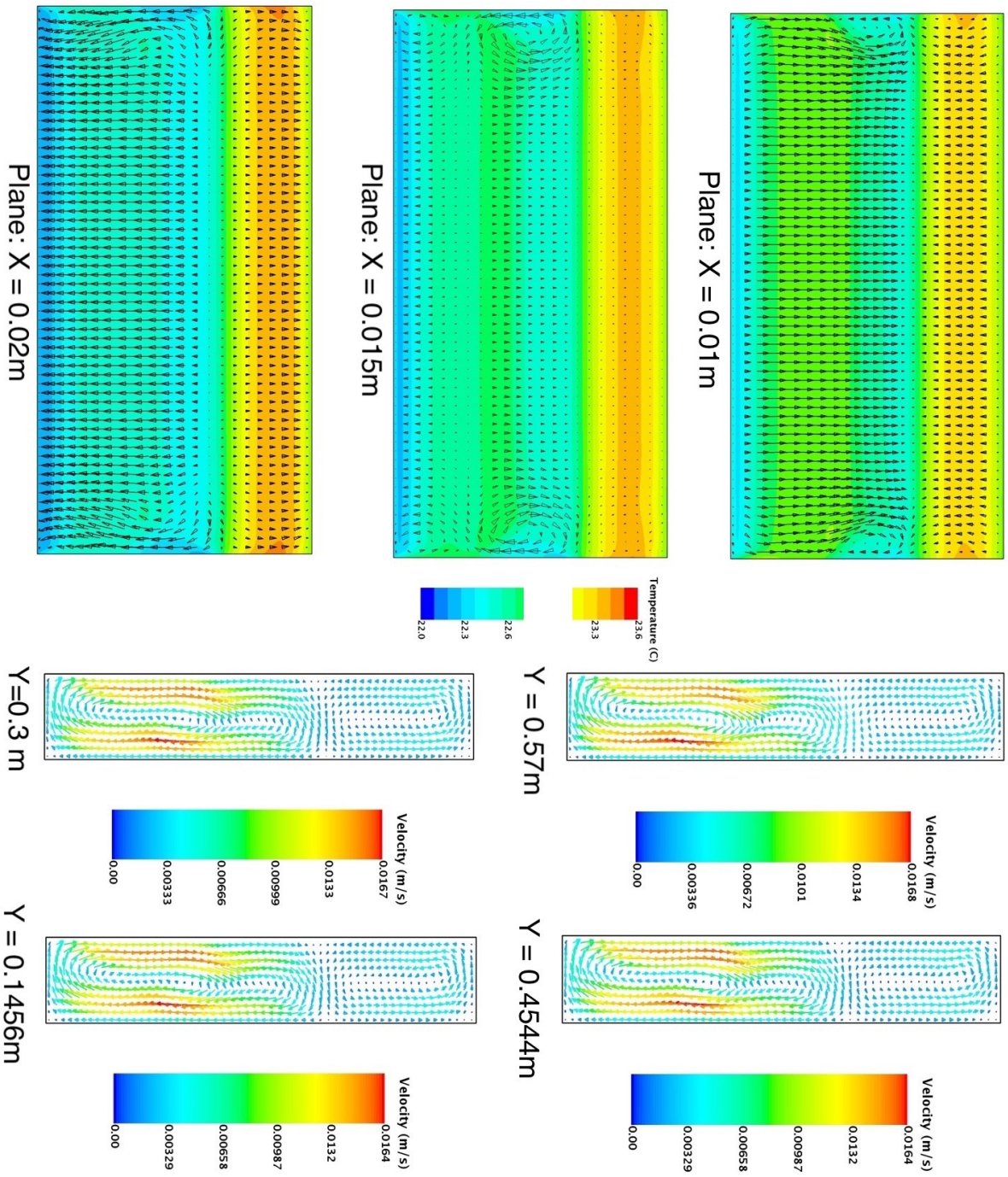

Figure 11.26: Temperature fields superimposed with vector plots for planes at x = 0.01m, 0.015m, 0.02m and vector plots for planes at y = 0.1456m, 0.3m, 0.4544, 0.57m for steady bi-cellular flow predicted at Ra = 3.08 x 10^6 using the 3D CFD model of rectangular cavity.
Note: Width of cavity (x-dimension) is scaled by *x*2 times for visualization purposes.

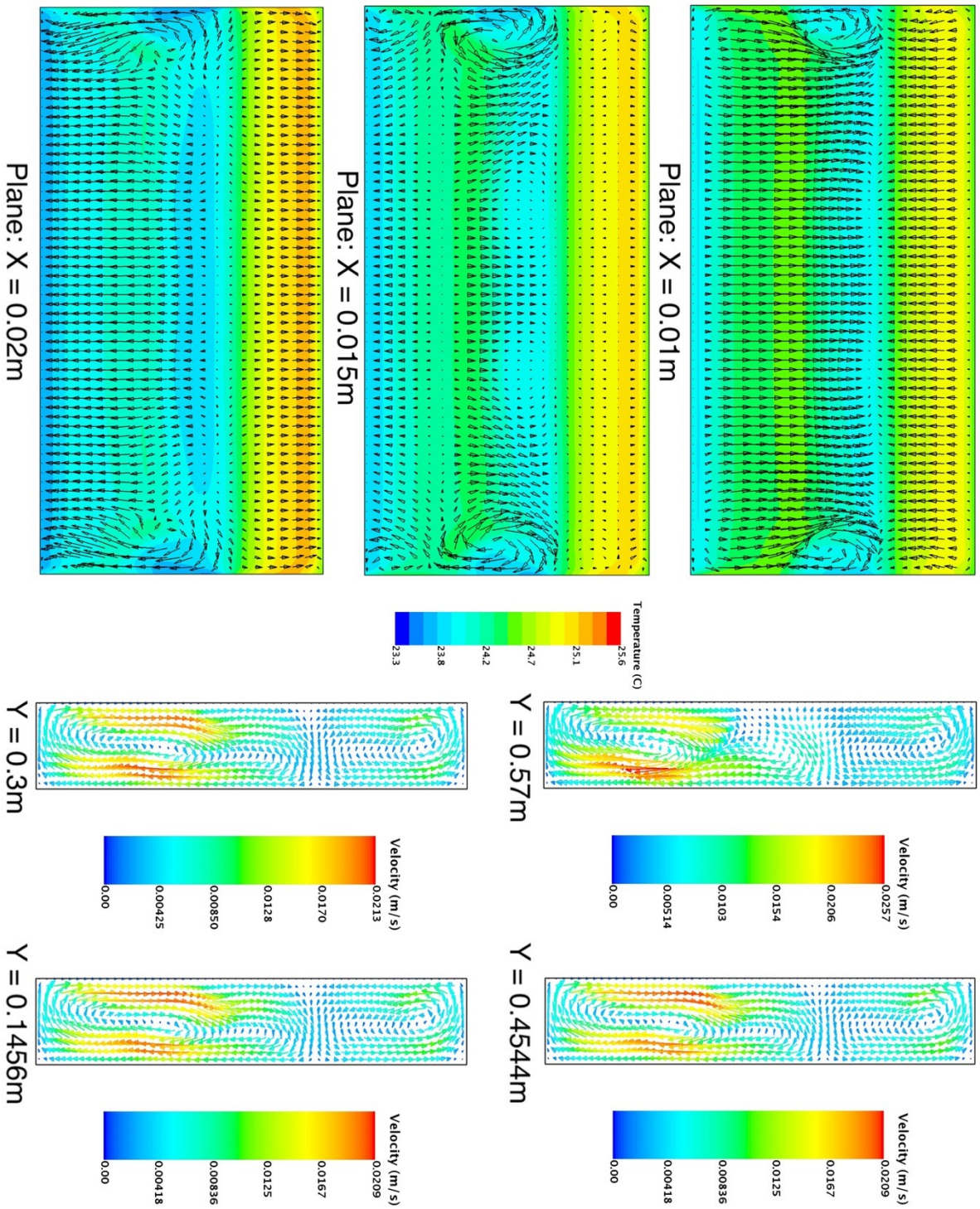

Figure 11.27: Temperature fields superimposed with vector plots for planes at x = 0.01m, 0.015m, 0.02m and vector plots for planes at y = 0.1456m, 0.3m, 0.4544, 0.57m for steady bi-cellular flow predicted at Ra = 4.66 x 10^6 using the 3D CFD model of rectangular cavity.
Note: Width of cavity (x-dimension) is scaled by *x*2 times for visualization purposes.

11.5.2 3D Steady Flow

Starting from the steady flow solution at Ra = 6.56 x 10^6, when the Rayleigh number was increased to 6.99 x 10^6, a 3D steady flow pattern was observed. Flow field now comprised of horizontal cells in cavity center and vertical convection cells in remaining portion of cavity. Both vertical and horizontal cells were stable, and the flow was time-invariant. This 3D steady flow is significantly different from the 2D steady flow pattern observed at lower Rayleigh numbers. Figures 11.28 and 11.29 show streamlines and isotherms inside the cavity and Fig. 11.30 shows vector plots at several YZ and XZ planes for 3D steady flow predicted at Ra = 6.99 x 10^6.

In vector plots on the x = 0.01m, 0.015m, and 0.02m planes, two horizontal cells/rolls are seen in the cavity interior. Vector plots on y = 0.1456m and y = 0.4544m planes show presence of the previously observed vertical upper and lower convection cells. Careful observation of isotherms indicates that fluid in central part of cavity near interface region of vertical convection cells is unstably stratified: with a hot horizontal fluid layer laying below a cold fluid layer.

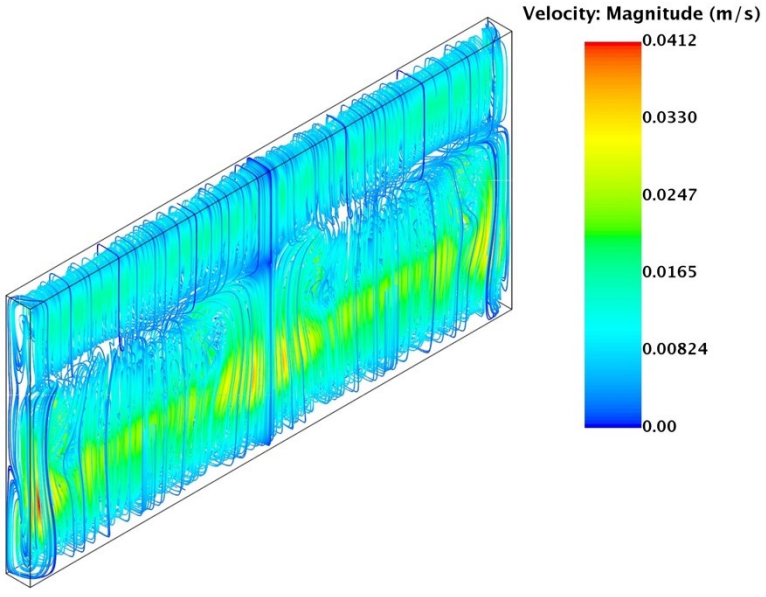

Figure 11.28: Streamlines for 3D steady flow predicted at Ra = 6.99 x 10^6 using the 3D CFD model of rectangular cavity.

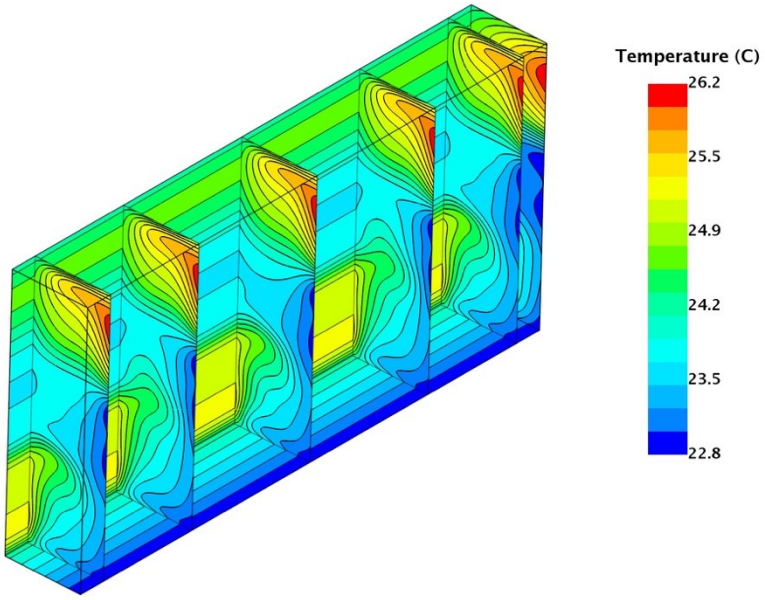

Figure 11.29: Isotherms for planes at y = 0.03m, 0.1456m, 0.3m, 0.4544m, 0.57m, 0.6m for steady flow predicted at Ra = 6.99 x 10^6 using the 3D CFD model of rectangular cavity.
Note: Width of cavity (x-dimension) is scaled by *x*3 times for visualization purposes.

At lower Rayleigh numbers, the hot fluid rises along heated bottom portions of one vertical wall (z-direction), turns (x-direction) and then falls along cooler portion of opposing wall. At higher Rayleigh numbers, temperature difference between the hot and cold horizontal fluid layers in the central portion of cavity increases and horizontal rolls/cells begin to form along cavity length. Hot fluid rises from bottom region of left vertical wall and instead of moving along the cold portion of opposing vertical wall (z-direction) to form a vertical lower convection cell, it begins to move into the cooler fluid layer above it in the y-direction to form a horizontal cell. These horizontal cells are similar to the horizontal rolls observed by Stork and Müller [90] in their experiments of Rayleigh -Bernard convection in rectangular boxes with a heated bottom wall. The horizontal cells are formed only in the cavity center, where the temperature difference between the hot and cold horizontal fluid layers is maximum. In the rest of the cavity, vertical convection cells are observed.

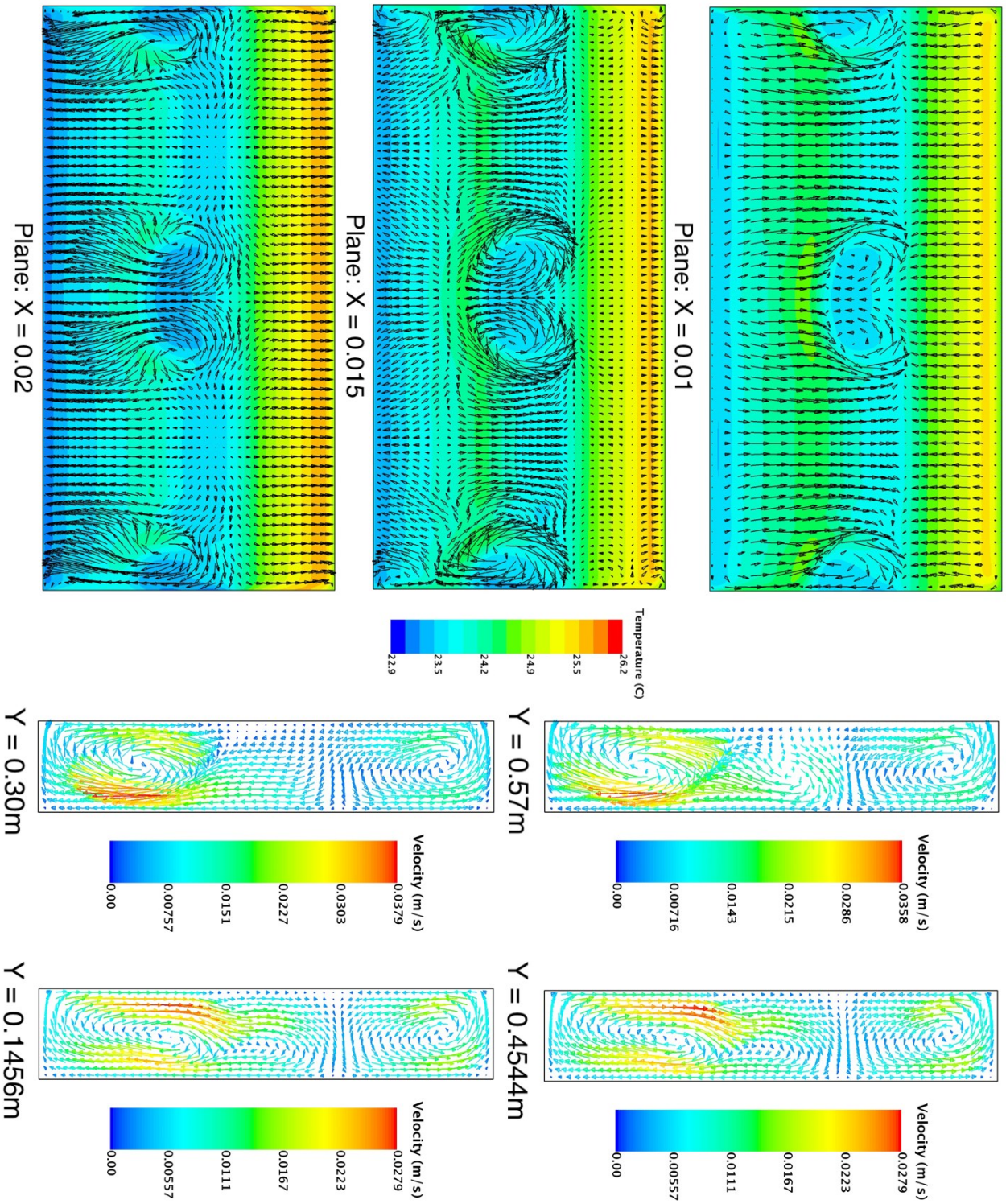

Figure 11.30: Vector plots for planes at y = 0.1456m, 0.3m, 0.4544, 0.57m and temperature fields superimposed with vector plots for planes at x = 0.01m, 0.015m, 0.02m for steady flow predicted at Rayleigh number Ra = 6.99 x 10^6 using the 3D CFD model of the rectangular cavity.
Note: Width of cavity (x-dimension) is scaled by x2 times for visualization purposes.

11.5.3 3D Oscillatory Flow

When Rayleigh number was increased to Ra = 7.32 x 10^6 starting from the 3D steady flow solution, a 3D periodic flow was obtained. Figure 11.31 shows temperature time series for several points inside the cavity. 3D flow oscillations are slow moving with a time period of 200 seconds.

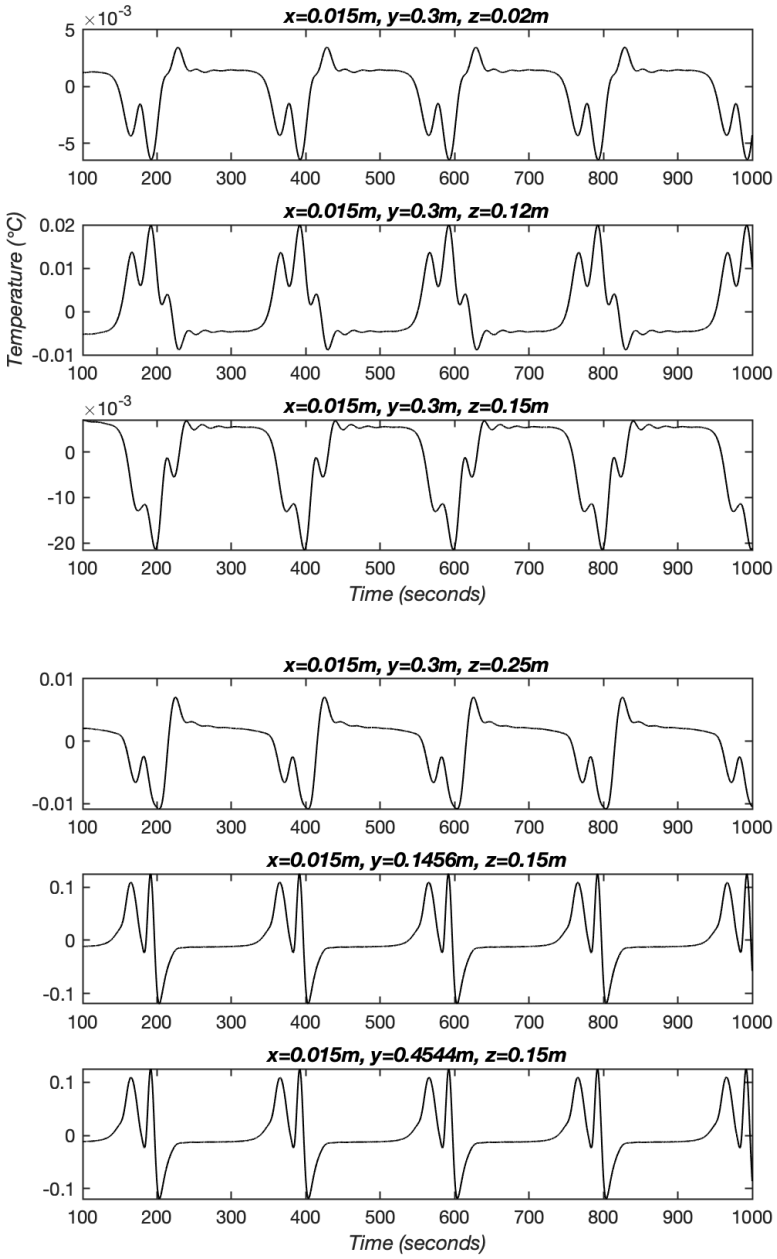

Figure 11.31: Temperature time series for six points inside the cavity for a 3D periodic flow predicted at Ra = 7.32 x 10^6.

Power spectral density plots for temperatures measured at four points inside the cavity are shown in Fig. 11.32. Flow is monoperiodic with the fundamental frequency of oscillation being 0.005 Hz. All measurement points show the same fundamental frequency with several harmonics also appearing in PSD plots. The shape of waveform of temperature oscillation, its amplitude and number of harmonics is sensitive to measurement location but not the fundamental frequency.

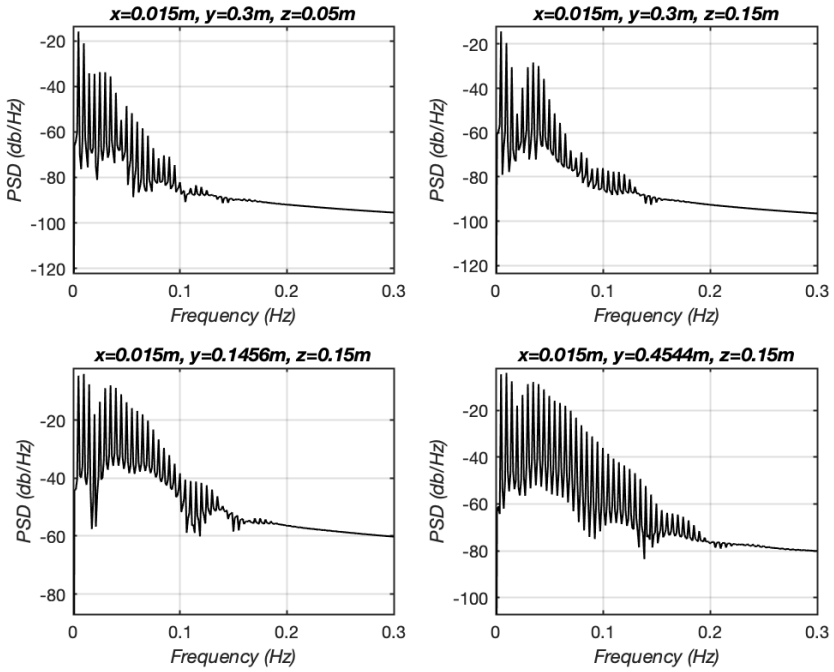

Figure 11.32: Power spectral density of temperature measurements at six points inside the cavity for a 3D periodic flow at Ra = 7.32 x 10^6.

Figure 11.33 shows the isotherms and vector plots along the YZ planes: x = 0.01m, 0.015m, 0.02m over one period of oscillation. The sequence of events that causes 3D oscillatory flow inside the cavity is as follows: At the start of the oscillation cycle there are 4 horizontal cells in the cavity: two at the center of the cavity and one at each end-wall. Next, two new horizontal cells are created adjacent to horizontal cells near the front and back end-walls. These cells start to move back and forth towards the cavity center.

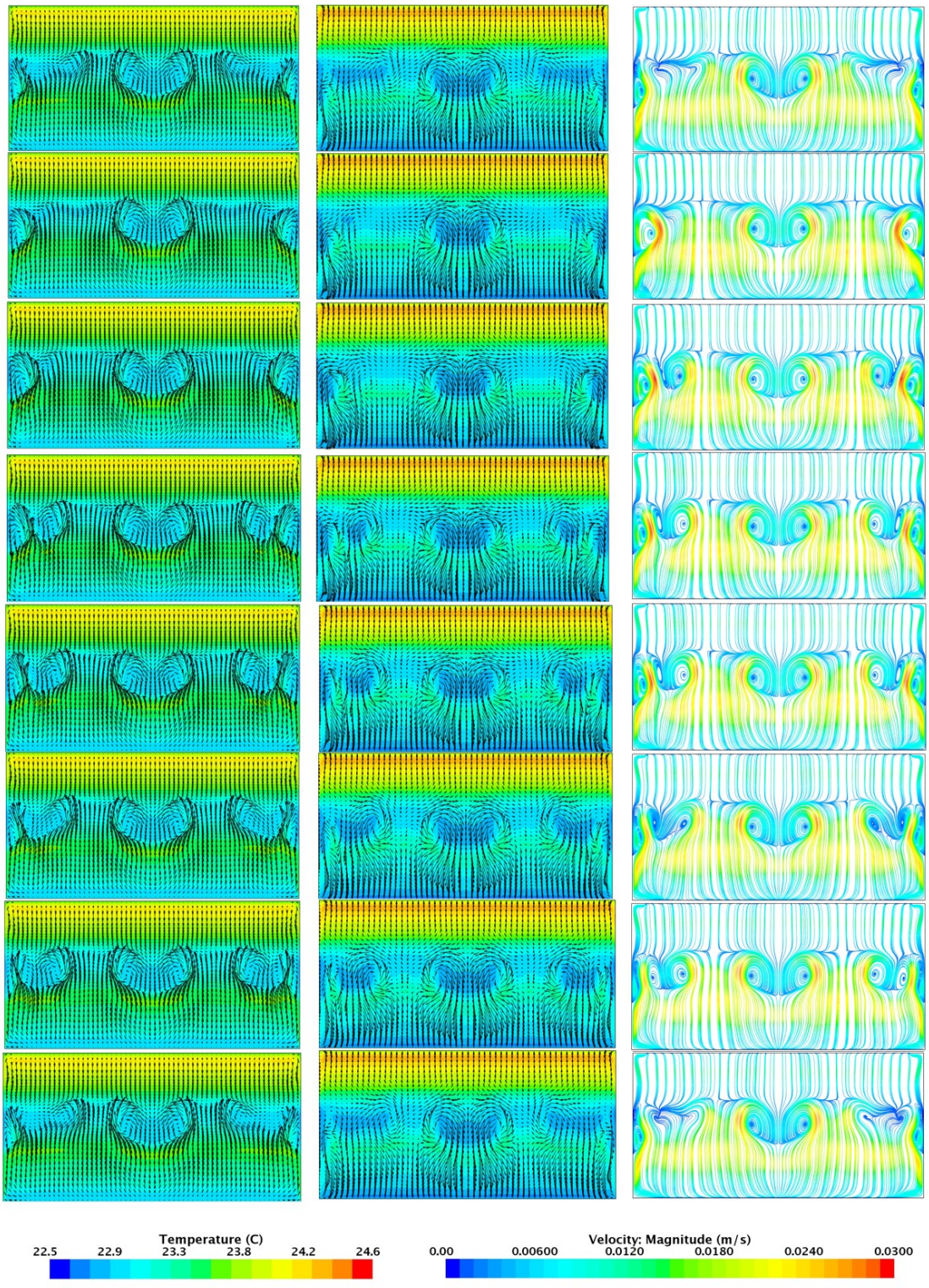

Figure 11.33: Temperature fields superimposed with vector plots for planes at x = 0.01m (left), 0.02m (center) and streamlines on the plane x = 0.01m (right) predicted for unsteady 3D periodic flow over one oscillation period (π = 200 seconds) corresponding to an experimental run at Ra = 7.32 x 10^6. using the 3D CFD model of the rectangular cavity.

At the midpoint of the oscillation cycle, there are now six horizontal cells observable on the YZ planes. By the end of the oscillation cycle, the two cells which were moving towards the cavity center begin to shrink in size and disappear during their forward motion. As the two old cells disappear, two new horizontal cells are again created adjacent to the horizontal cells near end-walls. This process continues *ad infinitum* to create a 3D periodic motion inside the cavity. Horizontal cell motion occurs in addtion to the two vertical convection cells which exist in regions where the horizontal cells are not present. The back and forth motion of the newly created horizontal cells in the Y- direction causes the vertical cells to move back and forth (up and down) in the Z-direction. This Z-movement of vertical convection cells can be seen in the vector plots on XZ plane at y = 0.1456m over one oscillation period, as shown in Fig. 11.34.

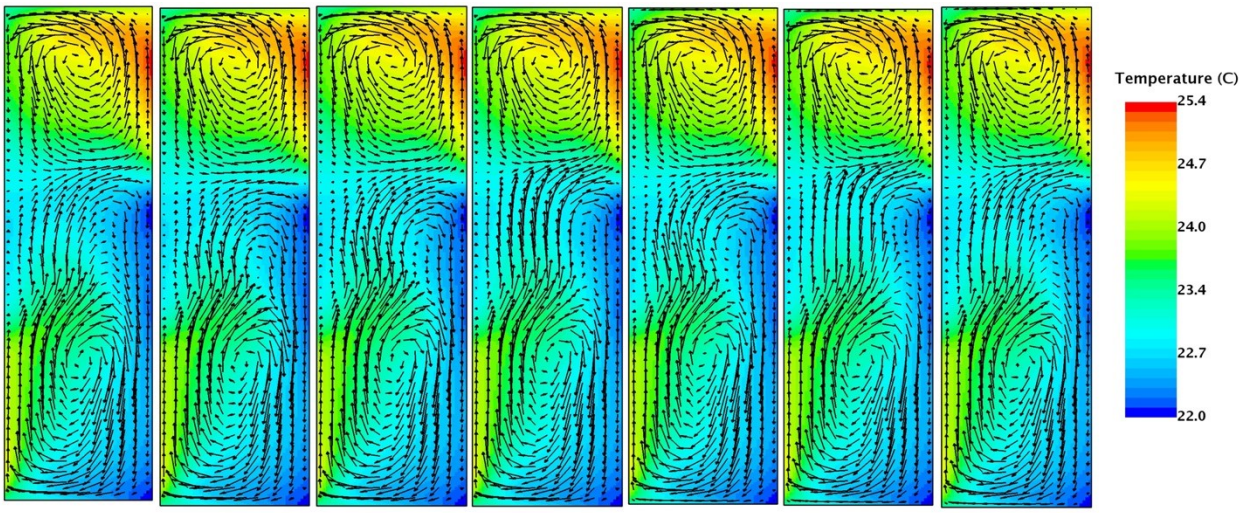

Figure 11.34: Flow vectors superimposed on temperature field plotted on the y = 0.1456m plane for unsteady 3D periodic flow over one oscillation period ($\pi = 200\ seconds$) for simulation at Ra = 7.32 x 10^6 using the 3D CFD model of rectangular cavity.
Note: Width of cavity (x-dim) is scaled by *x*3 times for visualization purposes

This 3D oscillatory motion of fluid is symmetric about the vertical midplane of the cavity (y = 0.3m). Figure 11.35 shows iso-surfaces of instantaneous X,Y and Z-velocity fluctuations at Ra = 7.32 x 10^6. These fluctuations create the symmetric back and forth motions of the horizontal and vertical convection cells.

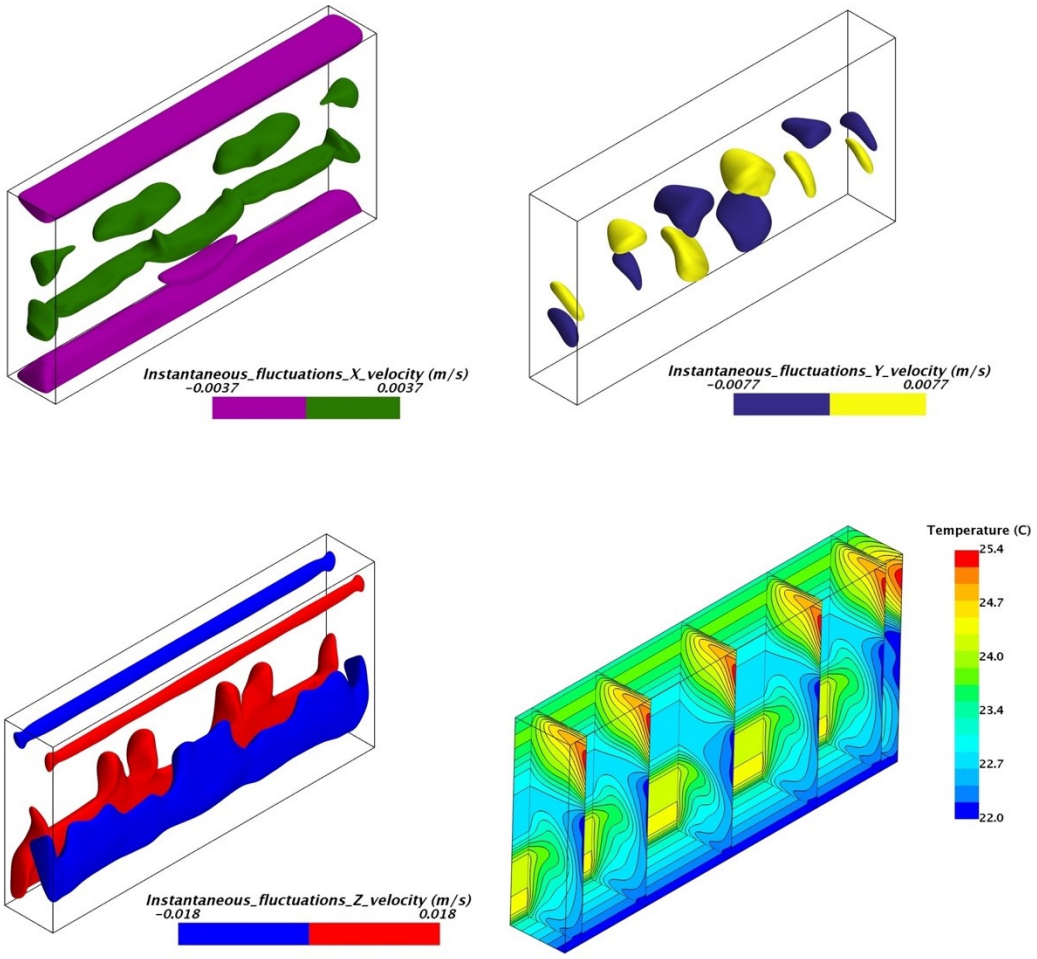

Figure 11.35: Iso-surfaces of instantaneous X,Y and Z-velocity fluctuations and isotherms for 3D periodic flow for simulation at Ra = 7.32 x 10^6 using the 3D CFD model of rectangular cavity.

Figures 11.36(a) shows time series for the X, Y and Z velocity components at three points in the cavity: one at vertical and horizontal center of the cavity and the other two at equal distances to right and left of cavity center. Figure 11.36(b) shows the velocity phase-space for four points inside the cavity. A stable limit cycle is visible in the phase-space plots.

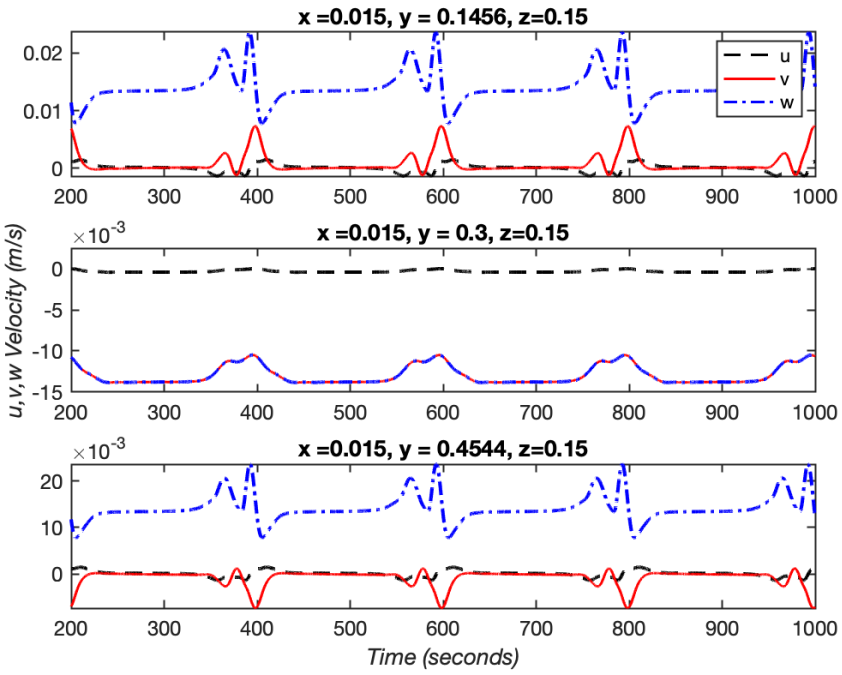

(a)

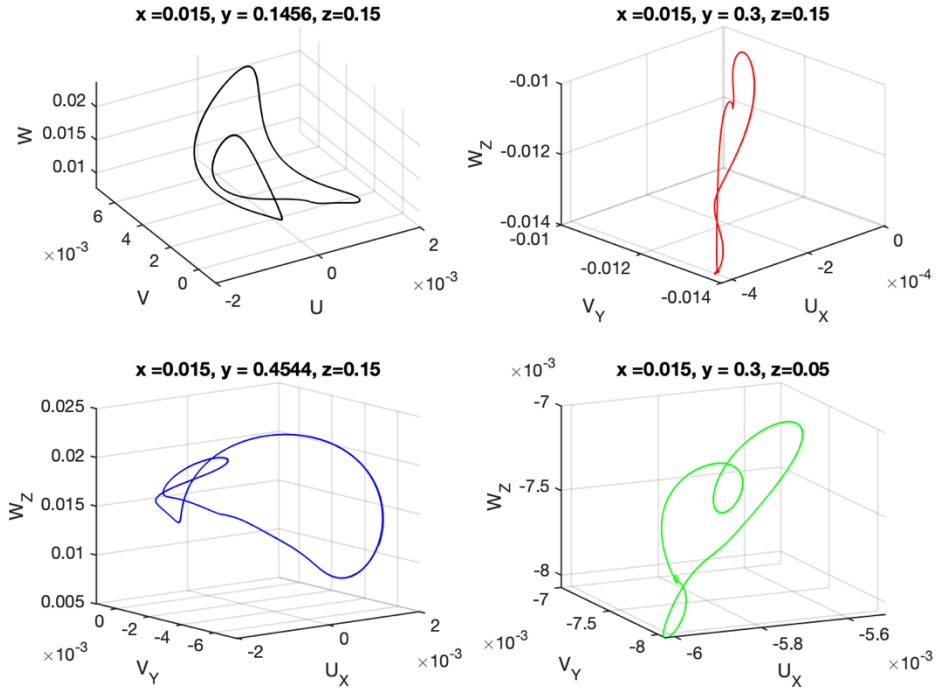

(b)

Figure 11.36: (a) X, Y and Z - Velocity time-series for three points inside the cavity for a 3D periodic flow predicted at Ra = 7.32 x 10^6; (b) Velocity phase space at four points inside the cavity for simulation at Ra = 7.32 x 10^6 showing a stable limit cycle.

11.5.4 Chaotic Flow

A chaotic flow solution was obtained when Rayleigh number was further increased to Ra = 8.71 x 10^6 starting from periodic solution at Ra = 7.32 x 10^6. Figure 11.37 shows temperature time series for several points inside the cavity for this chaotic flow solution over a time period of 400 seconds.

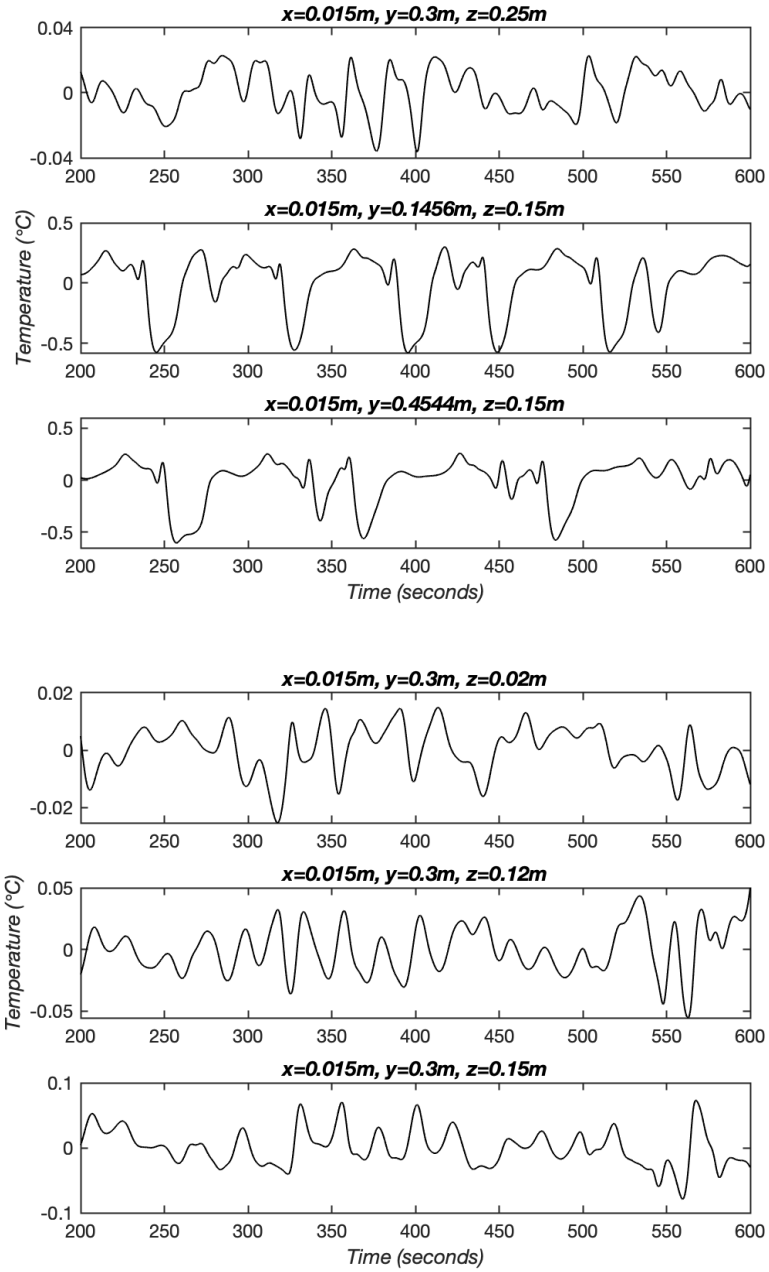

Figure 11.37: Temperature time series for six points inside the cavity for a 3D chaotic flow predicted for simulation at Ra = 8.71 x 10^6.

Power spectral density functions of temperature oscillations measured at different points inside the cavity are shown in Fig. 11.38. The PSD shows several frequency peaks in the range between 0 to 0.3 Hz. Based on PSD, the flow is not fully chaotic but is on the route to chaotic flow. Significant power is still present at frequencies between 0 to 0.05 Hz.

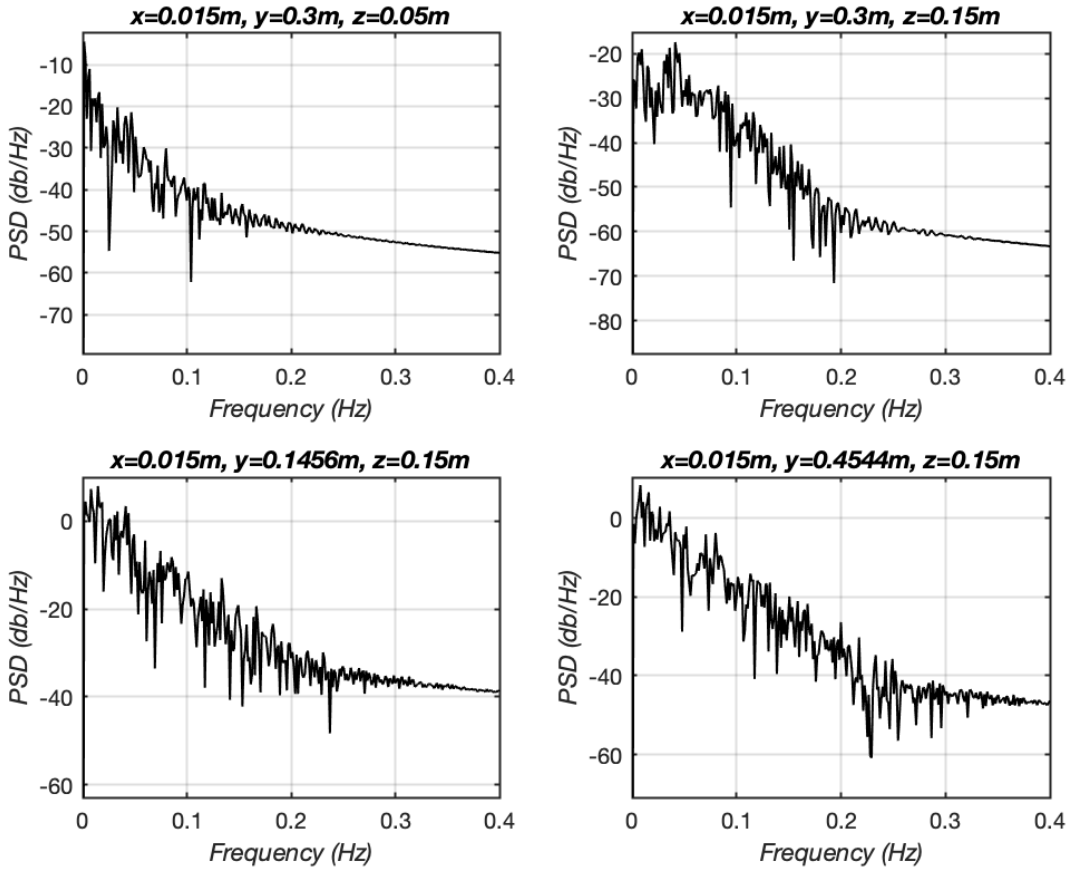

Figure 11.38: Power spectral density of temperature measurements at four points inside the cavity for a 3D chaotic flow predicted at Ra = 8.71 x 10^6.

The back and forth movement of the horizontal cells is no-longer periodic but is random, resulting in chaotic oscillations in temperature and velocity fields. Figures 11.39 and 11.40 show the isotherms and velocity vectors plots along five XZ planes and three YZ planes. The isotherms and vector plots at each XZ and YZ plane appear dissimilar. The symmetry of flow about the vertical midplane of the cavity (y = 0.3) observed in steady and period flow regimes is now lost.

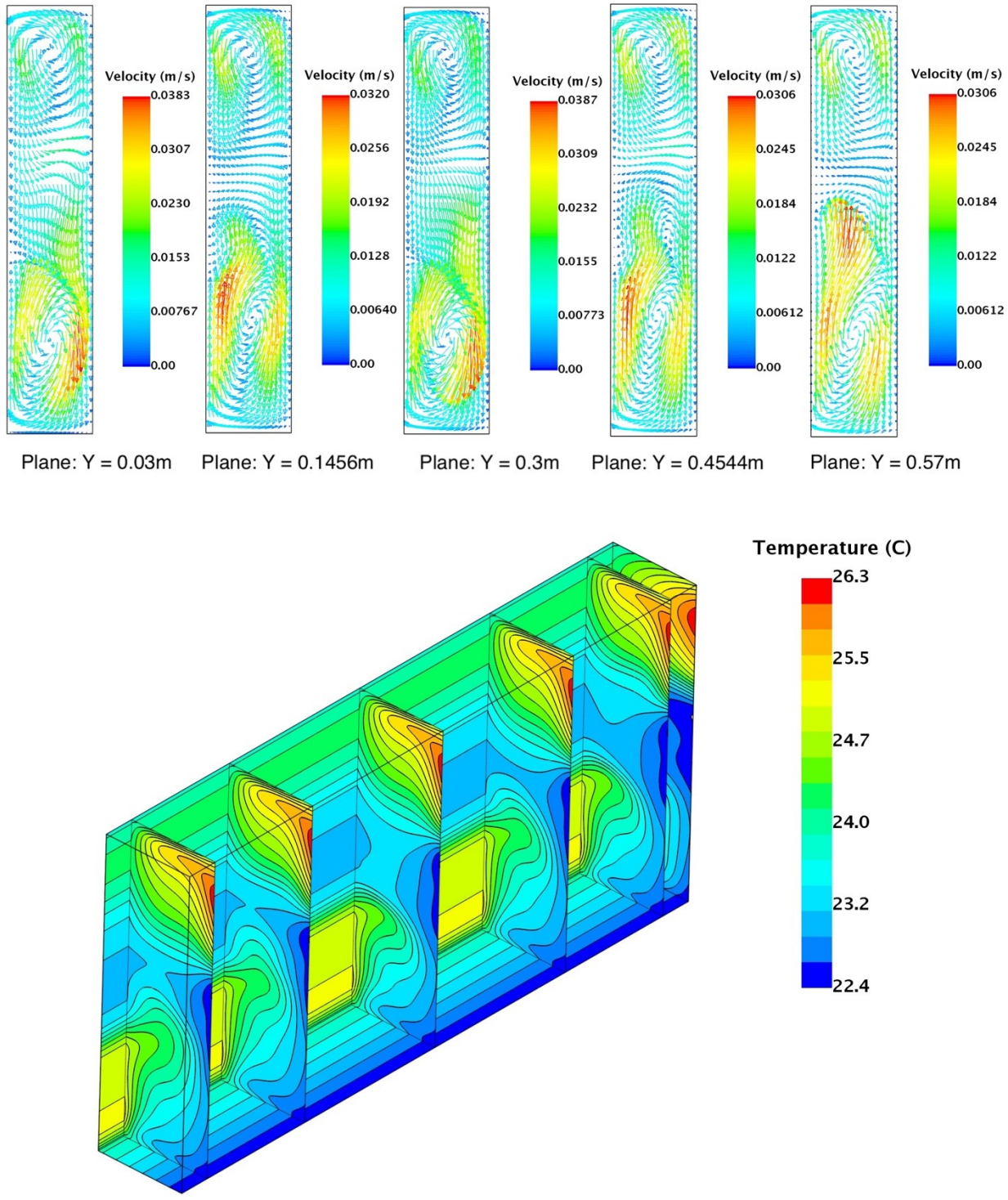

Figure 11.39: Vector plots (top) and isotherms (bottom) for planes at y = 0.03m, 0.1456m, 0.3m, 0.4544, 0.57m at a time instant for 3D chaotic flow predicted at Ra = 8.71 x 10^6 using the 3D CFD model of rectangular cavity.

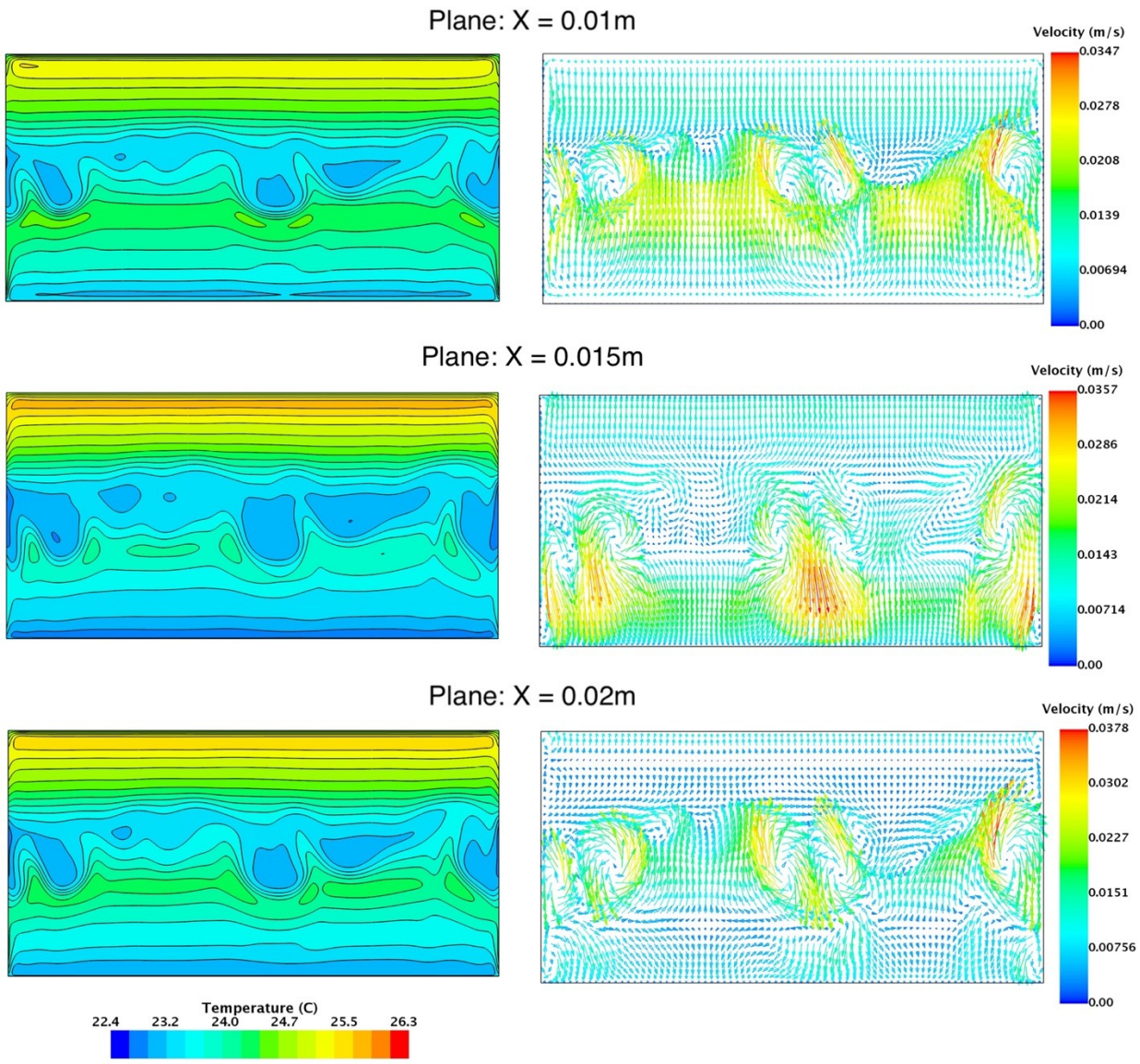

Figure 11.40: Isotherms (left) and Vector plots (right) for planes at x = 0.01m, 0.015m, 0.02m at a time instant for 3D chaotic flow predicted at Rayleigh number Ra = 8.71 x 10^6 using the 3D CFD model of the rectangular cavity.

Figure 11.41(a) shows the time series for the X, Y and Z velocity components at three points in the cavity and Fig. 11.36(b) shows the velocity phase space for four points inside the cavity for the chaotic flow solution obtained at Ra = 8.71 x 10^6.

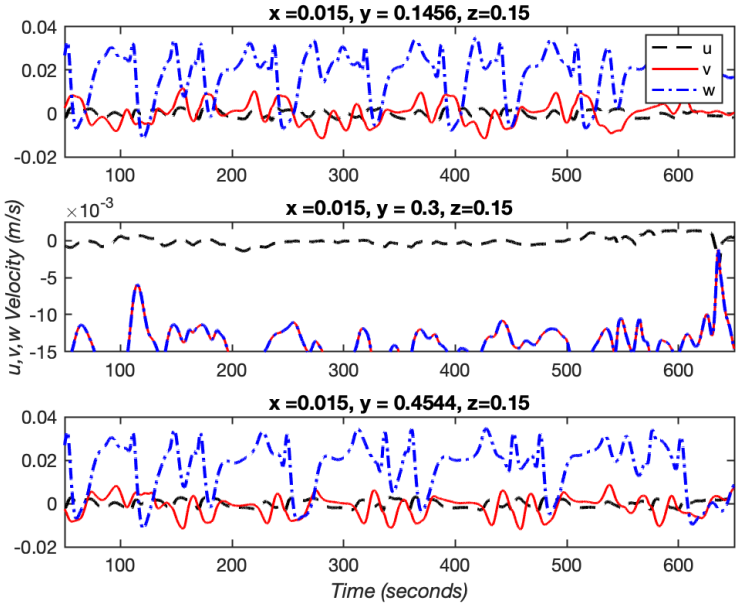

(a)

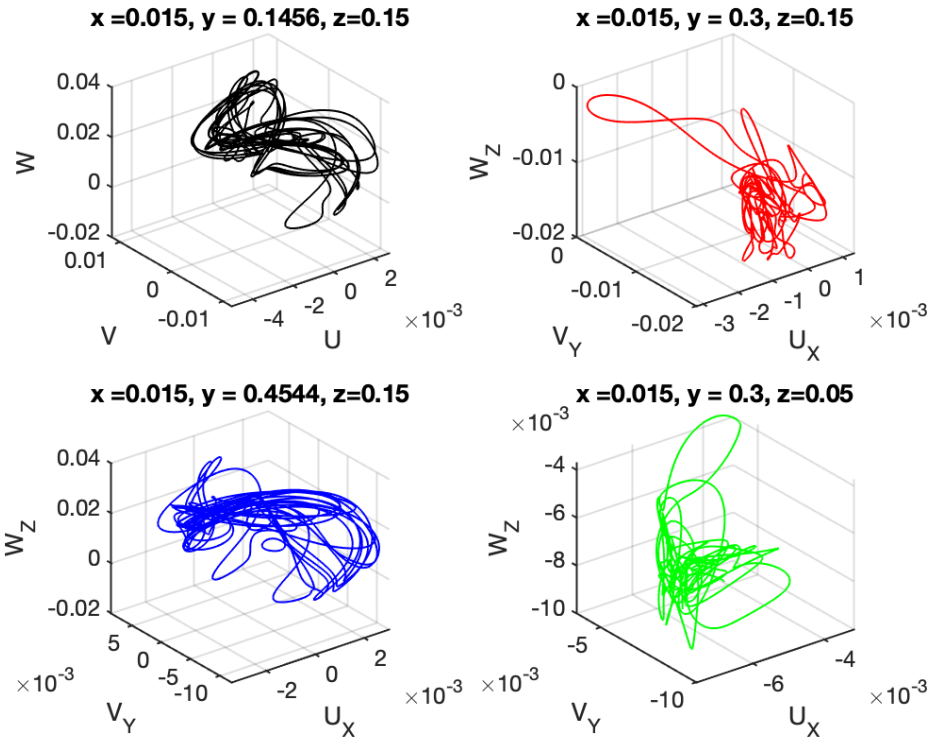

(b)

Figure 11.41: (a) X, Y and Z - Velocity time-series for three points inside the cavity for a 3D chaotic flow predicted at Ra = 8.71 x 10^6; (b) Velocity phase space at four points inside the cavity for simulation at Ra = 8.71 x 10^6

11.6 Key Results and Conclusions

11.6.1 Summary of 3D CFD Model Results

In the 3D numerical study for a rectangular cavity of aspect ratio A=10 and non-isothermal walls, steady, periodic, and chaotic flow regimes were predicted. At low Rayleigh numbers, a steady 2D bi-cellular flow pattern comprising of two vertical cells circulating fluid in the X-Z plane was predicted. As a result of the boundary conditions applied at cavity walls, a cooler horizontal fluid layer at the center of the cavity is sandwiched between two warmer fluid layers. As the Rayleigh number was increased, the temperature difference between the hot and cold horizontal fluid layers in the central part of the cavity began to increase. When the temperature difference was increased beyond a critical state (at higher Rayleigh numbers), two steady, horizontal cells, developed in the cavity interior along the cavity length. These horizontal cells were similar to those observed in Rayleigh-Bernard convection. Starting from the steady 3D convection when the Rayleigh number was increased further, the horizontal cells began to move in the cavity in an oscillatory manner leading to a 3D periodic flow. At even higher Rayleigh numbers, the motion of the cells became random, leading to a chaotic flow prediction.

11.6.2 Comparisons to Experiments and 2D Model Results

3D CFD simulations predicted steady, 3D periodic, and chaotic flows observed in rectangular cavity experiments. The 3D model correctly predicted the transition point from steady to 3D periodic flow. However, the fundamental frequency of oscillations and oscillation amplitudes predicted by the model were slightly lower than those seen in experiments. Table 11.3 shows the comparisons between flow predictions by 3D CFD model and experimental observations.

Table 11.3: Flow regimes, fundamental frequencies and oscillation amplitudes for experimental observations and 3D CFD model predictions at different Rayleigh numbers.

Rayleigh Number	Experiments			3D Simulations		
	Flow regime	Frequencies (Hz)	Amplitude	Flow regimes	Frequencies (Hz)	Amplitude
3.08×10^6	Steady	-	-	Steady	-	-
6.56×10^6	2D Periodic	0.051	0.06	Steady	-	-
6.99×10^6	3D Periodic	0.036	0.13	Steady	-	-
7.32×10^6	3D Periodic	0.029	0.15	3D Periodic	0.005	0.07
8.71×10^6	3D Periodic	0.024	0.35	Quasi-chaotic	0.005 to 0.05	0.30
9.06×10^6	3D Periodic	0.023	0.39	Quasi-chaotic	0.005 to 0.05	0.39
9.17×10^6	3D Periodic	0.022	0.40	Quasi-chaotic	0.005 to 0.05	0.44
1.05×10^6	Quasi-chaotic	0.005 to 0.08	0.43	-	-	-

Scaling of experimentally observed 3D periodic flow frequencies with the Brunt – Väisälä frequency suggests that the instability mechanism causing 3D oscillations might be related to the Rayleigh-Bernard instability mechanism. 3D CFD model results validate this postulation since the primary mechanism responsible for 3D oscillations in flow field is found to be formation and movement of Rayleigh-Bernard type horizontal cells/rolls.

A 2D steady bi-cellular flow at low Rayleigh numbers was predicted by both the 2D and 3D CFD models. However, the 3D model predicted a transition from 2D steady flow to a 3D steady flow before transitioning to a 3D oscillatory flow. No intermediate 2D periodic flows could be predicted by the 3D model for simulations performed corresponding to experimental runs.

Nonetheless, since the range over which 2D periodic flows were observed in experiments is very small, there is a possibility that a 2D periodic flow regime exists between the 2D steady flow and 3D steady flow regimes, similar to observations of Chait and Korpela [15]. The 2D periodic flow predicted by the 2D model could represent the kind of flow that could be expected in this small Rayleigh number range.

Unlike the 2D CFD model, the 3D CFD model was able to predict transition to chaotic flow. 3D simulations suggest that transitions to chaotic flow are linked to the movement of horizontal convection rolls seen in the 3D periodic regime. In the 2D CFD model, the absence of y – velocity (lengthwise) components due to the assumption of 2D flow in the governing equations rules out the possibility of forming horizontal cells/rolls; thus, making it impossible to predict 3D periodic and chaotic flows with the 2D flow assumption. Figures 11.42(a) and 11.42(b) show the comparison between the experimentally observed amplitudes and frequencies and those predicted by the 2D and 3D CFD models. It is quite evident that the predictions by the 3D model are in better agreement with the experiments as compared to those by the 2D model due to the afore-mentioned reasons.

In conclusion, the steady, 3D periodic and chaotic regimes observed in experiments were captured accurately by the 3D CFD model of the cavity. The 2D model was able to predict transition from steady to 2D periodic flow similar to those observed experimentally. However, the time periods, critical Rayleigh number of transition and amplitude of oscillations did not agree with experimental observations. On the other hand, 3D CFD model of the rectangular cavity was able to predict the instability mechanisms responsible for the 3D periodic and chaotic flow regimes observed in the rectangular cavity experiments albeit with limited accuracy in predicting oscillation time-periods.

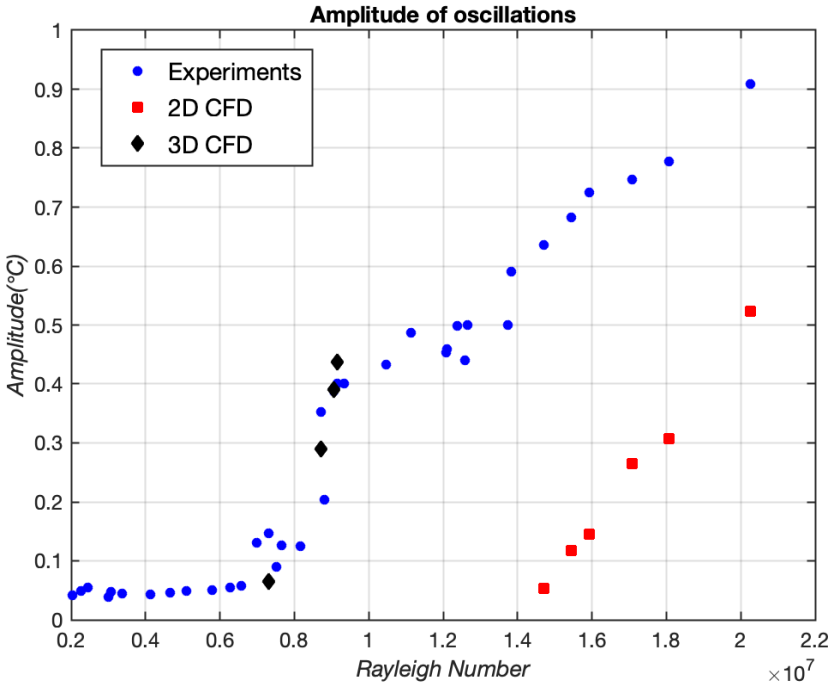

(a)

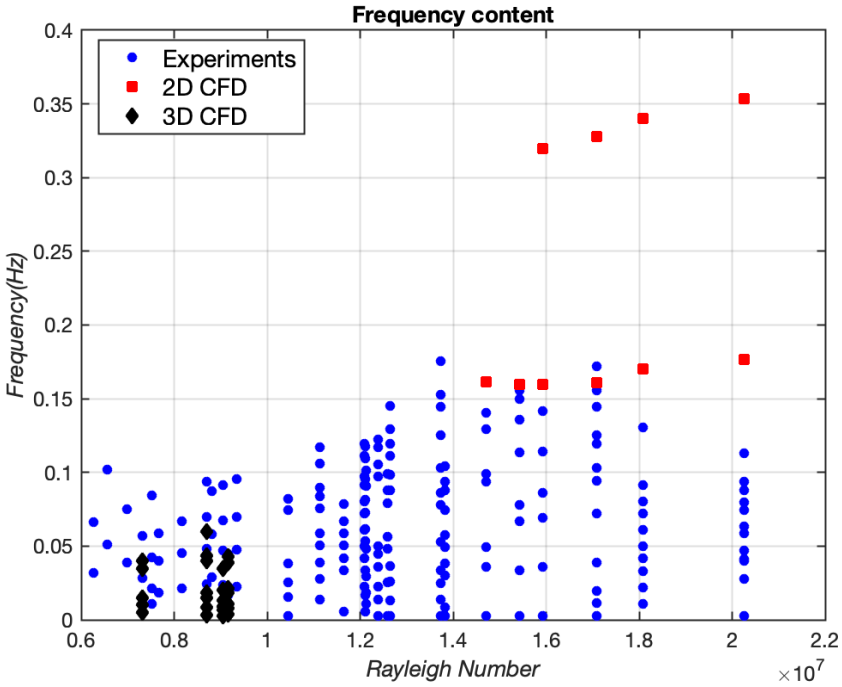

(b)

Figure 11.42: Comparison between (a) amplitude of oscillations (b) frequency content of unsteady flows observed in experiments and those predicted by 2D and 3D CFD models.

Chapter 12

12 CONCLUDING REMARKS

Natural convection instabilities observed in closed annular and rectangular cavities with non-isothermal walls were studied both experimentally and numerically. Key results from this work are as follows:

12.1 Experimental and Numerical Work for Annular Cavity with Non-Isothermal Walls

The stability of (base) bi-cellular natural convection air-flows in an annular cavity of radius ratio $\eta = 0.50$ and aspect ratio $A = 25.2$ was studied experimentally. When the buoyant potential of the upper cell of the bi-cellular flow was successively increased, the flow transitioned from steady to mono-periodic flow and then followed a quasi-periodic route to chaos. When the buoyant potential of the lower cell was successively increased, the flow transitioned from steady to mono-periodic flow, and then followed an intermittent route to chaos, indicating a Type I intermittency. In both sets of experiments, the very first bifurcations from steady bi-cellular flows to mono-periodic flows were subcritical and exhibited hysteresis. All of the flow behaviors in the periodic, quasi-periodic, quasi-chaotic, and chaotic flow regimes were experimentally observed to be 3D asymmetric. Fundamental frequencies, observed in the periodic regime for experiments with increasing buoyant potential of the upper cell, were scaled with the Brunt – Väisälä frequency. These non-dimensional frequencies showed relative invariance with Rayleigh number, potentially indicating a relation to the Rayleigh-Bernard instability mechanism.

3D numerical simulations were performed corresponding to the same experimental boundary conditions that were imposed. The 3D CFD model was able to predict asymmetric mono-periodic flows like those observed in the experiments, and the model predictions showed reasonable agreement with the trends observed in the periodic flow regime. At low Rayleigh numbers, 3D simulations revealed eight azimuthally oriented (radially directed) convection cells in the upper and lower portions of the cavity. The convection cells moved back and forth about the axis of the annulus, causing the 3D asymmetric oscillatory flows. The primary instability mechanism for these oscillating structures was identified as the Rayleigh-Bernard instability, triggered by unstably stratified fluid regions in the upper and lower cavity sections. Flow bifurcations were predicted, in which the number of convection cells were sequentially reduced from eight to six to two with increasing Rayleigh number.

The 3D CFD model was unable to predict transitions to quasi-periodic and chaotic flows. One possible cause for the 3D model's inability to predict chaotic flows could be that in order to fully capture the flow-dynamics of chaotic flows observed at higher Rayleigh numbers, a much finer grid than the one used in the present study is required. The use of a more refined grid than the one used could not be possible due to computational resource constraints. In future work on this problem, a DNS study using a spectral scheme could capture the chaotic flow dynamics at a much coarser grid. On the experimental side, Particle image velocimetry studies (PIV) might provide new insights on the interactions of the multiple convection cells inside the annular cavity, which are responsible for the 3D asymmetric flows.

12.2 Experimental and Numerical Work for Rectangular Cavity with Non-Isothermal Walls

The stability of (base) bi-cellular natural convection of air in a long, tall rectangular cavity of aspect ratio A = 10 was studied experimentally. When the buoyant potential of the bi-cellular base flow was increased, the flow transitioned first from steady to 2D mono-periodic flow via a Hopf bifurcation. With further increases in the buoyant potential (Rayleigh number), first, a transition from 2D mono-periodic flow to 3D mono-periodic flow occurred, followed directly by a transition to chaotic flow.

The 2D CFD model successfully predicted transition from steady to 2D mono-periodic flow, as observed in experiments. The steady flow was comprised of two counter-rotating cells. With successive increases in Rayleigh number, steady bi-cellular flow transitioned first to steady tri-cellular flow and then to 2D oscillatory (mono-periodic) flow, due to interactions between convection cells along their interfaces. The 2D CFD model was not able to predict chaotic flows.

The 3D CFD model was able to predict steady flow, 3D periodic and chaotic flows, like those observed in experiments. At low Rayleigh numbers, the 3D CFD model correctly predicted steady 2D flow comprised of two cells, as observed experimentally. As the Rayleigh number was increased, steady horizontal cells developed only in the central portion of the cavity. With further increases in Rayleigh number, additional horizontal cells appeared near the cavity ends and began to move back and forth towards the cavity center, causing periodic fluctuations in temperature and velocity fields. At even higher Rayleigh numbers, the motion of the cells became random, leading to 3D chaotic flow predictions. The primary instability modes identified by the 2D and 3D CFD models were substantially different, and it therefore seems likely that the 2D and 3D periodic flows

that were experimentally observed in the rectangular cavity arise from these two distinct instability mechanisms.

When comparing the 2D and 3D CFD model predictions with the experimental observations, it is evident that the 3D CFD model results are much more in agreement with the experimental observations than the 2D CFD model results. The frequencies of oscillations and the Rayleigh number corresponding to the transition from steady to 2D periodic flow predicted by the 2D CFD model were significantly higher than those observed in the experiments. On the other hand, the critical Rayleigh numbers corresponding to flow transitions and oscillation amplitudes predicted by the 3D CFD model agreed with experimental observations. Thus, the 3D CFD model could capture the flow dynamics observed in the experiments much more accurately than the 2D CFD model. This comparison between the predictive capabilities of the 2D and 3D CFD models also highlights the fact that while the 2D assumption proves useful for getting a general sense of fluid flow within the cavity, it should be used with caution for predicting unsteady flows and bifurcations, especially at higher Rayleigh numbers.

13 BIBILIOGRAPHY

[1] Reeve, Hayden Matane. "Effect of natural convection heat transfer during polymer optical fiber drawing." (2003), PhD thesis, University of Washington.

[2] Reeve, Hayden M., and Ann M. Mescher. "Effect of unsteady natural convection on the diameter of drawn polymer optical fiber." Optics express 11, no. 15 (2003): 1770-1779.

[3] Forest, M. Gregory, and Hong Zhou. "Unsteady analyses of thermal glass fibre drawing processes." European Journal of Applied Mathematics 12, no. 4 (2001): 479-496.

[4] Papamichael, H., C. Pellon, and I. N. Miaoulis. "Air flow patterns in the optical fibre drawing furnace." Glass technology38, no. 1 (1997): 22-29.

[5] Law, Susan H., Geoffrey W. Barton, and Thanh N. Phan. "The causes and nature of diameter variations along optical fiber." In Micro-and Nanotechnology: Materials, Processes, Packaging, and Systems II, vol. 5650, pp. 23-34. International Society for Optics and Photonics, 2005.

[6] Reeve, Hayden M., Ann M. Mescher, and Ashley F. Emery. "Investigation of steady-state drawing force and heat transfer in polymer optical fiber manufacturing." Journal of heat transfer 126, no. 2 (2004): 236-243.

[7] Eckert, E. R. G., and Walter O. Carlson. "Natural convection in an air layer enclosed between two vertical plates with different temperatures." International Journal of Heat and Mass Transfer 2, no. 1-2 (1961): 106-120.

[8] Elder, J. W. "Laminar free convection in a vertical slot." Journal of Fluid Mechanics 23, no. 1 (1965): 77-98.

[9] Vest, Charles M., and Vedat S. Arpaci. "Stability of natural convection in a vertical slot." Journal of Fluid Mechanics 36, no. 1 (1969): 1-15.

[10] Korpela, Seppo A. "A study on the effect of Prandtl number on the stability of the conduction regime of natural convection in an inclined slot." International Journal of Heat and Mass Transfer 17, no. 2 (1974): 215-222.

[11] ElSherbiny, Samy Morsy, G. D. Raithby, and K. G. T. Hollands. "Heat transfer by natural convection across vertical and inclined air layers." Journal of Heat Transfer 104, no. 1 (1982): 96-102.

[12] Simpkins, P. G., and J. E. Godreau. "Onset of periodic convection in a vertical slot." Physics of Fluids A: Fluid Dynamics 1, no. 9 (1989): 1479-1483.

[13] Shewen, E., K. G. T. Hollands, and G. D. Raithby. "Heat transfer by natural convection across a vertical air cavity of large aspect ratio." Journal of Heat Transfer 118, no. 4 (1996): 993-995.

[14] Lee, Yee, and Seppo A. Korpela. "Multicellular natural convection in a vertical slot." Journal of Fluid Mechanics 126 (1983): 91-121.

[15] Chait, Arnon, and Seppo A. Korpela. "The secondary flow and its stability for natural convection in a tall vertical enclosure." Journal of Fluid Mechanics 200 (1989): 189-216.

[16] Le Quéré, P. "A note on multiple and unsteady solutions in two-dimensional convection in a tall cavity." Journal of Heat Transfer 112, no. 4 (1990): 965-974.

[17] Wakitani, S. "Development of multicellular solutions in natural convection in an air-filled vertical cavity." Journal of heat transfer 119, no. 1 (1997): 97-101.

[18] Wakitani, Shunichi. "Flow patterns of natural convection in an air-filled vertical cavity." Physics of fluids 10, no. 8 (1998): 1924-1928.

[19] Zhao, Yie, W. P. Goss, and D. Curcija. Prediction of the multicellular flow regime of natural convection in fenestration glazing cavities. No. CONF-9702141--. American Society of Heating, Refrigerating and Air-Conditioning Engineers, Inc., Atlanta, GA (United States), 1997. ISSN 0001-2505

[20] Wright, John L., and Harry F. Sullivan. "A two-dimensional numerical model for natural convection in a vertical, rectangular window cavity." (1994).

[21] Batchelor, G. K. "Heat transfer by free convection across a closed cavity between vertical boundaries at different temperatures." Quarterly of Applied Mathematics 12, no. 3 (1954): 209-233.

[22] Choi, Inn G., and Seppo A. Korpela. "Stability of the conduction regime of natural convection in a tall vertical annulus." Journal of Fluid Mechanics 99, no. 4 (1980): 725-738.

[23] Bergholz, R. F. "Instability of steady natural convection in a vertical fluid layer." Journal of fluid Mechanics 84, no. 4 (1978): 743-768.

[24] Mizushima, Jiro, and Hiroki Tanaka. "Transitions of natural convection in a vertical fluid layer." Physics of Fluids 14, no. 4 (2002): L21-L24.

[25] Mizushima, Jiro, and Hiroki Tanaka. "Transition routes of natural convection in a vertical fluid layer." Journal of the Physical Society of Japan 71, no. 12 (2002): 2898-2906.

[26] Davis, G. De Vahl, and R. W. Thomas. "Natural convection between concentric vertical cylinders." The Physics of Fluids12, no. 12 (1969): II-198.

[27] Thomas, R. W., and Graham de Vahl Davis. NATURAL CONVECTION IN ANNULAR AND RECTANGULAR CAVITIES. A NUMERICAL STUDY. Univ. of New South Wales, Kensington, Australia, 1970.

[28] Korpela, Seppo A., Doğan Gözüm, and Chandrakant B. Baxi. "On the stability of the conduction regime of natural convection in a vertical slot." International Journal of Heat and Mass Transfer 16, no. 9 (1973): 1683-1690.

[29] Lee, Y., S. A. Korpela, and R. N. Horne. "Structure of multi-cellular natural convection in a tall vertical annulus." In Proc. 7th International Heat Transfer Conference, U. Grigul et al., eds., Hemisphere, Washington, DC, vol. 2, pp. 221-226. 1982.

[30] Le Quéré, P., and J. Pécheux. "Numerical simulations of multiple flow transitions in axisymmetric annulus convection." Journal of Fluid Mechanics 206 (1989): 517-544.

[31] Pécheux, J., P. Le Quéré, and F. Abcha. "Curvature effects on axisymmetric instability of conduction regime in a tall air- filled annulus." Physics of Fluids 6, no. 10 (1994): 3247-3255.

[32] Weng, Ling-Chia, and Hsin-Sen Chu. "Combined natural convection and radiation in a vertical annulusNatürliche Konvektion und Wärmestrahlung in einem vertikalen Ringkanal." Heat and mass transfer 31, no. 6 (1996): 371-379.

[33] McFadden, G. B., S. R. Coriell, R. F. Boisvert, and M. E. Glicksman. "Asymmetric instabilities in buoyancy-driven flow in a tall vertical annulus." The Physics of fluids 27, no. 6 (1984): 1359-1361.

[34] Prud'homme, Michel, and Patrick Le Quéré. "Stability of stratified natural convection in a tall vertical annular cavity." Physics of fluids 19, no. 9 (2007): 094106.

[35] Weidman, P. D., and G. Mehrdadtehranfar. "Instability of natural convection in a tall vertical annulus." The Physics of fluids 28, no. 3 (1985): 776-787.

[36] Fang, Q. T., M. E. Glicksman, S. R. Coriell, G. B. McFadden, and R. F. Boisvert. "Convective influence on the stability of a cylindrical solid–liquid interface." Journal of Fluid Mechanics151 (1985): 121-140.

[37] Lepiller, Valérie, Arnaud Prigent, Fabien Dumouchel, and Innocent Mutabazi. "Transition to turbulence in a tall annulus submitted to a radial temperature gradient." Physics of Fluids19, no. 5 (2007): 054101.

[38] Gray, Donald D., and Aldo Giorgini. "The validity of the Boussinesq approximation for liquids and gases." International Journal of Heat and Mass Transfer 19, no. 5 (1976): 545-551.

[39] Thangam, S., and C. F. Chen. "Stability analysis on the convection of a variable viscosity fluid in an infinite vertical slot." The Physics of fluids 29, no. 5 (1986): 1367-1372.

[40] Suslov, Sergey A., and Samuel Paolucci. "Stability of natural convection flow in a tall vertical enclosure under non-Boussinesq conditions." International Journal of Heat and Mass Transfer 38, no. 12 (1995): 2143-2157.

[41] Chenoweth, D. R., and S. Paolucci. "Natural convection in an enclosed vertical air layer with large horizontal temperature differences." Journal of Fluid Mechanics 169 (1986): 173-210.

[42] Darbandi, M., and S. F. Hosseinizadeh. "Numerical study of natural convection in vertical enclosures using a novel non-Boussinesq algorithm." Numerical Heat Transfer, Part A: Applications 52, no. 9 (2007): 849-873.

[43] Le Quéré, P., R. Masson, and P. Perrot. "A Chebyshev collocation algorithm for 2D non-Boussinesq convection." Journal of computational physics 103, no. 2 (1992): 320-335.

[44] Wright, John L., H. Jin, K. G. T. Hollands, and David Naylor. "Flow visualization of natural convection in a tall, air-filled vertical cavity." International Journal of Heat and Mass Transfer 49, no. 5-6 (2006): 889-904.

[45] Lartigue, Bérengère, Sylvie Lorente, and Bernard Bourret. "Multicellular natural convection in a high aspect ratio cavity: experimental and numerical results." International journal of heat and mass transfer 43, no. 17 (2000): 3157-3170.

[46] Sheriff, N. "experimental investigation of natural convection in single and multiple vertical annuli with high pressure carbon dioxide." In pp 132-8 of Proceedings of the Third International Heat Transfer Conference,

Chicago, Illinois, August 7--12, 1966. Volume II. New York, American Institute of Chemical Engineers, 1966. United Kingdom Atomic Energy Authority, Risley, Eng., 1967.

[47] Keyhani, M., F. A. Kulacki, and R. N. Christensen. "Free convection in a vertical annulus with constant heat flux on the inner wall." Journal of heat transfer 105, no. 3 (1983): 454-459.

[48] Khan, J. A., and R. Kumar. "Natural convection in vertical annuli: a numerical study for constant heat flux on the inner wall." Journal of heat transfer 111, no. 4 (1989): 909-915. DOI: 10.1115/1.3250805

[49] Rogers, B. B., and L. S. Yao. "Natural convection in a heated annulus." International journal of heat and mass transfer 36, no. 1 (1993): 35-47.

[50] Reeve, Hayden M., Ann M. Mescher, and Ashley F. Emery. "Unsteady natural convection of air in a tall axisymmetric, non-isothermal annulus." Numerical Heat Transfer, Part A: Applications 45, no. 7 (2004): 625-648.

[51] Dillon, Heather, Ashley Emery, and Ann Mescher. "Analysis of chaotic natural convection in a tall rectangular cavity with non-isothermal walls." Frontiers in Heat and Mass Transfer (FHMT) 4.2 (2013).

[52] Percival, Donald B., and Andrew T. Walden. Spectral analysis for physical applications. Cambridge university press, (1993).

[53] Kutz. J. N. Data-Driven Modeling & Scientific Computation: Methods for Complex Systems and Big Data. Oxford University Press, 1st edition, (2013).

[54] CD-adapco, S. "STAR CCM+ User Guide Version 12.04." CD-Adapco: New York, NY, USA (2017).

[55] Turkel, Eli. "Preconditioned methods for solving the incompressible and low speed compressible equations." Journal of computational physics 72, no. 2 (1987): 277-298.

[56] Turns, Stephen, and David Kraige. Properties Tables Booklet for Thermal Fluids Engineering. Vol. 10. Cambridge University Press, 2007.

[57] Le Quéré, Patrick, Catherine Weisman, Henri Paillère, Jan Vierendeels, Erik Dick, Roland Becker, Malte Braack, and James Locke. "Modelling of natural convection flows with large temperature differences: a benchmark problem for low Mach number solvers. Part 1. Reference solutions." ESAIM: Mathematical Modelling and Numerical Analysis 39, no. 3 (2005): 609-616.

[58] Paillère, Henri, Patrick Le Quéré, Catherine Weisman, Jan Vierendeels, Erik Dick, Malte Braack, Frédéric Dabbene et al. "Modelling of natural convection flows with large temperature differences: a benchmark problem for low Mach number solvers. Part 2. Contributions to the June 2004 conference." ESAIM: Mathematical Modelling and Numerical Analysis 39, no. 3 (2005): 617-621.

[59] Berg, Pierre., Pomeau, Yves. and Vidal, Christian. Order within chaos: Towards a deterministic approach to turbulence. Wiley, (1986).

[60] Strogatz, S. H. Nonlinear Dynamics and Chaos: with Applications to Physics, Biology, and Chemistry, and Engineering. Westview Press, 2nd edition, Boulder (2015)

[61] Le Quéré, P., and F. Penot. "Numerical and experimental investigation of the transition to unsteady natural convection of air in a vertical differentially heated cavity." ASME HTD 94 (1987): 75-82.

[62] Omega Engineering, Inc 2019a Technical reference—Thermocouples, Stamford, CT. Available online at https://www.omega.com/en-us/resources/thermocouples-response-time

[63] TS, NIST. "Thermocouple Database NIST Standard Reference Database 60, Version 2.0 (Web Version)." (90).

[64] MATLAB and Statistics Toolbox Release 2019a, The MathWorks, Inc., Natick, Massachusetts, United States.

[65] Lim, Kwang-Ok, Kwan-Soo Lee, and Tae-Ho Song. "Primary and secondary instabilities in a glass-melting surface." Numerical Heat Transfer: Part A: Applications 36, no. 3 (1999): 309-325.

[66] Zhang, Kun, Mo Yang, and Yuwen Zhang. "Numerical analysis of natural convection in a cylindrical envelope with an internal concentric cylinder with slots." Numerical Heat Transfer, Part A: Applications 59, no. 10 (2011): 739-754.

[67] Priestley, Maurice Bertram. Spectral analysis and time series. Vol. 1. London: Academic press, (1981).

[68] Sankar, M., Junpyo Park, and Younghae Do. "Natural convection in a vertical annuli with discrete heat sources." Numerical Heat Transfer, Part A: Applications 59, no. 8 (2011): 594-615.

[69] Roache, Patrick J. "Quantification of uncertainty in computational fluid dynamics." Annual review of fluid Mechanics 29, no. 1 (1997): 123-160.

[70] Kishor, Vimal, Singh, Suneet and Srivastava, Atul. "Investigation of Convective Heat Transfer Phenomena in Differentially-heated Vertical Closed Cavity: Whole Field Experiments and Numerical Simulations." Experimental Thermal and Fluid Science Vol. 99 (2018): pp. 71-84.

[71] Paolucci, Samuel, and Chenoweth, Donald R. "Transition to Chaos in a Differentially Heated Vertical Cavity." Journal of Fluid Mechanics Vol. 201 (1989): pp. 379-410.

[72] Henkes, R. A. W. M., and Hoogendoorn, C. J. "On the Stability of the Natural Convection Flow in a Square Cavity Heated from the Side." Applied Scientific Research Vol. 47 No. 3 (1990): pp. 195-220.

[73] Suslov, S.A. and Paolucci, S., 2004, "Stability of non-Boussinesq convection via the complex Ginzburg–Landau model," Fluid dynamics research, 35(3), pp.159-203.

[74] Suslov, S.A. and Paolucci, S., 1997, "Nonlinear analysis of convection flow in a tall vertical enclosure under non-Boussinesq conditions," Journal of Fluid Mechanics, 344, pp.1-41.

[75] Simpkins, P., 1989, "Transition to periodic convective states in an air-filled slot," Bull. Am. Phys. Soc., 34, p.2271.

[76] Bergman, T.L. and Incropera, F.P., 2011, Fundamentals of Heat and Mass Transfer, John Wiley & Sons.

[77] Paillere, H., C. Viozat, A. Kumbaro, and I. Toumi. "Comparison of low Mach number models for natural convection problems." Heat and mass transfer 36, no. 6 (2000): 567-573.

[78] Keshtiban, I. J., Belblidia, F., and Webster, M. F, "Compressible Flow Solvers for Low Mach Number Flows—A Review," Institute of Non-Newtonian Fluid Mechanics, University of Wales, Swansea, Wales, U.K., Report No.: CSR 2-2004. Available online at: http://www.cs.swan.ac.uk/reports/yr2004/CSR2-2004.pdf

[79] Guillard, Hervé, and Cécile Viozat. "On the behaviour of upwind schemes in the low Mach number limit." Computers & fluids 28, no. 1 (1999): 63-86.

[80] Weiss, Jonathan M., and Wayne A. Smith. "Preconditioning applied to variable and constant density flows." AIAA journal33, no. 11 (1995): 2050-2057.

[81] Tomboulides, Ananias G., and Steven A. Orzag. "A quasi-two-dimensional benchmark problem for low Mach number compressible codes." Journal of Computational Physics 146, no. 2 (1998): 691-706.

[82] Paolucci, S. "On the Filtering of Sound from the Navier-Stokes Equations, Sandia National Labs." In Technical Report. Sandia National Laboratories, 1982.

[83] Harlow, Francis H., and Anthony A. Amsden. "Numerical calculation of almost incompressible flow." Journal of Computational Physics 3, no. 1 (1968): 80-93.

[84] Clayborn lab, Technical reference. Available online at http://www.claybornlab.com/heat_tape_overview.html

[85] Drazin, Philip G., and William Hill Reid. Hydrodynamic stability. Cambridge university press, 2004.

[86] Ivey, G. N. "Experiments on transient natural convection in a cavity." Journal of Fluid Mechanics 144 (1984): 389-401.

[87] Nachtsheim, Philip R. "Stability of free-convection boundary-layer flows." (1963).

[88] Haaland, S. E., and E. M. Sparrow. "Wave instability of natural convection on inclined surfaces accounting for nonparallelism of the basic flow." (1973): 405-407.

[89] Gill, A. E., and A. Davey. "Instabilities of a buoyancy-driven system." Journal of Fluid Mechanics 35, no. 4 (1969): 775-798.

[90] Stork, K., and U. Müller. "Convection in boxes: experiments." Journal of Fluid Mechanics 54, no. 4 (1972): 599-611.

[91] Stork, K., and U. Müller. "Convection in boxes: an experimental investigation in vertical cylinders and annuli." Journal of Fluid Mechanics 71, no. 2 (1975): 231-240.

[92] Celik, I. B. "Journal of Fluids Engineering Editorial Policy Statement on the Control of Numerical Accuracy." (2000).

[93] Rubinov, A., V. Erenburg, A. Yu Gelfgat, E. Kit, P. Z. Bar-Yoseph, and A. Solan. "Three-dimensional instabilities of natural convection flow in a vertical cylinder with partially heated sidewall." J. Heat Transfer 126, no. 4 (2004): 586-599

[94] Selver, R., Y. Kamotani, and S. Ostrach. "Natural convection of a liquid metal in vertical circular cylinders heated locally from the side." (1998): 108-114.

[95] Ma, D. J., Daniel Henry, and H. Ben Hadid. "Three-dimensional numerical study of natural convection in vertical cylinders partially heated from the side." Physics of Fluids 17, no. 12 (2005): 124101.

[96] Neumann, G. "Three-dimensional numerical simulation of buoyancy-driven convection in vertical cylinders heated from below." Journal of Fluid Mechanics 214 (1990): 559-578.

[97] McMurtry, Patrick A., W-H. Jou, J. Riley, and R. W. Metcalfe. "Direct numerical simulations of a reacting mixing layer with chemical heat release." AIAA journal 24, no. 6 (1986): 962-970.

[98] McMurtry, P. A., James J. Riley, and R. W. Metcalfe. "Effects of heat release on the large-scale structure in turbulent mixing layers." Journal of Fluid Mechanics 199 (1989): 297-332.

Appendix A: Low Mach number compressible flow solver strategies

Natural convection flows under high temperature differences are compressible flows since the thermophysical properties vary significantly with temperature. There are two popular numerical methods approaches for solving the compressible natural convection flows at low Mach numbers. The first approach is using an elliptic solver in which the pressure term is treated implicitly in the momentum equation. The solution strategy of these type of solver is similar to the incompressible flow solvers and requires solution of an equation similar to the Poisson equation for pressure. These solvers can be pressure-based with pressure correction implemented for the scheme to work for compressible flows or they can be based on the asymptotic analysis of Navier-Stokes equations in the limit of low Mach number flows [77, 78, 97, 98]. The asymptotic methods usually involve splitting of the pressure into two parts – the thermodynamic pressure and dynamic pressure which results in a set of equations where the acoustic waves have been filtered out thereby making the compressible Navier-Stokes valid for low Mach numbers [77, 97, 98]. The second approach is using a hyperbolic solver like a compressible density-based solver and modifying it with a suitable preconditioning matrix to prevent the matrix from becoming ill conditioned at low Mach numbers and thereby making it accurate for solving compressible flows at low Mach numbers. [77, 79]

Two main families of solution techniques used by most commercial CFD codes are the pressure-based and density-based methods. Traditionally, pressure-based methods were developed to solve incompressible, low Mach number flows while the density-based methods were developed to solve highly compressible, high Mach number (supersonic, transonic) flows. Over the years, both these families of methods have introduced various types of modifications in order to solve

flows which are low Mach number but also compressible due to temperature dependent density variations.

A.1 Density-based solution strategies for low Mach number compressible flows

Traditional density-based implicit compressible solvers face accuracy and convergence issues due to the system of equations becoming ill-conditioned at low Mach numbers. To remedy this, two classes of techniques are usually employed, namely, the preconditioning methods and asymptotic-approximation methods. In the preconditioning methods approach, the solution matrix in the compressible density-based solver is modified with a suitable preconditioning matrix to prevent it from becoming ill conditioned at low Mach numbers [55,80]. The asymptotic method approach is based on the use of an asymptotic form of the compressible equations where, the pressure is split into two parts - the thermodynamic pressure and hydrodynamic pressure. The thermodynamic pressure appears only in the energy equation and equation of state whereas the dynamic pressure appears in the momentum equation. This pressure-splitting leads a form of equations where the acoustic waves have been filtered out and as a result, the system stiffness is reduced [81, 82, 97, 98]. A comparison between these two types of methods can be found in [77].

A.2. Pressure-based solution strategies for low Mach number compressible flows

Similar to density-based methods, pressure-based methods have been suitably modified to be used for compressible low Mach number flows [83]. A number of different strategies have been implemented to modify pressure-based methods like projection methods and pressure correction method for solving low-speed compressible flows. A review of the different pressure-based solution strategies available for solving low Mach number compressible flow is available at [78].

Appendix B : Uncertainty in furnace thermocouple positions

During the course of the annular cavity experiments described in Chapters 6,7 an estimation of the location of the 9 furnace thermocouples installed on custom made Thermcraft Inc. Marshall 1100 series furnace was carried out to quantify the uncertainty in the position of the thermocouple bead. It was discovered during the course of leveling the experimental system, that the outer casing of the furnace is tilted at an angle of 0.5° with respect to the axis of the ceramic furnace. Grooves extending from the outer casing up to the inner surface of the furnace were made in the furnace by the manufacturer to install thermocouples. Measurements of the insertion length of the thermocouples, inner and outer dimensions of the furnace wall, and tilt angle of the casing gave an estimate for the location of each of the thermocouple bead. Table D.1 shows the dimensions of the furnace, casing and nichrome power wire. Table D.2 shows the calculations for the insertion length and location of the thermocouple bead. Figure D.1 shows the locations of the 9 thermocouple beads along the cross-section of the furnace. Figure D.2 shows the uncertainty in the location for each thermocouple. Thermocouples 200 and 201 were found to be more than 7 mm away from the inner surface of the furnace wall. This resulted in a significant error in the temperature measurement at these two locations. Therefore, for the purposes of the determination of the furnace wall temperature profile the temperature measurements from those two sensors were not included in the polynomial fit.

Table B.1: Critical dimensions for the Thermcraft Inc. Marshall 1100 series furnace

Inner diameter of furnace	63.5 mm
Outer diameter of furnace	100 mm
Nichrome wire diameter	2.15 mm
Outer diameter of Casing	257 mm

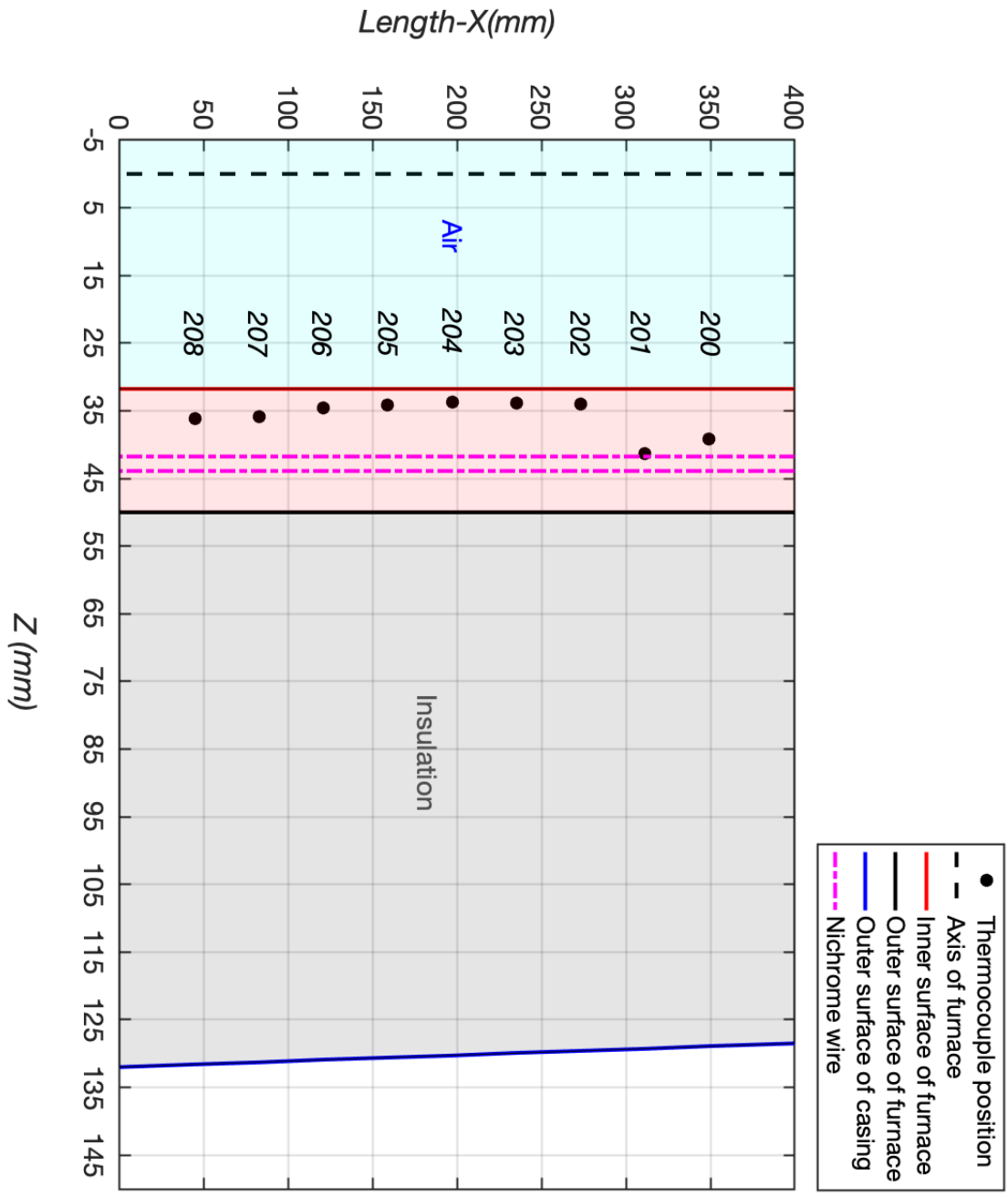

Fig B.1: Locations of the 9 thermocouple beads along the cross-section of the Thermcraft Inc. Marshall 1100 series furnace

Table B.2: Calulations for thermocouple insertion length and error in position for each of the 9 thermocouples installed on the inner surface of Thermcraft Inc. Marshall 1100 series furnace

Thermocouple	Corrected insertion length of thermocouple (mm)	Z (mm)	Distance between reference to thermocouple tip (mm)	Outside of Casing (mm)	Error in position of thermocouple (mm)
200	89.26	349.21	39.24	128.94	7.49
201	87.19	311.02	41.31	129.28	9.56
202	94.44	273.23	34.06	129.61	2.31
203	94.69	235.04	33.81	129.94	2.06
204	94.83	196.85	33.67	130.27	1.92
205	94.39	158.66	34.11	130.61	2.36
206	93.87	120.47	34.63	130.94	2.88
207	92.60	82.68	35.90	131.27	4.15
208	92.41	44.49	36.09	131.60	4.34

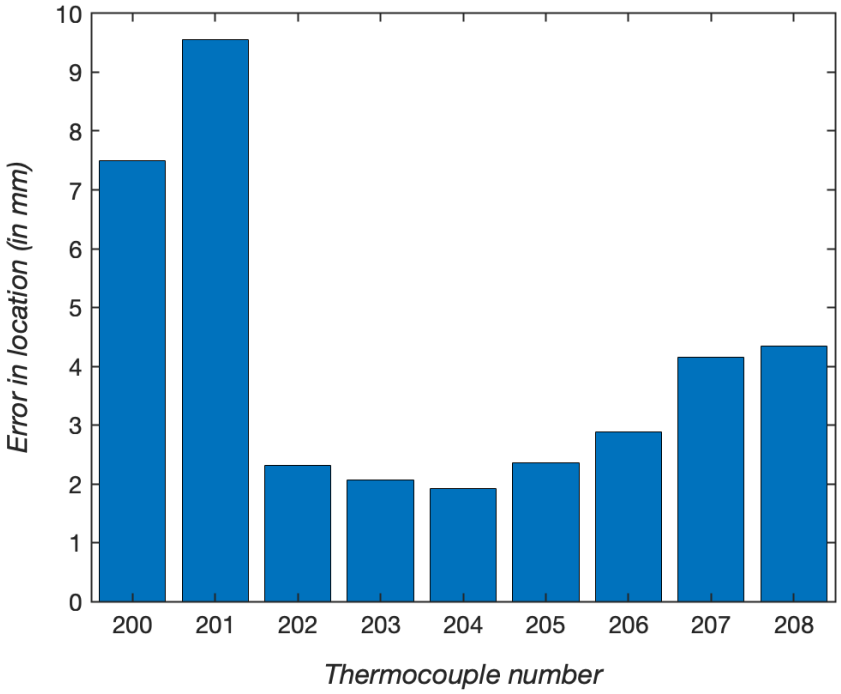

Fig B.2: Uncertainty in the location of each of the 9 thermocouples installed on the inner surface of Thermcraft Inc. Marshall 1100 series furnace

Appendix C: Grid refinement study for 2D CFD model for natural convection in rectangular cavity with non-isothermal walls.

A grid refinement study was performed for the 2D CFD model according to methods of Roache[69,92]. Grid refinement studies conducted for the 2D periodic solution found at Ra = 2.03 x 10^7 are presented here. Solutions were calculated at three different grids and two time-steps.

Table C.1: Grids and time-steps used for the grid convergence study of 2D CFD model of rectangular cavity with non-isothermal walls.

Grid	Time step (sec)	Number of cells in X	Number of cells in Z	h – Cell size (m)	Grid refinement ratio
1	0.005	200	2000	0.00015	2
1	0.0025	200	2000	0.00015	1
2	0.005	100	1000	0.0003	2
3	0.005	50	500	0.0006	-

Table C.2 Amplitude and time-period of oscillations for periodic solutions obtained on three grids.

Location of point in cavity	Amplitude of temperature oscillations (ºC)			%GCI		
	Grid 1	Grid 2	Grid 3	Grid 1 (200x2000)	Grid 2 (100x1000)	Grid 3 (50x500)
z = 0.02,x = 0.015	0.089	0.088	0.088	0.46	0.13	0.46
z = 0.05,x = 0.015	0.297	0.295	0.291	0.8	1.65	3.37
z = 0.10,x = 0.015	0.162	0.165	0.165	0.61	0.13	0.60
z = 0.12,x = 0.015	1.197	1.189	1.170	0.68	1.54	3.48
z = 0.15,x = 0.015	0.524	0.528	0.537	0.94	1.95	4.07
z = 0.18,x = 0.015	0.154	0.156	0.160	1.21	2.63	5.80
z = 0.20,x = 0.015	0.012	0.012	0.012	0.22	0.02	0.22
z = 0.25,x = 0.015	0.004	0.004	0.004	0.07	0.03	0.07
Time-period of oscillations (sec)	Grid 1	Grid 2	Grid 3	Grid 1 (200x2000)	Grid 2 (100x1000)	Grid 3 (50x500)
	5.695	5.693	5.683	0.01	0.06	0.27

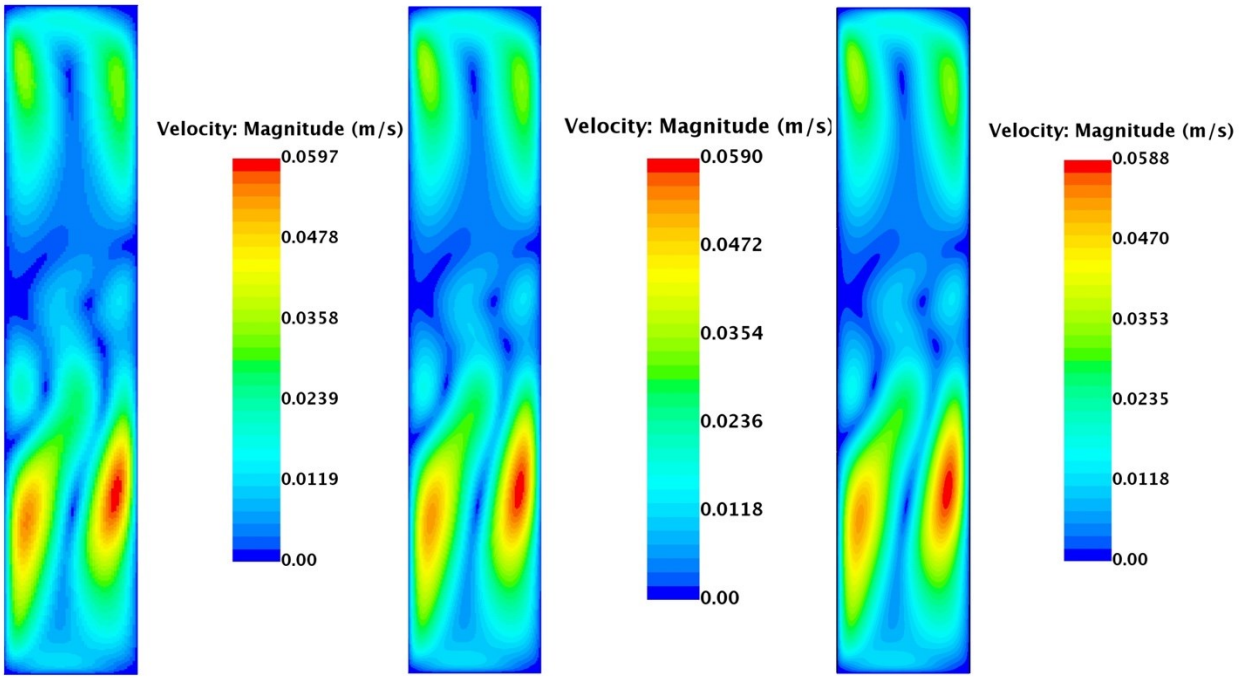

(a) (b) (c)

Figure C.1: Velocity field for periodic solution at t =150 seconds obtained on the three different grids (a) 50 x 500 (b) 100 x 1000 (c) 200 x 2000

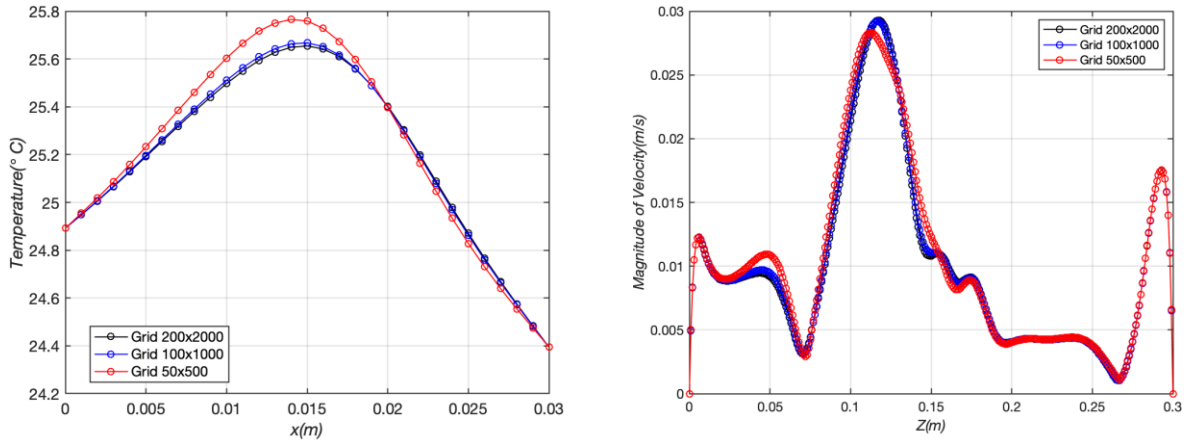

(a) (b)

Figure C.2: (a) Temperature along the plane z = 0.15m for periodic solution at t =150 seconds obtained on the three different grids.
(b) Magnitude of velocity along the plane x = 0.015m for periodic solution at t =150 seconds obtained on the three different grids.

To quantify the temporal error, simulations on the 2000 x 200 grid were done at two different time-steps: 0.0025s and 0.005s.

Table C.2: Amplitude of oscillations and time-period of oscillations calculated for the periodic solutions obtained on 200x2000 grid at two different time-steps.

Location of point in cavity	Amplitude of temperature oscillations (ºC)		%GCI	
	Timestep#1 = 0.0025s	Timestep#2 = 0.005s	Timestep#1 = 0.0025s	Timestep#2 = 0.005s
z = 0.02,x = 0.015	0.089	0.088	0.42	1.68
z = 0.05,x = 0.015	0.297	0.295	0.30	1.20
z = 0.10,x = 0.015	0.163	0.165	0.47	1.88
z = 0.12,x = 0.015	1.197	1.189	0.30	1.19
z = 0.15,x = 0.015	0.524	0.528	0.33	1.33
z = 0.18,x = 0.015	0.154	0.156	0.47	1.88
z = 0.20,x = 0.015	0.012	0.012	0.60	2.42
z = 0.25,x = 0.015	0.004	0.004	0.05	0.19
Time-period of oscillations (sec)	Timestep#1 = 0.0025s	Timestep#2 = 0.005s	Timestep#1 = 0.0025s	Timestep#2 = 0.005s
	5.696	5.693	0.02	0.09

Based on the results of the grid refinement study the grid with 2000 x 200 elements was selected and a time step size of 0.005s was selected. The maximum spatial and temporal errors associated with calculations of oscillation amplitude on this grid/time-step are 1.2% and 2.4% and the errors associated with oscillation time-period calculations are 0.01% and 0.1% respectively.